RAPPORTO TECNICO

Report di dettaglio sulla progettazione, preparazione e caratterizzazione analitica e funzionale delle biomolecole progettate e testate per il riconoscimento di ioni Hg^{2+} in ambienti acquosi marini o similari.

Le attività svolte sono:

Attività A1.1 Descrizione dettagliata delle caratteristiche delle biomolecole selezionionate

L'attività prevista dal progetto riguarda lo studio e la selezione di biomolecole da applicare a sensori per la rivelazione di Hg^{2+} in ambienti marini o similari (soluzioni acquose).

Descrizione dell'attività

La progettazione di biomolecole per il riconoscimento di Hg^{2+} è stata realizzata a partire dallo studio dello stato dell'arte sugli attuali biosensori disponibili per tale applicazione. La letteratura recente è ricca di molecole di varia natura e complessità che legano selettivamente ioni Hg^{2+} in un ampio spettro di condizioni. Si riportano di seguito le referenze di lavori che descrivono alcune di tali molecole:

1 – Shunmugam R., Gabriel G. J., Smith C. E., Aamer K. A., and Tew G. N.: A Highly Selective Colorimetric Aqueous Sensor for Mercury, *Chem. Eur. J.*, 14 (2008), 3904 – 3907.

2 - Thirupathi P., Lee H.K.: A new peptidyl fluorescent chemosensors for the selective detection of mercury ions based on tetrapeptide, *Bioorganic & Medicinal Chemistry*, 21 (2013), 7964–7970.

Le molecole descritte in questi lavori sono particolarmente interessanti e potenzialmente utilizzabili in applicazioni di rivelazione dello ione metallico, perché mostrano una elevata selettività per ioni Hg^{2+} in ambienti acquosi accoppiata ad una elevata affinità.

Di particolare rilievo sono le molecole riportate nella referenza 2 in quanto posseggono proprietà ottiche facilmente modulabili sulla base del pH, degli equivalenti di ioni Hg^{2+} o di percentuali di solventi organici. Il gruppo fluorescente dansile modula e rende selettivo il riconoscimento dei cationi metallici mediante complessazione con il gruppo sulfonammidico. Il riconoscimento si traduce in variazioni delle proprietà spettroscopiche (fluorescenza ed assorbanza) del dansile. Tali variazioni posso essere sfruttate per la messa a punto di saggi analitici in cui è possibile seguire la risposta dei sensori mediante misure di fluorescenza ed assorbanza.

Inoltre, le molecole fin qui riportate sono facilmente accessibili dal punto di vista sintetico mediante approcci di sintesi in fase solida. Dal punto di vista sintetico e della caratterizzazione analitica, nonché delle proprietà spettroscopiche e potenzialmente della stabilità in soluzioni acquose, la molecola descritta nella referenza 3, Composto **I** (Figura 1), dansyl metionina (Dansyl-L-Met-NH_2), è tra le due quella con le maggiori potenzialità. Infatti è riportato che il composto **I** è in grado di legare selettivamente lo ione mercurio in acqua con un meccanismo "turn-on" (aumento di fluorescenza, vedere Figura 2a) mentre lega altrettanto selettivamente lo stesso ione in solventi organici o misti organico-acquoso (acqua-acetonitrile 1:1) con un meccanismo invertito di "turn-off" (spegnimento della fluorescenza, vedere Figura 2b). L'ipotesi di maggiore stabilità è basata sulla struttura della molecola, sulle ridotte dimensioni e sulla generale elevata stabilità di amino acidi in soluzioni acquose.

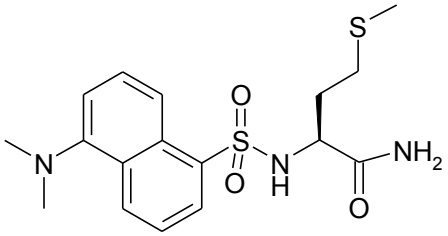

Figura. 1. Composto **I**: Dansyl-L-Met-NH_2.

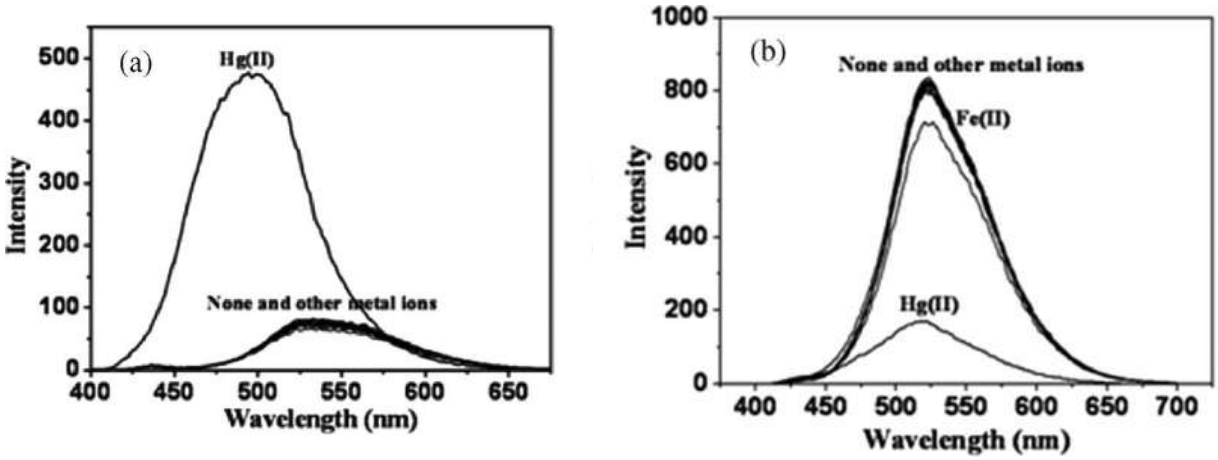

Figura 2a. Spetto di emissione in fluorescenza di I (λex = 380 nm) in tampone 10 mM HEPES pH 7.4, in presenza di ioni Hg2+ e di altri metalli, inclusi Hg^{2+}, Ca^{2+}, Cd^{2+}, Co^{2+}, Pb^{2+}, Ag+, Mg^{2+}, Cu^{2+}, Mn^{2+}, Ni^{2+}, Zn^{2+}, Na+, Al^{2+}, K^{2+}. **Figura 2b.** Spetto di emissione in fluorescenza di I (λex = 380 nm) in tampone acquoso in (acqua-acetonitrile 1:1) con 50% CH3CN, in presenza di ioni Hg^{2+} e di altri metalli, inclusi Hg^{2+}, Ca^{2+}, Cd^{2+}, Co^{2+}, Pb^{2+}, Ag+, Mg^{2+}, Cu^{2+}, Mn^{2+}, Ni^{2+}, Zn^{2+}, Na+, Al^{2+}, K^{2+}

La molecola di elezione su cui è stata sviluppata a progettazione di nuovi biosensori è stata quindi il Composto **I**. Derivati della dansyl metionina (Figura 3) differenti per lunghezza della catena laterale amminoacidica e tipo di sostituenti su *S*-terminale (zolfo terminale) sono stati proposti per valutare gli effetti

di tali modifiche sulle proprietà di complessazione di Hg^{2+}, sulla selettività di tale complessazione e sulle rispettive costanti di dissociazioni (K_d).

Nello specifico, i composti II e III sono analoghi della metionina da cui differiscono solo per lo stato di ossidazione dello zolfo in catena laterale. Il legame chimico dello zolfo nella metionina dà luogo a semireazioni di ossido-riduzione dando, nel primo stadio la metionina solfossido (Met(O), costituente il composto II) e, nel secondo stadio, metionina sulfone ($Met(O)_2$, costituente il composto III). Il composto IV è un derivato della cisteina, un amminoacido contenente zolfo in catena laterale che differisce dalla metionina per la lunghezza della catena laterale (solo una unità di $–CH_2$) e per la presenza del gruppo SH terminale libero. Il composto V è un derivato della omocisteina, un analogo della metionina da cui differisce solo per la presenza del gruppo SH terminale libero e non alchilato. Infine i composti VI e VII sono derivati della cisteina in cui è presente il gruppo acetamidometil (Acm) come gruppo protettore della funzione tiolica. Ai due composti sono associate le due configurazioni stereochimiche possibili: configurazione D per il composto VI e configurazione L per il composto VII.

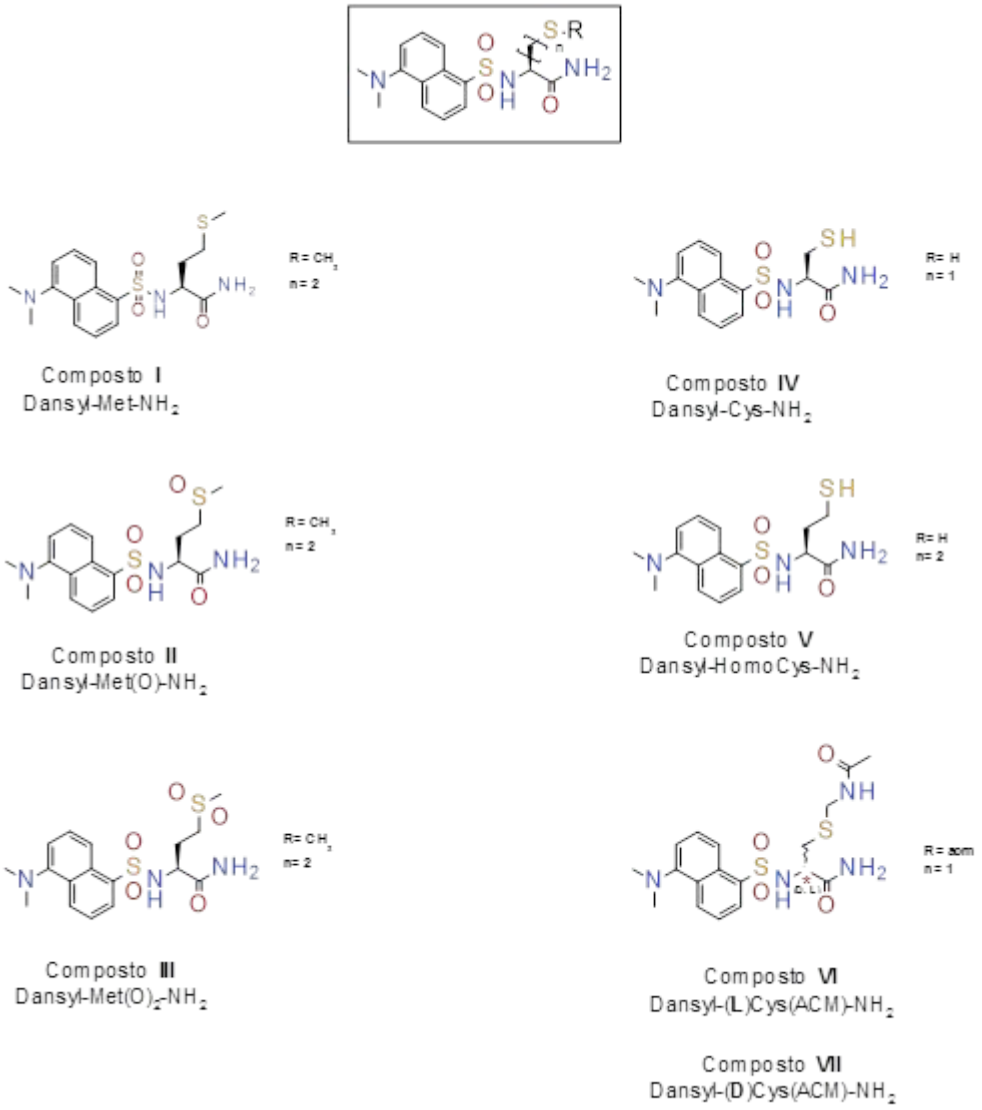

Figura 3. Lista di biomolecole proposte.

A corredo della progettazione delle biomolecole, sono stati anche valutati i possibili approcci tecnologici per l'impiego di tali molecole con sensori in fibra ottica. Le soluzioni tecnologiche individuate sono le seguenti (Figura 4):

a) Operatività diretta in soluzione

Tale approccio richiede la progettazione di un sensore in fibra ottica in grado di sfruttate le proprietà di binding selettivo e specifico delle molecole proposte con Hg^{2+} direttamente in soluzione. Il sensore in fibra ottica deve essere in grado di registrare variazioni negli spettri di assorbanza e/o emissione in fluorescenza in seguito alla complessazione con il catione metallico direttamente in soluzione (Figura 4).

b) Operatività mediata dalla funzionalizzazione del probe.

L'attuazione di tale modalità operativa necessita di uno step intermedio di immobilizzazione delle molecole proposte sul sensore in fibra ottica. Questo secondo approccio necessita della generazione di gruppi funzionali sulla superficie della fibra su cui ancorare i derivati fluorescenti sensibili allo ione Hg^{2+} (Figura 4)

La seconda soluzione tecnologica prevede l'inserimento nelle biomolecole di opportuni sostituenti che consentono di agganciare il probe alla superficie del sensore senza alterarne in maniera sostanziale le proprietà spettroscopiche. È necessario inoltre nello step di ancoraggio, l'inserimento di spaziatori molecolari (spacer) che permettono una elevata flessibilità del probe in soluzione ed in prossimità della superficie del sensore. Le problematiche di funzionalizzazione del probe fin ad ora esposte, legate all' impossibilità di rigenerare il probe funzionalizzato (probe usa e getta), limitano l'applicabilità di questi sensori in sistemi automatizzati tipo high throughput e richiedono di conseguenza anche costi maggiori.

L'operatività diretta in soluzione, invece, non prevede step intermedi di funzionalizzazione dei sensori in fibra, il sensore in fibra può essere applicato per misure di differenti spettri di assorbanza e fluorescenza e può essere integrato in sistemi di analisi in parallelo automatizzati. Sulla base di queste valutazioni, la soluzione tecnologica con operatività diretta in soluzione è stata prescelta per i successivi sviluppi del sensore.

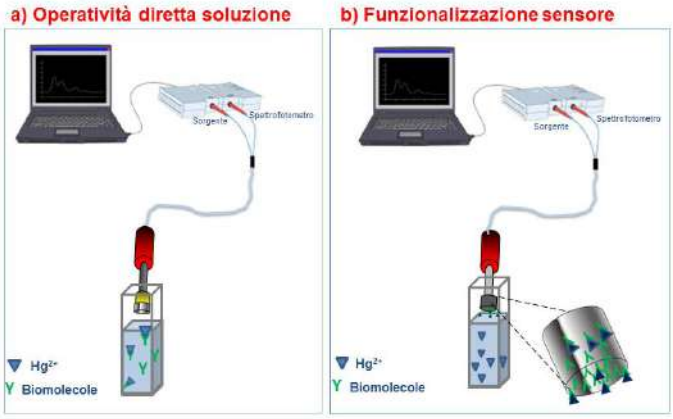

Figura 4: Schema dei due possibile approcci tecnologici: a) operatività diretta in soluzione; b) operatività mediata dalla funzionalizzazione del sensore.

Attività A1.2 Modalità di sintesi e purificazione delle biomolecole selezionate

L'attività prevista dal progetto riguarda la sintesi e la purificazione delle biomolecole selezionate nel corso dell'attività A1.1

<u>Descrizione dell'attività</u>

La metodica sintetica comune a tutti i derivati sintetizzati è stata messa a punto su fase solida, utilizzando una resina polistirenica di tipo Rink-ammide con grado di sostituzione di 0.77 mmol/g.

Il protocollo di sintesi, uguale per tutti i peptidi, è basato su cicli di accoppiamento composti dai seguenti moduli (Figura 5):

1. Deprotezione resina
2. Accoppiamento
3. Labelling con cloruro di dansile
4. Sblocco resina

Il modulo di deprotezione consiste di due trattamenti di 5 minuti con una soluzione al 20% e successivamente al 40% di Piperidina in dimetilformammide (DMF) .

Per il modulo di accoppiamento sono stati utilizzati 4 equivalenti di amminoacidi protetti con 9-fluorenylmethoxycarbonyl (Fmoc-AA), 3.8 equivalenti di 1-[Bis(dimethylamino)methylene]-1H-1,2,3-triazolo[4,5-b]pyridinium 3-oxid hexafluorophosphate (HATU) in DMF e 8 equivalenti di sim-collidina rispetto alla scala di sintesi. Il tempo di reazione per accoppiamento è stato di 60 minuti.

Per il modulo di labelling con cloruro di dansile sono stati utilizzati 2 equivalenti di Dansyl-Cl e 2 equivalenti di N,N-Diisopropylethylamine (DIPEA) con tempi di reazione di 12 ore .

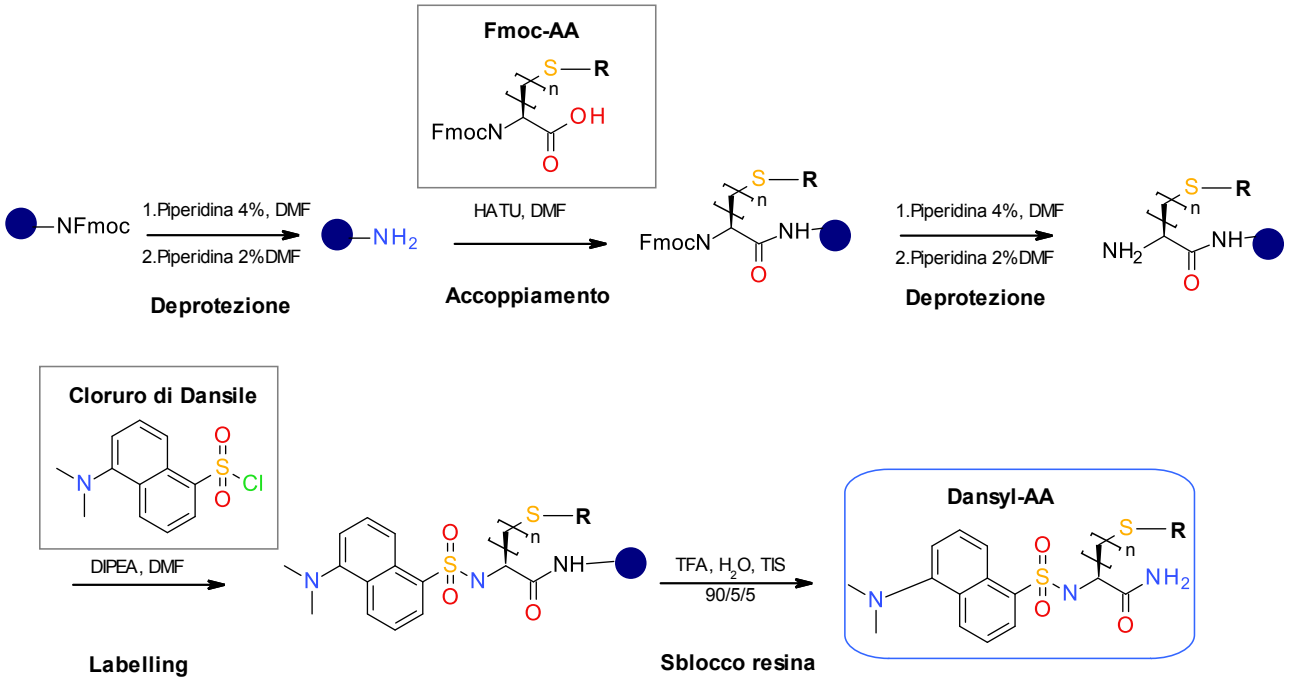

Figura 5: Schema sintetico per la preparazione dei dansyl derivati

Dopo ogni modulo sono stati effettuati quattro lavaggi con DMF per un minuto.

I peptidi sono stati staccati dalla resina, con contemporanea deprotezione delle catene laterali, trattando quest'ultima con una soluzione di acido trifluoroacetico (TFA)/ H_2O/tri-isoproprilsilano) nel rapporto 90/5/5

in volume per 4 h sotto agitazione a temperatura ambiente. La soluzione è stata poi filtrata, lavata con la minima quantità di TFA e liofilizzata.

Tutti i derivati sono stati caratterizzati analiticamente mediante LC-MS, UV, fluorimetria ed NMR. Le analisi LC-MS sono state eseguite con uno spettrometro Ion Trap (HCT-Ultra PTM discovery system, Bruker) accoppiato ad un sistema HPLC Waters Alliance Separation Module/ Detector 2998 PDA) equipaggiato con colonne a fase inversa (colonna Phenomenex OnxY C18). In figura 6 sono riportati gli spettri di massa che hanno confermato l'identità dei composti sintetizzati.

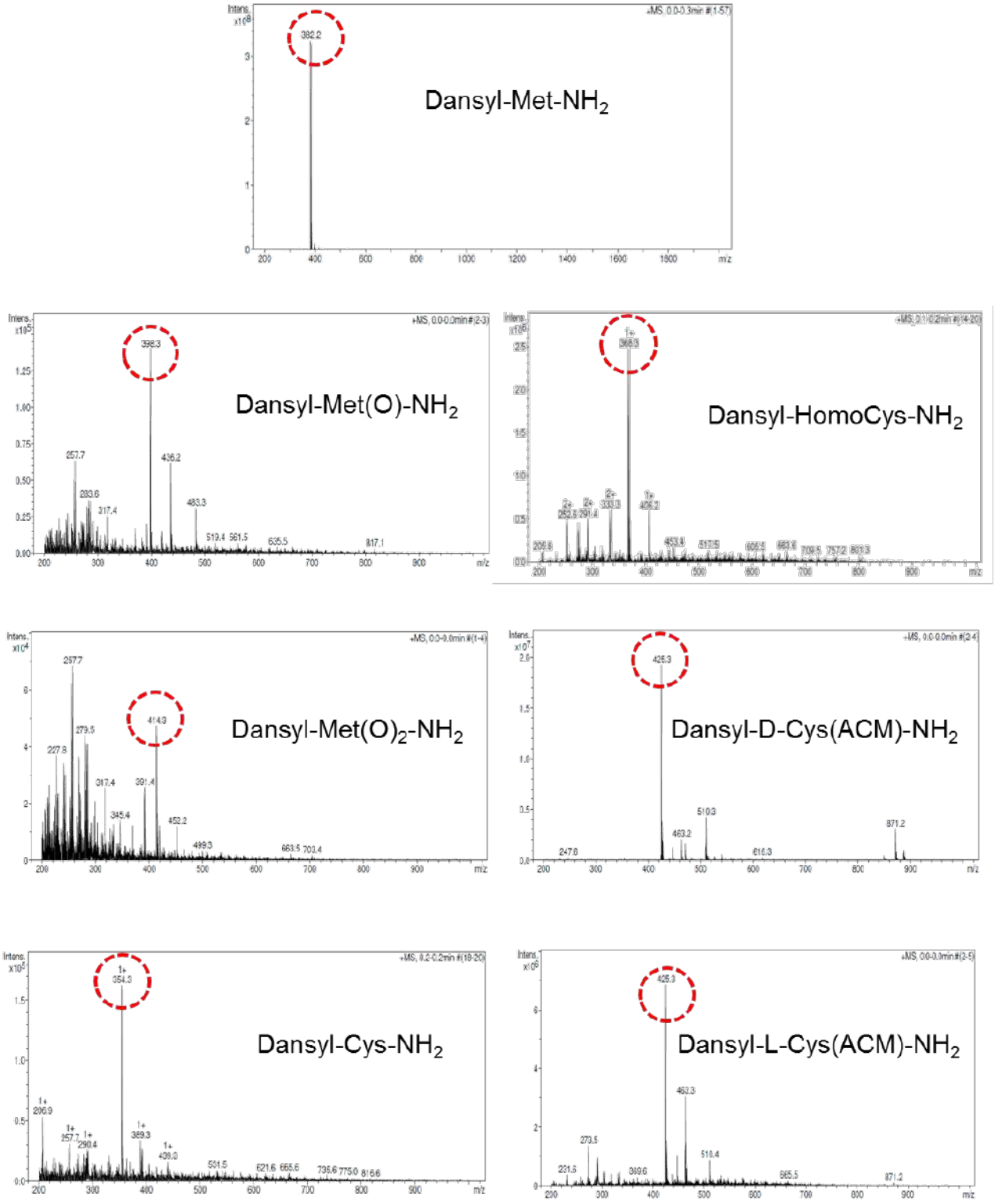

Figura 6:Spettri Esi Mass dei dansyl derivati sintetizzati

La purificazione del composto I è stata effettuata mediante RP-HPLC utilizzando gli eluenti H_2O/0.1% TFA (A) e CH_3CN/0.1% TFA (B) con un gradiente dal 5% al 50% di B in 15 minuti ad un flusso di 20 ml/min,

mentre per gli altri derivati è stato utilizzato un gradiente dal 5 al 70% di B in 15 minuti ad un flusso di 20 ml/min (Figura 7).

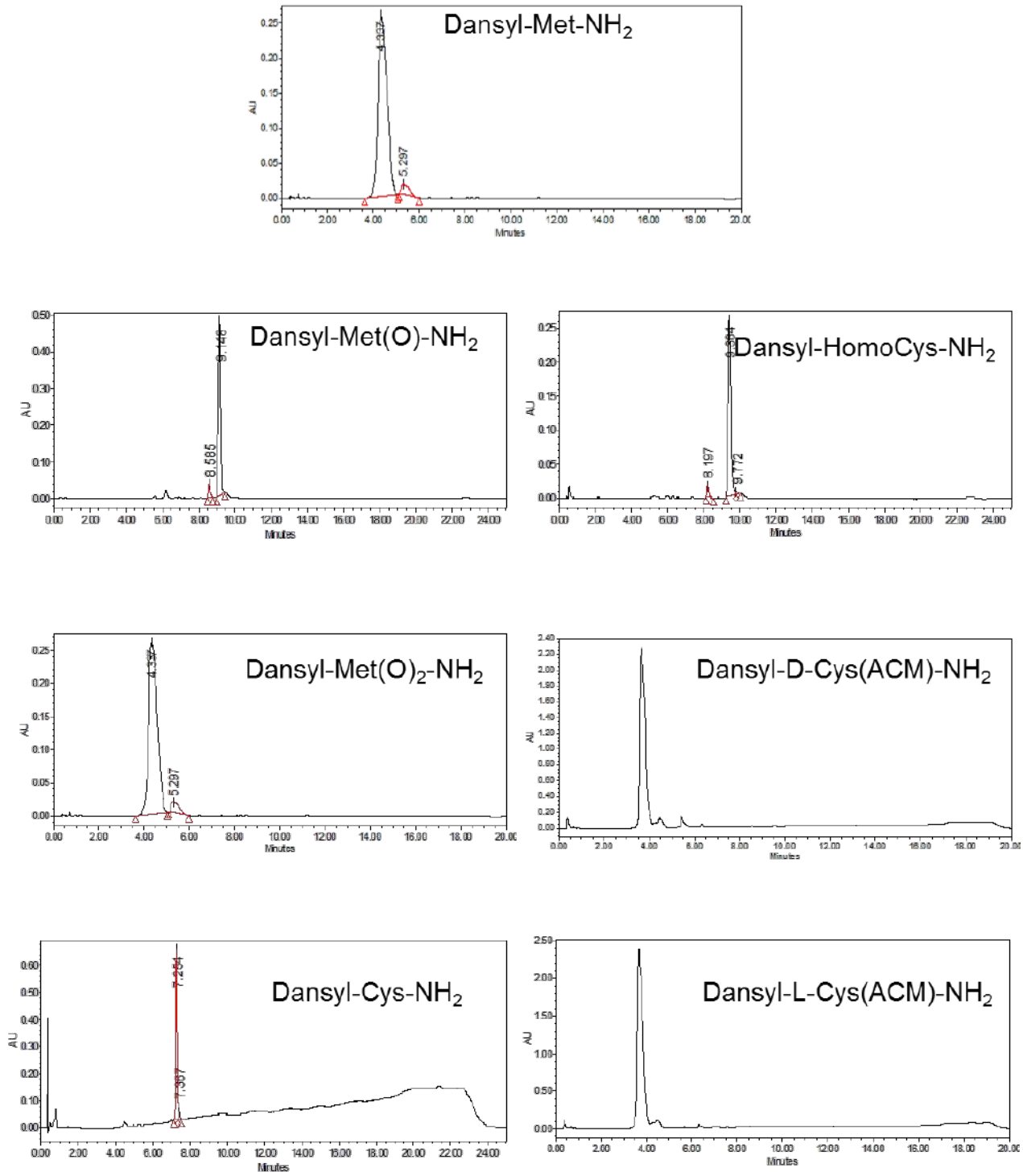

Figura 7: Cromatogrammi delle analisi HPLC dei dansyl derivati sintetizzati

La purezza dei derivati sintetizzati risulta essere ≥93%.

Le rese globali delle reazioni sono risultate essere ≥ 80 % per i composti I e II e ≥ 73 % per i restanti composti.

Attività A1.3 Metodiche per la caratterizzazione analitica di biomolecole con riferimento allo stato dell'arte nel campo ed alla letteratura scientifica recente per il riconoscimento di ioni Hg^{2+}

L'attività prevista dal progetto riguarda la caratterizzazione delle proprietà spettroscopiche (assorbimento UV e fluorescenza) delle molecole sintetizzate nell'attività A2.1. Per verificare la capacità di complessazione tali molecole con lo ione mercurio e/o con i vari metalli interferenti sono state condotte analisi UV e di fluorescenza.

Descrizione dell'attività

Analisi UV e di fluorescenza sono state effettuate per verificare le proprietà spettroscopiche sia delle molecole isolate sia dei complessi con i vari metalli. Gli spettri UV e di fluorescenza sono stati registrati con uno spettrofluorimetro EnSpire (Perkin Elmer) in piastre 96-multiwell OptiPlate.

Le titolazioni all'UV sono state eseguite acquisendo spettri di assorbimento nel range 200 nm – 500 nm e monitorando le variazioni spettrali in seguito all'aggiunta di ioni mercurio. Le titolazioni in fluorescenza sono state eseguite acquisendo spettri di fluorescenza nel range 400 nm – 700 nm in seguito ad eccitazione a 380 nm. Gli spettri di emissione di fluorescenza e di assorbimento UV-visibile sono stati registrati su soluzioni di dansyl derivati con concentrazione pari a 30 μM. Le misure sono state effettuate mantenendo costante in ogni campione la concentrazione di dansyl-derivato, in modo tale da poter trascurare in fase di elaborazione dati l'effetto di diluizione.

La caratterizzazione mediante UV e fluorescenza del binding agli ioni metallici è stata eseguita inizialmente in tamponi acquosi (HEPES 10 mM pH 7.4).

Gli spettri di emissione in fluorescenza del composto I per concentrazioni crescenti di Hg^{2+} (intervallo di concentrazioni 0.6 - 120 μM) sono riportati in Figura 8a. L'intensità e la posizione del picco di emissione del dansile sono funzione della concentrazione di Hg^{2+}. È stato osservato che per basse concentrazioni di Hg^{2+} (inferiori a 20 μM) si ha una diminuzione dell' emissione di fluorescenza (o quenching) e successivamente per concentrazioni crescenti una 'accensione' della intensità di emissione a 500 nm ed un blue-shift di 50 nm della massima intensità di emissione (550-500 nm). Tale risultato suggerisce la formazione di complessi di stechiometrica differente e dipendente dalle concentrazioni relative del composto I e dello ione mercurio. La stechiometria dei complessi è responsabile della risposta in fluorescenza dei sensori in esame; l'effetto sulle proprietà spettroscopiche dei diversi tipi di complessi è imputabile alla loro influenza sul trasferimento di carica interna tra il gruppo dimetilamino e/o il gruppo sulfamidico presenti nel fluoroforo.

Andamento analogo agli spettri di emissione in fluorescenza si registra per gli spettri di assorbimento: anche in questo caso l'intensità e la posizione dei picchi di assorbimento del dansile sono funzione della concentrazione di Hg^{2+} durante la titolazione (Figura 8b).

Per testare la selettività del binding del composto I verso Hg^{2+}, sono stai registrati gli spettri di emissione in fluorescenza del composto I (a 30 µM) in presenza di cationi metallici potenzialmente interferenti quali Ca^{2+}, Cd^{2+}, Co^{2+}, Pb^{2+}, Fe^{2+}, Pd^{2+}, Cu^{2+}, Na^{2+}, Ni^{2+}, Zn^{2+} (soluzioni preparate a partire dai cloruri, concentrazione di cationi pari a 120 µM). È stata testata dapprima la risposta del composto I in miscela con i singoli cationi metallici interferenti, ed in parallelo è stata anche valutata la risposta del composto I in presenza di miscele Hg^{2+}/ metallo interferente. In Figura 8c, sono riportate le intensità di emissioni in fluorescenza del composto I in presenza di metalli interferenti e miscele metalli / Hg^{2+}. Considerando l'emissione in fluorescenza a 500 nm, è stato osservato che in assenza di mercurio e per alte concentrazioni di interferenti (120 µM), non si ha una accensione della fluorescenza del composto I (Figura 8c, istogramma a barre rosse). In presenza di mercurio (120 µM), invece si ha un'accensione della fluorescenza a 500 nm pur essendo in presenza degli interferenti presi in esame (Figura 8c, istogramma a barre grigie). È necessario sottolineare che per metalli quali Pd^{2+}, Fe^{2+}, Cd^{2+}, l'intensità di emissione di fluorescenza registrata nelle miscele binarie ioni /Hg^{2+} risulta essere più bassa di quella attesa. È possibile che, in presenza di tali metalli, si instaurino complessi deboli in grado di alterare la risposta del sistema. Ulteriori prove di selettività per concentrazioni di mercurio ed interferenti più basse (caso reale) sono state successivamente approfondite.

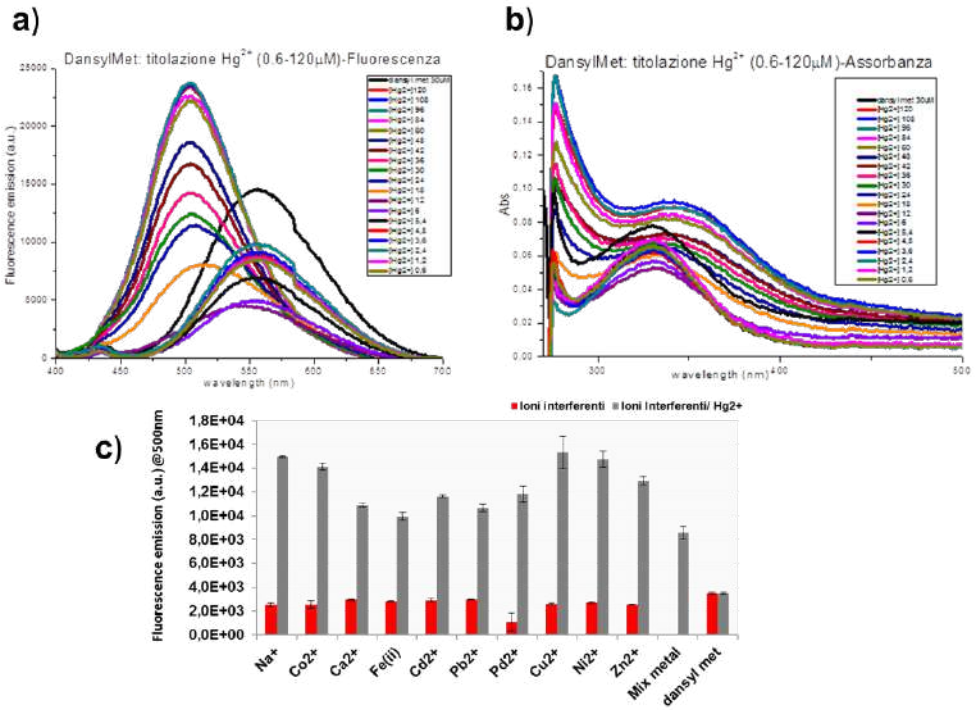

Figura 8: **a)** Spettri di emissione in fluorescenza e **b)** spettri di assorbimento del Composto I in presenza di concentrazioni crescenti di mercurio. **c)** Emissione in fluorescenza del Composto I in presenza di ioni interferenti e miscele di ioni interferenti/Hg^{2+} 1:1 registrata a 500 nm.

In Figura 9 sono riportati gli spettri di emissione in fluorescenza per i derivati II-VII in funzione di concentrazioni crescenti di mercurio.

Nel caso del composto II (dansyl-Met (O), Figura 9a), del composto III (dansyl-Met$(O)_2$, Figura 9b), del composto IV (dansyl-Cys, Figura 9c) e del composto V (dansyl-HomoCys, Figura 9d) si ha uno spegnimento dell'emissione della fluorescenza per concentrazioni crescenti di mercurio. Tale andamento è stato giustificato ipotizzando in questi casi la formazione di complessi con stechiometria diversa da quella responsabile dell'accensione della fluorescenza (come registrato per la dansyl metionina). Caso particolare risulta essere il composto IV (dansyl-Cys, Figura 9c), in cui l'andamento degli spettri di emissione in fluorescenza (aumento di emissione) nell'intervallo 6-30 μM sembra essere associato alla formazione di complessi con stechiometria diversa da quella responsabile dello spegnimento della fluorescenza. Nel caso dei composti VI (dansyl-(D)CysAcm, Figura 9e) e VII (dansyl-(L)CysAcm, Figura 9f), l'andamento degli spettri di emissione in fluorescenza è analogo a quello registrato nel caso della dansyl-Met.

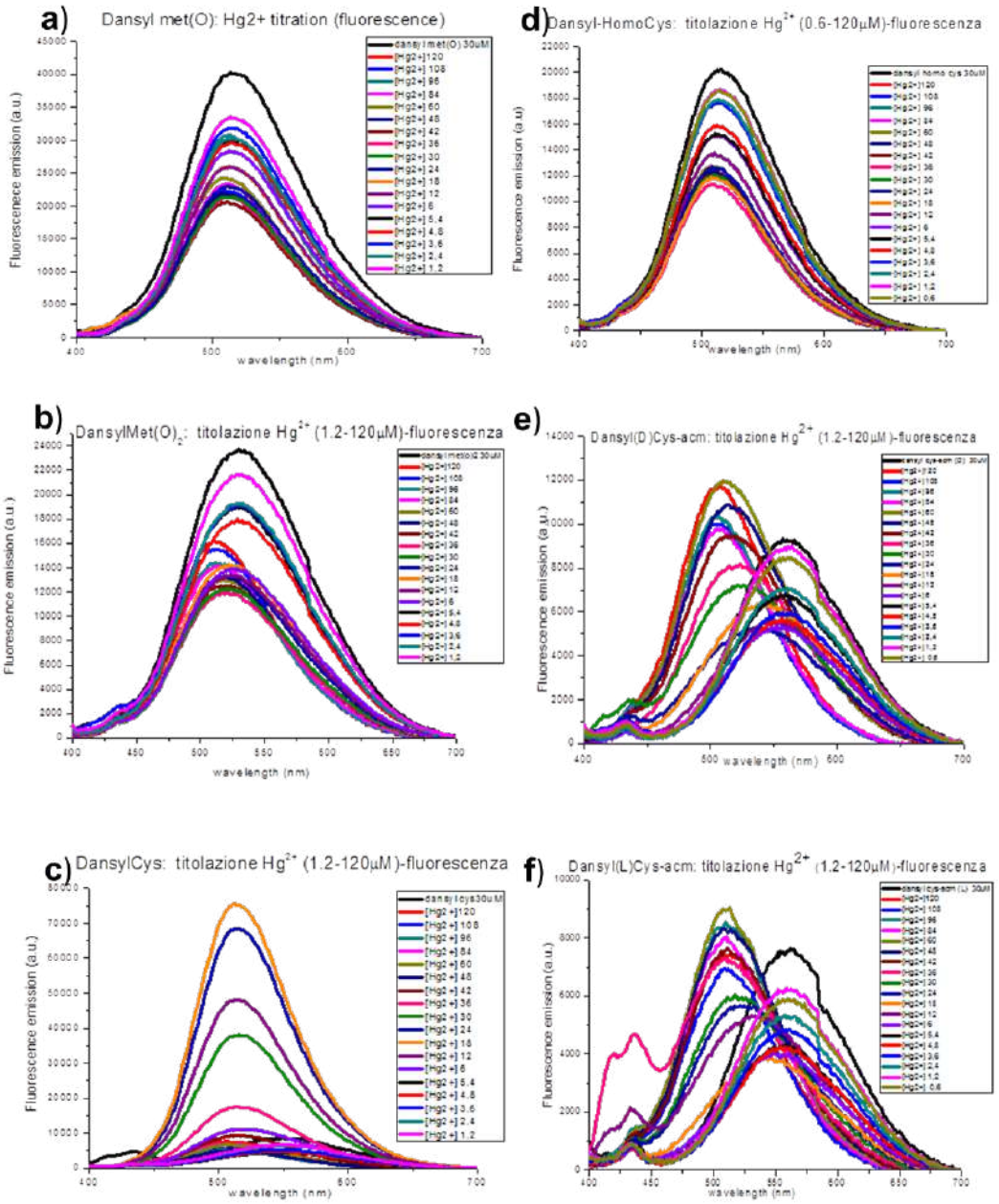

Figura 9.: Curve di titolazione in fluorescenza per concentrazioni crescenti di mercurio per i derivati: **a)** composto II (dansyl-Met(O)), **b)** composto III (dansyl-Met$(O)_2$), **c)** composto IV (dansyl-(L)Cys), **d)** composto V (dansyl-HomoCys), **e)** composto VI (dansyl-(L)CysAcm) e **f)** composto VII (dansyl-(D)CysAcm).

E' possibile distinguere anche per questi derivati una diversa stechiometria di complessazione: associata, per basse concentrazioni di mercurio, allo spegnimento della fluorescenza e per più alte concentrazioni di mercurio all'accensione della fluorescenza.

Analogamente sono stati acquisiti gli spettri di assorbanza per i vari derivati nei quali è stato possibile osservare lo shift dei massimi di assorbimento in funzione delle concentrazioni crescenti di Hg^{2+} durante la titolazione .

Sulla base degli spettri di emissione in fluorescenza dei derivati è stato possibile anche determinare le costante di dissociazione dansyl derivati –mercurio.

In generale per la determinazione delle costanti di dissociazione, l'interazione reversibile tra un generico substrato (S) e legante (L) viene trattata come un qualsiasi equilibrio chimico e descritta mediante la legge di azione di massa:

$$S\text{-}L \Longleftrightarrow S + L$$

$$Kd = [S]\,[L]/\,[S\text{-}L] \qquad \textbf{[1]}$$

valgono le seguenti definizioni:

$$[Stot] = [S] + [S\text{-}L] \qquad \textbf{[2]}$$

$$[Ltot] = [L] + [S\text{-}L] \qquad \textbf{[3]}$$

L'equazione [1] può essere riscritta nella forma:

$$[S\text{-}L] / [S] = [L] / Kd \qquad \textbf{[4]}$$

Combinando le equazioni [2] e [4] si ricava:

$$Y = [S\text{-}L]/\,[Stot] = [L]/\,Kd + [L] \qquad \textbf{[5]}$$

Se [SL] è direttamente proporzionale al cambiamento di "un segnale" rilevabile (fluorescenza), la rappresentazione grafica dell'equazione [5] è un'iperbole equilatera che ha [L] per ascissa e la variazione di segnalo rivelato (Y) per ordinata. Curve non iperboliche possono essere osservate ed indicano che lo schema di reazione è più complesso di quello descritto dall'equazione [1].

Quando [S-L] / [Stot] = 0,5 si ha [L] = Kd; questo comporta che la costante di dissociazione corrisponde alla concentrazione di legante libero necessaria per ottenere la semisaturazione del substrato (un valore spesso indicato come [L]50 o L50). Valori molto bassi di costanti di dissociazione corrispondono ad elevate affinità substrato/ligando.

Sulla base di queste considerazioni e, tendendo conto delle differenti stechiometrie dei complessi durante le titolazioni in presenza di concentrazioni crescenti di mercurio, i dati delle variazioni di emissioni in fluorescenza in funzione delle concentrazioni di mercurio sono stati elaborati con opportuni fitting e sono stati così determinati i valori delle costanti di dissociazione per i derivati sintetizzati (Tabella 1):

BIOMOLECOLE	$K_{d(1)}$ (μM)	$K_{d(2)}$ (μM)	Note
Composto I -Dansyl Met	17	45	2 differenti stechiometrie di complessazione
Composto II- Dansyl Met (O)	2	-	
Composto III- Dansyl Met $(O)_2$	-	-	
Composto IV- Dansyl Cys	30		
Composto V- Dansyl Homocys	5		
Composto VI- Dansyl Cys (L)-acm	10	36	2 differenti stechiometrie di complessazione
Composto VII- Dansyl Cys (D)-acm	30		

Tabella 1. Lista delle costanti di dissociazione determinate per i composti sintetizzati

Nel caso dei composti I e VI, è stato possibile determinare le due costanti di dissociazione relativi ai due complessi con diverse stechiometria. Considerando che valori bassi delle costanti di dissociazione corrispondono ad affinità maggiori tra il mercurio e il dansyl derivato, i derivati I, II, V, VI risultano essere quelli più affini al mercurio. Inoltre, poiché lo scopo ultimo dell'attività di ricerca è la determinazione quantitativa di ioni mercurio in campioni marini in cui la concentrazione di tale catione è al di sotto di una ppm, sui derivati a più alta affinità sono state effettuate nuove prove di titolazione per valutarne la risposta in intervalli di concentrazione di Hg^{2+} al di sotto di 0.6 μM (0.12 ppm) .

In particolare, per i composti I e VI sono stati registrati ulteriori spettri di emissione di fluorescenza e di assorbimento UV-visibile su soluzioni di dansyl derivati con concentrazione pari a 30 μM ed utilizzando concentrazioni crescenti di Hg^{2+} nel range 0.1-1.2 μM.

In figura 10 sono riportati gli spettri di emissione in fluorescenza per il composto I. Una prima analisi evidenzia che per concentrazioni di Hg^{2+}nel range 0.1-0.6 μM e 0.6-1.2 μM (Figura 10.b, 10.c) non è possibile delineare un andamento dell'emissione di fluorescenza in funzione di concentrazioni di Hg^{2+} al di sotto di 0.6 μM.

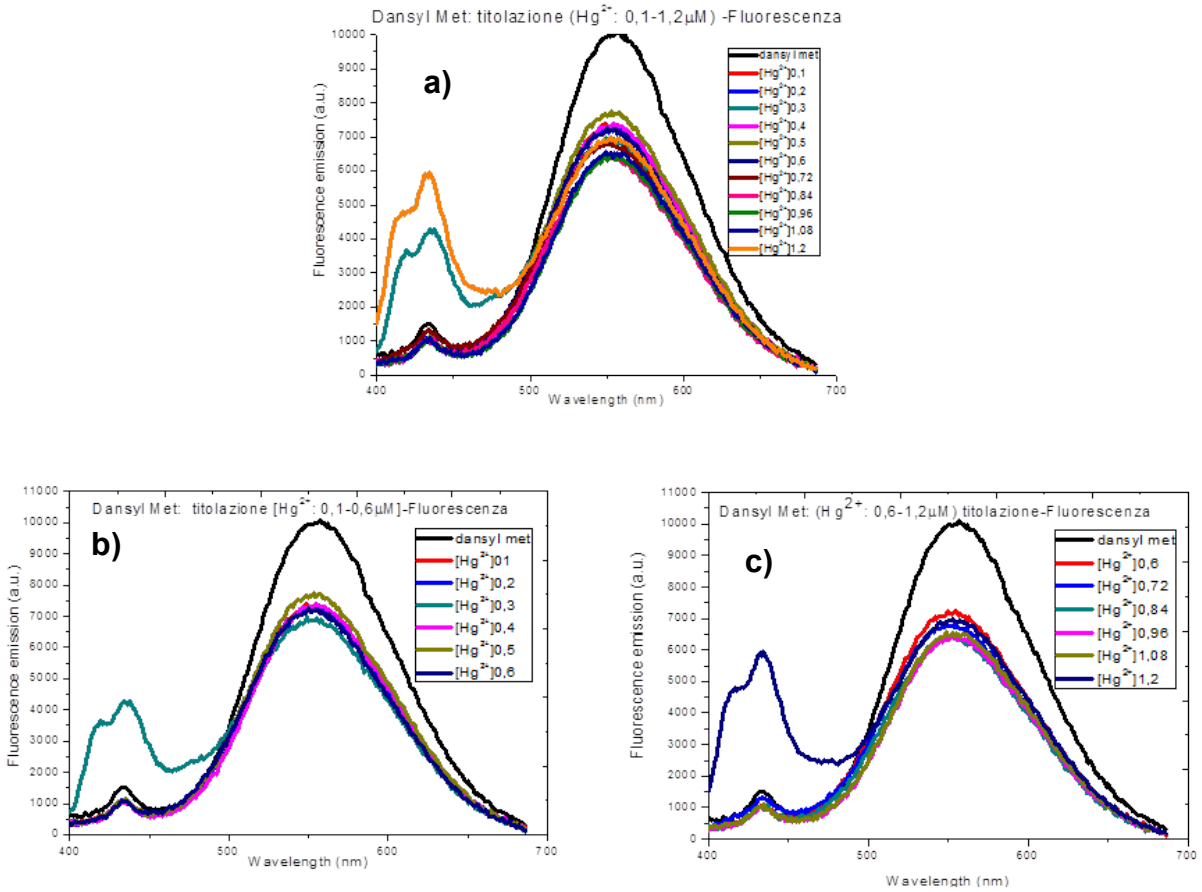

Figura 10: Spettri di emissione in fluorescenza del Composto I in presenza di concentrazioni crescenti di Hg^{2+} nel range: **a)** 0.1-1.2 mM; **b)** 0.1-0.6 µM; **c)** 0.6-1.2 µM.

Inoltre, per piccole variazioni di concentrazioni (Figura 11) le differenze degli spettri di emissione per concentrazioni di Hg^{2+} pari a 0.1 e 0.6 µM sono minime ed i relativi spettri sovrapponibili considerando le barre di errore ad essi associati. Le condizioni di acquisizione delle misure in fluorescenza fin qui adottate non hanno permesso di discriminare variazioni di concentrazione al di sotto di 0.6 µM.

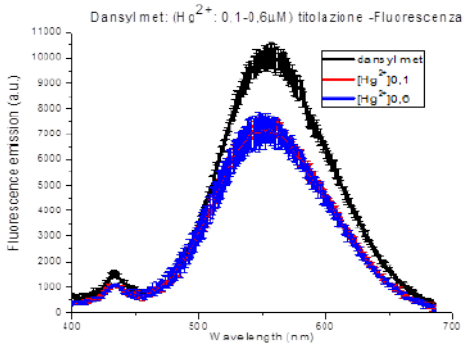

Figura 11: Spettri di emissione in fluorescenza del Composto I in presenza di concentrazioni di Hg^{2+} 0.1 µM e 0.6 µM con relative barre di errore.

Analogamente è stato effettuato anche uno studio degli spettri di assorbanza del composto I per concentrazioni di Hg^{2+}nel range 0.1-1.2 µM (Figura 12).

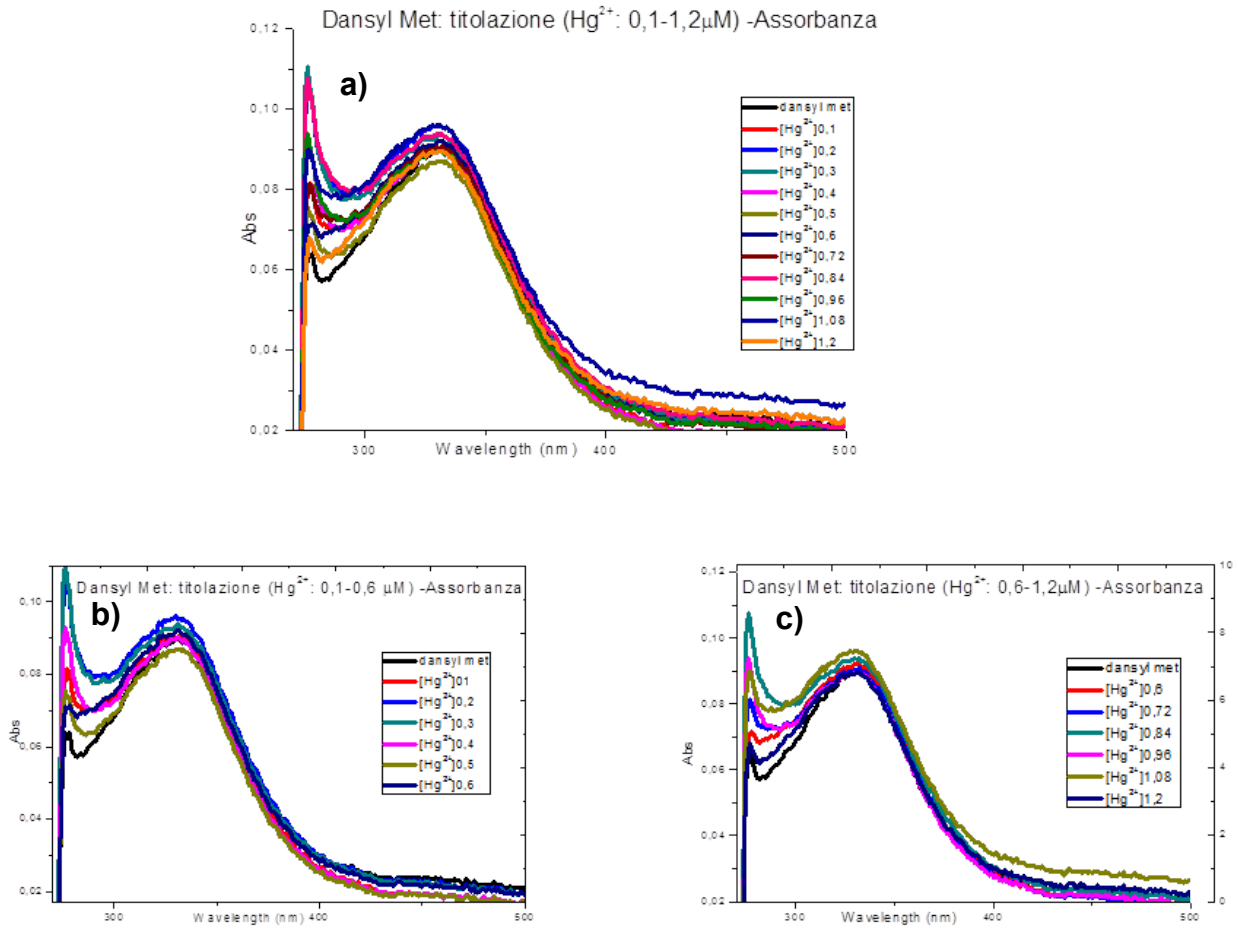

Figura 12: Spettri di assorbimento del Composto I in presenza di concentrazioni crescenti di Hg^{2+} nel range: **a)** 0.1-1.2 µM; **b)** 0.1-0.6 µM; **c)** 0.6-1.2 µM.

Una prima analisi evidenzia che anche in assorbanza per concentrazioni di Hg^{2+} nel range 0.1-0.6 µM e 0.6-1.2 µM (Figura 12.b, 12.c) non è possibile delineare un andamento degli spettri di assorbimento in funzione delle concentrazioni di Hg^{2+} al di sotto di 0.6 µM.

Inoltre, per piccole variazioni di concentrazioni (Figura 13) le differenze degli spettri di assorbimento sono minime e gli spettri per concentrazioni di Hg^{2+} pari a 0.1 e 0.6 µM sono sovrapponibili considerando le barre di errore ad essi associati. Le condizioni di acquisizione delle misure in assorbanza fin qui adottate non hanno permesso di discriminare variazioni di concentrazione al di sotto di 0.6 µM.

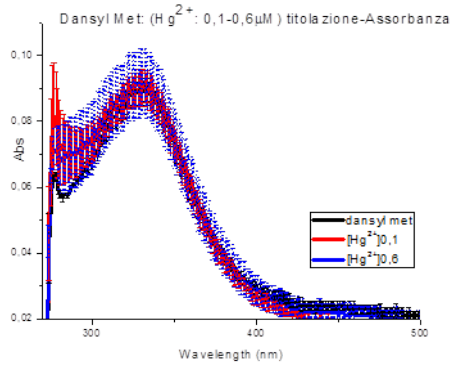

Figura 13: Spettri assorbimento del Composto I in presenza di concentrazioni di Hg^{2+} 0.1 µM e 0.6 µM con relative barre di errore.

Uno studio per concentrazioni di Hg^{2+} al di sotto di 0.6 µM è stato anche effettuato per il composto VI. In Figura 14 sono riportati gli spettri di emissione in fluorescenza per il composto VI. Una prima analisi evidenzia che per concentrazioni di Hg^{2+} nel range 0.1-0.6 µM e 0.6-1.2 µM (Figura 14.b, 14.c) non è possibile tracciare un andamento dell'emissione di fluorescenza in funzione delle concentrazioni di Hg^{2+} al di sotto di 0.6 µM.

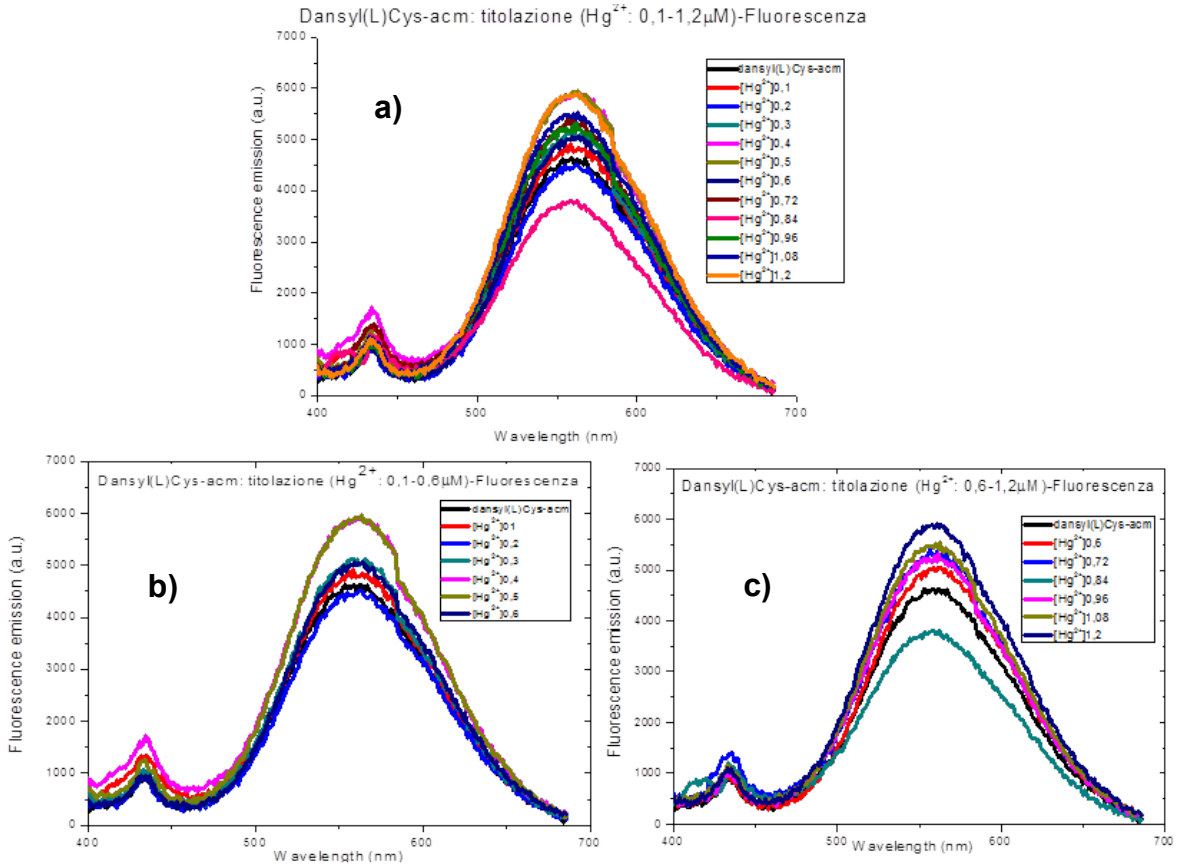

Figura 14: Spettri di emissione in fluorescenza del Composto VI in presenza di concentrazioni crescenti di Hg^{2+} nel range: **a)** 0.1-1.2 µM; **b)** 0.1-0.6 µM; **c)** 0.6-1.2 µM

Inoltre, per piccole variazioni di concentrazioni (Figura 15) le differenze degli spettri di assorbimento sono minime e per concentrazioni di Hg^{2+} pari a 0.1 e 0.6 µM gli spettri sovrapponibili considerando le barre di errore ad essi associati.

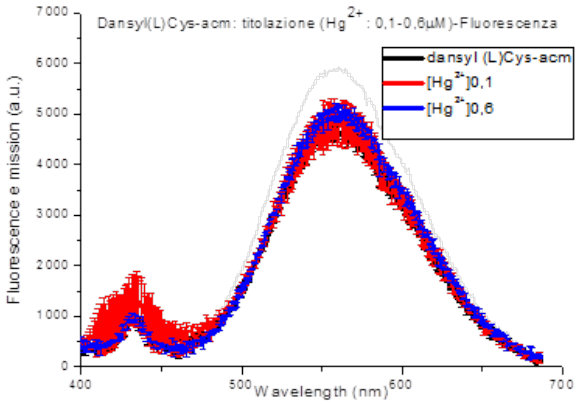

Figura 15: Spettri assorbimento del Composto VI in presenza di concentrazioni di Hg^{2+} 0.1 µM e 0.6 µM con relative barre di errore.

Analogamente, è stato effettuato anche uno studio degli spettri di assorbanza per il composto VI per concentrazioni di Hg^{2+} nel range 0.1-1.2 µM (Figura 16)

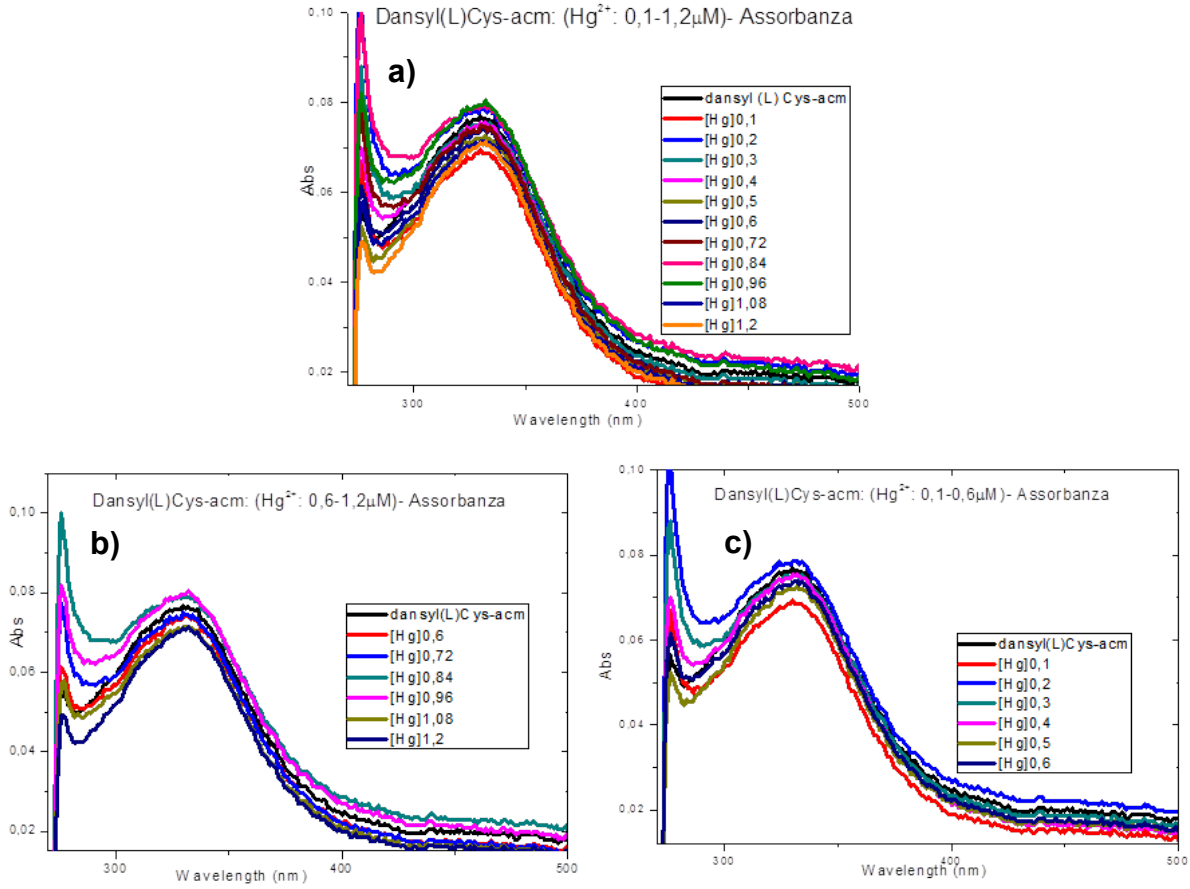

Figura 16: Spettri di assorbanza del Composto VI in presenza di concentrazioni crescenti di Hg^{2+} nel range: **a)** 0.1-1.2 µM; **b)** 0.1-0.6 µM; **c)** 0.6-1.2 µM.

Analizzando gli spettri si osserva che anche in assorbanza per concentrazioni di Hg^{2+} nel range 0.1-0.6 mM e 0.6-1.2 mM (Figura 16.b, 16.c) non è possibile delineare un andamento degli spettri di assorbimento in funzione delle concentrazioni di Hg^{2+} al di sotto di 0.6 mM.

Inoltre, per piccole variazioni di concentrazioni (Figura 17) le differenze degli spettri di assorbimento sono minime e gli spettri per le concentrazioni Hg^{2} 0.1 e 0.6 µM sono sovrapponibili considerando le barre di errore ad essi associati. Le condizioni di acquisizione delle misure in fluorescenza fin qui adottate non hanno permesso di discriminare variazioni di concentrazione al di sotto di 0.6 µM.

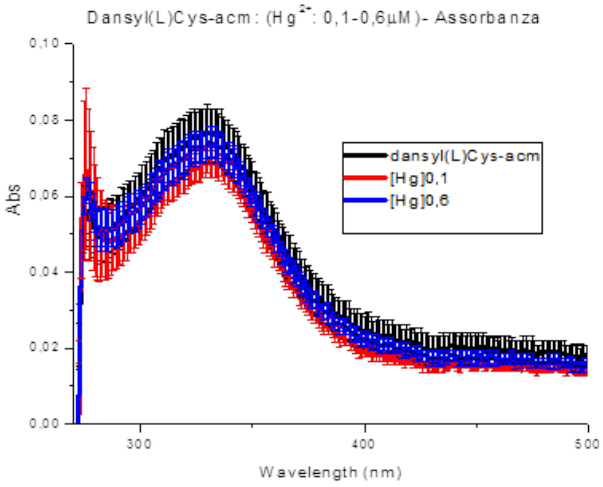

Figura 17: Spettri assorbimento del Composto VI in presenza di concentrazioni di Hg^{2+} 0.1 µM e 0.6 µM con relative barre di errore.

Per migliorare il limite di rilevabilità di Hg^{2+}e poter incrementare ulteriormente la sensibilità della risposta in fluorescenza a basse concentrazioni di Hg^{2+}, è stata valutata una fase successiva di ottimizzazione delle condizioni strumentali di acquisizione. Quindi si è cercato di ottimizzare nuovamente le condizioni del saggio e l'effetto dell'utilizzo di volumi piccoli su piastre da 384 pozzetti sulla sensibilità della riposta in fluorescenza dei composti I, II, V, VI.

Gli spettri di fluorescenza sono stati registrati con uno spettrofluorimetro EnSpire (Perkin Elmer) in piastre 384-multiwell Proxy Plate su soluzioni di dansyl derivati con concentrazione pari a 30 µM, operando su un volume di 30mL. Le misure sono state effettuate mantenendo costante in ogni campione la concentrazione di dansyl-derivato, in modo tale da poter trascurare in fase di elaborazione dati l'effetto di diluizione.

In Figura 18a, sono riportati gli spettri di emissione in fluorescenza registrati con il protocollo ottimizzato nel range di concentrazioni di Hg^{2+} 0.1-0.6 µM per il composto I. In figura 18.b sono stati comparati gli spettri di emissione con le relative deviazioni standard per le concentrazioni di Hg^{2+} 0.1 e 0.6 µM e del composto I. Pur avendo ottimizzato i nuovi parametri di acquisizione ed incrementato l'intensità di segnale acquisito a parità di concentrazione (rispetto alle precedenti condizioni di acquisizione), dalla comparazione degli spettri per basse concentrazioni, non è possibile individuare una sensibilità inferiore a 0.6 µM.

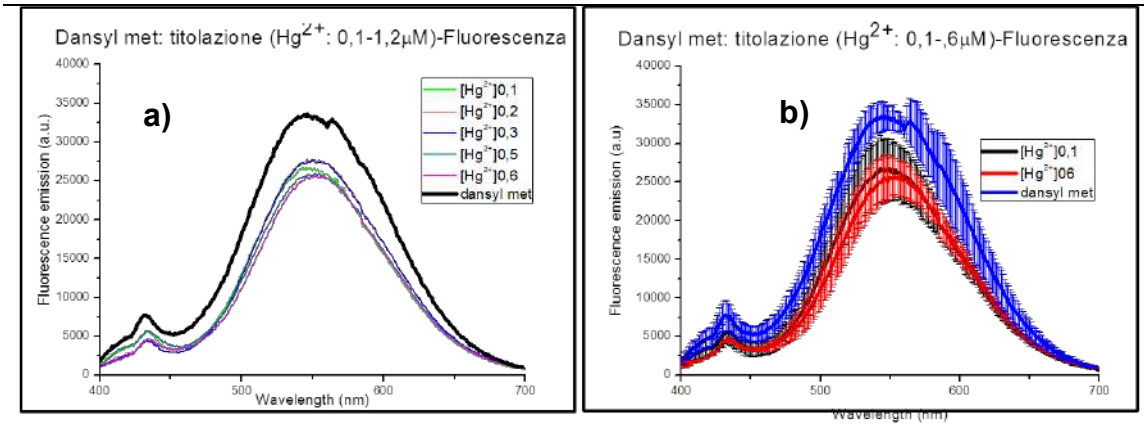

Figura 18: **a)** Spettri di emissione di fluorescenza del Composto I in presenza di concentrazioni crescenti di Hg^{2+} nel range: 0.1-0.6 μM;**b)** Spettri di emissione di fluorescenza per concentrazioni di Hg^{2+} 0.1 μM e 0.6 mM con relative barre di errore.

In Figura 19a, sono riportati gli spettri di emissione in fluorescenza registrati con il protocollo ottimizzato per il range di concentrazioni di Hg^{2+} 0.1-0.6 μM per il composto II. In Figura 19.b sono stati comparati gli spettri di emissione con le relative deviazioni standard per le concentrazioni Hg^{2+} 0.1 e 0.6 μM e del composto II. Pur avendo ottimizzato i nuovi parametri di acquisizione ed incrementato l'intensità di segnale acquisito, dalla comparazione degli spettri per basse concentrazioni, non è possibile individuare una sensibilità inferiore a 0.6 μM.

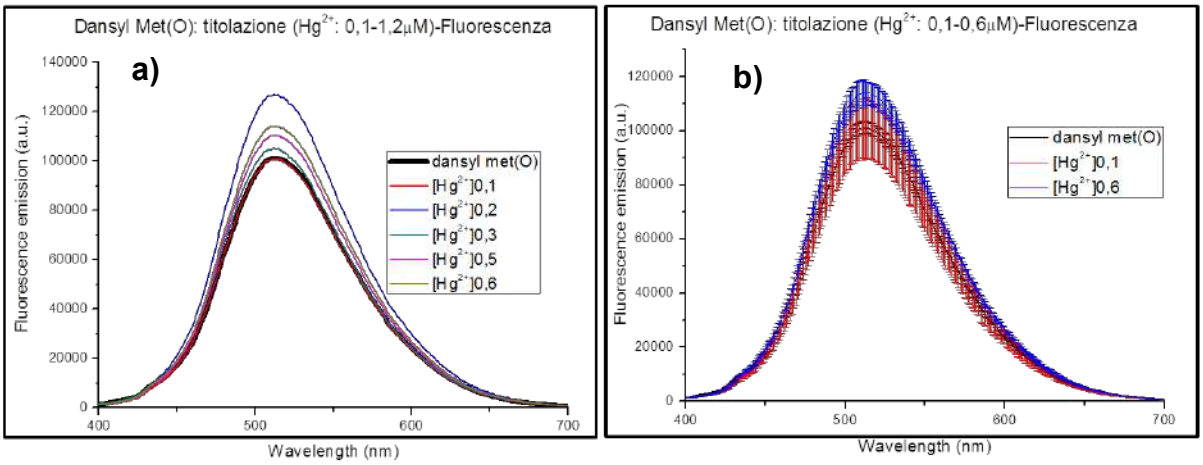

Figura 19: **a)** Spettri di emissione di fluorescenza del Composto II in presenza di concentrazioni crescenti di Hg^{2+} nel range: 0.1-0.6 μM; **b)** Spettri di emissione di fluorescenza per concentrazioni di Hg^{2+} 0.1 μM e 0.6 μM con relative barre di errore.

Studi analoghi con il nuovo protocollo ottimizzato sono stati condotti anche sul composto IV. In Figura 20a sono riportati gli spettri di emissione in fluorescenza registrati con il protocollo ottimizzato per il range di concentrazioni di Hg^{2+} 0.1-0.6 μM per il composto IV. In Figura 20b sono stati comparati gli spettri di

emissioni con le relative deviazioni standard per le concentrazioni Hg^{2+} 0.1 e 0.6 µM e del composto IV. Pur avendo ottimizzato i nuovi parametri di acquisizione ed incrementato l'intensità di segnale acquisito a parità di concentrazione, dalla comparazione degli spettri per basse concentrazioni, non è possibile individuare una sensibilità inferiore a 0.6 µM.

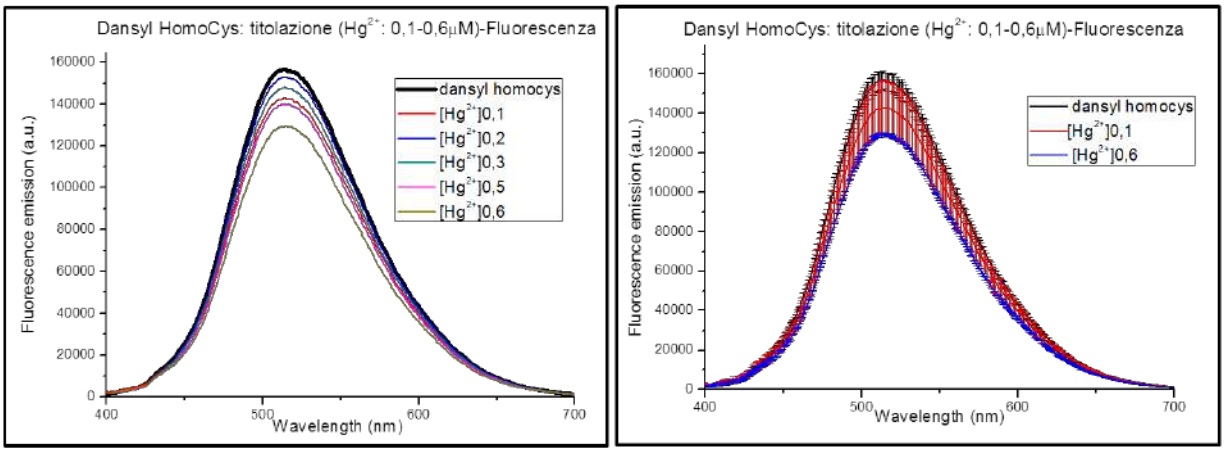

Figura 20: **a)** Spettri di emissione di fluorescenza del Composto IV in presenza di concentrazioni crescenti di Hg^{2+} nel range: 0.1-0.6 µM; **b)** Spettri di emissione di fluorescenza per concentrazioni di Hg^{2+} 0.1 µM e 0.6 µM con relative barre di errore.

Infine, sono state verificate le risposte in fluorescenza con il nuovo protocollo per l'ultimo derivato selezionato, il composto VI. In Figura 21a, sono riportati gli spettri di emissione in fluorescenza del composto VI registrati con il protocollo ottimizzato per il range di concentrazioni di Hg^{2+} 0.1-0.6 µM. In Figura 21b sono stati comparati gli spettri di emissioni con le relative deviazioni standard per le concentrazioni Hg^{2+} 0.1 e 0.6 µM e del Composto VI. Pur avendo ottimizzato i nuovi parametri di acquisizione ed incrementato l'intensità di segnale acquisito a parità di concentrazione, dalla comparazione degli spettri per basse concentrazioni, non è possibile individuare una sensibilità inferiore a 0.6 µM.

In conclusione, per migliorare la sensibilità del nostro saggio di riconoscimento di Hg^{2+}, si è proceduto con l'ottimizzazione delle condizioni di acquisizione (reader, piastra da 384 multiwell, volume 30 µL), ma pur avendo ottenuto una segnale in fluorescenza più intenso (a parità di concentrazione di dansyl derivato rispetto alle condizioni precedenti), non è stato possibile abbassare la sensibilità al di sotto di una concentrazione pari 0.6 µM.

Future acquisizioni con i probe in fluorescenza ed assorbanza su fibra potranno favorire l'ottenimento di sensibilità inferiori ai 0.12 ppm.

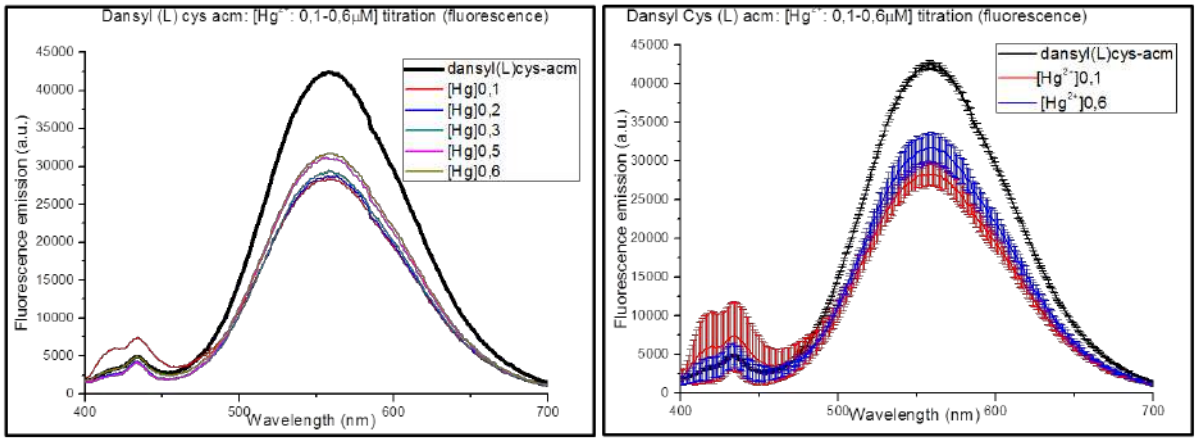

Figura 20: **a)** Spettri di emissione di fluorescenza del Composto VI in presenza di concentrazioni crescenti di Hg^{2+} nel range: 0.1-0.6 μM;**b)** Spettri di emissione di fluorescenza per concentrazioni di Hg^{2+} 0.1 μM e 0.6 μM con relative barre di errore.

Dopo il completamento degli studi sulla sensibilità dei dansyl derivati in saggi di riconoscimento di Hg^{2+}, è stato effettuato uno studio approfondito sulla selettività del riconoscimento di tale catione in presenza di cationi interferenti quali Ca^{2+}, Cd^{2+}, Co^{2+}, Pb^{2+}, Fe^{2+}, Pd^{2+}, Cu^{2+}, Na^{+}, Ni^{2+}, Zn^{2+} (soluzioni preparate a partire dai cloruri) e successivamente in acqua di mare sintetica.

Per valutare l'interferenza di altri cationi metallici sono stati effettuati differenti saggi di binding, utilizzando le seguenti condizioni sperimentali: i) concentrazione di dansyl-derivato pari a 30 μM; ii) concentrazioni limite di cationi interferenti 0.6 μM e 120 μM. L'effetto di tale cationi sulla fluorescenza del dansyl derivato è stato valutato in presenza ed assenza di Hg^{2+}. In particolare tali studi si sono concentrati sui derivati dansyl-Met (Composto I) e dansyl(L)Cys-Acm (composto VI), gli unici derivati a cui è associato uno shift della posizione del picco di emissione del dansile in seguito a complessazione con Hg^{2+}.

[1] Selettività Dansyl Met

- **<u>[0.6 μM] metalli interferenti + dansyl derivato [30 μM]</u>**

È stato valutato l'effetto sull'intensità di emissione di fluorescenza del composto I in presenza di concentrazioni di cationi interferenti pari a 0.6 μM. Lo scopo di tali misure è di valutare l'effetto dei cationi interferenti sulla fluorescenza del Composto I in assenza di Hg^{2+} ed in condizioni in cui la dansyl metionina è presente in largo eccesso (stechiometria 50:1) rispetto alla concentrazione dei cationi metallici (Figura 21).

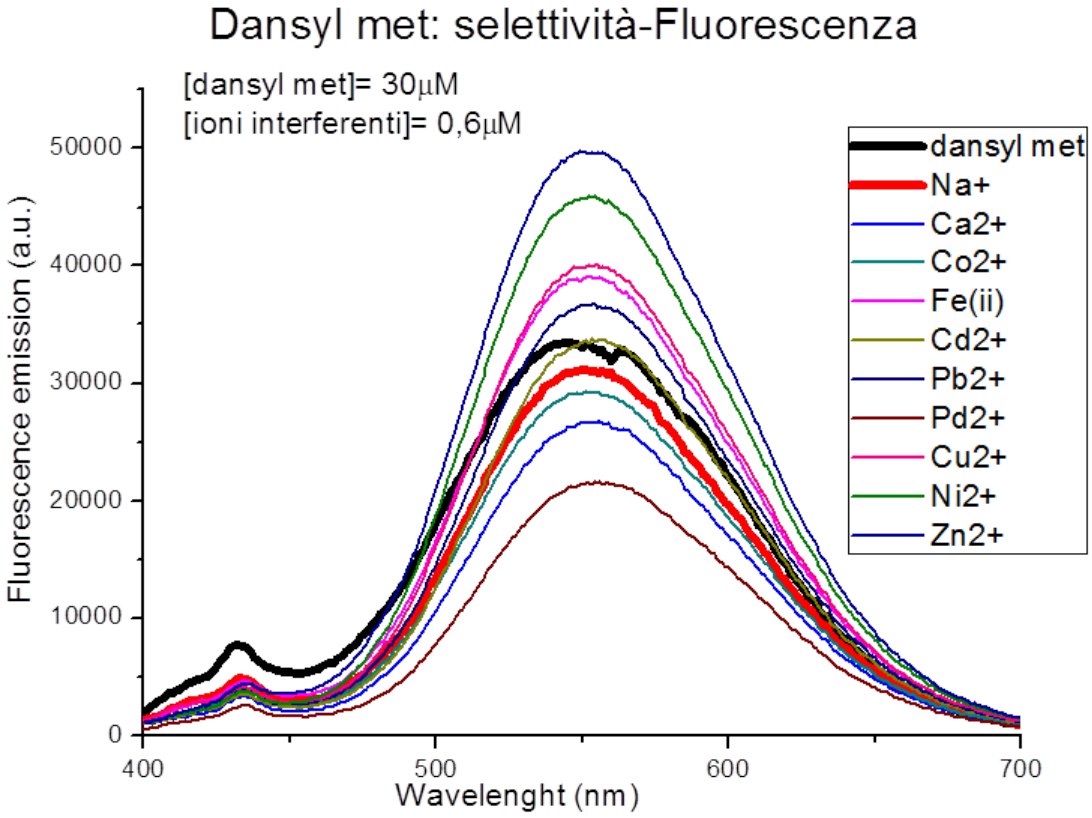

Figura 21: Spettri di emissione in fluorescenza del Composto I in presenza di ioni interferenti Ca^{2+}, Cd^{2+}, Co^{2+}, Pb^{2+}, Fe^{2+}, Pd^{2+}, Cu^{2+}, Na^{2+}, Ni^{2+}, Zn^{2+}

Per alcuni cationi, (Cu^{2+}, Pb^{2+}, Fe, $^{2+}$ Ca^{2+}) seppur presenti in bassa concentrazione (0.6 μM), si ha un incremento della fluorescenza della dansyl met di riferimento (curva nera). Tale incremento, o più in generale le variazioni di emissione in fluorescenza in presenza dei vari cationi sono attribuibili alla formazione di complessi o di interazioni di carica tra il composto I ed i cationi interferenti. Inoltre, particolare attenzione è da rivolgere catione Na^{+}, uno dei cationi presente in acqua di mare in concentrazioni elevate (0.6 M). Per basse concentrazioni, tale catione sembra non avere un effetto limitante sull'emissione in fluorescenza del composto I (curva nera per riferimento, curva rossa per Na^{+})

- **[0.6 μM] metalli interferenti + dansyl derivato [30 μM] + Hg^{2+} [0.6 μM]**

È stata valutata la risposta sull'intensità di emissione di fluorescenza del composto I in presenza di uguali concentrazioni (0.6 μM) di cationi interferenti e di Hg^{2+}. Lo scopo di tali misure è di valutare l'effetto dei cationi interferenti sulla risposta in fluorescenza del composto I in presenza di Hg^{2+} ed in condizioni in cui la dansyl-Met è presente in largo eccesso (stechiometria 50:1) rispetto alla concentrazione dei cationi metallici (Figura 22).

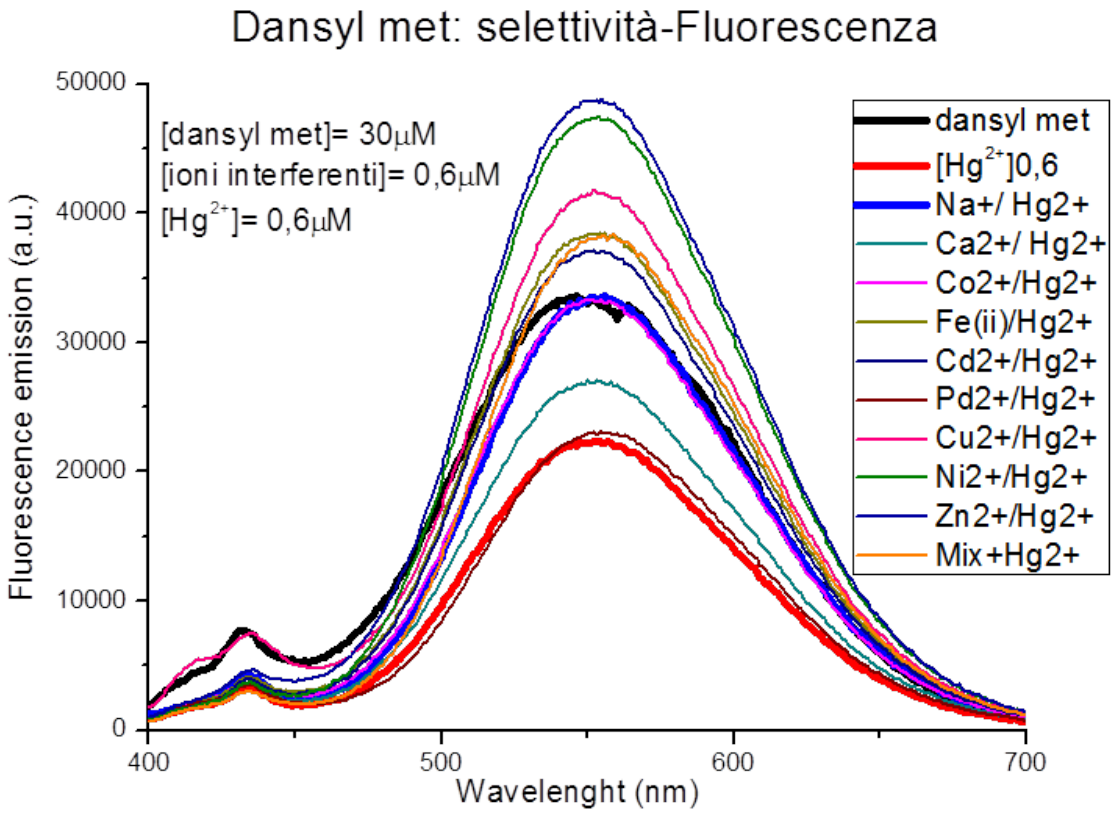

Figura 22: Spettri di emissione in fluorescenza del Composto I in presenza di Hg^{2+} e di ioni interferenti Ca^{2+}, Cd^{2+}, Co^{2+}, Pb^{2+}, Fe^{2+}, Pd^{2+}, Cu^{2+}, Na^{2+}, Ni^{2+}, Zn^{2+}

Molti cationi bivalenti seppur presenti in bassa concentrazione (0.6 μM) interferiscono con la risposta del dansyl-Met in presenza di Hg^{2+} 0.6 μM (curva rossa). In particolare, anche il catione Na^{+} (curva blu) risulta influenzare la risposta del composto I in presenza di Hg^{2}+, inibendo l'atteso spegnimento della fluorescenza del dansile in seguito alla complessazione con il mercurio.

- **<u>[120 μM] metalli interferenti + dansyl derivato [30 μM]</u>**

È stato valutato l'effetto sull'intensità di emissione di fluorescenza del composto I in presenza di concentrazioni di cationi interferenti pari a 120 μM. Lo scopo di tali misure è di valutare l'effetto dei cationi interferenti sulla sola fluorescenza del composto I in assenza di Hg^{2+} ed in condizioni in cui la dansyl-Met è presente in difetto (stechiometria 1:4) rispetto alla concentrazione dei cationi metallici (Figura 23).

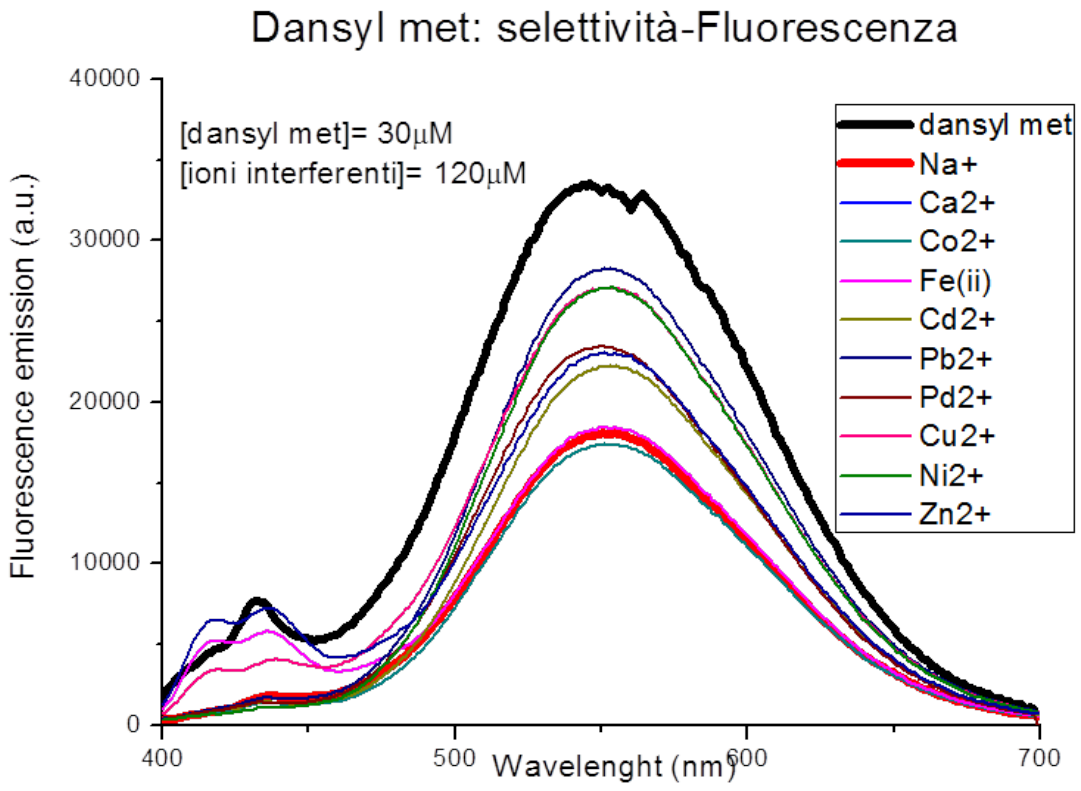

Figura 23: Spettri di emissione in fluorescenza del Composto I in presenza di ioni interferenti Ca^{2+}, Cd^{2+}, Co^{2+}, Pb^{2+}, Fe^{2+}, Pd^{2+}, Cu^{2+}, Na^{2+}, Ni^{2+}, Zn^{2+}

Tutti i cationi inibiscono l'emissione in fluorescenza della dansyl-Met di riferimento (curva nera). Tale effetto di quenching della fluorescenza, in presenza dei vari cationi è ancora una volta attribuibile alla formazione di complessi o di interazioni di carica non specifici tra il composto I ed i cationi. Inoltre, particolare attenzione è da rivolgere catione Na^{+} che dà luogo ad uno spegnimento dell'emissione di fluorescenza di circa il 50% rispetto alla fluorescenza di riferimento del composto I (curva nera per composto I, curva rossa per Na+).

- **[120 μM] metalli interferenti + dansyl derivato [30 μM] + Hg^{2+} [120 μM]**

È stata valutata la risposta sull'intensità di emissione di fluorescenza del composto I in presenza di uguali concentrazioni (120 μM) di cationi interferenti e di Hg^{2+}. Lo scopo di tali misure è di valutare l'effetto dei cationi interferenti sulla risposta in fluorescenza del composto I in presenza di Hg^{2+} ed in condizioni in cui la dansyl metionina è stechiometricamente in difetto (1:8) rispetto alla concentrazione dei cationi metallici (Figura 24).

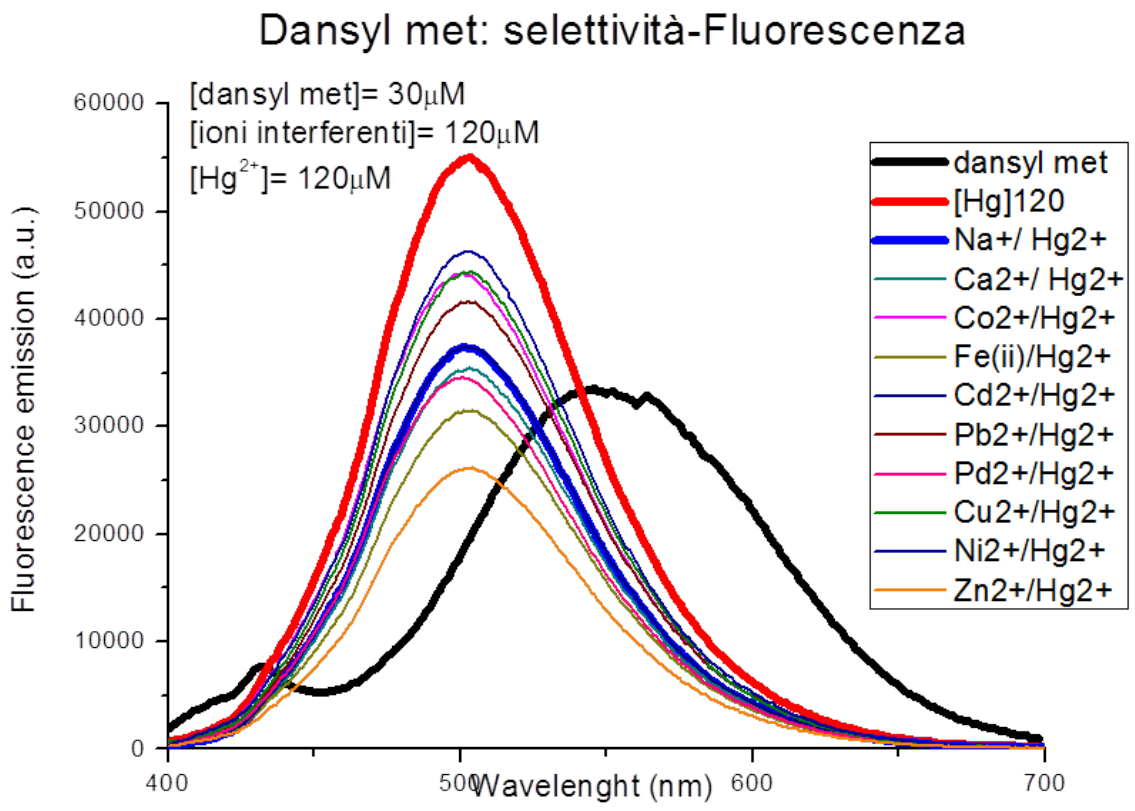

Figura 24: Spettri di emissione in fluorescenza del Composto I in presenza di Hg^{2+} e di ioni interferenti Ca^{2+}, Cd^{2+}, Co^{2+}, Pb^{2+}, Fe^{2+}, Pd^{2+}, Cu^{2+}, Na^{2+}, Ni^{2+}, Zn^{2+}

Tutti i cationi interferiscono con la risposta in fluorescenza del Composto I in presenza di una concentrazione di Hg^{2+} pari a 120 μM (curva rossa). È ancora possibile osservare uno shift della posizione del picco di emissione della fluorescenza in presenza di Hg^{2+}, ma la presenza dei cationi dà luogo un parziale spegnimento della fluorescenza.

[2] Selettività Dansyl(L)Cys-Acm

- **<u>[0.6 μM] metalli interferenti + dansyl derivato [30 μM]</u>**

È stato valutato l'effetto sull'intensità di emissione di fluorescenza del composto VI in presenza di concentrazioni di cationi interferenti pari a 0.6 μM. Lo scopo di tali misure è di valutare l'effetto dei cationi interferenti sulla fluorescenza del composto VI in assenza di Hg^{2+} ed in condizioni in cui il composto VI è presente in largo eccesso (stechiometria 50:1) rispetto alla concentrazione dei cationi metallici (Figura 25).

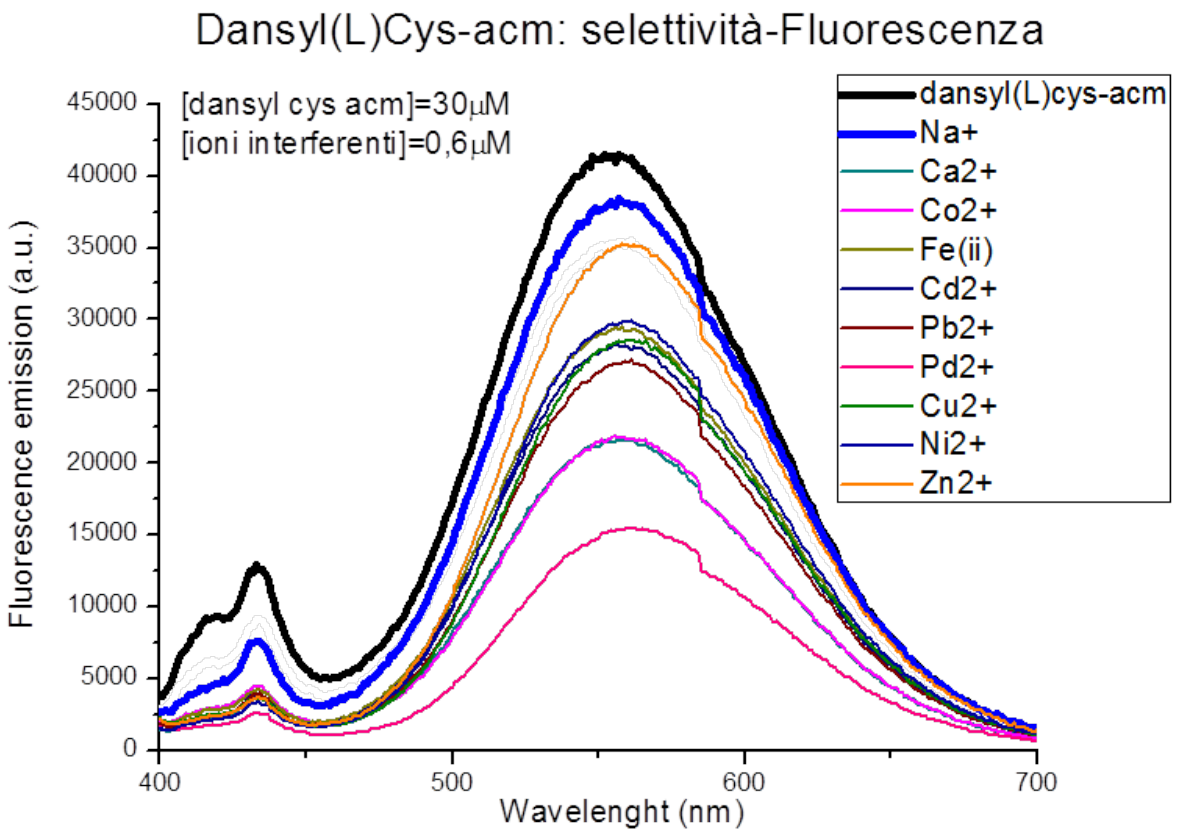

Figura 25: Spettri di emissione in fluorescenza del Composto VI in presenza di ioni interferenti Ca^{2+}, Cd^{2+}, Co^{2+}, Pb^{2+}, Fe^{2+}, Pd^{2+}, Cu^{2+}, Na^{2+}, Ni^{2+}, Zn^{2+}

Tutti i cationi, seppur in bassa concentrazione (0.6 μM), danno luogo ad uno spegnimento dell'emissione del composto VI di riferimento (curva nera). Tale effetto è da attribuire alla formazione di complessi o di interazioni di carica non specifici tra il composto VI ed i cationi interferenti. In particolare, la presenza di Na^{+} alla concentrazione in esame sembra non avere un effetto limitante sull'emissione in fluorescenza del composto VI (curva nera per riferimento, curva blu per Na^{+}).

- **[0.6 μM] metalli interferenti + dansyl derivato [30 μM] + Hg^{2+} [0.6 μM]**

È stata valutata la risposta sull'intensità di emissione di fluorescenza del composto VI in presenza di uguali concentrazioni (0.6 mM) di cationi interferenti e di Hg^{2+}. Lo scopo di tali misure è di valutare l'effetto dei cationi interferenti sulla risposta in fluorescenza del composto VI in presenza di Hg^{2+} ed in condizioni in cui il composto VI è presente in largo eccesso (stechiometria 50:1) rispetto ai cationi metallici (Figura 26).

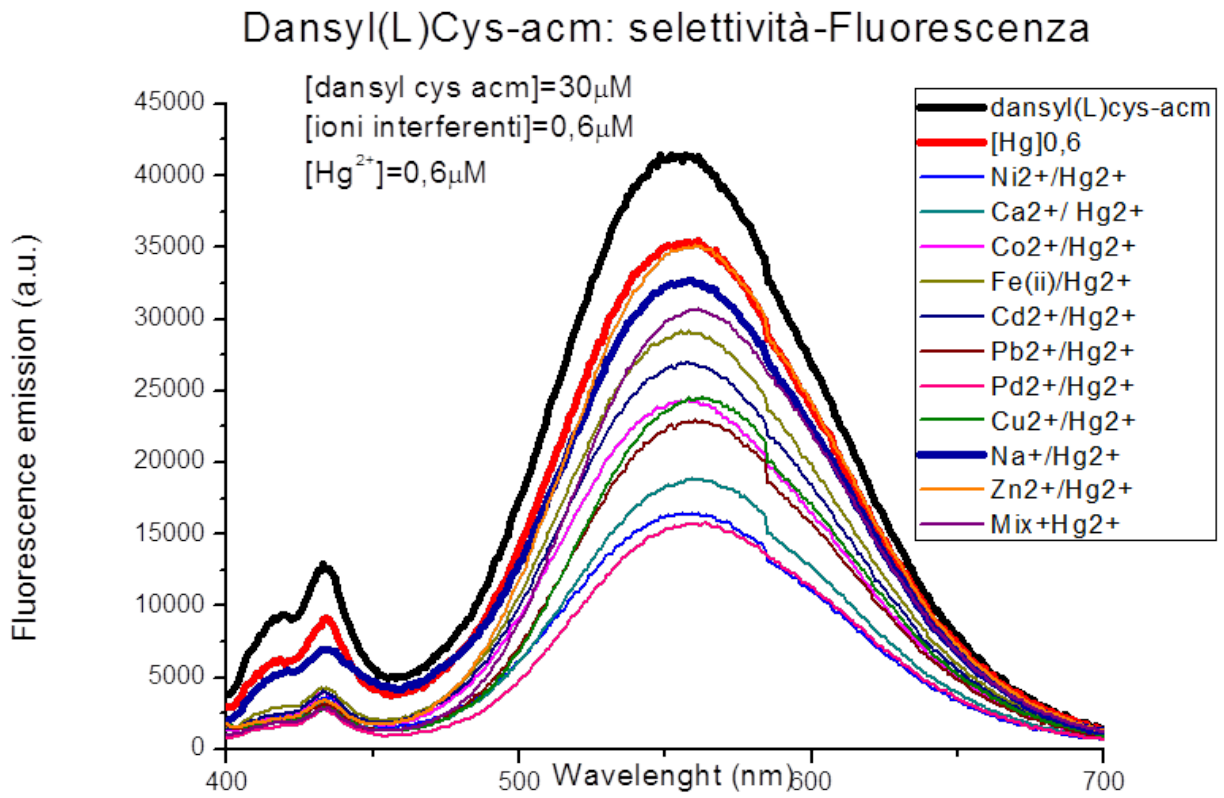

Figura 26: Spettri di emissione in fluorescenza del Composto VI in presenza di Hg^{2+} e di ioni interferenti Ca^{2+}, Cd^{2+}, Co^{2+}, Pb^{2+}, Fe^{2+}, Pd^{2+}, Cu^{2+}, Na^{2+}, Ni^{2+}, Zn^{2+}

Tutti i cationi bivalenti seppur presenti in bassa concentrazione (0.6 μM) interferiscono con la risposta del composto VI in presenza di Hg^{2+} 0.6 μM (curva rossa). In particolare, anche il catione Na^{+} (curva blu) risulta influenzare la risposta del composto VI in presenza di Hg^{2}+, dando luogo ad un ulteriore spegnimento della fluorescenza del complesso del dansyl derivato con il catione mercurio.

- **[120 μM] metalli interferenti + dansyl derivato [30 μM]**

È stato valutato l'effetto sull'intensità di emissione di fluorescenza del composto VI in presenza di concentrazioni di cationi interferenti pari a 120 μM. Lo scopo di tali misure è di valutare l'effetto dei cationi interferenti sulla fluorescenza del composto VI in assenza di Hg^{2+} ed in condizioni in cui il derivato dansyl(L)Cys-Acm risulta essere stechiometricamente in difetto (1:4) rispetto alla concentrazione dei cationi metallici (Figura 27).

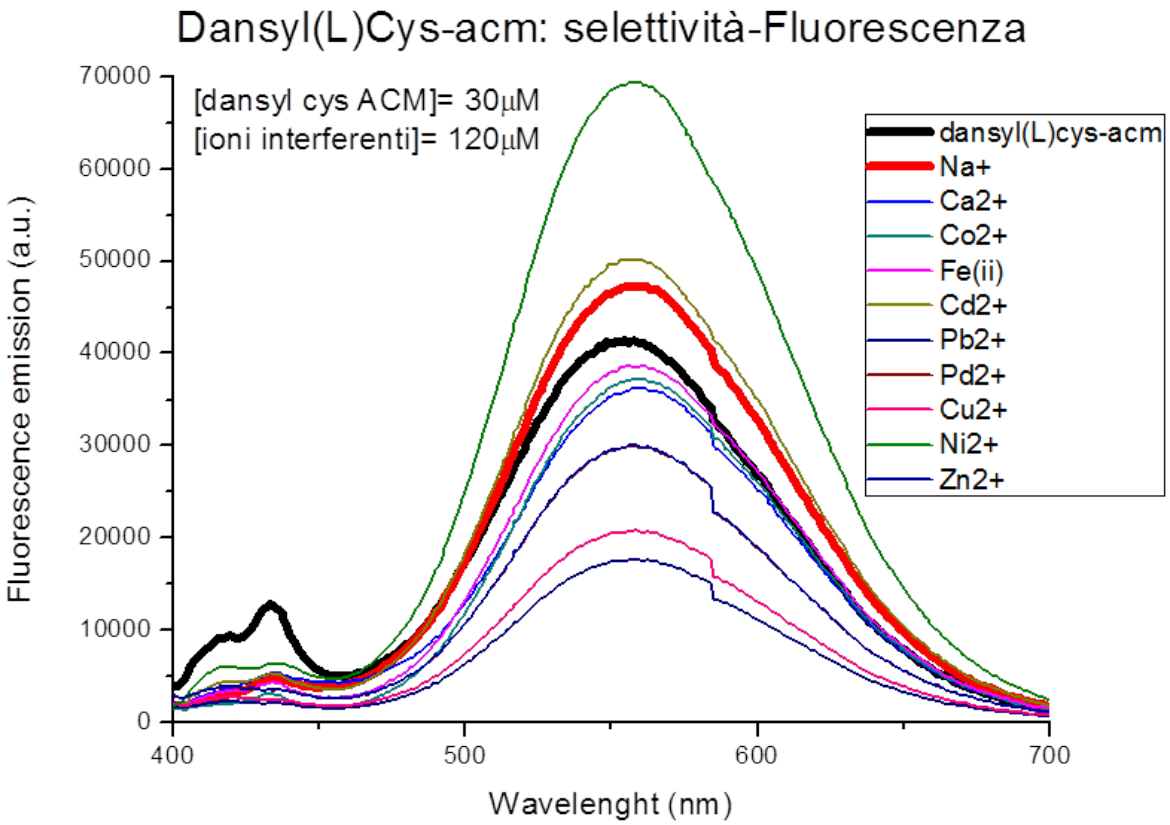

Figura 27: Spettri di emissione in fluorescenza del Composto VI in presenza di ioni interferenti Ca^{2+}, Cd^{2+}, Co^{2+}, Pb^{2+}, Fe^{2+}, Pd^{2+}, Cu^{2+}, Na^{2+}, Ni^{2+}, Zn^{2+}

I cationi Ca^{2+}, Co^{2+}, Na^{+} danno luogo ad un incremento dell'emissione di fluorescenza del composto VI di riferimento (curva nera). Nel caso particolare di Na^{+}(curva rossa), l'effetto sulla fluorescenza di tale catione risulta essere non molto pronunciato. Tutti gli altri cationi danno invece luogo ad uno spegnimento non trascurabile dell' emissione in fluorescenza della dansyl(L)Cys-Acm di riferimento (curva nera).

- **[120 µM] metalli interferenti + dansyl derivato [30 µM] + Hg^{2+} [120 µM]**

È stata la risposta sull'intensità di emissione di fluorescenza del composto VI in presenza di uguali concentrazioni (120 µM) di cationi interferenti e di Hg^{2+}. Lo scopo di tali misure è di valutare l'effetto dei cationi interferenti sulla risposta in fluorescenza del composto VI in presenza di Hg^{2+} ed in condizioni in cui il derivato dansyl(L)Cys-Acm risulta stechiometricamente in difetto (1:8) rispetto alla concentrazione dei cationi metallici (Figura 28).

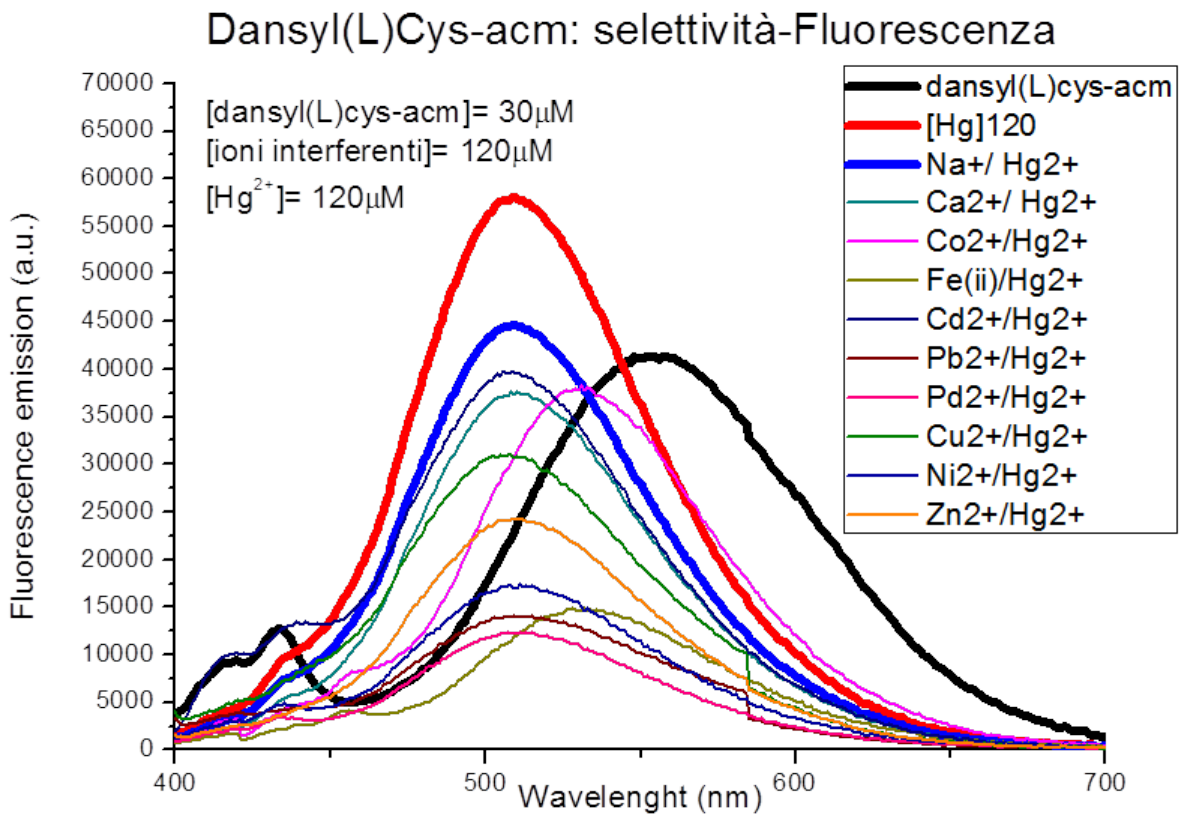

Figura 28: Spettri di emissione in fluorescenza del Composto VI in presenza di Hg^{2+} e di ioni interferenti Ca^{2+}, Cd^{2+}, Co^{2+}, Pb^{2+}, Fe^{2+}, Pd^{2+}, Cu^{2+}, Na^{2+}, Ni^{2+}, Zn^{2+}

Tutti i cationi interferiscono con la risposta in fluorescenza della dansyl(L)Cys-Acm in presenza di [Hg^{2+}] 120 μM (curva rossa). È ancora possibile osservare uno shift del picco di emissione del il derivato dansyl(L)Cys-Acm inseguito alla complessazione con Hg^{2+}, ma la presenza di alte concentrazioni di cationi genera un parziale spegnimento di tale fluorescenza.

Gli studi di selettività hanno evidenziato come per il composto I ed il composto VI si abbia una interferenza non trascurabile sugli spettri di emissione in fluorescenza dovuta alla presenza dei cationi interferenti presi in esame .Una situazione analoga è stata riscontrata in presenza di basse (0.6 μM) e d alte (120 μM) concentrazione di Hg^{2+} . Per alte concentrazioni di Hg^{2+} e di cationi interferenti si è osservato in tutti i casi l'atteso shift della posizione del picco di emissione di fluorescenza, ma con sostanziali effetti sull'intensità di emissione di tale picco.

Particolare attenzione è stata rivolta all'effetto non sottovalutabile del catione Na^{+}, uno dei cationi presenti in quantità elevate in ambiente marino, il cui effetto è stato definitivamente valutato effettuando prove di selettività in acqua di mare sintetica. Infatti, per completare quindi il pannello di saggi di selettività delle molecole prescelte (composti I e VI), sono stati effettuati titolazioni di Hg^{2+} in acqua di mare sintetica. La

composizione dell'acqua di mare sintetica utilizzata è la seguente: 0.6 M NaCl e 0.06 M $NaHCO_3$, ed il pH misurato è pari ad 8.

Per valutare le prestazioni del nostro saggio in acqua di mare sintetica la concentrazione di dansyl derivato è stata fissata 10 μM, e sono state usate concentrazioni di Hg^{2+} nell'intervallo 0.6-100 μM. Sono stati comparati gli spettri di emissione in fluorescenza nel buffer Hepes 10 mM (pH = 7.4) e quelli in acqua di mare sintetica in funzione di concentrazioni crescenti di Hg^{2+}.

Gli spettri di emissione in fluorescenza del composto I per concentrazioni crescenti di Hg^{2+} (intervallo di concentrazioni 0.6 - 100 μM) in Hepes buffer sono riportati in Figura 29. L'intensità e la posizione del picco di emissione del dansile sono funzione della concentrazione di Hg^{2+}. È stato osservato che per basse concentrazioni di Hg^{2+} (inferiori a 3.6 μM) si ha una diminuzione della emissione di fluorescenza (o quenching) e successivamente per concentrazioni crescenti una 'accensione' della intensità di emissione a 500 nm ed un blue-shift di 40 nm della massima intensità di emissione (550-500 nm).

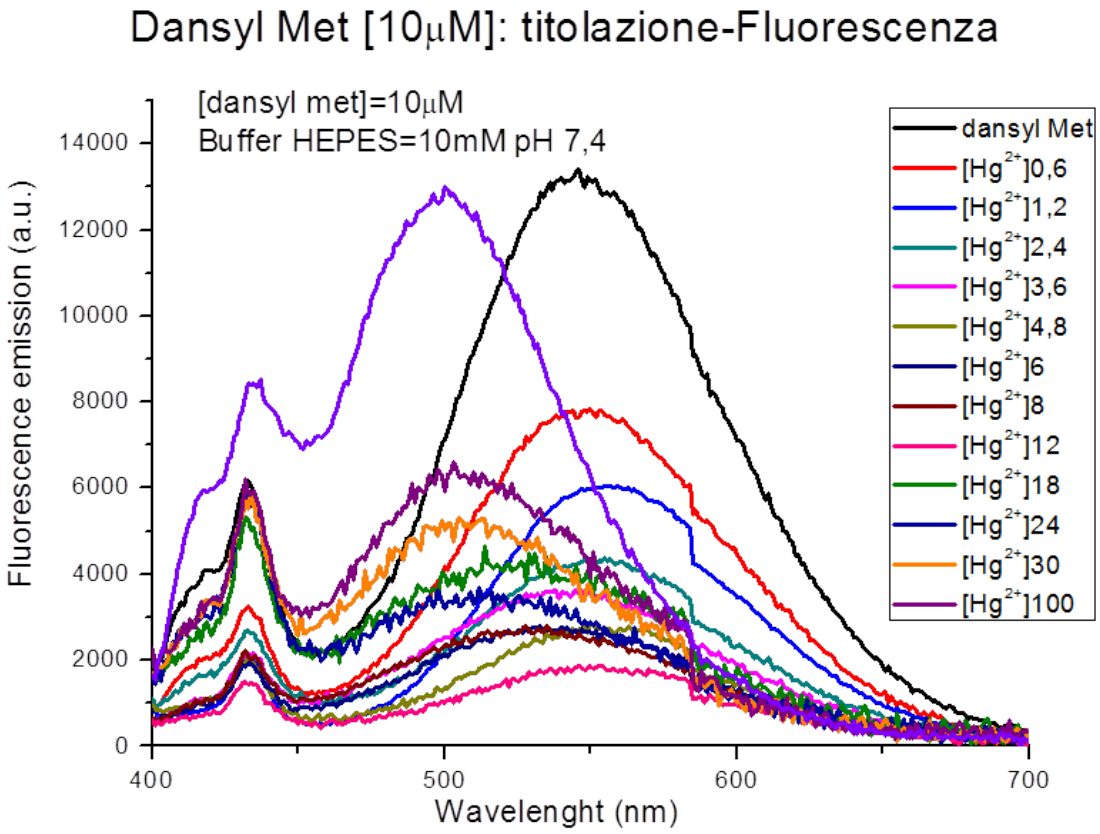

Figura 29: spettri di emissione in fluorescenza del composto I per concentrazioni crescenti di Hg^{2+} (intervallo di concentrazioni 0.6 - 100 μM) in Hepes buffer 10 mM.

Gli spettri di emissione in fluorescenza del composto I per concentrazioni crescenti di Hg^{2+} (intervallo di concentrazioni 0.6 - 100 μM) in acqua di mare sintetica sono riportati in Figura 30.

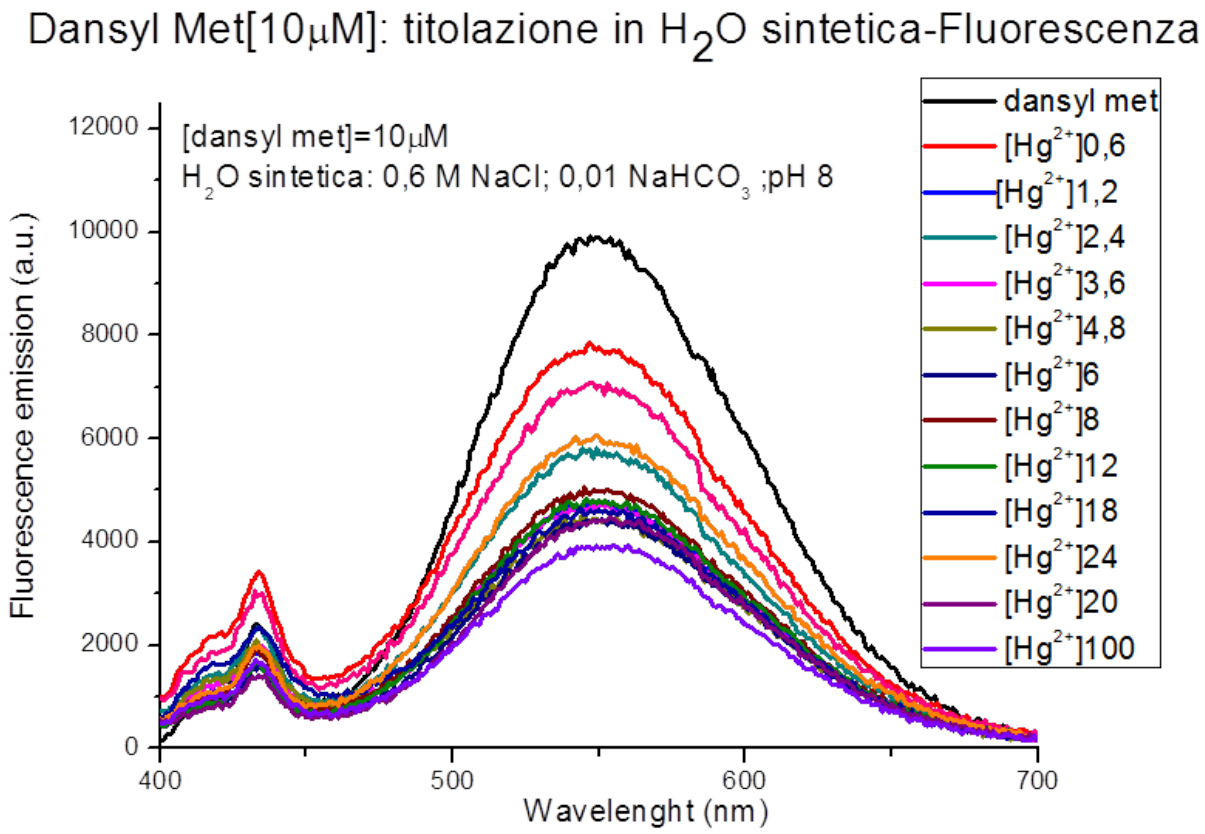

Figura 30: Spettri di emissione in fluorescenza del composto I per concentrazioni crescenti di Hg^{2+} (intervallo di concentrazioni 0.6 - 100 μM) in acqua di mare sintetica.

In acqua di mare è possibile seguire un andamento di spegnimento della fluorescenza ad un valore minimo corrispondente alla massima concentrazione di Hg^{2+} (100 μM). Probabilmente, per concentrazioni di NaCl così elevate (0.6 M), la presenza di sodio e di cloruri dà luogo ad equilibri di speciazione differenti che: i) possono interferire con la formazione del complesso Hg^{2+}/dansyl derivato; ii) possono interferire con il meccanismo di trasferimento elettronico responsabile dello shift e dell'accensione della fluorescenza.

La verifica delle performance del saggio in Hepes buffer ed acqua di mare sintetica è stata effettuata anche per il composto VI. Gli spettri di emissione in fluorescenza del composto VI per concentrazioni crescenti di Hg^{2+} (intervallo di concentrazioni 0.6 - 100 μM) in Hepes buffer sono riportati in Figura 31.

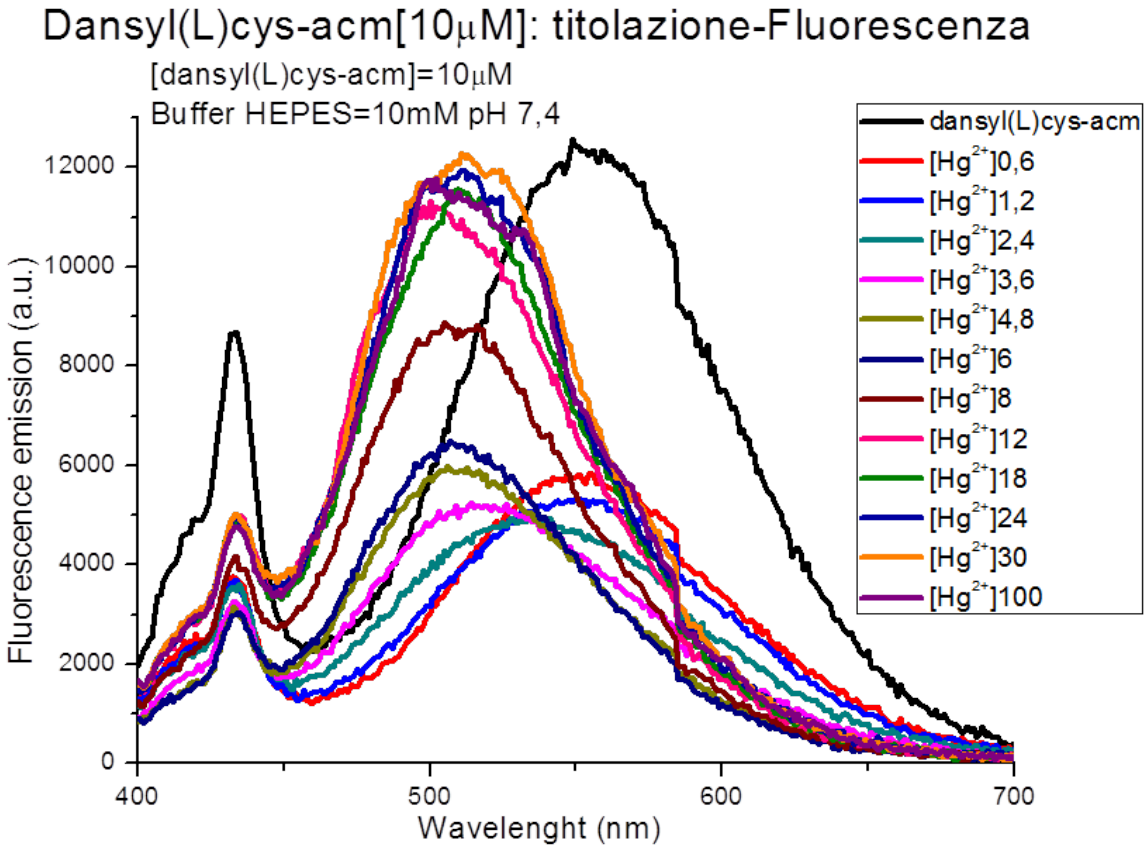

Figura 31: spettri di emissione in fluorescenza del composto VI per concentrazioni crescenti di Hg^{2+} (intervallo di concentrazioni 0.6 - 100 μM) in Hepes buffer 10 mM.

L'intensità e la posizione del picco di emissione del composto VI sono funzione della concentrazione di Hg^{2+}. È stato confermato anche per tale derivato che per basse concentrazioni di Hg^{2+} (inferiori a 3.6 μM) si ha una diminuzione dell' emissione di fluorescenza (o quenching) e successivamente per concentrazioni crescenti una 'accensione' della intensità di emissione a 500 nm ed un blue-shift di 40 nm della massima intensità di emissione (550-500 nm).

Gli spettri di emissione in fluorescenza del composto VI per concentrazioni crescenti di Hg^{2+} (intervallo di concentrazioni 0.6 - 100 μM) in acqua di mare sintetica sono riportati in Figura 32.

In acqua di mare sintetica è possibile seguire un andamento di spegnimento della fluorescenza fino ad una concentrazione di Hg^{2+} pari a 4.8 μM. A seguire, concentrazioni crescenti di Hg^{2+} generano il completo spegnimento della fluorescenza che si perde nel rumore di fondo della misure acquisite.

La risposta in fluorescenza del dansy(L)Cys-Acm, in presenza di Hg^{2+} e concentrazioni di cloruro di sodio elevate si discosta in modo rilevante da quella osservata nel buffer Hepes: valgono anche in questo caso le stesse considerazioni fatte in precedenza per la dansyl-Met.

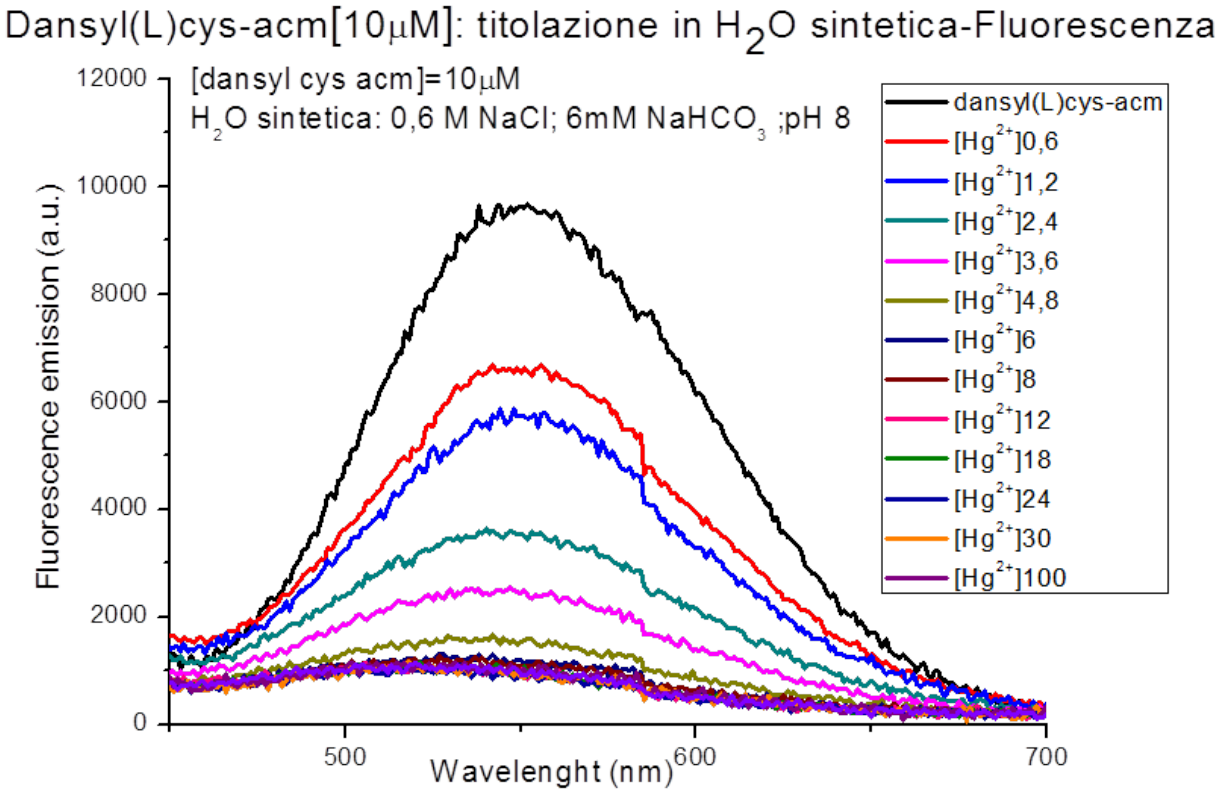

Figura 32: Spettri di emissione in fluorescenza del composto VI per concentrazioni crescenti di Hg^{2+} (intervallo di concentrazioni 0.6 - 100 μM) in acqua di mare sintetica.

Conclusioni

In conclusione:

- Un set di biomolecole è stato progettato sulla base della recente letteratura.
- È stata messa a punto una valida strategia sintetica delle biomolecole proposte che sono state ottenute in resa eccellente.
- È stato effettuata con successo la sintesi e caratterizzazione delle molecole selezionate.
- Sono stati effettuati saggi di titolazioni in presenza di concentrazioni crescenti di Hg^{2+} e valutata la risposta delle biomolecole in fluorescenza ed in assorbanza. La concentrazione di Hg^{2+} minima rilevabile nelle condizioni sperimentali qui descritte è pari a 0.6 μM (0.12 ppm).

Sono stati condotti studi di selettività in presenza di ioni interferenti a diverse concentrazioni.

Sono stati effettuati saggi di titolazione in acqua di mare sintetica per verificare la risposta delle molecole di elezione (derivati i e VI) in sistemi che mimano ambienti marini.

Le prove di selettività in acqua di mare sintetica evidenziano come non sia possibile effettuare i saggi di riconoscimento direttamente in acqua di mare. L'utilizzo dei dansyl derivati richiede quindi un pre-trattamento delle acque di mare che limiti la concentrazione salina. Sono in corso prove analitiche per valutare l'incidenza selettiva degli ioni sodio e ioni cloruro (che incide sulla speciazione dello ione Hg^{2+}), e a vari pH per verificare se modificando tale parametro è possibile ripristinare le proprietà del probe.

Saranno effettuate prove a diversa concentrazione salina, valutate le interferenze di altri cationi metallici nelle nuove soluzioni ed inquadrata una potenziale applicazione dei derivati della dansyl-Met per la determinazione di ioni mercurio in acque di transizione, ovvero in acque salmastre, originate dal mescolamento tra acque costiere e acque dolci dei fiumi, quali lagune, stagni costieri e laghi salmastri e zone di delta ed estuario.

RAPPORTO TECNICO 2

Progettazione, preparazione e caratterizzazione analitica di un biosensore in fibra ottica operante in soluzione con le biomolecole descritte nel Rapporto Tecnico 1 (RT1) per il riconoscimento di ioni Hg^{2+} in ambiente marino o in matrici acquose che mimano ambienti marini (acqua di mare sperimentale o sintetica).

Descrizione dell'attività

Il Rapporto Tecnico 2 (RT2) è orientato alla progettazione, realizzazione e caratterizzazione in laboratorio di un biosensore in fibra ottica per il riconoscimento di ioni Hg^{2+} in ambiente marino o in matrici che mimano ambienti marini.

L'attività in oggetto è stata rivolta alla progettazione di un biosensore in fibra ottica in grado di lavorare direttamente in soluzione, evitando dunque le problematiche di ancoraggio orientato delle molecole proposte nell'RT1 e degli spaziatori, e quindi del corretto binding sulla superficie.

In particolare, dovendo il biosensore essere in grado di registrare variazioni negli spettri di assorbanza e/o emissione in fluorescenza in seguito all'avvenuta complessazione con il catione metallico, sono state progettate ed implementate due diverse piattaforme tecnologiche:

- piattaforma per misure di assorbanza in soluzione;
- piattaforma per misure di fluorescenza in soluzione.

Le attività previste nel RT2 sono state così suddivise:

a - Progettazione e selezione della piattaforma tecnologica sulla base di uno studio dello stato dell'arte e dei risultati presentati nel RT1.

b - Preparazione dei biosensori in fibra ottica, sulla base della selezione effettuata in RT1.

c- Caratterizzazione in laboratorio dei biosensori in fibra ottica realizzati e quantificazione delle prestazioni.

a - Progettazione e selezione della piattaforma tecnologica sulla base di uno studio dello stato dell'arte e dei risultati riportati nell' RT1

Di seguito si riporta una descrizione delle due piattaforme progettate.

a.1 Progettazione di un biosensore per misure di assorbanza in soluzione

Il biosensore per misure di assorbanza in soluzione è stato progettato con lo scopo di ottenere informazioni circa lo spettro di assorbanza della soluzione in esame mediante una semplice misura di riflettanza,. Con

riferimento alla rappresentazione schematica riportata in Figura 1, il probe è essenzialmente composto da tre rami in fibra ottica:

i. un ramo per l'illuminazione del campione (la soluzione in esame) da collegare alla sorgente ottica mediante un connettore standard di tipo FC/PC; questo ramo è composto da un bundle di 6 fibre (dette "di illuminazione") aventi ciascuna un diametro pari a 200 µm;
ii. un ramo di raccolta della luce riflessa (anche detto di "detection"), da collegare allo spettrofotometro mediante un connettore standard di tipo FC/PC; questo ramo è composto da una sola fibra di lettura avente un diametro di 200 µm;
iii. un ramo la cui parte terminale (detta "tip" o "probe") è chiusa mediante un coperchio metallico rivestito internamente da uno strato completamente riflettente. Il gap presente tra la terminazione della fibra ottica e il coperchio riflettente (anche detta "cavità") ospita la soluzione in esame, che così è esposta alla luce emessa e riflessa nella cavità; questo ramo è composto da un bundle di 7 fibre ottiche, tutte aventi diametro pari a 200 µm, 6 di illuminazione ed 1 di detection, collocata al centro del bundle.

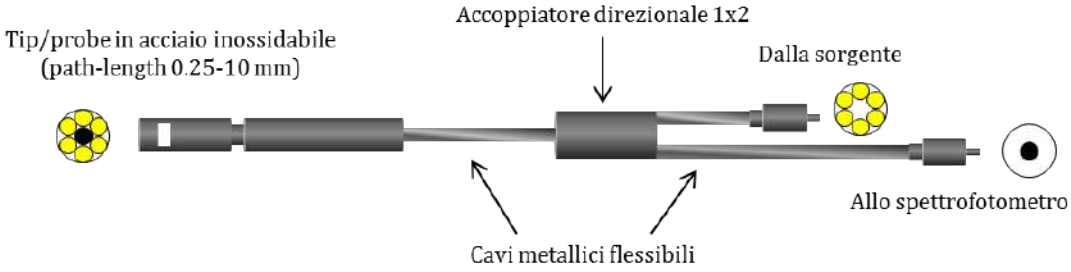

Figura 1: Rappresentazione schematica del biosensore per misure di assorbanza in soluzione.

Il biosensore, quindi, consiste essenzialmente di un probe in riflessione, che consente alla luce emessa dalla sorgente che fuoriesce dalla parte terminale della fibra di attraversare la soluzione in esame, di essere riflessa dal coperchio riflettente, di attraversare nuovamente la soluzione e rientrare nella fibra per raggiungere lo spettrofotometro (Figura 2).

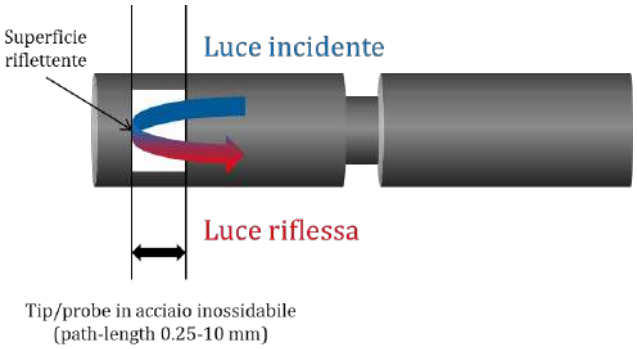

Figura 2: Rappresentazione schematica del percorso della luce all'interno del probe e della cavità a lunghezza variabile (tra 0.25 e 10 mm) del probe per misure di assorbanza in soluzione.

La fibra utilizzata per la raccolta della luce riflessa è collocata al centro del bundle di fibre di illuminazione, allo scopo di garantire un'efficiente raccolta di luce da parte del probe.

Nel punto centrale del biosensore è previsto l'inserimento di un accoppiatore direzionale 1x2, il quale ha il compito di separare le fibre nei rispettivi rami e direzionare la radiazione luminosa in ingresso verso il probe e quella riflessa verso lo spettrofotometro (Figura 1).

Per una maggiore flessibilità durante le misure di assorbanza, si è inoltre pensato di realizzare il probe in maniera tale da avere una cavità a lunghezza variabile tra un valore minimo di 0.25 mm ed un valore massimo di 10 mm (Figura 2).

Inoltre, al fine di garantire il funzionamento del biosensore anche per lunghezze d'onda nel range del basso ultravioletto (al di sotto dei 250 nm), sono state utilizzate fibre speciali (del tipo "resistenti alla solarizzazione") in grado di evitare la creazione di centri di colore dovuti all'assorbimento di luce, i quali possono portare nel tempo ad una graduale riduzione dell'intensità di luce trasmessa (ossia ad un aumento delle perdite ottiche).

Sia il ramo di illuminazione che quello di lettura sono entrambi a tenuta stagna, e sono ospitati all'interno di un rivestimento metallico flessibile realizzato in acciaio inox, mentre il probe è ospitato all'interno di un cilindro rigido, anch'esso a tenuta stagna e realizzato in acciaio inox.

a.2 Progettazione di un biosensore per misure di fluorescenza in soluzione

Il biosensore per misure di fluorescenza è stato progettato allo scopo di ottenere, mediante una semplice misura del segnale luminoso proveniente dal probe, informazioni sullo spettro di fluorescenza della soluzione in esame. Con riferimento alla rappresentazione schematica riportata in Figura 3, il biosensore per misure di fluorescenza è essenzialmente composto da tre rami in fibra ottica:

i. un ramo "d'illuminazione" del campione (per campione si intende la soluzione in esame) da collegare alla sorgente mediante un connettore standard di tipo FC/PC; al fine di massimizzare l'intensità del segnale di fluorescenza emesso dal campione, occorre illuminare lo stesso con la massima quantità di luce possibile: per questo motivo il ramo d'illuminazione è composto da un bundle di 12 fibre aventi ciascuna un diametro pari a 200 μm;
ii. un ramo di raccolta (anche detto di "detection") che trasmette il segnale di fluorescenza emesso dal campione fino allo spettrofotometro, con il quale è collegato mediante un connettore standard di tipo FC/PC; tale ramo è composto da una sola fibra di lettura con un diametro di 600 μm, un valore maggiore rispetto alle altre fibre scelto al fine di massimizzare l'efficienza di raccolta del segnale di fluorescenza (tipicamente debole) emesso dal campione;
iii. un ramo la cui parte terminale (detta "tip" o "probe") è inclinata a 45° e chiusa mediante uno speciale coperchio (detto "riflettore") che svolge il triplice compito di:

- minimizzare la quantità di luce che dall'ambiente entra nel probe interferendo con il segnale di fluorescenza emesso dal campione in esame;
- riflettere la radiazione luminosa di eccitazione nuovamente verso il campione in esame, incrementando l'intensità del segnale di fluorescenza emesso;
- convogliare nella fibra di raccolta la luce emessa anche in direzione diversa da quella della fibra di raccolta.

Il "canale" esistente tra la terminazione della fibra ottica e il riflettore ospita la soluzione in esame, esponendola al passaggio della luce e permettendone la raccolta del segnale di fluorescenza emesso. Questo ramo è composto da un bundle di 13 fibre ottiche, di cui 12 fibre di illuminazione con un diametro pari a 200 µm, ed 1 fibra di raccolta, posizionata al centro del bundle, con un diametro pari a 600 µm.

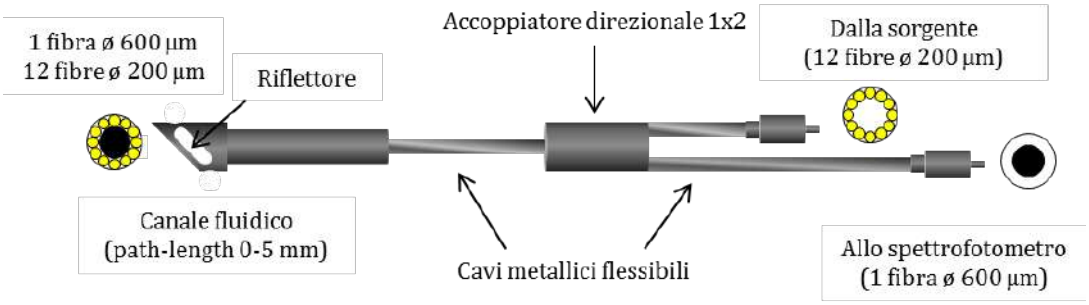

Figura 3: Rappresentazione schematica del biosensore per misure di fluorescenza in soluzione.

Il biosensore, quindi, consiste essenzialmente di un probe in riflessione, che consente alla luce emessa dalla sorgente che fuoriesce dalla terminazione della fibra di illuminare la soluzione in esame, e di generare l'emissione da parte di quest'ultima di un segnale di fluorescenza (Figura 4). Data la configurazione del probe e la caratteristica di isotropia dell'emissione, solo una piccola parte del segnale di fluorescenza rientra all'interno del probe attraverso la terminazione angolata della fibra e viene trasportata fino allo spettrofotometro dal ramo di raccolta.

Nel punto centrale del biosensore è previsto l'inserimento di un accoppiatore direzionale 1x2, il quale ha il compito di separare le fibre nei rispettivi rami e direzionare la radiazione luminosa in ingresso verso il probe e quella emessa verso lo spettrofotometro (Figura 3).

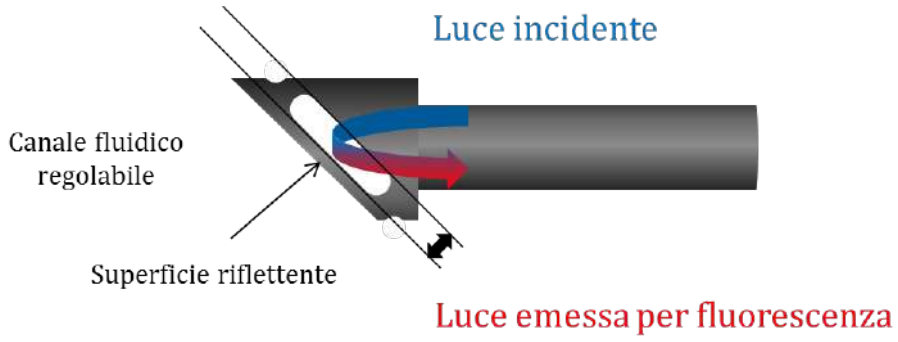

Figura 4: Rappresentazione schematica del percorso della luce all'interno del probe e del canale a lunghezza variabile (tra 0 e 5 mm) del probe per misure di fluorescenza in soluzione.

Per una maggiore flessibilità durante le misure di fluorescenza, si è inoltre pensato di realizzare il probe in maniera tale da avere una larghezza variabile del canale da 0 a 5 mm.

Inoltre, al fine di garantire il funzionamento del biosensore anche per lunghezze d'onda nel range del basso ultravioletto (al di sotto dei 250 nm) le fibre ottiche utilizzate sono fibre speciali (del tipo "resistenti alla solarizzazione") in grado di evitare la creazione di centri di colore dovuti all'assorbimento di luce, i quali possono portare nel tempo ad una graduale riduzione dell'intensità di luce trasmessa (ossia ad un aumento delle perdite).

Sia il ramo di illuminazione che quello di lettura sono entrambi a tenuta stagna, e sono ospitati all'interno di un rivestimento metallico flessibile realizzato in acciaio inox, mentre il probe è ospitato all'interno di un cilindro rigido, anch'esso a tenuta stagna e realizzato in acciaio inox.

b. Preparazione dei biosensori in fibra ottica.

Di seguito si riporta una descrizione delle due piattaforme realizzate.

b.1 Preparazione di un biosensore per misure di assorbanza in soluzione

Il biosensore per misure di assorbanza in soluzione è stato realizzato secondo le specifiche definite in fase di progettazione. Il biosensore per misure di assorbanza è stato realizzato allo scopo di ottenere informazioni sullo spettro di assorbanza della soluzione in esame mediante una semplice misura del segnale luminoso proveniente dal probe. Il biosensore consiste essenzialmente di un probe in trasmissione, che consente alla luce emessa dalla sorgente che fuoriesce dalla parte terminale della fibra di attraversare la soluzione in esame, di essere riflessa dal coperchio riflettente, di attraversare nuovamente la soluzione e rientrare nella fibra per raggiungere lo spettrofotometro (Figura 5). Come descritto in fase di progettazione, il biosensore per misure di assorbanza è costituito da tre rami:

i. un ramo per l'illuminazione della soluzione in esame da collegare alla sorgente ottica mediante un connettore standard di tipo FC/PC; questo ramo è composto da un bundle di 6 fibre (dette "di illuminazione") aventi ciascuna un diametro pari a 200 μm;

ii. un ramo di raccolta ("detection") della luce riflessa, da collegare allo spettrofotometro mediante un connettore standard di tipo FC/PC; questo ramo è composto da una sola fibra di lettura avente un diametro di 200 μm;

iii. un ramo la cui parte terminale (detta "tip" o "probe") è chiusa mediante un coperchio metallico rivestito internamente da uno strato completamente riflettente. Il gap presente tra la terminazione della fibra ottica e il coperchio riflettente (anche detta "cavità") ospita la soluzione in esame, che così è esposta alla luce emessa e riflessa nella cavità; questo ramo è composto da un bundle di 7 fibre ottiche, tutte aventi diametro pari a 200 μm, 6 di illuminazione ed una di detection, collocata al centro del bundle; per una maggiore flessibilità durante le misure di assorbanza, il probe è dotato di una cavità a lunghezza variabile tra un valore minimo di 0.25 mm ed un valore massimo di 10 mm (Figura 6).

Un accoppiatore direzionale 1x2 separa le fibre nei rispettivi rami di illuminazione e raccolta, direzionando la radiazione luminosa in ingresso verso il probe e quella riflessa verso lo spettrofotometro (Figura 5).

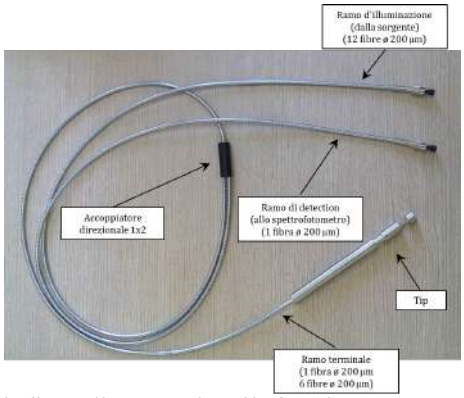

Figura 5: Foto del biosensore per misure di assorbanza in soluzione.

Al fine di garantire il funzionamento del biosensore anche per lunghezze d'onda nel range del basso ultravioletto (al di sotto dei 250 nm) le fibre ottiche utilizzate sono fibre speciali (del tipo "resistenti alla solarizzazione") in grado di evitare la creazione di centri di colore dovuti all'assorbimento di luce, i quali possono portare nel tempo ad una graduale riduzione dell'intensità di luce trasmessa (ossia ad un aumento delle perdite). Sia il ramo di illuminazione che quello di lettura sono entrambi a tenuta stagna, e sono ospitati all'interno di un rivestimento metallico flessibile realizzato in acciaio inox (Figura 5), mentre il probe è ospitato all'interno di un cilindro rigido, anch'esso a tenuta stagna e realizzato in acciaio inox (Figura 6).

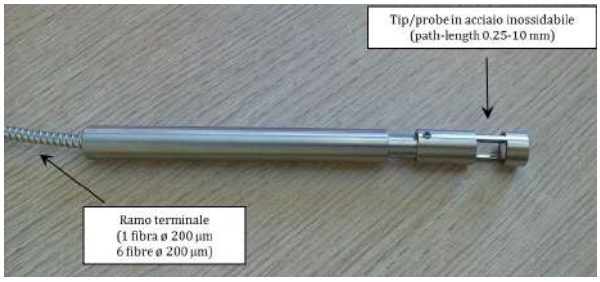

Figura 6: Particolare del probe (parte terminale) del biosensore per misure di assorbanza in soluzione.

b.2 Preparazione di un biosensore per misure di fluorescenza in soluzione

Il biosensore per misure di fluorescenza in soluzione è stato realizzato secondo le specifiche definite in fase di progettazione. Il biosensore per misure di fluorescenza è stato realizzato allo scopo di ottenere informazioni sullo spettro di fluorescenza della soluzione in esame mediante una semplice misura del segnale luminoso proveniente dal probe. Il biosensore consiste essenzialmente di un probe in riflessione, che consente alla luce emessa dalla sorgente che fuoriesce dalla parte terminale della fibra di attraversare la soluzione in esame, generando in tal modo l'emissione da parte di quest'ultima di un segnale di fluorescenza, raccolto nuovamente dal probe e trasmesso ad uno spettrofotometro per la rilevazione (Figura 7).

Come descritto in fase di progettazione, il biosensore per misure di assorbanza è costituito da tre rami:

i. un ramo "d'illuminazione" del campione (la soluzione in esame) da collegare alla sorgente mediante un connettore standard di tipo FC/PC; al fine di massimizzare l'intensità del segnale di fluorescenza emesso dal campione, occorre illuminare lo stesso con la massima quantità di luce possibile: per questo motivo il ramo d'illuminazione è composto da un bundle di 12 fibre aventi ciascuna un diametro pari a 200 μm;

ii. un ramo di raccolta (o di "detection") che trasmette il segnale di fluorescenza emesso dal campione fino allo spettrofotometro, con il quale è collegato mediante un connettore standard di tipo FC/PC; tale ramo è composto da una sola fibra di lettura con un diametro di 600 μm, un valore maggiore rispetto alle altre fibre scelto al fine di massimizzare l'efficienza di raccolta del segnale di fluorescenza (tipicamente debole) emesso dal campione;

iii. un ramo la cui parte terminale (detta "tip" o "probe") è inclinata a 45° e chiusa mediante uno speciale coperchio (detto "riflettore") che svolge il duplice compito di:
   - evitare che la luce dall'ambiente possa entrare nel probe ed interferire con il segnale di fluorescenza emesso dal campione in esame;
   - riflettere la radiazione luminosa di eccitazione nuovamente verso il campione in esame, incrementandone l'intensità del segnale di fluorescenza emesso.

Il "canale" esistente tra la terminazione della fibra ottica e il riflettore ospita la soluzione in esame, esponendola al passaggio della luce e permettendone la raccolta del segnale di fluorescenza emesso (Figura 8). Questo ramo è composto da un bundle di 13 fibre ottiche, di cui 12 fibre di illuminazione con un diametro pari a 200 μm, ed 1 fibra di raccolta, posizionata al centro del bundle, con un diametro pari a 600 μm.

Un accoppiatore direzionale 1x2 separa le fibre nei rispettivi rami di illuminazione e raccolta, direzionando la radiazione luminosa in ingresso verso il probe e quella riflessa verso lo spettrofotometro (Figura 7).

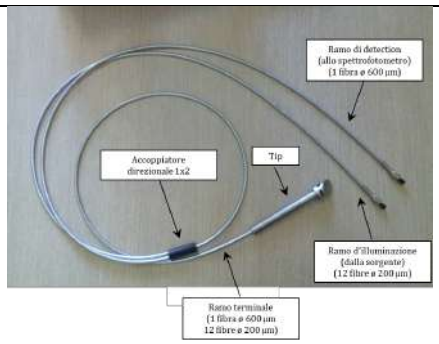

Figura 7: Sensore per misure di fluorescenza in soluzione.

Al fine di garantire il funzionamento del biosensore anche per lunghezze d'onda nel range del basso ultravioletto (al di sotto dei 250 nm) le fibre ottiche utilizzate sono fibre speciali (del tipo "resistenti alla solarizzazione") in grado di evitare la creazione di centri di colore dovuti all'assorbimento di luce, i quali possono portare nel tempo ad una graduale riduzione dell'intensità di luce trasmessa (ossia ad un aumento delle perdite). Sia il ramo di illuminazione che quello di lettura sono entrambi a tenuta stagna, e sono ospitati all'interno di un rivestimento metallico flessibile realizzato in acciaio inox (Figura 7), mentre il probe è ospitato all'interno di un cilindro rigido, anch'esso a tenuta stagna e realizzato in acciaio inox (Figura 8).

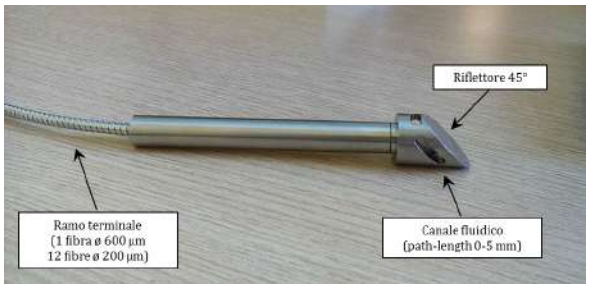

Figura 8: Particolare del probe (parte terminale) del biosensore per misure di fluorescenza in soluzione.

c. Caratterizzazione in laboratorio dei biosensori in fibra ottica realizzati e quantificazione delle prestazioni

Di seguito si riporta una descrizione della procedura di caratterizzazione adottata per i due biosensori realizzati e le rispettive prestazioni raggiunte.

c.1 Caratterizzazione in laboratorio del biosensore per misure di assorbanza in soluzione

Il biosensore per misure di assorbanza è stato caratterizzato attraverso la raccolta di misure di riflettanza (dalla quale è stato poi calcolato lo spettro di assorbanza) immergendolo in soluzioni contenenti il composto selezionato nell'OR1, vale a dire la dansyl metionina (in seguito indicato come *DansylMet*) con diverse concentrazioni di ioni Hg^{2+}.

Nel seguito di questo paragrafo sono riportati in dettaglio:

- le modalità di acquisizione degli spettri ottici;
- i dati sperimentali ottenuti e le relative curve di calibrazione.

c.1.1 Modalità di acquisizione degli spettri ottici per misure di assorbanza in soluzione

Ciascuna delle soluzioni impiegate per la caratterizzazione in laboratorio del probe per misure di assorbanza è posta all'interno di un provettone a fondo conico con una capacità di 50 mL.

Le soluzioni impiegate per la caratterizzazione (per un volume di 10 mL) sono state:

- Hepes filtrato, utilizzato come soluzione "buffer";
- DansylMet disciolta in Hepes con una concentrazione 30 μM;
- DansylMet (come sopra, 30 μM) con disciolte all'interno diverse concentrazioni di ioni Hg^{2+}, in un intervallo compreso tra 0.01 μM e 6 μM.

In una prima fase, il sensore per misure di assorbanza è stato immerso all'interno della soluzione buffer e in alcune soluzioni contenenti DansylMet e ioni Hg^{2+} per determinare il valore ottimale del tempo di integrazione dello spettrofotometro[1] così da massimizzare il segnale riflesso nell'intervallo di lunghezze d'onda di interesse (dove l'assorbanza delle soluzioni testate risulta essere più alta) e al tempo stesso evitare di incorrere nella saturazione dello spettrofotometro.

Una volta stabilito il tempo di integrazione ottimale, si spegne la sorgente e si acquisisce (e si salva su file) il segnale di "dark", vale a dire il segnale acquisito dallo spettrofotometro quando il biosensore non è illuminato dalla luce emessa dalla sorgente, rappresentando in pratica il rumore di sottofondo dello strumento di acquisizione. A questo punto, riaccesa (meccanicamente) la sorgente, si immerge il biosensore all'interno della soluzione "buffer" e si acquisisce il segnale riflesso (detto "scope"), avendo cura di impostare la correzione (sottrazione) del segnale di "dark" acquisito in precedenza (ottenendo lo "scope differenziale S_d").

[1] Per maggiori informazioni sullo spettrofotometro utilizzato, nonché sulle sorgenti, si faccia riferimento alla sezione dedicata nell'OR3.

$$S_d = (\text{scope} - \text{dark})$$

Tale segnale viene acquisito (e salvato su file) come segnale di riferimento (detto "reference"), per le successive acquisizioni che convertiranno in automatico la lettura del segnale riflesso in una lettura di assorbanza, secondo la formula:

$$A = -\log_{10}\left(\frac{\text{scope} - \text{dark}}{\text{reference} - \text{dark}}\right)$$

Si procede quindi all'immersione del probe all'interno delle soluzioni contenenti DansylMet e concentrazioni crescenti di ioni Hg^{2+}, nell'intervallo 0.01 μM e 6 μM. Ad ogni immersione, si effettua l'acquisizione e il salvataggio di un file, che memorizza, oltre alle informazioni sulle impostazioni di acquisizione, anche il segnale di "dark", il segnale di "reference", il segnale riflesso e l'assorbanza calcolata.
Per ogni concentrazione sono effettuate diverse immersioni successive, intervallate tra loro di alcune decine di secondi, allo scopo di ottenere uno spettro di assorbanza calcolato come media su più acquisizioni e quindi di minimizzare eventuali errori di misura.
Nel passaggio tra due diverse soluzioni, si procede con un rapido lavaggio del probe con acqua distillata (DDW) allo scopo di eliminare eventuali residui di sostanze lasciate dalla soluzione interrogata in precedenza.

Dati sperimentali ottenuti e relative curve di calibrazione per misure di assorbanza in soluzione

In Figura 9 sono riportati gli spettri acquisiti per tre diverse soluzioni: Hepes (in rosso), Dansyl-Met 30 μM (in verde), Dansyl-Met 30 μM con aggiunta di ioni Hg^{2+} 0.6 μM (in ciano), riportati secondo il calcolo dello "scope differenziale" e dell'assorbanza precedentemente descritti. Nel grafico relativo allo "scope differenziale" è possibile individuare un abbattimento dello spettro riflesso nel passaggio da Hepes a Dansyl-Met (anche con aggiunta di ioni Hg^{2+}). Il dato è interpretabile ancor meglio se si fa riferimento al grafico dell'assorbanza, a destra. Nel caso dell'Hepes, adottato come segnale di riferimento, il calcolo dell'assorbanza produce un valore nullo su tutto l'intervallo acquisito. Per le soluzioni contenenti DansylMet sono invece apprezzabili due picchi di assorbanza, localizzati intorno ai 247 nm e ai 330 nm. In corrispondenza di queste due lunghezze d'onda sono state tracciate delle linee tratteggiate, riportate anche nel grafico dello "scope differenziale", così da appurare che il valore di assorbanza letto (a destra) non sia condizionato da un segnale di partenza (a sinistra) troppo debole o saturato.

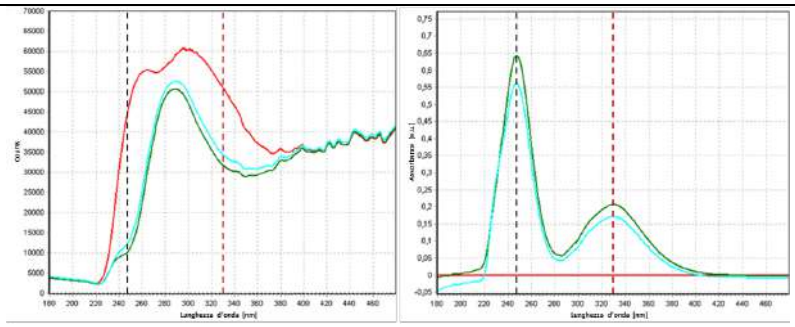

Figura 9: Scope differenziale e assorbanza per tre diverse soluzioni: Hepes (in rosso), Dansyl-Met 30 µM (in verde), Dansyl-Met 30 µM con aggiunta di ioni Hg^{2+} 0.6 µM (in ciano).

L'andamento dell'assorbanza ottenuta con il biosensore per le seguenti concentrazioni: Dansyl-Met 30 µM e Dansyl-Met 30 µM con aggiunta di ioni Hg^{2+} con concentrazioni crescenti: 0.01 – 0.05 – 0.1 – 0.3 – 0.6 – 1.2 – 2.4 – 3 – 6 µM, è riportato in Figura 10.

Tale andamento è stato confrontato con quello ottenuto attraverso l'uso di uno spettrofluorimetro (Reader) EnSpire (Perkin Elmer), riportato in Figura 11. È possibile apprezzare un incremento di un fattore 2 nell'assorbanza misurata con il biosensore in fibra ottica dovuto all'utilizzo di un cammino ottico circa il doppio rispetto a quello usato nel Reader.

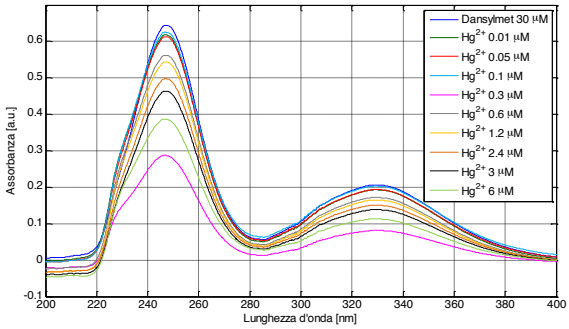

Figura 10: Andamento dell'assorbanza ottenuta con il biosensore in fibra ottica per soluzioni contenenti Dansyl-Met 30 µM con aggiunta di ioni Hg^{2+} con concentrazioni crescenti nell'intervallo 0 – 6 µM.

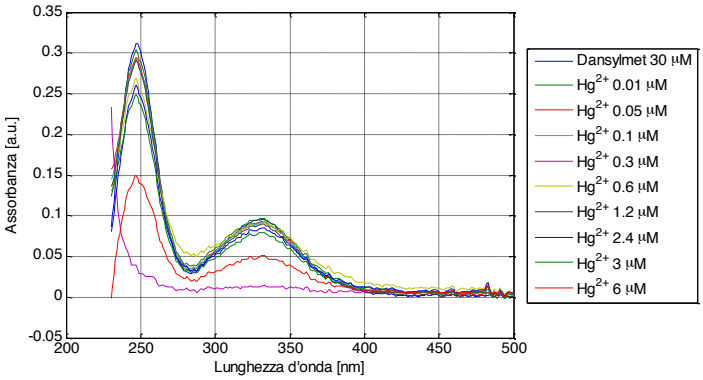

Figura 11: Andamento dell'assorbanza ottenuta con il Reader da banco per soluzioni contenenti Dansyl-Met 30 µM con aggiunta di ioni Hg^{2+} con concentrazioni crescenti nell'intervallo 0 – 6 µM.

Come accennato in precedenza, le acquisizioni svolte con il biosensore per misure di assorbanza hanno rivelato la presenza di due picchi nello spettro di assorbanza della Dansyl-Met (con aggiunta di ioni Hg^{2+}), localizzati intorno ai 247 nm e ai 330 nm.

Per apprezzare le differenze esistenti tra gli spettri relativi alle diverse concentrazioni di ioni Hg^{2+} si è deciso di individuare la posizione (in lunghezza d'onda) e l'assorbanza (in ampiezza) del punto di massimo di ciascuno dei due picchi individuati.

Per il picco centrato intorno ai 247 nm, il grafico relativo alla lunghezza d'onda è riportato in Figura 12. È immediato osservare che, a parte un'anomalia comparsa in corrispondenza della concentrazione 0.3 μM, non si ha alcuno spostamento della lunghezza d'onda del picco di assorbanza al variare della concentrazione. Si è deciso pertanto di non eseguire ulteriori analisi su questo parametro, focalizzando l'attenzione sul valore di assorbanza di picco.

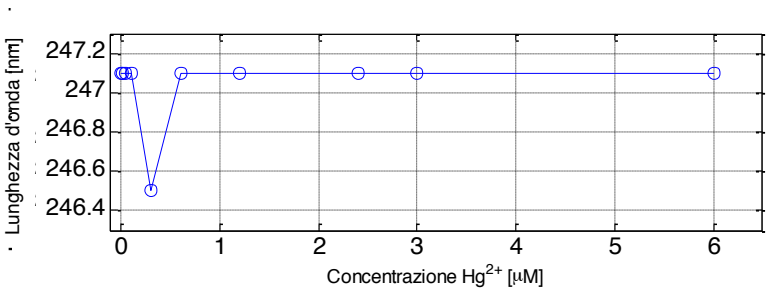

Figura 12: Andamento della lunghezza d'onda del punto di massima assorbanza (picco intorno ai 247 nm) ottenuta con il biosensore in fibra ottica per soluzioni contenenti Dansyl-Met 30 μM con aggiunta di ioni Hg^{2+} con concentrazioni crescenti nell'intervallo 0 – 6 μM.

L'assorbanza misurata nel picco a più basse lunghezze d'onda è riportata nel grafico mostrato in Figura 13. È possibile riscontrare un andamento complessivo decrescente dell'assorbanza massima all'aumentare della concentrazione di ioni Hg^{2+}. Nel grafico è evidenziato il punto a 0.3 μM, che non rispetta l'andamento monotono. Tale comportamento anomalo si è presentato nel corso di diverse prove sperimentali (anche con il Reader) eseguite su soluzioni preparate in momenti diversi, anche per concentrazioni vicine a 0.3 μM (0.2 e 0.4 μM). Ciò suggerisce che nell' intorno di questa concentrazione possa verificarsi una variazione della stechiometria e/o della conseguente geometria del complesso.

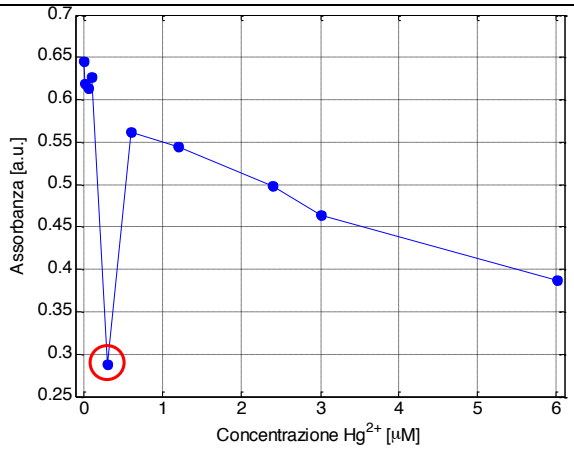

Figura 13: Andamento dell'assorbanza nel punto di massimo (picco intorno ai 247 nm) ottenuta con il biosensore in fibra ottica per soluzioni contenenti Dansyl-Met 30 µM con aggiunta di ioni Hg^{2+} con concentrazioni crescenti nell'intervallo 0 – 6 µM. È evidenziato il punto anomalo a 0.3 µM.

Allo scopo di verificare la capacità del biosensore di rilevare la presenza di basse concentrazioni di ioni Hg^{2+}, si è deciso di eseguire delle nuove prove focalizzandoci sulle basse concentrazioni, nell'intervallo 0 – 0.1 µM, come riportato in Figura 14. Tale grafico mostra l'assenza di linearità tra i punti 0, 0.01, 0.05 e 0.1 µM, indicando che in questo intervallo di concentrazioni non è possibile interpolare le concentrazione di ioni Hg^{2+} da misure di assorbanza. Si è deciso pertanto di non inserire queste concentrazioni nella successiva curva di calibrazione.

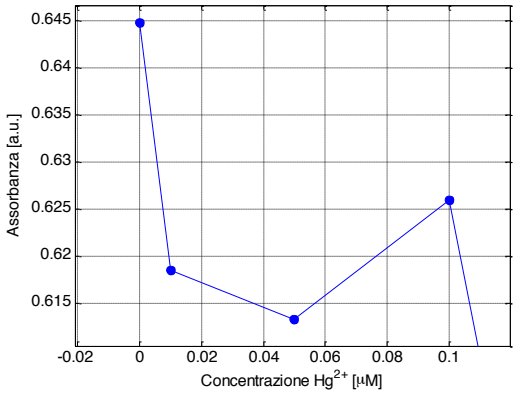

Figura 14: Andamento dell'assorbanza nel punto di massimo (picco intorno ai 247 nm) ottenuta con il biosensore in fibra ottica per soluzioni contenenti Dansyl-Met 30 µM con aggiunta di ioni Hg^{2+} con concentrazioni crescenti nell'intervallo 0 – 0.1 µM.

Sulla base di quanto mostrato in precedenza, si è deciso di costruire una curva di calibrazione con fitting lineare nell'intervallo 0.6 – 6 µM, scartando così le concentrazioni al di sotto di questo intervallo che non rispettano un andamento lineare (0 – 0.3 µM).

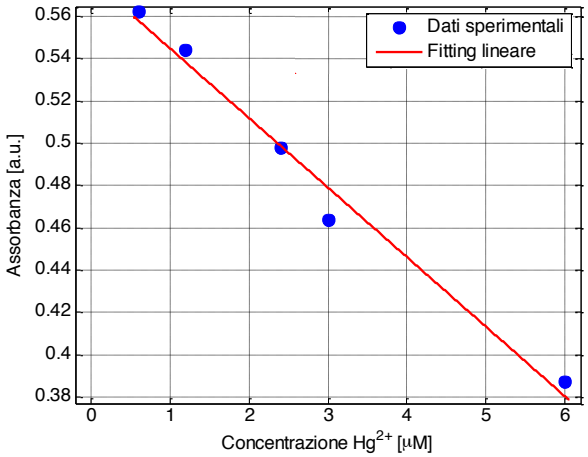

Figura 15: Curva di calibrazione e fitting lineare: assorbanza nel punto di massimo (picco intorno ai 247 nm) ottenuta con il biosensore in fibra ottica per soluzioni contenenti Dansyl-Met 30 µM con aggiunta di ioni Hg^{2+} con concentrazioni crescenti nell'intervallo 0.6 – 6 µM.

Prendendo in considerazione il grafico mostrato in Figura 15, è possibile constatare la bontà del fitting lineare, i cui parametri sono riportati nella Tabella 1 mostrata qui di seguito. In particolare, si può apprezzare un buon valore del parametro R^2, superiore al 98%.

Linear model Poly1:
f(x) = p1*x + p2
Coefficients (with 95% confidence bounds):
p1 = -0.0329 (-0.04083, -0.02497)
p2 = 0.5779 (0.5522, 0.6036)
Goodness of fit:
SSE: 0.0003298
R-square: 0.9831
Adjusted R-square: 0.9774
RMSE: 0.01049

Tabella 1: Parametri di fitting della curva di calibrazione per l'assorbanza nel punto di massimo (picco intorno ai 247 nm) ottenuta con il biosensore in fibra ottica per soluzioni contenenti Dansyl-Met 30 µM con aggiunta di ioni Hg^{2+} con concentrazioni crescenti nell'intervallo 0.6 – 6 µM.

Per il picco concentrato intorno ai 330 nm, il grafico relativo alla lunghezza d'onda è riportato in Figura 16. È immediato osservare che, a parte un'anomalia comparsa in corrispondenza della concentrazione 0.3 µM (come nel caso precedente), non si ha alcuno spostamento della lunghezza d'onda del picco di assorbanza al

variare della concentrazione. Si è deciso pertanto di non investigare ulteriormente questo parametro, focalizzando l'attenzione sul valore di assorbanza di picco.

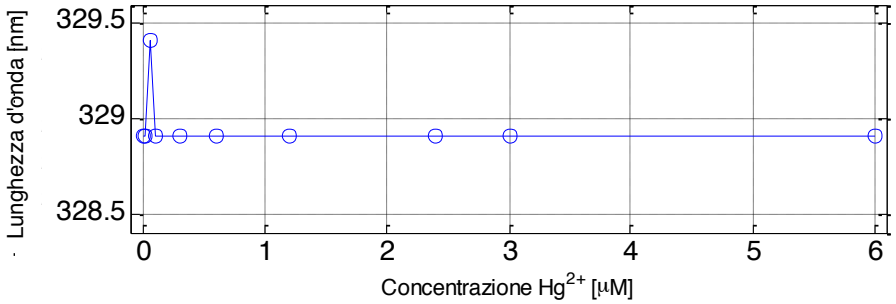

Figura 16: Andamento della lunghezza d'onda del punto di massima assorbanza locale (picco intorno ai 330 nm) ottenuta con il biosensore in fibra ottica per soluzioni contenenti Dansyl-Met 30 µM con aggiunta di ioni Hg^{2+} con concentrazioni crescenti nell'intervallo 0 – 6 µM.

L'assorbanza misurata nel picco a più alte lunghezze d'onda è riportata nel grafico mostrato in Figura 17. È possibile riscontrare un andamento complessivo decrescente dell'assorbanza di picco all'aumentare della concentrazione di ioni Hg^{2+}. Nel grafico è possibile individuare l'anomalia del punto a 0.3 µM, che non rispetta l'andamento monotono.

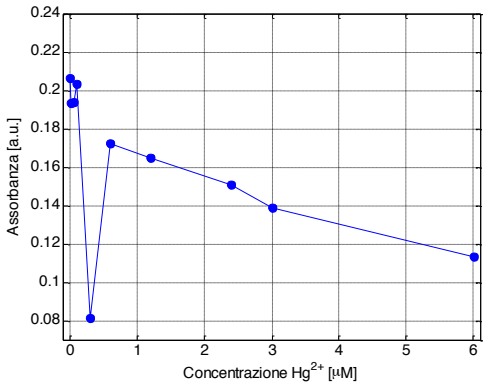

Figura 17: Andamento dell'assorbanza nel punto di massimo (picco intorno ai 330 nm) ottenuta con il biosensore in fibra ottica per soluzioni contenenti Dansyl-Met 30 µM con aggiunta di ioni Hg^{2+} con concentrazioni crescenti nell'intervallo 0 – 6 µM.

Allo scopo di verificare la capacità del biosensore di rilevare la presenza di basse concentrazioni di Hg^{2+} mediante misure di assorbanza si è deciso delle nuove prove focalizzandoci sulle basse concentrazioni, nell'intervallo 0 – 0.1 µM, come riportato in Figura 14. Tale grafico mostra l'assenza di linearità tra i punti 0, 0.01, 0.05 e 0.1 µM, permettendo di constatare che in questo intervallo di concentrazioni non è possibile interpolare le concentrazioni di ioni Hg^{2+} in soluzione a partire da una misura di assorbanza. Si è deciso pertanto di non inserire queste concentrazioni nella successiva curva di calibrazione.

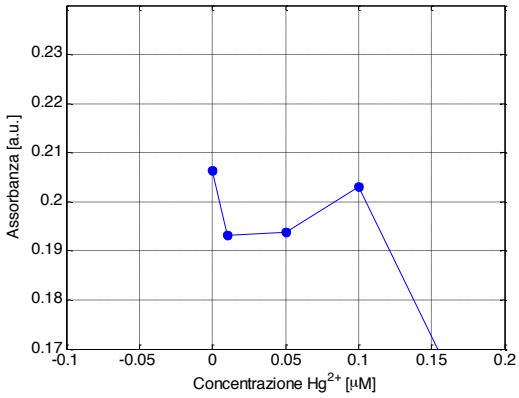

Figura 18: Andamento dell'assorbanza nel punto di massimo (picco intorno ai 330 nm) ottenuta con il biosensore in fibra ottica per soluzioni contenenti Dansyl-Met 30 μM con aggiunta di ioni Hg^{2+} con concentrazioni crescenti nell'intervallo 0 – 0.1 μM.

Sulla base di quanto mostrato in precedenza, si è deciso di costruire una curva di calibrazione con fitting lineare nell'intervallo 0.6 – 6 μM, scartando così le concentrazioni al di sotto di questo intervallo che non rispettano un andamento lineare (0 – 0.3 μM).

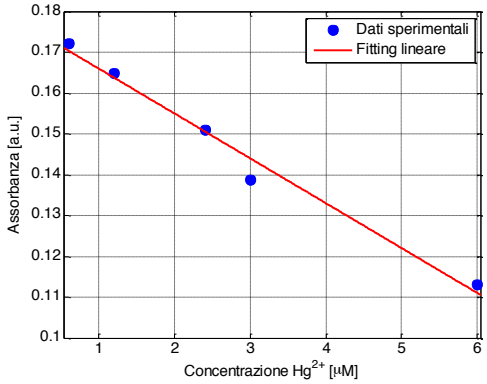

Figura 19: Curva di calibrazione e fitting lineare dell'assorbanza nel punto di massimo (picco intorno ai 330 nm) ottenuta con il biosensore in fibra ottica per soluzioni contenenti Dansyl-Met 30 μM con aggiunta di ioni Hg^{2+} con concentrazioni crescenti nell'intervallo 0.6 – 6 μM.

Prendendo in considerazione il grafico mostrato in Figura 19, è possibile constatare la bontà del fitting lineare, i cui parametri sono riportati nella Tabella 2 mostrata qui di seguito. In particolare, si può apprezzare un buon valore del parametro R^2, superiore al 98%.

Linear model Poly1:
f(x) = p1*x + p2
Coefficients (with 95% confidence bounds):
p1 = -0.01099 (-0.0136, -0.008371)
p2 = 0.177 (0.1685, 0.1855)

Goodness of fit:
SSE: 3.59e-005
R-square: 0.9835
Adjusted R-square: 0.978
RMSE: 0.003459

Tabella 2: Parametri di fitting della curva di calibrazione dell'assorbanza nel punto di massimo locale (picco intorno ai 330 nm) ottenuta con il biosensore in fibra ottica per soluzioni contenenti Dansyl-Met 30 μM con aggiunta di ioni Hg^{2+} con concentrazioni crescenti nell'intervallo 0.6 – 6 μM.

c.1.2 Caratterizzazione in laboratorio del biosensore per misure di fluorescenza in soluzione

Il biosensore per misure di fluorescenza è stato caratterizzato attraverso misure di riflettanza (dalla quale è stato poi calcolato lo spettro di fluorescenza) immergendolo in soluzioni contenenti il composto descritto nel RT1, vale a dire la Dansyl-Met con diverse concentrazioni di ioni Hg^{2+}.

Nel seguito sono riportati in dettaglio, nell'ordine:

- le modalità di acquisizione degli spettri ottici;
- i dati sperimentali ottenuti e le relative curve di calibrazione.

c.2.1 Modalità di acquisizione degli spettri ottici per misure di fluorescenza in soluzione

Ciascuna delle soluzioni impiegate per la caratterizzazione in laboratorio del probe per misure di fluorescenza è posta all'interno di provette a fondo conico con una capacità di 50 mL.

Le soluzioni impiegate per la caratterizzazione (per un volume di 10 mL) sono state:

- Hepes filtrato, utilizzato come soluzione "buffer";
- Dansyl-Met disciolta in Hepes con una concentrazione 30 μM;
- Dansyl-Met (come sopra, 30 μM) con disciolte all'interno diverse concentrazioni di ioni Hg^{2+}, in un intervallo compreso tra 0.01 μM e 6 μM.

In una prima fase, il sensore per misure di fluorescenza è stato immerso all'interno della soluzione buffer e in alcune soluzioni contenenti Dansyl-Met e ioni Hg^{2+} per determinare il valore ottimale del tempo di integrazione dello spettrofotometro, così da massimizzare il segnale riflesso nell'intervallo di lunghezze d'onda di interesse (dove la fluorescenza emessa dalle soluzioni testate risulta essere più alta) e al tempo stesso evitare di incorrere nella saturazione dello spettrofotometro.

Una volta stabilito il tempo di integrazione ottimale, si spegne la sorgente e si acquisisce (e si salva su file) il segnale di "dark", vale a dire il segnale acquisito dallo spettrofotometro quando il biosensore non è raggiunto dalla luce emessa dalla sorgente, rappresentando in pratica il rumore di sottofondo dello strumento di acquisizione. A questo punto, riaccesa (meccanicamente) la sorgente, si immerge il biosensore all'interno

della soluzione "buffer" e si acquisisce il segnale riflesso (detto "scope"), che viene assunto come il nuovo segnale di "dark". Tale segnale sarà poi sottratto mediante una misura differenziale allo scope acquisito nelle soluzioni contenenti Dansyl-Met e Hg^{2+}, ottenendo così lo "scope differenziale" che rappresenta il segnale di fluorescenza, secondo la definizione:

$$\text{Fluorescenza} = S_d = (\text{scope} - \text{dark})$$

La fluorescenza, secondo questa definizione, costituisce dunque la differenza tra il segnale acquisito in riflessione interrogando soluzioni contenenti Dansyl-Met e Hg^{2+} e il segnale acquisito in riflessione interrogando la soluzione "buffer" (Hepes).

Si procede quindi all'immersione del probe all'interno delle soluzioni contenenti Dansyl-Met e concentrazioni crescenti di Hg^{2+}, nell'intervallo 0.01 mM e 6 mM. Ad ogni immersione, si effettua l'acquisizione e il salvataggio di un file, che memorizza, oltre alle informazioni sulle impostazioni di acquisizione, anche il segnale di "dark", il segnale riflesso e lo scope differenziale, che rappresenta la fluorescenza calcolata.

Per ogni concentrazione sono effettuate diverse immersioni successive, intervallate tra loro per alcune decine di secondi, allo scopo di ottenere uno spettro di fluorescenza calcolato come media su più acquisizioni, al fine di compensare eventuali errori di misura.

Nel passaggio tra due diverse soluzioni, si procede con un rapido lavaggio del probe con acqua distillata (DDW) allo scopo di eliminare eventuali residui di sostanze lasciate dalla soluzione interrogata in precedenza.

Dati sperimentali ottenuti e relative curve di calibrazione per misure di fluorescenza in soluzione

In Figura 20 si riporta lo spettro ottenuto collegando una patch-cord in fibra ottica diretta tra la sorgente (solo Deuterio) e lo spettrofotometro, con un tempo di integrazione settato in modo da non incorrere nella saturazione dello strumento. La sorgente emette in un range di lunghezze d'onda in cui la Dansyl-Met presenta i suoi due picchi di assorbanza (~247 e ~330 nm), risultando in grado di eccitare l'emissione per fluorescenza da parte della Dansyl-Met.

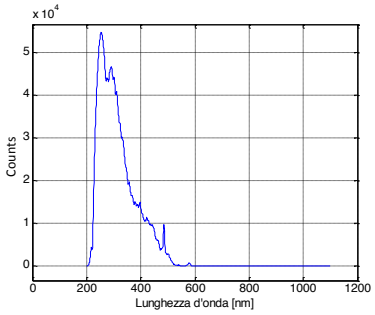

Figura 20: Spettro emesso dalla sorgente *AvaLight-DH-S-BAL Balanced Power* (solo Deuterio) con tempo di integrazione dello spettrofotometro di 150 ms.

Si osservi che il tempo di integrazione impostato per acquisire la sorgente è decisamente inferiore rispetto a quello necessario ad effettuare misure di fluorescenza. Infatti, a causa della bassa emissione in fluorescenza prodotta da basse concentrazioni di Dansyl-Met, tali misurazioni richiedono tempi di integrazione dell'ordine di qualche secondo. Si osservi inoltre che la scelta del tempo di integrazione dello spettrofotometro incide sull'intensità degli spettri acquisiti, ed essendo le misure di fluorescenza misure non normalizzate, ma misure di intensità del segnale, tale scelta si riflette sui valori di fluorescenza riportati in questo documento.

In Figura 21 sono mostrati gli spettri in riflessione per l'Hepes e per una soluzione contenente una specifica concentrazione di ioni Hg^{2+} (3 μM) acquisita tre volte a distanza di alcune decine di secondi. I quattro spettri mostrati sono sottratti del "dark". È possibile apprezzare una significativa differenza tra lo spettro in Hepes e quello in Dansyl-Met con aggiunta di ioni Hg^{2+} 3 μM nell'intervallo compreso tra 500 e 800 nm. Tale differenza può essere imputata all'emissione per fluorescenza da parte della Dansyl-Met.

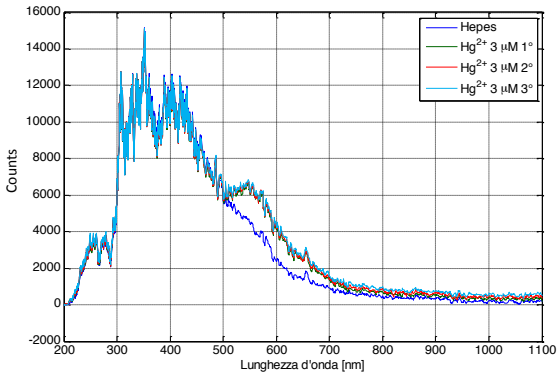

Figura 21: Spettri in riflessione acquisiti in Hepes e in una specifica concentrazione di ioni Hg^{2+} (3 μM) interrogata per tre volte a distanza di alcune decine di secondi. I quattro spettri sono sottratti del "dark".

In Figura 22 sono mostrati gli spettri in fluorescenza ottenuti con il biosensore in fibra ottica sottraendo lo spettro acquisito in Hepes a quello misurato in soluzioni contenenti Dansyl-Met 30 µM con aggiunta di ioni Hg^{2+} con concentrazioni crescenti nell'intervallo 0 – 6 µM ("scope differenziale"). Si può osservare un segnale positivo nell'intervallo 500 – 800 nm circa.

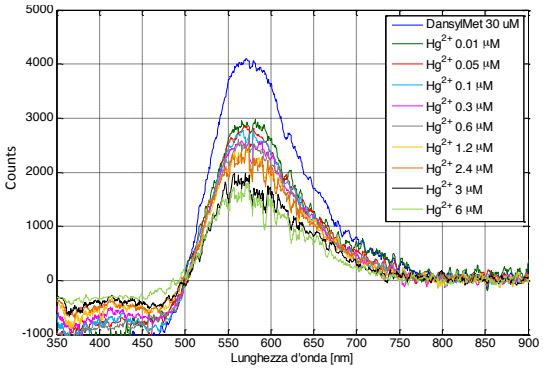

Figura 22: Spettri di fluorescenza ("scope" – Hepes) ottenuta con il biosensore in fibra ottica per soluzioni contenenti Dansyl-Met 30 µM con aggiunta di ioni Hg^{2+} con concentrazioni crescenti nell'intervallo 0 – 6 µM.

Osservando la figura precedente, appare evidente la necessità di filtrare lo spettro acquisito in modo tale da agevolare la successiva elaborazione degli spettri. A tale scopo, sono state valutate diverse strategie di filtraggio dello scope differenziale tenendo conto delle caratteristiche dei segnali in questione. Da questa analisi, il filtraggio più adeguato è risultato essere il filtro di Butterworth del secondo ordine con taglio pari a 0.02. I grafici mostrati in seguito riportano pertanto segnali sottoposti a questo tipo di filtraggio. Da un esame della Figura 23, è possibile individuare un picco di fluorescenza concentrato intorno ai 560 – 580 nm.

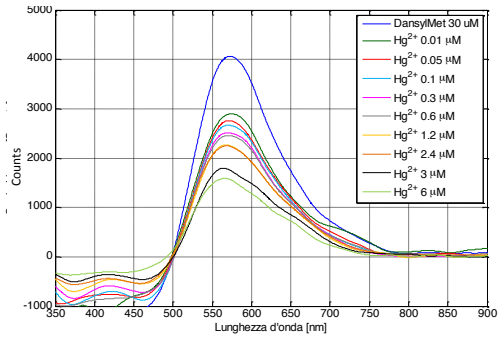

Figura 23: Filtraggio degli spettri di fluorescenza ("scope" – Hepes) ottenuta con il biosensore in fibra ottica per soluzioni contenenti Dansyl-Met 30 µM con aggiunta di ioni Hg^{2+} con concentrazioni crescenti nell'intervallo 0 – 6 µM.

In Figura 24 è invece riportato uno zoom della porzione di spettro di fluorescenza intorno al punto di massimo con le relative barre di errore in ogni punto (deviazione standard su tre acquisizioni ravvicinate). Osservando questo grafico è possibile apprezzare che le misurazioni eseguite con questo tipo di sensore sono caratterizzate, per questo intervallo di concentrazioni di Hg^{2+}, da un buon grado di ripetibilità, poiché le

diverse curve sono sufficientemente distanziate nel tratto in cui la fluorescenza è più elevata, evitando in questo modo di confondere tra loro le diverse concentrazioni. Ciò risulta vero ad eccezione delle concentrazioni 1.2 e 2.4 µM, che appaiono quasi sovrapposte in prossimità del punto di massimo.

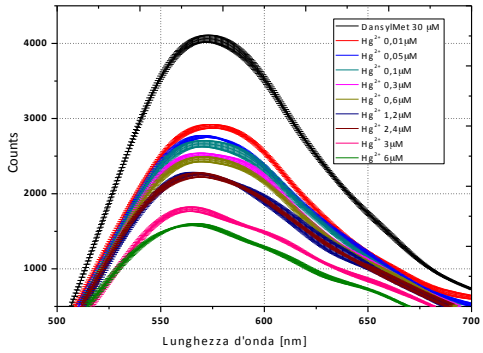

Figura 24: Zoom della porzione di spettro di fluorescenza intorno al punto di massimo con le relative barre di errore. Gli spettri, filtrati, sono ottenuti mediante il biosensore in fibra ottica per soluzioni contenenti Dansyl-Met 30 µM con aggiunta di ioni Hg^{2+} con concentrazioni crescenti nell'intervallo 0 – 6 µM.

In Figura 25 è riportato lo spettro di fluorescenza acquisito con il Reader da banco, adottando 380 nm come lunghezza d'onda di eccitazione per soluzioni contenenti Dansyl-Met 30 µM con aggiunta di ioni Hg^{2+} con concentrazioni crescenti nell'intervallo 0 e 0.6 – 6 µM. In Figura 26 sono riportate le stesse curve con le relative barre di errore (deviazione standard su tre acquisizioni ravvicinate). È importante sottolineare che le concentrazioni comprese nell'intervallo 0.01 – 0.3 mM interrogate dal Reader non producono degli spettri in fluorescenza distinguibili, pertanto, con questo setup, non si riesce a rilevare la presenza di concentrazioni di Hg^{2+} inferiori a 0.6 µM.

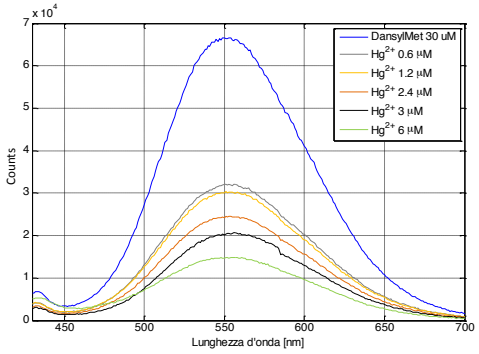

Figura 25: Spettri di fluorescenza ("scope" – Hepes) acquisiti con il Reader da banco interrogando soluzioni contenenti Dansyl-Met 30 µM con aggiunta di ioni Hg^{2+} con concentrazioni crescenti nell'intervallo 0, 0.6 – 6 µM.

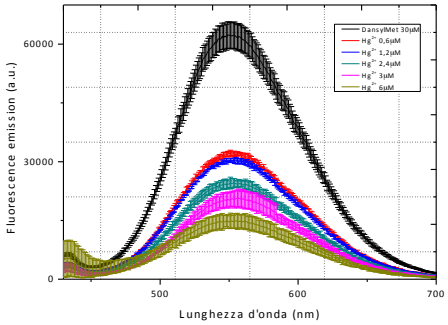

Figura 26: Spettri di fluorescenza ("scope" – Hepes) e relative barre di errore acquisiti con il Reader da banco interrogando soluzioni contenenti Dansyl-Met 30 µM con aggiunta di ioni Hg^{2+} con concentrazioni crescenti nell'intervallo 0, 0.6 – 6 µM.

Dal confronto tra le acquisizioni svolte con il Reader da banco e il sensore in fibra ottica, emerge una differenza nell'intensità, nella forma dello spettro di fluorescenza e nella posizione del punto di massimo, che nel Reader risulta essere collocato intorno ai 550 nm, rispetto ai 560 – 580 nm del picco avuto col sensore in fibra ottica. Tale differenza è imputabile alla differente metodologia di eccitazione adottata nei due setup: nel caso del Reader da banco, si è utilizzata una lunghezza d'onda di eccitazione di 380 nm, laddove per il sensore in fibra ottica si è adottata una sorgente a banda larga tra ~200 e ~500 nm.

Al fine di apprezzare le differenze esistenti tra gli spettri relativi alle diverse concentrazioni di Hg^{2+} si è deciso di individuare la posizione (in lunghezza d'onda) e l'intensità (in ampiezza) del punto di massima fluorescenza. Il grafico relativo alla lunghezza d'onda del massimo è riportato in Figura 27. Si può facilmente osservare che non si ha un andamento monotono, anche se, nel complesso, ad un aumento della concentrazione di Hg^{2+} corrisponde un abbassamento della lunghezza d'onda di picco.

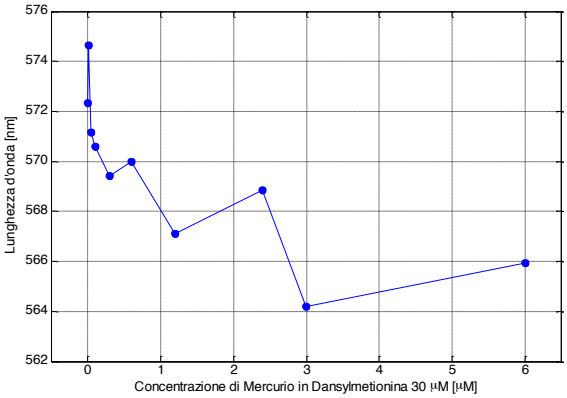

Figura 27: Andamento della lunghezza d'onda del punto di massima fluorescenza ottenuta con il sensore in fibra ottica per soluzioni contenenti Dansyl-Met 30 µM con aggiunta di ioni Hg^{2+} con concentrazioni crescenti nell'intervallo 0 – 6 µM.

Anche effettuando uno zoom per le concentrazioni più basse (Figura 28), non si riesce ad apprezzare una monotonia. Ciò spinge a non svolgere ulteriori analisi su questo parametro e a focalizzare l'attenzione sul valore di massima fluorescenza.

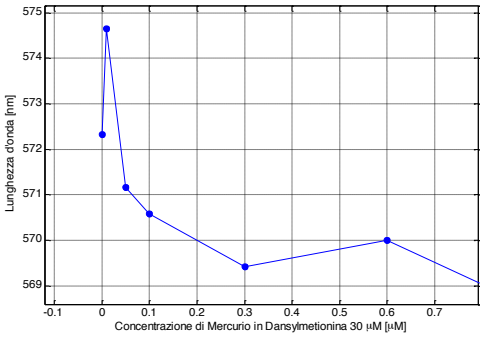

Figura 28: Zoom dell'andamento della lunghezza d'onda del punto di massima fluorescenza ottenuta con il sensore in fibra ottica per soluzioni contenenti Dansyl-Met 30 µM con aggiunta di ioni Hg^{2+} con concentrazioni crescenti nell'intervallo 0 – 0.6 µM.

L'andamento della massima fluorescenza è riportato nel grafico mostrato in Figura 29. È possibile riscontrare un andamento complessivo decrescente della massima fluorescenza all'aumentare della concentrazione di Hg^{2+}. Si nota tuttavia un'anomalia nel punto a 2.4 µM, troppo vicino a quello ottenuto per 1.2 µM.

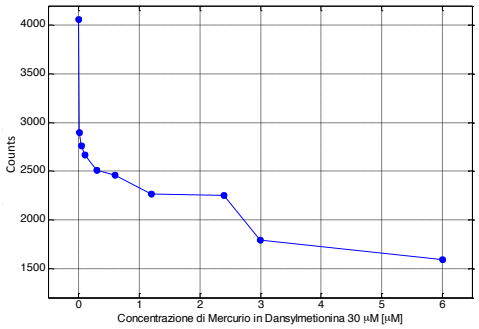

Figura 29: Andamento della massima fluorescenza ottenuta con il sensore in fibra ottica per soluzioni contenenti Dansyl-Met 30 µM con aggiunta di ioni Hg^{2+} con concentrazioni crescenti nell'intervallo 0 – 6 µM.

A partire da quest'analisi, si è deciso di costruire una curva di calibrazione con fitting esponenziale, considerando tutti i punti acquisiti nell'intervallo 0 – 6 µM, mostrata in Figura 30.

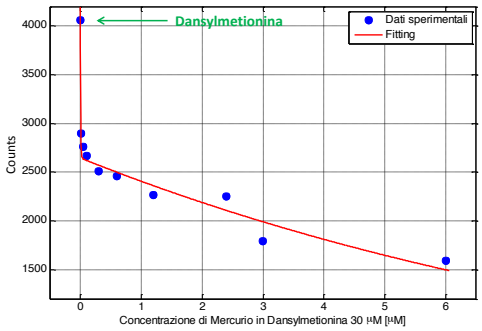

Figura 30: Curva di calibrazione e fitting esponenziale: massima fluorescenza ottenuta con il sensore in fibra ottica per soluzioni contenenti Dansyl-Met 30 µM con aggiunta di ioni Hg^{2+} con concentrazioni crescenti nell'intervallo 0.6 – 6 µM.

I parametri del fitting esponenziale sono riportati in Tabella 3.

General model Exp2:
f(x) = a*exp(b*x) + c*exp(d*x)
Coefficients (with 95% confidence bounds):
a = 1416 (1064, 1768)
b = -172.2 (-308.5, -35.93)
c = 2647 (2487, 2807)
d = -0.09492 (-0.1269, -0.06289)
Goodness of fit:
SSE: 9.858e+004
R-square: 0.9762
Adjusted R-square: 0.9643
RMSE: 128.2

Tabella 3: Parametri di fitting della curva di calibrazione della massima fluorescenza ottenuta con il sensore in fibra ottica per soluzioni contenenti Dansyl-Met 30 µM con aggiunta di ioni Hg^{2+} con concentrazioni crescenti nell'intervallo 0.6 – 6 µM.

Pur raggiungendo un valore accettabile di R^2 (97%), appare piuttosto evidente che la presenza dello zero nel set di punti riportati condiziona notevolmente l'andamento della curva di fitting. Si è deciso perciò di restringere l'intervallo di concentrazioni cui estendere la curva di calibrazione, prendendo in considerazione i punti compresi nell'intervallo 0.01 – 1.2 µM, escludendo così anche il punto anomalo a 2.4 µM. La nuova curva di calibrazione è riportata in Figura 31. Il fitting adottato è ancora di tipo esponenziale (Tabella 4), ma in questo caso il parametro R^2 è notevolmente migliorato, raggiungendo un valore superiore al 99%.

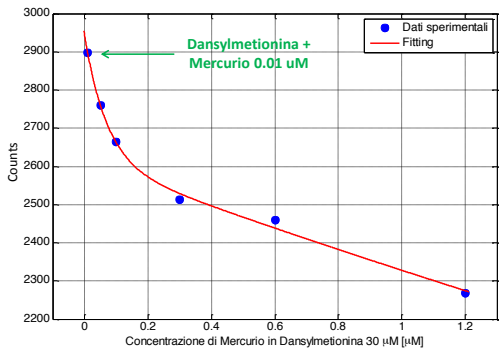

Figura 31: Curva di calibrazione e fitting esponenziale: massima fluorescenza ottenuta con il biosensore in fibra ottica per soluzioni contenenti Dansyl-Met 30 µM con aggiunta di ioni Hg^{2+} con concentrazioni crescenti nell'intervallo 0.01 – 1.2 µM.

General model Exp2:
f(x) = a*exp(b*x) + c*exp(d*x)
Coefficients (with 95% confidence bounds):
a = 331 (184.8, 477.3)

b = -14.4 (-28.51, -0.2947)
c = 2614 (2495, 2734)
d = -0.1159 (-0.1733, -0.0585)
Goodness of fit:
SSE: 726
R-square: 0.9972
Adjusted R-square: 0.9929
RMSE: 19.05

Tabella 4: Parametri di fitting della curva di calibrazione della massima fluorescenza ottenuta con il sensore in fibra ottica per soluzioni contenenti Dansyl-Met 30 µM con aggiunta di ioni Hg^{2+} con concentrazioni crescenti nell'intervallo 0.01 – 1.2 µM.

Si è tentato di monitorare il picco di fluorescenza seguendo anche altre strategie di elaborazione dei dati acquisiti, consistenti nel modificare la definizione di osservabile ottico. In particolare, in uno degli approcci qui riportati si è fissata una soglia in ampiezza a 1000 Counts (Figura 32), dopodiché è stata calcolata l'area di ciascuno spettro al di sopra della soglia fissata. Si ribadisce anche qui che le considerazioni fatte sugli spettri di fluorescenza sono dipendenti dalla strumentazione e dalle relative impostazioni adottate.

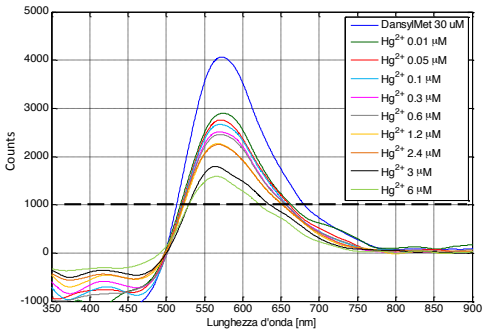

Figura 32: Spettri di fluorescenza ("scope" – Hepes) ottenuti con il sensore in fibra ottica per soluzioni contenenti Dansyl-Met 30 µM con aggiunta di ioni Hg^{2+} con concentrazioni crescenti nell'intervallo 0 – 6 mM con taglio fissato a 1000 Counts.

Il grafico dell'area calcolata al di sopra della soglia fissata a 1000 Counts è riportato in Figura 33. Si conferma un andamento decrescente all'aumentare della concentrazione di Hg^{2+} analogo a quello ottenuto sulla massima fluorescenza.

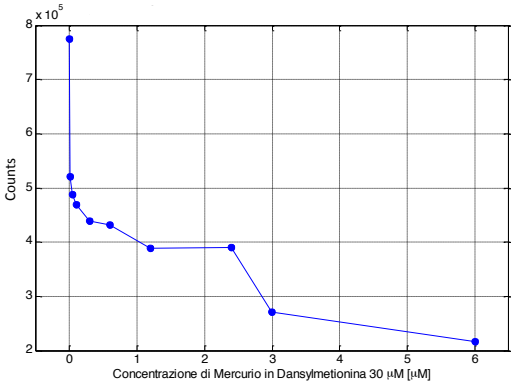

Figura 33: Andamento dell'area calcolata al di sopra di una soglia fissata a 1000 Counts nello spettro di fluorescenza ottenuto con il sensore in fibra ottica per soluzioni contenenti Dansyl-Met 30 µM con aggiunta di ioni Hg^{2+} con concentrazioni crescenti nell'intervallo 0 – 6 µM.

Anche in questo caso è stata ricavata una curva di calibrazione con fitting esponenziale, considerando tutti i punti acquisiti nell'intervallo 0 – 6 µM, mostrata in Figura 34.

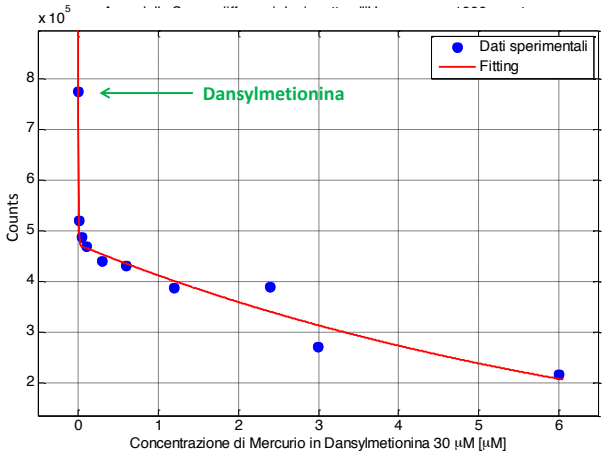

Figura 34: Curva di calibrazione e fitting esponenziale dell'area calcolata al di sopra di una soglia fissata a 1000 Counts nello spettro di fluorescenza ottenuto con il sensore in fibra ottica per soluzioni contenenti Dansyl-Met 30 µM con aggiunta di ioni Hg^{2+} con concentrazioni crescenti nell'intervallo 0.6 – 6 µM.

I parametri del fitting esponenziale sono riportati in **Tabella 5**.

General model Exp2:
f(x) = a*exp(b*x) + c*exp(d*x)
Coefficients (with 95% confidence bounds):
a = 3.018e+005 (2.214e+005, 3.821e+005)
b = -182.7 (-344.5, -20.92)
c = 4.729e+005 (4.355e+005, 5.103e+005)
d = -0.1364 (-0.1841, -0.08871)
Goodness of fit:
SSE: 5.067e+009
R-square: 0.9753
Adjusted R-square: 0.963
RMSE: 2.906e+004

Tabella 5: Parametri di fitting della curva di calibrazione dell'area calcolata al di sopra di una soglia fissata a 1000 Counts nello spettro di fluorescenza ottenuto con il sensore in fibra ottica per soluzioni contenenti Dansyl-Met 30 µM con aggiunta di ioni Hg^{2+} con concentrazioni crescenti nell'intervallo 0 – 6 µM.

Pur raggiungendo un valore accettabile di R^2 (97%), appare anche qui evidente che la presenza dello zero nel set di punti riportati condiziona notevolmente l'andamento della curva di fitting. Si è deciso perciò di restringere la curva di calibrazione e il conseguente fitting all'intervallo di concentrazioni 0.01 – 1.2 µM. La nuova curva di calibrazione è riportata in Figura 35.

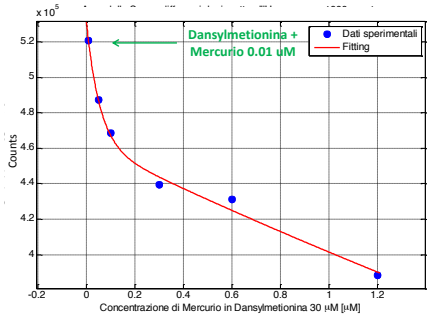

Figura 35: Curva di calibrazione e fitting esponenziale dell'area calcolata al di sopra di una soglia fissata a 1000 Counts nello spettro di fluorescenza ottenuto con il sensore in fibra ottica per soluzioni contenenti Dansyl-Met 30 µM con aggiunta di ioni Hg^{2+} con concentrazioni crescenti nell'intervallo 0.01 – 1.2 µM.

Il fitting adottato è ancora di tipo esponenziale (Tabella 6), ma in questo caso il parametro R^2 è notevolmente migliorato, raggiungendo un valore superiore al 99%.

General model Exp2:
f(x) = a*exp(b*x) + c*exp(d*x)
Coefficients (with 95% confidence bounds):
a = 7.007e+004 (2.701e+004, 1.131e+005)
b = -18.38 (-44.14, 7.374)
c = 4.63e+005 (4.305e+005, 4.955e+005)
d = -0.1424 (-0.2345, -0.05019)
Goodness of fit:
SSE: 6.346e+007
R-square: 0.9941
Adjusted R-square: 0.9853
RMSE: 5633

Tabella 6: Parametri di fitting della curva di calibrazione dell'area calcolata al di sopra di una soglia fissata a 1000 Counts nello spettro di fluorescenza ottenuto con il sensore in fibra ottica per soluzioni contenenti Dansyl-Met 30 µM con aggiunta di ioni Hg^{2+} con concentrazioni crescenti nell'intervallo 0.01 – 1.2 µM.

Un approccio alternativo consiste nel sottrarre allo spettro acquisito nella sola DansylMet (quello con il picco di fluorescenza più elevato) lo spettro acquisito nelle altre soluzioni, contenenti anche Hg^{2+}, ottenendo ancora una misura differenziale:

$$S_d = \left(\text{scope}_{\text{DansylMet}} - \text{scope}_{\text{DansylMet+Hg}^{2+}}\right)$$

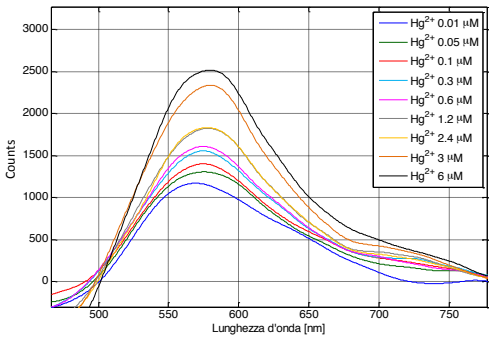

Figura 36: Spettro differenziale ottenuto sottraendo allo spettro in Dansyl-Met lo spettro acquisito in Dansyl-Met con aggiunta di ioni Hg^{2+} con concentrazioni crescenti nell'intervallo 0.01 – 6 µM. Gli spettri sono ottenuti con il sensore in fibra ottica per misure di fluorescenza.

Il risultato di questo differente approccio è ancora una curva con un picco concentrato intorno ai 560 – 580 nm (Figura 36).

L'andamento di tale picco è riportato in Figura 37. A causa della diversa definizione che è stata data allo scope differenziale rispetto agli approcci precedenti, in questo caso si ha un andamento crescente all'aumentare della concentrazione di Hg^{2+}, che conferma tra l'altro la presenza di un'anomalia a 2.4 µM.

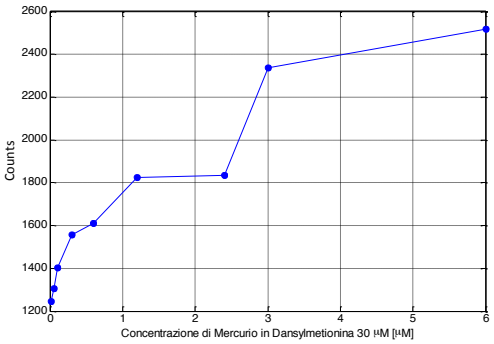

Figura 37: Andamento del massimo dello spettro differenziale ottenuto sottraendo allo spettro in DansylMet lo spettro acquisito in Dansyl-Met con aggiunta di ioni Hg^{2+} con concentrazioni crescenti nell'intervallo 0.01 – 6 µM. Gli spettri sono ottenuti con il sensore in fibra ottica per misure di fluorescenza.

La conseguente curva di calibrazione e il relativo fitting esponenziale (si riporta direttamente quello limitato all'intervallo 0.01 – 1.2 µM) sono riportati in Figura 38, mentre i parametri di fitting sono mostrati in Tabella 7, dove è possibile riscontrare un valore di R^2 analogo a quello raggiunto per il fitting nei due precedenti approcci, superiore al 99%.

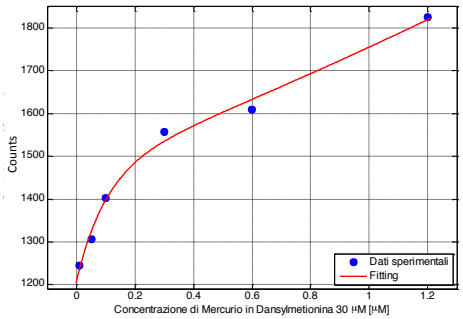

Figura 38: Curva di calibrazione e fitting esponenziale del massimo dello spettro differenziale ottenuto sottraendo allo spettro in Dansyl-Met lo spettro acquisito in DansylMet con aggiunta di ioni Hg^{2+} con concentrazioni crescenti nell'intervallo 0.01 – 1.2 µM. Gli spettri sono ottenuti con il sensore in fibra ottica per misure di fluorescenza.

General model Exp2:
f(x) = a*exp(b*x) + c*exp(d*x)
Coefficients (with 95% confidence bounds):
a = 1467 (1289, 1644)
b = 0.1796 (0.04875, 0.3104)
c = -257.5 (-456, -59.08)
d = -9.963 (-28.43, 8.509)
Goodness of fit:
SSE: 1455
R-square: 0.9937
Adjusted R-square: 0.9844
RMSE: 26.98

Tabella 7: Parametri di fitting della curva di calibrazione del massimo dello spettro differenziale ottenuto sottraendo allo spettro in Dansyl-Met lo spettro acquisito in DansylMet con aggiunta di ioni Hg^{2+} con concentrazioni crescenti nell'intervallo 0.01 – 1.2 µM. Gli spettri sono ottenuti con il sensore in fibra ottica per misure di fluorescenza.

Conclusioni

- Lo spettro di assorbanza mostra due picchi ben distinti: uno a ~247 nm e l'altro a ~330 nm. Analizzando il punto di massima assorbanza al variare della concentrazione di Hg^{2+}, per entrambi i picchi si è trovato un fitting lineare nell'intervallo 0.6 – 6 μM.
- Lo spettro di fluorescenza presenta un unico picco localizzato intorno a 570 nm. Analizzando il punto di massima fluorescenza al variare della concentrazione di Hg^{2+}, si è trovato un fitting esponenziale estendibile all'intervallo 0 – 6 μM e un fitting esponenziale, più accurato, limitato all'intervallo 0.01 – 1.2 μM. Sono stati proposti anche altri tipi di osservabili (area a soglia fissa, differenza rispetto alla Dansyl-Met), ottenendo trend e fitting analoghi a quelli basati sul massimo.
- Infine, confrontando le prestazioni del sistema ottenute mediante l'utilizzo del Reader da banco e del probe in fluorescenza, è possibile affermare che con il set up sperimentale in fibra ottica è possibile abbassare il limite di detection degli ioni Hg^{2+} al di sotto del valore di 0.6 μM raggiunto con il Reader. Infatti, con il probe in fluorescenza la minima concentrazione di Hg^{2+} rilevabile è dell'ordine di 0.01 μM.

Riconoscimento di ioni Hg^{2+} in ambiente marino o in matrici acquose che mimano ambienti marini

Sono stati eseguiti, mediante lettura con uno spettrofluorimetro EnSpire, saggi di titolazione in acqua di mare sintetica a diverse diluizioni per verificare la risposta della molecola selezionata (RT1). Le prove di selettività in acqua di mare sintetica, in precedenza condotte, hanno evidenziato come non sia possibile effettuare i saggi di riconoscimento direttamente in acqua di mare. L'utilizzo dei Dansyl derivati richiede quindi un pre-trattamento delle acque di mare che ne limiti la concentrazione salina.

A tale riguardo, sono state effettuate prove a diversa concentrazione salina, valutate le interferenze di altri cationi metallici nelle nuove soluzioni ed inquadrata una potenziale applicazione della Dansyl-Met per la determinazione di ioni Hg^{2+} in acque di transizione, ovvero in acque salmastre, originate dal mescolamento tra acque costiere e acque dolci dei fiumi, quali lagune, stagni costieri e laghi salmastri e zone di delta ed estuario.

La composizione dell'acqua di mare sintetica utilizzata è la seguente: 0.6 M NaCl e 0.06 M $NaHCO_3$, ed il pH misurato è pari ad 8.

Per valutare le prestazioni del nostro saggio in acqua di mare sintetica a diverse diluizioni la concentrazione di Dansyl-Met stata fissata a 10 µM, e sono state usate concentrazioni di Hg^{2+} nell'intervallo 0.6-18 µM. Sono stati comparati gli spettri di emissione in fluorescenza nel buffer Hepes 10 mM (pH = 7.4) e quelli in acqua di mare sintetica diluita a diverse diluizioni: 0.06M, 0.03M, 0.006M, 0.6mM, 0.06mM, 0.006mM.

1) <u>Diluizione 1/10 della concentrazione dell'acqua di mare sintetica</u>: comparando la risposta con il sistema nel buffer classico (Hepes pH 7.4) non si ha l'atteso quenching della fluorescenza e non si registra l'atteso shift del picco verso i 500 nm per concentrazioni più alte di Hg^{2+} (18 µM) (Figura 39).

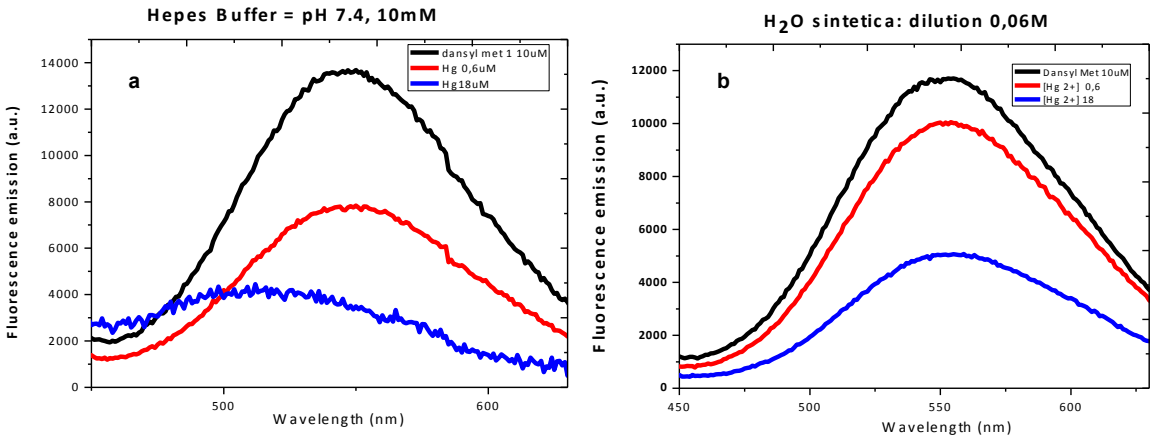

Figura 39: Spettri di emissione in fluorescenza della Dansyl-Met [10 µM] in presenza di concentrazioni di Hg^{2+} nell'intervallo 0.6-18 µM: a) Hepes 10 mM (pH = 7.4); b) acqua di mare sintetica ad una diluizione pari a 0.06M.

2) Diluizione 1/50 della concentrazione dell'acqua di mare sintetica: anche in tale soluzione, comparando la risposta con il sistema nel buffer classico (Hepes pH 7.4), non si ha l'atteso quenching della fluorescenza e non si registra l'atteso shift del picco verso i 500 nm per concentrazioni più alte di Hg^{2+} (18 µM) (Figura 40).

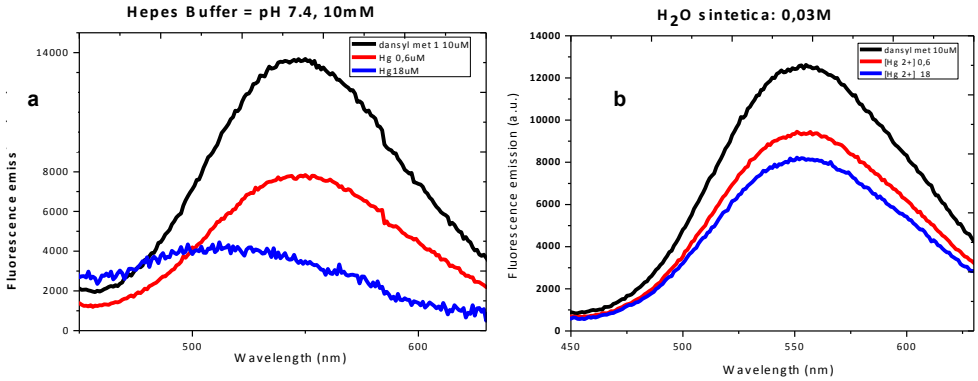

Figura 40: Spettri di emissione in fluorescenza della Dansyl-Met [10 µM] in presenza di concentrazioni di Hg^{2+} nell'intervallo 0.6 - 18 µM: a) Hepes 10 mM (pH = 7.4); b) acqua di mare sperimentale ad una diluizione pari a 0.03M.

3) Diluizione 1/100 della concentrazione dell'acqua di mare sperimentale: comparando la risposta con il sistema nel buffer classico (Hepes pH7.4) si osserva un quenching della fluorescenza che risulta non comparabile con quello osservato in buffer Hepes. Resta comunque non osservabile l'atteso shift del picco verso i 500 nm per concentrazioni più alte di Hg^{2+} (18 µM) (Figura 41).

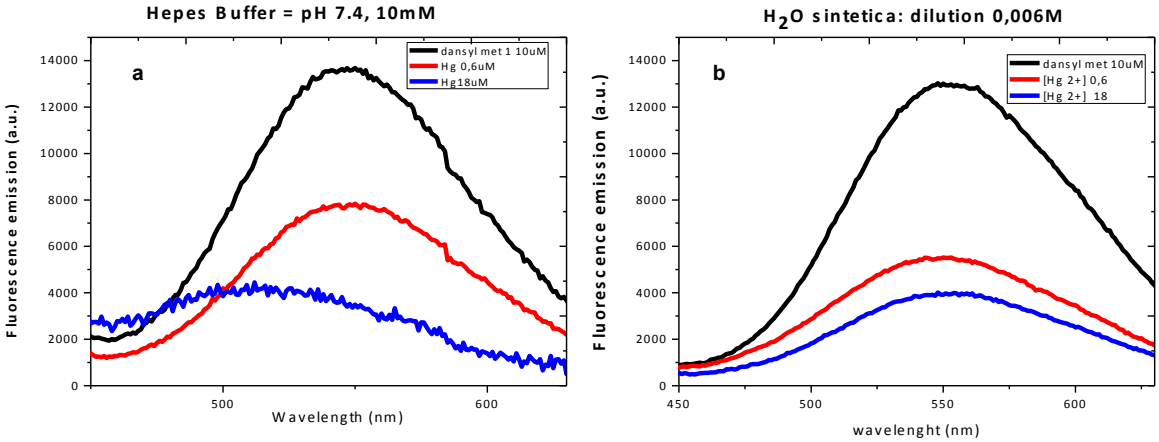

Figura 41: Spettri di emissione in fluorescenza della Dansyl-Met [10 µM] in presenza di concentrazioni di Hg^{2+} nell'intervallo 0.6-18 µM: a) Hepes 10 mM (pH = 7.4); b) acqua di mare sintetica ad una diluizione pari a 0.006M.

4) Diluizione 1/1000 della concentrazione dell'acqua di mare sintetica: comparando la risposta con il sistema nel buffer classico (Hepes pH 7.4) si osserva un quenching della fluorescenza che risulta non comparabile con quello osservato in buffer Hepes. Inoltre è possibile osservare un graduale shift del picco verso i 500 nm per concentrazioni più alte di Hg^{2+} (18 µM) (Figura 42).

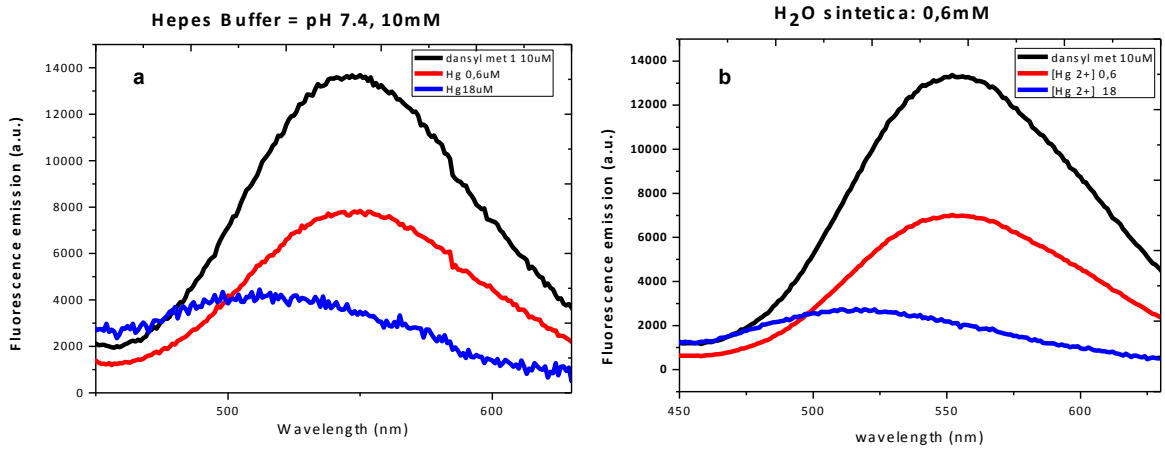

Figura 42: Spettri di emissione in fluorescenza della Dansyl-Met [10 μM] in presenza di concentrazioni di Hg^{2+} nell'intervallo 0.6-18 μM: a) Hepes 10 mM (pH = 7.4); b) acqua di mare sintetica ad una diluizione pari a 0.6 mM.

5) Diluizione 1/10000 della concentrazione dell'acqua di mare sintetica: comparando la risposta con il sistema nel buffer classico (Hepes pH7.4) si osserva un quenching della fluorescenza, comparabile con quello osservato in buffer Hepes. Inoltre, al diminuire della concentrazione di sale, risulta evidente il blueshift del picco verso i 500 nm per concentrazioni più alte di Hg^{2+} (18 μM) (Figura 43).

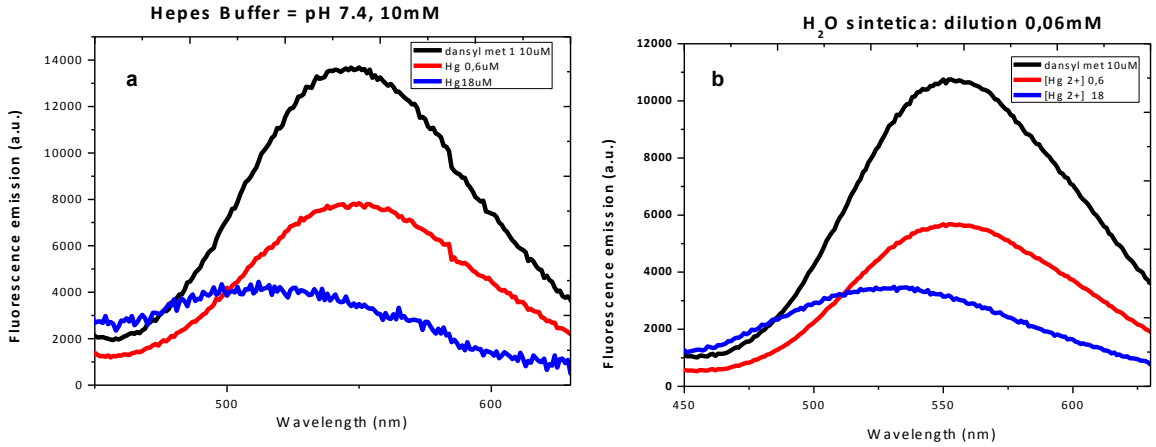

Figura 43: Spettri di emissione in fluorescenza della Dansyl-Met [10 μM] in presenza di concentrazioni di Hg^{2+} nell'intervallo 0.6-18 μM: a) Hepes 10 mM (pH = 7.4); b) acqua di mare sintetica ad una diluizione pari a 0.06 mM.

6) Diluizione 1/100000 della concentrazione dell'acqua di mare sintetica: per tali diluizioni il sistema ha recuperato le sue prestazioni in termini di quenching e shift della fluorescenza (Figura 44).

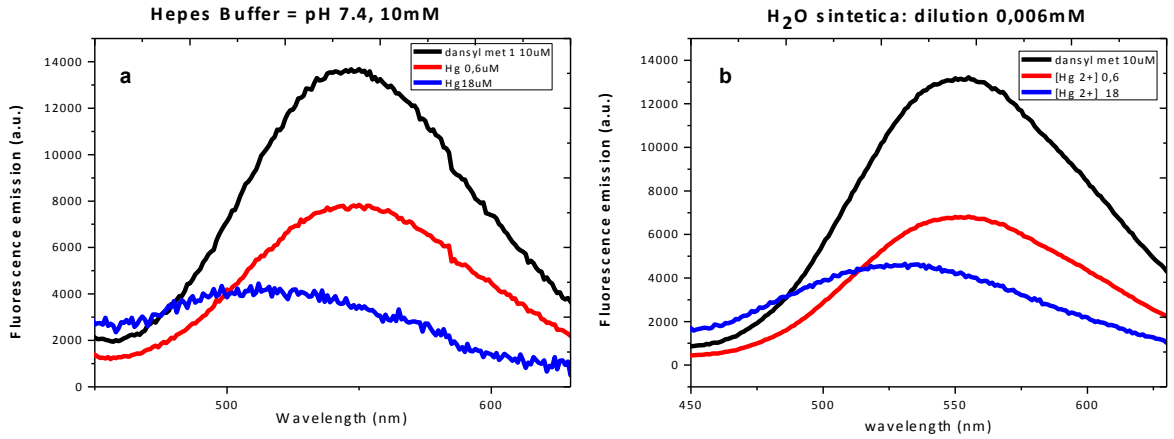

Figura 44: Spettri di emissione in fluorescenza della Dansyl-Met [10 μM] in presenza di concentrazioni di Hg^{2+} nell'intervallo 0.6-18 μM: a) Hepes 10 mM (pH = 7.4); b) acqua di mare sintetica ad una diluizione pari a 0.006 mM.

Lo studio in acqua di mare a diversa concentrazione salina ha evidenziato che per evitare l'interferenza di sali con le prestazioni del saggio è necessario diluire il campione almeno di un fattore 10000.

Dopo il completamento degli studi sulla risposta della Dansyl-Met in saggi di riconoscimento di Hg^{2+} in acqua diversa concentrazione salina, è stato prescelta la migliore concentrazione salina ([C]=0.006mM) ed effettuato uno studio sulla selettività del riconoscimento di tale catione.

E' stata valutata la selettività del riconoscimento di tale catione in presenza di cationi interferenti quali Ca^{2+}, Cd^{2+}, Co^{2+}, Pb^{2+}, Fe^{2+}, Pd^{2+}, Cu^{2+}, Na^{+}, Ni^{2+}, Zn^{2+} (soluzioni preparate a partire dai cloruri). Sono stati effettuati differenti saggi di binding, utilizzando le seguenti condizioni sperimentali:

i) concentrazione di Dansyl-derivato pari a 10 μM;

ii) concentrazioni limite di cationi interferenti 0.6 μM. L'effetto di tale cationi sulla fluorescenza del Dansyl-derivato è stato valutato in presenza ed assenza di Hg^{2+}.

a) Fe^{2+}, Cd^{2+}, Pd^{2+}

I cationi Fe^{2+}, Pb^{2+}, Cd^{2+} danno luogo ad uno spegnimento (~10-20%) dell'emissione di fluorescenza della Dansyl-Met di riferimento (curva nera) ed interferiscono con la risposta in fluorescenza della Dansyl-Met in presenza di $[Hg^{2+}]$ = 0.6 μM (curva rossa).

È ancora possibile osservare uno spegnimento dell'emissione della Dansyl-Met in seguito alla complessazione con Hg^{2+}, ma la presenza di cationi interferenti inibisce l'atteso spegnimento di tale fluorescenza (Figura 45).

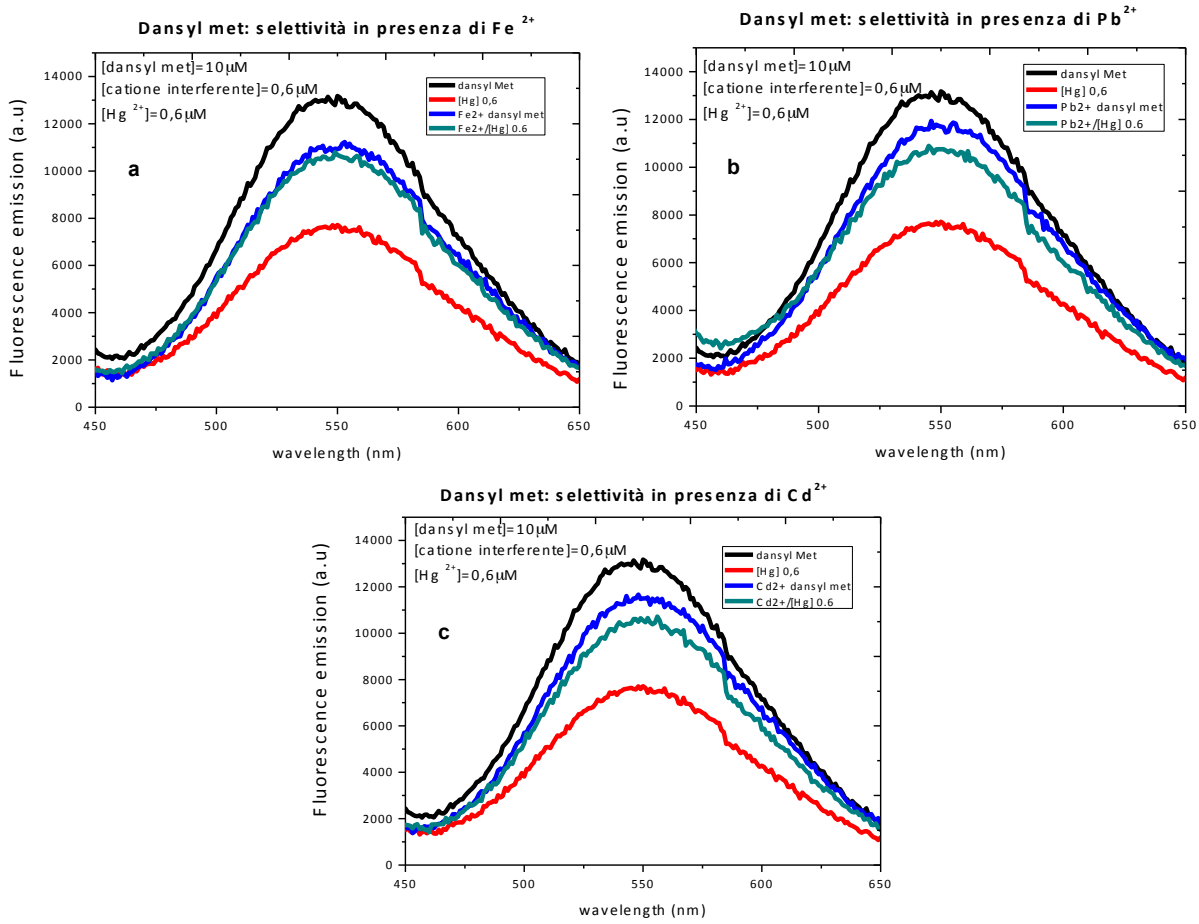

Figura 45: Spettri di emissione in fluorescenza della Dansyl-Met [10 µM] in presenza di concentrazioni di Hg^{2+} 0.6 µM e di metalli interferenti quali: a) Fe^{2+} ; b) Pb^{2+} ; c) Cd^{2+}.

b) Zn^{2+}, Cu^{2+}, Ni^{2+}

I cationi Ni^{2+}, Zn^{2} non interferiscono in modo sostanziale con l'emissione di fluorescenza della Dansyl-Met di riferimento (curva nera). Il catione Cu^{2+} genera uno spegnimento (~10-20%) dell'emissione di fluorescenza della Dansyl-Met di riferimento (curva nera).

I cationi Ni^{2+}, Zn^{2+}, Cu^{2+} interferiscono con la risposta in fluorescenza della Dansyl-Met in presenza di [Hg^{2+}] = 0.6 µM (curva rossa).

È ancora possibile osservare uno spegnimento dell'emissione della Dansyl-Met in seguito alla complessazione con Hg^{2+}, ma la presenza di cationi interferenti inibisce l'atteso spegnimento di tale fluorescenza (Figura 46).

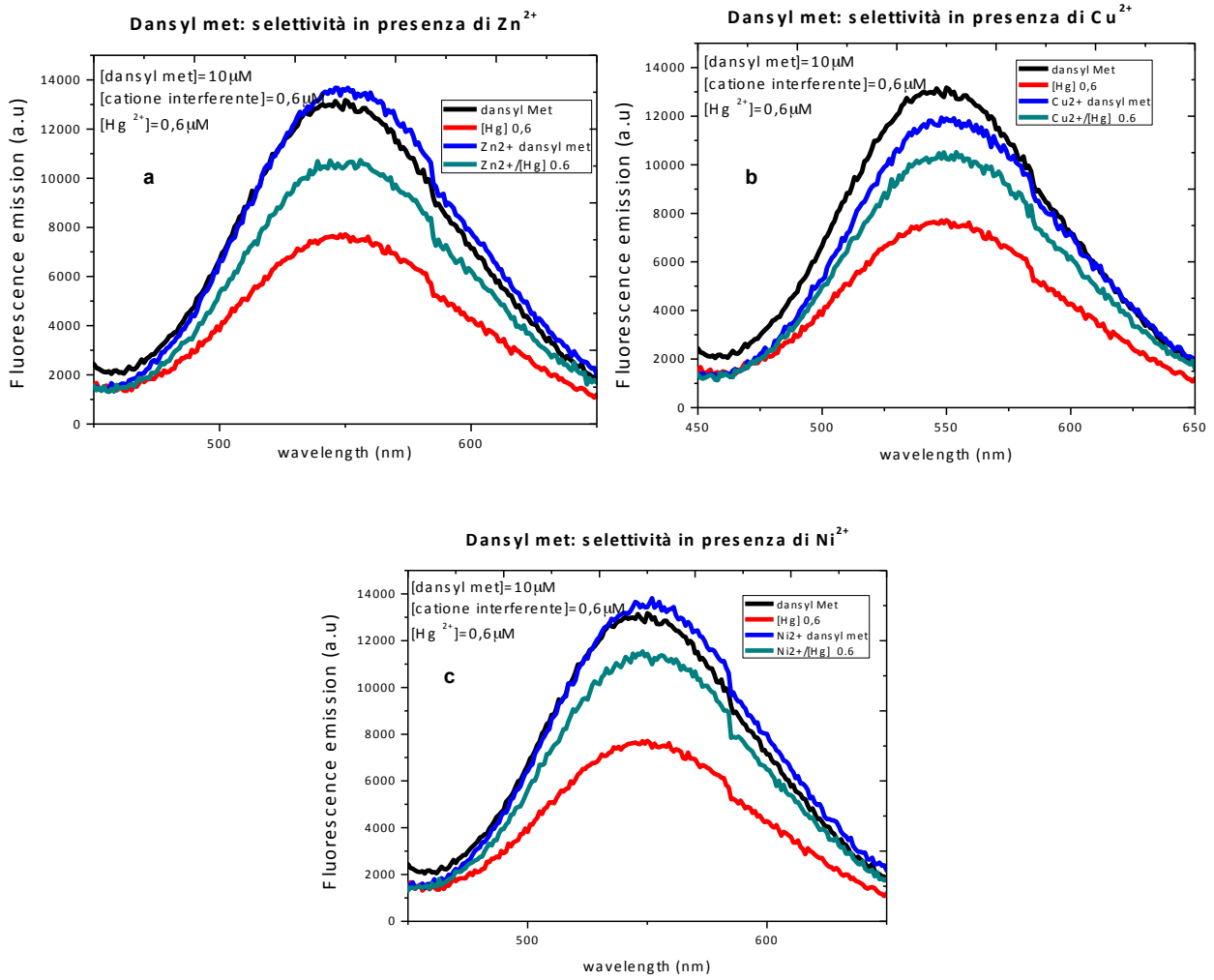

Figura 46: Spettri di emissione in fluorescenza della dansylMet [10 µM] in presenza di concentrazioni di Hg^{2+} 0.6 µM e di metalli interferenti quali: a) Zn^{2+}; b) Cu^{2+} ; c) Ni^{2+}.

c) Ca^{2+}, Co^{2+}, Pd^{2+}

Il catione Co^{2+} dà origine ad un incremento dell'emissione di fluorescenza della Dansyl-Met di riferimento (curva nera). Il catione Ca^{2+} genera uno spegnimento (~10-20%) dell'emissione di fluorescenza della Dansyl-Met di riferimento (curva nera).

I cationi Ca^{2+}, Co^{2+}, $^{+}$ interferiscono con la risposta in fluorescenza della Dansyl-Met in presenza di [Hg^{2+}] = 0.6 µM (curva rossa). Per i cationi Ca^{2+}, Co^{2+} è ancora possibile osservare uno spegnimento dell'emissione della Dansyl-Met in seguito alla complessazione con Hg^{2+}, ma la presenza di cationi interferenti inibisce l'atteso spegnimento di tale fluorescenza. Caso particolare risulta essere il catione Pd^{2+} per cui si ha il completo abbattimento dell'emissione in fluorescenza in presenza ed in assenza di Hg^{2+} (Figura 47).

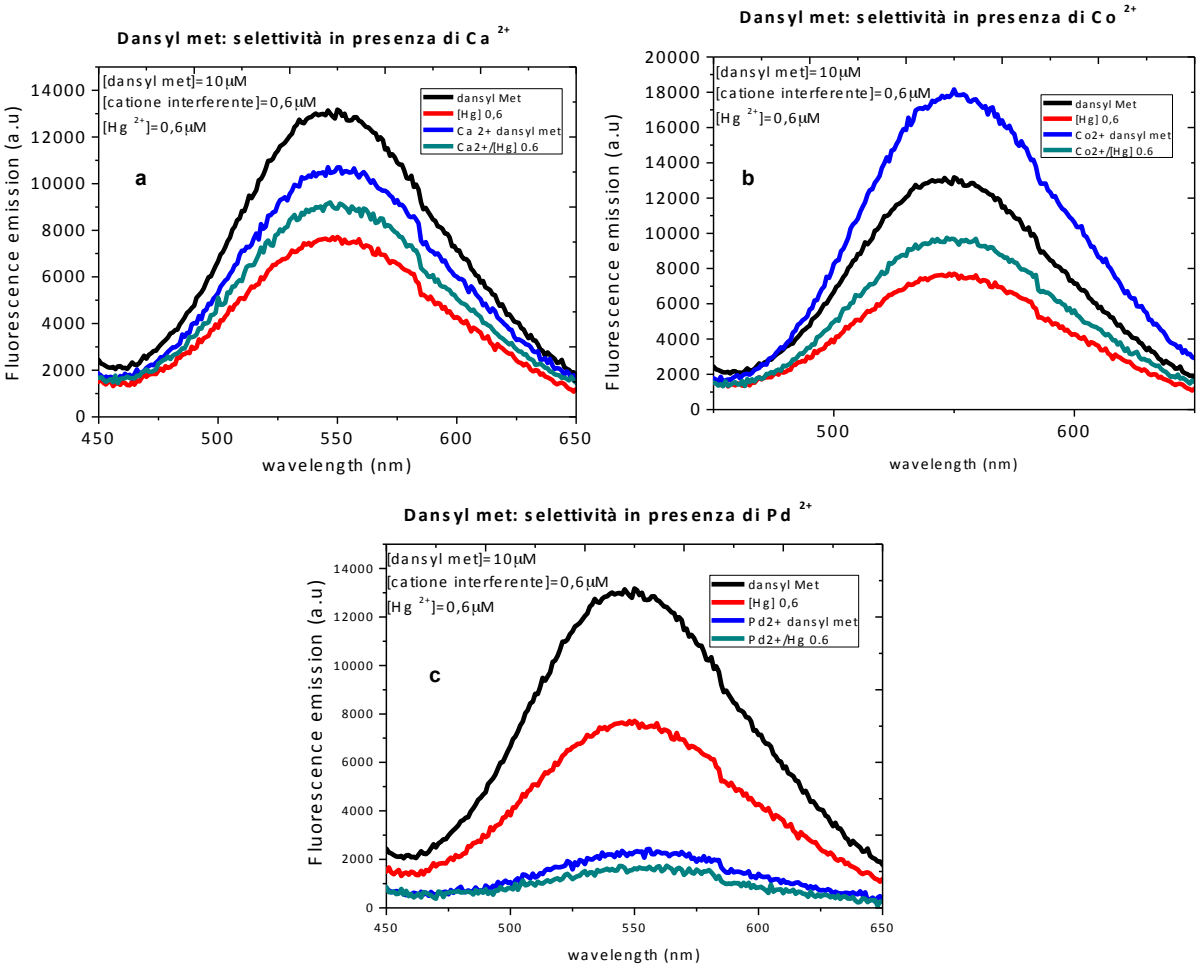

Figura 47: Spettri di emissione in fluorescenza della Dansyl-Met [10 µM] in presenza di concentrazioni di Hg^{2+} [0.6 µM] e di metalli interferenti quali: a) Ca^{2+}; b) Co^{2+} ; c) Pd^{2+}.

Gli studi di selettività hanno evidenziato come per la Dansyl-Met si abbia una interferenza non trascurabile sugli spettri di emissione in fluorescenza dovuta alla presenza dei cationi interferenti presi in esame (Ca^{2+}, Cd^{2+}, Co^{2+}, Pb^{2+}, Fe^{2+}, Pd^{2+}, Cu^{2+}, Na^{+}, Ni^{2+}, Zn^{2+}) anche in acqua di mare sintetica diluita.

Tali interferenze sono state riscontrate in presenza di basse concentrazioni di Hg^{2+} (0.6 µM). L'ipotesi è che in presenza di altri cationi, anche in acqua di mare sintetica, si formino complessi o si abbiano interazioni transienti, la cui stechiometria ed il cui effetto sulla fluorescenza dipendono dalle concentrazioni relative del dansyl derivato e del catione metallico.

Progettazione, preparazione e caratterizzazione analitica e funzionale di BODIPY per il riconoscimento di ioni Hg^{2+} in ambiente marino o in matrici acquose che mimano ambienti marini.

Un primo set di biomolecole è stato progettato e caratterizzato a partire dalla Dansyl-Met (Figura 48). Le molecole risultano essere particolarmente interessanti in quanto posseggono proprietà ottiche facilmente modulabili sulla base del pH, degli equivalenti di ioni Hg^{2+} o di percentuali di solventi organici. Inoltre la sintesi della Dansyl-Met e dei suoi derivati è particolarmente semplice e porta a delle rese superiori al 90% finale.

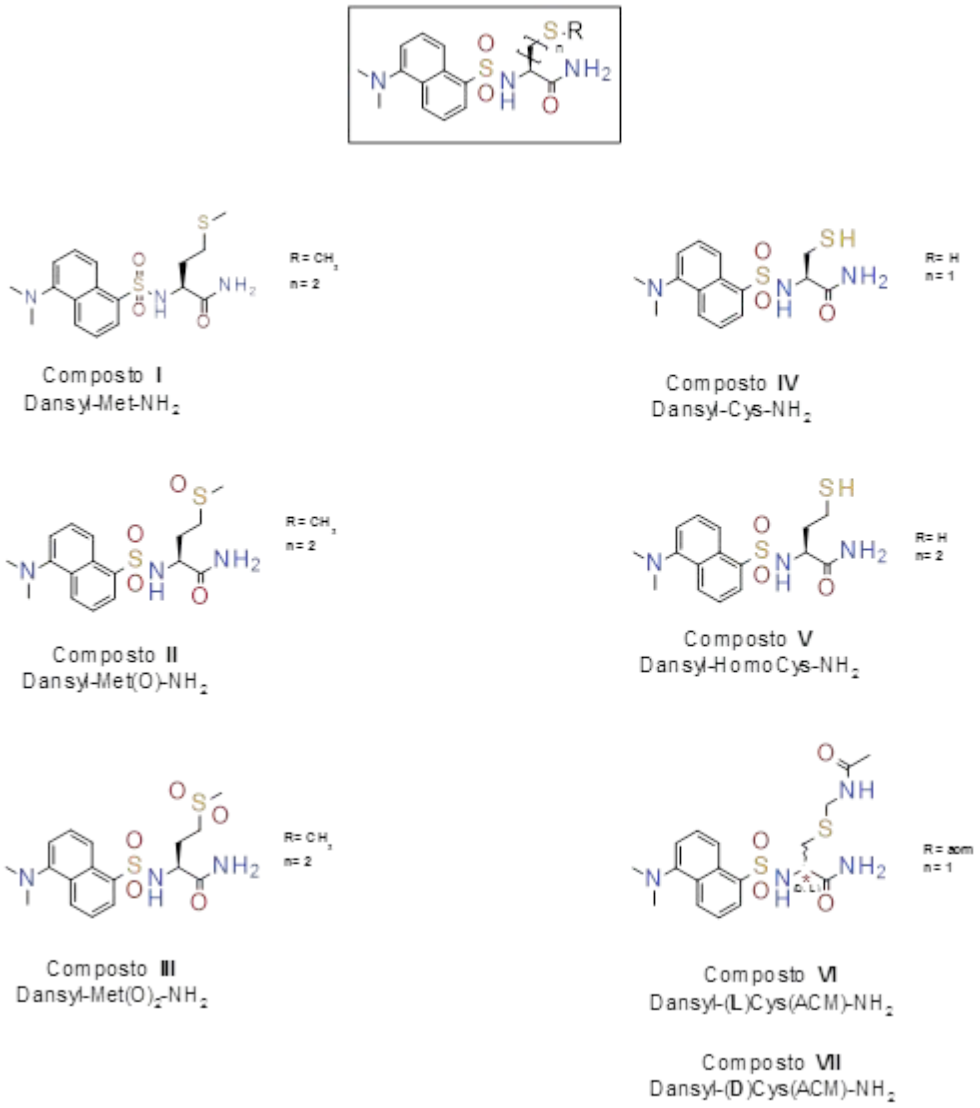

Figura 48: Lista dei dansyl derivati già studiati come probes per la rivelazione di Hg^{2+}.

In particolare, il gruppo fluorescente dansile modula e rende selettivo il riconoscimento dei cationi metallici mediante complessazione con il gruppo sulfonammidico. Il riconoscimento si traduce poi in variazioni delle

proprietà spettroscopiche (fluorescenza ed assorbanza) del dansile stesso che possono essere sfruttate per monitorare l'intensità e la specificità del legame dello ione al probe.

Per tali derivati è stata messa a punto una strategia sintetica semplice ed efficace che ha consentito di ottenere le molecole con rese eccellenti ed in tempi estremamente brevi. La caratterizzazione spettroscopica delle molecole selezionate è stata effettuata eseguendo delle titolazioni in presenza di concentrazioni crescenti di Hg^{2+} e valutando le variazioni spettrali sia in fluorescenza che in assorbanza. Impiegando la fluorescenza, la concentrazione di Hg^{2+} minima rilevabile nelle condizioni sperimentali ottimizzate è pari a 0.6 μM (0.12 ppm). Sono stati in seguito condotti studi di selettività in presenza di ioni interferenti a diverse concentrazioni e condotti saggi di titolazione in soluzioni acquose che mimano ambienti marini (acqua di mare sintetica/sperimentale) per verificare la risposta delle molecole selezionate in termini di selettività (derivati I e VI, RT1). Le prove di selettività in acqua di mare sintetica hanno evidenziato il limite dei Dansyl-derivati nel legare e rivelare lo ione mercurio in presenza di elevate concentrazioni di ioni cloruro, ma soprattutto alle concentrazioni previste nelle acque marine. L'interferente principale in questo caso è prevedibilmente proprio lo ione Cl^-, presente in elevatissime concentrazioni (circa 0.5 M), che è in grado di complessare anch'esso lo ione Hg^{2+}. L'utilizzo dei Dansyl-derivati richiederebbe quindi un eventuale pre-trattamento delle acque di mare che limiti la concentrazione di ioni cloruro. Alternativamente, l'impiego di tali molecole può essere ristretto alla rivelazione di ioni Hg^{2+} in matrici in cui la concentrazione di cloruro è notevolmente più bassa e i livelli di ione bivalente più alti come ad esempio nelle cosiddette "acque di transizione" (*C.G. Daughton / Environmental Impact Assessment Review 24 (2004) 711–732*). Per ovviare a questo inconveniente e permettere quindi la rivelazione di Hg^{2+} in matrici più simili all'acqua marina e con sensibilità più elevate, sono stati individuati derivati del difluoro-4-boro-3, 4-diaza-indacene (di seguito abbreviato come BODIPY, Figura 49).

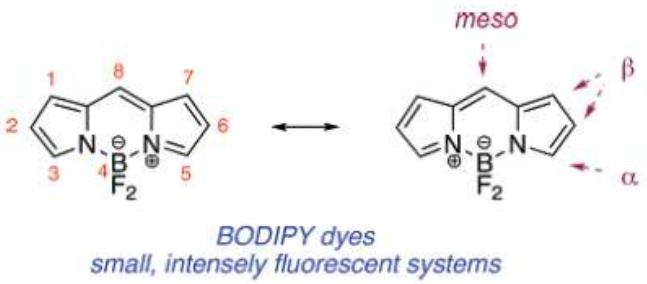

Figura 49: Struttura del Bodipy core.

Si riportano di seguito i riferimenti di lavori recenti che descrivono alcune molecole interessanti appartenenti a questa classe:

1) Burgess K. et al *Chem. Rev*. **2007,** 107, 4891–4932.

2) Dokyoung K. et al *Tetrahedron* **2012**, 68, 5279–5282.

3) Culzoni, M.J. et al *Anal. Methods*, **2013**, 5, 30–49.

4) Fan, J. et al *J Fluoresc* **2012**, 22, 945–951

I derivati del BODIPY sono molecole fluorescenti che tendono ad avere un forte assorbimento nell'UV e sono caratterizzate da picchi di emissione in fluorescenza ben definiti e con alte rese quantiche. Il grande coefficiente di estinzione molare (ε), l'elevata resa quantica in fluorescenza (Φ) e l'insensibilità a polarità del solvente e pH hanno permesso lo sviluppo di molecole fluorescenti a base di BODIPY come sensori fluorescenti efficienti per diversi analiti, tra cui Hg^{2+} (riferimento 4). Tali derivati sono ragionevolmente stabili in condizioni fisiologiche e piccole modifiche delle loro strutture consentono di modulare le loro caratteristiche di fluorescenza. Infatti, questi composti sono già stati utilizzati in letteratura per ottenere sistemi a trasferimento di energia o di elettroni in presenza di molecole che fungono da accettori di energia e di elettroni.

In particolare, partendo dallo studio riportato nel riferimento 4, si propone la sintesi del derivato BODIPY-amminofenolo (VIII), altamente selettivo e sensibile per il catione Hg^{2+} (Figura 50).

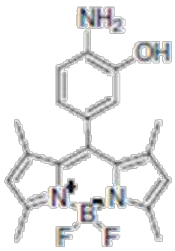

VIII

Figura 50: Struttura del BODIPY–amminofenolo.

Tale derivato è costituito da due unità: i) un core di BODIPY come molecola fluorescente; ii) l'amminofenolo che è in grado di formare un complesso stabile con Hg^{2+}. In presenza di concentrazioni crescenti di Hg^{2+} si ha un'accensione della fluorescenza (Figura 51.a), ed è stato riportato LOD (limit of detection) inferiore a 2 ppb (Figura 51.b).

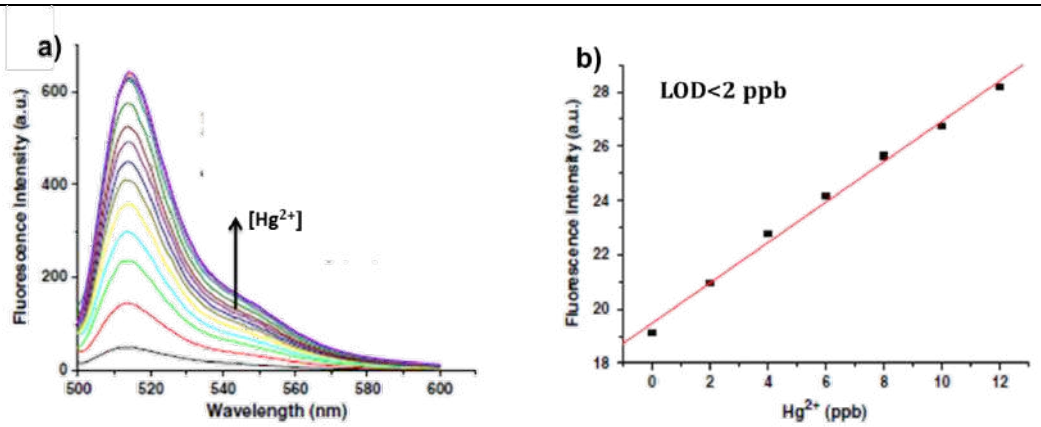

Figura 51. a) Spettro di emissione in fluorescenza di I (λex = 495 nm) in tampone 10 mM HEPES pH 7.4, in presenza di concentrazioni crescenti di Hg^{2+}. **b)** Le variazioni di intensità di fluorescenza del derivato VIII (5 µM) in seguito ad aggiunta di Hg^{2+} (0-12 ppb) in tampone 10 mM HEPES pH 7.4.

In questa molecola, il gruppo NH_2 è responsabile di un efficiente processo di trasferimento elettronico (PET) a partire dall'atomo di azoto al core del BODIPY. L'inibizione di tale processo fluorescente in seguito alla complessazione con lo ione Hg^{2+} è responsabile dell'accensione (o enhancement) della fluorescenza (Figura 52).

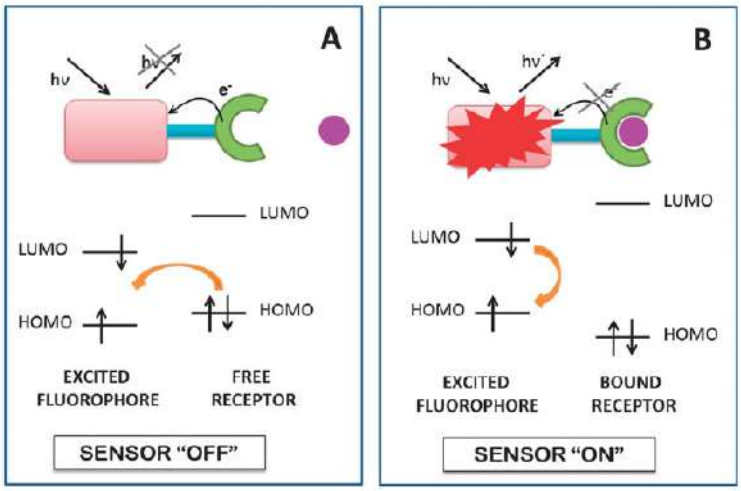

Figura 52: Processo di trasferimento elettronico (PET) per gli indicatori fluorescenti. **a)** Il formato a tre moduli permette il trasferimento di elettroni dal chelante al fluoroforo, spegnendo la fluorescenza del sensore. **b)** Quando il target si lega , il potenziale redox recettore viene perturbato e rallenta il processo di PET, con conseguente accensione del sensore.

Questo sensore presenta - in soluzioni acquose – un'elevata selettività e sensibilità per Hg^{2+} in presenza di vari ioni metallici e anioni (Figura 53a). Inoltre, anche la risposta di tale molecola è stata validata in ambienti ricchi di zolfo (Figura 53b) ed in condizioni naturali (campioni di acqua da ambienti marini, Figura 53c). Grazie a queste proprietà, tale derivato appare come un eccellente candidato per la rilevazione di Hg^{2+} in campo ambientale.

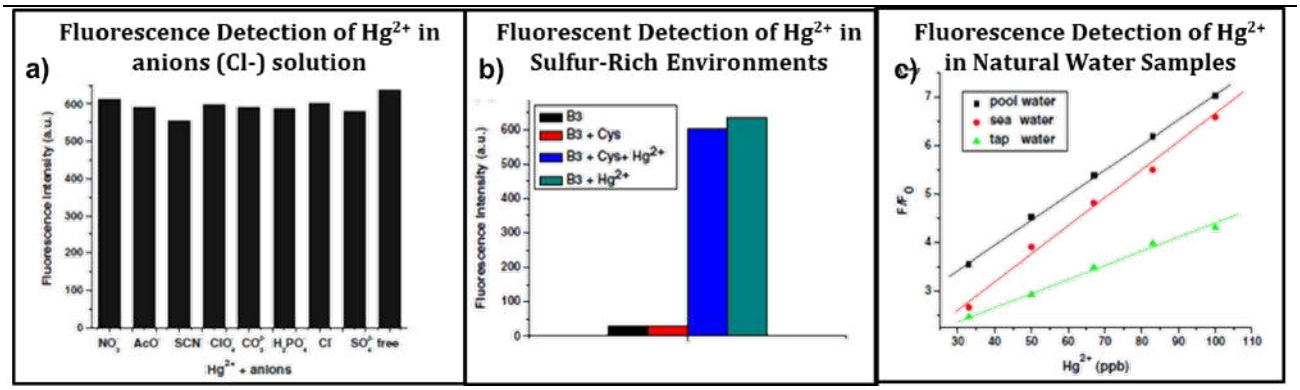

Figura 53. a) Risposte di fluorescenza del derivato VIII (10 μM) in presenza di 50 μM Hg^{2+} ed una soluzione di anioni selezionati (50 μM) in tampone HEPES pH 7.2 . Lunghezza d'onda di eccitazione è stata fissata a 495 nm e l'emissione è stata integrata tra 500-600 nm. **b)** Risposte di fluorescenza del derivato VIII (10 μM) in presenza di 50 μM Hg^{2+} ed in presenza di cisteina (50 μM) in tampone HEPES (20 mM HEPES). **c)** Risposta lineare in fluorescenza (F/F0) del derivato VIII (10 μM) dopo l'aggiunta di Hg^{2+} a diversi campioni di acqua naturale.

Nello specifico si propone quindi di preparare la molecole descritta, e caratterizzare dal punto di vista analitico le proprietà di complessazione di cationi metallici di varia natura. Il composto presenta una sintesi multisteps, come descritto in Figura 54.

La sintesi del derivato VIII si realizza a partire dal 2,4-dimetilpirrolo (X) e la 3-idrossi-4-nitrobenzaldeide (IX) e prevede 3 step di reazione. Tutti gli step di reazione richiedono ambiente anidro ed atmosfera inerte.

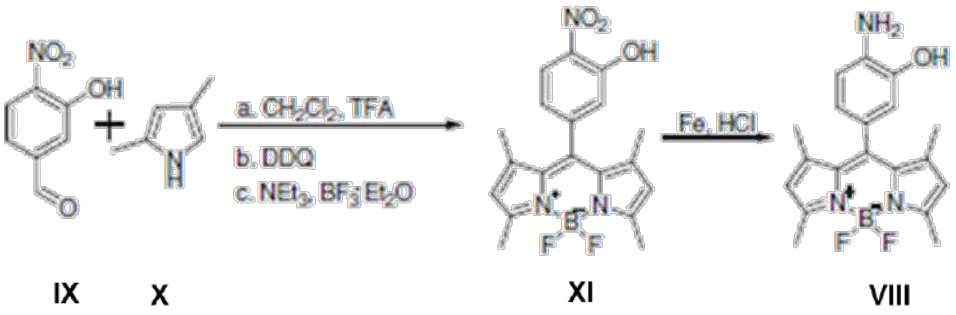

Figura 54: Schema sintetico per derivato VIII.

Sintesi – Parte sperimentale

In un pallone da 250 mL si introduce il 2,4-dimethylpirrolo (190 mg, 2 mmol) in 65 mL di diclorometano anidro in atmosfera inerte. Si aggiunge successivamente una goccia di acido trofluoroacetico (TFA), e mediante imbuto gocciolatore si aggiunge una soluzione di 3-idrossi-4-nitrobenzaldeide (167mg, 1 mmol) in diclorometano anidro (25 mL) (Figura 55). La miscela di reazione si lascia sotto agitazione per 5 ore (l'andamento della reazione è controllato via TLC).

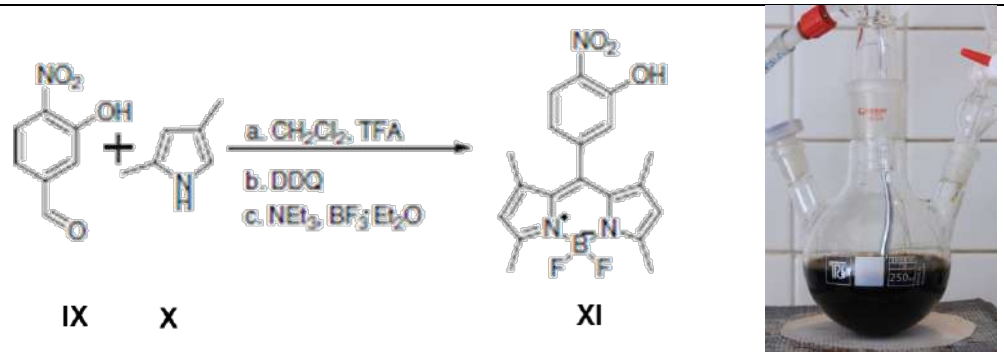

Figura 55: Schema sintetico per intermedio XI.

Il grezzo proveniente dalla reazione tra IX e X (un attacco al carbonile aldeidico sotto catalisi acida) è stato neutralizzato ed estratto prima di essere utilizzato nello step successivo di reazione. Nello step successivo sono aggiunti al pallone di reazione, nell'ordine 2,3-dicloro-5,6-dicianochinone (DDQ, 442 mg, 2 mmol) in 10 mL di diclorometano, trietilammina (2 mL) (per deprotonare l'NH pirrolico) e $BF3xOEt_2$. La miscela di reazione è stata lasciata sotto agitazione per 90 minuti .Tali passaggi hanno portato all'ottenimento del derivato XI. Alla miscela di reazione si aggiungono 40 mL di acqua e la fase acquosa. Viene estratta quindi con diclorometano (4x15 mL). Le fasi organiche ottenute (arancio scuro) sono riunite, anidrificate con Na_2SO_4 anidro e concentrate al rotavapor; la fase acquosa viene invece smaltita.
Si ottiene un solido rosso che viene purificato con colonna cromatografica di tipo Flash con eluente in gradiente di polarità (Esano/Acetato di Etile 7:1 -> 6:1 -> 5:1). Si ottiene un solido rosso (120 mg, 31%), come mostrato in Figura 56.

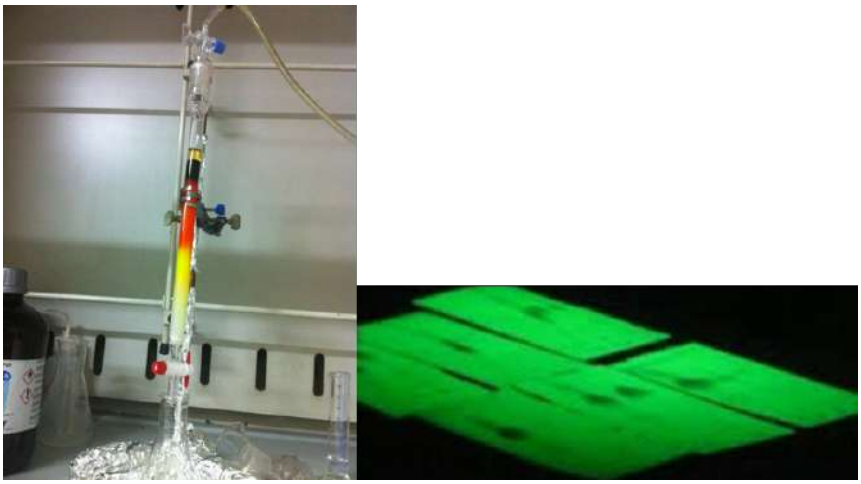

Figura 56: Colonna cromatografica di tipo Flash con eluente in gradiente di polarità (Esano/Acetato di Etile 7:1 -> 6:1 -> 5:1).

L'intermedio XI è stato caratterizzato analiticamente mediante LC-MS ed NMR. Le analisi LC-MS sono state eseguite con uno spettrometro HCT-Ultra PTM discovery system, Bruker con detector a trappola ionica (Ion Trap) accoppiato ad un sistema HPLC Waters Alliance Separation Module/Detector 2998 PDA) equipaggiato con colonne a fase inversa (colonna Phenomenex OnxY C18). In Figura 57 è riportato lo spettro di massa che ha confermato l'identità del composto sintetizzato.

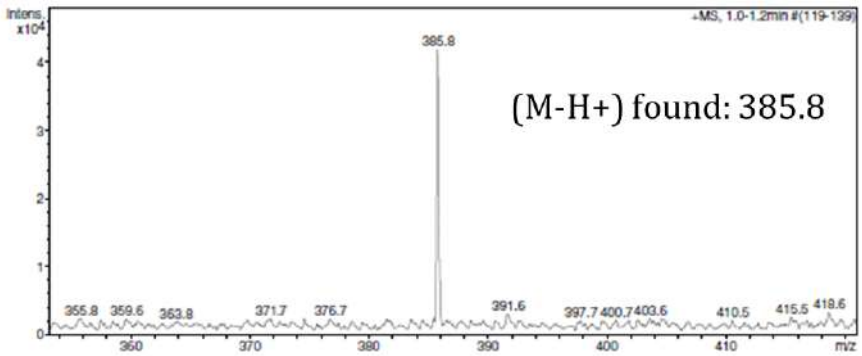

Figura 57: Spettro LC-MS del derivato XI.

Infine il derivato VIII è stato ottenuto mediante reazione di riduzione per cui si impiega Fe in polvere con HCl. In un pallone a tre colli si introduce il derivato XI (60 mg, 0.17 mmol) sciolto in 30 mL di metanolo, acqua (15 mL) a cui si aggiunge Fe in polvere 250 mg, 4.5 mmol (Figura 58). Si porta a riflusso la miscela di reazione riscaldando a 65 °C, si aggiunge HCl concentrato in metanolo (2 mL, 0.6 mol L^{-1}) e si lascia sotto agitazione a riflusso per 3 ore mL. L'andamento della reazione è controllato via TLC.

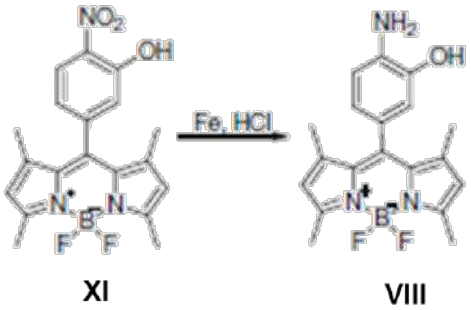

Figura 58: Schema sintetico per il composto finale VIII.

La miscela (soluzione rossa più precipitato giallo) viene poi raffreddata fino a temperatura ambiente e concentrate al rotavapor.

Si ottiene un solido rosso che viene purificato con colonna cromatografica di tipo Flash con eluente in gradiente di polarità (Esano/Acetato di Etile 5:1 -> 4:1 -> 3:1). Si ottiene un solido rosso (45 mg, 83%) (Figura 59).

Figura 59: Colonna cromatografica di tipo Flash con eluente in gradiente di polarità (Esano/Acetato di Etile 5:1 -> 4:1 -> 3:1).

Il composto finale VIII è stato caratterizzato analiticamente mediante LC-MS ed NMR. In Figura 60 è riportato lo spettro di massa che ha confermato l'identità del composto sintetizzato.

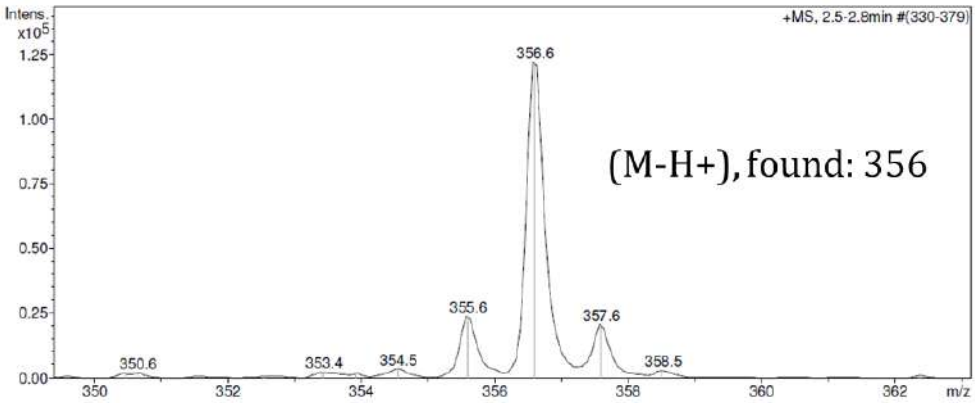

Figura 60: Spettro LC-MS del derivato VIII. Il peso molecolare teorico è 356.2

Si procederà successivamente alla caratterizzazione in assorbanza e fluorescenza del derivato VIII e saranno valutate le prestazioni in saggi di riconoscimento di ioni Hg^{2+}.

Caratterizzazione analitica e funzionale di BODIPY per il riconoscimento di ioni Hg^{2+} in ambiente marino o in matrici acquose che mimano ambienti marini.

E' stata inizialmente valutata la stabilità di emissione in fluorescenza del BODIPY-amminofenolo a tempi diversi: 1h e 3h dopo il caricamento in piastra (Figura 61). Le analisi in fluorescenza sono state eseguite acquisendo spettri di fluorescenza nel range 500 nm – 560 nm in seguito ad eccitazione a 480 nm. Gli spettri di emissione di fluorescenza sono stati registrati su soluzioni di BODIPY-amminofenolo con concentrazione pari a 5 µM.

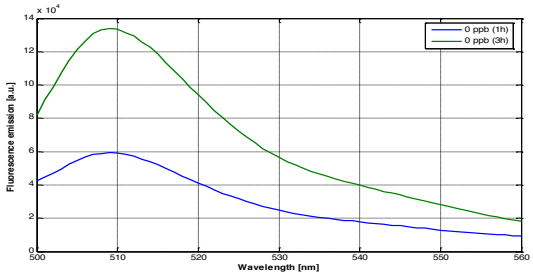

Figura 61: Spettri di emissione in fluorescenza del BODIPY-amminofenolo (λex = 480 nm) in tampone 10 mM HEPES/etanolo (9:1) pH 7.4.

Si osserva anche che a tempi diversi (1h e 3h) si ha un incremento della emissione in fluorescenza le cui cause possono essere attribuite a:

a) Variazioni di pH a seguito dell'assorbimento di CO_2;
b) Evaporazione nel tempo del solvente (in particolare l'etanolo che è presente al 10% nel Buffer Hepes 10 mM).

Queste ipotesi sono state verificate in modo tale da validare la stabilità del BODIPY-amminofenolo in soluzione.

a) <u>Variazioni di pH nel buffer a seguito dell'assorbimento di CO_2</u>

Sono stati preparati 3 campioni contenenti 2 ml di soluzione buffer Hepes 10 mM/etanolo (9/1) pH 7.4. Sono state monitorate nel tempo (1, 2, 3 ore) le variazioni del pH in seguito ad adsorbimento di CO_2 e/o all'evaporazione dell'etanolo (Tabella 7). Nell'arco temporale di 3 ore, i campioni sono stati esposti all'aria (temperatura dell'ambiente ~25°C) e si è registrato a fine misura una diminuzione di volume pari circa al 5% del volume iniziale.

	Tempo =0	Tempo= 1h	Tempo=2h	Tempo=3h
Campione 1	pH=7,24	pH=7,06	pH=7,07	pH=7,03
Campione 2	pH=7,21	pH=7,09	pH=7,07	pH=7,07
Campione 3	pH=7,15	pH=7,05	pH=7,06	pH=7,07

Tabella 7: Valori di pH misurati a diversi tempi nei campioni in esame.

Dopo 3 h si registra una variazione di pH pari a 0.14 unità. Tale variazione può essere trascurata considerando che il valore di pKa del BODIPY-amminofenolo è pari ~ 4, per cui le variazioni di pH così piccole intorno ad un valore di pH=7 non incidono sull'intensità di emissione in fluorescenza.

b) Evaporazione nel tempo del solvente (in particolare l'etanolo che è presente al 10% nel Buffer Hepes 10 mM)

L'effetto di evaporazione del buffer (in particolare dell'etanolo) sui valori di emissione in fluorescenza è stato valutato registrando gli spettri di emissione in fluorescenza del BODIPY-amminofenolo a diversi tempi (0,1,2,3 ore) con 2 diverse modalità:

i) Una piastra è stata caricata con 200 µL di soluzione di bodipy-amminofenolo 5 µM, lasciata in aria e conservata a temperatura ambiente (~25°C) per tutta la durata dell'esperimento (Figura 62.a).

ii) Invece, per minimizzare e controllare una eventuale evaporazione del buffer durante le acquisizioni nell'arco temporale di 3h, una seconda piastra è stata caricata con 200 µL di soluzione di BODIPY-amminofenolo 5 µM , accuratamente chiusa e tra le diverse misure conservata in frigo (Figura 62.b).

Dagli spettri di emissione in fluorescenza emerge che con la nuova modalità di conservazione della piastra è possibile controllare (a differenza della piastra lasciata aperta) le variazioni di emissione in fluorescenza nel tempo. Infatti, dopo 1h l'effetto dell'evaporazione è praticamente assente nella piastra conservata chiusa ed in frigo (Figura 62.b). Dopo 2h sulla stessa piastra si registra un incremento pari circa al 10% del segnale iniziale e dopo 3h si ha un incremento pari circa al 20% del segnale iniziale. Nel caso della piastra lasciata aperta a temperatura ambiente (Figura 62.a), si registra nel tempo un graduale incremento dell'emissione in fluorescenza che è possibile attribuire ad un solo effetto di evaporazione del solvente durante l'esperimento.

I parametri strumentali e di lettura fin qui ottimizzati, sono stati quindi utilizzati in saggi di riconoscimento di Hg^{2+} con soluzioni di BODIPY-amminofenolo.

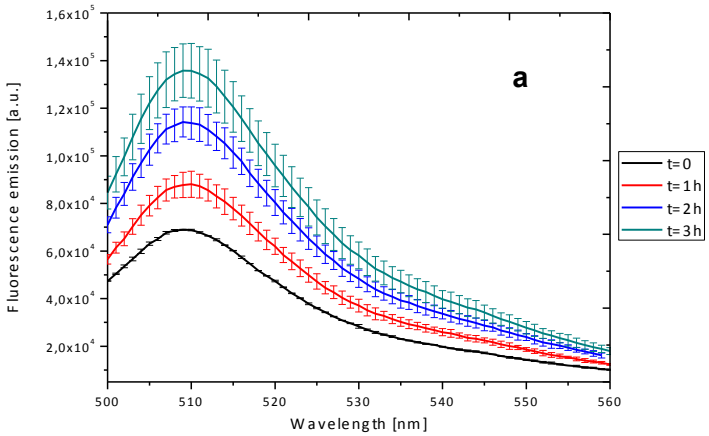

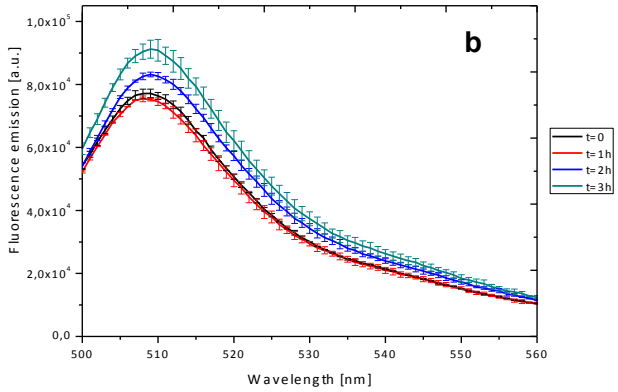

Figura 62: Spettri di emissione in fluorescenza del BODIPY-amminofenolo (λex = 480 nm) in tampone 10 mM HEPES/etanolo (9:1) pH 7.4 registrati: **a)** su piastra lasciata in aria; **b**) su piastra accuratamente chiusa e tra le diverse misure conservata in frigo

- **Saggi di binding BODIPY-amminofenolo/ Hg2+ in acqua di mare sperimentale**

Le titolazioni in fluorescenza sono state eseguite acquisendo spettri di fluorescenza nel range 500 nm – 560 nm in seguito ad eccitazione a 480 nm. Gli spettri di emissione di fluorescenza sono stati registrati su soluzioni di BODIPY-amminofenolo con concentrazione pari a 5 µM. Le misure sono state effettuate mantenendo costante in ogni campione la concentrazione di BODIPY-amminofenolo, in modo tale da poter trascurare in fase di elaborazione dati l'effetto di diluizione.

La caratterizzazione in fluorescenza del binding è stata eseguita in acqua di mare sperimentale /Etanolo 9:1, pH 7.4). Inoltre, poiché lo scopo ultimo dell'attività di ricerca è la determinazione quantitativa di ioni mercurio in campioni di acqua di mare in la cui concentrazione di tale catione è al di sotto di una ppm, sul BODIPY-amminofenolo sono state effettuate prove di titolazione per valutarne la risposta in intervalli di concentrazione di Hg^{2+} 0-15 ppb. In Figura 63, sono riportati gli spettri di emissione in fluorescenza registrati con il protocollo ottimizzato nel range di concentrazioni di Hg^{2+} 0-15 ppb.

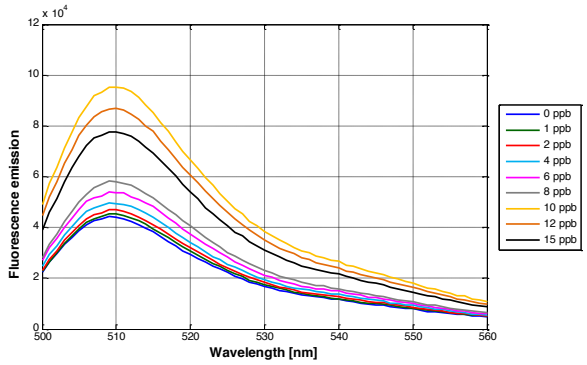

Figura 63: Spettri di emissione in fluorescenza del BODIPY-amminofenolo 5µM (λex = 480 nm) in acqua di mare sperimentale /etanolo (9:1) con aggiunta di ioni Hg^{2+} con concentrazioni crescenti nell'intervallo 0 – 15 ppb.

In Figura **24**63 sono riportati gli spettri di fluorescenza con le relative barre di errore in ogni punto (deviazione standard su triplicato). Osservando questo grafico è possibile apprezzare che le misurazioni eseguite con questo tipo di sensore sono caratterizzate, per questo intervallo di concentrazioni di Hg^{2+}, da un buon grado di ripetibilità, poiché le diverse curve sono sufficientemente distanziate nel tratto in cui la fluorescenza è più elevata, evitando in questo modo di confondere tra loro le diverse concentrazioni.

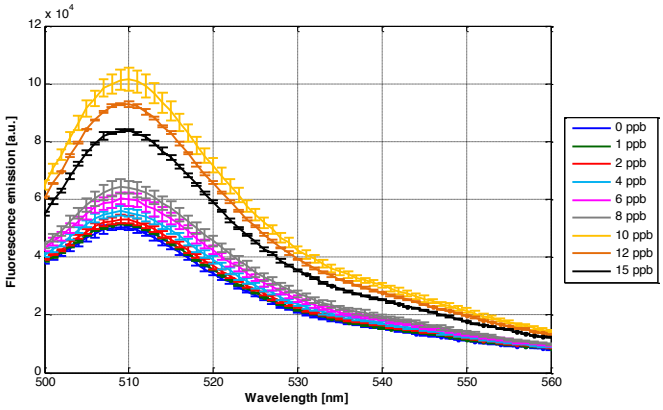

Figura 64: Spettri di emissione in fluorescenza e relative deviazioni standard del BODIPY-amminofenolo 5μM (λex = 480 nm) in acqua di mare sperimentale /etanolo (9:1) con aggiunta di ioni Hg^{2+} con concentrazioni crescenti nell'intervallo 0 – 15 ppb.

Per apprezzare le differenze esistenti tra gli spettri relativi alle diverse concentrazioni di ioni Hg^{2+} si è deciso di studiare la posizione (in lunghezza d'onda) e l'emissione (intensità) del punto di massimo di ciascuno dei due picchi individuati. Per il picco centrato intorno ai 510 nm, il grafico relativo alla lunghezza d'onda è riportato in Figura **12**64. È immediato osservare che si ha solo un piccolo spostamento della lunghezza d'onda del picco di emissione al variare della concentrazione nell'intorno di 510 nm. Si è deciso pertanto di non eseguire ulteriori analisi su questo parametro, focalizzando l'attenzione sul valore di intensità di emissione di picco.

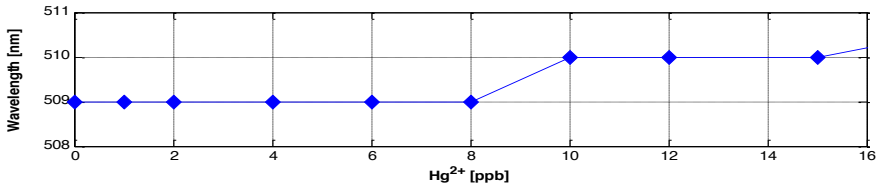

Figura 65: Andamento della lunghezza d'onda del punto di massima emissione in fluorescenza (picco intorno a 510 nm) per soluzioni di BODIPY-amminofenolo 5μM (λex = 480 nm) in acqua di mare sperimentale/etanolo (9:1) con aggiunta di ioni Hg^{2+} con concentrazioni crescenti nell'intervallo 0 – 15 ppb.

L'intensità di emissione in fluorescenza misurata nel picco intorno a 510 nm è riportata nel grafico mostrato in Figura 13. È possibile riscontrare un andamento complessivo crescente della fluorescenza massima all'aumentare della concentrazione di ioni Hg^{2+} fino ad un valore di 10 ppb. Dal grafico emerge che a partire dal punto a 10 ppb, non si rispetta l'andamento monotono. Ciò suggerisce che nell' intorno di questa concentrazione possa verificarsi una variazione della stechiometria e/o della conseguente geometria del complesso.

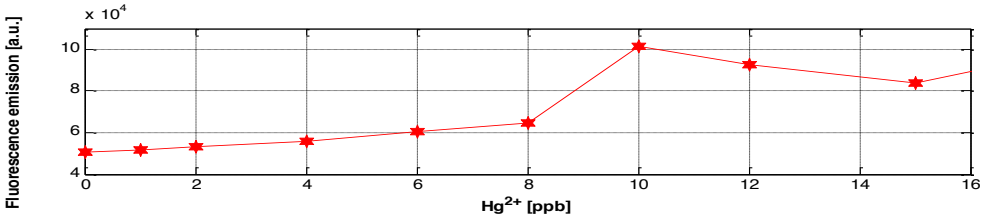

Figura 66: Andamento dell'intensità della massima emissione in fluorescenza (picco intorno a 510 nm) per soluzioni di BODIPY-amminofenolo 5μM (λex = 480 nm) in acqua di mare sperimentale/etanolo (9:1) con aggiunta di ioni Hg^{2+} con concentrazioni crescenti nell'intervallo 0 – 15 ppb.

Sulla base di quanto mostrato in precedenza, si è deciso di costruire una curva di calibrazione con fitting lineare nell'intervallo 0–8 ppb, scartando così le concentrazioni al di sopra di questo intervallo che non rispettano un andamento lineare. In Figura 66 è stato riportato uno zoom degli spettri di emissione in fluorescenza nell'intervallo Hg^{2+} 0-8 ppb con relative deviazioni standard nell'intervallo preso in esame per l'elaborazione del fitting.

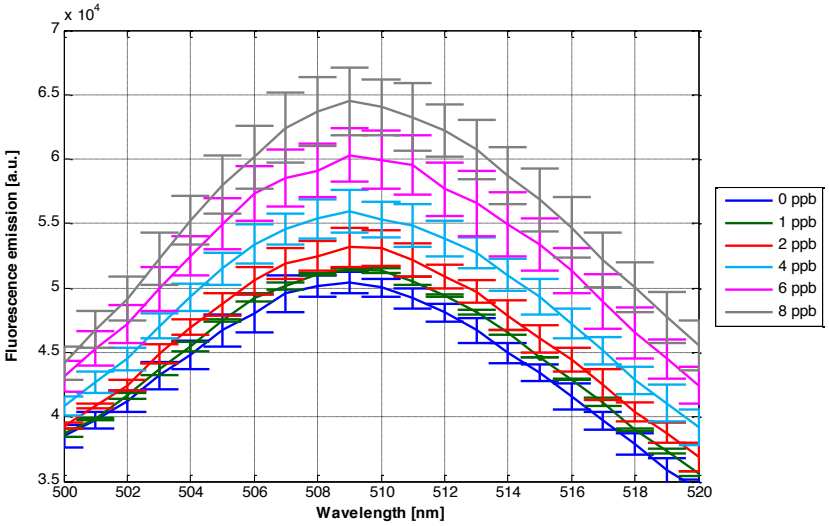

Figura 67: Zoom della porzione di spettro di fluorescenza intorno al punto di massimo con le relative barre di errore per soluzioni di BODIPY-amminofenolo 5μM (λex = 480 nm) in acqua di mare sperimentale/etanolo (9:1) con aggiunta di ioni Hg^{2+} con concentrazioni crescenti nell'intervallo 0 – 8ppb.

Prendendo in considerazione il grafico mostrato in Figura 19, è possibile constatare la bontà del fitting lineare, i cui parametri sono riportati nella Tabella 2 mostrata qui di seguito. In particolare, si può apprezzare un buon valore del parametro R^2, superiore al 98%.

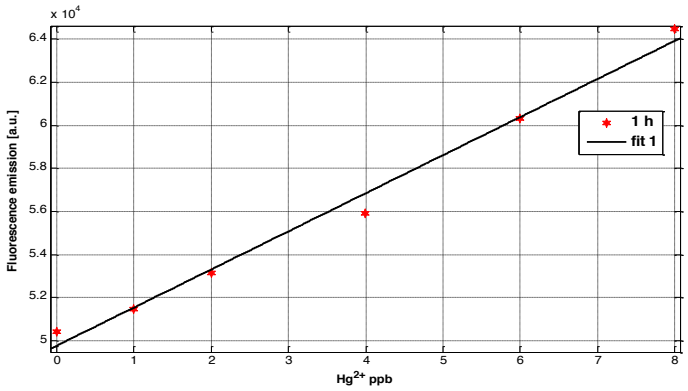

Figura 68: Curva di calibrazione e fitting lineare dell'emissione in fluorescenza nel punto di massimo (picco intorno a 510 nm) per soluzioni di BODIPY-amminofenolo 5 µM (λex = 480 nm) in acqua di mare sperimentale /etanolo (9:1) con aggiunta di ioni Hg^{2+} con concentrazioni crescenti nell'intervallo 0 – 8 ppb.

Linear model Poly1:
f(x) = p1*x + p2
Coefficients (with 95% confidence bounds):
p1 = 1769 (1514, 2024)
p2 = 4.997e+004 (4.863e+004, 5.092e+004)
Goodness of fit:
SSE: 1.60e+006
R-square: 0.9893
Adjusted R-square: 0.9866

Tabella 8: Parametri di fitting della curva di calibrazione dell'assorbanza nel punto di massimo locale (picco intorno ai 510 nm) per soluzioni di BODIPY-amminofenolo 5 µM (λex = 480 nm) in acqua di mare sperimentale/etanolo (9:1) con aggiunta di ioni Hg^{2+} con concentrazioni crescenti nell'intervallo 0 – 8 ppb.

Conclusioni

- Lo studio delle prove effettuate conferma che il BODIPY-amminofenolo è sensibile a concentrazioni di Hg^{2+} nel range di ppb.
- Lo spettro di fluorescenza del BODIPY-amminofenolo presenta un unico picco localizzato intorno a 510 nm. Analizzando il punto di massima fluorescenza al variare della concentrazione di Hg^{2+}, si è trovato una correlazione lineare nell'intervallo 0 – 8 ppb anche in acqua di mare sperimentale.
- Il BODIPY-amminofenolo rappresenta un potenziale ligando per ulteriori studi di selettività e specificità in saggi di riconoscimento di ioni mercurio (ppb) in matrici acquose complesse.

Light assisted antibody immobilization for bio-sensing

Bartolomeo Della Ventura,[1,2] Luigi Schiavo,[1] Carlo Altucci,[1] Rosario Esposito,[1] and Raffaele Velotta[1,*]

[1]*CNISM and Dipartimento di Scienze Fisiche, Università di Napoli "Federico II", Via Cintia, 26, Naples, 80126, Italy*

[2]*Dipartimento di Medicina, Seconda Università di Napoli, Via Costantinopoli, 16, Naples, 80132, Italy*

**rvelotta@unina.it*

Abstract: Ultrashort UV pulses at 258 nm with repetition rate of 10 kHz have been used to irradiate buffer solution of antibody. The tryptophan residues strongly absorb this radiation thus becoming capable to disrupt the disulfide bridges located next to them. Due to their high reactivity the opened bridges can anchor a gold plate more efficiently than other sites of the macromolecule giving rise to preferential orientations of the variable part of the antibody. UV irradiation has been applied to anchor antiIgG antibody to the electrode of a Quartz Crystal Microbalance (QCM) that lends itself as a sensor, the antibody acting as the bio-receptor. An increase of the QCM sensitivity and of the linear range has been measured when the antibody is irradiated with UV laser pulses. The photo-induced reactions leading to disulfide bridge breakage have been analyzed by means of a chemical assay that confirms our explanation. The control of disulfide bridges by UV light paves the way to important applications for sensing purpose since cysteine in combination with tryptophan can act as a hook to link refractory bio-receptors to surfaces.

©2011 Optical Society of America

OCIS codes: (280.1415) Biological sensing and sensors; (350.3450) Laser-induced chemistry; (170.0170) Medical optics and biotechnology.

References and links

1. M. A. Cooper and V. T. Singleton, "A survey of the 2001 to 2005 quartz crystal microbalance biosensor literature: applications of acoustic physics to the analysis of biomolecular interactions," J. Mol. Recognit. **20**(3), 154–184 (2007).
2. J. L. Arlett, E. B. Myers, and M. L. Roukes, "Comparative advantages of mechanical biosensors," Nat. Nanotechnol. **6**(4), 203–215 (2011).
3. Y. G. Lee and K. S. Chang, "Application of a flow type quartz crystal microbalance immunosensor for real time determination of cattle bovine ephemeral fever virus in liquid," Talanta **65**(5), 1335–1342 (2005).
4. X. Su, Y. J. Wu, and W. Knoll, "Comparison of surface plasmon resonance spectroscopy and quartz crystal microbalance techniques for studying DNA assembly and hybridization," Biosens. Bioelectron. **21**(5), 719–726 (2005).
5. E. Ostuni, L. Yan, and G. M. Whitesides, "The interaction of proteins with self-assembled monolayers of alkanethiolates on gold and silver," Colloids Surf. **13**, 3–30 (1999).
6. Y. Ruan, T. C. Foo, S. Warren-Smith, P. Hoffmann, R. C. Moore, H. Ebendorff-Heidepriem, and T. M. Monro, "Antibody immobilization within glass microstructured fibers: a route to sensitive and selective biosensors," Opt. Express **16**(22), 18514–18523 (2008).
7. J. R. Ott, M. Heuck, C. Agger, P. D. Rasmussen, and O. Bang, "Label-free and selective nonlinear fiber-optical biosensing," Opt. Express **16**(25), 20834–20847 (2008).
8. H. N. Daghestani and B. W. Day, "Theory and applications of surface plasmon resonance, resonant mirror, resonant waveguide grating, and dual polarization interferometry biosensors," Sensors (Basel Switzerland) **10**(11), 9630–9646 (2010).
9. M. T. Neves-Petersen, T. Snabe, S. Klitgaard, M. Duroux, and S. B. Petersen, "Photonic activation of disulfide bridges achieves oriented protein immobilization on biosensor surfaces," Protein Sci. **15**(2), 343–351 (2006).
10. C. A. Janeway, Jr., P. Travers, M. Walport, and M. J. Shlomchiket, *Immunobiology* (Garland Science, 2001).
11. M. T. Neves-Petersen, Z. Gryczynski, J. Lakowicz, P. Fojan, S. Pedersen, E. Petersen, and S. Bjørn Petersen, "High probability of disrupting a disulphide bridge mediated by an endogenous excited tryptophan residue," Protein Sci. **11**(3), 588–600 (2002).
12. J. R. Lakowicz, *Principles of Fluorescence Spectroscopy* (Springer, 2006).

#154574 - $15.00 USD Received 14 Sep 2011; revised 17 Oct 2011; accepted 17 Oct 2011; published 28 Oct 2011

13. R. Weinkauf, P. Aicher, G. Wesley, J. Grotemeyer, and E. W. Schlag, "Femtosecond versus nanosecond multiphoton ionization and dissociation of large molecules," J. Phys. Chem. **98**(34), 8381–8391 (1994).
14. B. Gu, K. Lou, H. T. Wang, and W. Ji, "Dynamics of two-photon-induced three-photon absorption in nanosecond, picosecond, and femtosecond regimes," Opt. Lett. **35**(3), 417–419 (2010).
15. DataBank RCSB PDB, IgG structure (*http://www.rcsb.org/pdb/explore/explore.do?structureId=3I75*).
16. T. R. Ioerger, C. Du, and D. S. Linthicum, "Conservation of cys-cys trp structural triads and their geometry in the protein domains of immunoglobulin superfamily members," Mol. Immunol. **36**(6), 373–386 (1999).
17. G. Z. Sauerbrey, "Verwendung von Schwingquarzen zur Wägung dünner Schichten und zur Mikrowägung," Z. Phys. **155**(2), 206–222 (1959).
18. G. L. Ellman, "Tissue sulfhydryl groups," Arch. Biochem. Biophys. **82**(1), 70–77 (1959).
19. C. Yao, T. Zhu, Y. Qi, Y. Zhao, H. Xia, and W. Fu, "Development of a quartz crystal microbalance biosensor with aptamer as bio-recognition element," Sensors (Basel Switzerland) **10**(6), 5859–5871 (2010).

1. Introduction

The quest for label free biosensors, in which no tag is applied to molecule to be detected, is underpinning the development of quartz-crystal-microbalance (QCM) based sensors [1]. Based on the measurement of the mass of the analyte, they also offer high versatility for different applications and are relatively low-priced and high sensitive, with the main constraint being the need of a specific binding partner (e.g. polyclonal antibody) for the molecule to be detected. Although this might appear a severe limitation for QCMs, the actual availability of antibodies for a wide range of analytes as well as their performances in terms of detection limit make these sensors very appealing for bio-sensing (an extensive review about the features of different types of biosensors can be found in ref [2].). As opposed to optical biosensors, QCMs are able to operate directly in complex liquids without the need for purification and their fast response and reliability have been proved even in the virus detection [3]. In applications like DNA assembly and hybridization no significant difference was found in comparison to a widespread technique such as Surface Plasmon Resonance with regard to linear range as well as limit of detection [4].

In QCMs the analyte is recognized by bio-receptors immobilized on the sensor surface: the larger the density of active bio-receptors, the higher the effectiveness of the biosensor. The strategies to anchor bio-receptors on the gold surface of the QCMs can be gathered into two basic categories: passive adsorption or covalent immobilization. The former relies upon non-specific interaction between the bio-receptor (e.g. antibody) and the gold surface. This procedure is fast and simple, but as a consequence of the nonspecific interaction it leads to relatively unstable anchoring as well as randomly oriented bio-receptors thus affecting the sensing effectiveness. On the opposite the covalent immobilization is based upon specific (covalent) interaction between the functional residues linked on the surface and the bio-receptors. This gives rise to specific and stable bonds, but the surface functionalization is generally achieved by time consuming procedures requiring qualified expertise and quite advanced technology [5,6]. Alternative tools to surface activation are of general interest in biosensing research since it is a non-avoidable step in biosensors based on fiber optics [7], surface plasmon resonance or interferometry [8].

As a method to overcome such drawbacks it has been proposed the use of UV light to break the disulfide bridges in protein upon absorption by nearby aromatic amino acids [9]. In fact, the bridge opening leads to the formation of reactive thiol groups that are very effective in bonding many surfaces, gold made plate among the other. Moreover, since the anchor link is determined by the position of the thiol group, the orientation of the bio-receptor on the plate can be controlled to a large extent. This is especially true when antibody is used as bio-receptor, since if the antibody were anchored to the plate through its variable part (the so-called Fab, Fragment Antigen Binding) the recognition would be hampered [10]. The disulfide bond breaking can be realized through the interaction with excited endogenous tryptophan residue [11], the latter being easily accomplished exploiting the high UV absorption by tryptophan [12].

In this paper we report on the antibody anchoring to a QCM gold electrode for sensing applications. Since the aromatic aminoacid absorption is the springboard for the bond breakage, high UV mean power is needed. Moreover, if the dissociation must be kept low,

#154574 - $15.00 USD Received 14 Sep 2011; revised 17 Oct 2011; accepted 17 Oct 2011; published 28 Oct 2011
(C) 2011 OSA

femtosecond rather than nanosecond pulses are appropriate in view of the resonant one photon excitation occurring in aromatic aminoacid in the UV range [13,14]. Thus, we have used the fourth harmonic of a 1030 nm femtosecond laser pulse delivered at 10 kHz repetition rate to irradiate the antiIgG from goat to detect IgG from mouse observing an increase in the detection efficiency explained in terms of improved orientation of antibody on the electrode. This antibody has 12 disulfide bridges at a distance from tryptophan not longer than approximately 5 Å [15,16]. These are located in such a way that their interaction with the gold surface prevents the antibody from anchoring upside down, which would impede the antigen recognition.

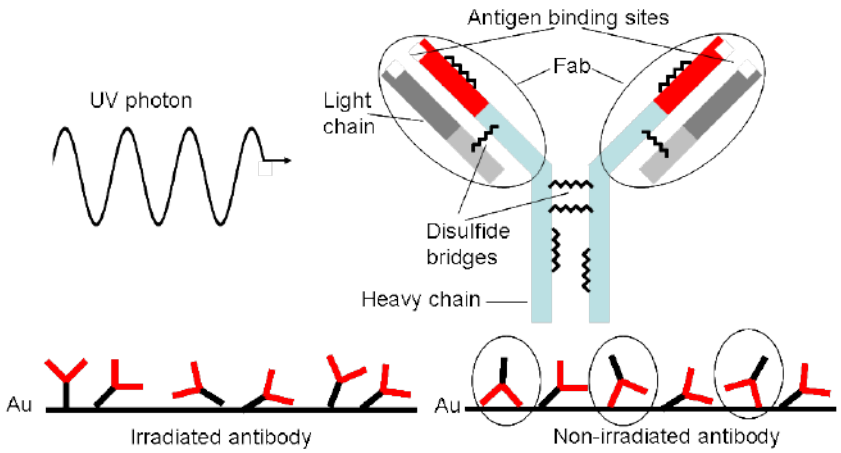

Fig. 1. (a) One UV photon is absorbed by the antibody and the disulfide bridge is opened thereby forming thiol groups. Their interaction with the gold surface leads to oriented Fab region so that the upside down position (circled in the right side of the picture) is hampered and the antigen binding is more effective.

The mechanism underlying the light induced antibody anchoring is described in Fig. 1. The tryptophan residues absorb in the UV range and relax by transferring the absorbed energy to its neighbors. The cysteines are close enough to the tryptophans so that the photon energy is virtually absorbed by the former. The resulting free thiol groups are highly reactive so that they can efficiently link the gold surfaces of a QCM.

2. QCM based biosensors and experimental procedure

A quartz crystal microbalance (QCM, µLibra, Technobiochip, Italy) with a fundamental frequency f_0 of 10 MHz and gold electrodes was used in the experiments. The frequency shift Δf of the quartz crystal after bio-receptor adsorption was measured at the first overtone order, i.e.10 MHz. The relation between the frequency change and the mass deposition Δm is given by the Sauerbrey equation [17] from which we have $\Delta f = -K(\Delta m)$, K being a constant depending on several experimental parameters (resonance frequency, piezoelectrically active crystal active area, quartz density and shear modulus for AT-cut crystal).

Figure 2 shows the pipeline system we have used to convey the solutions to the gold plate. The solution is drawn from a cuvette by peristaltic pump allowing a laminar flow onto the plate. To irradiate the antibody the laser was shined into the cuvette for 5′ before the pump was switched on and was kept on while the antibody was flowing into the pipeline circuit. The UV light was delivered by a femtosecond laser system (Pharos, Light Conversion, http://www.lightcon.com/) operating at 10 kHz repetition rate. The energy of the fourth harmonic (λ = 258 nm) was 30 µJ resulting in 0.3 W average power laser brought to the sample with no further focusing.

Libra microbalance uses 10 MHz AT-cut quartzes with gold electrodes on chromium layer. An alternating voltage applied to the electrodes causes the quartz to resonate at a particular frequency, and resonant frequency difference is directly proportional to the mass

#154574 - $15.00 USD Received 14 Sep 2011; revised 17 Oct 2011; accepted 17 Oct 2011; published 28 Oct 2011
(C) 2011 OSA

change. A simple model system, IgG mouse as antigen and anti-mouse IgG as antibody, has been used to evaluate the effect of the light assisted antibody immobilization on the biosensor.

Briefly, the experimental protocol was

1) Initial QCM wash with 1x Phosphate Buffer (PBS) pH 7.4 for basal resonant frequency stabilization.

2) Light- assisted adsorption or passive adsorption (as control) of anti-mouse IgG (Sigma, Milan).

3) Wash with PBS 1x to eliminate the excess of anti-mouse IgG from goat.

4) Blocking with Bovin Serum Albumin (BSA) solution (100 μg/mL) to avoid nonspecific-binding. In fact, the QCM gold surface used have a high affinity for proteins. Therefore, after the anti-mouse IgG immobilization, it is important to block the remaining gold surface to prevent non-specific binding of the detection antibodies during subsequent steps.

5) Wash with PBS 1x to eliminate BSA in excess.

6) Flowing of mouse-IgG (Sigma, Milan) to allow the specific antigen-antibody complex formation.

7) Final wash with PBS 1x to eliminate weakly bonded mouse IgG .

The experiment were performed in triplicate in both fluidic cells (working and reference) showing a good intra-assay accuracy and reproducibility between channels. The QCM response, i.e. Δf versus time, is shown in Fig. 3 for each of the seven protocol steps, for 5μg/mL of anti IgG and 1μg/mL of mouse IgG: The solid and dashed lines refer to the non-irradiated and irradiated antibody, respectively. The comparison between the two curves evidences a larger amount of detected antigen when the antibody is irradiated, while no significant change in the anchored antibody is observed. This is consistent with the

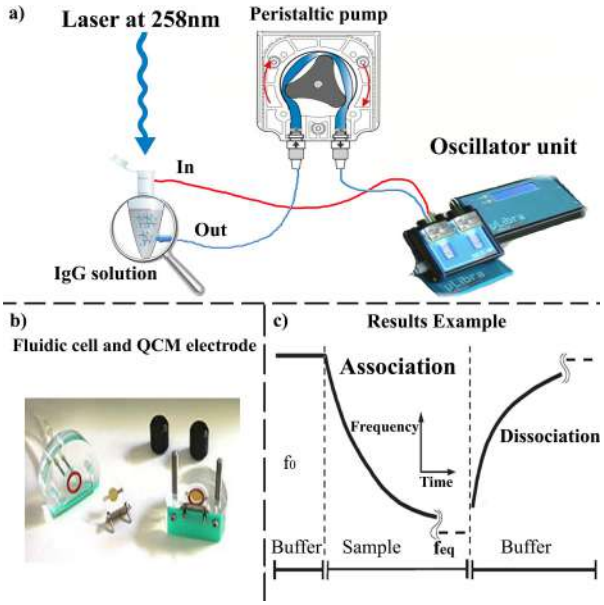

Fig. 2. (a) Experimental setup to convey the molecules to the electrode. (b) QCM cell for fluidic applications with gold electrodes. (c) Typical output showing the decrease of the frequency due to the association (anchoring) and the frequency rise produced by the dissociation (unanchoring).

#154574 - $15.00 USD Received 14 Sep 2011; revised 17 Oct 2011; accepted 17 Oct 2011; published 28 Oct 2011
(C) 2011 OSA

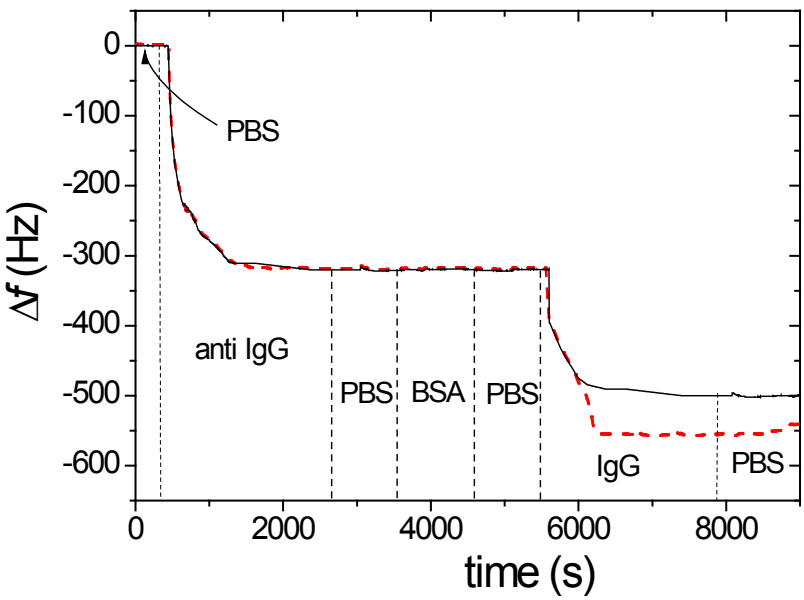

Fig. 3. QCM output obtained with with 5μg/mL of anti IgG) and 1μg/mL of mouse IgG of non-irradiated (black solid line) and irradiated antibody (red dashed line). The vertical dashed lines show the steps described in the text.

mechanism reported in Fig. 1, according to which the bond breakage facilitates the right orientation of the antibody on the plate, rather than increasing the number of anchored antibodies.

3. Results

3.1 Effect of antibody irradiation on QCM performances

In Fig. 4 we report the frequency shifts as a function of antigen concentration flowing onto the plate. We have analyzed two conditions: in the first the antibodies were adsorbed without any previous interaction with the UV light (black squares) whereas in the latter the antibodies were irradiated before and during the adsorption (see previous section) by the gold electrode of QCM (red circles). The clear enhancement of detector response is observed when the antibodies are previously irradiated with the UV light which can be interpreted by taking into account the steric effect induced by the disulfide bridge breaking when the antibody is irradiated. More specifically, the otherwise random antibody orientation on the gold plate is influenced by the opened disulfide bond in such a way that the Fab fragments are more exposed to the antigen [9,11]. The free sulphur favors the "right" antibody orientation and, hence, the antigen capture probability increases as well as the total amount of linkable antigen. In this view, the functional form of the curves in Fig. 4 and its dependence on the relevant experimental parameters can be deduced by the following argument.

The link between the antibody and the antigen occurs with a probability p, i.e. p is the probability for an antigen to be captured while passing onto the plate when all the N antibodies are free. As a consequence of the reduction of the available sites for antigen binding, the second antigen will have a probability $p(1-p)$ to be fixed on the plate, whereas for the third the probability will be $p[1-p(1-p)]$ and so on. The occupancy rate r of the N antibodies will be

$$r = p + p(1-p) + p\left[1-p(1-p)\right] + p\left\{1-p\left[1-p(1-p)\right]\right\}\ldots \qquad (1)$$

#154574 - $15.00 USD Received 14 Sep 2011; revised 17 Oct 2011; accepted 17 Oct 2011; published 28 Oct 2011
(C) 2011 OSA

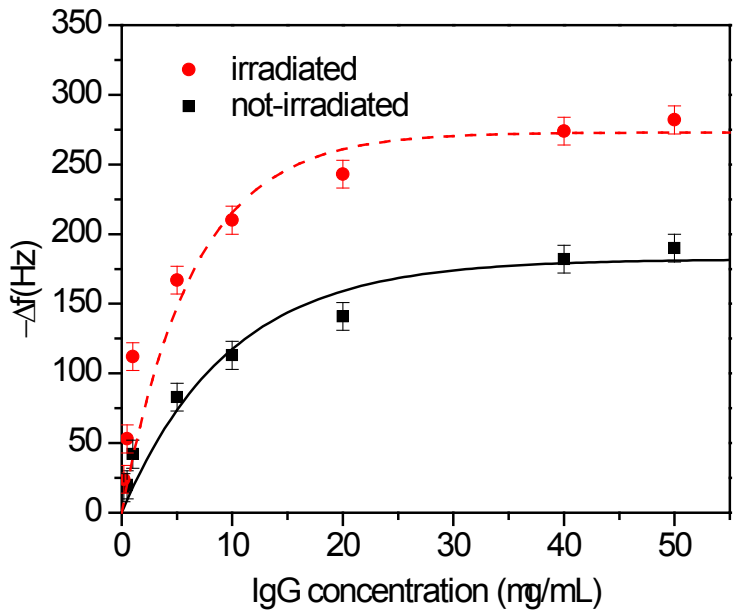

Fig. 4. Frequency shift measured with (red circle) irradiation and without (black square) antibody UV irradiation as a function of the antigen mass concentration. The best fit obtained with Eq. (3) provides $(\Delta f)_{max}$ = 182 Hz and $[M]_0$ = 9.6 μg/mL for the non-irradiated sample. For the irradiated sample the dashed curve is Eq. (3) with $(\Delta f)_{max,IRR}$ = 273 Hz and $[M]_{0,IRR}$ = 6.4 μg/mL.

where the summation is extended to M antigens interacting with N antibodies. As $M \to \infty$ and $p \to 0$ we have

$$r = 1 - \exp(-Mp) = 1 - \exp\left(-\frac{[M]}{[M]_0}\right) \tag{2}$$

The proportionality between Δf and the antigen mass deposited on the plate, which in turn is proportional to the concentration flowing in the fluidic circuit, leads to

$$\Delta f = (\Delta f)_{max}\left[1 - \exp\left(-\frac{[M]}{[M]_0}\right)\right] \tag{3}$$

where [M] is the mass concentration, $[M]_0$ a "characteristic mass concentration" whose value is an estimation of the linear range of the antigen sensor and $(\Delta f)_{max}$ a fit parameter. The best fit of the data obtained when the sample is not irradiated provides $(\Delta f)_{max}$ = 182 Hz and $[M]_0$ = 9.6 μg/mL and the resulting curve being in good agreement with the experimental results (black squares).

The experimental data obtained when the antibody is irradiated show an increase in the slope as well as in the saturation level. This can be explained by considering that the irradiation brings on oriented deposition of antibodies with their variable part facing up. As a consequence, more antibodies are effective for antigen linking thus increasing the probability p for an antigen to be linked during the flow. Since $[M]_0 \propto p^{-1}$ [Eq. (2)] the characteristic concentration decreases and the slope increases. The increase in the number of effective linking sites also accounts in a natural way for the larger saturation value for which $(\Delta f)_{max} \propto p$ is expected. This means that $(\Delta f)_{max}$ and $[M]_0$ should scale by the same factor when the effective antibody density is changed, i.e.

#154574 - $15.00 USD Received 14 Sep 2011; revised 17 Oct 2011; accepted 17 Oct 2011; published 28 Oct 2011
(C) 2011 OSA

$$\frac{(\Delta f)_{\max,IRR}}{(\Delta f)_{\max}} = \frac{[\mathrm{M}]_0}{[\mathrm{M}]_{0,IRR}} \equiv \frac{p_{IRR}}{p} \tag{4}$$

In Eq. (4) the subscript *IRR* refers to the values of the parameters when the antibody is irradiated. The fair fit of the experimental data (red dashed line in Fig. 4) has been obtained with $p_{IRR}/p = 1.5$ that yields $(\Delta f)_{\max,\mathrm{IRR}}$ = 273 Hz and $[\mathrm{M}]_{0,\mathrm{IRR}}$ = 6.4 μg/mL in Eq. (3). Assuming a linear dependence of the binding probability on the number of effective antibodies, Eq. (4) states that when irradiated approximately 50% more antiIgG are available to bind the antigen. Not only more bio-receptors on the electrode means more detectable antigens, thereby extending the linear range, but also larger antigen binding probability and, hence, higher sensitivity. With the help of Eq. (4), the latter can be easily worked out to be

$$S_{IRR} = \frac{\delta\left[(\Delta f)_{IRR}\right]}{\delta[\mathrm{M}]} = \frac{(\Delta f)_{\max,IRR}}{[\mathrm{M}]_{0,IRR}} = \left(\frac{p_{IRR}}{p}\right)^2 S \tag{5}$$

S_{IRR} and S being the sensitivity with and without the irradiation procedure. Thus, in our case the antibody irradiation more than doubles the sensor sensitivity.

3.2 Ellman assay

To verify the occurrence of disulfide bridge breaking we have carried out the Ellman assay based on a reagent [5,5′-dithiobis-(2-nitrobenzoic acid) or DTNB] able to quantify the concentration of thiol groups in a sample [18]. The reaction of the thiol with DTNB gives the mixed disulfide and 2-nitro-5-thiobenzoic acid (TNB) that is quantified by the absorbance of the anion (TNB^{2-}) at 412nm. The reagent has been widely used for the quantification of thiols in peptides and proteins and it has also been used to assay the disulfides present after blocking any free thiols and reducing the disulfides prior to reaction with the reagent [18].

The amount of free thiol groups as a function of the irradiation time and average irradiation power are reported in Figs. 5 and 6.

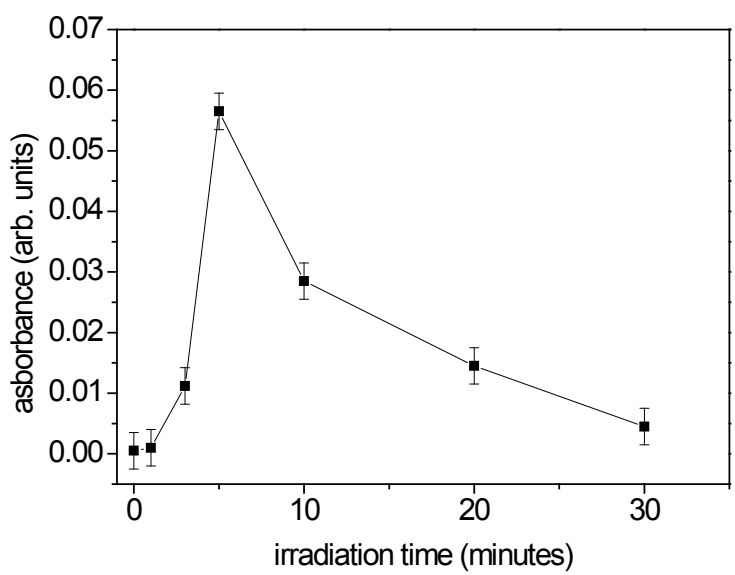

Fig. 5. Absorbance of antibody at 412 nm as a function of the irradiation time. The average laser power is 0.3 W. The reagent DTNB is added immediately after the laser exposure providing a measurement of the opened disulfide bridges.

#154574 - $15.00 USD Received 14 Sep 2011; revised 17 Oct 2011; accepted 17 Oct 2011; published 28 Oct 2011
(C) 2011 OSA

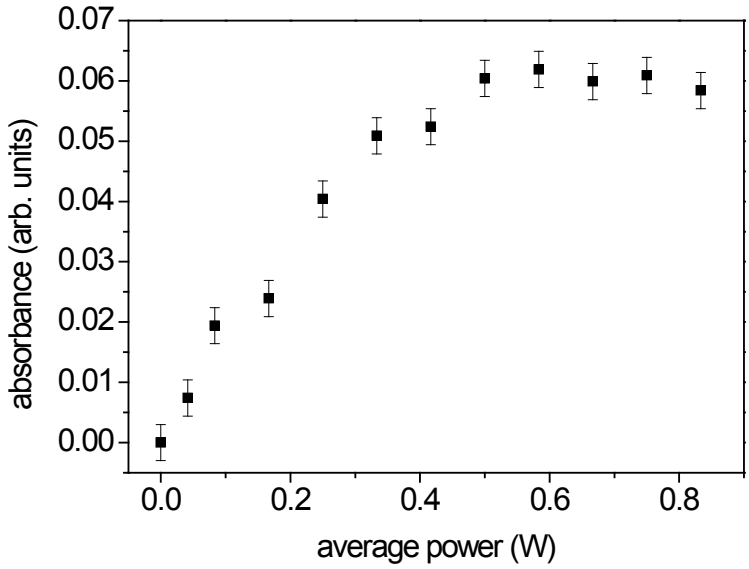

Fig. 6. Absorbance of antibody at 412 nm as a function of the average laser power. The irradiation time is 5′.

The existence of both an optimal irradiation time as well as a saturation effect when the energy per pulse (i.e. the average power) is increased suggests that the disulfide bridges have two loss channels after they have been opened by a UV photon: they can close again being available for a further opening or, alternatively, they can be "destroyed", e.g. by linking each other as a consequence of their high reactivity, thus giving rise to a net loss of molecule available for absorption. However, the Ellman assay demonstrates that the experimental conditions we have used really maximize the production of free thiol groups thereby supporting our description of the microscopic process.

4. Conclusions

Our work has demonstrated the effectiveness of ultrashort UV laser pulse in breaking the disulfide bridge in antibody thereby producing highly reactive free sulphurs that allow the right orientation of the antibody variable part (the so-called Fab region). This technique offers a powerful tool to steer the antibody orientation thus leading to more effective "hooks" available on the electrode of a QCM. The sensor performances in terms of linear range and sensitivity turn out to be significantly improved. Although we tested our method using antiIgG from goat to detect IgG from mouse, it is expected to observe similar behavior for any antibody since the presence of disulfide bridges is a common feature of all the antibodies. This opens interesting perspectives in the sensor research since it is possible to design peptide molecules that bind to a specific target molecule (aptamers) [19] and immobilize it on a QCM electrode by adding cysteines at one terminal. The ultrashort UV laser pulses would then be used to reduce the cysteines making them prone to fast binding to gold surface without any need for surface functionalization.

The photon assisted immobilization technique is competitive against alternative methods to anchor protein on to gold electrodes even if ultrafast UV pulses are to be used. This is because the functionalization is usually achieved by means of expensive toxic chemical reagents and requires long chemical procedures in well-equipped laboratories. On the contrary, femtosecond sources like that used in the present work are user friendly and can be safely run by non-expert personnel.

Since the high chemical reactivity of the opened bridges can lead them to different pathway other than surface binding (e.g. they can bind each other in solution), the optimal irradiation conditions have been found with the help of a chemical assay that allowed us to

#154574 - $15.00 USD Received 14 Sep 2011; revised 17 Oct 2011; accepted 17 Oct 2011; published 28 Oct 2011
(C) 2011 OSA

measure the amount of thiol groups in solution. Finally, the frequency shift measured by QCM has been interpreted by a simple statistical model that accounts for the experimental findings providing a physical insight of the microscopic phenomena involved in the UV light interaction with the antibody and its subsequent binding to gold electrode surface.

#154574 - $15.00 USD Received 14 Sep 2011; revised 17 Oct 2011; accepted 17 Oct 2011; published 28 Oct 2011
(C) 2011 OSA

UV-light-assisted functionalization for sensing of light molecules

Riccardo Funari*[a], Bartolomeo Della Ventura[b], Antonio Ambrosio[c],
Stefano Lettieri[c], Pasqualino Maddalena[a,c], Carlo Altucci[a] and Raffaele Velotta[a]
[a]Dept. of Physics, Univ. degli Studi di Napoli "Federico II", via Cinthia, 26, 80126 Napoli, Italy,
[b]Dept.of Physics, Univ. degli Studi di Roma "La Sapienza", p.le Aldo Moro, 5, 00185 Roma, Italy
[c]CNR-SPIN, Via Cintia 26, 80126 Napoli, Italy

ABSTRACT

An antibody immobilization technique based on the formation of thiol groups after UV irradiation of the proteins is shown to be able to orient upside antibodies on a gold electrode of a Quartz Crystal Microbalance (QCM). This greatly affects the aptitude of antibodies in recognizing small antigens thereby increasing the sensitivity of the QCM. The capability of such a procedure to orient antibodies is confirmed by the Atomic Force Microscopy (AFM) of the surface that shows different statistical distributions for the height of the detected peaks, whether the irradiation is performed or not. In particular, the distributions are Gaussian with a standard deviation smaller when irradiated antibodies are used compared to that obtained with no treated antibodies. The standard deviation reduction is explained in terms of higher order induced on the host surface resulting from the trend of irradiated antibodies to be anchored upside on the surface with their antigen binding sites free to catch recognized analytes. As a result the sensitivity of the realized biosensor is increased by even more than one order of magnitude.

Keywords: immunosensor; Quartz Crystal Microbalance; antibody orientation; parathion; ultrashort UV pulses

1. INTRODUCTION

Nowadays there is a strong interest in the development of measurement tools suitable for rapid and low cost analysis. Sensing and biosensing face this issue exploiting knowledge and technologies from different topics. The search of biological molecules able to bind the desired compound is extremely convenient since we can exploit what is already available in nature for our purposes. In this research area one of the crucial steps is the surface functionalization, especially in biosensors development. The immobilization of a biomolecule onto surfaces strongly affects function and activity of the anchored biomolecule, so it is extremely important to develop procedures which allow both good limit of detection (LOD) and high sensitivity, while preserving its attitude to recognize specific molecules[1].

The technological and biological characteristics of the system define the appropriate functionalization procedure to be applied. For example, technologies like QCM and Surface Plasmon Resonance (SPR) involve the use of gold plates and are widely employed in the development of immunosensors[2]. Gold is a biocompatible metal which can be easily cleaned by chemical treatment (e.g. piranha solution). The main advantage of gold electrodes in biosensing is the high stability of the gold-sulfur interaction which can be exploited for anchoring biomolecules exposing a free thiol group. This chemical function is usually present in proteins and can be easily added in chemical synthesis products.

It is well known that UV light affects protein structure and activity[3] and has interesting application in biosensing development[4]. Photonic Immobilization Technique (PIT) is a novel functionalization technology that results in spatially oriented anchoring of biomolecules onto thiol reactive surfaces (e.g. gold electrode)[5]. The only requirement to adopt this technique is the presence in the protein of a closely spaced Trp/Cys-Cys structural triad. Bioinformatic studies reveal that this structural characteristic is observable in all the IgSF (immunoglobulin superfamily) members and in many other proteins[6]. The protein structure of a typical IgG (1IGY)[7] is reported in figure 1 where the structural triad is also shown.

Optical Sensors 2013, edited by Francesco Baldini, Jiri Homola,
Robert A. Lieberman, Proc. of SPIE Vol. 8774, 87740K · © 2013
SPIE CCC code: 0277-786X/13/$18 · doi: 10.1117/12.2018510

Downloaded From: http://proceedings.spiedigitallibrary.org/ on 03/08/2016 Terms of Use: http://spiedigitallibrary.org/ss/TermsOfUse.aspx

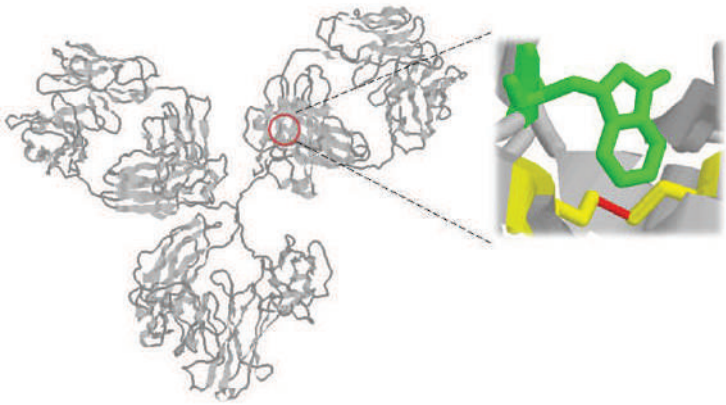

Figure 1. Crystallographic structure of a type G immunoglobulin (1IGY). Bioinformatic studies reveal that all the immunoglobulins have several triads of closely spaced aminoacids Trp/Cys-Cys.

The reaction mechanism behind this immobilization procedure involves the photonic activation of disulfide bridges: the UV photon is absorbed by tryptophan sidechain and its energy is subsequently released to the nearby cysteines so that the disulfide bridge breaks, resulting in the formation of two free thiol groups. These new chemical functions can easily react with a gold plate or a thiol-rich surface thus anchoring effectively the biomolecules[4].

In this paper we report the application of the PIT to the development of a QCM based immunosenor for the detection of parathion, a small and toxic molecule used as pesticide. Since QCM is sensitive to the mass and the molecular weight of parathion is relatively low (291.26 Da) we designed a procedure that allows the mixing of parathion with antibody in solution. This very heavy complex is subsequently conveyed to the QCM so that the exposed parathion is then recognized by the antibodies tethered on the gold electrode and well detected, thanks to an increased effective mass, by the QCM. We also report on the stationary fluorescence from a solution of irradiated antibodies that evidences change of conformation, but interestingly such a change does not affect the antibody capability to recognize the analyte. Moreover, AFM scans of the surface, after the antibodies are immobilized, demonstrate the effectiveness of PIT in orienting antibodies on a gold electrode.

2. METHODOLOGY

2.1 Chemicals

The following materials were from Sigma-Aldrich:

- Bovine serum albumin (BSA) (A2153)
- Parathion also called Ethylparathione, O,O-Diethyl O-(4-nitrophenyl) phosphorothioate or Parathion-ethyl (5607-100MG)
- Bisphenol A (BPA), IUPAC name 4,4'-(propane-2,2-diyl)diphenol (239658).
- p-nonylphenol (46018).
- Dichlorvos, IUPAC name 2,2-dichlorovinyl dimethyl phosphate (45441).
- Paraoxon, IUPAC name diethyl 4-nitrophenyl phosphate (36186).

The structure of parathion is reported in figure 2.

Downloaded From: http://proceedings.spiedigitallibrary.org/ on 03/08/2016 Terms of Use: http://spiedigitallibrary.org/ss/TermsOfUse.aspx

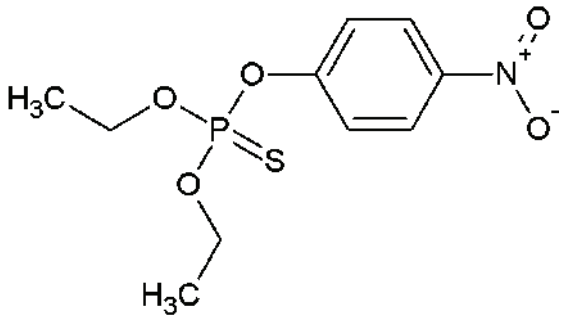

Figure 2. Chemical structure of parathion (molar mass 291.26 Da, IUPAC name O,O-Diethyl O-(4-nitrophenyl) phosphorothioate).

We used the Anti-Parathion polyclonal antibodies purchased from antibodies-online.com as rabbit serum (ABIN113883). The immunoglobulins were extracted by using Protein A agarose (Pierce) purchased from Thermo Scientific.

Other used materials are PBS 1x buffer solution pH 7.4, Helix water, sulfuric acid 98% and hydrogen peroxide 30%.

2.2 Fluorescence apparatus

The fluorescence spectra were acquired using a Perkin Elmer LS55 spectrofluorometer. The measurements were performed exciting the sample at 278 nm and collecting the emission between 290-390 nm with a resolution of 0.5 nm.

2.3 AFM

The AFM images were obtained using an atomic force microscope (XE-100 by Park Systems Corp.) working in non-contact mode. The data analysis has been performed using the standard producer-released software, SPIP 6.0.13 (Image Metrology) and OriginPro 8 (OriginLab). Each topographycal image is constituted by 512x512 pixels obtained by scanning squared areas 5 micrometers wide.

2.4 Protein irradiation

The proteins are irradiated by a custom femtosecond PHAROS laser system (Light Conversion Ltd – www.lightcon.com). This device has a highly tunable pulse repetition rate and UV laser pulses having a length of approximately 120 fs which are obtained by coupling the laser with a harmonic generator stage (HIRO). HIRO provides the 515 nm, 343 nm or 258 nm wavelengths components with high conversion efficiency from the IR fundamental radiation.

Samples of 1 mL with a protein concentration of 50 μg/mL have been irradiated using the fourth harmonic of the femtosecond laser system described above. The laser source operates at a repetition rate of 10 kHz and delivers 250 mW of average power at λ = 258 nm (resulting in an energy per pulse of 25 μJ). These conditions offer the maximum efficiency in the activation of the antibodies as demonstrated by Della Ventura et al.[5].

2.5 Quartz crystal microbalance (QCM) and experimental apparatus

The experimental setup consists of the following elements:

- QCM device a μLibra from Technobiochip, Italy.
- Peristaltic pump GILSON.
- Tygon silicone pipes.
- Fluidic cell in which the quartz crystal is placed.
- AT-cut quartz crystals with a fundamental frequency of 10 MHz purchased from ICM, Oklahoma city (USA).

The frequency variation of the QCM is displayed on a computer by a producer released software.

An especially designed procedure has been developed to selectively label the parathion molecules in order to make them heavier and easily detected by micro-gravimetric devices. A parathion sample is incubated with a free antibody solution

Downloaded From: http://proceedings.spiedigitallibrary.org/ on 03/08/2016 Terms of Use: http://spiedigitallibrary.org/ss/TermsOfUse.aspx

(50 μg/mL) and mechanically stirred for 10 minutes. The 1 mL samples, so prepared, are stored overnight at room temperature.

The QCM experiment consists of the following steps:

1) Basal frequency stabilization by flowing of 1x PBS in the fluidic circuit.
2) Adsorption on the electrode surface of previously irradiated Anti-parathion polyclonal antibodies (50 μg/mL).
3) Washing step with 1x PBS in order to eliminate weakly tethered antibodies.
4) Complete saturation of the gold lamina by flowing a BSA solution (50 μg/mL).
5) Washing step to remove the BSA solution.
6) Antigen (parathion-antibody complex previously prepared) recognition by the adsorbed antibodies.
7) Final washing with 1x PBS solution to remove weekly bonded antigen.

This procedure mimics the sandwich configuration widely used in the ELISA assay. Figure 3 shows the antigen binding described in step 6.

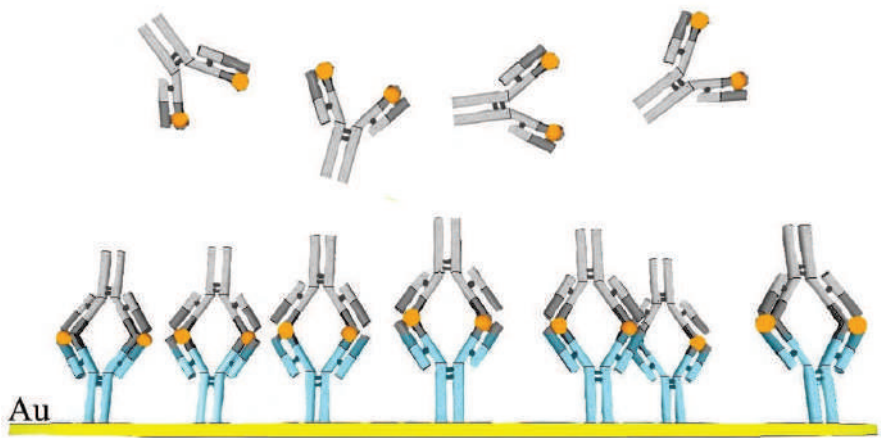

Figure 3. Binding of the antibody-parathion complexes by the anchored antibodies (in blue) which have been previously UV-activated.

The labeling procedure is crucial to detect parathion (291.26 Da) since, even if all the available antigen binding sites are occupied by the analytes, this will result in a frequency shift of only few Hz and, thus, not detectable by our biosensor.

3. RESULTS AND DISCUSSION

UV light affects the immunoglobulin sample in two different ways. Initially, the disulfide bridges are broken by means of the UV absorption through the near tryptophan residue as described by PIT mechanism. Subsequently, the protein is denaturated by long-time exposure to UV laser pulses. The optimal irradiation time has been found to be approximately 1 minute (0.25 W average power) and it corresponds to a maximum concentration of thiol groups as measured by Ellman's assay. Since with such a dose the antibodies still recognize the analytes, we deduce that UV light does not affect significantly the Fab region although conformational changes of the protein cannot be ruled out.

3.1 Fluorescence spectra

Stationary fluorescence is a rapid and low-cost method to investigate denaturation, folding and structural changes of proteins. Fluorescence emissions of intrinsic probes (Trp, Phe and Tyr) are strongly affected by changes in both chemical environment and protein structure. In our case, the protein irradiation results in the breakage of the disulfide

Downloaded From: http://proceedings.spiedigitallibrary.org/ on 03/08/2016 Terms of Use: http://spiedigitallibrary.org/ss/TermsOfUse.aspx

bridges placed nearby the tryptophan sidechain so that the protein structure becomes less compact. This new conformation allows the penetration of water molecules inside the protein resulting in the red shifting of the emission spectrum. This result is consistent with the immunoglobulin denaturation induced either by chaotropic agents or by temperature rising[8].

In the figure 4 we report the stationary fluorescence of antibody as a function of irradiation time. Essentially due to tryptophan fluorescence emission (λ_{ex} 278 nm), the collected fluorescence signal decreases with increasing irradiation time. In particular, the emission quickly drops after only 18 s irradiation time and changes slowly reaching a negligible value after several minutes of irradiation. Given the optimal irradiation time we have found (approximately 1 minute) the reduced emission has to be related to a prompt structural change that does not entail a complete denaturation, the latter occurring only after several minutes of irradiation. Thus, the conformational change induced by our laser source does not prevent the antibody from recognizing the analyte, while making more effective its upside tethering on gold. On the other side, it is plausible that the irradiated antibody may lose its ability to recruit the elements required for the immune response. This "immune function" is related to the Fc portion and does not affect the antigen recognition since it is due to a different part of the macromolecule.

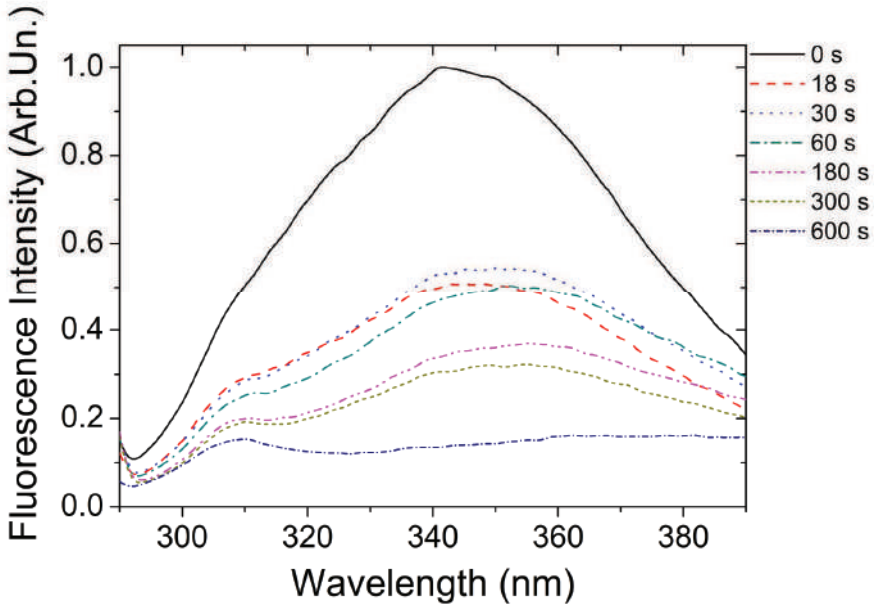

Figure 4. Fluorescence emission spectra of antibody sample as a function of irradiation time. The experimental data show that only few seconds of UV irradiation result in a consistent modification of the fluorescence spectra due to the changes in the surroundings of the tryptophan sidechain (e.g. disulfide bridges breakage). On the other side, irradiations longer than about 60 seconds lead to denaturation phenomena. These results are consistent with the Ellman's assay-based analysis reported by Della Ventura et al[5].

3.2 AFM analysis

As reported in literature[9], a significant difference in surface roughness is expected between random oriented and equally oriented adsorbed antibodies. The experimental data were analyzed by means of Origin Pro 8 software (OriginLab) in order to calculate the height distribution of the peak observed onto the gold surface. AFM outputs for QCM gold electrodes functionalized using either not- or irradiated antibodies are reported in figure 5. Five AFM scans were collected for both conditions.

Downloaded From: http://proceedings.spiedigitallibrary.org/ on 03/08/2016 Terms of Use: http://spiedigitallibrary.org/ss/TermsOfUse.aspx

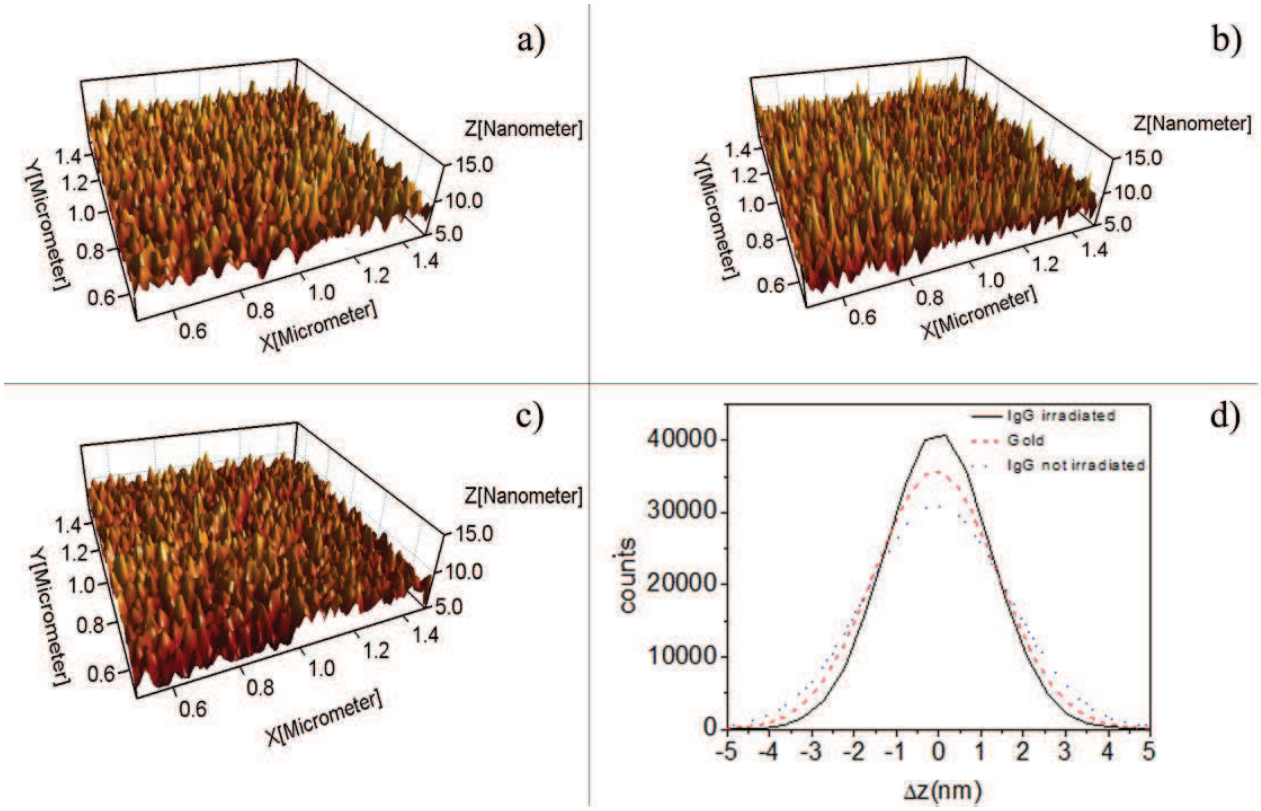

Figure 5. 3D plots of (a) gold electrode, (b) not-irradiated and (c) irradiated adsorbed samples respectively. (d) Height distributions of the three conditions.

The three height distributions in (a), (b), and (c) are Gaussian functions. The gold electrode is characterized by its own roughness which is related to the standard deviation of the distribution in (a). This parameter increases when the surface is functionalized by not-irradiated antibodies since the adsorbed proteins are randomly oriented. On the other side, the analysis shows that peak-to-valley excursion is smaller when the antibody solution is irradiated. This result suggests that using ultrashort UV laser pulses the adsorbed antibodies are preferentially oriented, thus inducing a higher degree of order onto the gold electrode.

3.3 QCM outputs

One of the main issue to face in biosensors development is surface functionalization, since the sensitive part of the biomolecule must be properly exposed to the sample in order to promote the analyte recognition. Figure 6 shows typical QCM outputs for both irradiated and not-irradiated antibodies in the detection of parathion (0.85 μM).

Downloaded From: http://proceedings.spiedigitallibrary.org/ on 03/08/2016 Terms of Use: http://spiedigitallibrary.org/ss/TermsOfUse.aspx

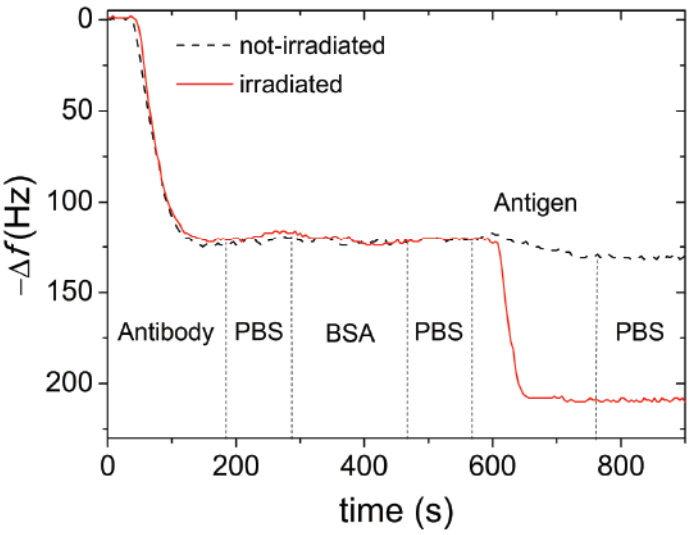

Figure 6. QCM outputs when the antibodies are irradiated (red solid line) and not-irradiated (black dashed line). The antibody concentration is 50 μg/mL whereas the antigen sample contains a parathion concentration of 0.85 μM.

The first frequency drop at approximately 50 s corresponds to the antibody adsorption onto the gold electrode. This frequency shift represents the amount of antibody adsorbed onto the gold electrode which turns out to be the same whether or not the antibodies are irradiated. The main striking difference between the two outputs lies in the antigen binding phase (second drop at ≈ 600 s). The sensor response is much better when PIT is used resulting in much higher sensitivity as well as a lower limit of detection. The sensor specificity for parathion has been verified by using different toxic and organophosphate compounds. The sensor response is negligible even for paraoxon, which differs from parathion for just one atom. This result is of great importance since it confirms that PIT does not affect the antigen-binding function of the antibodies. On the other side, UV-irradiation causes a structural change which results in forming an IgG layer onto the QCM gold electrode which reveals to be more effective in antigen recognition, thus, hugely increasing the sensor sensitivity.

4. CONCLUSIONS

In the present paper we report an interesting application of PIT in the development of a QCM based biosensor for the detection of a small and toxic molecule like parathion (291.26 Da). The procedure is inherently specific since antibodies are used in both labeling and recognition. The UV-activation of immunoglobulins has been characterized by means of three different techniques. Fluorescence analysis shows that the protein conformation changes significantly when the immunoglobulin sample is irradiated by UV laser pulses. The structural change does not affect the ability to bind the antigen in fact the irradiated adsorbed antibodies result to be much more sensitive to the organophosphate compound than not-irradiated ones. In addition, AFM outputs show that activated antibodies lead to a more ordered protein layer onto the electrodes, characterized by well exposed antigen binding sites. Since the presence of the triad Trp/Cys–Cys is the only requirement for the application of the PIT, UV light can be used to develop immunosensors for the detection of a wide range of toxic and harmful compounds.

*riccardo.funari@unina.it; phone 0039 081 676293; fax 0039 081 676352; phorlife.fisica.unina.it/

Downloaded From: http://proceedings.spiedigitallibrary.org/ on 03/08/2016 Terms of Use: http://spiedigitallibrary.org/ss/TermsOfUse.aspx

REFERENCES

[1] Y. Jung, J. Y. Jeong, and B. H. Chung, "Recent advances in immobilization methods of antibodies on solid supports.," *The Analyst* **133**(6), 697–701 (2008).

[2] B. Byrne, E. Stack, N. Gilmartin, and R. O'Kennedy, "Antibody-based sensors: principles, problems and potential for detection of pathogens and associated toxins.," *Sensors* **9**(6), 4407–4445 (2009).

[3] M. T. Neves-petersen, Z. Gryczynski, P. Fojan, S. Pedersen, E. Petersen, and S. B. Petersen, "High probability of disrupting a disulphide bridge mediated by an endogenous excited tryptophan residue," *Protein Science* **11**(3), 588–600 (2002).

[4] M. T. Neves-petersen, T. Snabe, S. Klitgaard, M. E. G. Duroux, and S. B. Petersen, "Photonic activation of disulfide bridges achieves oriented protein immobilization on biosensor surfaces," *Protein Science* **15**(2), 343–351 (2006).

[5] B. Della Ventura, L. Schiavo, C. Altucci, R. Esposito, and R. Velotta, "Light assisted antibody immobilization for bio-sensing.," *Biomedical optics express* **2**(11), 3223–3231 (2011).

[6] T. R. Ioerger, C. Du, and D. S. Linthicum, "Conservation of cys-cys trp structural triads and their geometry in the protein domains of immunoglobulin superfamily members.," *Molecular immunology* **36**(6), 373–386 (1999).

[7] L. J. Harris, E. Skaletsky, and a McPherson, "Crystallographic structure of an intact IgG1 monoclonal antibody.," *Journal of molecular biology* **275**(5), 861–872 (1998).

[8] P. Garidel, M. Hegyi, S. Bassarab, and M. Weichel, "A rapid, sensitive and economical assessment of monoclonal antibody conformational stability by intrinsic tryptophan fluorescence spectroscopy.," *Biotechnology journal* **3**(9-10), 1201–1211 (2008).

[9] S. Wang, M. Esfahani, U. a Gurkan, F. Inci, D. R. Kuritzkes, and U. Demirci, "Efficient on-chip isolation of HIV subtypes.," *Lab on a chip* **12**(8), 1508–1515 (2012).

Downloaded From: http://proceedings.spiedigitallibrary.org/ on 03/08/2016 Terms of Use: http://spiedigitallibrary.org/ss/TermsOfUse.aspx

analytical chemistry

Article

pubs.acs.org/ac

Detection of Parathion Pesticide by Quartz Crystal Microbalance Functionalized with UV-Activated Antibodies

Riccardo Funari, Bartolomeo Della Ventura, Luigi Schiavo, Rosario Esposito, Carlo Altucci, and Raffaele Velotta*

Department of Physics, Università di Napoli Federico II, Via Cintia, 26, Naples 80126, Italy

ABSTRACT: Photonic immobilization technique (PIT) has been used to develop an immunosensor for the detection of parathion. An antibody solution has been activated by breaking the disulfide bridge in the triad Trp/Cys-Cys through absorption of ultrashort UV laser pulses. The free thiol groups so produced interact with gold lamina making the antibody oriented upside, that is, with its variable parts exposed to the environment, thereby greatly increasing the detection efficiency. PIT has been applied to anchor polyclonal antiparathion antibodies to the gold electrode of a Quartz Crystal Microbalance (QCM) giving rise to very high detection sensitivity once the parathion is made heavier by complexion with BSA (bovine serum albumin), this latter step only required by the mass based transducer used in this case. The comparison of the sensor response with irradiated antibodies against different analytes shows that the high degree of antibody specificity is not affected by PIT nor is it by the complexion of parathion with BSA. These results pave the way to important applications in biosensing, since the widespread occurrence of the Trp/Cys-Cys residues triads in proteins make our procedure very general and effective to detect light analytes.

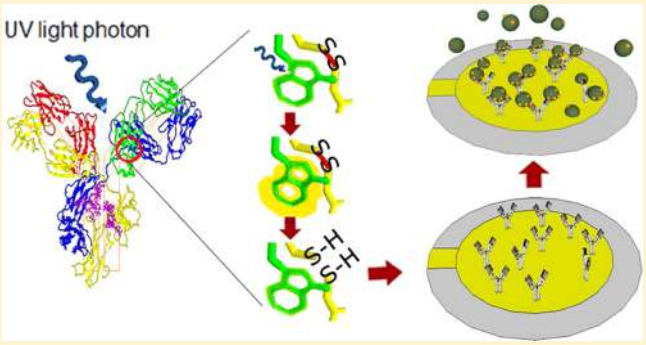

The high toxicity of pesticide residues and their bioaccumulation effects in human body underpins the research for fast response biosensors with high sensitivity and specificity for relatively light molecules.[1] Parathion (IUPAC name *O*,*O*-diethyl *O*-4-nitrophenil phosphorothioate) is an example of such compounds extensively used in agriculture as acaricide. As all the organophosphate insecticides, it is a selective inhibitor of acetylcholinesterase, an essential enzyme for nerve function in insects, humans, and many other animal species, thereby resulting highly toxic. The accumulation of this molecule leads to respiratory distress and muscular problems. Once absorbed, the parathion acts indirectly on the acetylcholinesterase since it is oxidized by enzymes of the host in its more reactive form, the paraoxon, which is capable of irreversible covalent binding the acetylcholinesterase.[2] The use of parathion is forbidden in the European Union.

Since the toxicity manifests its effects only several hours after exposure it is of paramount importance the availability of a tool allowing real-time analysis in environmental monitoring and particularly over agricultural waste. The lowest limit of detection (LOD) for parathion, and more in general measured for organophosphate, in aqueous solution has been achieved by Walker et al.[3] using a photonic crystal device. They developed a polymerized crystalline colloidal array (PCCA) photonic crystal sensing material that reaches a detection limit of 0.001 ppt. The crystals were coupled with acetylcholinesterase, which is irreversibly bonded by the organophosphate compound. The experiments were performed exposing the PCCAs to sample solutions as large as 100 mL thereby requiring up to 30 min for the analysis. Disadvantages of these devices include complex nanofabrication processes and the high cost of commercially modified substrates.

Amperometric devices allow rapid and low cost detection of organophosphates. A sensitive method for the detection of parathion has been developed by Zen et al.,[4] who reached a LOD of 50 nM (0.9 ppb) using a Nafion-coated glassycarbon electrode. Other detectors involve electrodes functionalized using organophosphorus hydrolase. Mulchandani et al.[5] reached a LOD of 20 nM (0.4 ppb) for both methyl-parathion and paraoxon, whereas Sacks et al.[6] efficiently detected parathion at nanomolar concentration. It is worth to mention that electrochemical devices are effective tools for analysis of aqueous solutions providing that the molecules to be detected are electroactive. In addition, this kind of sensors can be easily influenced by other oxidizable species that may well be present in a real sample.

Because of their cost-effectiveness, flexibility, and reliability, quartz crystal microbalance (QCM) based sensors have received an increasing interest in recent years[7,8] with wide applications to liquid samples. For instance, Bi and Yang[9] detected pesticides in aqueous environment using a QCM based method. They used molecular imprinted monolayers (MIMs), obtained from hexadecanethiol self-assembling on the

Received: March 21, 2013
Accepted: May 31, 2013
Published: May 31, 2013

 © 2013 American Chemical Society

QCM gold electrode, to detect imidacloprid and thiacloprid in celery juice reaching a LOD of 1 μM by using an extremely sensitive QCM apparatus with a resolution of 0.1 Hz. Marx et al.[10] developed a sol−gel functionalization method based on MIP (molecularly imprinted polymer) films for the detection of parathion. They applied this technique for the development of both cyclic voltammetry devices and QCM based sensors, but despite their high sensitivity, sol−gel-based functionalizations can be easily affected by cross-sensitivity phenomena.

The sensor specificity is inherently warranted when antibodies are used as linkers, but in this case, the surface functionalization becomes a crucial phase in the realization of the sensor, the antibody orientation being one of the main issues.[11] Usually a biological molecule moves into aqueous environment and its functions are characterized by parameters, which can change significantly when the same molecule is, instead, immobilized. So, there is a strong interest in the research of new immobilization and functionalization techniques which allows better sensitivity and lower LOD as witnessed by the vast literature on this topics.[12,13]

The most suitable functionalization procedure depends both on the nature of the biological sensitive element and on the transduction principle. Besides that, functionalization of gold laminas entices many efforts in view of their use not only in QCM-based immunosensors[14−17] but also in surface plasmon resonance (SPR).[18−20] Moreover, gold is an inert metal having a low tendency to oxidize and is biocompatible and easily cleaned by chemical treatments such as piranha solution (a mixture of sulfuric acid and hydrogen peroxide). The stability of gold−sulfur interaction is one of the mechanisms exploited to immobilize molecules on a support, since the only requirement is the availability of a thiol group. To this end, it is possible both to use a chemical marker of the molecule, usually easy to realize by chemical synthesis, or to exploit existing thiol groups within proteins and peptides.[21]

UV induced immobilization is a novel technology that results in spatially oriented and spatially localized anchoring of biomolecules onto thiol-reactive surfaces as demonstrated by Neves-Petersen et al.[22] The reaction mechanism behind this immobilization technique involves the photonic activation of disulfide bridges, that is, the light-induced breakage of disulfide bridges in proteins through UV illumination of nearby aromatic amino acids.

In a previous paper, we have demonstrated that no pretreatment to the surface is necessary, the presence of this structural characteristic being the only condition required to apply this approach that we will refer as photonic immobilization technique (PIT).[23] The mechanism of photonic activation of the Trp/Cys-Cys triads and the crystallographic structure of a type G immunoglobulin (IgG)[24] are shown in figure 1. Basically, the UV photon energy is absorbed by Tryptophan and then transferred to the close Cys-Cys thereby forming free reactive thiol groups which interact with thiol-reactive surfaces (like gold plates or surfaces treated with alkanethiols). Thus, the "driving force" for a possible side-up orientation of the antibody onto the gold surface is provided by the open disulfide bridges; these are produced in a selective way because the occurrence of a solvent accessible triad Try/Cys-Cys, which is required by PIT, is limited to interdomain region.[22]

The UV radiation may reduce or vanish the biological activity of proteins and enzymes, causing also structural changes in the biomolecules,[25] but PIT preserves the native structure and the

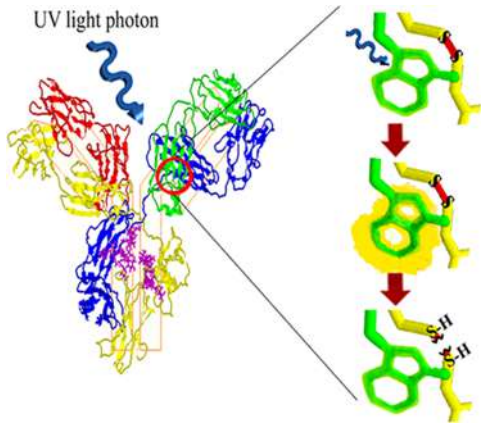

Figure 1. UV photonic activation of a generic IgG (1IGY). (a) The protein solution is irradiated. (b) One UV photon is absorbed by a tryptophan side-chain which transfers the energy to the near cysteines. (c) The disulfide bridge opens and the thiol groups so produced can effectively interact with the gold surface.

functional properties of the immobilized proteins while favoring the proper orientation of the biomolecule on the support,[23] and this is achieved by avoiding any chemical and thermal treatment.

One of the advantages of PIT relies in the wide field of application since the closely spaced triad of residues Trp/Cys−Cys is present in all members of the immunoglobulin superfamily. Every IgG has twelve intradomain disulfide bridges near a tryptophan residue, one of them being present in every domain of the protein. It is likely to induce the opening of these disulfide bonds through UV irradiation of the near aromatic residue. With the breaking of these disulfide bridges there is an increase of free thiol groups, which can react with a gold or thiol-rich surface. The same geometry of the Trp/Cys−Cys triad is observable in structures of several IgSF (immunoglobulin superfamily) molecules as well as in TCRs (T cell receptors), MHCs (major histocompatibility complex),[26] cell surface antigens (CD4 and CD8), and various cell-adhesion molecules. It is suggested that the conservation of the geometrical relationship between this three aminoacids is due to the role played by tryptophan in stabilizing or protecting the disulfide bridge.[27]

The proof of principle of PIT reported in our previous paper concerned the detection of murine immunoglobulin by QCM based immunosensor for which the sensitivity improved only by a factor of 2.[23] This result is in agreement with the findings reported in a recent paper by Trilling et al.[28] who show that the effect of the antibody orientation on the capture of the analyte is strongly dependent on the mass of the analyte. In particular, lighter analytes are more sensitive to the side-up orientation of the antibodies, so that PIT can render effective several techniques (e.g., QCM) otherwise impractical.

In this paper, we demonstrate how PIT improves the sensitivity of a QCM by about 1 order of magnitude compared to that achieved when the antibodies are tethered randomly oriented. The main drawback of a mass-based transducer like QCM in detecting light molecules (parathion weighs only about 300 Da), is the small frequency shift associated with their tethering to the antibody. We overcame this problem through a procedure that makes the molecules heavier so that a LOD of 4 ppb was achieved with an analysis requiring less than 10 min. We also demonstrate that PIT does not affect the specificity

features of the antibody as the test with similar compounds have shown.

■ EXPERIMENTAL SECTION

Chemicals. Antiparathion polyclonal antibodies were purchased from antibodies-online.com as rabbit serum (ABIN113883). Protein A agarose (Pierce) from Thermo Scientific has been used for the antibodies purification, whereas bovine serum albumin (A2153), parathion (45607), bisphenol A (239658), *p*-nonylphenol (46018), dichlorvos (45441), and paraoxon (36186) were purchased from Sigma-Aldrich. Since these compounds are highly toxic, all the samples were prepared in the fume hood. Other materials we have used are PBS 1× buffer solution pH 7.4, Helix water, sulfuric acid 98%, and hydrogen peroxide 30%.

Experimental Apparatus. The QCM is a μLibra from Technobiochip, Italy. The frequency variation of the balance in the cell is displayed on a connected computer by a producer-released software. The quartz crystals are from ICM Manufacturer, Oklahoma city (U.S.A.). They are AT-CUT quartz with a fundamental frequency of 10 MHz. The crystal diameter is 1.37 cm while the diameter of the gold lamina is 0.68 cm. The electrodes are cleaned using the Piranha solution (3:1 ratio between concentrated sulfuric acid and 30% hydrogen peroxide solution).

The fluidic apparatus consists of a GILSON peristaltic pump, Tygon silicone tubes with different diameters (0.51 mm for input into the cell and 0.64 mm for output) and the cell which contains the crystal placed on the electronic console for the measurement of frequency oscillation. The volume just above the electrode is approximately 40 μL and the fluidic apparatus is designed so that the whole replacement of the solution takes about 80 s when the flow rate is 3.3 μL/s. This was tested by measuring the time required by PBS to remove completely a colored solution (Flavin adenine dinucleotide) from the cell. The permanence of BSA above the electrode entails that this protein is still present when the parathion reaches the cell, so that a complex between the protein and the analyte is formed as a consequence of unspecific interactions. This is sketched in figure 2 where the BSA and the analyte are represented as big green and small orange balls, respectively. To check the complex formation between parathion and BSA we measured the BSA fluorescence spectrum (λ_{ex} = 278 nm) observing a strong reduction of the yield as a function of the parathion concentration. This quenching effect of parathion on BSA fluorescence shows the interaction between these two partners.

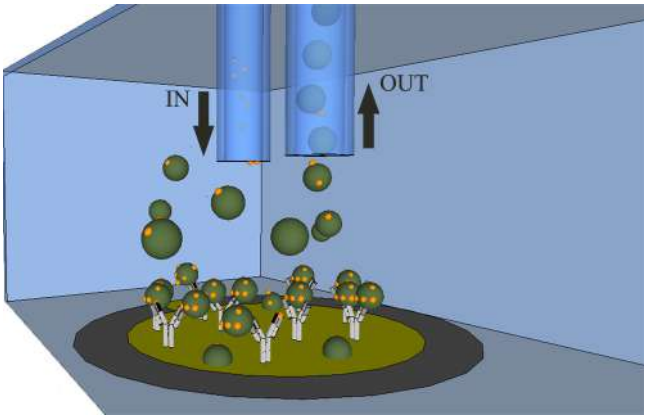

Figure 2. Antigen binding on the functionalized gold electrode. The big green spheres are the BSA macromolecules which are complexed with the smaller antigens (orange spheres). The model is not in scale.

The UV light source used is a custom femtosecond PHAROS laser system having a high tunable pulse repetition rate (Light Conversion, Ltd., www.lightcon.com). UV laser pulses having a length of approximately 120 fs are obtained coupling the laser with a harmonic generator stage (HIRO), which provides the conversion to 515, 343, or 258 nm wavelengths of the IR fundamental radiation.

UV Activation of the Antibody Solution. Aliquots of 1 mL, containing 5 μg of antiparathion polyclonal antibody, have been irradiated by means of the femtosecond laser system previously described. The laser source operates, in this case, at a pulse repetition rate of 10 kHz and delivers 250 mW of average power at λ = 258 nm (resulting in energy per pulse of 25 μJ). These irradiation conditions guarantee the maximum efficiency in disulfide bond breaking as demonstrated by Della Ventura et al.[23] through the Ellman's assay.[29]

QCM Protocol. The experimental protocol consists of the following steps: (1) Reaching of the basal frequency stabilization by washing the electrode surface with 1× phosphate buffer (PBS) pH 7.4. (2) UV-assisted adsorption or passive adsorption of antiparathion polyclonal antibodies. (3) Blocking the remaining gold free surface with bovin serum albumin (BSA) solution (50 μg/mL) to avoid nonspecific-interactions. (4) Flowing of parathion solution in the fluidic circuit that interacts with BSA solution still inside the volume above the electrode. The complex so formed is subsequently recognized by the antibody (see Figure 2). (5) Final washing step with PBS 1× to eliminate weakly bonded antigen.

Figure 3 shows typical QCM outputs obtained when the antibodies are irradiated (black continuous line) and not-irradiated (red dashed line). To be noted that the first drop in the frequency shift (∼−300 Hz, step 2 of the protocol) is the same in both cases (irradiated and not irradiated) so that we can assume that PIT does not change the amount of antibody

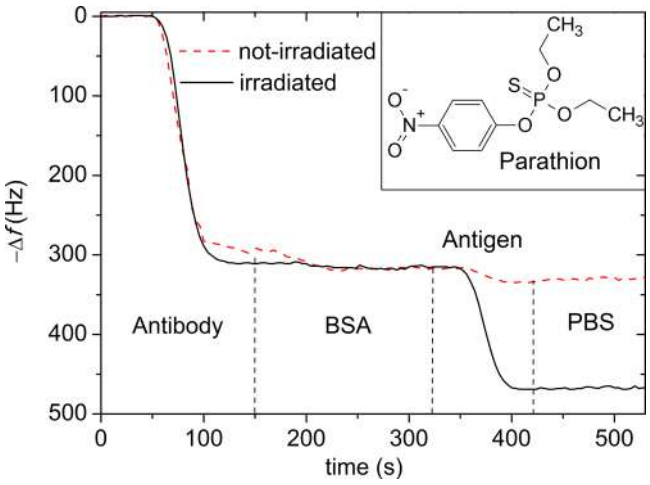

Figure 3. QCM responses of irradiated (black solid line) and not-irradiated (red dashed line) antibody samples with a protein concentration of 5 μg/mL. The first drop at ∼50 s corresponds to the antibodies tethered to the electrode and is not affected by PIT, whereas the second drop at ∼350 s is given by an antigen solution (parathion 51.5 μM) conveyed to the cell and is much larger when PIT is used. The vertical dashed lines show the steps described in the text.

tethered to the electrode. This is in fair agreement with the surface density measurements reported by Peluso et al. who studied the effects produced by orientation on both full-sized antibodies and Fab' fragments, finding comparable surface densities between aligned and not-aligned antibodies in three different cases (Mab602, Mab208, and Mab9647).[30]

When BSA reaches the electrode (step 3) no frequency shift is observed demonstrating that the surface is fully covered by antibodies. Subsequently, the analyte is conveyed to the electrode (step 4) and a completely different response is observed whether PIT is used or not. Such a difference is kept even when the electrode is washed by means of PBS (step 5).

RESULTS AND DISCUSSION

Sensitivity and LOD. The response of the QCM is proportional to the mass tethered to the electrode[31] so that the frequency shift $\Delta f(P)$, P being the concentration of parathion, is a measure of the amount of analyte bound to the antibodies. As reported in the Experimental Section, when the parathion reaches the volume above the electrode, the BSA solution is still there in high concentration thereby allowing the complex formation. The BSA molecules (approximately 66 kDa) bind the organophosphate compound by means of unspecific interactions and plays a "ballast" role, making the analyte "heavier" and detectable by a balance. In fact, even if all the antibodies on the electrode bound one parathion molecule (~300 Da), the QCM frequency shift would be only few hertz and, thus, not detectable by our device. This has been verified by washing the fluidic circuit, thus removing the BSA, and checking that the parathion is not detectable any more, even if PIT is used. It is worth to stress that this unconventional labeling of the analyte does not affect the features of the sensor which is fully insensitive to BSA once the antibodies are tethered to the electrode. Figure 3 shows that when BSA is conveyed to the QCM the crystal oscillation frequency keeps constant (see the signal in the interval 150−330 s). Thus, with a relatively high concentration of BSA in the fluidic circuit we have compared the response of QCM to irradiated (PIT) and nonirradiated antibodies obtaining the results shown in figure 4.

It is readily seen that no significant signal is measurable when the parathion concentration is lower than 50 μM (15 μg/mL) if the antibodies are not irradiated, the signal being already in the saturation region in the opposite case. By considering the law of mass action and given the free diffusion conditions of our experiment, the analysis of the interaction kinetic between the analyte and the antibody leads to a Michaelis−Menten type equation:

$$\Delta f(P) = \frac{(\Delta f)_{sat} P}{P + K_M} \quad (1)$$

where $(\Delta f)_{sat}$ contains the instrument response and K_M is the so-called Michaelis−Menten constant. The former parameter includes the number of antibodies tethered on the balance as well as their effectiveness in capturing the analyte, that is, their orientation, whereas the latter provides estimation for the range of linearity of the realized sensor. The fitting of the experimental results obtained with irradiated antibodies by eq 1 (solid line in figure 4) provides $(\Delta f)_{sat}$ = 151 ± 5 Hz and K_M = 2.2 ± 0.7 μM. The uncertainty in our measurements is due to instrumental limitations in the performances of our QCM, as well as to the fluctuations in some steps of the procedure. Although we expect a remarkable improvement of the

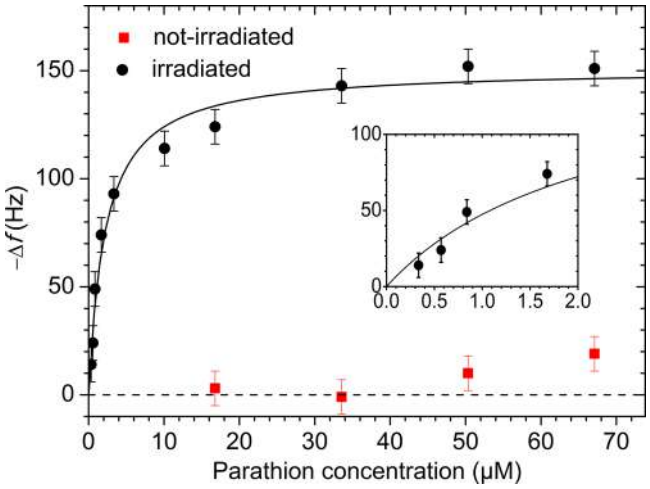

Figure 4. Response of the QCM versus the parathion concentration with irradiated (circles) and not-irradiated (squares) antibodies. The experimental points obtained with the irradiated antibody are fitted by a Michaelis−Menten type equation (black solid line). The low frequency change achieved when the antibody is not irradiated does not allow any significant fit of the experimental data. The inset is the enlargement of the low concentration region.

reproducibility by an up-to-date QCM as well as an improved fluidic circuit setup, currently we consider a conservative frequency error of 15 Hz (see also the inset in figure 4). Thus, a minimum frequency change $(\Delta f)_{min}$ = 15 Hz is required for a measurement to be significantly different from zero. An evaluation of the lower LOD can, then, be obtained by inverting eq 1

$$\mathrm{LOD} \approx \frac{(\Delta f)_{min} K_M}{(\Delta f)_{sat}} \approx 2 \times 10^{-7}\,\mathrm{M} \approx 60\,\frac{\mathrm{ng}}{\mathrm{mL}} \quad (2)$$

Since the concentration of water is about 55 M a LOD better than 4 ppb for parathion in water results from our functionalization technique applied to a QCM.

By considering the response at the concentration of 51.5 μM (see figure 4) we can estimate an increase in the sensitivity by at least 1 order of magnitude when PIT is used. Such a result can only be attributed to the side-up orientation of the antibodies and is much more significant than that achieved with heavier analytes,[23] in agreement with the mass dependence effects of antibody orientation recently reported by Trilling et al.[28]

Specificity. To test the sensor specificity, the same experimental procedure has been used for four compounds, progressively similar to parathion, from the chemical and structural point of view. They are bisphenol A (4,4′-(propane-2,2-diyl)diphenol), *p*-nonylphenol, dichlorvos (2,2-dichlorovinyl dimethyl phosphate), and paraoxon (diethyl 4-nitrophenyl phosphate). At concentrations of approximately 1.7 μM, where parathion exhibits a significant response (see inset of Figure 4), all the four compounds showed no detectable frequency shift when they were tested separately. Thus, we tested the sensor response with a mixture of the four compounds at an even higher concentration (3.5 μM). thereby mimicking a real complex matrix. The results are reported in Figure 5a, where the last steps of the protocol are highlighted. The frequency shift measured when only the four compounds are in the solution is just few hertz (mix), but the frequency goes back to the previous value when PBS is made to flow (blue dotted line).

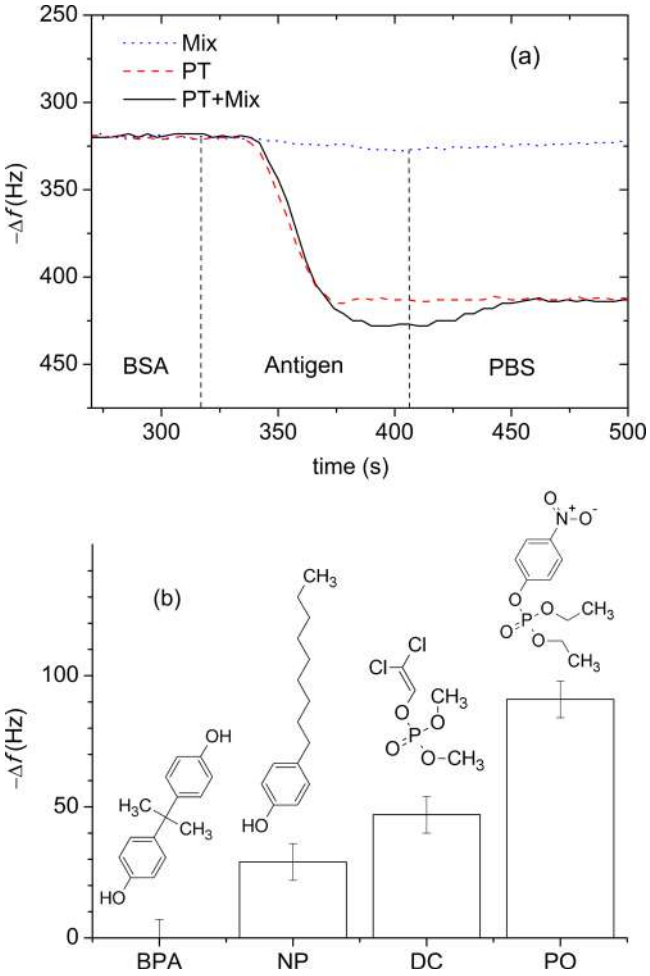

Figure 5. Sensor specificity i.e. sensor responses against different pollutants similar to parathion (their structures are reported in the panel b). (a) QCM response to parathion (PT) (red dashed line), to a mixture (mix) of bisphenol A (BPA), *p*-nonylpheno (NP), dichlorvos (DC), paraoxon (PO) (blue dotted line), and to PT + mix (solid black line). The concentration of all the compounds is 3.5 μM. (b) Frequency shift of the single compounds at the concentration of 172 μM, that is, one hundred times higher than that for which the parathion yields approximately 70 Hz.

The parathion alone at 3.5 μM gives rise to a frequency shift of approximately 90 Hz (red dashed line). The addition of the four compounds (Pt + mix) produces a slightly larger shift (solid black line) that disappear after purging with PBS. Thus, the concentrations were increased by 2 orders of magnitude (170 μM) compared to the initial one (1.7 μM), but despite such high concentration, the QCM responses were always lower than those provided by parathion in the saturation regime of the dose−response curve. It is also noticeable to look at the sensor response as a function of "similarity" with the parathion, reported in Figure 5b. Such data are internally consistent showing once again that the recognition capability of antibodies is unaffected by PIT.

■ CONCLUSIONS

The side-up orientation of antibodies is the most effective way to improve the sensitivity of immunosensors designed for light molecules and becomes a necessary condition when QCMs are going to be used. By applying the novel photonic immobilization technique to antibodies to be tethered to the gold electrodes of a QCM, we have been able to achieve a sensitivity that allows the detection of a light molecule like parathion (291.26 Da) in water with a LOD lower than 4 ppb (60 ng/mL). This value has been reached with a QCM capable to detect frequency shift of approximately 10 Hz and, although the resulting LOD is already competitive with those obtained with similar devices, we anticipate a significant improvement if an up-to-date QCM capable to detect frequency shift as low as o.1 Hz is used.[9] Thus, in principle, by adopting PIT, as well as the complexion with a heavy molecule like BSA, we expect to be able to reach LOD much better than 1 ppb. This kind of immunosensor is inherently highly specific and provides fast response (only few minutes are required for the whole analysis). Moreover, in view of its flexibility and portability, such a device is suitable for in situ analysis. On the basis of our microscopic interpretation of the experimental findings and given the widespread presence of the triad Trp/Cys-Cys in all the antibodies, PIT can be considered as a general technique to anchor oriented antibodies on thiol reactive surfaces thereby paving the way to use this cost-effective technology for the detection of a variety of analytes.

■ AUTHOR INFORMATION

Corresponding Author

*E-mail: rvelotta@unina.it.

Notes

The authors declare no competing financial interest.

■ REFERENCES

(1) Liu, S.; Zheng, Z.; Li, X. *Anal Bioanal. Chem.* **2013**, *405*, 63−90.
(2) Milles, H. L.; Salt, H. *Br. Med. J.* **1950**, *2*, 444.
(3) Walker, J. P.; Asher, S. A. *Anal. Chem.* **2005**, *77*, 1596−1600.
(4) Zen, J.-M.; Jou, J.-J.; Senthil Kumar, A. *Anal. Chim. Acta* **1999**, *396*, 39−44.
(5) Mulchandani, P.; Chen, W.; Mulchandani, A. *Environ. Sci. Technol.* **2001**, *35*, 2562−2565.
(6) Sacks, V.; Eshkenazi, I.; Neufeld, T.; Dosoretz, C.; Rishpon, J. *Anal. Chem.* **2000**, *72*, 2055−2058.
(7) Cooper, M. A.; Singleton, V. T. *J. Mol. Recognit.* **2007**, *20*, 154−184.
(8) Becker, B.; Cooper, M. *J. Mol. Recognit.* **2011**, *24*, 754−787.
(9) Bi, X.; Yang, K.-L. *Anal. Chem.* **2009**, *81*, 527−532.
(10) Marx, S.; Zaltsman, A.; Turyan, I.; Mandler, D. *Anal. Chem.* **2004**, *76*, 120−126.
(11) Trilling, A. K.; Beekwilder, J.; Zuilhof, H. *Analyst* **2013**, *138*, 1619−1627.
(12) Nicu, L.; Leïchlé, T. *J. Appl. Phys.* **2008**, *104*, 111101.
(13) Jung, Y.; Jeong, J. Y.; Chung, B. H. *Analyst* **2008**, *133*, 697−701.
(14) Caruso, F.; Rodda, E.; Furlong, D. N. *J. Colloid Interface Sci.* **1996**, *178*, 104−115.
(15) Přibyl, J.; Hepel, M.; Halámek, J.; Skládal, P. *Sens. Actuators, B* **2003**, *91*, 333−341.
(16) Hao, R.; Wang, D.; Zhang, X.; Zuo, G.; Wei, H.; Yang, R.; Zhang, Z.; Cheng, Z.; Guo, Y.; Cui, Z.; Zhou, Y. *Biosens. Bioelectron.* **2009**, *24*, 1330−1335.
(17) Sharma, H.; Mutharasan, R. *Anal. Chem.* **2013**, *85*, 2472−2477.
(18) Byrne, B.; Stack, E.; Gilmartin, N.; O'Kennedy, R. *Sensors* **2009**, *9*, 4407−4445.
(19) Jiang, X.; Li, D.; Xu, X.; Ying, Y.; Li, Y.; Ye, Z.; Wang, J. *Biosens. Bioelectron.* **2008**, *23*, 1577−1587.
(20) Wang, Y.; Knoll, W.; Dostalek, J. *Anal. Chem.* **2012**, *84*, 8345−8350.
(21) Karyakin, A. A.; Presnova, G. V; Rubtsova, M. Y.; Egorov, A. M. *Anal. Chem.* **2000**, *72*, 3805−3811.
(22) Neves-Petersen, M. T.; Snabe, T.; Klitgaard, S.; Duroux, M. E. G.; Petersen, S. B. *Protein Sci.* **2006**, *15*, 343−351.

(23) Della Ventura, B.; Schiavo, L.; Altucci, C.; Esposito, R.; Velotta, R. *Biomed. Opt. Express* **2011**, *2*, 3223−3231.
(24) Harris, L. J.; Skaletsky, E.; McPherson, A. *J. Mol. Biol.* **1998**, *275*, 861−72.
(25) Neves-Petersen, M. T.; Gryczynski, Z.; Fojan, P.; Pedersen, S.; Petersen, E.; Petersen, S. B. *Protein Sci.* **2002**, *11*, 588−600.
(26) Snabe, T.; Røder, G. A.; Neves-Petersen, M. T.; Buus, S.; Petersen, S. B. *Biosens. Bioelectron.* **2006**, *21*, 1553−1559.
(27) Ioerger, T. R.; Du, C.; Linthicum, D. S. *Mol. Immunol.* **1999**, *36*, 373−386.
(28) Trilling, A. K.; Harmsen, M. M.; Ruigrok, V. J. B.; Zuilhof, H.; Beekwilder, J. *Biosens.Bioelectron.* **2013**, *40*, 219−226.
(29) Ellman, G. L. *Arch. Biochem. Biophys.* **1959**, *82*, 70−77.
(30) Peluso, P.; Wilson, D. S.; Do, D.; Tran, H.; Venkatasubbaiah, M.; Quincy, D.; Heidecker, B.; Poindexter, K.; Tolani, N.; Phelan, M.; Witte, K.; Jung, L. S.; Wagner, P.; Nock, S. *Anal. Biochem.* **2003**, *312*, 113−124.
(31) Sauerbrey, G. *Z. Phys.* **1959**, *155*, 206−222.

Appl. Phys. A
DOI 10.1007/s00339-014-8340-4

Applied Physics A
Materials Science & Processing

Nano- and femtosecond UV laser pulses to immobilize biomolecules onto surfaces with preferential orientation

S. Lettieri · A. Avitabile · B. Della Ventura · R. Funari · A. Ambrosio · P. Maddalena · M. Valadan · R. Velotta · C. Altucci

Received: 4 November 2013 / Accepted: 23 February 2014
© Springer-Verlag Berlin Heidelberg 2014

Abstract By relying on the photonic immobilization technique of antibodies onto surfaces, we realized portable biosensors for light molecules based on the use of quartz crystal microbalances, given the linear dependence of the method on the laser pulse intensity. Here, we compare the quality of the anchoring method when using nanosecond (260 nm, 25 mJ/pulse, 5 ns, 10 Hz rep. rate) and femtosecond (258 nm, 25 μJ/pulse, 150 fs, 10 kHz rep. rate) laser source, delivering the same energy to the sample with the same average power. As a reference, we also tethered untreated antibodies by means of the passive adsorption. The results are striking: When the antibodies are irradiated with the femtosecond pulses, the deposition on the gold plate is much more ordered than in the other two cases. The effects of UV pulses irradiation onto the antibodies are also analyzed by measuring absorption and fluorescence and suggest the occurrence of remarkable degradation when nanosecond pulses are used likely induced by a larger thermal coupling. In view of the high average power required to activate the antibodies for the achievement of the photonic immobilization technique, we conclude that femtosecond rather than nanosecond laser pulses have to be used.

S. Lettieri · A. Avitabile · R. Funari · A. Ambrosio · P. Maddalena · M. Valadan · R. Velotta · C. Altucci (✉)
Dipartimento di Fisica, Università degli Studi di Napoli Federico II, Complesso Universitario Monte S. Angelo, Via Cintia, Naples 80126, Italy
e-mail: carlo.altucci@unina.it

S. Lettieri · A. Ambrosio
CNR-SPIN, UOS Napoli, Complesso Universitario Monte S. Angelo, Via Cintia, Naples 80126, Italy

B. Della Ventura
Dipartimento di Fisica, Università di Roma, La Sapienza, Rome, Italy

R. Velotta · C. Altucci
Consorzio Nazionale Interuniversitario per le Scienze Fisiche della Materia, Naples, Italy

1 Introduction

The quest for developing more and more sophisticated and efficient techniques for surface functionalization is of extreme importance in the current scenario of applied sciences, ranging from sensing [1, 2] to bioelectronics [3]. Here, we report on the role played by a pulsed UV radiation source in the surface functionalization of a quartz crystal microbalance (QCM) by means of the Photonic Immobilization Technique (PIT) for the detection of a light pesticide such as parathion (IUPAC name *O*,*O*-diethyl *O*-4-nitrophenil phosphorothioate) [2, 4]. In QCMs, the detection of the analyte occurs thanks to its specific recognition by bio-receptors (antibodies) immobilized on the sensor surface. The strategy to anchor bio-receptors on a metallic surface element is a key issue to improve the sensor performances and for any requirement of surface functionalization. We demonstrated an increase in the QCM sensitivity and its linear range extension when antibodies were irradiated with 258-nm laser pulses [2, 5]. It is important stressing that the increase in the antibodies efficiency due to laser pulse irradiation is linear with the peak intensity, namely the pulse power per unit surface, of the UV laser pulses in the investigated intensity range, as demonstrated in [2]. This has the consequence to rule out any nonlinear phenomenon essentially based on two-photon absorption in the antibody response, thus indicating the delivered energy dose as the laser source key parameter for antibody treatment. Such linear response, moreover, would somehow entail that any source delivering the same energy dose to the target, even

Published online: 14 March 2014

conventional lamps of photo-reactors, should be equally efficient in triggering the PIT mechanism. Nonetheless, we have found here that different UV sources imply very much different efficiencies in triggering PIT, due to the different nature of the stimulated molecular dynamics, once a single UV photon has been absorbed by an antibody. Here, we compare the quality of the PIT-based anchoring method when using nanosecond (260 nm, 25 mJ/pulse, 5 ns, 10 Hz rep. rate) and femtosecond (258 nm, 25 μJ/pulse, 150 fs, 10 kHz rep. rate) laser source, delivering the same energy dose to the sample. The results show that QCM is effective in the antigen detection only when PIT is realized with fs UV pulses.

The mechanism underlying the PIT relies on the photonic activation of disulfide bridges into the antibody, i.e., the light-induced breakage of the disulfide bridges in proteins through UV illumination of nearby aromatic amino acids [4]. Such a mechanism favors the proper orientation of the biomolecule on the surface so as the antibody can easily catch its antigen.

Nevertheless, irradiating biomolecules with 260-nm light leads to the denaturation of the molecules. Proteins and enzymes, for instance, can substantially reduce their biological activity as a consequence of induced structural changes [6]. Thus, we seek for the best trade-off between efficient tethering of the antibodies onto the surface, due to UV irradiation, and the lowest possible damage produced to the biomolecules. This latter feature was characterized by analyzing molecular absorption and fluorescence UV spectra: Differently from the femtosecond treatment case and likely due to thermal coupling, nanosecond UV pulses induce severe damages to the antibodies, as witnessed by significant changes in absorption and fluorescence spectra. Thus, femtosecond UV pulses confirm their capability to trigger important processes, otherwise inaccessible, even in antibodies beside their effectiveness already demonstrated in nucleic acids both in vitro [7] and in living cells [8].

2 PIT and its application to bio-sensing

We have recently demonstrated PIT to be an efficient method to anchor antibodies onto gold surfaces in order to realize sensors for the detection of heavy [2] and light [5] molecules. Briefly, the underlying idea is that, thanks to PIT based on fs UV pulse irradiation of antibodies, these proteins are tethered to the gold surface of a QCM-based biosensor with their variable part (i.e., the region that recognize the antigen,) pointing up[9–12]. The driving force for such a mechanism is provided by disulfide bridges disrupted by absorption of 260-nm photons; these are selectively produced since the occurrence of a solvent accessible triad Tryptophan/Cysteine–Cysteine, which is required by PIT, is limited to the specific interdomain region of the antibody [4].

Details of device realization to detect heavy and light analytes, based on PIT, can be found elsewhere [2, 5]. Here, it is useful to summarize that the frequency variation of the quartz crystal microbalance is displayed and acquired in real time on a computer by producer-released software. The quartz crystal fundamental frequency is in our case 10 MHz. Antibodies and, successively, antigens are circulated in liquid phase by means of a fluidic apparatus consisting of a peristaltic pump and a cell containing the quartz crystal. The suitable antibody aqueous solution needed to detect the analyte is pre-treated by means of a preliminary irradiation in cuvette, to obtain the desired UV activation. In the case reported in Fig. 1, we detected a light pesticide, parathion, and used its polyclonal antibody having a concentration of 50 μg/1 mL. When using fs UV laser pulses, we utilized the fourth harmonic (258 nm, ≈180 fs, 25 μJ/pulse) of a PHAROS system operated at a repetition rate of 10 kHz, thus reaching the UV average power of 250 mW. The maximum efficiency in disulfide bond breaking was reached in this case after 60 s irradiation and monitored by the Ellman's assay on the irradiated antibodies that quantify the amount of thiol groups produced by UV absorption [13]. We tried also PIT with ns UV sources, by using the fourth harmonic (260 nm, ≈3 ns, 25 mJ/pulse) of a Nd:YAG system operated at 10-Hz repetition rate. The maximum efficiency in disulfide bond breaking was reached again after

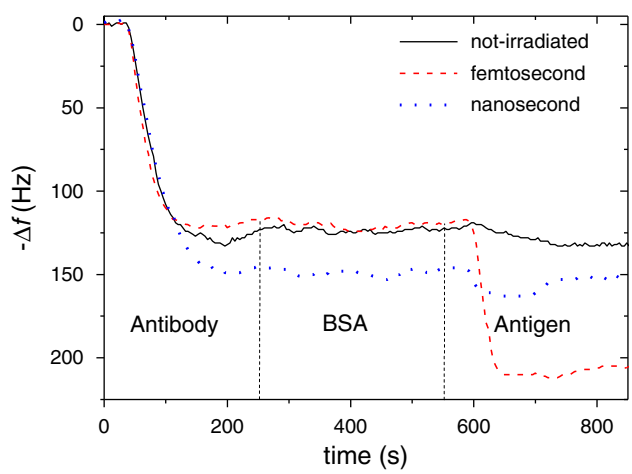

Fig. 1 QCM-based biosensor response for parathion detection in real time. *Black solid line* no PIT is used. *Red dashed line* femtosecond-based PIT is carried out. *Blue dotted line* nanosecond-based PIT is used. The first drop between ~0 and 150 s corresponds to the antibodies tethered to the electrode and is poorly affected by PIT only with nanosecond irradiation, whereas the second drop at ~550 s is given by an antigen solution (parathion 1.5 μM) conveyed to the cell and is effective only when femtosecond-based PIT is carried on. *The vertical dashed lines* show the steps of the protocol described in the text. The reported experiment was performed at a parathion concentration of 1.5 μM

60 s irradiation, although the corresponding Ellman's assay indicated that the number of opened disulfide bonds by fs treatment was about double than that for ns. Moreover, no measurable response of the sensor was detected for ns irradiation of the antibody in the above as well as in other tested conditions, indicating that PIT is highly efficient only when coupled to fs antibody irradiation.

A typical biosensor response for parathion detection is reported in Fig. 1, where the ordinary QCM response with no PIT is compared to PIT with fs and ns pulses, in the conditions of antibody concentration and laser irradiation reported above. The experimental protocol, which mimics the so-called SANDWICH [14] method widely spread in several biochemical assays, consists of the following steps. (1) Reaching of the basal frequency stabilization by washing the electrode surface with 1× phosphate buffer (PBS). (2) UV-assisted adsorption or passive adsorption of antiparathion polyclonal antibodies. (3) Wash with PBS to eliminate the excess of IgG. (4) Blocking the remaining gold-free surface with bovin serum albumin (BSA) solution (50 μg/mL) to avoid nonspecific interactions. (5) Flowing of PBS to clean the fluidic circuit. (6) Flowing of a parathion-antibody sample where the labeled antigen is captured by the immobilized antibodies. The mixture of pesticide and protein solution has been prepared 24 h before the experiment. By using a SANDWICH-type protocol, we can make heavier and detectable the light parathion analyte ($\sim$300 Da), the antibody molecules playing the twofold role of "specific ballasts", rendering the device inherently specific. (7) Final washing step with PBS 1× eliminates weakly bonded antigen. We notice also that the first drop in the frequency shift (~ -150 Hz, step 2 of the protocol) is nearly the same in all the cases, being the ns irradiation shift slightly higher than the other two cases, likely due molecular fragmentation induced by ns pulse irradiation, with the consequence of a partial deposit of small antibody peptides with no active recognition function. Thus, in fair agreement with previous results [15], we can assume that PIT does not change the amount of antibody immobilized onto the electrode. As a final result, we have that no measurable response is provided by the device both when the antibodies are tethered by spontaneous adsorption, and the PIT is realized with ns UV pulses, in contrast to the nice and very well detectable response of the QCM when fs-based PIT is used ($\approx$100 Hz frequency shift is detected with a solution of 1 μM).

3 Optical characterization of activated antibodies

It is well known for long that technologies based on UV irradiation of biomolecules in general, and in particular proteins, imply a nonnegligible disadvantage as both molecular structure and biological activity can be severely affected. Thus, we characterized the effect of irradiating antibodies with UV fs laser pulses, which is an essential step of PIT [2, 5], in order to verify two important issues of our application: (1) Finding the irradiation conditions allowing the best trade-off between UV activation in PIT and protein denaturation and (2) Assuring that the fundamental biological properties of the irradiated antibodies are preserved, in particular looking at the antigen-binding capability. This has been done by investigating the absorption and fluorescence UV spectra of irradiated proteins (nanosecond and femtosecond) in comparison with those of the nonirradiated species.

A typical UV absorption spectrum (recorded with the Jenway 6715 UV–visible spectrophotometer) displays two peaks at 220 nm (ammidic bond) and $\approx$280 nm (aromatic amino acids, particularly tryptophan). Generally, a nice and well-behaved peak at 280 nm indicates a protein well folded with its natural conformation. This is, indeed, the case of the curves obtained for no irradiation (initial species) in Fig. 2 (a) and (b), where the UV absorption spectra of the anti-parathion are reported at several irradiation times for fs (a) and ns (b) laser irradiation. In both cases, the irradiation leads to a significant change in the protein spectrum with the consequent almost complete disappearance of the peak at 280 nm. This phenomenon requires much shorter irradiation times if the protein sample is irradiated using the ns rather than the fs laser source. It is worth noticing that after short irradiation times (18, 30 and 60 s), there is still a shoulder at 280 nm. Spectral changes, in this case, can be due to a structural modification of the protein which does not affect the ability of the immunoglobulin to bind the antigen. This means that most likely such changes occurred in a region of the immunoglobulin far from the structural characteristic involved in the photonic activation (cys–cys trp triads), since PIT-enhanced immuno-recognition of the antibody is properly working, as demonstrated by a very effective response of the QCM-based sensor.

Stationary fluorescence is a rapid, low-cost, and effective method to monitor structural changes and is based on the emissions of intrinsic protein probes (the aromatic amino acids: tryptophan, phenylalanine, and tyrosine) which are strongly affected by both chemical environment and protein structure [16]. The photonic activation of antibodies results in the breakage of the sulfur–sulfur bonds placed nearby the tryptophan side chain so that the protein structure becomes less compact. The new conformations allow the penetration of water molecules inside the protein resulting in a change of the fluorescence spectrum. The data are acquired using a Perkin Elmer LS55 spectrofluorometer, the excitation wavelength being 278 nm. The fluorescence emission is mainly due to the tryptophan residues which strongly absorb at that wavelength. In

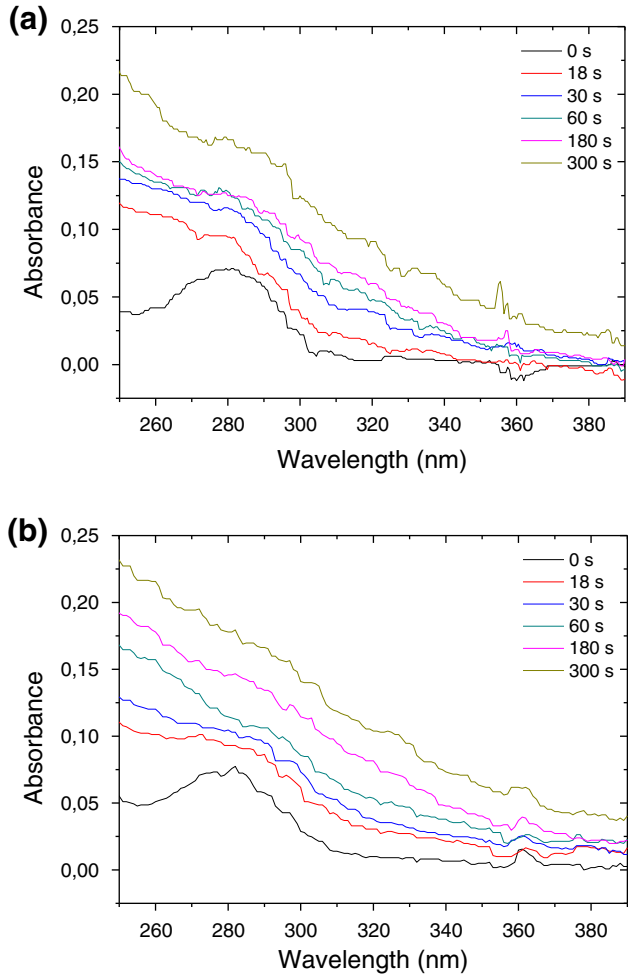

Fig. 2 UV Absorption spectra of antiparathion solutions for **a** fs and **b** ns UV pulse pre-treatment at various irradiation times. The antibody concentration is 50 μg/1 mL, whereas the laser source irradiation conditions are 25 μJ/pulse—10 kHz repetition rate for the 150-fs system and 25 mJ/pulse—10 Hz for the 3-ns source. In this way, the same UV dose is delivered to the target in the two cases in correspondence with the same irradiation time

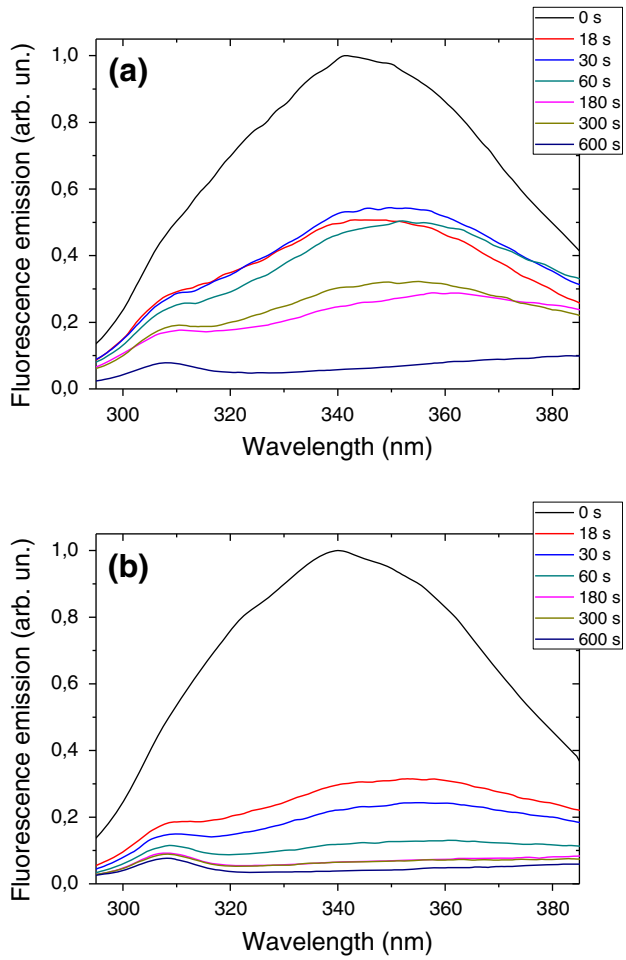

Fig. 3 UV Fluorescence spectra of antiparathion solutions for **a** fs and **b** ns UV pulse pre-treatment at various irradiation times. The excitation wavelength is 278 nm. Experimental parameters concerning antibody concentration and laser irradiation are the same as in Fig. 2

Fig. 3 (a) and (b), we report the stationary fluorescence of antibody samples as function of the irradiation time using either fs (a) or ns (b) laser source. UV irradiation leads to two different phenomena: protein activation and denaturation. Given the optimal irradiation time for maximizing the sensor efficiency (60 s), we have found that the reduced emission has to be related to a prompt structural change that does not entail a complete denaturation, the latter occurring only after several minutes of irradiation. These two phenomena can be easily observed in Fig. 4 where the fluorescence signal integrated in the 320–370 nm range is reported. If the protein sample is irradiated using fs laser pulses, there is a prompt rapid variation in fluorescence emission related to protein activation and a subsequent decrease due to the denaturation. This difference is not so evident if the antibodies are irradiated using much more energetic UV pulses. Nanosecond irradiated antibodies show a more rapid drop in fluorescence emission due to denaturation phenomena.

The conformational change induced by the femtosecond laser source does not prevent the antibody from recognizing the analyte, while making more effective its orientation once immobilized on the gold surface of a QCM. On the other side, it is plausible that the irradiated antibody may lose its ability to recruit the elements required for the immune response. This "immune function" is related to a different part of the biomolecule and does not affect the antigen recognition [16, 17].

The solid lines in Fig. 4 are the result of best fits to the experimental points. For the nanosecond measurement, a single exponential model has been used, whereas a double exponential best fits the femtosecond behavior for which, indeed, we observed a much longer tail. The amplitudes of the

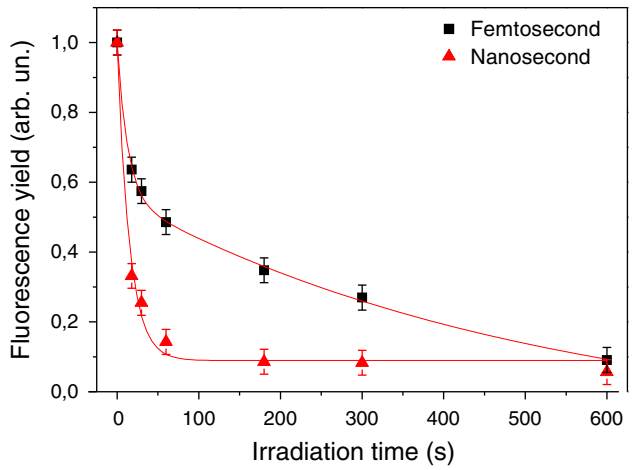

Fig. 4 Integrated fluorescence emission in the 320–370 nm spectral window for antiparathion activated with fs (*black squares*) and ns (*red triangles*) pulses versus the UV laser irradiation time. Red bold lines: best fits using a double exponential model for (**a**) and a single exponential model for (**b**)

two exponential decays turn out to be $A_{\text{short}} = 0.44 \pm 0.03$ and $A_{\text{long}} = 0.7 \pm 0.1$ for the short- and for long-lived decay, respectively. Most likely, such a substantial difference between nanosecond and femtosecond irradiation indicates a conformational change in the antibody occurring when femtosecond rather than nanosecond pulses are used for PIT. It is well known the fluorescence of proteins in the UV is mostly due to aromatic amino acids, and in particular to tryptophan, which has a fluorescence quantum yield about one order of magnitude higher than that of the tyrosine and phenylalanine [18]. It is also known that in a large number of cases, tryptophan fluorescence yield and dynamics in proteins are closely related to the molecular conformation as demonstrated for the electron transfer in myoglobins [19], for protein photoactivation in bacteria [20], and for the influence of tryptophan in ligand recognition of nicotinic receptors [21]. Such a change might be induced in the antibody only by shining femtosecond and not nanosecond pulses, as tryptophan exhibits two fluorescence lifetimes in the UV equal to ≈ 0.4 and ≈ 2.8 ns [22], in correspondence with the $S_0 \rightarrow {}^1L_a$ and $S_0 \rightarrow {}^1L_b$ transitions. These lifetimes are much longer than our femtosecond pulses, whereas they are shorter than the used nanosecond pulses. As a consequence, conformational changes induced in the antibody by the dynamics triggered by the $S_0 \rightarrow {}^1L_a$ and $S_0 \rightarrow {}^1L_b$ transitions in tryptophan can be observed only when using femtosecond pulse irradiation, since our relatively long nanosecond pulses will likely also deplete the excited ${}^1L_a$ and ${}^1L_b$ states due to stimulated emission. This has the natural counterpart, typical of the nanosecond regime, of inducing stronger damages than in the femtosecond case, due to thermal coupling.

4 Conclusions

We have shown here a successful application of fs pulse-based PIT to the realization of a portable immune-sensor for the detection of a light pesticide such as parathion. In particular, the application of fs pulse-based PIT to functionalize the electrode of a QCM sensor makes the difference between the possibility of a good sensing against no response at all from the device. Such a negative result occurs indeed both when passive adsorption and nanosecond PIT are used to functionalize the gold electrode.

We then characterized the effects of a robust 260-nm pulse irradiation onto the antiparathion molecules by measuring absorption and fluorescence spectra for initial and irradiated species in several different experimental conditions. We found that using fs pulse irradiation of the antibodies represents the best trade-off between efficient tethering of the antibodies onto the surface and the lowest possible damage induced to the biomolecules by UV radiation. This finding strongly suggests to carry on a dynamic study of the tryptophan UV photo-excitation into the antibody with the consequent relaxation and related conformational dynamics.

Acknowledgments Partial funding for this research was provided by the Italian Ministry for Research and Education through the Grant PON01_01517.

References

1. J.L. Arlett, E.B. Myers, M.L. Roukes, Nat. Nanotechnol. **6**(4), 203–215 (2011)
2. B. Della Ventura, L. Schiavo, C. Altucci, R. Esposito, R. Velotta, Biomed. Opt. Expr. **2**(11), 3223–3231 (2011)
3. J. Cheng, G. Zhu, L. Wu, X. Du, H. Zhang, B. Wolfrum, Q. Jin, J. Zhao, A. Offenhäuser, Y. Xu, J. Neurosci. Methods **213**(2), 196–203 (2013)
4. M.T. Neves-Petersen, T. Snabe, S. Klitgaard, M. Duroux, S.B. Petersen, Protein Sci. **15**(2), 343–351 (2006)
5. R. Funari, B. Della Ventura, L. Schiavo, R. Esposito, C. Altucci, R. Velotta, Anal. Chem. **85**, 6392–6397 (2013)
6. M.T. Neves-Petersen, Z. Gryczynski, Z. Fojan, S. Pedersen, E. Petersen, S.B. Petersen, Protein Sci. **11**, 588–600 (2002)
7. C. Russmann, M. Beato, J. Stollhof, C. Weiss, R. Beigang, Nucl. Acid Res. **26**, 3697 (1998)
8. C. Altucci, A. Nebbioso, R. Benedetti, R. Esposito, V. Carafa, M. Conte, M. Micciarelli, L. Altucci, R. Velotta, Laser Phys. Lett. **9**, 234–239 (2012)
9. F. Caruso, E. Rodda, D.N. Furlong, J. Colloid Interface Sci. **178**, 104–115 (1996)
10. J. Pribyl, M. Hepel, J. Halámek, P. Skládal, Sens. Actuators, B **91**, 333–341 (2003)
11. R. Hao, D. Wang, X. Zhang, G. Zuo, H. Wei, R. Yang, Z. Zhang, Z. Cheng, Y. Guo, Z. Cui, Y. Zhou, Biosens. Bioelectron. **24**, 1330–1335 (2009)
12. H. Sharma, R. Mutharasan, Anal. Chem. **85**, 2472–2477 (2013)
13. G.L. Ellman, Arch. Biochem. Biophys. **82**, 70–77 (1959)

14. C. Davies, *The immunoassay handbook* (Stockton Press, New York, 1994)
15. P. Peluso, D.S. Wilson, D. Do, H. Tran, M. Venkatasubbaiah, D. Quincy, B. Heidecker, K. Poindexter, N. Tolani, M. Phelan, K. Witte, L.S. Jung, P. Wagner, S. Nock, Anal. Biochem. **312**, 113–124 (2003)
16. P. Garidel, M. Hegyi, S. Bassarab, M. Weichel, Biotechnol. J. **3**, 1201–1211 (2008)
17. C.A. Janeway Jr., P. Travers, M. Walport, and M.J. Schlomchiket, Immunobiology, Garland Science Ed. (2001)
18. J.R. Lakowicz, *Principles of fluorescence spectroscopy*, 3rd edn. (Springer, New York, 2006)
19. C. Consani, G. Auböck, F. van Mourik, M. Chergui, Science **339**, 1586–1589 (2013)
20. J. Léonard, E. Portuondo-Campa, A. Cannizzo, F. Van Mourik, G. Van der Zwan, J. Tittor, S. Haacke, M. Chergui, Proc. Nat. Ac. Sci. **106**, 7718–7723 (2009)
21. S.B. Hansen, Z. Radi¢, T.T. Talley, B.E. Molles, T. Deerinck, I. Tsigelny, P. Taylor, J. Biol. Chem. **277**, 41299–41302 (2002)
22. J.R. Albani, J. Fluoresc. **19**, 1061–1071 (2009)

Biosensors and Bioelectronics 67 (2015) 224–229

Contents lists available at ScienceDirect

Biosensors and Bioelectronics

journal homepage: www.elsevier.com/locate/bios

Detection of parathion and patulin by quartz-crystal microbalance functionalized by the photonics immobilization technique

Riccardo Funari [a], Bartolomeo Della Ventura [a], Raffaele Carrieri [b], Luigi Morra [b], Ernesto Lahoz [b], Felice Gesuele [a], Carlo Altucci [a], Raffaele Velotta [a,*]

[a] CNISM and Dipartimento di Fisica, Università di Napoli "Federico II", Via Cintia, 26, Naples 80126, Italy
[b] Consiglio per la Ricerca e la Sperimentazione in Agricoltura – Unità di Ricerca per le Colture Alternative al Tabacco, Via P. Vitiello, 108, Scafati 84018, Italy

ARTICLE INFO

Article history:
Received 6 June 2014
Received in revised form
28 July 2014
Accepted 8 August 2014
Available online 19 August 2014

Keywords:
Parathion
Patulin
Immunosensor
Quartz crystal microbalance
Photonics immobilization technique

ABSTRACT

Oriented antibodies are tethered on the gold surface of a quartz crystal microbalance through the photonics immobilization technique so that limit of detection as low as 50 nM and 140 nM are achieved for parathion and patulin, respectively. To make these small analytes detectable by the microbalance, they have been weighed down through a "sandwich protocol" with a second antibody. The specificity against the parathion has been tested by checking the immunosensor response to a mixture of compounds similar to parathion, whereas the specificity against the patulin has been tested with a real sample from apple puree. In both cases, the results are more than satisfactory suggesting interesting outlook for the proposed device.

© 2014 Elsevier B.V. All rights reserved.

1. Introduction

The effective detection of small molecular weights analytes is of paramount importance in a wide range of scientific topics like investigating the molecular recognition phenomena and sensing of toxic molecules (Cooper and Singleton, 2007; Geschwindner et al., 2012; Jones et al., 2013; Vashist and Vashist, 2011). In particular, in the field of environmental monitoring it would be of great importance the availability of cost-effective and sensitive tools allowing the detection of low soluble and harmful compounds like steroids, herbicides, pesticides, toxins and combustion products like polycyclic aromatic hydrocarbon (PAH). As case studies to test our approach, we focused on parathion (IUPAC name O,O-diethyl O-4-nitrophenil phosphorothioate, MW=297 Da) and patulin (IUPAC name 4-hydroxy-4,6-dihydrofuro[3,2-c]pyran-2-one, MW=154 Da), which share a relatively low molecular weight and high interest for environment and health safety. Parathion is an organophosphate pesticide widely used to enhance agricultural production, but for its toxicity (Milles and Salt, 1950) it is now forbidden within the European Union which sets the limits of pesticide residues in food between 50 and 100 μg/kg (Commission Regulation (EC) no. 839/2008). Patulin is an example of mycotoxin which is most likely to be found in crops as a result of fungal infection. Both molecules are highly resistant to degradation and the patulin high toxicity for human and animal health has been recently pointed out in a review by Puel et al. (2010). Patulin level in food is strictly regulated in European countries (Commission Regulation (EC) no. 1881/2006) which set a maximum level of 50 μg/kg for fruit juices and derived products, 25 μg/kg for solid apple products and 10 μg/kg for baby foods. Both parathion and patulin are usually quantified by exploiting expensive, time consuming and relatively complex techniques like high-performance-liquid-chromatography (HPLC) and/or mass spectrometry [see (Blasco et al., 2004; Carabias Martinez et al., 1992; Kwakman et al., 1992) for parathion and (Berthiller et al., 2014; Pereira et al., 2014) for patulin]. Thus, the lack of any commercial and standard immunochemical methods underpins the research for biosensor based detection allowing *in situ* and real-time analysis for environmental monitoring and food quality control.

Amperometric devices are used for parathion in view of their feature to provide cheap, rapid and effective analysis of aqueous samples if the molecules to be detected are electroactive. Zen et al. (1999) developed a sensitive technique for the detection of parathion using a Nafion-coated glassycarbon electrode thus reaching a limit of detection (LOD) of 50 nM. Other sensing strategies are based on electrodes functionalized using enzymes like organophosphorus hydrolase. Exploiting this principle Mulchandani et al. (2001) were able to detect methyl-parathion and paraoxon with a LOD of 20 nM. Even if this kind of devices

* Corresponding author. Tel.: +39 081 6 76148.
E-mail address: rvelotta@unina.it (R. Velotta).

http://dx.doi.org/10.1016/j.bios.2014.08.020
0956-5663/© 2014 Elsevier B.V. All rights reserved.

offers several advantages for water analysis, electrochemical detection can be easily influenced by other oxidizable molecules eventually present in a real sample.

Electrochemical (Vidal et al., 2013), optical (Pereira et al., 2014) and piezoelectric (Pohanka et al., 2007; Prieto-Simón and Campàs, 2009), sensors and biosensors for the detection of mycotoxins are reported in literature, but quite few results are reported for patulin detection. A fluorescence assay was proposed by De Champdoré et al. (2007) with a LOD of 10 μg/L (less than 0.1 μM), but no test on a real sample was carried out. Damián Chanique et al. (2013) have developed a detection method based on the electrochemical reduction of patulin using glassy carbon electrodes. With this strategy they reached a LOD of 300 nM quantifying patulin in commercial apple juices. Starodub and Slishek (2012) proposed a nano-porosus silicon based immunosensor for measuring the level of patulin and T2 mycotoxin in real samples reaching a sensitivity of about 10 ng/mL for both pollutants. More recently, Pennacchio et al. (2014) proposed a competitive surface plasmon resonance (SPR) based bioassay with an estimated LOD of 0.1 nM, but it is worth noticing that the accuracy of SPR measurements can be influenced by interfering effects like temperature and sample composition fluctuation which produce a change in the refractive index not related to the analyte binding.

In view of their robustness, flexibility and cost-effectiveness, quartz crystal microbalance (QCM) technology has achieved an important role in fields like sensing, material science, environmental monitoring and protein studying (Vashist and Vashist, 2011). It is possible use QCM devices for small molecule detection exploiting several principles and configurations (Cooper and Singleton, 2007). All these advantages led to a wide range of publications involving QCM based detection of both pesticides and mycotoxins. For instance, Bi and Yang (2009) used molecular imprinted monolayers (MIMs) self-assembled onto the QCM gold electrode to effectively detect imidacloprid and thiacloprid pesticides in celery juice. They used an extremely sensitive QCM device getting a LOD of 1 μM. Concerning mycotoxin detection an indirect competitive immunological strategy has been adopted by Jin et al. (2009) for the quantification of aflatoxin B1. They significantly improved the sensitivity of the QCM based biosensor coupling the indirect competitive immunoassay with biocatalyzed deposition amplification using enzyme labeled secondary antibodies. Horseradish peroxidase was used to catalyze the oxidation of 4-chloro-1-naphthol to form an insoluble product which deposits onto the QCM electrode thus resulting in a huge increase in the sensor response. This procedure requires several time consuming incubation steps and allows to reach a LOD of about 32 pM.

Surface functionalization is one the main issue in biosensor development, in fact, recent publications show the strong interest in the research of innovative immobilization and functionalization strategies which provide better sensitivity and lower LOD (Jung et al., 2008; Nicu and Leïchlé, 2008). In particular, protein orientation is of paramount importance for immobilized antibodies which have to well expose their sensitive parts, the so called antigen binding sites, to effectively capture the antigens. Trilling et al. (2013) have recently investigated the relationship between analyte characteristics and capture molecule anchoring showing that the uniform orientation of the recognition elements provides a huge systematic improvement in sensitivity for weak interactions. They observed that the smaller the molecule, the lower the epitope number per analyte and, hence, the more important is the orientation of the sensitive biomolecule. By an appropriate antibody surface functionalization, Funari et al. (2013) were able to use a simple transducer like quartz-crystal microbalance (QCM) to detect a concentration of about 200 nM of parathion. This result was achieved by adopting the photonic immobilization technique (PIT) (Della Ventura et al., 2011), so that a gold surface fully covered by oriented antibodies was realized, but also by "weighing down" the molecule through the complexion of parathion with bovine serum albumin (BSA). Since not all the molecules are able to complex with BSA, in this paper we propose a more general approach leading to higher sensitivity and specificity. Essentially, parathion and patulin are "weighed down" by the same antibodies used for the detection onto QCM, mimicking the so called sandwich configuration widely used in the ELISA assays. To this end, the pollutant sample is mixed with an antibody solution before the latter is conveyed to the QCM and LODs of approximately 50 nM and 140 nM are achieved for parathion and patulin, respectively.

2. Materials and methods

2.1. Chemicals

Parathion (45607) and patulin (P1639) were purchased from Sigma-Aldrich. Anti-parathion (ABIN113883) and anti-patulin (AS11-1699) polyclonal antibodies were purchased as rabbit sera from antibodies-online.com and Agrisera respectively. The type G immunoglobulins were purified using the Protein A Antibody Purification Kit (PURE1A) from Sigma-Aldrich. 5,5′-dithiobis-(2-nitrobenzoic acid) also known as Ellman's reagent (D8130), bovine serum albumin (A2153) and the compounds used for the specificity tests, bisphenol A (239658), p-nonylphenol (46018), dichlorvos (45441), diazinon (45428) and paraoxon (36186), were from Sigma-Aldrich. The pollutant samples were prepared using PBS 1 × buffer solution in the fume hood. Helix water, sulfuric acid 98% and hydrogen peroxide 40% were used for the cleaning procedure of the QCM gold surfaces.

2.2. Patulin extraction from real sample

For the specificity test, we used real samples of patulin extracted from apple puree obtained from apple processing plant. To this end a commercial kit (Polyintell Affinimip® SPE cartridges) was used. The extraction was performed as follows: 10 g of apple puree were treated with 150 μL of a pectinase enzyme solution followed by 10 mL water and mixed. Solution was left at room temperature overnight, or for 2 h at 40 °C, centrifuged at 4500*g* for 5 min and then filtered with a 0.2 μM filter. This solution is used as the loading solution. SPE Cartridge was conditioned with 2 mL of acetonitrile (ACN), then with 1 mL of deionised water. 5 mL of the loading solution was put in the cartridge, which was subsequently washed with 4 mL of deionized water containing 1% of acetic acid. Water was forced down into the cartridge. The cartridge was treated with 1 mL of $CHCl_3$ and patulin was eluted with 2 mL of ACN containing 1% acetic acid. The SPE procedure lasted approximately 30 min. The elution fraction was then evaporated and dissolved in water containing 0.1% acetic acid. This fraction was submitted to a Perkin Elmer HPLC with UV detector to determine the patulin concentration. The same sample was used in QCM validation analysis.

2.3. UV laser source

The immunoglobulin samples were irradiated using the UV laser pulses provided by a custom femtosecond PHAROS laser system with high tunable pulse repetition rate coupled with a harmonic generator stage (HIRO) which allows the conversion to 515 nm, 343 nm and 258 nm wavelengths of the IR fundamental radiation. Both PHAROS and HIRO were from Light Conversion Ltd.

2.4. Quartz crystals

The quartz oscillators (151218) are from ICM, Oklahoma city (USA). They are AT-CUT quartz with a fundamental frequency of 10 MHz. The crystal and the gold electrode diameters are 1.37 cm and 0.68 cm respectively. The gold surfaces are cleaned by immersing the oscillators for 1 min in a glass beaker containing Piranha solution (5:1 ratio between concentrated sulfuric acid and 40% hydrogen peroxide solution), then the quartzes are washed with helix water. The whole cleaning procedure is performed in the hood and can be repeated 3–4 times before the quartz needs to be changed. The QCM device is a μLibra from Technobiochip, Italy. The gold-quartz wafer is placed on the electronic console and the resonance frequency of the oscillator is monitored by producer released software. The QCM is integrated in a microfluidic circuit consisting of the cell which contains the oscillator, platinum threated silicon tubes and a GILSON peristaltic pump. The volume of the circuit is about 300 μL and the flow rate is 3 μL/s. A gentle cleaning with glycine HCl 0.2 M at pH 2.8 allows the removal of only the antigen without significant loss of the tethered antibodies thus leading to the regeneration of the functionalized gold surface. This procedure can be safely applied approximately three times.

2.5. UV activation of antibody solution

Photonic immobilization technique (PIT) (Della Ventura et al., 2011) is a method to immobilize antibodies onto gold based on the photonic reduction of disulfide bridges in proteins by UV illumination of near aromatic amino acid (Neves-Petersen et al., 2002). PIT leads to antibodies oriented side-up i.e. they expose the Fab onto thiol-reactive surfaces like gold plates. The only requirement for applying this technique is the presence into the protein of a closely spaced tryptophan/cysteine–cysteine (Trp/Cys–Cys) triad which is a typical structural characteristic of the immunoglobulin family (Ioerger et al., 1999). The details of this photonic activation have been recently reported by Neves-Petersen et al. (2012). Basically the UV-excitation of tryptophan can result in its photoionization thus generating solvated electrons which are captured by the near electrophillic species like cystines. In this case the result is the breakage of the disulfide bridge thereby generating new thiol functions (red part in the constant region of the antibody) which can easily react with other free thiol groups or with thiol reactive surfaces like gold plates. The rise of the number of the SH groups onto the protein allows new structural conformation for the immobilized immunoglobulin which are characterized by a well exposure of the antigen binding sites thus greatly improving sensor sensitivity. It is well known that UV radiation strongly affects both structure and activity of biomolecules, but we have recently demonstrated that the photonic activation of immunoglobulins by femtosecond UV pulses does not affect their ability to capture the antigen (Funari et al., 2013; Lettieri et al., 2014).

To realize the PIT, antibody samples of 500 μL with a protein concentration of 50 μg/mL were activated using the UV laser source previously described (Fig. 1). In order to find the irradiation conditions which maximize the number of thiol groups per molecule we exploited the so called Ellman's assay (Ellman, 1959) (data not shown). For both anti-parathion and anti-patulin antibodies, the irradiation conditions are $\lambda = 258$ nm, 10 kHz repetition rate, 250 mW of average power, and 1 min irradiation time.

2.6. QCM measurements

Before the experiment each pollutant sample has been incubated for 30 min with the same volume of immunoglobulin solution at a fixed concentration (25 μg/mL), corresponding to an initial concentration of Ab_{free} (*free* antibody in solution) of $[Ab_{free}]_0 \approx 0.17$ μM. This mixture is then tested by the QCM based immunosensor. The experimental procedure consists in the flowing of different solutions onto the gold sensitive surface of the crystal using the fluidic apparatus previously described. Typical QCM outputs involving either irradiated or non-irradiated antibodies in the detection of parathion are shown in Fig. 2.

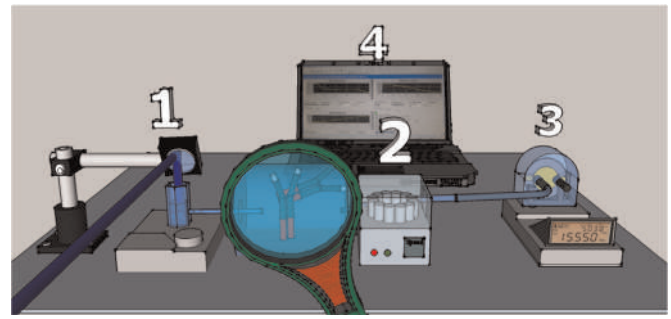

Fig. 1. Experimental layout for PIT. The antibodies are "activated" in the cuvette (1) and conveyed through a peristaltic pump (2) to the QCM (3). The electronics of the QCM is interfaced with a PC (4) so that the frequency shift due to the antibody tethering is controlled in real time. The white end of the antibodies in the pipe is the antigen binding site, whereas the red part highlights the region where the free thiols are produced. (For interpretation of the references to color in this figure legend, the reader is referred to the web version of this article.)

The first step is the reaching of the basal frequency stabilization by flowing PBS solution. Then the surface is functionalized using either irradiated or non-irradiated antibody sample. This step gives rise to a first frequency drop of about 140 Hz, which is the same in both conditions showing that PIT does not affect significantly the total amount of tethered antibodies. This result is in fair agreement with the surface density measurements reported by Peluso et al. (2003) and can be explained by considering that even oriented side up the antibodies can tether with an arbitrary azimuthal, which prevents the possibility to line them up. Subsequently, a washing step with PBS is used to purge the circuit from the excess of immunoglobulins. Then a BSA solution (50 μg/mL) flows into the cell filling the remaining free space on the gold surface. This blocking step is crucial in order to avoid non-specific

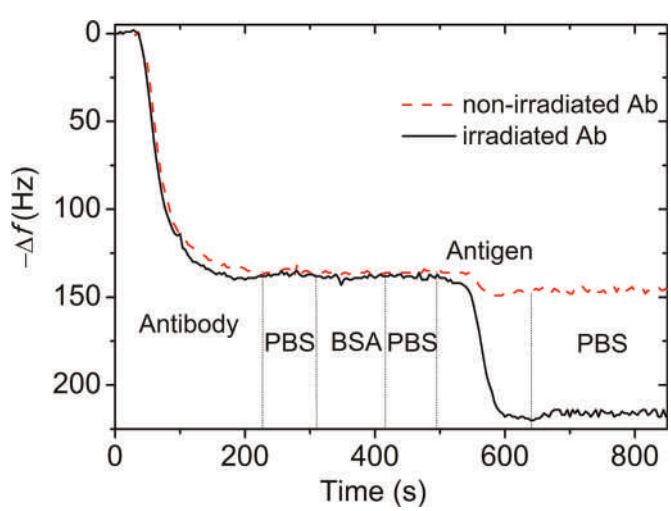

Fig. 2. QCM-based immunosensor outputs for parathion detection using either irradiated (black solid line) or non-irradiated (red dashed line) antibodies. The first frequency shift at about 150 s corresponds to the antibody immobilization onto the sensor surface, while the second drop at about 550 s is due to the detection of analyte–antibody complex (parathion 0.85 μM). The vertical dashed lines highlight the phases of the protocol described in the text. (For interpretation of the references to colour in this figure legend, the reader is referred to the web version of this article.)

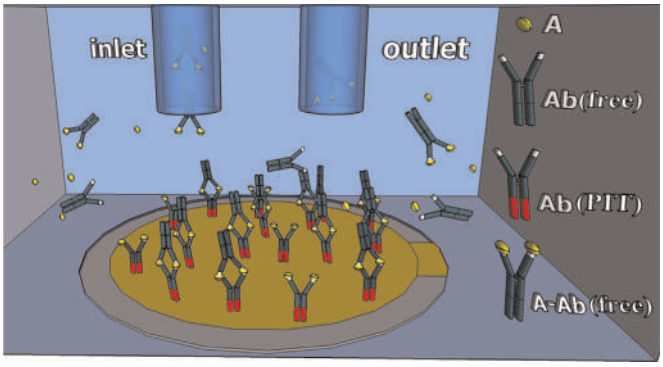

Fig. 3. Sketch of the cell containing the surface detector. The antibodies activated by the PIT are shown with their lower part in red and are tethered side-up on the gold electrode. The solution flowing through the cell contains analyte (small yellow particles) bound to the Ab (green Y-shape), but also "free" Ab and "free" analytes. When a free analyte is recognized by the Ab tethered to the gold, there is no effect on the QCM frequency since the deposited mass is too small. Only when the "sandwich" configuration is realized there is a detectable response. (For interpretation of the references to colour in this figure legend, the reader is referred to the web version of this article.)

interactions between the further flowing molecules and the gold plate. It is worth notice that this phase results in a negligible change in the resonance frequency, therefore proving that the gold surface is quite completely covered by the antibodies. After another cleaning step with PBS, the analyte–antibody sample flows into the circuit and the labeled antigens are captured by the immobilized antibodies, thus resulting in the second frequency shift. This signal is much bigger when the sensor surface is functionalized using UV activated antibodies. A final washing step is then used to remove weakly bonded analytes.

It is important to highlight that in this scheme three species can interact with the sensor (Fig. 3): A (antigen), A–Ab_{free} (antigen–antibody complex) and Ab_{free} (antibody).

The advantage of the simultaneous injection of the three species (A, Ab_{free} and A–Ab_{free}) rather than the sequential injection of A and Ab_{free}, as it occurs in the "standard sandwich ELISA" protocol (Crowther, 1995), relies in the higher *effective* concentration of the analyte in the interaction volume. In fact, due to the stationary equilibrium conditions occurring in the interaction volume of the QCM, when the antibodies are mixed with the solution to be analyzed, the *effective* antigen concentration in the interaction volume coincides with the antigen concentration in the original solution. On the opposite, when the original solution is injected first into QCM and the antibody is injected in a second step after a necessary washing (as in the "standard sandwich ELISA" protocol), the *effective* antigen concentration is lower since there are no free antigens that could replace those detached from the QCM plate by the free antibodies. This, in turn, leads to a reduction of the QCM frequency shift which we measured to be approximately two. Since the aim of this work was the search for the highest sensitivity, the injection of the solution mixed with antibodies was preferred. The drawback of such an approach relies in the need of high antibody concentration in the original solution so that virtually all the antigens are bound and the probability of finding free antigen is negligible. At antigen concentration much higher than the antibody concentration there will be free antigens that would bind the antibodies tethered to the gold plate. In this case the QCM will not provide a detectable signal because of the low antigen mass giving rise to the so-called "hook effect" which can be shifted to high analyte concentration by simply increasing the antibody concentration (Amarasiri Fernando and Wilson, 1992).

3. Results and discussion

The response of the QCM is proportional to the mass tethered to the electrode (Sauerbrey, 1959) so that through the measurement of the frequency shift $\Delta f([A]_0)$, we measure the concentration of the analyte in the solution. While a detailed description of the process in terms of chemical kinetic would require a complex analysis which should also include the diffusion of the several species, we can easily model the observed dynamics by considering the law of mass action and the free diffusion conditions of our experiment. In fact, in this case a Michaelis–Menten type equation is expected to well describe the process when $[A]_0 \ll [Ab_{free}]_0$:

$$\Delta f([A]_0) = \frac{(\Delta f)_{sat}[A]_0}{K_M + [A]_0} \quad (1)$$

In Eq. (1) $(\Delta f)_{sat}$ contains the instrument response and K_M is the so-called Michaelis–Menten constant. The former parameter includes the number of antibodies tethered on the balance as well as their effectiveness in capturing the analyte, i.e. their orientation, whereas the latter provides an estimation of the linear range of the sensor. As explained in Section 2.6, an excess of analyte concentration in the original solution ($[A]_0 \gg [Ab_{free}]_0$) makes high the probability that tethered antibodies bind the analytes (A) rather than the complexed analytes (A–Ab_{free}), but due to the small mass of the analyte such a recognition does not lead to a measurable frequency shift. Thus, when [A] increases and the

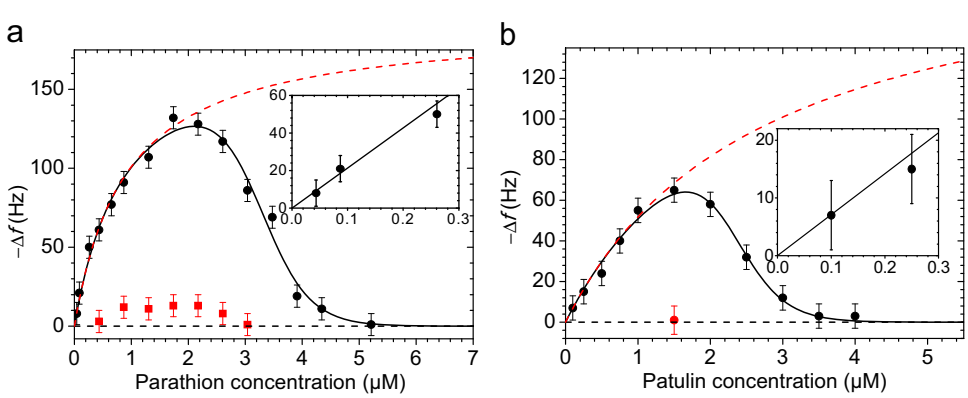

Fig. 4. Response of the QCM to (a) parathion and (b) patulin concentrations when the antibody is irradiated (circle points) and not irradiated (square points). The points achieved with the irradiated antibody are fitted by Eq. (2) (bold line). The low frequency change achieved when the antibody is not irradiated does not allow any significant fit of the experimental data. The inset is the enlargement of the low concentration region, whereas the dashed red lines are the plots of Eq. (1), i.e. the inhibition effect of the free antigens is hampered by high Ab_{free} concentration. (For interpretation of the references to color in this figure legend, the reader is referred to the web version of this article.)

Table 1
Values of the three free parameters as deduced from the best fit of the experimental data.

	K_M [μM]	b [μM]$^{-1}$	$[A]_M$ [μM]
Parathion	0.90 ± 0.05	2.4 ± 0.1	3.3 ± 0.1
Patulin	2.70 ± 0.05	3.0 ± 0.1	2.3 ± 0.1

condition $[A]_0 \approx [Ab_{free}]_0$ is reached an "inhibition effect" starts and further increase of [A] results in a reduction of Δf rather than in its increase. This is observable in Fig. 4 where at low [A] the frequency shift follows Eq. (1), whereas a reduction of the frequency shift occurs at high analyte concentration. A simple way to model the inhibition role played by the free analyte is through a two parameters logistic function, in which one parameter accounts for the analyte concentration at which the inhibition becomes important and the other takes into account the decay rate of the available recognition site. Thus, we can fit our experimental results with the following function:

$$\Delta f([A]_0) = \frac{(\Delta f)_{sat}[A]_0}{K_M + [A]_0} \times \frac{1}{1 + e^{b([A]_0 - [A]_M)}} \quad (2)$$

In the Eq. (2) b and $[A]_M$ are two free parameters accounting for the different kinetics the analytes and antibodies may have, whereas $(\Delta f)_{sat} = 192 \pm 2$ Hz has been determined by measuring the saturation value one measures when a layer of antibodies covers the surface. Although such a value refers to irradiated antibodies, it is essentially the same even when the antibodies are not irradiated (Della Ventura et al., 2011).

The fitting of the experimental results obtained with irradiated antibodies by Eq. (2) (solid black lines in both panels of Fig. 4) provides the results reported in Table 1, while the square red points in Fig. 4 are the results obtained if PIT is not adopted and the antibodies are only tethered spontaneously on the gold. In this latter case it is readily seen that no significant signal is measurable. The dashed red lines in Fig. 4 are the plots of Eq. (1), i.e. the response one obtains when $[Ab_{free}]_0 \gg K_M$, showing that an initial Ab concentration of 1 mg/mL is more than enough in many practical conditions to achieve a monotonic response from our sensor.

The uncertainty in our measurements is due to instrumental limitations in the performances of our QCM as well as to the unavoidable fluctuations in the several steps of the procedure. Assuming an overall error of 10 Hz, (see also the insets in Fig. 4) so that a minimum frequency change $(\Delta f)_{min} = 10$ Hz is required for a measurement to be significantly different from zero, an evaluation of the lower LOD can be obtained by inverting Eq. (1)

$$LOD \approx \frac{(\Delta f)_{min} K_M}{(\Delta f)_{sat}}. \quad (3)$$

Eq. (3) leads to a LOD in water of approximately 50 nM and 140 nM, for parathion and patulin, respectively.

To ascertain the sensor specificity, the same experimental procedure has been used to test the response of the QCM when compounds similar to the analytes to be detected are in the solution. For parathion, we prepared a mixture of bisphenol A (4,4′-(propane-2,2-diyl)diphenol), p-nonylphenol, dichlorvos (2,2-dichlorovinyl dimethyl phosphate), diazinon (O,O-diethyl O-[4-methyl-6-(propan-2-yl)pyrimidin-2-yl] phosphorothioate), and paraoxon (diethyl 4-nitrophenyl phosphate) each of them at a concentration of 2 μM. When only this mixture is made to flow into the QCM no response is provided by the sensor (black solid line in Fig. 5(a)). On the opposite, when parathion at 0.2 μM is added to this mixture, the sensor exhibits a frequency shift of approximately 35 Hz (dashed red line in Fig. 5(a)) in very good agreement with the curve shown in Fig. 4(a) (see the inset), thereby evidencing that pollutants other than parathion have no effect in the QCM response.

As it concerns patulin, Fig. 5(b) reports the QCM response to real samples previously analyzed by HPLC. When there is no patulin in the extract from apple puree, no frequency shift is observed (black solid line); on the opposite, when we analyze extracts from apple puree containing 0.2 μM and 1.0 μM of patulin measured by HPLC, the response of QCM (−12 Hz and −43 Hz, for the two concentrations, respectively) is in very satisfactory agreement with the calibration curve reported in Fig. 4(b). It is worth mentioning, that the real samples we analyzed contained all the possible analytes which could potentially interfere with the patulin measurement; nevertheless, our results show that the technique and the protocol adopted is robust and highly specific.

4. Conclusion

We report here a method to detect light molecules which combines the recently proposed Photonic Immobilization Technique for the antibody functionalization of the gold surfaces, and the antibody-sandwich protocol, to realize an immunosensor based on a QCM. Essentially, in our device the antigen is recognized by its own antibody and the resulting solution is conveyed to the balance. While PIT is shown to largely increase the sensitivity of QCM, the sandwich protocol has a twofold effect: on the one hand it weighs down light molecules, so that they can be "weighed" by QCM, on the other hand it inherently increases even more the

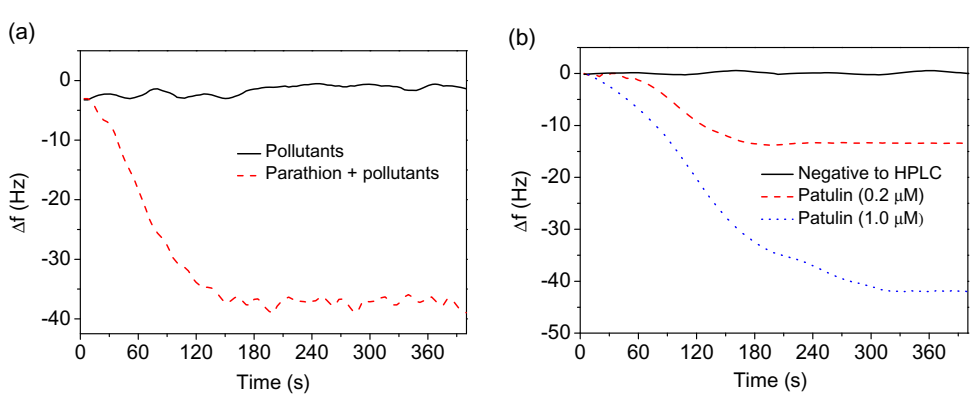

Fig. 5. Sensor specificity i.e.. QCM responses against different pollutants. (a) Parathion at 0.2 μM tested against bisphenol A, p-nonylphenol, dichlorvos, diazinon and paraoxon each of them at 2 μM. (b) Extract from apple puree previously analyzed by HPLC. (—) Negative to patulin; (---) 0.2 μM patulin; (····) 1 μM patulin. (For interpretation of the references to color in this figure, the reader is referred to the web version of this article.)

specificity of the whole device. The sandwich protocol proposed here considers the inclusion of free antibody in the solution to be analyzed, so that the formation of the analyte-antibody complex takes place in the cuvette, and a subsequent injection of the whole solution into QCM. Compared to the typical sandwich ELISA protocol, in which the solution is conveyed as it is to the tethered antibodies and the second antibody is added after a washing, our approach leads to higher sensitivity, the drawback of the decrease of the signal in presence of high analyte concentration being easily overcome by using higher antibody concentration in the mixing volume. On the opposite, one of the advantages of our immunosensors relies in its generality, since in practice antibodies can be produced for any analyte. We have applied our device to parathion and patulin for which LODs of 50 nM and 140 nM were achieved, respectively. In a scenario with lack of simple and reliable immunochemical analysis for two important analytes such as parathion and patulin, our QCM based immunosensor has noticeable advantages in terms of rapidity in the response (only few minutes are required), flexibility and portability, lending itself appropriate for *in situ* analysis.

Acknowledgments

We acknowledge the financial support of the “Fondazione con il Sud” (Project no. 2011-PDR-18, “Biosensori piezoelettrici a risposta in tempo reale per applicazioni ambientali e agro-alimentari”) and the Italian Ministry for Reaserch (MIUR) under the Grant no. PON_0101517.

References

Amarasiri Fernando, S., Wilson, G.S., 1992. J. Immunol. Methods 151, 47–56.
Berthiller, F., Burdaspal, P.A., Crews, C., Iha, M.H., Krska, R., Lattanzio, V.M.T., MacDonald, S., Malone, R.J., Maragos, C., Solfrizzo, M., Stroka, J., Whitaker, T. B., 2014. World Mycotoxin J. 7, 3–33.
Bi, X., Yang, K.-L., 2009. Anal. Chem. 81, 527–532.
Blasco, C., Fernández, M., Picó, Y., Font, G., 2004. J. Chromatogr. A 1030, 77–85.
Carabias Martinez, R., Rodriguez Gonzalo, E., Amigo Moran, M.J., Hernandez Mendez, J., 1992. J. Chromatogr. A 607, 37–45.
Cooper, M.A., Singleton, V.T., 2007. J. Mol. Recognit. 20, 154–184.
Crowther, J.R., 1995. ELISA: Theory and Practice. Humana Press, Totowa, NJ.
Damián Chanique, G., Heraldo Arévalo, A., Alicia Zon, M., Fernández, H., 2013. Talanta 111, 85–92.
De Champdoré, M., Bazzicalupo, P., De Napoli, L., Montesarchio, D., Di Fabio, G., Cocozza, I., Parracino, A., Rossi, M., D’Auria, S., 2007. Anal. Chem. 79, 751–757.
Della Ventura, B., Schiavo, L., Altucci, C., Esposito, R., Velotta, R., 2011. Biomed. Opt. Express 2, 3223–3231.
Ellman, G.L., 1959. Biophysics 82, 70–77.
Funari, R., Della Ventura, B., Schiavo, L., Esposito, R., Altucci, C., Velotta, R., 2013. Anal. Chem. 85, 6392–6397.
Geschwindner, S., Carlsson, J.F., Knecht, W., 2012. Sensors 12, 4311–4323.
Ioerger, T.R., Du, C., Linthicum, D.S., 1999. Mol. Immunol. 36, 373–386.
Jin, X., Jin, X., Liu, X., Chen, L., Jiang, J., Shen, G., Yu, R., 2009. Anal. Chim. Acta 645, 92–97.
Jones, A.M., Grossmann, G., Danielson, J.Å., Sosso, D., Chen, L.-Q., Ho, C.-H., Frommer, W.B., 2013. Curr. Opin. Plant Biol. 16, 389–395.
Jung, Y., Jeong, J.Y., Chung, B.H., 2008. Analyst 133, 697–701.
Kwakman, P.J.M., Vreuls, J.J., Brinkman, U.A.T., Ghijsen, R.T., 1992. Chromatographia 34, 41–47.
Lettieri, S., Avitabile, A., Della Ventura, B., Funari, R., Ambrosio, A., Maddalena, P., Valadan, M., Velotta, R., Altucci, C., 2014. Appl. Phys. A, http://dx.doi.org/10.1007/s00339-014-8340-4, in press.
Milles, H.L., Salt, H.B., 1950. Brit Med. J. 2, 444.
Mulchandani, P., Chen, W., Mulchandani, A., 2001. Sci. Technol. 35, 2562–2565.
Neves-Petersen, M.T., Petersen, S., Gajula, G.P., 2012. In: Satyen Saha (Ed.). UV Light Effects on Proteins: From Photochemistry to Nanomedicine in Molecular Photochemistry: Various Aspects. Tech-Open Access Company. http://dx.doi.org/10.5772/37947. Available from: http://www.intechopen.com/books/molecular-photochemistry-various-aspects/uv-light-effects-on-proteins-from-photochemistry-to-nanomedicine.
Neves-Petersen, M.T., Gryczynski, Z., Lakowicz, J., Fojan, P., Pedersen, S., Petersen, E., Bjørn Petersen, S., 2002. Protein Sci. 11, 588–600.
Nicu, L., Leïchle, T., 2008. J. Appl. Phys. 104, 111101.
Peluso, P., Wilson, D.S., Do, D., Tran, H., Venkatasubbaiah, M., Quincy, D., Heidecker, B., Poindexter, K., Tolani, N., Phelan, M., Witte, K., Jung, L.S., Wagner, P., Nock, S., 2003. Anal. Biochem. 312, 113–124.
Pennacchio, A., Ruggiero, G., Staiano, M., Piccialli, G., Oliviero, G., Lewkowicz, A., Synak, A., Bojarski, P., D’Auria, S., 2014. Opt. Mater. (Amst) 36, 1670–1675.
Pereira, V.L., Fernandes, J.O., Cunha, S.C., 2014. Trends Food Sci. Technol. 36, 96–136.
Pohanka, M., Jun, D., Kuca, K., 2007. Drug Chem. Toxicol. 30, 253–261.
Prieto-Simón, B., Campàs, M., 2009. Monatshefte für Chem. – Chem. Mon. 140, 915–920.
Puel, O., Galtier, P., Oswald, I.P., 2010. Toxins 2, 613–631.
Sauerbrey, G., 1959. Z. Phys. 155, 206–222.
Starodub, N.F., Slishek, N.F., 2012. Adv. Biosens. Bioelectron. 2, 7–15.
Trilling, A.K., Harmsen, M.M., Ruigrok, V.J.B., Zuilhof, H., Beekwilder, J., 2013. Biosens. Bioelectron. 40, 219–226.
Vashist, S.K., Vashist, P., 2011. J. Sensors 2011, 1–13.
Vidal, J.C., Bonel, L., Ezquerra, A., Hernández, S., Bertolín, J.R., Cubel, C., Castillo, J.R., 2013. Biosens. Bioelectron. 49, 146–158.
Zen, J.-M., Jou, J.-J., Senthil Kumar, A., 1999. Anal. Chim. Acta 396, 39–44.

DISPOSITIVO PORTATILE E METODO PER LA RIVELAZIONE E LA MISURA DI ANTIGENI SPECIFICI

Rivendicazioni

1) Dispositivo per la rivelazione e la misura di sostanze inquinanti, come gli idrocarburi policiclici aromatici (IPA) quale ad esempio il Benzo[a]Pirene (B[a]p); che comprende un mezzo per la misurazione del peso (5), come e non solo una microbilancia a cristalli di quarzo, un circuito fluidico (7), una macchina operatrice (3), come ma non solo una pompa peristaltica, contenitori per fluidi (1) e (2), un sistema informatico di elaborazione(6), atto alla lettura e all'analisi dei dati in uscita dal sistema (5), **caratterizzato dal fatto che** comprende un mezzo per la produzione di impulsi di luce ultravioletta (8), quale ma non solo laser o lampade UV, irraggiante il liquido contenuto nel contenitore (2), atto alla funzionalizzazione dell'elettrodo (4) del mezzo per la misurazione del peso (5).
2) Dispositivo come nella rivendicazione 1, caratterizzato dal fatto che detto mezzo per la misurazione del peso (5) è collegato attraverso il circuito fluidico (7) ai mezzi contenitori (1) e (2) e alla macchina operatrice (3), atta a far circolare i fluidi nel dispositivo.
3) Dispositivo come nella rivendicazione 1, caratterizzato dal fatto che detto mezzo per la misurazione del peso (5) comprende un elettrodo funzionalizzato mediante la deposizione di anticorpi specifici.
4) Metodo per la rivelazione e la misura di anticorpi in tempo reale di sostanze inquinanti, come gli idrocarburi policiclici aromatici (IPA) quale ad esempio il Benzo[a]Pirene (B[a]p), detto metodo prevede, in una delle sue forme, le seguenti fasi:
    a. prelievo, condensazione e filtraggio del campione;
    b. scioglimento del campione in un solvente, come, ma non solo, il diclorometano;
    c. deposizione degli anticorpi sull'elettrodo della microbilancia ai cristalli di quarzo;
    d. ancoraggio degli antigeni zavorrati agli anticorpi monoclonali;
    e. rivelamento e misurazione degli antigeni;
    f. elaborazione dei dati;

    Caratterizzato dal fatto che detto metodo comprende una fase di irraggiamento degli anticorpi monoclonali con impulsi di luce ultravioletta e una successiva fase di zavorramento mediante l'utilizzo di anticorpi policlonali.

5) Metodo come nella rivendicazione 4, caratterizzato dal fatto che detta fase di irraggiamento di anticorpi monoclonali, realizzata mediante mezzo per la produzione di impulsi di luce ultravioletta (8), è atta a garantire la deposizione degli stessi sull'elettrodo del sensore.
6) Metodo come nella rivendicazione 4, caratterizzato dal fatto che detta fase di zavorramento prevede l'utilizzo di anticorpi policlonali atti a legarsi all'antigene da rivelare.
7) Metodo come nelle rivendicazioni 4, caratterizzato dal fatto che la fase di irraggiamento avviene a monte della fase di deposizione.
8) Metodo come nelle rivendicazioni 4, caratterizzato dal fatto che la fase di zavorramento avviene a monte della fase di rivelamento.

DISPOSITIVO PORTATILE E METODO PER LA RIVELAZIONE E LA MISURA DI ANTIGENI SPECIFICI

CAMPO DI APPLICAZIONE

Forma oggetto del seguente trovato un metodo e un dispositivo per la rivelazione e la misura di idrocarburi policiclici aromatici (Antigeni), come ma non solo il Benzo[a]pirene (B[a]p), basato sull'uso di anticorpi specifici.

STATO DELLA TECNICA

Sono noti dispositivi che esplicano funzioni similari al trovato, cioè la rivelazione ed il monitoraggio di idrocarburi policiclici aromatici (Antigeni).

Una soluzione è la Gas-Cromatografia - Spettrometria di Massa (GC-MS), costituita essenzialmente da un gascromatografo per la separazione dei composti presenti nel campione, accoppiato ad uno spettrometro di massa per la rivelazione dei composti stessi.

Un'altra soluzione è la cromatografia liquida ad alta prestazione (HPLC), costituita essenzialmente da contenitori per la fase mobile, pompe, sistemi di introduzione del campione, colonna, riempimento della colonna, rivelatori.

Le soluzioni viste presentano il limite di essere di grosse dimensioni e di conseguenza fanno riferimento a grossi laboratori in genere localizzati anche lontani dai siti di interesse. Tali grandi dispositivi hanno costi di acquisto, di esercizio e di manutenzione rilevanti e richiedono l'impiego di operatori specializzati. Per tali ragioni possono essere fatte misurazioni di antigeni una tantum.

Un'altra soluzione, il brevetto KR20110040159, è un kit per la diagnosi di contaminazione da Benzo[a]pirene in vivo contenente un antigene che si lega

specificamente ad un marcatore, se il valore del marcatore supera un certo livello di soglia vi è contaminazione.

Il brevetto US6676904, invece, atto ad isolare un generico analita in un campione di prova, consiste in una membrana semipermeabile con pori per la trattenuta dell'analita, dove la membrana è stata modificata chimicamente; marcatori che avranno un'affinità di legame con i modificatori di membrana in presenza dell'analita e una sostanziale differenza di affinità di legame in assenza dell'analita; un sistema di rilevamento dei marcatori per il rilevamento della loro presenza sulla membrana.

Entrambe le soluzioni presentano delle differenze sostanziali da quello oggetto della richiesta di brevetto. Le differenze fondamentali risiedono nelle tecnologie utilizzate che sono solo di tipo chimico e non anche elettro – meccanico e di non essere abili a misurare il quantitativo di antigene ma solo di rilevarne la presenza, inoltre con il limite di non poter essere utilizzate in tempo reale, di non avere lo stesso grado di sensibilità e di specificità.

Il brevetto WO2007000163 si riferisce a metodi per la rivelazione di biomolecole, come polipeptidi. In particolare, la presente invenzione riguarda metodi e vettori utili per accoppiare un polipeptide ad un vettore tramite un legame disolfuro. L'invenzione oggetto del trovato si riferisce invece alla rivelazione di idrocarburi, attraverso l'utilizzo di anticorpi monoclonali e policlonali.

Per ovviare a tutti gli inconvenienti su menzionati ed ottenere ulteriori vantaggi, il Richiedente ha studiato e realizzato il presente trovato.

ESPOSIZIONE DEL TROVATO

Il presente trovato è esposto e caratterizzato nelle sue rivendicazioni principali.

Altre caratteristiche sono presenti nelle rivendicazioni secondarie.

Scopo del seguente trovato è quello di realizzare un immunosensore e definire un metodo per la rivelazione e la misurazione di particolari sostanze inquinanti, che possa esser utilizzato in tempo reale e che sia pratico, funzionale, compatto, portatile e che possa esser utilizzato in condizioni di assoluta sicurezza anche da da parte di utenti non esperti.

Il funzionamento del dispositivo si basa sull'uso di anticorpi specifici per la rivelazione di un antigene, quale ma non solo il Benzo[a]pirene, attraverso l'uso di microbilance a cristalli di quarzo. Gli elettrodi di tale microbilancia sono funzionalizzati mediante dispositivi per la produzione di luce impulsata ultravioletta. La sorgente di luce impulsata può essere costituita da apparati, quali ma non solo lampade impulsate UV e/o laser ultravioletti; tale sorgente impulsata è atta alla funzionalizzazione degli elettrodi della microbilancia a cristalli di quarzo. La funzionalizzazione, che avviene *una tantum* e comunque a monte del processo di misura, serve a consentire la deposizione, sul piatto di tale bilancia, di anticorpi specifici, in grado di individuare l'antigene oggetto della ricerca.

Caratteristica fondamentale dell'apparato di rivelazione, oggetto del trovato, consiste in un dispositivo analitico atto alla misurazione della massa dell'antigene, contenuto in campioni in fase liquida, che deposita sulla bilancia in condizioni di flusso laminare controllato. L'antigene può essere un qualsiasi idrocarburo policiclico aromatico (IPA), quale ma non solo il Benzo[a]pirene.

Secondo il trovato viene ideato un metodo per l'utilizzo di anticorpi monoclonali e policlonali per la rivelazione di idrocarburi come, ma non solo Benzo[a]pirene disciolte in una soluzione.

Il modello di funzionalizzazione del trovato si basa su una metodologia di deposizione di anticorpi come, ma non solo Photonic Immobilization Technique (PIT), associata al protocollo di appesantimento tipo sandwich, adoperato ad

esempio nel Enzyme-Linked ImmunoSorbent Assay (saggio ELISA), per essere rivelata con un sensore gravimetrico, come ma non solo quello basato su microbilancia. Secondo il trovato, nella sua seconda rivendicazione principale, un anticorpo policlonale è utilizzato come zavorra per l'appesantimento di tipo sandwich.

Infatti, tra le molecole utilizzabili come possibili zavorre, la scelta dell'anticorpo stesso è altamente raccomandabile per la sua specificità verso l'analita e la sua massa elevata. La fase di appesantimento della molecola viene eseguita in una fase preliminare.

Per il processo di deposizione di anticorpi monoclonali e policlonali per la rivelazione di idrocarburi come, ma non solo Benzo[a]pirene disciolti in una soluzione viene, secondo il trovato, utilizzato un particolare protocollo di appensantimento. Il protocollo fa uso di anticorpi monoclonali, per la funzione di immuno-riconoscimento e cattura dell'antigene, e policlonali, per la funzione di appesantimento. Questo tipo di protocollo raggiunge il miglior compromesso tra specificità, che predilige l'uso di anticorpi monoclonali a scapito dell'efficienza, ed efficienza stessa, per la quale è invece richiesto l'uso di anticorpi policlonali, più efficienti e meno specifici.

ILLUSTRAZIONE DEI DISEGNI

Attraverso la descrizione di una forma preferenziale di realizzazione di tale trovato saranno più chiare queste ed altre caratteristiche dello stesso. Tale forma del trovato è fornita a titolo esemplificativo, non limitativo, nell'annesso disegno in cui:

La Fig. illustra una schematizzazione di un dispositivo secondo il trovato.

DESCRIZIONE DI UNA FORMA PREFERENZIALE DEL TROVATO

Con riferimento alla Figura, un sensore secondo il presente trovato atto alla rivelazione e misurazione di sostanze inquinanti contenute in un campione contenuto in una cuvette 1.

Tala sensore comprende un dispositivo per la produzione di luce impulsata 8 atta alla funzionalizzazione mediante metodologia PIT degli anticorpi anti-B[A]P presenti in una cuvette 1, un circuito fluidico 7 con pompa peristaltica 3, un elemento sensibile, elettrodo 4, inserito nella microbilancia a cristallo di quarzo 5, un PC con software per la lettura/analisi in tempo reale 6.

Il metodo per il rivelamento e la misurazione di sostanze inquinanti dove il campione da misurare, dopo il prelievo e successivo filtraggio, è condensato e successivamente risciolto in un solvente, come ma non solo il Diclorometano. Il campione è prelevato tramite variazione di pressione, indotta nel circuito dalla pompa peristaltica 3, mediante luce impulsata, quale ad esempio quella prodotta mediante lampade UV o laser ultravioletti 2, si ottiene la funzionalizzazione degli anticorpi presenti in una cuvette che successivamente vanno ad ancorarsi all’elettrodo 4 della bilancia a microcristalli di quarzo 5. Il sensore rileva la variazione di frequenza dalla bilancia a microcristalli di quarzo 5 ed invia il segnale digitale al sistema di lettura informatico 6 che ne evidenzia il salto in frequenza.

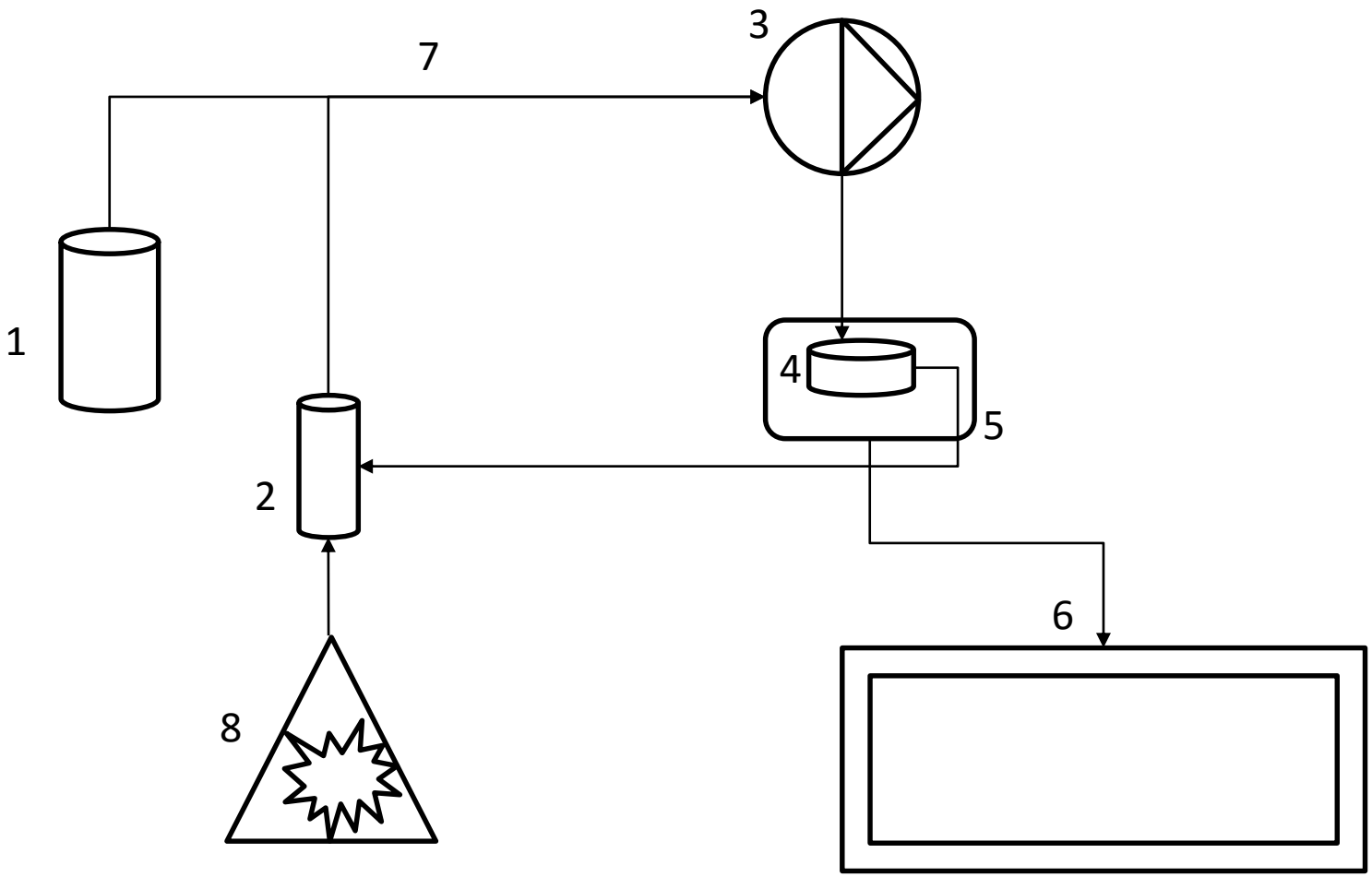
3
7
1
4
5
2
6
8

This article was downloaded by: [Stazione Zoologica], [Giovanna Romano]
On: 22 March 2012, At: 10:47
Publisher: Taylor & Francis
Informa Ltd Registered in England and Wales Registered Number: 1072954 Registered office: Mortimer House, 37-41 Mortimer Street, London W1T 3JH, UK

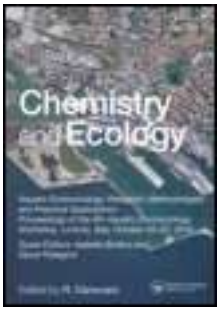

Chemistry and Ecology
Publication details, including instructions for authors and subscription information:
http://www.tandfonline.com/loi/gche20

Study of apoptosis induction using fluorescent and higher harmonic generation microscopy techniques in Acartia tonsa nauplii exposed to chronic concentrations of nickel

Isabella Buttino [a b], David Pellegrini [b], Giovanna Romano [a], Jiang-Shiou Hwang [c], Tzu-Ming Liu [d e], Davide Sartori [b], Chi-Kuang Sun [e f], Simona Macchia [b] & Adrianna Ianora [a]

[a] Stazione Zoologica Anton Dohrn, Naples, Italy

[b] Istituto Superiore per la Protezione e Ricerca Ambientale, ISPRA-STS, Livorno, Italy

[c] Institute of Marine Biology, National Taiwan Ocean University, Keelung, Taiwan

[d] Institute of Biomedical Engineering, National Taiwan University, Taipei, Taiwan

[e] Molecular Imaging Center, National Taiwan University, Taipei, Taiwan

[f] Department of Electrical Engineering, National Taiwan University, Taipei, Taiwan

Available online: 01 Nov 2011

To cite this article: Isabella Buttino, David Pellegrini, Giovanna Romano, Jiang-Shiou Hwang, Tzu-Ming Liu, Davide Sartori, Chi-Kuang Sun, Simona Macchia & Adrianna Ianora (2011): Study of apoptosis induction using fluorescent and higher harmonic generation microscopy techniques in Acartia tonsa nauplii exposed to chronic concentrations of nickel, Chemistry and Ecology, 27:sup2, 97-104

To link to this article: http://dx.doi.org/10.1080/02757540.2011.625944

PLEASE SCROLL DOWN FOR ARTICLE

Full terms and conditions of use: http://www.tandfonline.com/page/terms-and-conditions

This article may be used for research, teaching, and private study purposes. Any substantial or systematic reproduction, redistribution, reselling, loan, sub-licensing, systematic supply, or distribution in any form to anyone is expressly forbidden.

The publisher does not give any warranty express or implied or make any representation that the contents will be complete or accurate or up to date. The accuracy of any instructions, formulae, and drug doses should be independently verified with primary sources. The publisher shall not be liable for any loss, actions, claims, proceedings, demand, or costs or damages whatsoever or howsoever caused arising directly or indirectly in connection with or arising out of the use of this material.

Downloaded by [Stazione Zoologica], [Giovanna Romano] at 10:47 22 March 2012

Chemistry and Ecology
Vol. 27, No. S2, December 2011, 97–104

Downloaded by [Stazione Zoologica], [Giovanna Romano] at 10:47 22 March 2012

Study of apoptosis induction using fluorescent and higher harmonic generation microscopy techniques in *Acartia tonsa* nauplii exposed to chronic concentrations of nickel

Isabella Buttino[a,b]*, David Pellegrini[b], Giovanna Romano[a], Jiang-Shiou Hwang[c], Tzu-Ming Liu[d,e], Davide Sartori[b], Chi-Kuang Sun[e,f], Simona Macchia[b] and Adrianna Ianora[a]

[a]*Stazione Zoologica Anton Dohrn, Naples, Italy;* [b]*Istituto Superiore per la Protezione e Ricerca Ambientale, ISPRA-STS, Livorno, Italy;* [c]*Institute of Marine Biology, National Taiwan Ocean University, Keelung, Taiwan;* [d]*Institute of Biomedical Engineering, National Taiwan University, Taipei, Taiwan;* [e]*Molecular Imaging Center, National Taiwan University, Taipei, Taiwan;* [f]*Department of Electrical Engineering, National Taiwan University, Taipei, Taiwan*

(*Received 14 June 2011; final version recived 16 September 2011*)

In this study, we applied different fluorescent techniques to analyse the induction of apoptosis in the copepod *Acartia tonsa* nauplii exposed to low concentrations of nickel chloride ($NiCl_2$). Newly hatched and later naupliar stages were exposed to increasing concentrations of $NiCl_2$ (0.016, 0.025 and 0.063 $mg \cdot L^{-1}$) for 7 days and then stained with annexin V–FITC, a vital fluorescent probe commonly used to visualise apoptotic cells in live samples. Nauplii were also stained with TUNEL, a non-vital fluorescent probe used to detect apoptosis in fixed copepods. Moreover, we used for the first time, two-photon fluorescence (2PF) microscopy and higher harmonic generation microscopy (second SHG and third THG harmonic generation) to study apoptosis induction in *A. tonsa* nauplii without the use of fluorescent probes. 2PF and THG intensity increased in samples exposed to higher Ni concentrations, with respect to the control, whereas SHG signals were similar in all treated samples and visualised muscles. Future perspectives on the use of these new technologies to reveal apoptosis are discussed.

Keywords: confocal microscopy; two-photon fluorescence microscopy; heavy metals; ecotoxicology

1. Introduction

Apoptosis or programmed cell death is determined by precise genetic and molecular signals [1], triggered by physiological events such as metamorphosis in amphibians and fetal development in mammals, or by external factors such as exposure to toxic compounds or environmental stress [2]. Apoptotic processes induce certain peculiar characteristic events leading to morphological and biochemical alterations [3]. Among the morphological modifications are cell shrinkage, nuclear blebbing and condensation, with formation of membrane-bound vesicles called apoptotic bodies. Alteration of DNA, with consequent fragmentation and degradation, and the inversion of

*Corresponding author. Email: isabella.buttino@isprambiente.it

ISSN 0275-7540 print/ISSN 1029-0370 online
© 2011 Taylor & Francis
http://dx.doi.org/10.1080/02757540.2011.625944
http://www.tandfonline.com

plasma membrane permeability, coupled with the exposure of phosphatidyl serine residues to the cell surface, are other morphological events common to apoptosis in many biological systems. Moreover, specific biochemical and molecular signals, such as activation of cysteine-dependent proteases (caspases in mammals or cysteine protease homologues in non mammals) and/or release of cytochrome *c* from the mitochondrial intermembrane space to the cytosol, are part of a regulatory network consisting of pro- and anti-apoptotic factors [4]. By contrast, necrosis generally occurs when cells are exposed to extreme conditions and results in damage to the plasma membrane, with an impairment of the cell's ability to maintain homeostasis. An influx of water and extracellular ions leads to cell swelling and lysis with the release of cytoplasmic contents into the extracellular fluid. Generally, necrosis follows apoptotis in a temporal sequence depending on the intensity of the initial insult or the prevalence of one process over another [5,6]. The complexity of events inducing cellular suicide in pluricellular organisms is under continuous study, especially in humans where the characteristics of cell death are considered diagnostic.

Biochemical mechanisms of apoptosis have recently been studied in crustaceans [7], but whether apoptosis is mainly regulated, as in other arthropods (involving killer proteins as for *Drosophila melanogaster*), or rather is controlled by pro- and anti- apoptotic proteins (Bcl-2 family proteins), as occurs in vertebrates, needs to be confirmed.

From a morphological point of view, observation of cells in light microscopy, commonly used as a first screen to differentiate between apoptosis and necrosis, is not possible in crustaceans, due to the presence of a thick chitinous wall surrounding embryos, nauplii and adults. Therefore, specific fluorescent probes are the only tool to visualise apoptosis in copepods. A recent review [8] reported progress in the detection of apoptosis in marine zooplankton and described different fluorescent techniques used to visualise and differentiate apoptosis from necrosis in whole-mount copepods.

Here, we report progress in the detection of apoptosis in the marine zooplanktonic copepod *Acartia tonsa* after exposure to nickel chloride ($NiCl_2$), In addition to being ubiquitous in the biosphere and as trace element in water [9], Ni is also widely used in industry or is produced from sources such as mining, extraction and refining, and food processing. In natural waters, Ni concentrations range between 1 and 75 $\mu g \cdot L^{-1}$ [10]. It is known that Ni is toxic for humans at high concentrations, inducing nephrotoxicity, hepatotoxicity and teratogenesis [11,12], and it has been classified as carcinogenic [13]. In mammals, Ni generates reactive oxygen species [12] leading to an increase in lipid peroxidation and a loss of membrane integrity [14,15]. In aquatic environments, Ni acts as a respiratory toxicant in the cladoceran *Daphina magna* after chronic exposure [16]. Oxidative damaging effects on metallothionein synthesis have been found in the harpacticoid copepod *Tigriopus japonicus* chronically exposed to Ni [16].

With this study, we propose different microscopy techniques to identify apoptosis in copepods exposed to low concentrations of $NiCl_2$. We compare classical methods using fluorescent probes such as annexin V or TUNEL staining, with new, promising microscopy techniques such as second and third harmonic generation microscopy (SHG, THG), which can reveal apoptotic tissues in whole-mount copepods without any fluorescent probes.

2. Materials and methods

Almost 20 mature adult *A. tonsa* pairs, from a 50-L aquarium rearing tank, were sorted and incubated in a 1000 mL beaker filled with 500 mL 0.45-μm mesh net filtered seawater (Millipore 90 mm Holder YY 3009000) containing a mixture of the phytoplanktonic algae *Isochrysis galbana*, *Tetraselmis suecica* and *Rhinomonas reticulate* at a final concentration of 10^4 cells$\cdot$mL^{-1}. After 24 h, newly spawned *A. tonsa* eggs were collected from the bottom of the beaker and incubated

Downloaded by [Stazione Zoologica], [Giovanna Romano] at 10:47 22 March 2012

individually for different lengths of time (48 h, 7 days) in 2.5-mL multiwell plates containing two of these algae (*I. galbana* and *T. suecica*) provided at the above concentrations. Groups of 24 newly spawned eggs were incubated in 0.016, 0.025 and 0.063 mg·L^{-1} $NiCl_2 \times 6H_2O$ (Sigma-Aldrich, Milan, Italy). Another control group of 24 embryos was incubated in 0.45-μm filtered seawater without toxicants. Nickel solutions and food concentrations were renewed after 48 h and after 5 days.

After 7 days, the percentage of surviving nauplii was assessed. Only live nauplii were collected and incubated for 20 min with annexin V–fluorescein isothiocyanate (FITC) (Alexis Biochemicals, Switzerland) at a final concentration of 40 μl·mL^{-1}. Annexin V–FITC is a vital fluorescent probe able to bind phosphatidyl serine residues that are externalised on the plasma membrane surface during the early phases of apoptosis [17,18]. Therefore, cells undergoing apoptosis show positive green fluorescence. Nauplii were maintained in the dark and at a temperature of 20 °C and then fixed in 4% formaldehyde dissolved in seawater. They were then observed using a confocal inverted microscope Zeiss-LSM 510 with 20× to 40× objectives, and the percentage of positively stained nauplii was assessed.

Fixed nauplii were treated as reported in Buttino et al. [19] for terminal deoxynucleotidyl transferase (TdT)-mediated dUTP nick end labelling (TUNEL) staining, and observed using the confocal microscope. The same samples were also incubated with Hoechst 33342 to stain DNA, as reported in Buttino et al. [20]. For SHG and THG microscopy, 7-day-old *A. tonsa* nauplii were fixed in 4% formaldehyde for 2–4 weeks, rinsed in phosphate-buffered saline and observed with the SHG, THG and 2PF microscopy systems at the Molecular Imaging Center, National Taiwan University, Taiwan.

The nonlinear microscopy systems were excited by a home-built femtosecond Cr : forsterite laser operating around 1230 nm, which is less invasive and has deeper penetration than commonly used Ti : sapphire lasers (700–100 nm) [21,22]. The corresponding SHG and THG signals fall within the visible wavelength range, making it compatible with microscope optics. The scanned laser beam was guided to an upright microscope and focused by a 60× water immersion objective with NA = 1.2. Focusing on biological samples, the SHG contrast can reveal the distribution of structural proteins like collagens, microtubules, neurons and muscle fibres. The THG contrast can reveal the discontinuity of the refractive index by which the morphology of cells membranes, lipid vesicles, pigments and elastic fibres can be imaged. The 2PF contrast is mainly due to bilins, porphyrins, chlorophylls and their metabolites.

Because apoptosis results in apoptotic bodies enclosed by lipid membranes, such bodies can be detected by THG. Moreover, apoptosis also causes morphological abnormalities, and internal changes in copepods can be tomographically observed with SHG and THG sectioning images. These contrast mechanisms characteristic of 2PF, SHG and THG microscopy allow the imaging system to correlate intensity changes with apoptotic events.

3. Results

$NiCl_2$ was below lethal concentrations inducing 50% mortality in *A. tonsa* hatched nauplii (LC_{50}) after 48 h (0.19 to 0.25 mg·L^{-1}) and 7 days (0.038 to 0.063 mg·L^{-1}) (unpublished data). In our incubation experiments, the percentage of live nauplii after 7 days was >70% in controls, 35% in 0.025 mg·L^{-1} Ni and only 4% in 0.063 mg·L^{-1} Ni.

Figure 1 shows a 3D reconstruction of an *A. tonsa* nauplius incubated for 7 days in 0.025 mg·L^{-1} $NiCl_2$ (Figure 1a, b), and the corresponding control (Figure 1c), both of which were stained with the vital fluorescent probe annexin V–FITC and observed using the confocal laser scanning microscope. Two positively stained structures (green) are visible in the region corresponding to

Downloaded by [Stazione Zoologica], [Giovanna Romano] at 10:47 22 March 2012

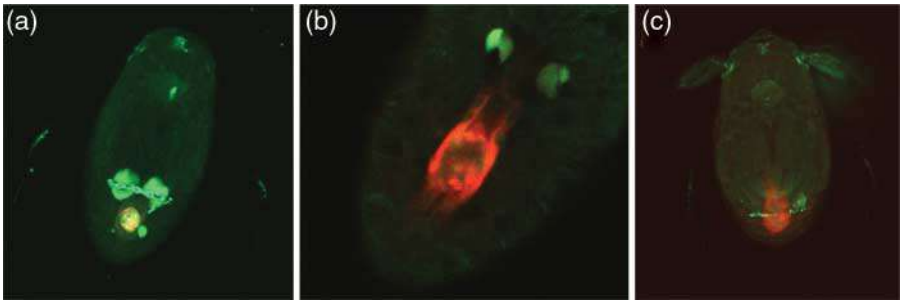

Figure 1. Three-dimensional reconstruction of *Acartia tonsa* nauplius stained with annexin V–FITC (green) and observed using a confocal laser scanning microscope. (a) Nauplius exposed to 0.025 mg·L^{-1} $NiCl_2$ for 7 days: two large structures and one small structure are positively stained with annexin (green) in the posterior part of the nauplius, while in the central and posterior part of the body, a terminal part of the digestive apparatus is stained both green and red. The red colour is due to chlorophyll autofluorescence. (b) Close-up of the posterior body of a nauplius exposed for 7 days to 0.025 mg·L^{-1} $NiCl_2$, two structures are positively stained with annexin lateral to the digestive organ which contains chlorophyll (red). (c) Control nauplius. The brightness has been increased to show diffuse and nonspecific green fluorescence. Chlorphyll (in red) is visible at the bottom of the digestive apparatus.

Downloaded by [Stazione Zoologica], [Giovanna Romano] at 10:47 22 March 2012

the beginning of the genital system (Figure 1a). A small green structure is also visible in the lower part of the body, while both red and green structures are visible in the central and posterior parts of the body. The red colour is caused by chlorophyll autofluorescence probably due to recent feeding of the animals.

Figure 1b shows a higher magnification of a nauplius incubated in 0.025 mg·L^{-1} $NiCl_2$; red fluorescence is due to chlorophyll inside the posterior digestive apparatus. Again, two structures are positively stained with annexin, laterally to the gut. Figure 1c is a control nauplius showing only the red fluorescence in the posterior part of the digestive apparatus, due to chlorophyll autofluorescence. Image brightness has been increased to highlight the very low intensity of green fluorescence. Of the live nauplii exposed to 0.025 mg·L^{-1} $NiCl_2$, >66% were positively stained with annexin V, whereas 85% showed TUNEL positivity, in contrast to controls with 30% positivity with both probes, probably due to natural apoptosis caused by imminent metamorphosis. Only 2% of nauplii exposed to 0.063 mg·L^{-1} $NiCl_2$ survived and these were not stained with TUNEL or annexin V because of the small sample size.

Fixed nauplii incubated with 0.025 mg·L^{-1} $NiCl_2$ were stained with TUNEL; when cells enter apoptosis, lysis of endonucleases triggers the cleavage of DNA into specific oligonucleosomic fragments that can be labelled on the free radical 3′OH by a fluorescent marker dUTP using TdT [23,24]. Figure 2a is a 3D reconstruction of a nauplius incubated in $NiCl_2$ and observed with three different excitation lights to visualise TUNEL (green), Hoechst (violet) and chlorophyll (red). Many nuclei appeared positively stained with TUNEL; in some areas nuclei were so bright that they covered other fluorescence (i.e. violet and red). Figure 2b is a 3D reconstruction of a control nauplius; the whole body is stained with Hoechst (violet). Green fluorescence due to TUNEL is only visible at the top of the legs, probably indicating natural apoptosis occurring during development.

Harmonic generation microscopy (HGM) is a laser scanning nonlinear microscopy technique that acquires optical sectioning images with submicron spatial resolution. The intensity of two photon red fluorescence images (Figure 3e, f, g, h) was represented with a flame-like colour scale and the fluorescence level of the control was amplified 100× to show greater detail (Figure 3e). Nauplii exposed to increasing concentrations of $NiCl_2$ (0.016, 0.025 and 0.063 mg·L^{-1}) showed an increased 2PF fluorescence in the region corresponding to the digestive apparatus (arrows in Figure 3f, g, h), compared to the control. Similarly, THG signals (M = magenta) increased in nauplii exposed to $NiCl_2$ at 0.063 mg·L^{-1}, in contrast to a weak fluorescence of control nauplii

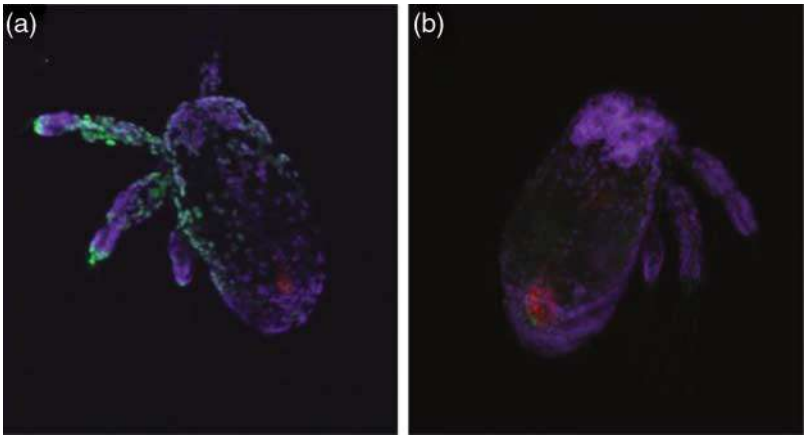

Figure 2. Three-dimensional reconstruction of *Acartia tonsa* nauplius stained with Hoechst 33342 (violet) and TUNEL (green) and observed using the confocal laser scanning microscope. (a) Nauplius exposed to 0.025 mg·L^{-1} $NiCl_2$ for 7 days was positively stained with TUNEL. Red autofluorescence is visible at the bottom of the digestive apparatus, due to chlorophyll (red). (b) Control nauplius.

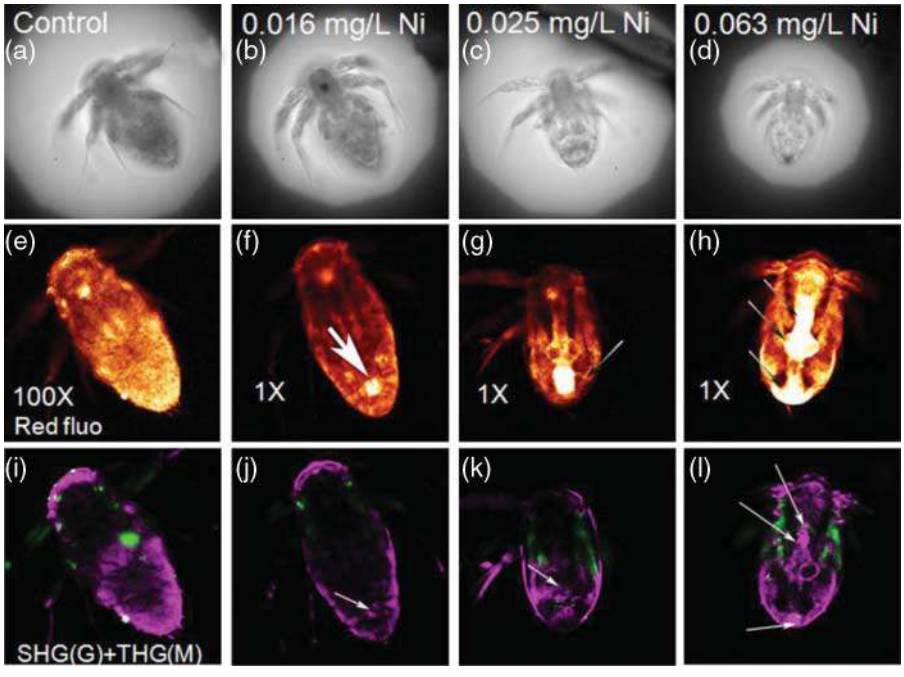

Figure 3. *Acartia tonsa* nauplius observed with light microscopy (first row), two photon fluorescence (2PF) microscopy (second row), and second (SHG) and third (THG) harmonic generation microscopy (third row). Control nauplius shows a weak autofluorescence when observed with 2PF; fluorescence output was increased 100× to visualize the structures (e). Nauplius incubated in 0.016, 0.025 and 0.063 mg·L^{-1} $NiCl_2$ for 7 days show an increased 2PF fluorescence in the region corresponding to the digestive apparatus (arrows) (f, g, h). SHG microscopy (green) shows muscles; the magenta colour represents the THG microscopy signals which increased in nauplii exposed to the highest $NiCl_2$ concentrations, in the same regions as for 2PF fluorescence (see arrows) (j, k, l). In the combined images, the strong fluorescence in nauplii exposed to 0.063 mg·L^{-1} $NiCl_2$ is evident in the inner part of the gut and in the posterior part of the body (arrows) (l).

Downloaded by [Stazione Zoologica], [Giovanna Romano] at 10:47 22 March 2012

(Figure 3i) and to those exposed to lower nickel concentrations (arrows in Figure 3j, k, l). The THG signals, evident in the inner part of the gut, could be due to the production of apoptosis-related vesicles. By contrast, SHG microscopy (G = green) revealed muscles resulting in a fluorescent signal similar to those recorded for all treatments.

4. Discussion

The use of copepods for ecotoxicological tests is not new [25]. In our study, the calanoid copepod *A. tonsa* appears to be very sensitive to Ni exposure; 0.025 $mg \cdot L^{-1}$ $NiCl_2$ strongly reduced naupliar viability to only 35% after 7 days exposure, with 85% of the surviving nauplii marked positively for apoptotis as revealed with TUNEL staining. This suggests that only 6% of the naupliar population would be recruited to adulthood in 25 $\mu g \cdot L^{-1}$ $NiCl_2$-polluted waters, a Ni concentration found in many estuaries and rivers [10].

The identification of active programmed cell death (apoptosis) in copepods is relatively new [8,26–28]. Among the classical non vital fluorescent probes used to detect apoptosis, the *in situ* nick-end labelling of DNA strand breaks (TUNEL) has been successfully used to stain copepod embryos, nauplii and adults [17,26,28]. Moreover, vital fluorescent probes such as fluorescein diacetate or its homologous Sytox green and 7-aminoactinomycin have been used to discriminate between live or dead cells in copepods. These latter stains do not differentiate between necrosis and apoptosis even though their application may be useful to rapidly detect copepod embryo viability without having to wait for eggs to hatch [18,29]. Poulet et al. [27] used a double-labelling method to stain *Calanus helgolandicus* nauplii with annexin V–FITC coupled with propidium iodide, to differentiate between apoptotic and necrotic cells in live copepod nauplii. However, use of fluorescent probes in copepods and more generally in crustaceans is difficult, due to their chitinous wall which needs to be permeabilised [8].

Our results obtained with annexin V reveal two large structures in the posterior part of the body, in the region corresponding to the gonad buds. These structures are not visible in samples stained with TUNEL, probably because of the different staining protocols. In fact, annexin V is a viable fluorescent probe and the protocol consists of the incubation of live animals in a solution. In this manner, live copepods actively ingest the probe which stains the internal organs. By contrast, the permeability of TUNEL is limited to sub-superficial body cells because the animals are fixed and then stained. Hence, the two staining methodologies (TUNEL versus annexin V) can, at times, lead to different results.

Our data obtained with non-invasive SHG and THG microscopy show that these techniques, applied in copepods for the first time, can be useful to detect apoptosis in both live and fixed copepods, without any preliminary treatment or fluorescent probes. Therefore, both techniques may represent an innovative approach to study copepod toxicology. THG microscopy can depict the boundaries of cells or the distribution of vesicles. Its signal intensity is determined by the contrast of the refractive index and a material-related constant [24,30,31]. SHG microscopy has been shown to reveal the distribution and orientation of structured proteins such as collagens or microtubules [24]. In a recent article, strong THG signals were found associated to the apoptotic bodies in the hind brain of zebrafish. The same apoptotic bodies were positively stained with acridine orange and detected by 2PF [32,33]. In our experiments 2PF increased in nauplii exposed to higher concentrations of heavy metals. The signals detected are in the same regions that are positively stained with annexin V. Moreover, THG fluorescence increased in nauplii exposed to higher concentrations of Ni, as also demonstrated in zebrafish embryos, suggesting that this method is able to visualise apoptosis induction. If this hypothesis is confirmed by further studies, this noninvasive technique can be used to predict naupliar mortality in live organisms without using any fluorescent probes.

Downloaded by [Stazione Zoologica], [Giovanna Romano] at 10:47 22 March 2012

Interestingly, the three different approaches used in this study revealed different sensitive regions: TUNEL was able to differentiate cells and their fluorescence in apopototic regions including small spots, annexin-V stained organs with a particular affinity to lipid structures, such as the gonadic buds, whereas 2PF microscopy was able to detect apoptotic tissues with a diffuse fluorescence, including the autofluorescence due to chlorophyll emission. In general, the image quality obtained using SHG and THG fluorescence microscopy was more detailed, with THG able to reveal very fine structures inside the copepod gut. Whether these signals are, in fact, due to apopototis must be further investigated, possibly using different molecular approaches.

Our preliminary results open up new and unexpected possibilities for predicting embryo and naupliar viability in zooplanktonic communities using fluorescent probes and new imaging techniques such as 2PF and THG microscopy in addition to confocal microscopy. Because some apparently normal copepod embryos or deformed nauplii are positive for apoptotic markers such as annexin and TUNEL, the possibility to predict egg, naupliar and adult mortality appears realistic and this approach should be considered in future ecotoxicology studies.

Downloaded by [Stazione Zoologica], [Giovanna Romano] at 10:47 22 March 2012

Acknowledgements

This research has partially been supported by the National Health Research Institute of Taiwan, through grant NHRI-EX98-9201EI and grant NHRI-EX100-993EI, by the National Science Council of Taiwan through grant NSC 98-2112-M-002-022; by the bilateral project SZN-NSC grant NSC 99-2923-B-019-001-MY2, and by ISPRA. Special thanks are due to Mario Di Pinto and Dr. Francesco Esposito for their support.

References

[1] G.T. Williams, *Programmed cell death: Apoptosis and oncogenesis*, Cell. 65 (1991), pp. 1097–1098.
[2] R.P. Rastogi, R. Richa, and R.P. Sinha, *Apoptosis: Molecular mechanisms and pathogenicity*, EXCLI J. 8 (2009), pp. 155–181.
[3] D.V. Krysko, T.V. Berghe, K. D'Herde, and P. Vandenabeele, *Apoptosis and necrosis: Detection, discrimination and phagocytosis*, Methods. 44 (2008), pp. 205–221.
[4] J. Yuan, S. Shaham, S. Ledoux, H.M. Ellis, and R.H. Horvitz, *The* C. elegans *cell death gene* ced-3 *encodes a protein similar to mammalian interleukin-1β-converting enzym*e, Cell. 75 (1993), pp. 641–652.
[5] E.J. Behilarz, C.E. Williams, M. Dragunow, E.S. Sirimanne, and P.D. Gluckman, *Mechanisms of delayed cell death following hypoxic–ischemic injury in the immature rat: Evidence for apoptosis during selective neuronal loss*, Mol. Brain Res. 29 (1995), pp. 1–14.
[6] M. Leist and P. Nicotera, *The shape of cell death*, Biochem. Biophys. Res. Commun. 236 (1997), pp. 1–9.
[7] M.A. Menze, G. Fortner, S. Nag, and S.C. Hang, *Mechanisms of apoptosis in Crustacea: What conditions induce versus suppress cell death?* Apoptosis 15 (2010), pp. 293–312.
[8] I. Buttino, J.-S. Hwang, C.-K. Sun, C.-T. Hsieh, T.-M. Liu, D. Pellegrini, A. Ianora, D. Sartori, G. Romano, S.-H. Cheng, and A. Miralto, *Apoptosis to predict copepod mortality: State of the art and future perspectives*, Hydrobiologia 666 (2011), pp. 257–264.
[9] S. Woo, S. Yum, H.S. Park, T.K. Lee, and J.C. Ryu, *Effects of heavy metals on atioxidatns and stress-responsive gene expression in Javanese medaka* (Oryzias javanicus), Comp. Biochem. Physiol. C 149 (2009), pp. 289–299.
[10] R. Eisler, *Nickel hazards to fish, wildilife, and invertebtrates: A synoptic review*, US Geological Survey, Biological Resources Division, Biological Science Report, 1998, pp. 1998–2001.
[11] A. Mas, D. Holt, and M. Webb, *The acute toxicity and teratogenicitiy of nickel in pregnant rats*, Toxicology 35 (1985), pp. 47–57.
[12] K. Vijayavel, S. Gopalakrishnan, R. Thiagarajan, and H. Thilagam, *Immunotoxic effects of nickel in the mud crab* Scylla serrata, Fish Shellfish Immun. 26 (2009), pp. 133–139.
[13] L.T. Haber, L. Erdreicht, G.L. Diamond, A.M. Maier, R. Ratney, Q. Zhao, and M.L. Dourson, *Hazard identification and dose response of inhaled nichel-soluble salts*, Regul. Toxicol. Pharmacol. 31 (2000), pp. 210–230.
[14] M.D. Ptashynski, R.M. Pedlar, R.E. Evans, K.G. Wautier, C.B. Baron, and J.F. Klaverkamp, *Accumulation, distribution, and toxicology of dietary nickel in lake whitefish* (Coregonus clupeaformis) *and lake trout* (Salvelinus namaycush), Comp. Biochem. Physiol. C 130 (2001), pp. 145–162.
[15] M.D. Ptashynski, R.M. Pedlar, R.E. Evans, C.B. Baron, and J.F. Klaverkamp, *Toxicology of dietary nickel in lake whitefish* (Coregonus clupeaformis), Aquat. Toxicol. 58 (2002), pp. 229–247.
[16] E.F. Pane, C. Smith, J. McGeer, and C.M. Wood, *Mechanisms of acute and chronic waterborne nickel toxicity in the freshwater cladoceran,* Daphnia magna, Environ. Sci. Technol. 37 (2003), pp. 4382–4389.

[17] J.P. Aubry, A. Blaeckem, S. Lecoanet-Henchoz, P. Jeannin, N. Herbault, G. Caron, V. Moine, and J.Y. Bonnefoy, *Annexin-V used for measuring apoptosis in the early events of cellular cytotoxicity*, Cytometry 37 (1999), pp. 197–204.

[18] E. Bossy-Wetzel and D.R. Green, *Detection of apoptosis by annexin V labeling*, in *Methods in Enzymology*, J.C. Reed, ed., Academic Press, San Diego, 2000, pp. 15–18.

[19] I. Buttino, G. De Rosa, Y. Carotenuto, M. Mazzela, A. Ianora, F. Esposito, V. Vitiello, F. Quaglia, M.I. La Rotonda, and A. Miralto, *Aldehyde-encapsulating liposomes impair marine grazer survivorship*, J. Exp. Biol. 211 (2008), 1426–1433.

[20] I. Buttino, A. Ianora, Y. Carotenuto, and A. Miralto, *Use of the confocal laser scanning microscope in studies on the developmental biology of marine crustaceans*, Microsc. Res. Tech. 60 (2003), pp. 458–464.

[21] I.-H. Chen, T.-M. Liu, P.-C. Cheng, C.-K. Sun, and B.-L. Lin, *Multimodal nonlinear spectral microscopy based on a femtosecond Cr:forsterite laser*, Opt. Lett. 26 (2001), pp. 1909–1911.

[22] C.-K Sun, S.-W. Chu, S.-Y. Chen, T.-H. Tsai, T.-M. Liu, C-H. Lin, and H.-J. Tsai, *Higher harmonic generation microscopy for developmental biology*, J. Struct. Biol. 147 (2004), pp. 19–30.

[23] S. Iseki and T. Mori, *Histochemical detection of DNA strand scissions in mammalian cells by in situ nick translation*, Cell Biol. Int. Report 9 (1985), pp. 471–477.

[24] S.H. Kaufmann, P.W. Mesner, K. Samejima, S. Toné, and W.C. Earnshaw, *Detection of DNA cleavage in apoptotic cells*, in *Methods in Enzymology, Apoptosis*, J.C. Reed, ed., Academic press, San Diego, 2000, pp. 3–11.

[25] S. Raisuddin, K.W.H. Kwok, K.M.Y. Leung, D. Schlenk, and J-S Lee, *The copepod* Tigriopus*: a promising marine model organism for ecotoxicology and environmental genomics*, Aquat. Toxicol. 83 (2007), pp. 161–173.

[26] G. Romano, G.L. Russo, I. Buttino, A. Ianora, and A. Miralto, *A marine diatom derived aldehyde induces apoptosis in copepod and sea urchin embryos*, J. Exp. Biol. 206 (2003), pp. 3487–3494.

[27] S.A Poulet, M. Richer de Forges, A. Cueff, and J.F. Lennon, *Double-labelling methods used to diagnose apoptotic and necrotic cell degradations in copepod nauplii*, Mar. Biol. 143 (2003), pp. 889–895.

[28] A. Ianora, A. Miralto, S.A. Poulet, Y. Carotenuto, I. Buttino, G. Romano, R. Casotti, G. Pohnert, T. Wichard, L. Colucci-D'Amato, G. Terrazzano, and V. Smetacek, *Aldehyde suppression of copepod recruitment in blooms of a ubiquitous planktonic diatom*, Nature 429 (2004), pp. 403–407.

[29] I. Buttino, M. do Espirito Santo, A. Ianora, and A. Miralto, *Rapid assessment of copepod embryo viability using fluorescent probes*, Mar. Biol. 145 (2004), pp. 393–399.

[30] S.-W. Chu, S.-Y. Chen, T.-H. Tsai and T.-M. Liu, C.-Y. Lin, H.-J. Tsai, and C.-K. Sun, *In vivo developmental biology study using non invasive multi-harmonic generation microscopy*, Opt. Expr. 11 (2003), pp. 3093–3099.

[31] T.-M. Liu, Y.-W. Lee, C.-F. Chang, S.-C. Yeh, C.-H. Wang, S.-W. Chu, and C.-K. Sun, *Imaging polyhedral inclusion bodies of nuclear polyhedrosis viruses with second harmonic generation microscopy*, Opt. Expr. 16 (2008), pp. 5602–5608.

[32] S.-Y. Chen, C.-S. Hsieh, S.-W. Chu, C.-H. Lin, C.-Y. Ko, Y.- C. Chen, H.-J. Tsai, C.-H. Hu, and C.-K. Sun, *Noninvasive harmonics optical microscopy for long-term observation of embryonic nervous system development in vivo*, J. Biomed. Opt. 11 (2006), pp. 054022 1–8.

[33] C.-S. Hsieh, C.-Y. Ko, S.-Y. Chen, T.-M. Liu, J.-S. Wu, C.-H. Hu, and C.-K. Sun, *In vivo long-term continuous observation of gene expression in zebrafish embryo nerve systems by using harmonic generation microscopy and morphant technology*, J. Biomed. Opt. 13 (2008), pp. 064041 1-7.

Downloaded by [Stazione Zoologica], [Giovanna Romano] at 10:47 22 March 2012

ARTICLE IN PRESS

Ecotoxicology and Environmental Safety ∎ (∎∎∎∎) ∎∎∎–∎∎∎

Contents lists available at ScienceDirect

Ecotoxicology and Environmental Safety

journal homepage: www.elsevier.com/locate/ecoenv

Detection of malformations in sea urchin plutei exposed to mercuric chloride using different fluorescent techniques

Isabella Buttino [a,*], Jiang-Shiou Hwang [b], Giovanna Romano [c], Chi-Kuang Sun [d], Tzu-Ming Liu [d], David Pellegrini [a], Andrea Gaion [a], Davide Sartori [a,e]

[a] Istituto Superiore per la Protezione e la Ricerca Ambientale, ISPRA_ STS-Livorno, Piazzale dei marmi 12, 57123, Italy
[b] Institute of Marine Biology, National Taiwan Ocean University, Keelung 20224, Taiwan
[c] Stazione Zoologica Anton Dohrn, Villa Comunale, 80121 Napoli, Italy
[d] Graduate Institute of Photonics and Optoelectronics and Department of Electrical Engineering, National Taiwan University, Taipei 10617, Taiwan
[e] CAISIAL, Academic Centre for Innovation and Development in the Food Industry, 80055 Portici (Na), Italy

ARTICLE INFO

Article history:
Received 25 March 2015
Received in revised form
22 July 2015
Accepted 23 July 2015

Keywords:
Harmonic generation microscopy
Two-photon microscopy
Confocal microscopy
Skeletal rod
Apoptosis

ABSTRACT

Embryos of Mediterranean sea urchin *Paracentrotus lividus* and subtropical *Echinometra mathaei* were exposed to 5,10, 15 and 20 μg L^{-1} and to 1, 2, 3 and 4 μg L^{-1} mercuric chloride ($HgCl_2$), respectively. The effective concentration (EC_{50}) inducing malformation in 50% of 4-arm pluteus stage (P4) was 16.14 μg L^{-1} for *P. lividus* and 2.41 μg L^{-1} for *E. mathaei.* Two-photon (TP), second (SHG) and third harmonic generation (THG) microscopy techniques, TUNEL staining, propidium iodide (PI) and Hoechst 33342 probes were used to detect light signals or to stain apoptotic and necrotic cells in fixed and alive plutei. Signals were detected differently in the two species: TP fluorescence, commonly associated with apoptotic cells, did not increase with increasing $HgCl_2$ concentrations in *P. lividus* and in fact, the TUNEL did not reveal induction of apoptosis. PI fluorescence increased in *P. lividus* in a dose-dependent manner, suggesting a loss of cell permeability. In *E. mathaei* plutei TP fluorescence increased at increasing $HgCl_2$ concentrations. THG microscopy revealed skeletal rods in both species. Different fluorescent techniques, used in this study, are proposed as early-warning systems to visualize malformations and physiological responses in sea urchin plutei.

© 2015 Elsevier Inc. All rights reserved.

1. Introduction

Mercury (Hg) is one of the most toxic and persistent elements in the environment, deriving both from natural and anthropogenic sources. This metal can enter the ecosystem through the breakdown of minerals, although significant amounts originate as a result of human activities and discharges from metal smelting, coal-burning power plants, municipal waste incineration, coal and other fossil fuel combustion (Satoh, 2000). In aquatic ecosystems, mercury is present mainly in inorganic elemental (Hg°, Hg^{2+}) or organic methylated form and its bioavailability is influenced by physical-chemical factors such as pH, dissolved organic carbon or temperature of the water (Driscoll et al., 1994). Between the two ionized states, the bivalent form is more stable and more frequently found, and can bond with chloride ($HgCl_2$) in salt water. Mercury concentrations in aquatic environments are highly variable, ranging from very low concentrations in open ocean to concentrations as high as 16 μg L^{-1} in very polluted areas close to industrial discharges (Plaschke et al., 1997; De Riso et al., 2000).

Toxic effects of mercury have been widely studied on fish (Driscoll et al., 1994; Devil, 2006; Sinaie et al., 2010), due to their relevance in human consumption. On the other hand, the impact of mercury on marine environment has been investigated using animal models, belonging to different trophic levels, and taking into consideration various end-points such as behavior, reproduction, embryo and larval mortality or morbidity (Fernandez and Beiras, 2001). In ecotoxicology studies, echinoderms are considered excellent bioindicators due to their dual role in pelagic and benthic compartments (Bellas et al., 2005; Salamanca et al., 2009). Furthermore, echinoderm gametes are easy to collect and fertilization and larval development are well known (Pagano et al., 1986). Studies on the toxicity of mercury on sea urchin species have mainly been focused on the evaluation of the effective concentration (EC_{50}) inducing 50% embryo and larval mortality, as well as deformities, or sperm fertilization inhibition (Fernandez and Beiras, 2001; Warnau et al., 1996).

In this study we analyzed the effect of increasing

* Corresponding author.
E-mail address: isabella.buttino@isprambiente.it (I. Buttino).

http://dx.doi.org/10.1016/j.ecoenv.2015.07.027
0147-6513/© 2015 Elsevier Inc. All rights reserved.

Please cite this article as: Buttino, I., et al., Detection of malformations in sea urchin plutei exposed to mercuric chloride using different fluorescent techniques. Ecotoxicol. Environ. Saf. (2015), http://dx.doi.org/10.1016/j.ecoenv.2015.07.027

concentrations of mercuric chloride ($HgCl_2$) on the larval development of two different sea urchin species: *Echinometra mathaei*, the most ubiquitous and abundant shallow-water sea urchin in tropical and subtropical regions, and *Paracentrotus lividus. E. mathaei* is commonly found at depth up to 130 mt and in a temperature range between 24 and 27 °C. It has a flexible behavior and diet, high reproduction and recruitment rates and low resource requirements (McClanahan and Muthiga, 2007). Although genetic, morphological, biochemical, ecological and reproductive studies have been carried out on *Echinometra* species, few data are available on its sensitivity to organic and inorganic contaminants (Kominami and Takata, 2003; Mahdavi et al., 2008; Sadripour et al., 2013). *Paracentrotus lividus* is common in the temperate Mediterranean areas, with winter water temperatures of around 11 to 12 °C and summer temperatures ranging from 18 to 25 °C (Boudouresque and Verlaque, 2007). This species has largely been used as a model animal to study the impact of toxicants (Bellas et al., 2008; Pinsino et al., 2010; Gaion et al., 2013) or natural toxins (Romano et al., 2011, 2003, 2010).

Here we evaluated the effective concentration of $HgCl_2$ inducing malformations in the 4-arm plutei stage (P4) in both temperate and subtropical species. Furthermore, harmonic generation (HGM) and two-photon (TP) microscopy techniques were used to verify whether fluorescence signals could be associated with chemical stress. Harmonic generation and TP microscope are the least invasive laser scanning techniques enabling visualization of autofluorescent and endogenous harmonic generation signals from the whole-mount samples, with submicron spatial resolution and without the use of fluorescent probes. Optical sections along the depth of the sample can detect different cell morphology and physiological activity (Chu et al., 2003). Furthermore, we used TUNEL staining to detect apoptotic cells in *P. lividus* P4 stage exposed to $HgCl_2$, propidium iodide (PI) to visualize necrotic cells in live plutei and Hoechst 33342 to stain cell nuclei. Apoptosis or programmed cell death is a form of cell suicide showing characteristic morphological and biochemical alterations such as cell shrinkage, blebbing and activation of specific caspases that lead to enzymatic breakdown of DNA (Lockshin et al., 1998). Apoptosis is a physiological process occurring during embryo development and metamorphosis (Roccheri et al., 2002; Thurber and Epel, 2007; Agnello and Roccheri, 2010), but can also be activated by external stimuli such as the presence of bioactive molecules and pollutants (Romano et al., 2003; Agnello et al., 2007). Different fluorescent techniques applied in this study, could be used as early stress indicators in sea urchin bioassay tests.

2. Materials and methods

2.1. Gamete collection

P. lividus and *E. mathaei* adults were collected from an intertidal rocky site along the coast of Livorno (Italy) [43° 25′ 31.79″ N, 10° 23′ 37.51″ E] and Keelung (Taiwan) [25° 8′ 30.79″ N, 121° 48′ 11.79″ E] respectively, and immediately transported in an insulated box to the laboratory. Animals were injected with 1 ml of 0.5 M KCl solution into the coelom, through the peristome, to obtain gametes, soon after their arrival. Sperm obtained from at least three males was collected dry from each male using a Pasteur pipette, pooled and conserved in an Eppendorf tube at 4 °C until fertilization within 2 h. Sperm concentration was determined diluting 50 µl of semen in 25 ml tap water to enlarge sperm head, through osmotic shock, which was then measured with a hemocytometer (Thoma chamber) under the Olympus inverted-microscope (Milan, Italy) using a 40*x* objective. Oocytes obtained from at least three females were pooled into 1 L beaker filled with 0.22 µm filtered seawater (FSW) collected at the corresponding sampling site (36 ± 1 psu salinity, pH$=8.0 \pm 0.2$). The final concentration of 1000 eggs mL^{-1} was prepared by counting subsamples of a known volume with the inverted Olympus microscope at 4*x* objective. Fertilization occurred diluting sperm and eggs in 1 L FSW beaker at 15,000:1 and 10,000:1 sperm:egg ratio, for *P. lividus* and *E. mathaei*, respectively (Rahman et al., 2000; Lera and Pellegrini, 2006). Few minutes after fertilization, an aliquot of embryos was observed under the inverted microscope to verify the presence of the fertilization membrane. The acceptability of the sample was fixed at a fertilization rate above 90%, as also suggested by other authors (from 70% to 95%) (Warnau et al., 1996; Arizzi Novelli et al., 2002; Lera and Pellegrini, 2006).

2.2. Incubation experiments

Each solution was prepared dissolving 135.75 g of $HgCl_2$ in 500 mL bi-distilled water (BDW) to obtain a final concentration of 1M $HgCl_2$ solution. Nominal concentrations of 10, 20, 30, 40, 50, 80, 100, 150, 200 and 250 µg L^{-1} $HgCl_2$ (corresponding approximatively to 3.6–92 µM $HgCl_2$) were then obtained diluting 1M solution in FSW and stirring at the test temperature (1 µg L^{-1} $HgCl_2$ corresponds to 0.74 µg L^{-1} Hg^{2+}). One milliliter of each solution was then added to 9 ml FSW in each well plate containing about 1000 *P. lividus* and *E. mathei* embryos, to obtain final concentrations of 5, 10, 15, 20 and 25 µg L^{-1} for *P. lividus* and 1, 2, 3, 4 and 8 µg L^{-1} for *E. mathaei. Paracentrotus lividus* embryos were maintained at 18 ± 2 °C (Cakal Arslan et al., 2007) while *E. mathaei* where maintained at 24 ± 1 °C (Kominami and Takata, 2003). An untreated control for each species was incubated in FSW alone; six replicates for each condition were applied.

Larval growth followed until the controls reached P4 stage for more than 80%. For *P. lividus* this stage occurred 72 h after fertilization, 48 h for *E. mathaei*. The acceptability of the results was fixed when the percentage of normal plutei was higher than 80% in the controls. Normal and abnormal P4 were identified according to Pagano et al. (1986); the fully developed P4 larvae were considered normal, whereas retarded gastrulae, preastrulae, prism stages and those malformed (showing defects in the skeleton and/or digestive apparatus) were considered abnormal (De Nicola et al., 2007). Median effective concentration inducing 50% of abnormal P4 stages (EC_{50}) was determined for each species, considering the percentage of abnormal P4 stage in each concentration.

2.3. Harmonic generation microscopy analyses

To verify HGM or TP fluorescent signals in living plutei, P4 embyos from both sea urchin species were observed with the second (SHG) and third harmonic generation (THG) microscopy techniques and TP contrast using an adapted upright microscope Olympus BX51 microscope (Taipei, Taiwan) (Hsieh et al., 2008). The scanned SHG and THG images were obtained with a 60x water immersion objectives at numerical aperture of 1.2. The HGM microscopy system is based on a femto-second Cr:forsterite laser operating at wavelengths (λ) of 1230 nm, which can achieve deepest penetration and causes less damage compared with the most commonly used Ti:sapphire laser (700–1000 nm λ) (Chen et al., 2001; Sun et al., 2004). Harmonic generation microscopy is related to the interaction of intense light with matter; in particular the SHG intensity generated depends on the square of the incident light intensity (Chu et al., 2002) and signals are generated at dense, non-centro symmetric structures, such as collagen fibers and striated muscle myosin (Rehberg et al., 2011). The THG fluorescence generated depends on the cubic of the incident light intensity and associated signals were found to be associated with

optical property in homogeneity in unfixed tissues. Furthermore, it can illustrate cell boundaries or the vesicles distribution (Hsieh et al., 2008). By using such intrinsic contrasts, fluorescent probes are not required and dye-related problems (permeability, photodamage, phototoxicity, photobleaching, availability or eventual toxicity) can all be eliminated. Analyses were performed 3 times with 3 replicates and at least 10 embryos, among the most abundant larval stage present in each treatment, were observed.

2.4. TUNEL staining

P. lividus embryos exposed to 5, 10, and 15 μg L^{-1} $HgCl_2$ were stained with terminal deoxy-nucleotidyl-transferase-mediated dUTP nick end labelling (TUNEL, Promega Italia, Milan, Italy). This assay is able to detect apoptotic cells in fixed samples, which appeared with positive, green fluorescent nuclei (Gavrieli et al., 1992). When untreated controls reached the P4 stage a group of almost 200 embryos was fixed for 1 h in 4% paraformaldehyde (PFA), rinsed in phosphate buffer saline solution (PBS) and incubated at 4 °C in 0.1% triton in PBS for 30 min. After being rinsed twice in PBS and once in PBS with 1% bovine serum albumin (SIGMA ALDRICH, Milan, Italy), plutei were incubated for 1 h at 37 °C in the TUNEL, according to the manufacturer instructions. The enzyme was diluted 1:10 with the equilibration buffer to avoid unspecific background. An additional aliquot of the same plutei (almost 50 larvae) was pre-treated for 10 min with 1 Unit mL^{-1} DNAase (Biolab, UK) at 37 °C before TUNEL staining. Another group of almost 50 larvae was incubated with TUNEL labeling without the enzyme, as a negative TUNEL control. All samples were then observed with an inverted ZEISS 510 confocal laser scanning microscopy (CLSM, Oberkochen, Germany) using a 488 nm λ laser.

2.5. Hoechst and propidium iodide staining

Propidium iodide and Hoechst 33342 (Sigma-Aldrich, Milan) are viable probes used to stain not-fixed samples; PI marks dead cells with compromised cell-membrane integrity in red, while Hoechst 33342 stains the nuclei of both living and dead cells specifically in blue (Fried et al., 1976). An aliquot of almost 200 alive *P. lividus* plutei exposed to 5, 10, and 15 μg L^{-1} $HgCl_2$ were incubated 30 min in 1 μg mL^{-1} Hoechst 33342 and 15 min in 2 μg mL^{-1} PI. After being rinsed in FSW samples were fixed for 1 h in 4% PFA at room temperature, then rinsed again in PBS and observed with the inverted CLSM using 405 and 543 nm λ lasers for Hoechst 33342 and PI, respectively.

2.6. Statistical analyses

Probit analysis was used to estimate the concentration that caused an abnormal development in 50% (EC_{50}) of P4 stage (Hamilton et al., 1978). To guarantee the accuracy of the test, EC_{50} and coefficient of variation were calculated. Analyses of variance (One-way ANOVA) and Student–Newman–Keuls (SNK) tests were applied to evaluate differences in deformed P4 embryos between treatments. The SNK method was used as post-hoc test, whenever a significant difference between tested concentration was revealed by ANOVA.

3. Results

The percentage of normally developed *P. lividus* and *E. mathei* plutei exposed to different $HgCl_2$ concentrations is reported in Fig. 1. A significant decrease in the percentage of normal *P. lividus* P4 stages was observed at concentrations ≥ 15 μg L^{-1} $HgCl_2$ ($73.8 \pm 7.5\%$ standard deviation s.d., SNK test $p < 0.05$). At 20 μg L^{-1} $HgCl_2$ only $6 \pm 2.1\%$ were normally developed plutei. The subtropical species *E. mathaei* exhibit the highest sensitivity in respect to the Mediterranean sea urchin; in fact, at 2 μg L^{-1} $HgCl_2$ the percentage of normal P4 was significantly reduced ($51 \pm 3.6\%$, SNK test $p < 0.01$) and at 3 μg L^{-1} $HgCl_2$ this percentage was further reduced to less than $40 \pm 6.7\%$. Normal plutei sharply declined to $18.3 \pm 4.4\%$ at 4 μg L^{-1} $HgCl_2$ and to less than 10% at 8 μg L^{-1}. The EC_{50} calculated for *E. mathei* was 2.41 ± 1.7 μg L^{-1} whereas for *P. lividus* this was 16.14 ± 1.5 μg L^{-1} $HgCl_2$. Living P4 stages exposed to $HgCl_2$ were observed with TP, SHG and THG microscopy to verify whether autofluorescent and HG signals were differently detected in plutei exposed at increasing concentrations (Fig. 2). *P. lividus* plutei showed very weak TP (Fig. 2a–e) and SHG signals in all treatments (Fig. 2f–l). Few spots of TP fluorescent signals were visible in plutei exposed from 5 to 15 μg L^{-1} $HgCl_2$ (Fig. 2b–d), whereas an unspecific background was observed in plutei exposed to the concentration of 20 μg L^{-1} $HgCl_2$ (Fig. 2e). Samples exposed to concentrations from 5 to 15 μg L^{-1} $HgCl_2$ showed SHG signals in the same fluorescent cells observed with TP (Fig. g–i) and no specific fluorescence was observed at the highest concentration (Fig. 2l). Signals from THG revealed a strong contrast of skeletal rods in the controls (Fig. 2m) that disappeared in almost all the exposed plutei (Fig. 2n, o, q). At 15 μg L^{-1} $HgCl_2$ few spicules appeared THG-bright in only one arm (Fig. 2p). *Paracentrotus lividus* plutei stained with the TUNEL are shown in Fig. 3. Control plutei observed in transmitted light appeared normally developed and negatively stained with the TUNEL (Fig. 3a, b) suggesting that at this stage physiological induction of apoptosis was not activated. In the positive DNAase-treated sample, DNA breaks are similar to those induced by apoptosis and nuclei were fluorescent in green (Fig. 3c is a merge of bright light and fluorescent microscopy images). Fig. 3d shows an untreated control pluteus stained with PI (red) and Hoechst 33342 (violet); due to DNA staining only the violet fluorescence was evident, whereas red fluorescence (dead cells) was not visible. An increasing red fluorescence was observed in plutei exposed at the increasing $HgCl_2$ concentrations suggesting that cell membrane permeability was progressively lost in these plutei with a dose-dependent correlation (Fig. 3f, h, l). Green fluorescence due to the TUNEL was evident only in a few cells in plutei exposed from 5 to 15 μg L^{-1} $HgCl_2$ (Fig. 3e, g, l, arrows), similar to those observed with TP microscopy at the same concentrations (Fig. 2b, c, d).

Two-photon, SHG and THG microscopy images of *E. mathaeii* plutei are shown in Fig. 4. Plutei exposed to 2 and 4 μg L^{-1} $HgCl_2$ observed with TP microscopy showed a significant increase in fluorescent signals (Fig. 4c, d), with respect to the control group (Fig. 4a), while, more than 80% of malformed plutei at 4 μg L^{-1}

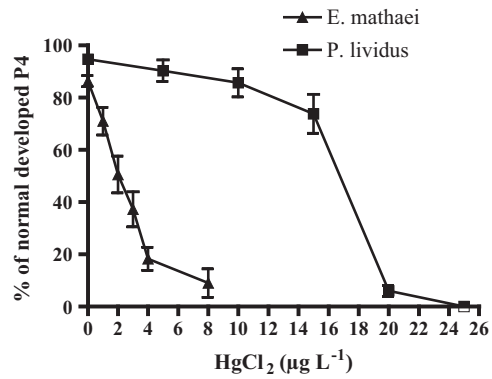

Fig. 1. Percentage of normally developed 4-arm larval stage of *Paracentrotus lividus* and *Echinometra mathaei* incubated soon after fertilization at different $HgCl_2$ concentrations. Each data point represents the mean of three independent experiments, while the vertical bars represent standard deviation.

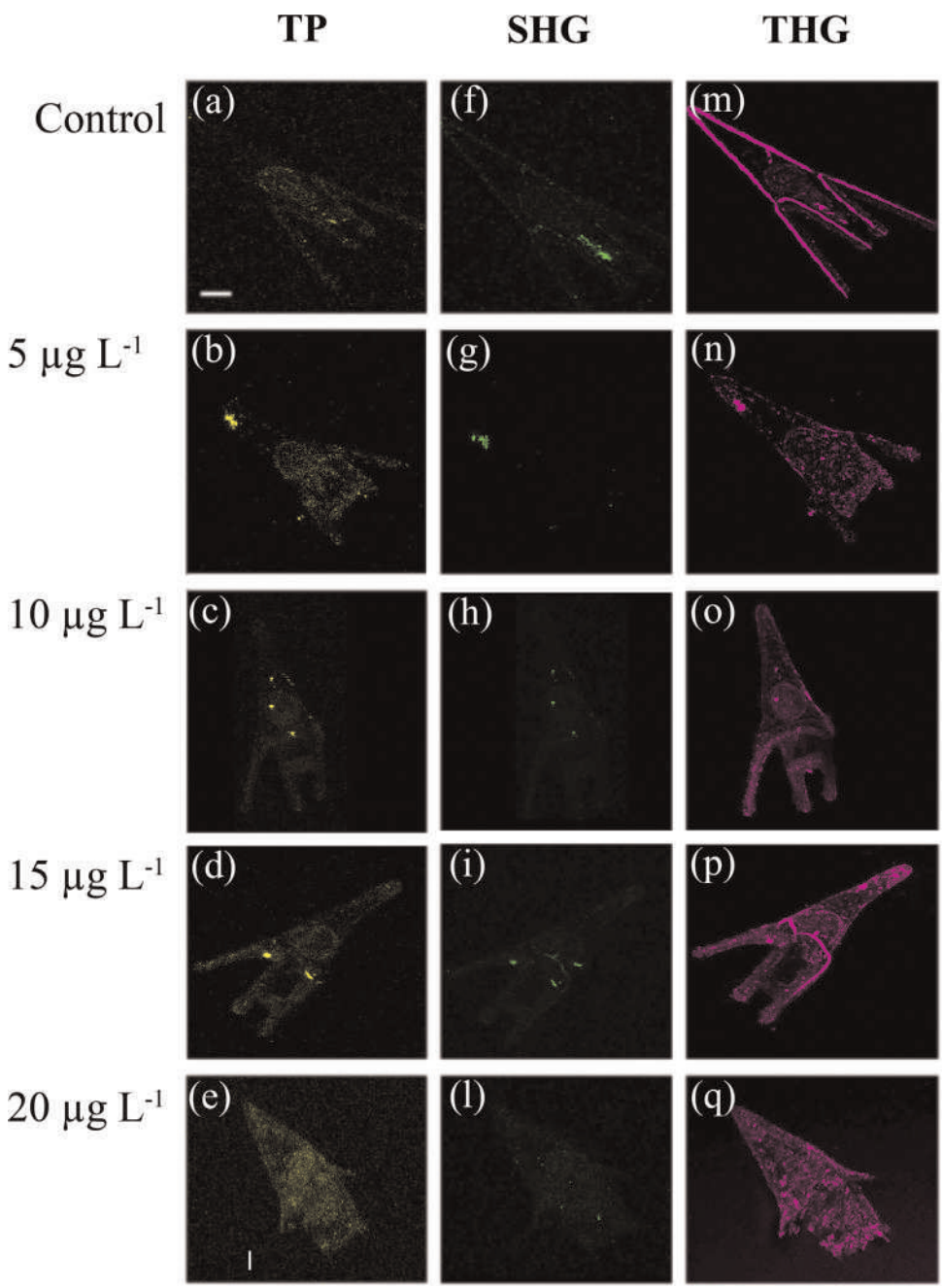

Fig. 2. *Paracentrotus lividus* plutei exposed to different $HgCl_2$ concentrations (row) have been observed with different fluorescent techniques (column). (a–e) two photon microscopy (TP); (f–l) second harmonic generation microscopy (SHG); (m–q) third harmonic generation microscopy (THG). (Bar = 40 µm).

$HgCl_2$ lost the signal (Fig. 4e). SHG signals were low in all the observed plutei at any concentration (Fig. 4f–i), whereas THG fluorescence marked spicules in all treated samples, including strongly deformed plutei (Fig. 4m–q).

4. Discussion

Embryos of two sea urchin species, one inhabiting temperate areas and the second subtropical sea, were exposed to different $HgCl_2$ concentrations; EC_{50} was determined taking into consideration the percentage of abnormal P4 stage. This stage was deemed the end-point, allowing us to detect malformations induced by mercury in both species. Malformations in the P4 stage were analyzed in terms of defects to shape and skeletal rods, using the following optical techniques: i) HGM and TPF microscopy, which facilitates analysis of living, whole-mount plutei without the use of fluorescent probes; ii) the classical TUNEL staining protocol, which identify early apoptosis induction in fixed samples, and iii) the vital fluorescent probes PI and Hoechst 33342, chemicals that penetrate only dead, necrotic cells with compromised cell membrane integrity, or stains nucleic acids respectively.

In terms of dose–response effects, results showed an increasing number of malformed P4 stage at higher Hg concentrations. However, the two species showed different sensitivity; the most sensitive species was the subtropical *E. mathaei*, with an EC_{50} value that was 8-folds lower compared to the temperate sea urchin *P. lividus*. Toxicity of $HgNO_3$ on *E. mathaei* species was studied by Sadripour et al. (2013) which found variable and higher EC50 values (17/42 µg L^{-1} $HgNO_3$), compared to our results. However, the

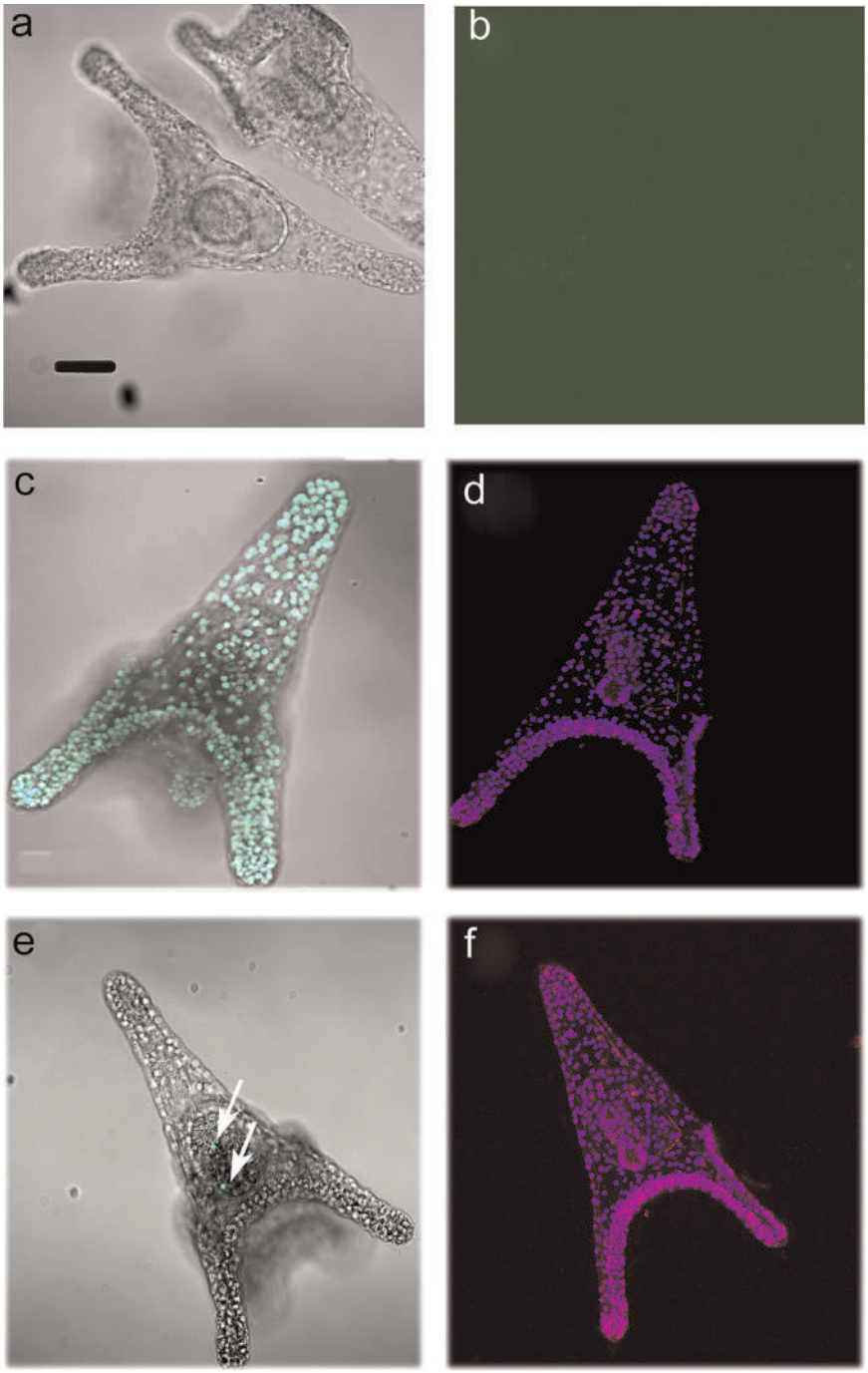

Fig. 3. *Paracentrotus lividus* plutei observed with confocal laser scanning microscopy. (a), (b), (c), (e) and (g) fixed plutei stained with the TUNEL to detect apoptosis, observed in transmitted light and in fluorescence using a 488 nm wavelength laser to detect apoptotic cells. (d), (f), (h), (l) living plutei stained with propidium iodide (PI) and observed with a 543 nm wavelength laser (red), to detect necrotic cells, and with Hoechst 33342, observed with a 405 nm wavelength laser (violet), to detect nucleic acids. (a) Untreated control plutei observed in transmitted light and (b) the corresponding TUNEL staining pluteus did not show any fluorescence even at a very high contrast (green background). (c) Pluteus treated with DNAse enzyme, in which TUNEL stains fluorescent nuclei in green (positive control). The figure is a merge of the transmitted light microscopy and the fluorescent images. (d) Untreated, control pluteus stained with the Hoechst 33342 probe and the PI showing only the violet fluorescence of nucleic acids. (e) Pluteus developed within 5 $\mu g\ L^{-1}$ $HgCl_2$ showing two cells positively stained with TUNEL (arrows). (f) Pluteus exposed as in (e) showing an increase in red fluorescence. (g) Pluteus developed within 10 $\mu g\ L^{-1}$ $HgCl_2$ appeared with two cells positively stained with TUNEL (arrows). (h) Pluteus exposed as in (g) showing deformities and a strong red fluorescence in the whole body. (i) Pluteus developed within 15 $\mu g\ L^{-1}$ $HgCl_2$ appeared severely deformed with few nuclei positively stained in green (arrows). (l) Plutei exposed as in (i) strongly malformed and highly fluorescent in red. (Bar = 40 μm).

authors incubated embryos after the first embryonic cleavage while, in our study, embryos were incuabated immediately after fertilization. It is well known that heavy metal toxicity is associated with the incubation stage of sea urchins, with gametes and zygotes being more sensitive than later developmental stages (Kobayashi, 1995; Kobayashi and Okamura, 2004).

For *P. lividus*, results are comparable with those reported by Kobayashi (1995) in which deformed plutei were recorded at Hg concentrations above to 6.8 $\mu g\ L^{-1}$. The concentration of total mercury in aquatic environment is highly variable, with values ranging from less than 3 $ng\ L^{-1}$ in unpolluted seawater to more than 10 $\mu g\ L^{-1}$ in polluted coastal and estuarine areas (De Riso

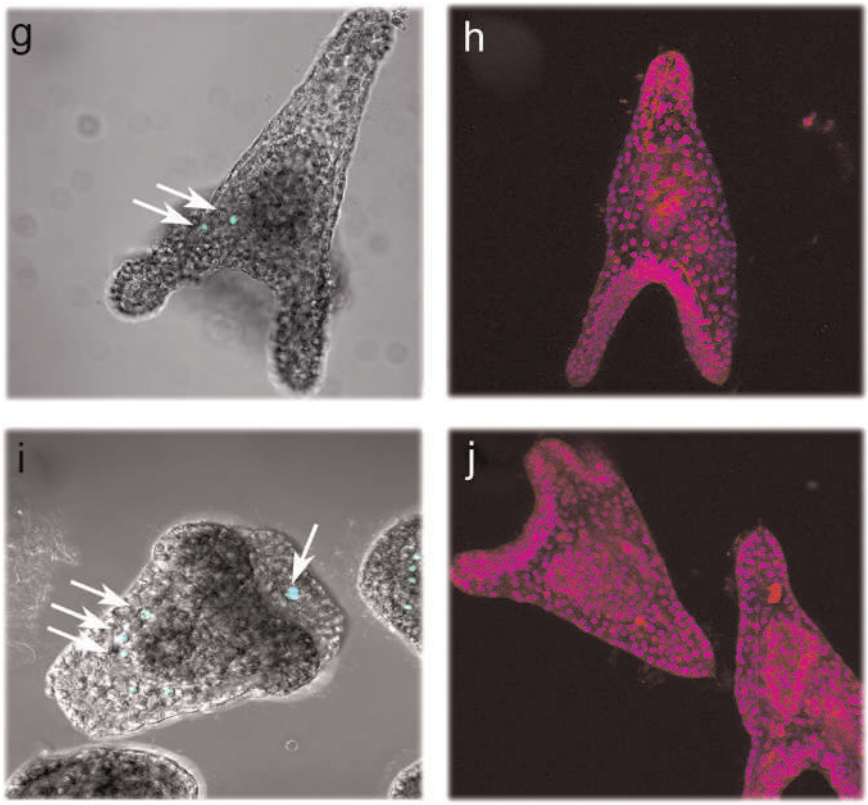

Fig. 3. (*continued*)

et al., 2000), where sea urchin development could be disrupted.

It has been reported that mercury toxicity increases with higher temperatures for a wide range of species (Chaudhary and Gupta, 2006; Tsui and Wang, 2006; Fernández and Beiras, 2001). Our study does not rule out the possibility that the different temperatures used in our protocol could influence the different sensitivity recorded for the two species. However, larvae of *P. lividus* and *E. mathaei* were exposed to their typical environmental median temperatures, which can be considered as the actual exposure scenario during their life cycle. In addition, tropical organisms live in more stable environments, likely explaining the great sensitivity of *E. mathaei* compared with eurytherm Mediterranean species *P. lividus*.

The sea urchin embryo development test is considered a standard bioassay by which to evaluate the toxicity of specific pollutants (Gaion et al., 2013; Beiras et al., 2003). The ratio between normally and abnormally developed larvae (such as deformities in skeletal rods) is an important evaluation criterion and should be clearly determined and described. Recently, skeletal integrity has been suggested as a more sensitive criterion with respect to the classical normally-shaped larval description or EC_{50} determination. Carballeira et al. (2012) classified abnormalities according to the severity of skeletal alteration. In our study, we showed that THG microscopy was able to detect skeletal rod (see Figs. 2 and 4) and this technique can be useful to investigate skeletal malformations during pluteus development. Skeletal alterations in sea urchins have been observed after exposure to different classes of toxicants, including heavy metals and effluents, therefore their description can be considered a fast early-warning test in bioassay studies. In both *P. lividus* and *E. mathaei* malformations of P4, induced by $HgCl_2$, is dose-dependent, although THG microscopy revealed different mechanisms of toxicity in the two species: a loss of THG signal in the skeleton of *P. lividus* was observed with all tested concentrations could be due to incorrect tissutal organization in the skeletal structures (Fig. 2). By contrast, the THG signals by skeletal rod fluorescence was always evident in *E. mathaei*, suggesting correct tissue formation (Fig. 4). This also suggests that the induced morphological anomalies were not determined by incorrect skeletal structures. This technique is useful as a fast screening assay of the anomalies induced by toxicants during sea urchin larval development.

In the last decade, detection of apoptosis or programmed cell death in marine invertebrates exposed to bioactive molecules has opened new perspectives in marine ecotoxicology and physiology studies (Romano et al., 2003, 2010; Agnello et al., 2007; Ianora et al., 2004; Buttino et al., 2011). The feasibility of identifying apoptosis before the appearance of macroscopic aberrations is useful for predicting toxic effects (Buttino et al., 2011). Apoptosis in sea urchin occurs as physiological process to mold the organism during larval development (Roccheri et al., 2002; Voronina and Wessel, 2001), but it could also be activated in response to different external stresses (Romano et al., 2003). Recently, Filosto et al. (2008) demonstrated that Cd^{2+} induced an apoptotic response in *P. lividus* embryos exposed to subacute/sublethal concentrations. It was previously demonstrated that apoptosis can be activated to remove cells with a heavily damaged DNA structure: this process can be considered as a part of a defense strategy from pollutant-induced toxicity (Filosto et al., 2008). There is growing evidence that mercury is an effective apoptogenic toxicant for humans (Sutton and Tchounwou, 2006); to our knowledge, however, this aspect has never been investigated in marine organisms. In the present study, different approaches were applied to detect apoptosis in sea urchin plutei: the classical protocol using the TUNEL and HGM microscopy. It is interesting to note that *P. lividus* plutei exposed in 5–15 $\mu g\ L^{-1}$ $HgCl_2$ showed only few positive cells marked with the TUNEL and signals were similar to those found using TP and SHG microscopy (Figs. 2 and 3). Our results suggest that a general increase in TP signals, recorded in *E. mathei*

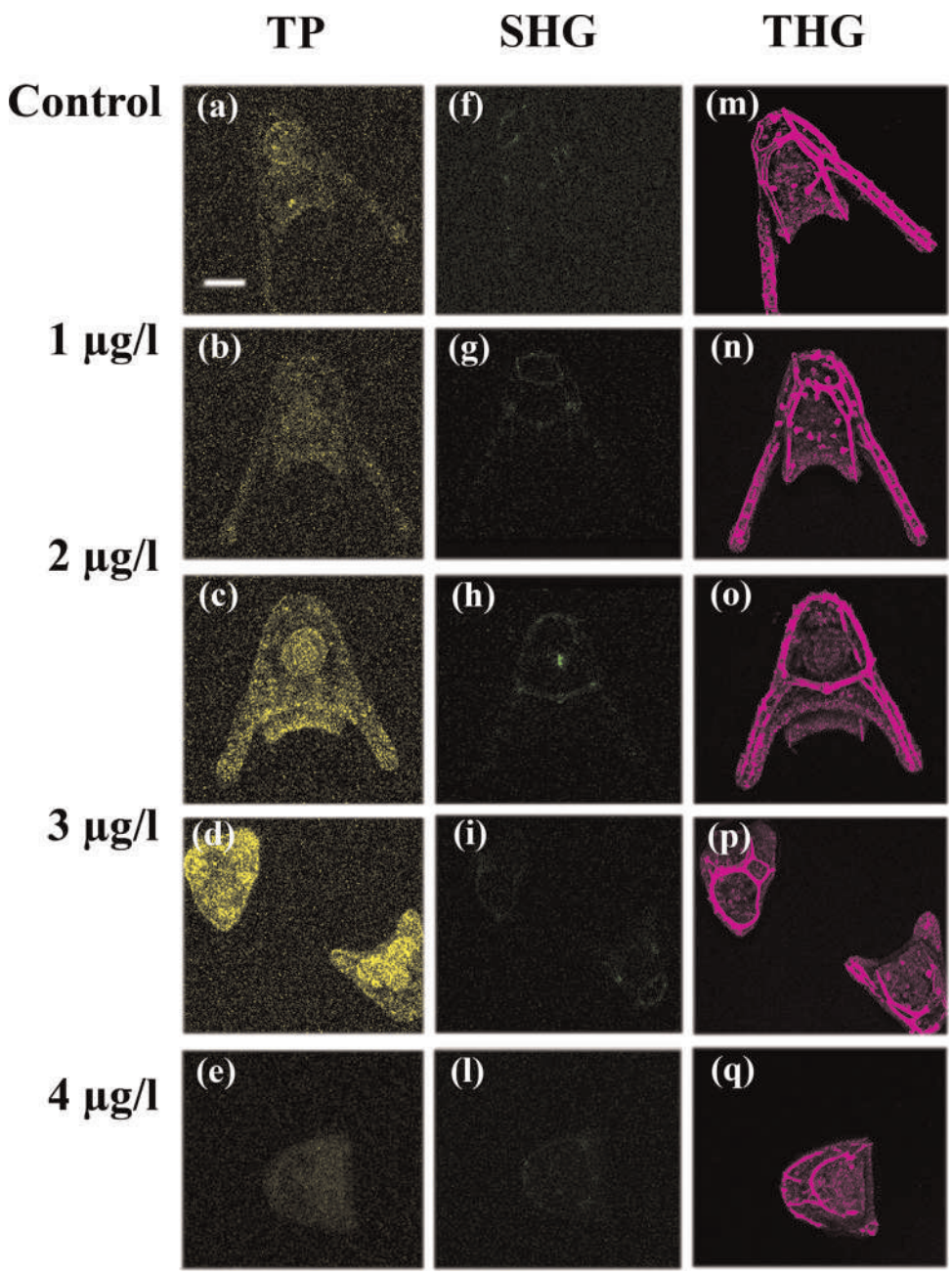

Fig. 4. *Echinometra mathaei* plutei exposed to different $HgCl_2$ concentrations (row) were observed using different fluorescent techniques (column). (a–e) two photon microscopy (TP); (f–l) second harmonic generation microscopy (SHG); (m–q) third harmonic generation microscopy (THG). (Bar = 64.3 μm).

plutei exposed to increasing $HgCl_2$ concentrations, could be due to an apoptotic-like mechanism. At the highest $HgCl_2$ concentration TP autofluorescence disappeared in both species, probably due to an unspecific inhibition of metabolic activities occurring in such highly abnormal plutei. Previous studies have confirmed that strong TP autofluorescence is associated with apoptotic cells; for example TP signals were associated with apoptotic bodies in the hind brain of zebrafish (Hsieh et al., 2008) and in copepods (Buttino et al., 2011).

In *P. lividus* an increase in red fluorescence associated with the PI probe was clearly observed starting from 5 μg L^{-1} $HgCl_2$, suggesting that cell permeability increased in a dose-dependent manner as a consequence of chemical stress. This result is consistent with the hypothesis of an interaction between Hg^{2+} and cell transport/membrane permeability processes (Bonacker et al., 2004). Changes in membrane permeability due to physical or chemical stress is well known (Bischof et al., 1995), in particular, exposure to inorganic mercury altered calcium channel conductance in human cell lines with corresponding effects on membrane permeability (Bischof et al., 1995; Parran et al., 2001; Hajela and Peng, 2003). This phenomenon has never been observed in *P. lividus* embryos; $HgCl_2$ was able to increase membrane fluidity by stimulating interaction with Ca^{2+} channels (Allemand et al., 1988). In addition, Allemand et al. (1993) demonstrated that $HgCl_2$ can alter the intracellular pH of *P. lividus* fertilized sea urchin eggs, prompting an increase of Ca^{2+} influx corresponding an H^+ mobilizations in the acidic intracellular compartments. Alternatively, PI staining could be associated with the presence of organelles such as lysosomes, which concentrate heavy metals as a de-toxification mechanism (Viarengo, 1989). It is also known that PI-positive staining, in living cells, could be associated with high RNA contents, which may not necessarily be followed by protein

synthesis (Rieger et al., 2010). Further investigations are needed to better clarify cellular mechanism induced by $HgCl_2$ and it remains to be verified whether cell permeability increases, thus also exposing P4 larvae to other toxicants. At present, PI can be proposed as a rapid *in vivo* probe to detect chemical stress in *P. lividus* plutei exposed to mercury.

In conclusion, our results suggest that two sea urchin species activate different mechanisms in response to mercury exposure; the less-sensitive temperate species lost selective permeability of the membrane, and the apoptotic mechanism is not induced at the tested concentrations. In the more sensitive tropical species, plutei showed an increase in apoptotic-like signals. These different approaches can be useful for the rapid evaluation of toxicity in living organisms and can be considered early-warning systems in bioassay tests.

Acknowledgements

This research has been partially funded by the National Science Council of Taiwan, grant from the Summer Program 2011 and a bilateral project comprising the Stazione Zoologica Anton Dohrn, Naples, Italy and the National Science Council of Taiwan [Grant no. NSC 101-2923-B-019-001-MY2].

We are extremely grateful to all the staff of STS-ISPRA Livorno, the Institute of Marine Biology of National Taiwan Ocean University, the Molecular Imaging Center at National Taiwan University and the National Health Research Institute, for technical and qualified assistance during the project.

Appendix A. Supplementary material

Supplementary data associated with this article can be found in the online version at http://dx.doi.org/10.1016/j.ecoenv.2015.07.027.

References

Satoh, H., 2000. Occupational and environmental toxicology of mercury and its compounds. Indus. Health 38, 153–164.
Driscoll, C.T., Yan, C., Schofield, C.L., Munson, R., Holsapple, J., 1994. The mercury cycle and fish in the Adirondak Lakes. Environ. Sci. Technol. 28, 136–143.
Plaschke, R., Dal Pont, G., Butler, E.C.V., 1997. Mercury in waters of the Derwent Estuary - sample treatment and analysis. Mar. Pollut. Bull. 34, 177–185.
De Riso, R., Waeles, M., Mombet, P., Chaumery, C.J., 2000. Measurements of trace concentrations of mercury in sea water by stripping chronopotentiometry with gold disk electrode: influence of copper. Anal. Chim. Acta 410, 97–105.
Devil, E.W., 2006. Acute toxicity, uptake and histopathology of aqueous methyl mercury to fathead minnow embryos. Ecotoxicology 15, 97–110.
Sinaie, M., Bastami, K.D., Ghorbanpour, M., Najafzadeh, H., Shekari, M., Haghparast, S., 2010. Metallothionein biosynthesis as a detoxification mechanism in mercury exposure in fish, spotted scat (Scatophagus argus). Fish Physiol. Biochem. 36, 1235–1242.
Fernandez, N., Beiras, R., 2001. Combined toxicity of dissolved mercury with copper, lead and cadmium on embryogenesis and early larval growth of the *Paracentrotus lividus* sea-urchin. Ecotoxicology 10, 263–271.
Bellas, J., Granmo, A., Beiras, R., 2005. Embryotoxicity of the antifouling biocides zinc pyrithione to sea urchin (*Paracentrotus lividus*) and mussel (*Mytilus edulis*). Mar. Pollut. Bull. 50, 1382–1385.
Salamanca, M.J., Fernández, N., Cesar, A., Antón, R., Lopez, P., Delvalls, Á., 2009. Improved sea-urchin embryo bioassay for in situ evaluation of dredged material. Ecotoxicology 18, 1051–1057.
Pagano, G., Cipollaro, M., Corsale, G., Esposito, A., Ragucci, E., Giordano, G.G., Trieff, N.M., 1986. The sea urchin, bioassay for the assessment of damage from environmental contaminants. In: Cairns, J. Jr (Ed.), Community Toxicity Testing. American Society for Testing and Materials, Philadelphia, pp. 66–92.
Warnau, M., Iaccarino, M., De Biase, A., Temara, A., Jangoux, M., Dubois, P., Pagano, G., 1996. Spermiotoxicity and embryotoxicity of heavy metals in the Echinoid *Paracentrotus lividus*. Environ. Toxicol. Chem. 15, 1931–1936.
McClanahan, T.R., Muthiga, N.A., 2007. Ecology of Echinometra. In: Lawrence, J.M. (Ed.), Edible Sea Urchins: Biology and Ecology Developments in Aquaculture and Fisheries Science. Elsevier Science B.V, pp. 297–317.
Kominami, T., Takata, H., 2003. Timing of early developmental events in embryos of a tropical sea urchin *Echinometra mathaei*. Zool. Sci. 20, 617–626.
Mahdavi, S.N., Haghighat, K.Z., Karamzadeh, S., Naseri, F., Esteki, A.A., Rameshi, H., 2008. Reproductive cycle of the sea urchin *Echinometra mathaei* (Echinodermatidea: Echinoidea) in Bostaneh, Persian Gulf, Iran. J. Biol. Sci. 8, 1138–1148.
Sadripour, E., Mortazavi, M.S., Mahdavi Shahri, N., 2013. Effects of mercury on embryonic development and larval growth of the sea urchin *Echinometra mathaei* from the Persian Gulf. Iran. J. Fish. Sci 12, 898–907.
Boudouresque, C.F., Verlaque, M., 2007. Ecology of *Paracentrotus lividus*. In: Lawrence, J.M. (Ed.), Edible Sea Urchins: Biology and Ecology Developments in Aquaculture and Fisheries Science. Elsevier Science B.V, pp. 243–285, Edible Sea Urchins: Biology and Ecology (ed.), In J.M. Lawrence, ed..
Bellas, J., Saco-Alvarez, L., Nieto, O., Beiras, R., 2008. Ecotoxicological evaluation of polycyclic aromatic hydrocarbons using marine invertebrate embryo-larval bioassays. Mar. Pollut. Bull. 57, 493–502.
Pinsino, A., Matranga, V., Trinchella, F., Roccheri, M.C., 2010. Sea urchin embryos as an in vivo model for the assessment of manganese toxicity: developmental and stress response effects. Ecotoxicology 19, 555–562.
Gaion, A., Scuderi, A., Pellegrini, D., Sartori, D., 2013. Arsenic exposure affects embryo development of sea urchin, *Paracentrotus lividus* (Lamarck, 1816). Bull. Environ. Contam. Toxicol. 91, 565–570.
Romano, G., Costantini, M., Buttino, I., Ianora, A., Palumbo, A., 2011. Nitric oxide mediates the stress response induced by diatom aldehydes in the sea urchin *Paracentrotus lividus*. PLoS ONE 6, e25980. http://dx.doi.org/10.1371/journal.pone.0025980.
Romano, G., Russo, G.L., Buttino, I., Ianora, A., Miralto, A., 2003. A marine diatom-derived aldehyde induces apoptosis in copepod and sea urchin embryos. J. Exp. Biol. 206, 3487–3494.
Romano, G., Miralto, A., Ianora, A., 2010. Teratogenic effects of diatom metabolites on sea urchin *Paracentrotus lividus* embryos. Mar. Drugs 8, 950–967.
Chu, S.-W., Chen, S.-Y., Tsai, T.-H., Liu, T.-M., Lin, C.-Y., Tsai, H.-J., Sun, C.-K., 2003. In vivo developmental biology study using non invasive multi-harmonic generation microscopy. Opt. Express 11, 3093–3099.
Lockshin, R.A., Zakeri, Z., Tilly, J.L., 1998. When Cells Die: A Comprehensive Evaluation of Apoptosis and Programmed Cell Death. Wiley-Liss, New York.
Roccheri, M.C., Tipa, C., Bonaventura, R., Matranga, V., 2002. Physiological and induced apoptosis in sea urchin larvae undergoing metamorphosis. Int. J. Dev. Biol. 46, 801–806.
Thurber, R.V., Epel, D., 2007. Apoptosis in early development of the sea urchin strongylocentrotus purpuratus. Dev. Biol. 303, 336–346.
Agnello, M., Roccheri, M.C., 2010. Apoptosis: focus on sea urchin development. Apoptosis 15, 322–330.
Agnello, M., Filosto, S., Scudiero, R., Rinaldi, A.M., Roccheri, M.C., 2007. Cadmium induces an apoptotic response in sea urchin embryos. Cell Stress Chaperones 12, 44–50.
Rahman, M.A., Uehara, T., Aslan, L.M., 2000. Comparative viability and growth of hybrid between sympatric species of sea urchin (genus Echinometra) in Okinawa. Aquaculture 183, 45–56.
Lera, S., Pellegrini, D., 2006. Evaluation of the fertilization capability of *Paracentrotus lividus* sea urchin storage gametes by the exposure to different aqueous matrices. Environ. Monit. Assess. 119, 1–13.
Arizzi Novelli, A., Argese, E., Tagliapietra, D., Bettiol, C., Ghirardini, A. Volpi, 2002. Toxicity of tributyltin and triphenyltin towards early life stages of *Paracentrotus lividus* (Echinodermata: Echinoidea). Environ. Toxicol. Chem. 21, 859–864.
Lera, S., Pellegrini, D., 2006. Evaluation of the fertilization capability of *Paracentrotus lividus* sea urchin storaged gametes by the exposure to different aqueous matrices. Environ. Monit. Assess. 119, 1–13.
Cakal Arslan, O., Parlak, H., Oral, R., Katalay, S., 2007. The effects of nonylphenol and octylphenol on embryonic development of sea urchin (*Paracentrotus lividus*). Arch. Environ. Contam. Toxicol. 53, 214–219.
De Nicola, E., Meric, S., Gallo, M., Iaccarino, M., Della Rocca, C., Lofrano, G., Russo, T., Pagano, G., 2007. Vegetable and synthetic tannins induced hormesis/toxicity in sea urchin early development and in algal growth. Environ. Pollut. 146, 46–54.
Hsieh, C.-S., Ko, C.-Y., Chen, S.-Y., Liu, T.-M., Wu, J.-S., Hu, C.-H., Sun, C.-K., 2008. In vivo long- term continuous observation of gene expression in zebrafish embryo nerve system by using harmonic generation microscopy and morphant technology. J. Biomed. Opt. 13, 064041-1–064041-7.
Chen, I.-H., Liu, T.-M., Cheng, P.-C., Sun, C.-K., Lin, B.-L., 2001. Multimodal nonlinear spectral microscopy based on a femtosecond Cr:forsterite laser. Opt. Lett. 26, 1909–1911.
Sun, C.-K., Chu, S.-W., Chen, S.-Y., Tsai, T.-H., Liu, T.-M., Lin, C.-H., Tsai, H.-J., 2004. Higher harmonic generation microscopy for developmental biology. J. Struct. Biol. 147, 19–30.
Chu, S.-W., Chen, I.-H., Liu, T.-M., Sun, C.-K., Lee, S.-P., Lin, B.-L., Cheng, P.-C., Kuo, M.-X., Lin, D.-J., Liu, H.-L., 2002. Nonlinear bio-photonic crystal effects revealed with multimodal nonlinear microscopy. J. Microsc. 208, 190–200.
Rehberg, M., Krombach, F., Pohl, U., Dietzel, S., 2011. Label-free 3D visualization of cellular and tissue structures in intact muscle with second and third harmonic generation microscopy. PLoS One 6, e28237. http://dx.doi.org/10.1371/journal.pone.0028237.
Hsieh, C.-S., Chen, S.-U., Lee, Y.-W., Yang, Y.-S., Sun, C.-K., 2008. Higher harmonic generation microscopy of in vitro cultured mammal oocytes and embryos. Opt. Express 16, 11574–11588.

Gavrieli, Y., Sherman, Y., Ben-Sasson, S.A., 1992. Identification of programmed cell death in situ via specific labeling of nuclear DNA fragmentation. J. Cell Biol. 119, 493–501.
Fried, J., Perez, A., Clarkson, B., 1976. Flow cytofluorometric analysis of cell cycle distributions using propidium iodide. Properties of the method and mathematical analysis of the data. J. Cell. Biol. 71, 172–181.
Hamilton, M.A., Russo, R.C., Thurston, R.V., 1978. Trimmed Spearman-Karber method for estimating median lethal concentrations in toxicity bioassays. Environ. Sci. Technol. 12, 714–720.
Kobayashi, N., 1995. Bioassay data for marine pollution using echinoderms. In: Cheremisinoff, P.N. (Ed.), Environmental control technology Vol. 9. Gulf Publ., Houston, pp. 536–609.
Kobayashi, N., Okamura, H., 2004. Effects of heavy metals on sea urchin embryo development. 1 Tracing the cause by the effects. Chemosphere 55, 1403–1412.
Chaudhary, P., Gupta, A.K., 2006. Impact of water hardness and temperature on the acute toxicity of copper and mercury to a freshwater copepod, Cyclops Indian. J. Environ. Sci. 10 (2), 139–143.
Tsui, M.K., Wang, W.X., 2006. Acute, toxicity of mercury to Daphnia magna under different conditions. Environ. Sci. Technol. 40, 4025–4030.
Fernández, N., Beiras, R., 2001. Combined toxicity of dissolved mercury with copper, lead and cadmium on embryogenesis and early larval growth of the *Paracentrotus lividus* sea-urchin. Ecotoxicology 10, 263–271.
Beiras, R., Fernández, N., Bellas, J., Besada, V., González-Quijano, A., Nunes, T., 2003. Integrative assessment of marine pollution in Galician estuaries using sediment chemistry, mussel bioaccumulation, and embryo-larval toxicity bioassays. Chemosphere 52, 1209–1224.
Carballeira, C., Ramos-Gómez, J., Martín-Díaz, L., DelValls, T.A., 2012. Identification of specific malformations of sea urchin larvae for toxicity assessment: application to marine pisciculture effluents. Marine Environ. Res. 77, 12–22.
Ianora, A., Miralto, A., Poulet, S.A., Carotenuto, Y., Buttino, I., Romano, G., Casotti, R., Pohnert, G., Wichard, T., Colucci-D'Amato, L., et al., 2004. Aldehyde suppression of copepod recruitment in blooms of a ubiquitous planktonic diatom. Nature 429, 403–407.
Buttino, I., Pellegrini, D., Romano, G., Hwang, J.-S., Liu, T.-M., Sartori, D., Sun, C.-K., Macchia, S., Ianora, A., 2011. Study of apoptosis induction in Acartia tonsa nauplii exposed to chronic concentration of Nickel. Chem. Ecol. 27, 97–104.
Buttino, I., Hwang, J.-S., Sun, C.-K., Hsieh, C.-T., Liu, T.-M., Pellegrini, D., Ianora, A., Sartori, D., Romano, G., Cheng, S.-H., Miralto, A., 2011. Apoptosis to predict copepod mortality: state of the art and future perspectives. Hydrobiologia 666, 257–264.
Voronina, E., Wessel, G.M., 2001. Apoptosis in sea urchin oocytes, eggs, and early embryos. Mol. Reprod. Dev. 60, 553–561.
Filosto, S., Roccheri, M.C., Bonaventura, R., Matranga, V., 2008. Environmentally relevant cadmium concentrations affect development and induce apoptosis of *Paracentrotus lividus* larvae cultured in vitro. Cell Biol. Toxicol. 24, 603–610.
Sutton, D.J., Tchounwou, P.B., 2006. Mercury-induced externalization of phosphatidylserine and caspase 3 activation in human liver carcinoma ($HepG_2$), cells. Int. J. Environ. Res. Public Health 3, 38–42.
Hsieh, C.-S., Ko, C.-Y., Chen, S.-Y., Liu, T.-M., Wu, J.-S., Hu, C.-H., Sun, C.-K., 2008. In vivo long- term continuous observation of gene expression in zebrafish embryo nerve system by using harmonic generation microscopy and morphant technology. J. Biomed. Opt. 13, 064041-1–064041-7.
Bonacker, D., Stiber, T., Wang, M., Bhöm, K.J., Prots, I., Unger, E., Their, R., Bolt, H.M., Degen, G.H., 2004. Genotoxicity of inorganic mercury salts based o disturbed microtubule function. Arch. Toxicol. 78, 575–583.
Bischof, J.C., Padanilam, J., Holmes, W.H., Ezzell, R.M., Lee, R.C., Tompkins, R.G., Yarmush, M.L., Toner, M., 1995. Dynamics of cell membrane permeability changes at supraphysiological temperatures. Biophys. J. 68, 2608–2614.
Parran, D.K., Mundy, W.R., Barone, Jr. S., 2001. Effects of methylmercury and mercuric chloride on differentiation and cell viability in PC12 cells. Toxicol. Sci. 59, 278–290.
Hajela, R.K., Peng, S.Q., 2003. Comparative effects of methylmercury and Hg^{2+} on human neuronal N and R type high voltage activated calcium channels transiently expressed in human embryonic kidney 293 cells. J. Pharmacol. Exp. Therap. 306, 1129–1136.
Allemand, D., De Renzis, G., Payan, P., Girard, J.-P., Vaissiere, R., 1988. $HgCl_2$-induced cell injury. Differential effects on membrane-located transport systems in unfertilized and fertilized sea urchin eggs. Toxicology 50, 217–230.
Allemand, D., De Renzis, G., Payan, P., 1993. Effects of $HgCl_2$ on intracellular pH in sea urchin eggs : activation of H^+ excretion and Na^+/H^+ exchange activity. Aquat. Toxicol. 26, 171–184.
Viarengo, A., 1989. Heavy metals in marine invertebrates: mechanisms of regulation and toxicity at the cellular level. CRC Crit. Rev. Aquat. Sci. 1, 295–317.
Rieger, A.M., Hall, B.E., Luong, I.E.T., Schang, L.M., Barrreda, D.R., 2010. Conventional apoptosis assays using propidium iodide generate a significant number of false positives that prevent accurate assessment of cell death. J. Immunol. Methods 358, 81–92.

Please cite this article as: Buttino, I., et al., Detection of malformations in sea urchin plutei exposed to mercuric chloride using different fluorescent techniques. Ecotoxicol. Environ. Saf. (2015), http://dx.doi.org/10.1016/j.ecoenv.2015.07.027

Provided for non-commercial research and education use.
Not for reproduction, distribution or commercial use.

(This is a sample cover image for this issue. The actual cover is not yet available at this time.)

This article appeared in a journal published by Elsevier. The attached copy is furnished to the author for internal non-commercial research and education use, including for instruction at the authors institution and sharing with colleagues.

Other uses, including reproduction and distribution, or selling or licensing copies, or posting to personal, institutional or third party websites are prohibited.

In most cases authors are permitted to post their version of the article (e.g. in Word or Tex form) to their personal website or institutional repository. Authors requiring further information regarding Elsevier's archiving and manuscript policies are encouraged to visit:

http://www.elsevier.com/copyright

Author's personal copy

Journal of Experimental Marine Biology and Ecology 418-419 (2012) 46–58

Contents lists available at SciVerse ScienceDirect

Journal of Experimental Marine Biology and Ecology

journal homepage: www.elsevier.com/locate/jembe

Multi-generation cultivation of the copepod *Calanus helgolandicus* in a re-circulating system

Ylenia Carotenuto *, Francesco Esposito, Fabio Pisano, Chiara Lauritano, Massimo Perna, Antonio Miralto, Adrianna Ianora

Stazione Zoologica Anton Dohrn, Villa Comunale 1, 80121 Napoli, Italy

ARTICLE INFO

Article history:
Received 2 November 2011
Received in revised form 15 March 2012
Accepted 16 March 2012
Available online xxxx

Keywords:
Calanus helgolandicus
Copepod population growth
Mass cultivation
Thalassiosira weissflogii

ABSTRACT

We tested the amenability of the calanoid copepod *Calanus helgolandicus* to be mass cultivated in a large volume system. The copepod was reared on two different occasions (during 2009 and 2010), for at least four generations and six months with a mixed flagellate diet of *Isochrysis galbana*, *Rhodomonas baltica* and *Prorocentrum minimum*, or a mixed diet of *I. galbana*, *R. baltica* and the diatom *Thalassiosira weissflogii*. The generation time of *C. helgolandicus* from nauplius to adult was 21 days, with relative duration of naupliar and copepodid phases of 7 and 14 days, respectively. Population growth rates when the second generation of adults developed and reproduced in the tank, were ~2-times higher (0.067 d^{-1} vs. 0.038 d^{-1}) and abundances increased 6-times more (40-fold vs. 6.7-fold) during 2010 than 2009. This higher production was related to the addition of *T. weissflogii* to the mixed *R. baltica* + *I. galbana* diet at low concentrations (0.17 mg C l^{-1}) and for short periods (<2 months), which induced higher egg production rate and percentage of spawning females and lower copepodid mortality in the population. However, supplementation of *T. weissflogii* at higher concentrations (0.40 mg C l^{-1}) or longer feeding times (>3 months), reduced copepod egg hatching success, and hence population growth of *C. helgolandicus*. In conclusion, our study shows that by using an appropriate mixed diatom assemblage for short periods, it is possible to obtain healthy individuals of all larval stages of *C. helgolandicus* for biological, toxicological and gene expression studies year-round.
© 2012 Elsevier B.V. All rights reserved.

1. Introduction

Copepods are dominant members of the zooplankton, both in terms of biomass and abundance (Verity and Smetacek, 1996), and are considered a critical component of most marine and freshwater environments. They dominate the zooplankton literature due to their worldwide distribution, central role in marine food webs, contribution to fisheries and, indirectly, to human nutrition, and role as indicators of environmental pollution (Mauchline, 1998). Most of this copepod literature, however, is based on small-scales laboratory cultivation experiments performed on one copepod generation, e.g. from egg to adult (Carlotti et al., 2007; Carotenuto et al., 2002, 2011; Halsband-Lenk et al., 2002; Huntley et al., 1987; Koski et al., 1998; Rey-Rassat et al., 2002a). In a few cases, the spawning activity of adult females of the second generation has also been assessed (Bonnet and Carlotti, 2001; Hygum et al., 2000; Rey-Rassat et al., 2002b). At best, copepods have been raised for a maximum of two generations, from late copepodid stages to the next adult generation (Campbell et al., 2001).

More than 60 copepod species have been successfully raised (Mauchline, 1998) and a World Copepod Culture Database started at Roskilde University (Denmark) now provides information on cultivation conditions for about 30 copepod cultures worldwide (http://copepod.ruc.dk/main.htm) (Drillet et al., 2011). Most of these cultures are for three relevant calanoid genera, such as *Acartia*, *Eurytemora* and *Temora*, even though individual cultures of other ecologically-important copepod species are also included (*Oithona* and *Centropages*). Among the listed species, *Acartia tonsa*, *Temora stylifera*, *Centropages typicus* and *Gladioferens imparipes*, have been cultivated through multiple generations in intensive systems directed to commercial or ornamental fish aquaculture (Buttino et al., 2012; Payne and Rippingale, 2001; Støttrup et al., 1986). Although the maximum copepod density obtained in these systems is lower than that obtained for harpacticoid and cyclopoid copepods (Drillet et al., 2011), these studies have shown that calanoids can be maintained in long-term cultivation systems over multiple generations. In contrast to small neritic calanoid copepods, larger sized species such as *Calanus finmarchicus* and *C. helgolandicus* have received less attention for mass cultivation, mainly because of their lower temperature optima that slow down copepod generation times (Støttrup, 2000). *C. finmarchicus* is a key species living from the open ocean to coastal environments in the North Atlantic and North Sea (Bonnet et al., 2005), and has been extensively studied in the past ten years for its

* Corresponding author. Tel.: +39 0815833235; fax: +39 0817641355.
E-mail addresses: ylenia@szn.it (Y. Carotenuto), esposito@szn.it (F. Esposito), fabio.pisano@szn.it (F. Pisano), chiara.lauritano@szn.it (C. Lauritano), perna@szn.it (M. Perna), miralto@szn.it (A. Miralto), ianora@szn.it (A. Ianora).

0022-0981/$ – see front matter © 2012 Elsevier B.V. All rights reserved.
doi:10.1016/j.jembe.2012.03.014

Author's personal copy

link between phytoplankton standing stocks and fish secondary production (Tande and Miller, 2000). Recently, this species is also a model for ecotoxicological studies on the molecular effects of oil and other xenobiotics on copepod reproduction, survival and gene expression (Hansen et al., 2007, 2008a, 2008b, 2010). The first experiment to rear *C. finmarchicus* through multiple generations dates back to the end of the 1980s (Marcus and Alatalo, 1989), and was carried out in 10–20 l carboys using a mixed dinoflagellate diet. Recently, a static 100-l system for the cultivation of multiple generations of *C. finmarchicus* was reported for long-term testing on the biological effects of oil contaminants on all developmental stages (Jensen et al., 2006). For the same aims, a mass cultivation of *C. finmarchicus* has also been established at the SINTEF/NTNU (Norwegian University of Science and Technology) Sealab in Trondheim (Norway) since 2004 (http://www.sintef.no/Projectweb/Calanus—home/), although a detailed technical description of this culturing system is currently not available in the literature. *C. helgolandicus*, on the other hand, is very abundant in the temperate Atlantic Ocean and in the Mediterranean basin, particularly in the Adriatic Sea and off the coast of Spain (Bonnet et al., 2005). Due to an increase in water temperatures recorded in the last ten years, *C. helgolandicus* is gradually expanding its distribution northwards, showing higher abundances in the North Sea. As a consequence, *C. finmarchicus* is being confined to colder waters of the North Sea (Bonnet et al., 2005). In light of these distributional changes over the last decade, and considering the predicted further increase in water temperatures due to general global warming, the relevance of *C. helgolandicus* for the European system may become more important in the future.

C. helgolandicus is among the most widely studied copepod species when investigating the influence of temperature and food on development, growth, egg production and hatching success (Bonnet et al., 2009; Cook et al., 2007; Guisande and Harris, 1995; Jónasdóttir et al., 2005; Kang et al., 2000; Pond et al., 1996; Rey-Rassat et al., 2002a, 2002b). This species has also been the subject of several experimental and field studies focused on the negative effects of diatom secondary metabolites deriving from the oxidative metabolism of fatty acids (oxylipins), on hatching success and naupliar fitness (Buttino et al., 2008; Ianora and Miralto, 2010; Ianora et al., 2004; Irigoien et al., 2000a; Laabir et al., 1995; Miralto et al., 2003; Poulet et al., 1995, 2006, 2007; Wichard et al., 2008). These experiments have traditionally been conducted on wild-caught specimens kept for a few days or weeks in small volume containers, but so far, the species has never been reared for multiple generations. However, in order to perform year-round experiments with all larval stages, addressing basic questions concerning copepod physiology, ecotoxicology and gene expression studies, it would be useful to cultivate the species over multiple generations using a large-volume re-circulating system. Such systems have been previously used for the cultivation of the calanoid copepods *G. imparipes* (Payne and Rippingale, 2001), *T. stylifera* and *C. typicus* (Buttino et al., 2012).

The aim of our work was to employ the re-circulating water system located at the Stazione Zoologica Anton Dohrn and previously used by Buttino et al. (2012), to establish a massive multi-generation cultivation of *C. helgolandicus*. We maintained two copepod cultures over two successive years (2009 and 2010), during which we monitored time–course abundances of juveniles, copepodids and adults, as well as egg production, faecal pellet production and hatching success of females bred in the tank. The algae administered in mixed treatments were among the most widely used in small scale and intensive copepod cultures (World Copepod Culture Database, http://copepod.ruc.dk/main.htm): the prymnesiophyte *Isochrysis galbana*, the cryptophyte *Rhodomonas baltica*, the dinoflagellate *Prorocentrum minimum* and the diatom *Thalassiosira weissflogii*.

Although no detectable amount of any known deleterious oxylipins has been reported for the *T. weissflogii* strain used for our cultivation experiments (d'Ippolito pers comm), in order to reduce any possible harmful effect on population growth in our re-circulating system, this diatom was supplied in different food concentrations during the two experiments in 2009 and 2010. Thus, our set-up also offered a unique opportunity to investigate the influence of a changing food regime on total *C. helgolandicus* population growth, as well as on individual life-history parameters such as egg production and hatching success.

The output of our long-term multi-generation cultivation of *C. helgolandicus* was the harvesting of nearly 3000 healthy females in 2009, and nearly 800 females throughout 2010. These individuals were used to investigate the toxic effects of the oxylipin-producing diatom *Skeletonema marinoi* on gene expression patterns of *C. helgolandicus* (Lauritano et al., 2011a, 2011b; Carotenuto pers. comm.).

2. Methods

2.1. The re-circulating water system

A complete and detailed description of the re-circulating water system (Innovaqua srl, Reggio Emilia, Italy) located at the SZN is given in Buttino et al. (2012). Briefly, the system consisted of: a 400 l water accumulation tank (A); a bio-mechanical filter unit (B); two 500 l cylindrical fibreglass rearing tanks (C), each one connected to a 40 l cylindrical pre-tank for water temperature control (D), and provided with a suspended 50-μm-mesh size net (E); a UV lamp (F); a skimmer (G); three thermostats (H) (Fig. 1). The system was able to work in total water re-circulation mode, in which the water from both rearing tanks was biologically and mechanically purified in the filter unit; and a partial water re-circulation mode, in which the water from the cultivation tanks was maintained at the appropriate temperature through the pre-tank circulation. Circulation mode and timing were set and controlled by a Programmable Logic Control (PLC). The re-circulating water system, located in a temperature-controlled room set at 18 °C, was filled with 0.6-μm natural filtered seawater and left in total circulation mode for one month. The water temperature was set at 18 °C and the salinity at 38‰. The tank was gently aerated to allow 100% oxygen saturation level and illuminated from above with dim light on a 12:12 h L:D cycle.

2.2. Cultivation set-up

Calanus helgolandicus females, males and copepodids were sorted from zooplankton samples collected in the Adriatic Sea using a 200-μm-mesh size net. Specimens were incubated in several 1 l flasks filled with 0.2-μm filtered seawater and the dinoflagellate *P. minimum* (6000 cells ml^{-1}). Flasks were kept in a temperature-controlled chamber at 18 °C and brought to Naples in an insulated box within 24 h. A pre-culture of *C. helgolandicus* females, males, and copepodids feeding on *P. minimum* at 6000 cells ml^{-1} was kept in 10 l glass jars for 1 week. The culture was renewed three times per week and the eggs were collected, allowed to hatch and nauplii added to the pre-culture glass jar. The mixed *C. helgolandicus* population was placed in one of the 500 l rearing tanks to start the cultivation experiment in the re-circulating water system. Two experiments were conducted over two years: EXP1 in 2009, from mid-March to the beginning of September and EXP2 in 2010, from mid-May to the end of November. After the introduction of *C. helgolandicus* specimens, the re-circulating water system was set for 2 h of total circulation, allowing 40% renewal of the water through the biomechanical filter, followed by 6 h of partial circulation, allowing temperature maintenance but no algal loss.

2.3. Phytoplankton

C. helgolandicus in the re-circulating water system was fed with a mixed phytoplankton assemblage of the cryptophyte *R. baltica*, the

Author's personal copy

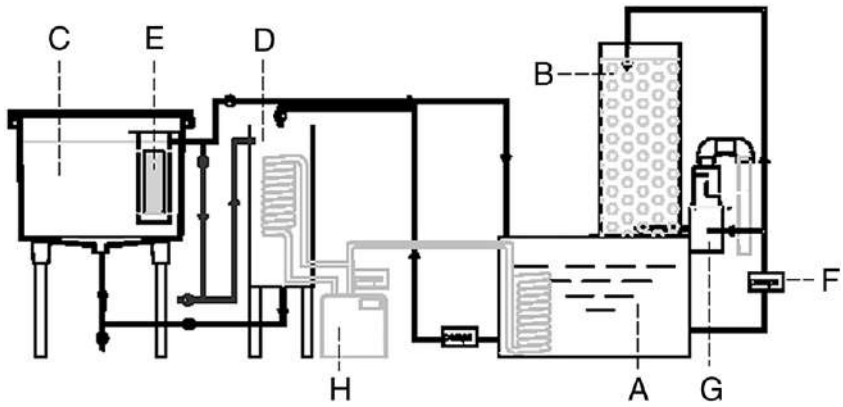

Fig. 1. Schematic drawing of the re-circulating system located at SZN and used for the intensive cultivation of *Calanus helgolandicus*: A, 400 l water accumulation tank; B, biomechanical filter unit; C, 500 l cylindrical fibreglass rearing tank; D, 40 l cylindrical pre-tank for water temperature control; E, suspended 50-μm-mesh size net; F, UV lamp; G, skimmer; H, thermostat.
After Buttino et al. (2012).

prymnesiophyte *I. galbana*, the dinoflagellate *P. minimum* and the diatom *T. weissflogii*, which have already been used in previous intensive copepod cultivations (Buttino et al., 2012; Jensen et al., 2006). Algal species were grown as semi-continuous batch cultures to late-exponential phase of growth in 10 l polycarbonate carboys containing K medium (Keller et al., 1987) (*R. baltica*, *P. minimum* and *I. galbana*), or f/2 medium (Guillard and Lorenzen, 1972) (*T. weissflogii*). Cultures were grown in a temperature-controlled chamber kept at 18 °C and on a 12:12 h light:dark cycle and gently aerated. Cell concentrations of each batch culture were determined daily and, depending on the algal cellular carbon content, an appropriate volume was supplied after the total water re-circulating mode. We ensured a total daily carbon food concentration in the cultivation tank of ~1.2 mg C l^{-1}, which is above the food saturation threshold for most calanoid copepods (Mauchline, 1998). Different algae and concentrations were supplied during the two cultivation experiments in 2009 and 2010. In 2009 (EXP1), we supplied *R. baltica* + *I. galbana* + *P. minimum* first (33:33:33 in terms of carbon), and *R. baltica* + *I. galbana* + *T. weissflogii* after (33:33:33 in terms of carbon). The diatom was introduced later to increase egg production and population growth of *C. helgolandicus*. Based on the results of the previous experiment, in 2010 (EXP2), we first supplied *R. baltica* + *I. galbana* + *T. weissflogii* at lower concentrations (50:34:15 in terms of carbon), and then switched to *R. baltica* + *I. galbana* + *P. minimum* (33:33:33 in terms of carbon) (Table 1).

2.4. Abundance and secondary production of C. helgolandicus

Abundances of *C. helgolandicus* juveniles and adults in the 500 l re-circulating tank were assessed in both EXP1 and EXP2. The water collected with a 5 l beaker from two opposite areas of the rearing tank was poured through a 50-μm-mesh size net to retain all larval stages of the population. The total number of nauplii, copepodids, adult males and females were assessed in each sample under a stereomicroscope, in order to calculate the average number of juveniles (nauplii and copepodids), and adults (males and females) in the rearing tank (ind. $tank^{-1}$). Specific population growth rate (r) of the *C. helgolandicus* culture was calculated using the following equation (Lee et al., 2006):

$$r = (\ln N_e - \ln N_i)/I$$

where, I is culture days when copepod density was the highest, N_i and N_e are the initial and highest copepod (from nauplii to adult) abundances, respectively.

Faecal pellet production, egg production and egg viability of females reared in the tank, were also determined weekly in both EXP1 and EXP2. Ten females were incubated individually in 100-ml crystallising dishes containing 100-μm filtered seawater from the rearing tank, after the addition of the mixed diet. Crystallising dishes were kept at 20 °C under a 12:12 h light:dark cycle. After 24 h, females were removed and transferred back to the rearing tank, whereas the eggs were counted under an inverted microscope. They were left to hatch and incubated again at 20 °C under a 12:12 h light:dark cycle. After 24 h the total number of hatched eggs was determined by counting the number of empty egg membranes, and the percentage of hatching success was assessed with respect to the eggs produced.

During EXP2, we also collected the eggs weekly from the sediment of the tank to determine egg hatching success. After gently syphoning the bottom of the tank, water was poured on a 50-μm-mesh size filter

Table 1
Algal species, algal cellular carbon content and total food concentrations supplied daily to the 500-l tank (cells ml^{-1} and mg C l^{-1}) during the cultivation of *Calanus helgolandicus* in 2009 (EXP1) and 2010 (EXP2).

Algal species	Cellular carbon content	Food concentration							
		EXP1				EXP2			
		MIX		MIX + high-*T. weissflogii*		MIX + low-*T. weissflogii*		MIX	
	(pg C $cell^{-1}$)	(Cells ml^{-1})	(mg C l^{-1})	(Cells ml^{-1})	(mg C l^{-1})	(Cells ml^{-1})	(mg C l^{-1})	(Cells ml^{-1})	(mg C l^{-1})
Isochrysis galbana	13.0	3×10^4	0.39	3×10^4	0.39	3×10^4	0.39	3×10^4	0.39
Rhodomonas baltica	130.5	3×10^3	0.39	3×10^3	0.39	4.5×10^3	0.59	3×10^3	0.39
Prorocentrum minimum	177.1	2.4×10^3	0.42	–	–	–	–	2.4×10^3	0.42
Thalassiosira weissflogii	113.2	–	–	3.5×10^3	0.40	1.5×10^3	0.17	–	
Total		3.5×10^4	1.20	3.6×10^4	1.18	3.6×10^4	1.15	3.5×10^4	1.20

Author's personal copy

to retain the eggs. From 100 to 400 eggs were collected with a wide-mouth pipette under the stereomicroscope and incubated in filtered seawater. They were counted under the inverted microscope and then left to hatch at 20 °C under a 12:12 h light:dark cycle. After 24 h the percentage of hatching success was assessed as described before.

2.5. Egg production experiments

During 2010, we tested the effect of *T. weissflogii*, *R. baltica* and a mixed *T. weissflogii* + *R. baltica* diet, on the reproduction of *C. helgolandicus*. These algae have never been tested before on this copepod and since many diatoms have been reported to have deleterious effects on copepods (Ianora and Miralto, 2010) we wanted to investigate if our *T. weissflogii* strain was harmful for *C. helgolandicus*. Fifteen females were sorted from the zooplankton sampled in the Adriatic Sea in 2010, and incubated in 100-ml crystallising dishes containing 0.22-μm filtered seawater and one of three algal diets: a monoalgal diet of *T. weissflogii* at a concentration of 9000 cells ml^{-1} (1 mg C l^{-1}), a monoalgal diet of *R. baltica* at a concentration of 8000 cells ml^{-1} (1 mg C l^{-1}) as control, and a 50:50 mixed diet of *R. baltica* + *T. weissflogii* (MIX) at a concentration of 4000 cells ml^{-1} (0.5 mg C l^{-1}) + 4500 cells ml^{-1} (0.5 mg C l^{-1}). Crystallising dishes were incubated as described before, at 20 °C under 12:12 h light: dark cycle. The algal medium was changed every day and daily egg production, pellet production, as well as percentage hatching success, were assessed for fifteen days.

Statistical analysis between life-history parameters for different diets was performed using GraphPad Prism v. 4.02 (GraphPad Software, Inc. 2004).

3. Results

3.1. EXP1

3.1.1. Population census

The first cultivation experiment (EXP1) started in March 2009 with 1556 total individuals inoculated in the 500 l re-circulating tank (800 nauplii, 130 copepodids, 420 females and 206 males), and terminated after 167 days with the collection of 3450 individuals (350 copepodids, 2850 females and 250 males). *C. helgolandicus* were fed with a mixed diet of *R. baltica* + *I. galbana* + *P. minimum* (33:33:33 in terms of carbon) from day 0 till day 117, and with *R. baltica* + *I. galbana* + *T. weissflogii* (33:33:33 in terms of carbon), from day 118 to day 161 (Table 1).

Three maximum population abundances consisting mainly of nauplii (66–86%) were recorded during the overall experiment: 12,550 ind. $tank^{-1}$ on day 15, 10,350 ind. $tank^{-1}$ on day 50, and 9600 ind. $tank^{-1}$ on day 127 (Fig. 2A, B). These population maxima corresponded to specific population growth rates of 0.14 d^{-1}, 0.038 d^{-1}, and 0.014 d^{-1}, respectively, and 8-fold, 6.7-fold, and 6-fold increase, compared to the initial number of individuals introduced in the breeding tank.

Naupliar abundance increased 13-fold after two weeks of cultivation, (10,750 ind. $tank^{-1}$), and this corresponded to the highest naupliar density measured during the experiment (Fig. 2A). The abundance decreased during the following weeks down to 1250 ind. $tank^{-1}$, peaked a second time on day 43 (9-fold increase, 7350 ind. $tank^{-1}$), and decreased afterwards to <500 ind. $tank^{-1}$ till day 105. A third and last maximum abundance of nauplii was detected on day 127 (9-fold increase, 7550 ind. $tank^{-1}$), nine days after the introduction of the diatom *T. weissflogii* to the diet (Fig. 2A). The census was then interrupted for one month, but the population was regularly fed with *R. baltica* + *I. galbana* + *T. weissflogii* at the same cell concentrations as before. Naupliar abundance had dropped to zero at the next census on day 161, and it did not increase in the following and last week of the experiment, even after *T. weissflogii* had been substituted with *P. minimum*.

Copepodids showed a first and highest peak on day 22 (5750 ind. $tank^{-1}$), which corresponded to a 44-fold increase with respect to initial copepodid numbers introduced in the tank. Their abundance decreased sharply afterwards, peaked again on day 50 with 3400 ind. $tank^{-1}$, and gradually reached very low values on day 69 (Fig. 2A). Copepodid numbers remained steady and low from day 79 till day 119 (<300 ind. $tank^{-1}$), showed a third and last maximum on day 127 (1550 ind. $tank^{-1}$), and dropped to <300 ind. $tank^{-1}$ at the termination of the cultivation experiment on day 167 (Fig. 2A).

Abundances of males and females decreased from ~200 and ~400 ind. $tank^{-1}$, respectively, introduced into the breeding tank, to 50 ind. $tank^{-1}$ during the first 22 days of cultivation. Male abundances remained low till day 119, with no males at all from day 69 to day 99, but increased and remained stable around the highest value of 300 ind. $tank^{-1}$, with the mixed *R. baltica* + *I. galbana* + *T. weissflogii* diet till the end of the cultivation experiment. In contrast, female abundances increased from day 22 to day 36 up to a maximum of 350 ind. $tank^{-1}$, and then decreased and levelled off to 150 ind. $tank^{-1}$, until day 119. Abundances of females slightly improved afterwards (300 ind. $tank^{-1}$ on day 127), and were highest on day 167(2850 ind. $tank^{-1}$), about fifty days after the introduction of the *R. baltica* + *I. galbana* + *T. weissflogii* diet to the re-circulating system (Fig. 2B).

Dominance of females over males was also clear from the dynamics of male:female sex ratios. The initial sex ratio of 0.5 increased to 1 after 2–3 weeks of cultivation, but was usually <0.5 for most of the experiment; it dropped to zero from day 69 to day 99, indicating the absence of males from the culture. Male:female ratio increased slightly afterwards, remaining between 0.3 and 0.7 for a month, but dropped again to <0.1 at the end of the experiment (Fig. 2C).

Dynamics of copepodid and naupliar abundances were positively correlated with a 7-d delay (Pearson rank correlation, $r_p = 0.93$, $N = 17$, $p < 0.0001$); hence the duration of the naupliar phase of *C. helgolandicus* in the re-circulating system was seven days. Moreover, because maximum copepodid and adult abundances occurred on days 22 and 36, respectively, the duration of the copepodid phase of *C. helgolandicus* was fourteen days, and the total generation time from nauplius to adult was twenty-one days. Comparing abundances of nauplii, copepodids and adults at their maxima on days 15, 22 and 36, respectively, we estimated a loss of 46.5% from nauplii to copepodids, 93% from copepodids to adults and a total population loss of 96.3% from nauplius to adult.

3.1.2. Secondary production

Faecal pellet production for *C. helgolandicus* females incubated in unfiltered seawater collected from the 500 l tank, ranged from 27.8 pellets · fem^{-1} d^{-1} to 71.3 pellets fem^{-1} d^{-1}, during the *R. baltica* + *I. galbana* + *P. minimum* food treatment, and from 43.1 pellets fem^{-1} d^{-1} to 106.4 pellets fem^{-1} d^{-1}, during the *R. baltica* + *I. galbana* + *T. weissflogii* diet (Fig. 3A). The presence of *T. weissflogii*, thus, significantly increased the average pellet production of *C. helgolandicus* (78.2 ± 26.7 pellets · fem^{-1} d^{-1} compared to 44.0 ± 15.2 pellets fem^{-1} d^{-1}, respectively. Unpaired *t* test, $t_{11} = 300$, $p < 0.05$).

Similarly, lower egg production rates were measured with the *R. baltica* + *I. galbana* + *P. minimum* diet (from 0.3 eggs fem^{-1} d^{-1} to 9.4 eggs fem^{-1} d^{-1}), compared to when *T. weissflogii* replaced *P. minimum* (from 10.2 eggs fem^{-1} d^{-1} to 20.3 eggs fem^{-1} d^{-1}) (Fig. 3B). Mean egg production, thus, was significantly higher in presence of the mixed food assemblage containing the diatom (13.5 ± 4.7 eggs fem^{-1} d^{-1} vs. 3.3 ± 2.7 eggs fem^{-1} d^{-1}, respectively. Unpaired *t* test, $t_{11} = 5.0$, $p < 0.001$). Temporal dynamics of egg production was mirrored by that of the percentage of spawning females, which ranged between 11% and 70% when copepods were feeding on *R. baltica* + *I. galbana* + *P. minimum*, and from 60% to 100% in the presence of *R. baltica* + *I. galbana* + *T.*

Author's personal copy

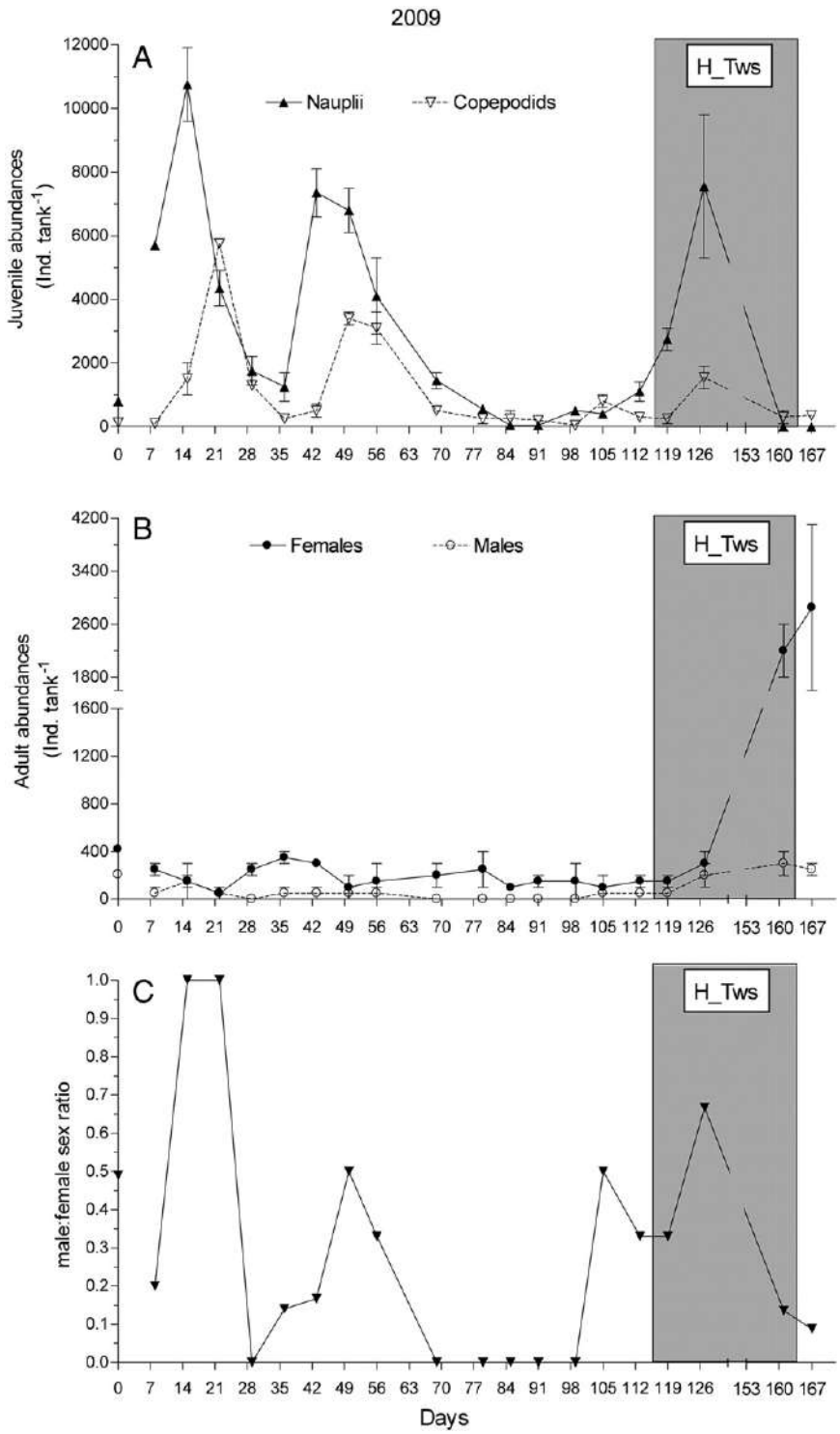

Fig. 2. Temporal dynamics for total A, juveniles (nauplii and copepodids) and B, adults (males and females), and C, male : female sex ratio of *Calanus helgolandicus* collected from the 500 l re-circulating system during the cultivation experiment in 2009 (EXP1). White area: with a *Rhodomonas baltica* + *Isochrysis galbana* + *Prorocentrum minimum* mixed diet (33:33:33 in terms of carbon). Dark grey area: with a *R. baltica* + *I. galbana* + *Thalassiosira weissflogii* mixed diet (33:33:33 in terms of carbon). Symbols are means ± se.

weissflogii. Average percentage of spawning females during this treatment was significantly higher than that with the previous diet (87.5 ± 18.9% vs. 34.6 ± 18.0%, respectively. Unpaired *t* test, $t_{11} = 4.8$, $p < 0.001$).

Egg hatching success ranged from 0.0% to 88.0%, when the copepods were feeding on *R. baltica* + *I. galbana* + *P. minimum*, and from 33.2% to 86.0%, during the following *R. baltica* + *I. galbana* + *T. weissflogii* treatment (Fig. 3C). However, the reasons for the lower values in both periods were probably different. Males were absent from the re-circulating system when the lowest percentages of hatching success were measured (from 0.0% to 13.2% from day 56 to day 99), (see Fig. 2B, C). These eggs were probably un-fertilised, as suggested by the absence of embryo blastomers 24 h after spawning, and by the leakage of cytoplasm from the egg (unpublished observations), a sign of loss of membrane integrity that has been previously reported in un-fertilised eggs (Turner et al., 2001). In contrast, eggs spawned on days 139 and 161 during the *R. baltica* + *I. galbana* + *T.*

Author's personal copy

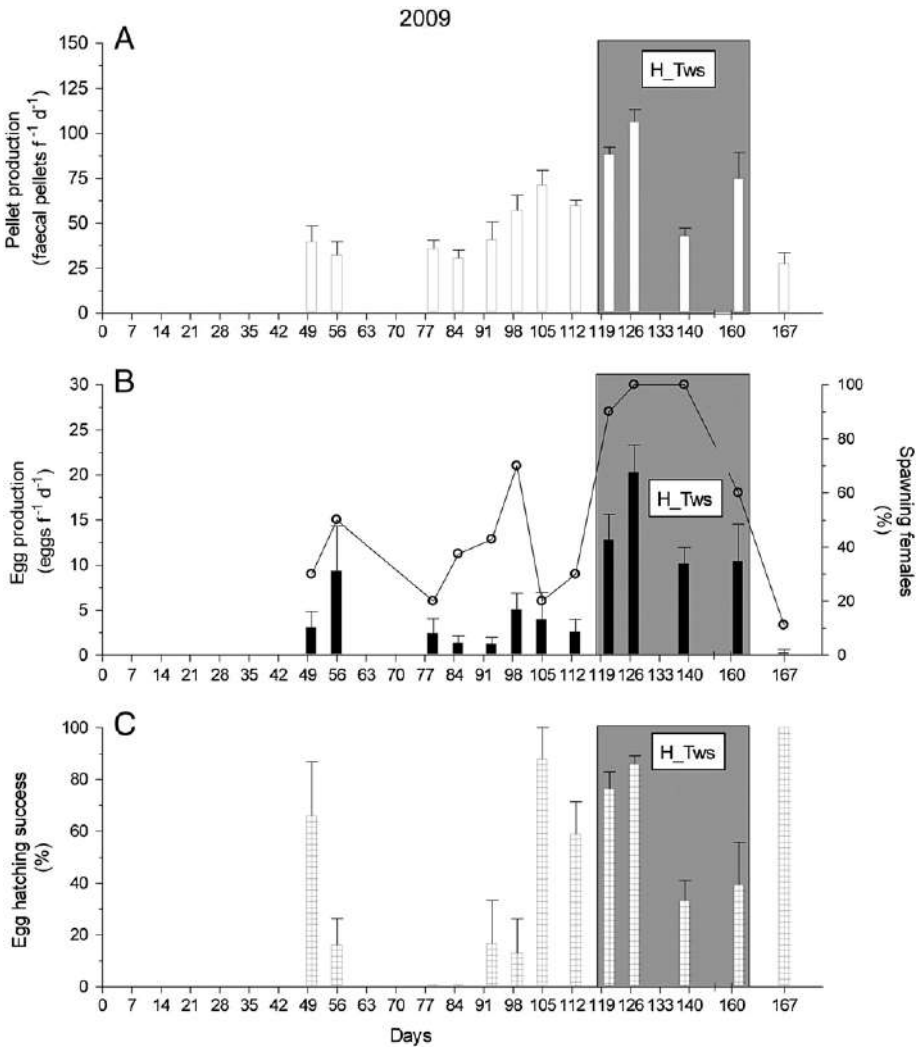

Fig. 3. Temporal dynamics for A, faecal pellet production, B, egg production and % of spawning females, C, hatching success of *Calanus helgolandicus* collected from the 500 l recirculating system during the cultivation experiment in 2009 (EXP1). White area: with a *Rhodomonas baltica* + *Isochrysis galbana* + *Prorocentrum minimum* mixed diet (33:33:33 in terms of carbon). Dark grey area: with a *R. baltica* + *I. galbana* + *Thalassiosira weissflogii* mixed diet (33:33:33 in terms of carbon). Bars are means ± se.

weissflogii feeding, having a hatching success of 33.2% and 39.4%, remained blocked at advanced embryonic developmental stages for 48 h, and did not show any cytoplasm leakage. In this period, males reached their maximum abundance (see Fig. 2B, C).

3.2. EXP2

3.2.1. Population census

The second cultivation experiment (EXP2) started on May 2010 with less individuals compared to EXP 1 due to a lower sampling frequency of the zooplankton in the Adriatic Sea. In total, 230 individuals were introduced in the 500 l cultivation tank (150 nauplii, 60 adult females and 20 adult males). The experiment was terminated after 186 days, when no more individuals were present. *C. helgolandicus* was fed with *R. baltica* + *I. galbana* + *T. weissflogii*, at lower concentrations compared to EXP1 (50:34:15 in terms of carbon), from day 0 till day 104, and with *R. baltica* + *I. galbana* + *P. minimum* (33:33:33 in terms of carbon) from day 105 to day 186 (Table 1). Only one maximum population abundance, consisting mainly of nauplii (65%), was recorded during the overall experiment, with 9150 ind. tank^{-1}on day 55, in presence of the mixed flagellate + diatom diet (Fig. 4A, B). This corresponded to a specific population growth rate of 0.067 d^{-1} and a 40-fold increase compared to the initial number of individuals introduced in the breeding tank.

Naupliar abundance increased 12-fold after 26 days of cultivation (1850 ind. tank^{-1}), remained stable for the following three weeks and peaked on day 55 with 5950 ind. tank^{-1} (40-fold increase), which corresponded to the highest naupliar density ever measured (Fig. 4A). Number of nauplii constantly decreased during the following weeks, when copepods were receiving *R. baltica* + *I. galbana* + *T. weissflogii*, and was zero on day 102. The abundance slightly increased after the diet was switched to *R. baltica* + *I. galbana* + *P. minimum* (up to 650 ind. tank^{-1} on day 146), but then ultimately declined to zero on day 186, when the experiment was terminated (Fig. 4A).

Copepodid abundances ranged from 400 to 1000 ind. tank^{-1} during the first six weeks of cultivation; it then increased linearly to the highest value of the experiment of 3500 ind. tank^{-1} on day 61 (Fig. 4A). As observed for nauplii, copepodid numbers also decreased gradually till day 102, to 150 ind. tank^{-1}. After the diet was changed to *R. baltica* + *I. galbana* + *P. minimum*, two more high abundances were observed (250 ind. tank^{-1} and 150 ind. tank^{-1} on days 130 and 160, respectively). No copepodids were found in the sampling during the last census on day 186 (Fig. 4A).

Abundance of females increased gradually from 60 individuals introduced into the tank, to the highest value of 1300 ind. tank^{-1} on day 76. It then decreased constantly to a minimum of 50 ind. tank^{-1} on day 146, and remained low until the last day of the experiment,

Author's personal copy

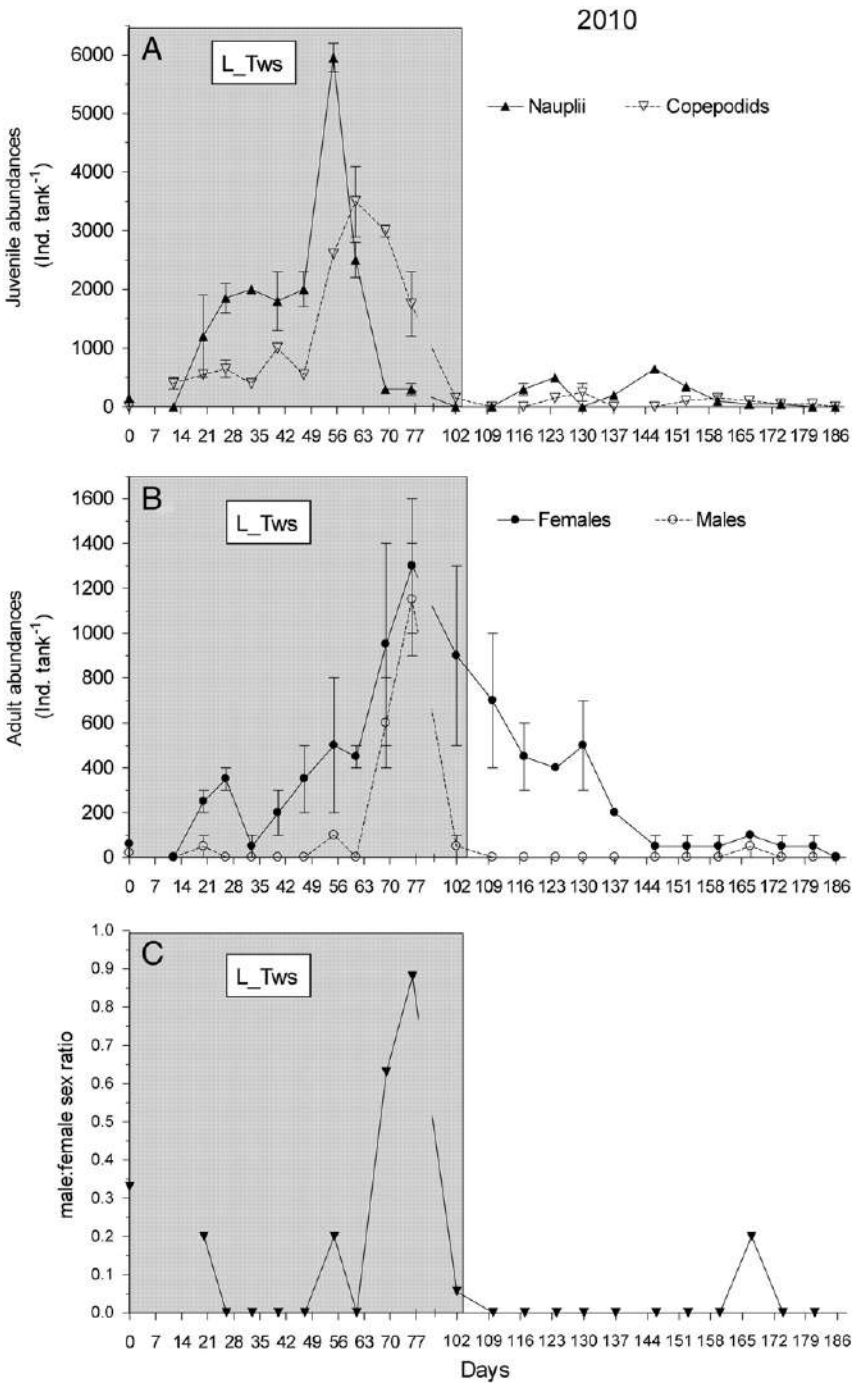

Fig. 4. Temporal dynamics for total A, juveniles (nauplii and copepodids) and B, adults (males and females), and C, male : female sex ratio of *Calanus helgolandicus* collected from the 500 l re-circulating system during the cultivation experiment in 2010 (EXP2). Light grey area: with a *Rhodomonas baltica* + *Isochrysis galbana* + *Thalassiosira weissflogii* mixed diet (50:34:15, in terms of carbon). White area: with a *R. baltica* + *I. galbana* + *Prorocentrum minimum* mixed diet (33:33:33 in terms of carbon). Symbols are means ± se.

when no females were detected at all (Fig. 4B). Abundance of males was much lower then that of females, with not a single male detected on most of the sampling dates. However, the number of males also peaked on day 76 as females, with 1150 ind. $tank^{-1}$. The very low number of males was mirrored by the male:female sex ratio, which was 0.3 at the beginning of the experiment but was usually between 0 and 0.2, except on days 69 and 76 when it was close to 1 (Fig. 4C).

As occurred in EXP1, dynamics of copepodid and naupliar abundances were positively correlated with a 7-d delay (Pearson rank correlation, $r_p = 0.82$, $N = 22$, $p < 0.0001$); as were dynamics of adult stages and copepodid abundances positively correlated with a 14-d delay (Pearson rank correlation, $r_p = 0.89$, $N = 23$, $p < 0.0001$). Hence, once again durations of naupliar and copepodid phases of *C. helgolandicus* were seven and fourteen days, respectively; and the total generation time from nauplius to adulthood was twenty-one days. Comparing abundances of nauplii, copepodids and adults at their maxima (on days 55, 61 and 76, respectively), we estimated a loss of 41.2% from nauplii to copepodids, 30.0% from copepodids to adults, and a total population loss of 58.8% from nauplii to adults.

3.2.2. Secondary production

Faecal pellet production for *C. helgolandicus* females in EXP2 ranged from 37.2 pellets $fem^{-1}\,d^{-1}$ to 120.8 pellets $fem^{-1}\,d^{-1}$ with *R. baltica* + *I. galbana* + *T. weissflogii*, and from 10.6 pellets $fem^{-1}\,d^{-1}$

Author's personal copy

to 55.2 pellets fem^{-1} d^{-1} with *R. baltica* + *I. galbana* + *P. minimum* (Fig. 5A). On average, pellet production was significantly higher with the mixed food assemblage containing the diatom (64.8 ± 24.6 pellets fem^{-1} d^{-1}, compared to 33.5 ± 14.4 pellets fem^{-1} d^{-1}, respectively. Unpaired *t* test, $t_{19} = 3.60$, $p < 0.01$).

Similarly, higher egg production rates were measured with *R. baltica* + *I. galbana* + *T. weissflogii* (from 1.6 eggs fem^{-1} d^{-1} to 15.1 eggs fem^{-1} d^{-1}), compared to *R. baltica* + *I. galbana* + *P. minimum* (from 0.0 eggs fem^{-1} d^{-1} to 6.3 eggs fem^{-1} d^{-1}) (Fig. 5B). Mean egg production in the presence of *T. weissflogii* was, in fact, significantly higher than that with the mixed flagellate diet (9.8 ± 3.9 eggs fem^{-1} d^{-1} vs. 3.2 ± 2.7 eggs fem^{-1} d^{-1}, respectively. Unpaired *t* test, $t_{19} = 4.57$, $p < 0.001$).

Again, temporal dynamics of the percentage of spawning females and egg production rates were positively correlated (Pearson rank correlation, $r_p = 0.82$, $N = 21$, $p < 0.0001$) (Fig. 4B). However, the spawning activity of the females did not change depending on the mixed food assemblages, being on average 53.4 ± 19.8% and 34.4 ± 29.3%, respectively (unpaired *t* test, $t_{19} = 1.72$, $p > 0.05$).

Egg hatching success was very high at the beginning of the cultivation experiment (85.5%), but gradually decreased with the *R. baltica* + *I. galbana* + *T. weissflogii* diet to 41.4% on day 76 and 0% on day 102 (Fig. 5C). After the diatom was removed from the assemblage (diet switched to *R. baltica* + *I. galbana* + *P. minimum*), hatching success partially recovered during the following weeks (50.0% on day 146). It definitely dropped to zero toward the end of the experiment, probably due to the production of a high number of unfertilised eggs (Fig. 5C).

The same trend in hatching success was also observed for eggs sampled from the bottom of the 500 l tank, which was usually above 60% until day 76, then ranged from 0% to 2.7% from day 102 to day 117, and from 51.3% to 82.6% from day 137 to day 160 (Fig. 6).

3.3. Copepod incubation experiments

Faecal pellet production of *C. helgolandicus* females feeding on a unialgal *R. baltica* diet decreased during the 2-week incubation experiment from 76.1 pellets fem^{-1} d^{-1} on day 1, to 43.9 pellets fem^{-1} d^{-1} on day 15 (Fig. 7). Similarly, initial egg production was 19.1 eggs fem^{-1} d^{-1}, but was reduced to 6.7 eggs fem^{-1} d^{-1} after three days of feeding, remaining almost stable for the rest of the experiment. Hatching success was high and stable during the experiment, from 90.1% to 76.5% (Fig. 7).

A monoalgal diet of *T. weissflogii* induced an initially high faecal pellet production in *C. helgolandicus*, which then decreased toward the end of the experiment (from 141.1 pellets fem^{-1} d^{-1} on day 1 to 23.0 pellets fem^{-1} d^{-1} on day 15) (Fig. 7). This trend mirrored that for egg production, which decreased from 21.1 eggs fem^{-1} d^{-1}

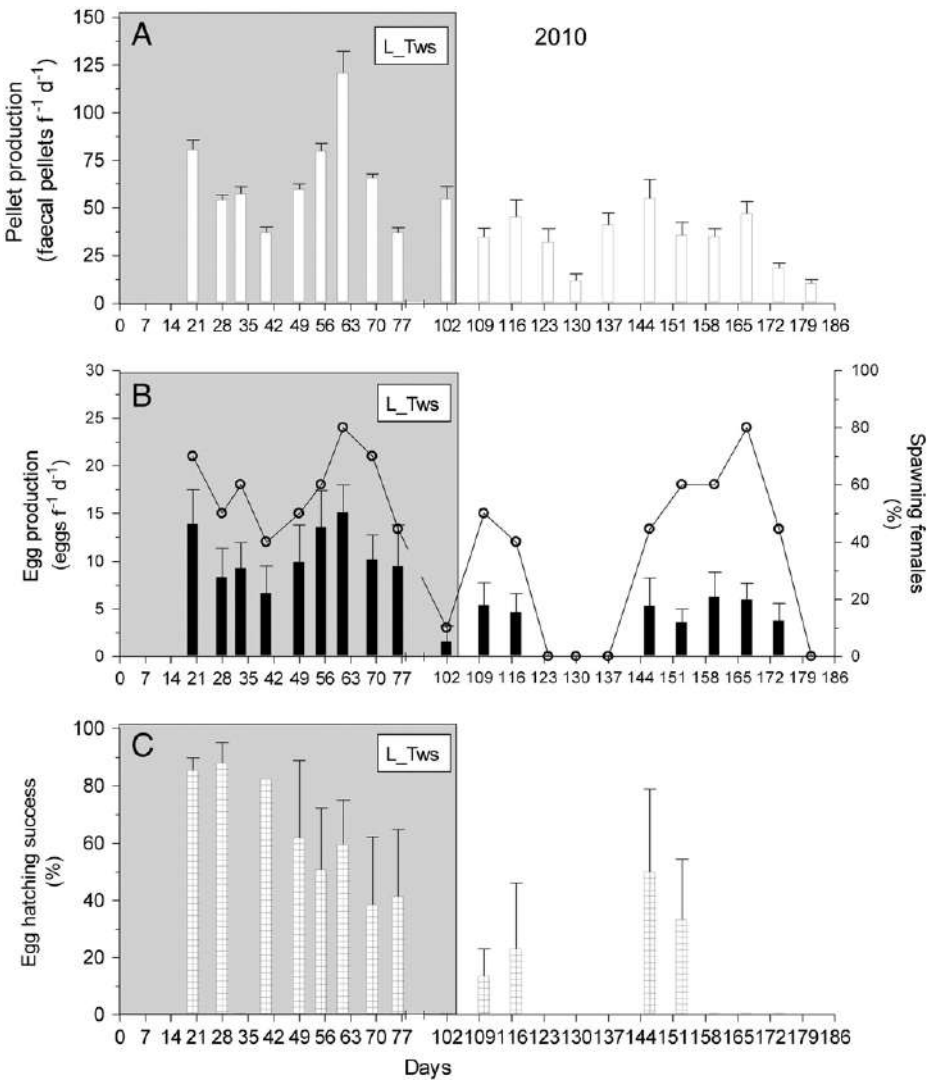

Fig. 5. Temporal dynamics for A, faecal pellet production, B, egg production and % of spawning females, and C, hatching success of *Calanus helgolandicus* collected from the 500 l recirculating system during the cultivation experiment in 2010 (EXP2). Light grey area: with a *Rhodomonas baltica* + *Isochrysis galbana* + *Thalassiosira weissflogii* mixed diet (50:34:15, in terms of carbon). White area: with a *R. baltica* + *I. galbana* + *Prorocentrum minimum* mixed diet (33:33:33 in terms of carbon). Bars are means ± se.

Author's personal copy

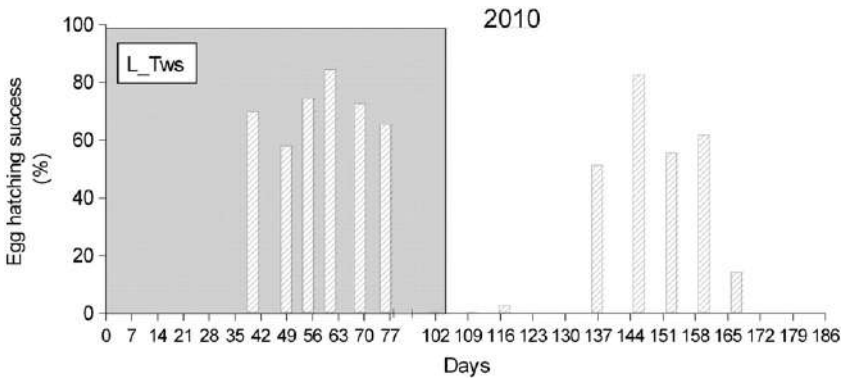

Fig. 6. Temporal dynamics for *Calanus helgolandicus* egg hatching success for eggs collected from the bottom of the 500 l tank during the cultivation experiment in 2010 (EXP2). Light grey area: with a *Rhodomonas baltica* + *Isochrysis galbana* + *Thalassiosira weissflogii* mixed diet (50:34:15, in terms of carbon). White area: with a *R. baltica* + *I. galbana* + *Prorocentrum minimum* mixed diet (33:33:33 in terms of carbon). Bars are values from a pooled egg sample.

to 0.0 eggs fem^{-1} d^{-1}. The diatom diet also reduced egg hatching success from 91.4% to 30.0% after five days of feeding, and to 0.0% at the end of the experiment (Fig. 7).

Compared to both algae used as single diets, the mixed *R. baltica* + *T. weissflogii* diet induced a higher and steady faecal pellet production rate (from 145.6 pellets fem^{-1} d^{-1} on day 1, to 70.2 pellets fem^{-1} d^{-1} on day 15), a slightly higher egg production rate (from 12.9 eggs fem^{-1} d^{-1} to 2.2 eggs fem^{-1} d^{-1}), and an intermediate egg hatching success (from 91.3% to 46.4%) (Fig. 7).

On average, production of faecal pellets during the 15-day incubation experiment was significantly higher with *R. baltica* + *T. weissflogii* and *T. weissflogii* (139.1 ± 34.8 pellets fem^{-1} d^{-1} and 116.5 ± 45.7 pellets fem^{-1} d^{-1}) than with *R. baltica* (54.5 ± 14.7 pellets fem^{-1} d^{-1}) (ANOVA, $F_{(2,42)} = 24.5$, $p < 0.001$). Egg production, in contrast, was only significantly higher with *R. baltica* + *T. weissflogii* compared to *R. baltica* (16.1 ± 7.3 eggs fem^{-1} d^{-1}, and 7.2. ± 4.1 eggs fem^{-1} d^{-1}, respectively) (ANOVA, $F_{(2,42)} = 6.34$, $p < 0.01$). Egg hatching success was significantly higher with *R. baltica* (89.1 ± 7.0%), intermediate with *R. baltica* + *T.*

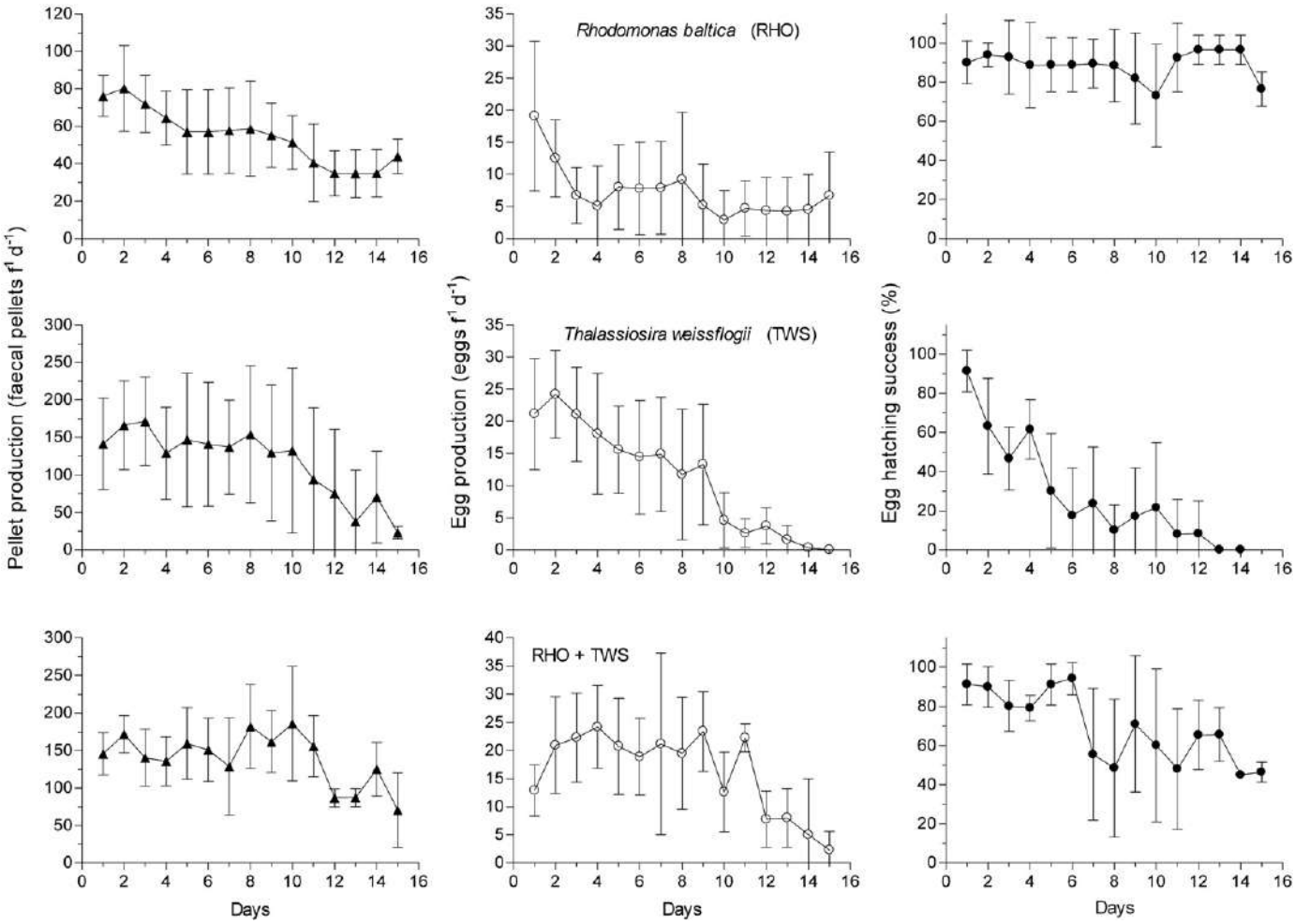

Fig. 7. Daily faecal pellet production, egg production and hatching success for *Calanus helgolandicus* during feeding experiments with *Rhodomonas baltica* (upper panel), *Thalassiosira weissflogii* (middle panel) and mixed *R. baltica* + *T. weissflogii* (lower panel) diets. Symbols are means ± sd.

Author's personal copy

weissflogii (68.8 ± 18.0%) and lower with *T. weissflogii* (28.5 ± 27.3%) (ANOVA, $F_{(2,41)} = 37.6$, $p < 0.001$).

4. Discussion

Our study is the first reporting the intensive cultivation of the calanoid copepod *C. helgolandicus* through multiple generations. In two separate cultivation experiments carried out in 2009 and 2010, we show that a mixed diet of the prymnesiophyte *I. galbana*, the cryptophyte *R. baltica*, the dinoflagellate *P. minimum* and the diatom *T. weissflogii*, was able to sustain the development and reproduction of the copepod continuously for six months. In 2009, the culture was terminated because all adult females generated in the breeding tank were used in gene expression studies (Lauritano et al., 2011a, 2011b; Carotenuto et al. unpubl data), whereas in 2010, the experiment was terminated due to ageing of the population and the lack of individuals in the tank.

Our findings show that open-water calanoids such as *C. helgolandicus* are amenable to intensive cultivation over multiple generations in large-scale facilities, though lower densities are attained with respect to smaller neritic species, such as *T. stylifera* and *C. typicus* (Buttino et al., 2012), *A. tonsa* (Drillet et al., 2006), and *G. imparipes* (Payne and Rippingale, 2001). This was probably related to the higher reproductive activity of these neritic species compared to *C. helgolandicus* previously reported in laboratory feeding experiments (Carotenuto et al., 2006; Miralto et al., 1999), or to the greater sensitivity of *C. helgolandicus* to crowding.

The generation time of *C. helgolandicus* from nauplius to adult in our system was 21 days in both experiments, with relative durations of naupliar and copepodid phases of 7 and 14 days, respectively. These are shorter than times reported in previous *C. helgolandicus* rearing experiments conducted in the laboratory, in which development from nauplius to adulthood at a temperature of 20 °C ranged from 26 to 28 days on a monoalgal diet of *P. minimum* (Ianora et al., 2004). The reduced development time was not due to a higher rearing temperature in the re-circulating system (18 °C), but more likely to the mixed diet that shortened copepod development times.

C. helgolandicus population reached the highest instantaneous growth rate of in 2009 after only two weeks of cultivation (0.14 d^{-1}), which corresponded to a 8-fold increase in the total number of copepods, with respect to initial numbers introduced into the 500 l tank. Since this population was mainly formed by nauplii (86%), it is likely that the adult females introduced at the beginning into the system were well fed and had a high amount of lipid reserves that sped up initial naupliar production. A similar high initial population increase has been reported during the mass cultivation of *T. stylifera* (26-fold) and *C. typicus* (10-fold), with a mixed diet of *I. galbana* + *R. baltica* + *P. minimum* (Buttino et al., 2012), and whose nauplii were collected daily for use as live feed for clownfish larvae (Olivotto et al., 2008). This early high population growth of *C. helgolandicus* was not observed in 2010, probably because the females introduced into the tank were collected later that year (May) and had lower lipid reserves than those introduced in 2009 and sampled in March. Despite this, however, the second generation of copepods that had developed and were actively reproducing in the tank during 2010, was more productive than the previous year. Comparing values in both cultivation experiments after 50–55 days, in fact, population growth rates were ~2-times higher (0.067 d^{-1} vs. 0.038 d^{-1}) and abundances increased 6-times more (40-fold vs. 6.7-fold) during 2010 than in 2009. This higher population growth rate was related to both a higher egg production rate and percentage of spawning females (see Figs. 3 and 5), and also to a lower loss from copepodids to adults (30% in 2010 vs. 93% in 2009). The only difference between the two cultivation experiments was the diet supplied to the population: a mixed *R. baltica* + *I. galbana* + *P. minimum* in 2009 and a mixed *R. baltica* + *I. galbana* + *T. weissflogii* in 2010. In addition, the overall fecundity of *C. helgolandicus* females during 2010 was significantly higher in the presence of *T. weissflogii* than with *P. minimum*. We therefore conclude that even if a diet of the flagellates *R. baltica* and *I. galbana* was a suitable food for the development and survival of *C. helgolandicus* nauplii, the addition of the diatom *T. weissflogii* to the mixed assemblage at low concentrations (0.17 mg C l^{-1}) and for short time intervals (<2 months), reduced copepodid mortality, improved female egg production and spawning activity, and in turn, increased population growth rate.

These findings confirm previous results obtained in copepod incubation experiments and mass cultivation facilities. *I. galbana* and *R. baltica* have already been shown to support high development rates and survival in several calanoids such as *T. stylifera* (Buttino et al., 2009; Carotenuto et al., 2002), *C. typicus* (Buttino et al., 2009), *A. tonsa* (Ismar et al., 2008) and *G. imparipes* (Payne and Rippingale, 2001). Additionally, *P. minimum* sustained the development of *C. helgolandicus* from hatching to the spawning of the resulting adult female population (Ianora et al., 2004; Rey-Rassat et al., 2002a, 2002b). Fast development and high gross growth efficiency (body carbon/carbon ingestion) was also reported for this copepod species when fed *I. galbana* and *R. baltica*, possibly due to the ease of assimilation of these small naked algae (Rey et al., 2001). A mixed *I. galbana* + *R. baltica* diet was also optimal for the mass cultivation of *G. imparipes* (Payne and Rippingale, 2001), *Acartia tranteri* (Morehead et al., 2005), *T. stylifera* and *C. typicus* (Buttino et al., 2012). Similarly, the diatom *T. weissflogii* supported fast development and high naupliar production in *A. tonsa* (Ismar et al., 2008), *Temora longicornis* (Arendt et al., 2005; Klein Breteler et al., 2005; Koski, 2008), *Pseudocalanus elongatus* (Klein Breteler et al., 2005) and *C. typicus* (Bonnet and Carlotti, 2001). This diatom has also been used at low concentrations (100–1000 cells ml^{-1}) for the cultivation of *C. finmarchicus* for up to three generations (Jensen et al., 2006). Diatoms are usually rich in polyunsaturated fatty acids and sterols (Brown et al., 1997; Hassett, 2004; Jónasdóttir, 1994), and have been reported to sustain higher egg production in copepods compared to flagellates. For example, fecundity of *T. longicornis* was higher in the presence of *T. weissflogii* than with the chlorophyte *Dunaliella tertiolecta* (Arendt et al., 2005), and the same was observed for *A. tonsa* feeding on *T. weissflogii* compared to *P. minimum* (Dam and Colin, 2005).

A side effect of the addition of the diatom to our re-circulating system, however, was a significant reduction in *C. helgolandicus* egg hatching success in both cultivation experiments when *T. weissflogii* was supplied in higher carbon concentration (0.40 mg C l^{-1}) or for longer periods (>3 months) (see Figs. 3C, 5C, and Fig. 6). As a consequence, reduced naupliar abundance in the 500 l tank was registered during the same periods (see Figs. 2A and 4A), thus, leading to a reduced population growth of *C. helgolandicus*. The deleterious effect of *T. weissflogii* on *C. helgolandicus* hatching success was confirmed by our results monitoring the copepod reproduction in 100-ml crystallising dishes. In these short-term feeding experiments, hatching success after fifteen days were 0% and 46.5% in the presence of *T. weissflogii* and *R. baltica* + *T. weissflogii*, respectively (Fig. 7). The longer feeding times in our re-circulating system during both 2009 and 2010 may have further reduced copepod hatching success to zero even if the diatom was supplied in combination with the two flagellates. Removing *T. weissflogii* from the mixed diet in 2010 improved copepod hatching success to 50–80% (see Figs. 5C and 6, from day 102 onwards), thus allowing production of two new naupliar cohorts in the tank (see Fig. 4A, days 124 and 145). A similar reversible effect on copepod hatching success when a diatom diet is replaced by a dinoflagellate diet has been reported previously. Egg viability in the copepod *Calanus pacificus* fed the diatoms *T. weissflogii* or *Chaetoceros difficilis* for 10–12 days, and then switched to *P. minimum* increased from 30% and 10%, respectively, to 90% in only two days (Uye, 1996). The same was observed for *C. helgolandicus* fed *Thalassiosira rotula* and then switched to *P. minimum*, with hatching success recovering from zero to 80% in 2–3 days (Ianora et al., 2003).

Author's personal copy

In recent years, it has been shown that marine diatoms release several products derived from the oxidative metabolism of lipids and fatty acids that are termed oxylipins (Fontana et al., 2007). These molecules impair hatching success and naupliar viability in many copepod species, inducing apoptosis in embryos, nauplii and females (for a review see Ianora and Miralto, 2010). Diatoms and diatom oxylipins have also been suggested to impair the recruitment of *C. helgolandicus* populations at sea (Ianora et al., 2004). Reduced copepod population growth in the presence of diatom diets has also been reported in large-volume copepod incubation experiments and intensive cultures. The body-carbon-specific naupliar production in *C. helgolandicus* females kept in natural-seawater-enriched mesocosms was lowest in diatom-dominated mesocosms ($<5.2\%\,d^{-1}$) compared to those where a flagellate–microzooplankton bloom developed ($10.6\%\ d^{-1}$) (Nejstgaard et al., 2001). Similarly, highest fecundity but lower naupliar viability and population growth was reported in the intensive cultivation of *Parvocalanus* sp. with the monospecific diatom diet *Chaetoceros* sp., compared to *I. galbana* alone or a mixed *Chaetoceros* sp. + *I. galbana* diet (Shields et al., 2005). A reduction in egg viability from 80% to 35% was reported during the mass culturing of several copepod species in the Philippines with a mixed diet of flagellates and the diatoms *Chaetoceros* sp. or *Skeletonema* sp. (O'Bryen, and Lee, 2005).

Diatoms can thus sustain very high copepod fecundity but also reduce embryo viability and, in turn, copepod population growth in intensive cultivation systems. The reasons for reduced hatching success and naupliar production of *C. helgolandicus* in our study are not clear. Since no detectable amount of any known deleterious oxylipins has been found in the *T. weissflogii* strain used in our cultivation (d'Ippolito pers comm), we do not know whether this diatom produced other unknown harmful compounds impairing copepod embryo viability, or if the causes leading to lower embryo viability and naupliar production are more complex. As suggested by others, for example, incomplete digestion of diatom cells during gut passage may lead to nutritional deficiencies that impair copepod hatching (Dutz et al., 2008); or such a deficiency might occur due to the depletion of diatom polyunsaturated fatty acids which are converted into oxylipins during diatom cell disruption and grazing (Wichard et al., 2007). Whatever the reasons, our results confirm previous findings on the use of appropriate mixed diatom assemblages for short periods in order to fuel egg production without impairing embryo viability and allow long-term copepod mass cultivation (Shields et al., 2005).

Two common problems often encountered during copepod cultivations are the scarcity of males and the ageing of the culture. The reasons for unbalanced sex ratio have been related to starvation (Gusmão and Mckinnon, 2009; Irigoien et al., 2000b), sex-specific mortality (Avery et al., 2008), impaired male development (Carotenuto et al., 2011), and age-related mortality (Rodríguez-Graña et al., 2010). This latter study, in particular, reported that during prolonged cultivation, copepod males showed stronger oxidative damage compared to females, probably due to their lower biomass turnover compared to females (spermatophore production vs. egg production). Thus, a reduced male abundance in copepod cultures could be explained by their higher age-related mortality rates. In our experiments, the male : female sex ratio of *C. helgolandicus* was usually quite low, but it affected the copepod population growth only marginally. In particular, no males were found from day 69 to day 99 during 2009, thus explaining the zero hatching success measured in that period (see Figs. 2C and 3C). Whereas during 2010, the absence of males was a limiting factor only toward the end of the experiment, when no males were found in the tank for at least three months and naupliar abundance, as well as egg hatching success was very low. It is likely that the lack of female fertilisation in this latter period reduced naupliar recruitment of *C. helgolandicus*. This is supported by the observation that the eggs produced dissolved as soon as they were laid, as occurs in unfertilised eggs where the membrane is very soft (unpublished observations). Possibly, the co-occurrence of low mating success and the senescence of females, eventually led to the final crash of the culture in 2010.

Recently, Rodríguez-Graña et al. (2010) showed that *A. tonsa* females kept in culture for up to 50 days, from senescence to death, gradually reduced their egg production, hatching success and naupliar production rate. This was possibly related to maternal-mediated oxidative damage in eggs and first-feeding nauplii, as indicated by the high level of oxidative modified proteins in nauplii spawned by older females. There was also a correlation between age and the food administered to the females, with nauplii produced by *T. weissflogii*-fed females showing significantly higher oxidative damage compared to nauplii produced by *R. baltica*-fed females (Rodríguez-Graña et al., 2010). The reasons for such higher oxidative damage induced by *T. weissflogii* could be related to the co-occurring production of oxylipins and Reactive Oxygen Species (ROS) in diatoms that have been previously reported to induce oxidative stress in *T. stylifera* nauplii (Fontana et al., 2007). A progressive ageing of the copepod population, thus, can be one reason why many copepod cultures tend to have lower vitality after 8–10 generations (Kleppel et al., 2005). The introduction of freshly caught wild copepods to the culture may refresh the population and improve production.

In conclusion, long-term intensive cultivation of copepods has been mainly developed for use of copepods as live food for commercial and ornamental fish farming (for a review see Drillet et al., 2011). However, copepod amenability to laboratory culturing and maintenance through multiple generations may also be applied to research addressing fundamental biological questions about reproduction, developmental biology, diapause, and toxicological and eco-toxicogenomic studies. For example, the harpacticoid copepod *Tigriopus japonicus* is being used as a model species to investigate the physiological response to environmental stressors, including temperature and heavy metal contamination (Raisuddin et al., 2007). Also the calanoid *Eurytemora affinis* is currently being cultivated through multiple generations as a genetic model for studying adaptation to novel environments (Lee et al., 2007). Similarly, specimens of *C. finmarchicus* harvested from a mass-cultivation facility have been employed in studies to assess molecular processes related to diapause (Tarrant et al., 2008), reproduction (Hansen et al., 2008b) or exposure to xenobiotic contaminants (Hansen et al., 2007, 2008a, 2010). Our findings suggest that other ecologically-relevant model copepods, such as *C. helgolandicus*, may be mass cultivated through multiple generations, to obtain year-round individuals of all larval stages. However, we recommend the use of mixed flagellate diets alternated to short feeding-times with diatom species no longer than two months, in order to fuel copepod reproduction and reduce any possible deleterious effects of diatom diets.

Acknowledgements

We thank the VI.S.MA PESCATORI PICCOLA PESCA, Chioggia, Venezia (Italy), for zooplankton collection in the Adriatic Sea. We also thank Isabella Buttino for her suggestions during the start-up of the re-circulating water system, and Mario Di Pinto and Flora Palumbo for their technical assistance with culture algal medium. The establishment of the re-circulating water system at the Stazione Zoologica Anton Dohrn was supported by the Regione Campania (project DGR no. 889-30/06/2006). **[SS]**

References

Arendt, K.E., Jónasdóttir, S.H., Hansen, P.J., Gärtner, S., 2005. Effects of dietary fatty acids on the reproductive success of the calanoid copepod *Temora longicornis*. Mar. Biol. 146, 513–530.

Avery, D.E., Altand, K.K., Dam, H.G., 2008. Sex-related differential mortality of a marine copepod exposed to a toxic dinoflagellate. Limnol. Oceanogr. 53, 2627–2635.

Bonnet, D., Carlotti, F., 2001. Development and egg production in *Centropages typicus* (Copepoda: Calanoida) fed different food types: a laboratory study. Mar. Ecol. Prog. Ser. 224, 133–148.

Author's personal copy

Bonnet, D., Richardson, A., Harris, R., Hirst, A., Beaugrand, G., Edwards, M., Ceballos, S., Diekman, R., Lopez-Urrutia, A., Valdes, L., Carlotti, F., Molinero, J.C., Weikert, H., Greve, W., Lucic, D., Albaina, A., Yahia, N.D., Umani, S.F., Miranda, A., dos Santos, A., Cook, K., Robinson, S., de Puelles, M.L.F., 2005. An overview of *Calanus helgolandicus* ecology in European waters. Prog. Oceanogr. 65, 1–53.

Bonnet, D., Harris, R.P., Yebra, L., Guilhaumon, F., Conway, D.V.P., Hirst, A.G., 2009. Temperature effects on *Calanus helgolandicus* (Copepoda: Calanoida) development time and egg production. J. Plankton Res. 31, 31–44.

Brown, M.R., Jeffrey, S.W., Volkman, J.K., Dunstan, G.A., 1997. Nutritional properties of microalgae for mariculture. Aquaculture 151, 315–331.

Buttino, I., De Rosa, G., Carotenuto, Y., Mazzaella, M., Ianora, A., Esposito, F., Vitiello, V., Quaglia, F., La Rotonda, M.I., Miralto, A., 2008. Aldehyde-encapsulating liposomes impair marine grazer survivorship. J. Exp. Biol. 211, 1426–1433.

Buttino, I., Ianora, A., Buono, S., Vitello, V., Sansone, G., Miralto, A., 2009. Are monoalgal diets inferior to plurialgal diets to maximize cultivation of the calanoid copepod *Temora stylifera*? Mar. Biol. 156, 1171–1182.

Buttino, I., Ianora, A., Buono, S., Vitiello, V., Malzone, M.G., Rico, C., Langellotti, A.L., Sansone, G., Gennari, L., Miralto, A., 2012. Experimental cultivation of the Mediterranean calanoid copepods *Temora stylifera* and *Centropages typicus* in a pilot recirculating system. Aquac. Res. 43, 247–259.

Campbell, R.G., Wagner, M.M., Teegarden, G.J., Boudreau, C.A., Durbin, E.G., 2001. Growth and development rates of the copepod *Calanus finmarchicus* reared in the laboratory. Mar. Ecol. Prog. Ser. 221, 161–183.

Carlotti, F., Bonnet, D., Halsband-Lenk, C., 2007. Development and growth rates of *Centropages typicus*. Prog. Oceanogr. 72, 164–194.

Carotenuto, Y., Ianora, A., Buttino, I., Romano, G., Miralto, A., 2002. Is postembryonic development in the copepod *Temora stylifera* negatively affected by diatom diets? J. Exp. Mar. Biol. Ecol. 276, 49–66.

Carotenuto, Y., Ianora, A., Di Pinto, M., Sarno, D., Miralto, A., 2006. Annual cycle of early developmental stage survival and recruitment in the copepods *Temora stylifera* and *Centropages typicus*. Mar. Ecol. Prog. Ser. 314, 227–238.

Carotenuto, Y., Ianora, A., Miralto, A., 2011. Maternal and neonate diatom diets impair development and sex differentiation in the copepod *Temora stylifera*. J. Exp. Mar. Biol. Ecol. 396, 99–107.

Cook, K.B., Bunker, A., Hay, S., Hirst, A.G., Speirs, D.C., 2007. Naupliar development times and survival of the copepods *Calanus helgolandicus* and *Calanus finmarchicus* in relation to food and temperature. J. Plankton Res. 29, 757–767.

Dam, H.G., Colin, S.P., 2005. *Prorocentrum minimum*(clone Exuv) is nutritionally insufficient, but not toxic to the copepod *Acartia tonsa*. Harmful Algae 4, 575–584.

Drillet, G., Jepsen, P.M., Højgaard, J.K., Jørgensen, N.O.G., Hansen, B.W., 2006. Strain-specific vital rates in four *Acartia tonsa* cultures II: life history traits and biochemical contents of eggs and adults. Aquaculture 279, 47–57.

Drillet, G., Frouël, S., Sichlau, M.H., Jepsen, P.M., Højgaard, J.K., Joarder, A.K., Hansen, B.W., 2011. Status and recommendations on marine copepod cultivation for use as live feed. Aquaculture 315, 155–166.

Dutz, J., Koski, M., Jónasdóttir, S.H., 2008. Copepod reproduction is unaffected by diatom aldehydes or lipid composition. Limnol. Oceanogr. 53, 225–235.

Fontana, A., d'Ippolito, G., Cutignano, A., Romano, G., Lamari, N., Massa Gallucci, A., Cimino, G., Miralto, A., Ianora, A., 2007. LOX-induced lipid peroxidation mechanism responsible for the detrimental effect of marine diatoms on zooplankton grazers. ChemBioChem 8, 1810–1818.

GraphPad Prism® 4 Software for windows, version 4.02, Inc., 2004.

Guillard, R.R., Lorenzen, C.J., 1972. Yellow-green algae with chlorophyllidae c. J. Phycol. 8, 10–14.

Guisande, C., Harris, R., 1995. Effect of total organic content of eggs on hatching success and naupliar survival in the copepod *Calanus helgolandicus*. Limnol. Oceanogr. 40, 476–482.

Gusmão, L.F.M., McKinnon, A.D., 2009. Sex ratios, intersexuality and sex change in copepods. J. Plankton Res. 31, 1101–1117.

Halsband-Lenk, C., Hirche, H.J., Carlotti, F., 2002. Temperature impact on reproduction and development of congener copepod populations. J. Exp. Mar. Biol. Ecol. 271, 121–153.

Hansen, B.H., Altin, D., Nordtug, T., Olsen, A.J., 2007. Suppression subtractive hybridization library prepared from the copepod *Calanus finmarchicus* exposed to a sublethal mixture of environmental stressors. Comp. Biochem. Physiol. D: Genomics Proteomics 2, 250–256.

Hansen, B.H., Altin, D., Vang, S.-H., Nordtug, T., Olsen, A.J., 2008a. Effects of naphthalene on gene transcription in *Calanus finnmarchicus* (Crustacea: Copepoda). Aquat. Toxicol. 86, 157–165.

Hansen, B.H., Altin, D., Hessen, K.M., Dahl, U., Breitholtz, M., Nordtug, T., Olsen, A.J., 2008b. Expression of ecdysteroids and cytochrome P450 enzymes during lipid turnover and reproduction in *Calanus finmarchicus* (Crustacea: Copepoda). Gen. Comp. Endocrinol. 158, 115–121.

Hansen, B.H., Altin, D., Booth, A., Vang, S.-H., Frenzel, M., Sørheim, K.R., Brakstad, O.G., Størseth, T.R., 2010. Molecular effects of diethanolamine exposure on *Calanus finmarchicus* (Crustacea: Copepoda). Aquat. Toxicol. 99, 212–222.

Hassett, R.P., 2004. Supplementation of a diatom diet with cholesterol can enhance copepod egg-production rates. Limnol. Oceanogr. 49, 488–494.

Huntley, M.E., Ciminiello, P., Lopez, M.D.G., 1987. Importance of food quality in determining development and survival of *Calanus pacificus*. Mar. Biol. 95, 103–113.

Hygum, B.H., Rey, C., Hansen, B.W., Tande, K., 2000. Importance of food quantity to structural growth rate and neutral lipid reserves accumulated in *Calanus finmarchicus*. Mar. Biol. 136, 1057–1073.

Ianora, A., Miralto, A., 2010. Toxigenic effects of diatoms on grazers, phytoplankton and other microbes: a review. Ecotoxicology 19, 493–511.

Ianora, A., Poulet, S., Miralto, A., 2003. The effects of diatoms on copepod reproduction: a review. Phycologia 42, 351–363.

Ianora, A., Miralto, A., Poulet, S.A., Carotenuto, Y., Buttino, I., Romano, G., Casotti, R., Pohnert, G., Wichard, T., Colucci-D'Amato, L., Terrazzano, G., Smetacek, V., 2004. Aldehyde suppression of copepod recruitment in blooms of a ubiquitous planktonic diatom. Nature 429, 403–407.

Irigoien, X., Harris, R.P., Head, R.N., Harbour, D., 2000a. The influence of diatom abundance on the egg production rate of *Calanus helgolandicus* in the English Channel. Limnol. Oceanogr. 45, 1433–1439.

Irigoien, X., Obermuller, B., Head, R.N., Harris, R.P., Rey, C., Hansen, B.W., Hygum, B.H., Heath, M.R., Durbin, E.G., 2000b. The effect of food on the determination of sex ratio in *Calanus* spp.: evidence from experimental studies and field data. ICES J. Mar. Sci. 57, 1752–1763.

Ismar, S., Hansen, T., Sommer, U., 2008. Effect of food concentration and type of diet on *Acartia* survival and naupliar development. Mar. Biol. 154, 335–343.

Jensen, L.K., Carroll, J., Pedersen, G., Hylland, K., Dahle, S., Bakke, T., 2006. A multi-generation *Calanus finmarchicus* culturing system for use in long-term oil exposure experiments. J. Exp. Mar. Biol. Ecol. 333, 71–78.

Jónasdóttir, S.H., 1994. Effects of food quality on the reproductive success of *Acartia tonsa* and *Acartia hudsonica*, laboratory observations. Mar. Biol. 121, 67–81.

Jónasdóttir, S.H., Trung, N.H., Hansen, F., Gartner, S., 2005. Egg production and hatching success in the calanoid copepods *Calanus helgolandicus* and *Calanus finmarchicus* in the North Sea from March to September 2001. J. Plankton Res. 27, 1239–1259.

Kang, H.K., Poulet, S., Lacoste, A., Kang, Y.J., 2000. A laboratory study of the effect of non-phytoplankton diets on the reproduction of *Calanus helgolandicus*. J. Plankton Res. 22, 2171–2179.

Keller, M.D., Selvin, R.C., Claus, W., Guillard, R.R.L., 1987. Media for the culture of oceanic ultraphytoplankton. J. Phycol. 633–638.

Klein Breteler, W.C.M., Schogt, N., Rampen, S., 2005. Effect of diatom nutrient limitation on copepod development: role of essential lipids. Mar. Ecol. Prog. Ser. 291, 125–133.

Kleppel, G.S., Hazzard, S.E., Burkart, C.A., 2005. Maximizing the nutritional values of copepods: implications for population growth and fatty acid composition. In: Lee, C.S., et al. (Ed.), Copepods in Aquaculture. Blackwell Publishing Professional, Iowa 50014, USA, pp. 209–224.

Koski, M., 2008. "Good" and "bad" diatoms: development, growth and juvenile mortality of the copepod *Temora longicornis* on diatom diets. Mar. Biol. 154, 719–734.

Koski, M., Klein Breteler, W., Schogt, N., 1998. Effect of food quality on rate of growth and development of the pelagic copepod *Pseudocalanaus elongatus* (Copepoda, Calanoida). Mar. Ecol. Prog. Ser. 170, 169–187.

Laabir, M., Poulet, S.A., Ianora, A., Miralto, A., Cueff, A., 1995. Reproductive response of *Calanus helgolandicus*. 2. In situ inhibition of embryonic development. Mar. Ecol. Prog. Ser. 129, 97–105.

Lauritano, C., Borra, M., Carotenuto, Y., Biffali, E., Miralto, A., Procaccini, G., Ianora, A., 2011a. First molecular evidence of diatom effects in the copepod *Calanus helgolandicus*. J. Exp. Mar. Biol. Ecol. 404, 79–86.

Lauritano, C., Borra, M., Carotenuto, Y., Biffali, E., Miralto, A., Procaccini, G., Ianora, A., 2011b. Molecular evidence of the toxic effects of diatom diets on gene expression patterns in copepods. PLoS One 6 (10), e26850.

Lee, K.W., Park, H.G., Lee, S.-M., Kang, H.-K., 2006. Effects of diets on the growth of the brackish water cyclopoid copepod *Paracyclopina nana* Smirnov. Aquaculture 256, 346–353.

Lee, C.E., Remfert, J.L., Chang, Y.M., 2007. Response to selection and evolvability of invasive populations. Genetica 129, 179–192.

Marcus, N.H., Alatalo, P., 1989. Conditions for rearing *Calanus finmarchicus* (Gunnerus, 1770) (Copepoda, Calanoida) through multiple generations in the laboratory. Crustaceana 57, 101–103.

Mauchline, J., 1998. The biology of calanoid copepods. In: Blaxter, J.H.S., et al. (Ed.), Advances in Marine Biology. Academic Press, USA, p. 710.

Miralto, A., Barone, G., Romano, G., Poulet, S.A., Ianora, A., Russo, G.L., Buttino, I., Mazzarella, G., Laabir, M., Cabrini, M., Giacobbe, M.G., 1999. The insidious effect of diatoms on copepod reproduction. Nature 402, 173–176.

Miralto, A., Guglielmo, L., Zagami, G., Buttino, I., Granata, A., Ianora, A., 2003. Inhibition of population growth in the copepods *Acartia clausi* and *Calanus helgolandicus* during diatom blooms. Mar. Ecol. Prog. Ser. 254, 253–268.

Morehead, D.T., Battaglene, S.C., Metillo, E.B., Bransden, M.P., Dunstan, G.A., 2005. Copepods as live feed for striped trumpeter *Latris lineata* larvae. In: Lee, C.S., et al. (Ed.), Copepods in Aquaculture. Blackwell Publishing Professional, Iowa 50014, USA, pp. 209–224.

Nejstgaard, J.C., Hygum, B.H., Naustvoll, L.J., Bamstedt, U., 2001. Zooplankton growth, diet and reproductive success compared in simultaneous diatom- and flagellate–microzooplankton-dominated plankton blooms. Mar. Ecol. Prog. Ser. 221, 77–91.

O'Bryen, P.J., Lee, C.E., 2005. Culture of copepods and applications to marine finfish larval rearing. Workshop discussion summary. In: Lee, C.S., et al. (Ed.), Copepods in Aquaculture. Blackwell Publishing Professional, Iowa 50014, USA, pp. 209–224.

Olivotto, I., Buttino, I., Borroni, M., Piccinetti, C.C., Malzone, M.G., Carnevali, O., 2008. The use of the Mediterranean calanoid copepod *Centropages typicus* in Yellowtail clownfish (*Amphiprion clarkii*) larviculture. Aquaculture 284, 211–216.

Payne, M.F., Rippingale, R.J., 2001. Intensive cultivation of the calanoid copepod *Gladioferens imparipes*. Aquaculture 201, 329–342.

Pond, D.W., Harris, R., Head, R., Harbour, D., 1996. Environmental and nutritional factors determining seasonal variability in the fecundity and egg viability of *Calanus helgolandicus* in coastal waters off Plymouth, UK. Mar. Ecol. Prog. Ser. 143, 45–63.

Poulet, S.A., Laabir, M., Ianora, A., Miralto, A., 1995. Reproductive response of *Calanus helgolandicus*.1. Abnormal embryonic and naupliar development. Mar. Ecol. Prog. Ser. 129, 85–95.

Poulet, S., Wichard, T., Ledoux, J.B., Lebreton, B., Marchetti, J., Dancie, C., Bonnet, D., Cueff, A., Morin, P., Pohnert, G., 2006. Influence of diatoms on copepod reproduction. I. Field

Author's personal copy

and laboratory observations related to *Calanus helgolandicus* egg production. Mar. Ecol. Prog. Ser. 308, 129–142.

Poulet, S.A., Cueff, A., Wichard, T., Marchetti, J., Dancie, C., Pohnert, G., 2007. Influence of diatoms on copepod reproduction. III. Consequences of abnormal oocyte maturation on reproductive factors in *Calanus helgolandicus*. Mar. Biol. 152, 415–428.

Raisuddin, S., Kwok, K.W.H., Leung, K.M.Y., Schlenk, D., Lee, J.-S., 2007. The copepod *Tigriopus*: a promising marine model organism for ecotoxicology and environmental genomics. Aquat. Toxicol. 83, 161–173.

Rey, C., Harris, R., Irigoien, X., Head, R., Carlotti, F., 2001. Influence of algal diet on growth and ingestion of *Calanus helgolandicus* nauplii. Mar. Ecol. Prog. Ser. 216, 151–165.

Rey-Rassat, C., Irigoien, X., Harris, R., Head, R., Carlotti, F., 2002a. Growth and development of *Calanus helgolandicus* reared in the laboratory. Mar. Ecol. Prog. Ser. 238, 125–138.

Rey-Rassat, C., Irigoien, X., Harris, R., Head, R., Carlotti, F., 2002b. Egg production rates of *Calanus helgolandicus* females reared in the laboratory: variability due to present and past feeding conditions. Mar. Ecol. Prog. Ser. 238, 139–151.

Rodríguez-Graña, L., Calliari, D., Tiselius, P., Hansen, B.W., Sköld, H.N., 2010. Gender-specific ageing and non-Mendelian inheritance of oxidative damage in marine copepods. Mar. Ecol. Prog. Ser. 401, 1–13.

Shields, R.J., Kotani, T., Molnar, A., Marion, K., Kobashigawa, J., Tang, L., 2005. Intensive cultivation of a subtropical paracalanid copepod, *Parvocalanus* sp., as prey for small marine fish larvae. In: Lee, C.S., et al. (Ed.), Copepods in Aquaculture. Blackwell Publishing Professional, Iowa 50014, USA, pp. 209–224.

Støttrup, J.G., 2000. The elusive copepods: their production and suitability in marine aquaculture. Aquac. Res. 31, 703–711.

Støttrup, J.G., Richardson, K., Kirkegaard, E., Pihl, N.J., 1986. The cultivation of *Acartia tonsa* Dana for use as a live food source for marine fish larvae. Aquaculture 52, 87–96.

Tande, K.S., Miller, C.B., 2000. Population dynamics of *Calanus* in the North Atlantic: results from the trans-Atlantic study of *Calanus finmarchicus*. ICES J. Mar. Sci. 57, 1527.

Tarrant, A.M., Baumgartner, M.F., Verslycke, T., Johnson, C.L., 2008. Differential gene expression in diapausing and active *Calanus finmarchicus* (Copepoda). Mar. Ecol. Prog. Ser. 355, 193–207.

Turner, J.T., Ianora, A., Miralto, A., Laabir, M., Esposito, F., 2001. Decoupling of copepod grazing rates, fecundity and egg-hatching success on mixed and alternating diatom and dinoflagellate diets. Mar. Ecol. Prog. Ser. 220, 187–199.

Uye, S., 1996. Induction of reproductive failure in the planktonic copepod *Calanus pacificus* by diatoms. Mar. Ecol. Prog. Ser. 133, 89–97.

Verity, P.G., Smetacek, V., 1996. Organism life cycles, predation, and the structure of marine pelagic ecosystems. Mar. Ecol. Prog. Ser. 130, 277–293.

Wichard, T., Gerecht, A., Boersma, M., Poulet, S.A., Wiltshire, K., Pohnert, G., 2007. Lipid and fatty acid composition of diatoms revisited: Rapid wound-activated change of food quality parameters influences herbivorous copepod reproductive success. ChemBioChem 8, 1146–1153.

Wichard, T., Poulet, S.A., Boulesteix, A.-L., Ledoux, J.B., Lebreton, B., Marchetti, J., Pohnert, G., 2008. Influence of diatoms on copepod reproduction. II. Uncorrelated effects of diatom-derived α β χ δ-unsaturated aldehydes and polyunsaturated fatty acids on *Calanus helgolandicus* in the field. Prog. Oceanogr. 77, 30–44.

Provided for non-commercial research and education use.
Not for reproduction, distribution or commercial use.

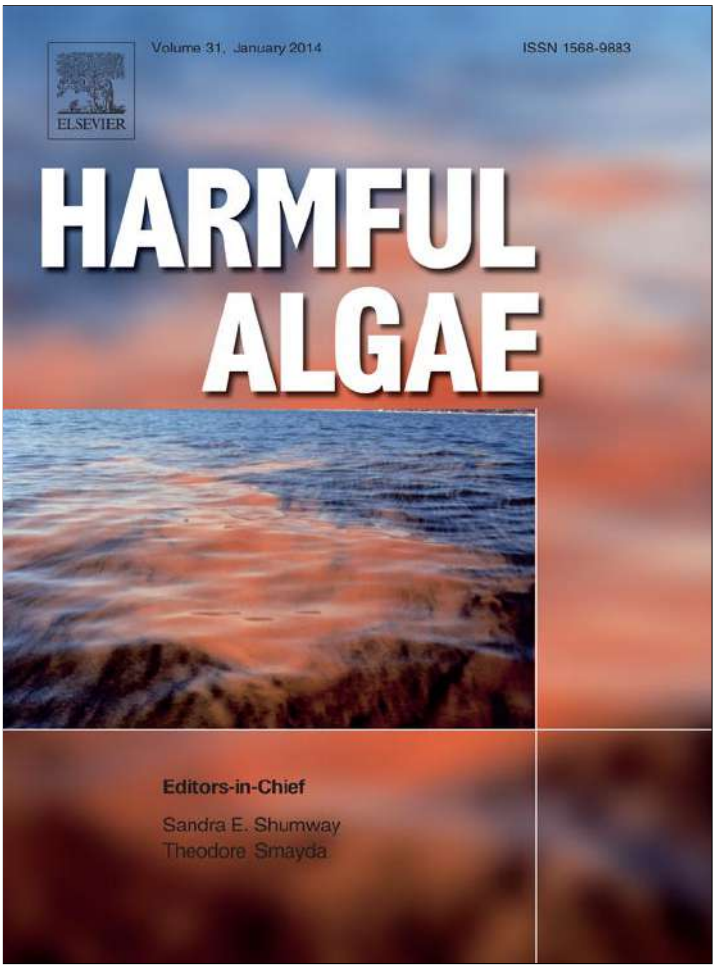

This article appeared in a journal published by Elsevier. The attached copy is furnished to the author for internal non-commercial research and education use, including for instruction at the authors institution and sharing with colleagues.

Other uses, including reproduction and distribution, or selling or licensing copies, or posting to personal, institutional or third party websites are prohibited.

In most cases authors are permitted to post their version of the article (e.g. in Word or Tex form) to their personal website or institutional repository. Authors requiring further information regarding Elsevier's archiving and manuscript policies are encouraged to visit:

http://www.elsevier.com/authorsrights

Author's personal copy

Harmful Algae 31 (2014) 153–162

Contents lists available at ScienceDirect

Harmful Algae

journal homepage: www.elsevier.com/locate/hal

Insights into the transcriptome of the marine copepod *Calanus helgolandicus* feeding on the oxylipin-producing diatom *Skeletonema marinoi*

Ylenia Carotenuto *, Emanuela Dattolo, Chiara Lauritano, Fabio Pisano, Remo Sanges, Antonio Miralto, Gabriele Procaccini, Adrianna Ianora

Stazione Zoologica Anton Dohrn, Villa Comunale, Napoli, Italy

ARTICLE INFO

Article history:
Received 9 May 2013
Received in revised form 12 November 2013
Accepted 12 November 2013

Keywords:
Calanus helgolandicus
Cellular Stress Response
Gene expression
Oxylipins
Skeletonema marinoi
Suppression subtractive hybridization

ABSTRACT

Diatoms dominate productive regions in the oceans and have traditionally been regarded as sustaining the marine food chain to top consumers and fisheries. However, many of these unicellular algae produce cytotoxic oxylipins that impair reproductive and developmental processes in their main grazers, crustacean copepods. The molecular mode of action of diatoms and diatom oxylipins on copepods is still unclear. In the present study we generated two Expressed Sequence Tags (ESTs) libraries of the copepod *Calanus helgolandicus* feeding on the oxylipin-producing diatom *Skeletonema marinoi* and the cryptophyte *Rhodomonas baltica* as a control, using suppression subtractive hybridization (SSH). Our aim was to investigate differences in the transcriptome between females fed toxic and non-toxic food and identify differentially expressed genes and biological processes targeted by this diatom. We produced 947 high quality ESTs from both libraries, 475 of which were functionally annotated and deposited in GenBank. Clustering and assembling of ESTs resulted in 376 unique transcripts, 200 of which were functionally annotated. Functional enirchment analysis between the two SSH libraries showed that ESTs belonging to biological processes such as response to stimuli, signal transduction, and protein folding were significantly over-expressed in the *S. marinoi*-fed *C. helgolandicus* compared to *R. baltica*-fed *C. helgolandicus* library. These findings were confirmed by RT-qPCR analysis. In summary, 2 days of feeding on *S. marinoi* activated a generalized Cellular Stress Response (CSR) in *C. helgolandicus*, by over-expressing genes of molecular chaperones and signal transduction pathways that protect the copepod from the immediate effects of the diatom diet. Our results provide insights into the response of copepods to a harmful diatom diet at the transcriptome level, supporting the hypothesis that diatom oxylipins elicit a stress response in the receiving organism. They also increase the genomic resources for this copepod species, whose importance could become ever more relevant for pelagic ecosystem functioning in European waters due to global warming.

© 2013 Elsevier B.V. All rights reserved.

1. Introduction

Diatoms are responsible for approximately 50% of marine primary production and play a major role in the transfer of energy through marine food chains (Mauchline, 1998). However, upon cell damage several species produce cytotoxic compounds such as poly-unsaturated aldehydes (PUAs) and other oxylipins deriving from the oxidative metabolism of fatty acids (d'Ippolito et al., 2004; Fontana et al., 2007; Pohnert, 2000). Oxylipins and PUAs in particular impair several reproductive and developmental processes in copepods, such as gametogenesis (Poulet et al., 2007a), embryogenesis (Ianora et al., 1995), egg viability (Ianora et al., 2003), larval development (Carotenuto et al., 2002) and sex differentiation (Carotenuto et al., 2011). They also induce malformations (teratogenesis) and apoptosis in newly hatched nauplii (Ianora et al., 2004). Reduced copepod fecundity, hatching success and larval fitness have been reported during major spring diatom blooms in the Mediterranean Sea (Northern Adriatic Sea) (Miralto et al., 1999), the Northern Eastern Pacific Ocean (Dabob Bay, Washington, USA) (Halsband-Lenk et al., 2005; Pierson et al., 2005), the Northern Eastern Atlantic Ocean (English Channel) (Poulet et al., 2006) and in upwelling areas of the South-Eastern Pacific Ocean (off the coast of Chile) (Poulet et al., 2007b; Vargas et al., 2006).

The diatom *Skeletonema marinoi* is an ubiquitous bloom-forming species found in both northern and southern temperate

* Corresponding author. Tel.: +39 081 5833235; fax: +39 081 7641355.
E-mail address: ylenia.carotenuto@szn.it (Y. Carotenuto).

1568-9883/$ – see front matter © 2013 Elsevier B.V. All rights reserved.
http://dx.doi.org/10.1016/j.hal.2013.11.002

Author's personal copy

latitudes (Kooistra et al., 2008). The strain used in the present study originates from the Northern Adriatic Sea, where the species dominates the winter-spring phytoplankton bloom (Aubry et al., 2004). This *S. marinoi* strain is reported to produce up to 14 different oxylipins, including PUAs, oxoacids, hydroxyacid, epoxy alcohols, and fatty acid hydroperoxides, which reduce egg hatching success and cause malformations in the offspring of the copepod *Calanus helgolandicus* during in vitro incubation assays (Fontana et al., 2007).

Calanus helgolandicus is one of the most widely studied copepod species in terms of development, growth, reproduction and recruitment (Bonnet et al., 2009; Cook et al., 2007; Ianora and Miralto, 2010; Pond et al., 1996; Rey-Rassat et al., 2002). It is one of the dominant zooplankton species in European waters, living in open and coastal waters from the temperate Eastern Atlantic Ocean to the Mediterranean basin (Northern Adriatic Sea) (Bonnet et al., 2009). A recent survey on the distribution of *C. helgolandicus* in European waters has shown that the species is gradually expanding northwards, with peaks in abundance moving from Mediterranean coasts to the North Sea, due to an increase in water temperatures in the last decade (Bonnet et al., 2005). Considering the predicted further increase in water temperatures due to general global warming, *C. helgolandicus* could replace its congener *Calanus finmarchicus* and become the dominant *Calanus* species in the North Sea (Bonnet et al., 2009). Despite extensive studies on *C. helgolandicus*, the molecular mode of action of diatoms and diatom oxylipins on this species is still not clear. Only recently has it been shown, using RT-qPCR, that 2 days of feeding on *Skeletonema marinoi* inhibits a series of genes involved in aldehyde detoxification, apoptosis regulation and cytoskeleton structure (Lauritano et al., 2011a,b, 2012).

To enrich these studies and identify a wider set of differentially expressed genes and biological processes induced by a *Skeletonema marinoi* diet, we used suppression subtractive hybridization (SSH) (Diatchenko et al., 1996) to generate two reciprocal Expressed Sequences Tags (ESTs) libraries of *Calanus helgolandicus* fed for 2 days on *S. marinoi* and the control algae *Rhodomonas baltica*. The obtained *C. helgolandicus* ESTs were further assembled into contiguous transcripts (contigs), which were functionally annotated and used for quantitative gene expression analysis using RT-qPCR.

Genomic and transcriptomic studies are still under-explored in copepods, being mainly limited to species such as the fish parasites *Lepeoptheirus salmonis* and *Caligus rogercresseyi*, the tidepool *Tigriopus californicus* and the planktonic congener *Calanus finmarchicus* (Bron et al., 2011). To date, there are only 196 nucleotide sequences for *Calanus helgolandicus* deposited in GenBank (October 2013), 26 cDNA/mRNA sequences of which correspond to those deposited by (Lauritano et al., 2011a,b, 2012).

Our study shows that the *Skeletonema marinoi*-fed *Calanus helgolandicus* library was significantly enriched in ESTs encoding for genes involved in protein folding, response to stimuli and cytoskeleton functioning, and that up-regulation of molecular chaperones and signal transduction genes was confirmed in *S. marinoi*-fed *C. helgolandicus* using RT-qPCR. These results suggest that 2 days of feeding on *S. marinoi* activates a generalized Cellular Stress Response (CSR) in *C. helgolandicus*, and that these genes help protect the copepod from the harmful effects of the diatom diet.

2. Materials and methods

2.1. Copepods collection and feeding experiments

Calanus helgolandicus females were collected in September 2009 from a 500-L re-circulating copepod cultivation system established at the Stazione Zoologica Anton Dohrn (Carotenuto et al., 2012) and originating from specimens collected in the North Adriatic Sea from March to April 2009. The copepod culture was fed a mixed food assemblage of *Rhodomonas baltica*, *Prorocentrum minimum* and *Isochrysis galbana* and kept at 18 °C and 38‰ salinity. Adult *C. helgolandicus* females sampled from the breeding tank (~1200 specimens) were sorted under a stereomicroscope (Leica) and transferred to several 10 L beakers filled with 0.22 μm filtered sea water enriched with either the diatom *Skeletonema marinoi* (SKE) (45,000 cells/ml, 1 mgC/L) or the control diet *R. baltica* (RHO) (8000 cells/ml, 1 mgC/L) known to support high egg hatching success and survival in this copepod species (Carotenuto et al., 2012). Both algae were grown as semi-continuous batch cultures to late-exponential phase of growth in 2-L glass jar containing K medium (Keller et al., 1987) or f/2 medium (Guillard and Lorenzen, 1972), for *R. baltica* or *S. marinoi*, respectively. Algal cultures were grown in a temperature-controlled chamber kept at 18 °C and on a 12:12 h light:dark cycle. After 48 h of feeding, *C. helgolandicus* females from each of the two groups were transferred to filtered seawater (FSW) for an additional 24 h, in order to allow gut evacuation. A total of 500 *R. baltica*-fed *C. helgolandicus* females and 500 *S. marinoi*-fed *C. helgolandicus* females were collected, washed in FSW and transferred to two 14-mL polypropylene tubes with 5 ml Trizol Reagent (Invitrogen, San Diego, CA, USA). Samples were frozen directly in liquid nitrogen and stored at −80 °C until RNA extraction.

2.2. RNA extraction and mRNA purification

Total RNA of *Calanus helgolandicus* was extracted from each group using Trizol Reagent and a phenol:chloroform separation according to the manufacturer's protocol. The procedure was the same as reported in (Lauritano et al., 2011b, 2013). RNA quantity and purity were checked by Nano-Drop (ND-1000 UV-Vis spectrophotometer; NanoDrop Technologies Inc., Wilmington, DE, USA), and by gel electrophoresis. Poly A^+ RNA of each sample was purified from total RNA using the Dynabeads® mRNA Purification Kit (Dynal Biotech ASA, Smestad, Norway) and the concentration and purity were assessed by Nano-Drop.

2.3. Suppression subtractive hybridization libraries

Suppression subtractive hybridization (SSH) libraries were performed using the PCR-Select™ cDNA subtraction kit (Clontech, USA) following the manufacturer's instructions. Briefly, 2 μg of poly A^+ RNA from each total RNA *Calanus helgolandicus* sample were used for double strand (ds) cDNA synthesis, followed by *Rsa I* digestion, adaptors ligation and two hybridization steps. We performed two SSH: a forward subtraction where the cDNA from *C. helgolandicus* fed *Skeletonema marinoi* was used as tester and the cDNA from *C. helgolandicus* fed *Rhodomonas baltica* was used as driver, to obtain a library enriched for transcripts whose expression was induced during *S. marinoi* feeding; and a reverse subtraction, where the cDNA from *C. helgolandicus* fed *R. baltica* was used as tester and the cDNA from *C. helgolandicus* fed *S. marinoi* was used as driver, to obtain a library enriched for transcripts whose expression was induced during *R. baltica* feeding. The last two steps of suppressive PCR reactions were performed using the 50× Advantage® cDNA Polymerase Mix (Clonthech, USA).

The amplified subtracted cDNAs of *Calanus helgolandicus* were cloned into the pCR®II-TOPO® TA Cloning® vector (Invitrogen) and transferred into One Shot® TOP10F′ Competent Cells (Invitrogen). The chemically transformed cells were plated onto LB agar supplemented with 100 μg ml^{-1} of ampicillin, 40 mg ml^{-1} of X-Gal and 100 mM of isopropyl β-D-1-thiogalactopyranoside (IPTG), and incubated at 37 °C overnight for the blue-white colony screening. All white and light blue clones were randomly picked and transferred into 2 ml LB-ampicillin (100 μg ml^{-1}) tube and

Author's personal copy

incubated overnight at 37 °C. A pre-screening of a subset of these clones was performed with PCR and 1% agarose gel electrophoresis. The PCR reactions were performed using 1 μl of bacterial culture, primers T3 and M13Reverse, and Taq DNA Polymerase (Roche). PCR amplifications were carried out as follows: 5 min at 94 °C; 35 cycles of 1 min at 94 °C, 45 s at 52 °C, 90 s at 72 °C; and 10 min at 72 °C for the final extension. Since 90% of these clones incorporated a fragment of the appropriate length (longer than 150 bp) (data not shown), all picked white and light blue clones were preserved in 200 μl of 12.5% glycerol + LB-ampicillin without further screening, and stored at −80 °C until shipping to the Biologisch-Technische Produkte Service of the Max Planck Institute for Molecular Genetics (Molgen) (Berlin, Germany). Clones were sequenced using ABI 3730xl automated DNA sequencers (Applied Biosystems, USA) to generate single-pass 3′-end Expressed Sequence Tags (ESTs).

2.4. Sequence pre-processing, clustering and functional annotation

Sequences and quality values were extracted by chromatograms using the program phred (Ewing and Green, 1998; Ewing et al., 1998), trimming the low quality ends. Vector masking and cleaning were performed using the on-line bioinformatics resource EGassembler (Masoudi-Nejad et al., 2006) which produced high-quality Expressed Sequence Tags (ESTs) sequences clipping the vector, the adaptors and removing short sequences from the dataset (<80 bp). Analyses of the un-assembled high quality ESTs gave us a quantitative picture of the transcriptome. High-quality ESTs were assigned a putative protein function by sequence similarity comparison against the NCBI non-redundant protein database (nr) using the BLASTx algorithm (*E*-value cut-off set to 1E−3), and then annotated according to different Gene Onthology (GO) functional categories (*E*-value cut-off set to 1E−6), using the bioinformatics tool Blast2GO v.2.5.1 (Conesa et al., 2005; Goetz et al., 2008). For each ESTs, putative gene function, GO terms and, whenever possible, enzyme commission (EC) number, were assigned. Functional enrichment analysis between annotated ESTs from the forward and the reverse library was also performed by Blast2GO using the Fisher's Exact Test with Multiple Testing Correction of False Discovery Rate (FDR < 0.01) (Benjamini and Hochberg, 1995). This analysis returned a list of significant GO terms, ranked by their FDR value, which differed between the two subtractive libraries, thus allowing the identification of treatment-specific differentially enriched GO terms. High-quality ESTs sequences from both libraries were subsequently grouped into clusters, based on their similarity, and assembled into single contiguous transcripts (contigs) or single sequence clusters (singletons) by EGassembler using the CAP3 program (Huang and Madan, 1999). This analysis gave us a qualitative picture of the functional landscape of the transcriptome. The output was a set of contigs (formed by at least two contiguous ESTs) and singletons, which together represent tentative unigenes (TUGs). Contigs and singletons were functionally annotated using the Blast2GO tool following the same procedure described previously.

2.5. RT-qPCR quantitative gene expression analysis

To confirm up-regulation of genes enriched in the forward SSH library and down-regulation of genes enriched in the reverse library, in *Calanus helgolandicus* fed *Skeletonema marinoi* versus those fed *Rhodomonas baltica*, we selected a number of annotated contigs from both libraries to be tested quantitatively using RT-qPCR. These contigs belonged to differentially enriched GO terms and were formed by the highest number of ESTs. Primers were designed on sequence contigs using Primer 3 software to obtain amplicon lengths in the range of 100–200 bp and synthesized commercially by Primm Labs (Milan, Italy). PCRs were performed on a GeneAmp PCR System 9700 (Perkin Elmer, Applied Biosystems, Foster City, CA) and amplified products were sequenced following standard procedures reported in (Lauritano et al., 2012). RT-qPCR experiments were performed in a MicroAmp Optical 384-Well reaction plate (Applied Biosystem, Foster City, CA) using a Viia7 Real Time PCR System (Applied Biosystem), following standard procedures reported in (Lauritano et al., 2012). The cDNA template was a 1:100 dilution (0.5 ng) of the original unsubtracted double strand (ds) cDNA of *C. helgolandicus* fed *S. marinoi* or *R. baltica*, prior to *Rsa I* digestion and used in the Clontech PCR-Select^{TM} cDNA subtraction kit (Clontech, USA). All RT-qPCR reactions were carried out in triplicate to capture intra-assay variability. Each assay included three no-template controls for each primer pair. Five serial dilutions of cDNA were used to calculate reaction efficiencies (E) for all primer pairs using the equation $E = 10^{-1/\text{slope}}$, where the slope was obtained from a standard curve between Cycle Threshold (Ct) values and the $\log_{10}$ of each dilution factor. All gene amplifications fitted in the optimal detection window from 19 to 26 cycles. Full sequences of these target genes are deposited in GenBank with accession numbers from KC521529 to KC521538. The relative expression ratio (*R*) of each target gene and its statistical significance was calculated using the Excel-applet REST tool and the Pair Wise Fixed Reallocation Randomization Test (Pfaffl et al., 2002). The calculation is based on the efficiency (*E*) and the Ct difference in the sample group (copepods fed on *S. marinoi*) versus the control group (copepods fed on *R. baltica*), of the target gene normalized to the reference gene ribosomal protein S20, which had previously been identified as the best reference gene under these same experimental conditions (Lauritano et al., 2011a).

3. Results

3.1. Suppression subtractive hybridization library

We sequenced a total of 1248 clones from both suppression subtractive cDNA libraries (960 from the forward SKE-fed *Calanus helgolandicus* library and 288 from the reverse RHO-fed *C. helgolandicus* library), obtaining 947 high quality ESTs, with 787 ESTs from the forward and 160 ESTs from the reverse library, respectively. ESTs ranged in size from 81 to 764 bp, with an average length of 370 bp. Of these 947 high quality ESTs, those that were longer than 100 bp have been deposited in GenBank dbESTs. Blast2GO analysis using BLASTx showed that 583 out of 947 ESTs (62%), significantly matched known proteins from the non-redundant protein database (nr), with the top occurring most similar species being the fruit fly *Drosophila melanogaster* and the red flour beetle *Tribolium castaneum*, followed by *Mus musculus*, *Homo sapiens* and the parasitic copepod sea lice *Lepeophtheirus salmonis*. The remaining nearly 40% of ESTs that did not match any known protein in the database, probably represented unknown gene functions or modified genes. Further analysis of Blast2GO showed that 475 out of 583 ESTs were functionally annotated and distributed into the following GO functional categories, biological process (BP), molecular function (MF) and cellular component (CC), at different hierarchical levels (Table 1). As expected, the majority of sequences belonging to BP are involved in cellular (94%) and metabolic (85%) processes. However, a relevant part of annotated sequences were also related to regulation (47%), response to stimuli (28%), development (23%), signaling (18%), or biogenesis of cellular component (21%). For MF, most of the ESTs encoded for proteins involved in molecular binding (protein: 41%, nucleotide: 34%, ion: 22%, nucleic acid: 18%), as well as for enzymes involved in several cellular catalytic activities (oxidoreductase: 19%, hydrolase: 21% and transferase: 16%). Finally, for CC, most of the

Author's personal copy

Table 1
Distribution of annotated ESTs into GO functional categories.

GO term	ESTs	%
Biological process	397	100.0
Cellular process	374	94.2
Metabolic process	339	85.4
Biological regulation	188	47.4
Response to stimulus	111	28.0
Localization	110	27.7
Cellular component organization	91	22.9
Developmental process	90	22.7
Cellular component biogenesis	83	20.9
Multicellular organismal process	79	19.9
Signaling	70	17.6
Reproduction	36	9.1
Locomotion	26	6.5
Death	20	5.0
Growth	19	4.8
Cell proliferation	17	4.3
Immune system process	15	3.8
Biological adhesion	13	3.3
Rhythmic process	8	2.0
Molecular function	453	100.0
Protein binding	187	41.3
Nucleotide binding	153	33.8
Ion binding	98	21.6
Hydrolase activity	96	21.2
Oxidoreductase activity	87	19.2
Nucleic acid binding	80	17.7
Transferase activity	73	16.1
Structural constituent of ribosome	57	12.6
Transmembrane transporter activity	48	10.6
Cofactor binding	26	5.7
Phosphatase regulator activity	21	4.6
Signal transducer activity	12	2.6
Lipid binding	8	1.8
Ligase activity	8	1.8
Superoxide dismutase activity	6	1.3
Kinase regulator activity	5	1.1
Peroxidase activity	4	0.9
Cellular component	364	100.0
Intracellular	336	92.3
Intracellular organelle part	144	39.6
Membrane	113	31.0
organelle lumen	63	17.3
Organelle membrane	44	12.1
organelle envelope	30	8.2
Endomembrane system	16	4.4
Cell surface	15	4.1
Membrane-bounded vesicle	13	3.6
Extracellular space	12	3.3
Nuclear-ER network	7	1.9
Receptor complex	4	1.1
Intercellular bridge	4	1.1

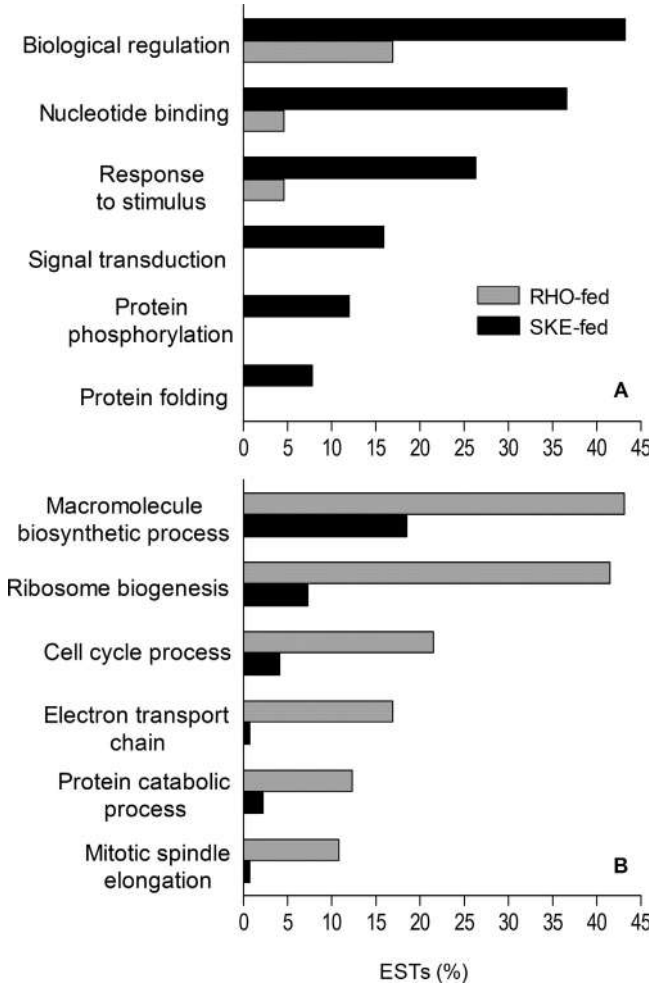

Fig. 1. Gene enrichment analysis in the copepod *Calanus helgolandicus*. Significantly enriched GeneOnthology (GO) terms in *Skeletonema marinoi*-fed (SKE-fed) (A) or *Rhodomonas baltica*-fed (RHO-fed) *C. helgolandicus* ESTs libraries (B), after Fisher's Exact Test with Multiple Testing Correction of FDR (FDR < 0.01). Bars represented percentages of ESTs, for each GO term, in SKE-fed (black) or RHO-fed (gray) *C. helgolandicus* libraries.

sequences are proteins localized in the intracellular matrix (92%), whereas membrane-bound proteins represented a lower fraction of the dataset (31%).

To obtain information on the specific mechanism affected by *Skeletonema marinoi*, we performed the Fisher's Exact Test with Multiple Testing Correction of False Discovery Rate (FDR < 0.01), on the forward SKE-fed *Calanus helgolandicus* library versus the reverse RHO-fed *C. helgolandicus* library. This analysis showed that the GO terms biological regulation (43%), nucleotide binding (37%), response to stimuli (26%), signal transduction (16%), protein phosphorylation (12%) and protein folding (8%), were significantly enriched in SKE-fed *C. helgolandicus* compared to RHO-fed *C. helgolandicus* libraries (Fig. 1A). Among the proteins included into these GO terms, there were the following: 14-3-3 (FTT) protein zeta, serine/threonine casein/kinases CK2, aquaporin, arsenical pump-driving ATPase, carboxypeptidase, chaperonin-containing T-complex protein 1 (TCP-1), cyclin a and b, cyclophilin a and b, disco-interacting protein 2, epithelial membrane protein, glycoprotein 93 (gp93), various heat shock proteins (HSP70, HSP70p, HSP90), nucleoside diphosphate kinase (NDK), pyruvate dehydrogenase isoform b, protein phosphatase 1, ras-related protein rab-40c and ring finger protein 121 (RNF-121). All these proteins have in common multiple functions of binding and catalitic activity and are essential for various biological processess, such as transmembrane transport of ions, long-chain fatty acids and proteins, signaling pathways (GTPase mediated signal transduction and Wnt signaling), regulation of gene expression, DNA and protein stability, embryonic development, cytoskeleton organization and response to stress. On the contrary, the GO terms macromolecule biosynthetic processes (43%), ribosome biogenesis (42%), cell cycle processes (22%), electron transport chain (17%), protein catabolic processes (12%) and mitotic spindle elongation (11%), were significantly enriched in the reverse RHO-fed *C. helgolandicus* library compared to the forward SKE-fed *C. helgolandicus* library (Fig. 1B). These terms included various 40S and 60S ribosomal proteins involved in translation, or proteins with oxidoreductase and catalitic activity taking part in the energy metabolism of the cell (ATP synthase, cytochrome b and c1, cytochrome oxidase, glyoxylate reductase, hydroxypyruvate reductase, isocitrate dehydrogenase, nadh dehydrogenase subunit 4).

Author's personal copy

Table 2
List of annotated contigs used for RT-qPCR validation.

Sequence	ESTs	Length	Organism	Hit acc.	*E*-value	Similarity (%)	Score	Putative protein	EC
Contig72	41	1291	*Tribolium castaneum*	XP_967459	3.84E−50	92	204	t-Complex protein 1 subunit eta	
Contig154	13	734	*Xenopus laevis*	NP_001081266	7.22E−21	75	105	Cyclin b1	
Contig51	12	634	*Drosophila grimshawi*	XP_001991282	2.99E−40	88	169	Ring finger protein 121	
Contig56	9	682	*Ciona intestinalis*	XP_002123476	1.63E−21	88	107	Nucleoside diphosphate kinase	2.7.4.6
Contig81	8	941	*Apis mellifera*	XP_391841	1.28E−96	96	357	14-3-3 protein zeta	
Contig14	7	315	*Tribolium castaneum*	XP_971540	4.11E−25	89	118	Glycoprotein 93	
Contig138	6	577	*Tigriopus japonicus*	ACA03523	1.93E−67	92	258	Heat shock protein 70 precursor	
Contig148	6	696	*Lepeophtheirus salmonis*	ACO12708	2.54E−49	87	200	40S ribosomal protein s4e	3.6.5.3
Contig15	6	356	*Xantho poressa*	CAR82602	4.17E−38	88	161	Mitochondrial manganese superoxide dismutase	1.15.1.1
Contig156	5	438	*Daphnia pulex*	EFX69073	7.45E−56	92	220	Proteasome subunit alpha type-5	3.4.25.0

For each contig is reported: number of clustered ESTs, length, organism name and hit accession number, mean *E*-value, mean similarity, score, putative protein function, and Enzyme Commission number (EC).

3.2. Assembly, functional annotation and quantitative RT-qPCR analysis

The 947 high quality ESTs were assembled into 376 Tentative Unigenes (TUGs) (167 contigs and 209 singletons), with lengths ranging from 80 to 1291 bp, and an average of 420 bp. The greatest part of the contigs (96.4%) were assembled from unique ESTs to the forward or to the reverse libraries, with 40% assembled from two ESTs, 16% from three ESTs and 44% from more than three ESTs. Of the total number of TUGs, 264 putative genes (121 contigs and 143 singletons), 70%, significantly matched known proteins from the non-redundant protein database (nr), whereas the remaining 30% did not match any known protein. The top species with the highest number of BLAST hits were, again, *Tribolium castaneum*, *Drosophila melanogaster*, *Mus musculus* and *Lepeoptheirus salmonis*, but also *Daphnia pulex* and *Aedes aegypti*. Thus, assembling ESTs into longer contigs increased the information available for the nucleotide sequence and gave better results in the BLASTx search compared to the raw ESTs sequence. Blast2GO software was able to functionally annotate 200 out of 264 TUGs (94 contigs and 106 singletons), which were further distributed into 158 BP, 191 MF and 148 CC terms at various hierarchical levels, similar to what is reported for ESTs (data not shown).

The following eight contigs assembled from the highest number of unique ESTs to the forward library and belonging to the significantly enriched GO-terms after the Fisher's Test, were selected for RT-qPCR validation: contig 72 (chaperonin-containing T-complex protein 1, TCP-1, subunit eta), contig 154 (cyclin b1), contig 51 (ring finger protein 121, RNF-121), contig 56 (nucleoside diphosphate kinase, NDK), contig 81 (14-3-3, FTT, protein zeta), contig 14 (glycoprotein 93, gp93), contig 138 (heat shock protein 70 precursor, HSP70p), and contig 15 (Mn superoxide dismutase, MnSOD). Only two contigs unique to the reverse library, containing the highest number of ESTs and belonging to the significantly enriched GO-terms after the Fisher's Test, were selected for RT-qPCR, due to the lower number of abundant and physiologically relevant contigs in this library: contig 148 (40S ribosomal protein s4e) and contig 156 (proteasome subunit alpha type-5) (Table 2). Amplicon size, primers' sequences, efficiency (*E*), correlation coefficient (R^2) and NCBI' accession numbers for all these Genes of Interest (GOIs) are listed in Table 3. The identity of these sequences was verified and confirmed using BLASTx. REST analysis and the Pair Wise Fixed Reallocation Randomization Test performed on RT-qPCR results showed that six out of eight contigs selected from the forward library were significantly up-regulated in *Calanus helgolandicus* fed on *Skeletonema marinoi* compared to those fed on *Rhodomonas baltica*. Fig. 2 shows the corresponding relative expression ratio (*R*) for each target gene. Contigs 138 (HSP70p), 154 (cyclin b1), and 14 (gp93), were the most over-expressed (3.4-fold, 2.5-fold and 2.5-fold up-regulated, respectively; $p < 0.001$); followed by contigs 72 (TCP-1, 1.9-fold up-regulated, $p < 0.001$), 56 (NDK, 1.7-fold up-regulated, $p < 0.001$) and 51 (RNF-121, 1.6-fold up-regulated, $p < 0.05$). In contrast, expression levels of contig 81 (14-3-3 FTT protein) and contig 15 (MnSOD) did not change significantly (1.3-fold and 1.0-fold up-regulated, respectively; $p > 0.05$). Relative expression ratio of both contigs from the reverse library, did not change significantly in *C. helgolandicus* fed on *S. marinoi*, being 1.2-fold down-regulated in the case of contig 156 (proteasome subunit alpha type-5, $p > 0.05$) and 1.2-fold up-regulated in the case of contig 148 (40S ribosomal protein s4e, $p > 0.05$).

4. Discussion

Our study is the first large-scale transcriptional profiling of a free-living planktonic copepod, *Calanus helgolandicus*, feeding on

Table 3
Statistics of primers used in RT-qPCR amplification of annotated contigs.

Sequence	Putative protein	GeneBank acc. no.	Primer forward (5′–3′)	Primer reverse (5′–3′)	Amplicon size	*E*	R^2
Contig72[a]	t-Complex protein 1 subunit eta	KC521529	GGCAGGTACTTGCTCAGCTC	ACTGAGAGGTCCCTTCACGA	110	100%	0.995
Contig154[a]	Cyclin b1	KC521530	CCCCTCCACGCAGAGATA	GAAGATGAGGGGTGTGTTGG	131	100%	0.982
Contig51	Ring finger protein 121	KC521531	GAGGCATTTGGAGACGGATA	TCGGGAACATTCTCTTCAGG	206	100%	0.982
Contig56	Nucleoside diphosphate kinase	KC521532	CAATCCTGCTGACTCAATGC	GCTATCTCCTGGTTGGCTGA	136	97.4%	0.998
Contig81	14-3-3 protein zeta	KC521533	ACAAGTTCCTCATCGCCAAG	GCATCCTGGTAAGCCTTCTG	151	99.9%	0.998
Contig14	Glycoprotein 93	KC521534	CATGATGCCAAGCTACCTCA	GTCCAGAGTCTTGCGGACA	139	100%	0.999
Contig138	Heat shock protein 70 precursor	KC521535	GACAATGCTCTGCTTGGACA	TGGTGAGATAGGGGAGGTTG	166	100%	0.992
Contig148	40S ribosomal protein s4e	KC521536	AGATCCAGGACACCATCAGG	TGCCGATGACAAAGACGTAG	186	100%	0.999
Contig15[a]	Mitochondrial manganese superoxide dismutase	KC521537	CCAGTCTTGCTCCAACATCA	CTGGACTGGTGCCTCTCTTT	132	100%	0.994
Contig156	Proteasome subunit alpha type-5	KC521538	AAGGATCACAAGCCCTCTCA	TCGTCGTAGGTGAACCAGTG	159	97%	0.998

GeneBank accession numbers, primer sequences, amplicon sizes (base pair), oligo efficiencies (*E*) and correlation factors (R^2).
[a] Primers have been designed on the complementary strand.

Author's personal copy

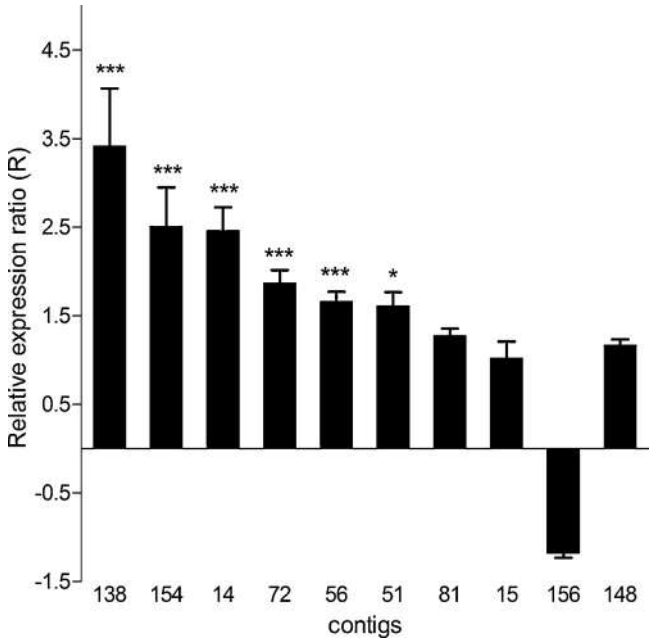

Fig. 2. Gene expression level of annotated contigs in the copepod *Calanus helgolandicus*. Relative expression ratio (*R*) (mean ± SD) of target genes of interest in *C. helgolandicus* specimens fed *S. marinoi* for 2 days, versus specimens fed on the control *Rhodomonas baltica*, and using the ribosomal protein S20 as reference gene to normalize the data. Contigs 138 (heat shock protein 70 precursor), 154 (cyclin b1), 14 (glycoprotein 93), 72 (chaperonin-containing T-complex protein 1 subunit eta), 56 (nucleoside diphosphate kinase), 51 (ring finger protein 121), 81 (14-3-3 protein) and 15 (Mn superoxide dismutase), were unique to the forward *S. marinoi*-fed *Calanus helgolandicus*, whereas contigs 156 (proteasome subunit alpha type-5), and 148 (40S ribosomal protein s4e), were unique to the reverse *R. baltica*-fed *C. helgolandicus* library. Significant values resulting from the Pair-Wise Fixed Reallocation Randomization Test are indicated with asterisks ($^{*}p < 0.05$, $^{***}p < 0.001$).

a cytotoxic diatom, *Skeletonema marinoi*, which induces reproduction failure, offspring abnormalities and larval mortality in copepods (Ianora et al., 2003). We were able to sequence 947 ESTs and generate 376 unigenes of *C. helgolandicus* from two suppression subtractive hybridization (SSH) libraries built to investigate differences in the transcriptome between females fed toxic and non-toxic food. In our study, we showed that the forward (*S. marinoi*-fed *C. helgolandicus*) and the reverse (*Rhodomonas baltica*-fed *C. helgolandicus*) libraries were significantly enriched in genes belonging to dissimilar GO-functional categories. In addition, 96% of *C. helgolandicus* unigenes were unique sequences to either the forward or the reverse library. And ultimately, six out of eight unigenes selected from the forward library for RT-qPCR validation, were significantly up-regulated in *S. marinoi*-fed *C. helgolandicus*, coherently with the results of the SSH library. All these findings suggest that both the forward (*S. marinoi*-fed *C. helgolandicus*) and reverse (*R. baltica*-fed *C. helgolandicus*) subtractions were successful. Although we cannot rule out that some of our results could have been affected by the lack of statistical replicates in the SSH procedure, which was performed on only one treatment sample, we conclude that they are representative of the treatment since they include 500 female copepods collected over a single experimental trial and from a stable and uniform cultivation system.

Skeletonema marinoi is a well know producer of various oxylipins, including highly reactive α,β-unsaturated aldehydes (PUAs), such as 2,4-heptadienal, 2,4-octadienal, and 2,4,7-octatrienal, produced from the oxidative metabolism of lipids and fatty acids (Fontana et al., 2007). These lipid peroxidation products share a common structure with other widely studied aldehydes, such as 4-hydroxy-2-nonenal, malondialdehyde, and 2,4-decadienal (DDE). In particular, DDE has been detected in the diatom *Thalassiosira rotula* (d'Ippolito et al., 2002) and has traditionally been used as a model α,β-unsaturated aldehyde to test the deleterious effect of diatom secondary metabolites on copepods and other animal models (Ianora and Miralto, 2010). PUAs are widely reported to be cytotoxic due to adducts formation with proteins and DNA, induction of altered mitochondrial functionality and activation of cell signaling cascades leading to cell death through necrosis or apoptosis (Hansen et al., 2004; Loureiro et al., 2000; West and Marnett, 2005, 2006).

Previous studies aimed at investigating the molecular response of *Calanus helgolandicus* to the same *Skeletonema marinoi* strain used in this study, were based on a target gene approach and were mainly focused on detoxification and stress genes (Lauritano et al., 2011a,b). These studies showed that the genes encoding for aldehyde dehydrogenase 9, 8 and 6, cellular apoptosis susceptibility protein, inhibitor of apoptosis protein, and alpha- and beta-tubulins, were down-regulated in *C. helgolandicus* after 2 days of feeding, suggesting that these genes may act as early warning signals denoting a deterioration in copepod fitness. The present study enriches these previous observations, by showing that the whole transcriptomic machinery of the copepod to *S. marinoi* was strongly altered in comparison to the control diet *Rhodomonas baltica*. Copepods feeding on *R. baltica*, in fact, showed higher expression of genes involved in basic cellular and organismal processes such as protein synthesis (ribosome biogenesis, macromolecule biosynthetic process) and energy metabolism (electron transport). On the contrary, 2 days of feeding on *S. marinoi* induced higher expression of genes involved in protein folding or degradation, re-organization of actin and tubulin filaments, and processing of environmental and cellular information (biological regulation, signal transduction, response to stimuli). A similar response to stress, that inhibited protein synthesis, was reported for the cladoceran crustacean *Daphnia magna* exposed to the chlorinate fungicide fenarimol (Soetaert et al., 2007) and the blue crab *Callinectis sapidus* under chronic hypoxia exposure (Brown-Peterson et al., 2005). In particular, daphnids exposed for 96 h to the compound showed reduced growth and reproduction and decreased expression of several ribosomal protein genes involved in protein synthesis (Soetaert et al., 2007). The results of the gene enrichment analysis on the two subtraction libraries was confirmed by the RT-qPCR results, which showed that genes encoding for various chaperonin proteins involved in repairing or degrading un-folded and/or damaged proteins (heat shock protein 70 precursor HSP70p, glycoprotein 93 gr93, and chaperonin containing T-complex protein 1 TCP-1), as well as genes encoding for proteins involved in cellular and signal transduction pathways (RING finger protein 121 RNF-121, and nucleoside diphosphate kinase NDK), were significantly up-regulated in *C. helgolandicus* feeding on *S. marinoi* as compared to copepods feeding on the control *R. baltica* diet.

On the whole, genes encoding for molecular chaperones, signal transduction factors, macromolecule processing and stabilization proteins, are highly conserved in the animal kingdom, being part of a core stress proteome typically associated with a generalized Cellular Stress Response (CSR). They are required when there is the need for repairing or degrading mis-folded macromolecules (proteins and DNA), and for activating specific gene networks that re-establish cellular homeostasis, at the expense of reduced metabolic activity (Kültz, 2003). The finding that these genes are over-expressed in *Calanus helgolandicus* feeding on *Skeletonema marinoi* suggests that this diatom induces a CSR in *C. helgolandicus* and that these genes may be involved in the coordinated protection of the copepod against the toxic diet. Combining our findings with previous results reported for *C. helgolandicus* exposed to the same

Author's personal copy

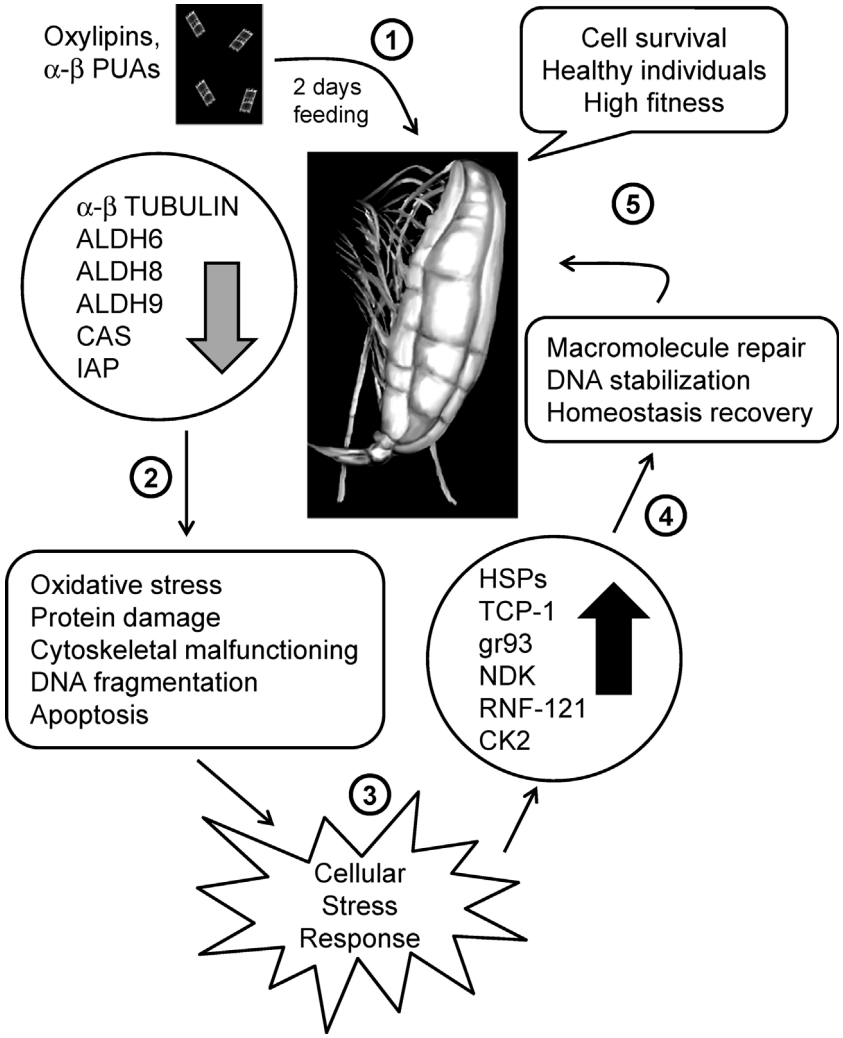

Fig. 3. Hypothetical cascade effects of *S. marinoi* feeding on *C. helgolandicus*. Ingestion of *S. marinoi* (1) induced down-regulation of aldehyde dehydrogenases genes (ALDH 6, 8 and 9), cellular apoptosis susceptibility (CAS) and inhibitor of apoptosis (IAP) genes, and α- and β-tubulin genes, leading to oxidative stress, protein damage, cytoskeletal malfunctioning, DNA fragmentation and apoptosis (2). This elicited a Cellular Stress Reponse (CSR) (3) characterized by over-expression of molecular chaperones (HSPs, TCP-1, gr93) and signal transduction pathways genes (RNF-121, NDK, CK2), which re-established cellular homeostasis and macromolecular structure and function (4). The net effect is high *C. helgolandicus* cell viability and fitness (5).

experimental conditions as the present study, we propose the following cascade effects prompted by short feeding trials of *S. marinoi* on *C. helgolandicus* (Fig. 3). The ingestion of *S. marinoi* (1) induces the down-regulation of several genes encoding for aldehyde dehydrogenases (ALDH 6, 8 and 9), cellular apoptosis susceptibility (CAS) and inhibitor of apoptosis (IAP) proteins, and α- and β-tubulins (Lauritano et al., 2011a,b). Lack of inactivation of aldehydes could lead to their excessive accumulation, reaction with DNA and proteins potentially leading to damage, cytoskeletal malfunctioning, DNA fragmentation and, ultimately, apoptosis (2). This alteration of the cellular homeostasis elicites a (3) Cellular Stress Reponse (CSR) characterized by an over-expression of genes encoding for molecular chaperones (HSPs, TCP-1, gr93) and proteins involved in signal transduction pathways (RNF-121, NDK, CK2). This mechanism is aimed at conserving metabolic energy for re-establishing cellular homeostasis, and stabilizing macromolecular structure and function (4). The net effect is high *C. helgolandicus* cell viability and fitness, in terms of adult survival and reproduction (hatching success is >90% after 48 h feeding on *S. marinoi*, see Fontana et al., 2007, supporting material) (5).

Among the above mentioned chaperonin proteins, the glycoprotein gr93 is reported in *Drosophila melanogaster* to be homologous to the mammalians glycoprotein gp96, an endoplasmic reticulum (ER) chaperone HSP90 involved in the folding of several transmembrane receptors that play a role in cell–cell and cell–tissue interactions (Morales et al., 2009). Likewise, TCP-1 acts specifically in conjunction with other cytosolic chaperones (Hartl, 1996), and assists the folding and polymerization of the cytoskeletal proteins actin and tubulin, being thus involved in microtubule polymerization (Martin et al., 2004). Interestingly, earlier findings showed that diatom polyunsaturated aldehydes (PUAs) blocked tubulin-polymerization in sea urchins (Buttino et al., 1999; Hansen et al., 2004) and actin re-organization in the ascidian *Ciona intestinalis* (Tosti et al., 2003). Thus, our observed higher expression of TCP-1 in *Calanus helgolandicus* after feeding on *Skeletonema marinoi* might be related to the need of repairing misfolded or degraded cytoskeleton proteins induced by the diatom diet. Similarly, up-regulation of RNF-121 could be associated to a possible deleterious effect of this diatom on *C. helgolandicus* oocyte development (Poulet et al., 2007a). This protein belongs to the zinc-finger protein class, which are involved in numerous cellular mechanisms, such as regulation of gene transcription, protein synthesis, cytoskeleton organization, protein folding and chromatin remodeling (Laity et al., 2001). Recently, over-expression of the

Author's personal copy

RNF-121 gene during early stages of gonad development of the nematode *Caenorhabditis elegans*, was related to aberrations in germline development and gonad migration (Darom et al., 2010).

Interestingly, up-regulation of HSP70 has been recently reported in sea urchins embryos exposed to low concentrations of 2,4-decadienal, thus protecting the embryos against the toxic effects of this aldehyde (Romano et al., 2011). Higher expression of this chaperonin protein was also observed in the copepod *Calanus finmarchicus* exposed to thermal stress (Voznesensky et al., 2004) or to chemicals such as naphthalene (Hansen et al., 2008) and diethanolamine DEA (Hansen et al., 2010), or in active animals living in shallow waters, and hence exposed to stress due to temperature, starvation and turbulence, compared to animals living in more stable deeper environments (Aruda et al., 2011). It is worth mentioning that our *Calanus helgolandicus* HSP70p showed the highest BLASTx sequence similarity with that of the harpacticoid copepod *Tigriopus japonicus* (hit accession no. ACA03523). Similar to our findings, the expression level of the harpacticoid HSP70p gene is up-regulated during exposure to heat stress, trace metals, and the endocrine-disrupting chemical (EDC) bisphenol A (Rhee et al., 2009), thus suggesting that HSP70 can be considered a stress-related protein involved in the protection of copepods to various stressors, including lipid peroxidation products.

A similar role as potential stress-responsive protein was also recently suggested for the nucleoside diphosphate kinase NDK (Clavero-Salas et al., 2007). This enzyme is required for the ATP dependent synthesis of nucleoside triphosphates from the respective nucleoside diphosphates. It is a fundamental enzyme encoded by the *nm23* human oncogene, and is implicated in several cellular functions, such as DNA replication, lipid biosynthesis, microtubule dynamics, and various signal transduction pathways, such as the G-protein signaling (Steeg et al., 2011). In *Drosophila melanogaster*, this enzyme is involved in the development of the imaginal discs and a mutation in its corresponding *nm23* homolog, the *abnormal wing disk* (*awd*) gene, induces aberrant development and deformities in insects (Rosengard et al., 1989). Recently, a *nm23* cDNA encoding for the same nucleoside diphosphate kinase, was identified in the transcriptome of the shrimp *Litopenaeus vannamei* and was found to be over-expressed in shrimps infected by the White Spot Syndrome Virus (WSSV) (Clavero-Salas et al., 2007), thus suggesting to be part of the defensive system of the shrimp.

In addition to the above mentioned genes that were up-regulated in *Calanus helgolandicus* feeding on *Skeletonema marinoi*, several other ESTs encoding for proteins involved in various signal transduction pathways were also enriched in the *S. marinoi*-fed *C. helgolandicus* library. For example, the serine/threonine casein/kinases CK2, which controls gene expression by activating a large number of transcription factors (Withmarsh and Davis, 1996), and is involved in the Wnt receptor signaling pathway, and several GTPases of the Ras superfamily, which play a role in vescicle transport, cytoskeleton adjustments associated with cell volume and regulate proliferation, shape, development and protein transport. In particular, Rab GTPases are fundamental components of the cross talks between receptor signaling and endoplasmic reticulum trafficking, a key process in most signaling pathways (von Zastrow and Sorkin, 2007). Recently, a Ras-like GTP-binding protein Rho and a Ras-related protein Rab-6A, were found in a SSH library prepared from the white spot syndrome virus (WSSV)-resistant shrimp *Penaeus japonicus*, thus suggesting that they may be involved in the signal transduction of the shrimp to cope with the viral infection (Pan et al., 2005).

In conclusion, we propose that 2 days of feeding on the oxylipin producing diatom *Skeletonema marinoi* induces a CSR in the copepod *Calanus helgolandicus*. Although our dataset depicts the short term molecular response of a copepod to a diatom diet, it is expected to provide the building blocks for a future discovery of the molecular pathways that might explain copepod reduced hatching success, production of abnormal offspring and apoptosis induced by diatoms during longer feeding trials (5–7 days, see (Ianora and Miralto, 2010). In more general terms, our publicly available dataset for *C. helgolandicus* could provide a basis for finding new candidate genes for elucidating the molecular mechanisms underlying key physiological processes in copepods (diapause, growth and reproduction), or to cope with environmental contaminants, global warming and ocean acidification. These processes may have strong implications for public benefits considering the central role that copepods play for fisheries, ecosystem functioning and global ecosystem health.

Author's contributions

Y.C. conceived the study, designed and performed the experiments, analyzed the data and drafted the manuscript. E.D. partecipated in the SSH experiments and analysis of the data. C.L. partecipated in the design of the study and in the performing of the feeding and RT-qPCR experiments. F.P. helped in the bioinformatic analysis of the data. R.S. partecipated in the bioinformatic analysis of the data and helped to draft the manuscript. A.M. carried out the zooplankton collection. G.P. partecipated in the design of the study and helped to draft the mansucript. A.I. partecipated in the conceivement and design of the study and coordinated the drafting of the mansucript. All authors have read and approved the final manuscript.

Competing interests

The authors declare that they have no competing interests.

Funding

This research received no specific grant from any funding agency in the public, commercial or not-for-profit sectors.

Acknowledgements

We thank F. Esposito for algal stock maintenance and cultivation, M. di Pinto, M. Perna and F. Palumbo for their technical assistance during the experiments. We thank E. Biffali and M. Borra from the Servizio di Biologia Molecolare (SBM) of the SZN for sequence analysis and sample preparation. We also thank Dr. O. Giovanardi from ISPRA, Istituto Superiore per la Protezione e la Ricerca Ambientale, Chioggia (Venezia, Italy), for logistic support during zooplankton sampling in the Adriatic Sea.[SS]

References

Aruda, A.M., Baumgartner, M.F., Reitzel, A.M., Tarrant, A.M., 2011. Heat shock protein expression during stress and diapause in the marine copepod *Calanus finmarchicus*. J. Insect Physiol. 57 (5) 665–675.

Aubry, F.B., Berton, A., Bastianini, M., Socal, G., Acri, F., 2004. Phytoplankton succession in a coastal area of the NW Adriatic, over a 10-year sampling period (1990–1999). Continent. Shelf Res. 24 (1) 97–115.

Benjamini, Y., Hochberg, Y., 1995. Controlling the false discovery rate: a practical and powerful approach to multiple testing. J. R. Stat. Soc. Ser. B (Methodol.) 57 (1) 289–300.

Bonnet, D., Richardson, A., Harris, R., Hirst, A., Beaugrand, G., Edwards, M., Ceballos, S., Diekman, R., Lopez-Urrutia, A., Valdes, L., Carlotti, F., Molinero, J.C., Weikert, H., Greve, W., Lucic, D., Albaina, A., Yahia, N.D., Umani, S.F., Miranda, A., dos Santos, A., Cook, K., Robinson, S., de Puelles, M.L.F., 2005. An overview of *Calanus helgolandicus* ecology in European waters. Prog. Oceanogr. 65 (1) 1–53.

Bonnet, D., Harris, R.P., Yebra, L., Guilhaumon, F., Conway, D.V.P., Hirst, A.G., 2009. Temperature effects on *Calanus helgolandicus* (Copepoda: Calanoida) development time and egg production. J. Plankton Res. 31 (1) 31–44.

Author's personal copy

Bron, J., Frisch, D., Goetze, E., Johnson, S., Lee, C., Wyngaard, G., 2011. Observing copepods through a genomic lens. Front. Zool. 8 (1) 22.

Brown-Peterson, N.J., Larkin, P., Denslow, N., King, C., Manning, S., Brouwer, M., 2005. Molecular indicators of hypoxia in the blue crab *Callinectes sapidus*. Mar. Ecol. Prog. Ser. 286, 203–215.

Buttino, I., Miralto, A., Ianora, A., Romano, G., Poulet, S.A., 1999. Water-soluble extracts of the diatom *Thalassiosira rotula* induce aberrations in embryonic tubulin organisation of the sea urchin Paracentrotus lividus. Mar. Biol. 134 (1) 147–154.

Carotenuto, Y., Ianora, A., Buttino, I., Romano, G., Miralto, A., 2002. Is postembryonic development in the copepod *Temora stylifera* negatively affected by diatom diets? J. Exp. Mar. Biol. Ecol. 276 (1–2) 49–66.

Carotenuto, Y., Ianora, A., Miralto, A., 2011. Maternal and neonate diatom diets impair development and sex differentiation in the copepod *Temora stylifera*. J. Exp. Mar. Biol. Ecol. 396, 99–107.

Carotenuto, Y., Esposito, F., Pisano, F., Lauritano, C., Perna, M., Miralto, A., Ianora, A., 2012. Multi-generation cultivation of the copepod *Calanus helgolandicus* in a recirculating system. J. Exp. Mar. Biol. Ecol. 418–419, 46–58.

Clavero-Salas, A., Sotelo-Mundo, R.R., Gollas-Galván, T., Hernández-López, J., Peregrino-Uriarte, A.B., Muhlia-Almazán, A., Yepiz-Plascencia, G., 2007. Transcriptome analysis of gills from the white shrimp *Litopenaeus vannamei* infected with White Spot Syndrome Virus. Fish Shellfish Immunol. 23 (2) 459–472.

Conesa, A., Gotz, S., Garcia-Gomez, J.M., Terol, J., Talon, M., Robles, M., 2005. Blast2GO: a universal tool for annotation, visualization and analysis in functional genomics research. Bioinformatics 21 (18) 3674–3676.

Cook, K.B., Bunker, A., Hay, S., Hirst, A.G., Speirs, D.C., 2007. Naupliar development times and survival of the copepods *Calanus helgolandicus* and *Calanus finmarchicus* in relation to food and temperature. J. Plankton Res. 29 (9) 757–767.

Darom, A., Bening-Abu-Shach, U., Broday, L., 2010. RNF-121 is an endoplasmic reticulum-membrane E3 ubiquitin ligase involved in the regulation of beta-integrin. Mol. Biol. Cell 21 (11) 1788–1798.

Diatchenko, L., Lau, Y.-F.C., Aaron, P.C., Chenchik, A., Moqadam, F., Huang, B., Lukyanov, S., Lukyanov, K., Gurskaya, N., Sverdlov, E.D., Siebert, P.D., 1996. Suppression subtractive hybridization: a method for generating differentially regulated or tissue-specific cDNA probes and libraries. Proc. Natl. Acad. Sci. U. S. A. 93 (12) 6025–6030.

d'Ippolito, G., Iadicicco, O., Romano, G., Fontana, A., 2002. Detection of short-chain aldehydes in marine organisms: the diatom *Thalassiosira rotula*. Tetrahedron Lett. 43 (35) 6137–6140.

d'Ippolito, G., Tucci, S., Cutignano, A., Romano, G., Cimino, G., Miralto, A., Fontana, A., 2004. The role of complex lipids in the synthesis of bioactive aldehydes of the marine diatom *Skeletonema costatum*. Biochim. Biophys. Acta 1686, 100–107.

Ewing, B., Green, P., 1998. Base-calling of automated sequencer traces using phred. II. Error probabilities. Genome Res. 8 (3) 186–194.

Ewing, B., Hillier, L.D., Wendl, M.C., Green, P., 1998. Base-calling of automated sequencer traces using phred. I. Accuracy assessment. Genome Res. 8 (3) 175–185.

Fontana, A., d'Ippolito, G., Cutignano, A., Romano, G., Lamari, N., Massa Gallucci, A., Cimino, G., Miralto, A., Ianora, A., 2007. LOX-induced lipid peroxidation mechanism responsible for the detrimental effect of marine diatoms on zooplankton grazers. Chem. Biol. Chem. 8 (15) 1810–1818.

Goetz, S., Garcia-Gomez, J.M., Terol, J., Williams, T.D., Nagaraj, S.H., Nueda, M.J., Robles, M., Talon, M., Dopazo, J., Conesa, A., 2008. High-throughput functional annotation and data mining with the Blast2GO suite. Nucleic Acids Res. 36 (10) 3420–3435.

Guillard, R.R., Lorenzen, C.J., 1972. Yellow-green algae with chlorophyllidae c. J. Phycol. 8, 10–14.

Halsband-Lenk, C., Pierson, J.J., Leising, A.W., 2005. Reproduction of *Pseudocalanus newmani* (Copepoda: Calanoida) is deleteriously affected by diatom blooms – a field study. Prog. Oceanogr. 67 (3–4) 332–348.

Hansen, E., Even, Y., Geneviere, A.-M., 2004. The α,β,γ,∂-unsaturated aldehyde 2-trans-4-trans-decadienal disturbs DNA replication and mitotic events in early sea urchin embryos. Toxicol. Sci. 81 (1) 190–197.

Hansen, B.H., Altin, D., Vang, S.-H., Nordtug, T., Olsen, A.J., 2008. Effects of naphthalene on gene transcription in *Calanus finnmarchicus* (Crustacea: Copepoda). Aquat. Toxicol. 86, 157–165.

Hansen, B.H., Altin, D., Booth, A., Vang, S.-H., Frenzel, M., Sørheim, K.R., Brakstad, O.G., Størseth, T.R., 2010. Molecular effects of diethanolamine exposure on *Calanus finmarchicus* (Crustacea: Copepoda). Aquat. Toxicol. 99 (2) 212–222.

Hartl, F.U., 1996. Molecular chaperones in cellular protein folding. Nature 381, 571–580.

Huang, X., Madan, A., 1999. CAP3: a DNA sequence assembly program. Genome Res. 9, 868–877.

Ianora, A., Miralto, A., 2010. Toxigenic effects of diatoms on grazers, phytoplankton and other microbes: a review. Ecotoxicology 19, 493–511.

Ianora, A., Poulet, S.A., Miralto, A., 1995. A comparative study of the inhibitory effect of diatoms on the reproductive biology of the copepod *Temora stylifera*. Mar. Biol. 121 (3) 533–539.

Ianora, A., Poulet, S., Miralto, A., 2003. The effects of diatoms on copepod reproduction: a review. Phycologia 42 (4) 351–363.

Ianora, A., Miralto, A., Poulet, S.A., Carotenuto, Y., Buttino, I., Romano, G., Casotti, R., Pohnert, G., Wichard, T., Colucci-D'Amato, L., Terrazzano, G., Smetacek, V., 2004. Aldehyde suppression of copepod recruitment in blooms of a ubiquitous planktonic diatom. Nature 429, 403–407.

Keller, M.D., Selvin, R.C., Claus, W., Guillard, R.R.L., 1987. Media for the culture of oceanic ultraphytoplankton. J. Phycol. (23) 633–638.

Kooistra, W.H.C.F., Sarno, D., Balzano, S., Gu, H., Andersen, R.A., Zingone, A., 2008. Global diversity and biogeography of *Skeletonema* species (Bacillariophyta). Protist 159 (2) 177–193.

Kültz, D., 2003. Evolution of the cellular stress proteome: from monophyletic origin to ubiquitous function. J. Exp. Biol. 206, 3119–3124.

Laity, J.H., Lee, B.M., Wright, P.E., 2001. Zinc finger proteins: new insight into structural and functional diversity. Curr. Opin. Struct. Biol. 11, 39–46.

Lauritano, C., Borra, M., Carotenuto, Y., Biffali, E., Miralto, A., Procaccini, G., Ianora, A., 2011a. First molecular evidence of diatom effects in the copepod *Calanus helgolandicus*. J. Exp. Mar. Biol. Ecol. 404 (1–2) 79–86.

Lauritano, C., Borra, M., Carotenuto, Y., Biffali, E., Miralto, A., Procaccini, G., Ianora, A., 2011b. Molecular evidence of the toxic effects of diatom diets on gene expression patterns in copepods. PLoS ONE 6 (10) e26850.

Lauritano, C., Carotenuto, Y., Miralto, A., Procaccini, G., Ianora, A., 2012. Copepod population-specific response to a toxic diatom diet. PLoS ONE 7 (10) e47262.

Lauritano, C., Carotenuto, Y., Procaccini, G., Turner, J.T., Ianora, A., 2013. Changes in expression of stress genes in copepods feeding upon a non-brevetoxin producing strain of the dinoflagellate *Karenia brevis*. Harmful Algae 28, 23–30.

Loureiro, A.P.M., Di Mascio, P., Gomes, O.F., Medeiros, M.H.G., 2000. trans,trans-2,4-Decadienal-induced 1,N-2-etheno-2′-deoxyguanosine adduct formation. Chem. Res. Toxicol. 13 (7) 601–609.

Martin, J., Gruber, M., Lupas, A.N., 2004. Coiled coils meet the chaperone world. Trends Biochem. Sci. 29, 455–458.

Masoudi-Nejad, A., Tonomura, K., Kawashima, S., Moriya, Y., Suzuki, M., Itoh, M., Kanehisa, M., Endo, T., Goto, S., 2006. EGassembler: online bioinformatics service for large-scale processing, clustering and assembling ESTs and genomic DNA fragments. Nucleic Acids Res. 34 (Suppl. 2) W459–W462.

Mauchline, J., 1998. The biology of Calanoid Copepods. In: Blaxter, J.H.S., Southward, A.J., Tyler, P.A. (Eds.), Advances in Marine Biology. Academic Press, USA, p. 710.

Miralto, A., Barone, G., Romano, G., Poulet, S.A., Ianora, A., Russo, G.L., Buttino, I., Mazzarella, G., Laabir, M., Cabrini, M., Giacobbe, M.G., 1999. The insidious effect of diatoms on copepod reproduction. Nature 402 (6758) 173–176.

Morales, C., Wu, S., Yang, Y., Hao, B., Li, Z.H., 2009. Drosophila glycoprotein 93 is an ortholog of mammalian heat shock protein gp96 (grp94, HSP90b1, HSPC4) and Retains disulfide bond-independent chaperone function for TLRs and integrins. J. Immunol. 183 (8) 5121–5128.

Pan, D., He, N., Yang, Z., Liu, H., Xu, X., 2005. Differential gene expression profile in hepatopancreas of WSSV-resistant shrimp (*Penaeus japonicus*) by suppression subtractive hybridization. Dev. Comp. Immunol. 29 (2) 103–112.

Pfaffl, M.W., Horgan, G.W., Dempfle, L., 2002. Relative expression software tool (REST) for group-wise comparison and statistical analysis of relative expression results in real-time PCR. Nucleic Acids Res. 30 (9) e36.

Pierson, J.J., Halsband-Lenk, C., Leising, A.W., 2005. Reproductive success of *Calanus pacificus* during diatom blooms in Dabob Bay, Washington. Prog. Oceanogr. 67 (3–4) 314–331.

Pohnert, G., 2000. Wound-activated chemical defense in unicellular planktonic algae. Angew. Chem. Int. Ed. 39 (23) 4352–4354.

Pond, D.W., Harris, R., Head, R., Harbour, D., 1996. Environmental and nutritional factors determining seasonal variability in the fecundity and egg viability of *Calanus helgolandicus* in coastal waters off Plymouth, UK. Mar. Ecol. Prog. Ser. 143, 45–63.

Poulet, S., Wichard, T., Ledoux, J.B., Lebreton, B., Marchetti, J., Dancie, C., Bonnet, D., Cueff, A., Morin, P., Pohnert, G., 2006. Influence of diatoms on copepod reproduction. I. Field and laboratory observations related to *Calanus helgolandicus* egg production. Mar. Ecol. Prog. Ser. 308, 129–142.

Poulet, S.A., Cueff, A., Wichard, T., Marchetti, J., Dancie, C., Pohnert, G., 2007a. Influence of diatoms on copepod reproduction. III. Consequences of abnormal oocyte maturation on reproductive factors in *Calanus helgolandicus*. Mar. Biol. 152 (2) 415–428.

Poulet, S.A., Escribano, R., Hidalgo, P., Cueff, A., Wichard, T., Aguilera, V., Vargas, C.A., Pohnert, G., 2007b. Collapse of *Calanus chilensis* reproduction in a marine environment with high diatom concentration. J. Exp. Mar. Biol. Ecol. 352 (1) 187–199.

Rey-Rassat, C., Irigoien, X., Harris, R., Head, R., Carlotti, F., 2002. Growth and development of *Calanus helgolandicus* reared in the laboratory. Mar. Ecol. Prog. Ser. 238, 125–138.

Rhee, J.-S., Raisuddin, S., Lee, K.-W., Seo, J.S., Ki, J.-S., Kim, I.-C., Park, H.G., Lee, J.-S., 2009. Heat shock protein (Hsp) gene responses of the intertidal copepod *Tigriopus japonicus* to environmental toxicants. Comp. Biochem. Physiol. C 149 (1) 104–112.

Romano, G., Costantini, M., Buttino, I., Ianora, A., Palumbo, A., 2011. Nitric oxide mediates the stress response induced by diatom adehydes in the sea urchin *Paracentrotus lividus*. PLoS ONE 6, e25980.

Rosengard, A.M., Krutzsch, H.C., Shearn, A., Biggs, J.R., Barker, E., Margulies, I.M.K., King, C.R., Liotta, L.A., Steeg, P.S., 1989. Reduced Nm23/Awd protein in tumour metastasis and aberrant *Drosophila* development. Nature 342 (6246) 177–180.

Soetaert, A., van der Ven, K., Moens, L.N., Vandenbrouck, T., van Remortel, P., De Coen, W.M., 2007. Daphnia magna and ecotoxicogenomics: gene expression profiles of the anti-ecdysteroidal fungicide fenarimol using energy-, molting- and life stage-related cDNA libraries. Chemosphere 67 (1) 60–71.

Steeg, P., Zollo, M., Wieland, T., 2011. A critical evaluation of biochemical activities reported for the nucleoside diphosphate kinase/Nm23/Awd

Author's personal copy

family proteins: opportunities and missteps in understanding their biological functions. Naunyn-Schmiedeberg's Arch. Pharmacol. 384 (4) 331–339.

Tosti, E., Romano, G., Buttino, I., Cuomo, A., Ianora, A., Miralto, A., 2003. Bioactive aldehydes from diatoms block the fertilization current in ascidian oocytes. Mol. Reprod. Dev. 66 (1) 72–80.

Vargas, C.A., Escribano, R., Poulet, S., 2006. Phytoplankton food quality determines time windows for successful zooplankton reproductive pulses. Ecology 87 (12) 2992–2999.

von Zastrow, M., Sorkin, A., 2007. Signaling on the endocytic pathway. Curr. Opin. Cell Biol. 19, 436–445.

Voznesensky, M., Lenz, P.H., Spanings-Pierrot, C.I., Towle, D.W., 2004. Genomic approaches to detecting thermal stress in *Calanus finmarchicus* (Copepoda: Calanoida). J. Exp. Mar. Biol. Ecol. 311 (1) 37–46.

West, J.D., Marnett, L.J., 2005. Alterations in gene expression induced by the lipid peroxidation product, 4-hydroxy-2-nonenal. Chem. Res. Toxicol. 18 (11) 1642–1653.

West, J.D., Marnett, L.J., 2006. Endogenous reactive intermediates as modulators of cell signaling and cell death. Chem. Res. Toxicol. 19 (2) 173–194.

Withmarsh, A.J., Davis, R.J., 1996. Transcription factor AP-1 regulation by mitogen-activated protein kinase signal transduction pathways. J. Mol. Med. (Heidelberg, Ger.) 74, 589–607.

Provided for non-commercial research and education use.
Not for reproduction, distribution or commercial use.

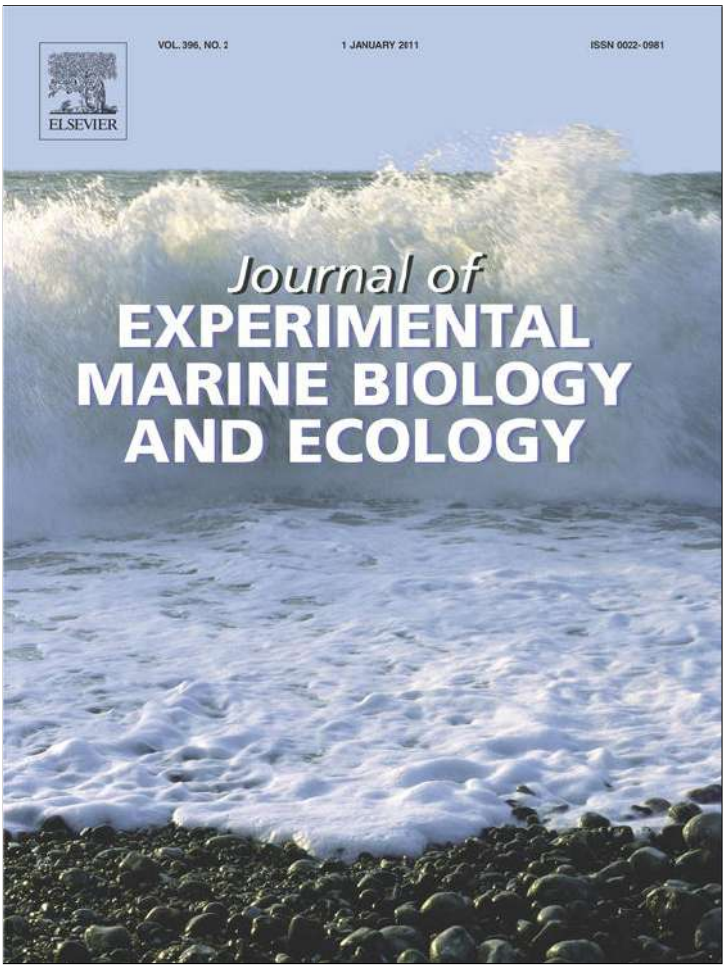

(This is a sample cover image for this issue. The actual cover is not yet available at this time.)

This article appeared in a journal published by Elsevier. The attached copy is furnished to the author for internal non-commercial research and education use, including for instruction at the authors institution and sharing with colleagues.

Other uses, including reproduction and distribution, or selling or licensing copies, or posting to personal, institutional or third party websites are prohibited.

In most cases authors are permitted to post their version of the article (e.g. in Word or Tex form) to their personal website or institutional repository. Authors requiring further information regarding Elsevier's archiving and manuscript policies are encouraged to visit:

http://www.elsevier.com/copyright

Author's personal copy

Journal of Experimental Marine Biology and Ecology 404 (2011) 79–86

Contents lists available at ScienceDirect

Journal of Experimental Marine Biology and Ecology

journal homepage: www.elsevier.com/locate/jembe

First molecular evidence of diatom effects in the copepod *Calanus helgolandicus*

Chiara Lauritano *, Marco Borra, Ylenia Carotenuto, Elio Biffali, Antonio Miralto, Gabriele Procaccini, Adrianna Ianora

Stazione Zoologica Anton Dohrn, Villa Comunale I, 80121 Napoli, Italy

ARTICLE INFO

Article history:
Received 1 February 2011
Received in revised form 11 May 2011
Accepted 12 May 2011
Available online xxxx

Keywords:
Copepod
Diatom
PUA
Reference genes
RT-qPCR
Tubulin

ABSTRACT

In this study we develop gene expression tools in *Calanus helgolandicus* to study the effects of toxic diatom diets on copepod fitness and survival. We demonstrate that when adult females are fed on the control dinoflagellate *Prorocentrum minimum* and the flagellate *Rhodomonas baltica*, which are not known to produce toxic oxylipins, there are no significant changes in alpha- and beta-tubulin (microtubule subunits) gene expression levels. By contrast, the oxylipin-producing diatom *Skeletonema marinoi* influences tubulin expression levels which were markedly down-regulated. We scored a panel of putative reference genes (ACT, EFA, GAPDH, 18S, S7, S20, ATPs, UBI and IST) and found that two (S20 and S7) were highly stable in the tested conditions and can be used for further experiments. To normalize reverse transcription-quantitative real time polymerase chain reaction (RT-qPCR) data we also used the third best reference gene, GAPDH, considering the possibility that the two ribosomal proteins could be co-regulated. This pilot study will pave the way for further investigations on which genes are affected by diatom diets and clarify when and if a stress response or a detoxification mechanism becomes visible in *C. helgolandicus*. Moreover, the RT-qPCR analysis presented here may also be useful to study the effects of other diets and/or environmental factors such as salinity, temperature, pollution and other toxic compounds, on gene expression levels in this copepod species.

© 2011 Elsevier B.V. All rights reserved.

1. Introduction

Diatoms are eukaryotic unicellular plants that constitute one of the major components of marine phytoplankton, comprising up to 40% of annual productivity at sea (Falkowski, 1994) and representing 25% of global carbon-fixation (Nelson et al., 1995). Diatoms have traditionally been considered a preferential food for zooplankton grazers such as copepods and for the transfer of organic carbon to higher trophic levels sustaining important fisheries (Mauchline, 1998). In the last two decades, however, this beneficial role has been challenged after the discovery that several genera of diatoms produce secondary metabolites such as short-chain polyunsaturated aldehydes (PUAs) and other oxygenated fatty acid degradation products such as hydroxides, oxo-acids, epoxy alcohols, and hydroperoxides, collectively termed oxylipins, that induce reproductive failure in zooplankton grazers (Fontana et al., 2007; Ianora et al., 2004; Miralto et al., 1999; Romano et al., 2010). These compounds are not constitutively present in the diatom cells but are produced from fatty acid precursors by enzymes activated within seconds after membrane damage due to senescence or grazing (as reviewed by Ianora and Miralto, 2010).

Oxylipins, and PUAs in particular, have important biological and biochemical properties including the disruption of gametogenesis, gamete functionality, fertilization, embryonic mitosis and larval fitness and competence (Caldwell, 2009). Buttino et al.(1999) were the first to show that water-soluble extracts of the diatom *Thalassiosira rotula* induced aberrations in embryonic tubulin organization leading to cell blockage and the absence of spindle formation in the sea urchin *Paracentrotus lividus*, but the molecules responsible for these effects were unknown at the time. Miralto et al.(1999) later isolated the PUAs 2-trans-4-cis-7-cis-decatrienal, 2-trans-4-trans-7-cis-decatrienal and 2-trans-4-trans-decadienal and showed that they arrested embryonic development of copepod and sea urchin embryos in a dose-dependent manner, and also had antiproliferative and apoptotic effects on human carcinoma cells. Hansen et al.(2004)) studied the effects of decadienal on the sea urchin *Sphaerechinus granularis* and showed that this PUA inhibited cyclin B/Cdk1 kinase activity and DNA replication. Staining of alpha-tubulin subunits showed that tubulin polymerization was disrupted and aberrations were induced in mitotic spindles (Hansen et al., 2004).

Tubulins are proteins that are the building blocks of microtubules (MTs), one of the active components of the cytoskeleton. MTs play an important role in many cellular functions including development and maintenance of cell shape, growth, signaling, protein movement, intracellular vesicle transport, organization and positioning of membranous organelles, and segregating replicated chromosomes into daughter cells during mitosis and meiosis (Calligaris et al., 2010; Harrison et al., 2009; Jordan Mary Ann, 2004; Nogales et al., 1998).

* Corresponding author. Tel.: +39 0815833235; fax: +39 0817641355.
E-mail addresses: chiara.lauritano@szn.it (C. Lauritano), borra@szn.it (M. Borra), ylenia@szn.it (Y. Carotenuto), elio@szn.it (E. Biffali), miralto@szn.it (A. Miralto), gpro@szn.it (G. Procaccini), ianora@szn.it (A. Ianora).

0022-0981/$ – see front matter © 2011 Elsevier B.V. All rights reserved.
doi:10.1016/j.jembe.2011.05.009

Author's personal copy

MTs consist in α- and β-tubulin monomers which constantly switch between a state of polymerization and depolymerization (Calligaris et al., 2010; Nogales et al., 1998), the ratio of which can be altered by many natural products and drugs, especially anti-cancer compounds targeting MTs (Calligaris et al., 2010; Harrison et al., 2009; Jordan Mary Ann, 2004; Sashidhara et al., 2009). Compounds that bind to tubulins modify the formation and function of MTs and can affect the proper functioning and formation of the mitotic spindle. If MT function is altered and spindle dynamics is compromised, a mitotic block or the slowing down in cell cycle progression occurs at the metaphase-anaphase transition, eventually leading to apoptosis (Jordan Mary Ann, 2004).

The aim of this study was to evaluate, for the first time, the effects of ingestion of the oxylipin-producing diatom *Skeletonema marinoi* (SKE) by the copepod *Calanus helgolandicus* on α- and β-tubulin gene expression levels using the reverse transcription-quantitative real time polymerase chain reaction (RT-qPCR). Previous studies have already shown that a diet of *S. marinoi* which contains high levels of PUAs and other oxylipins (same strain as in this study) reduces egg hatching success and female survival in this copepod species (Fontana et al., 2007; Ianora et al., 2004), with a concomitant appearance of apoptosis in both copepod embryos and female tissues (Buttino et al., 2008), but there are no studies on gene expression analyses in the copepod *C. helgolandicus*. We also investigated tubulin gene expression levels in *C. helgolandicus* feeding on the non-oxylipin producing flagellate *Rhodomonas baltica* (RHO) and dinoflagellate *Prorocentrum minimum* (PRO) currently being used to rear *C. helgolandicus* in our laboratory. *P. minimum* was considered the control diet since several previous studies have shown that *C. helgolandicus* reproduces and grows well on this diet (Ianora et al., 2004). Although the biology of *C. helgolandicus* species is rather well known (Mauchline, 1998), very little is known about its genome, except for the gene sequences of cytochrome oxidase subunit I, antennapedia proteins 1 and 2, cytochrome b, and 16S, 18S and 28S ribosomal RNA as reported in the public database PubMed. Since there are few studies on gene expression analysis via qPCR in copepods (Frost and Nilsen, 2003; Hansen et al., 2008a; Hansen et al., 2008b; Hansen et al., 2009; Hansen et al., 2010; Kvamme et al., 2004; Lee et al., 2007; Lee et al., 2008; Seo et al., 2006; Skern-Mauritzen et al., 2009; Tarrant et al., 2008), and none of these focus on *C. helgolandicus*, here we also describe the first evaluation of reference genes (RGs) as internal controls for RT-qPCR analyses in *C. helgolandicus*. It is important to note that the analyses of potential RGs were conducted according to the MIQE suggestions and checklist (Bustin et al., 2009; Bustin et al., 2010).

2. Methods

2.1. Collection of copepods

Calanus helgolandicus specimens were collected in the North Adriatic Sea from March to April 2009 and transported to Naples where they were placed in a 500 l re-circulating copepod breeding system (Buttino et al., in press) maintained at 20 °C, 38 ppm salinity, 12 h:12 h light:dark cycle, and a mixed diet of the flagellates *R. baltica*, *P. minimum* and *Isochrysis galbana*.

Adult female *C. helgolandicus* specimens were sampled from the culturing tanks, isolated under a Leica stereomicroscope and transferred to 10 l beakers filled with 0.22 μm filtered sea water at 20 °C. Beakers containing from 5 to 40 adult females were fed either unialgal diets of the control non-oxylipin producing dinoflagellate *P. minimum* (PRO) (6000–8000 cells/ml), or test diets of the oxylipin-producing diatom *S. marinoi* (SKE) (45,000–60,000 cells/ml) and the non-oxylipin producing flagellate *R. baltica* (RHO) (7500–8000 cells/ml). The strains belong to the Stazione Zoologica Anton Dohrn culture collection. *R. baltica* and *P. minimum* were cultured in 2-l glass jars with 0.22 μm-filtered FSW enriched with *k* medium at 20 °C and on a 12:12 h dark:light cycle. The diatom *S. marinoi* was cultured under the same experimental conditions but with F2 medium.

Copepods were collected from the culturing tank on three different occasions (Table 1). The first sampling was conducted in May 2009 when two replicates of 20 adult *C. helgolandicus* were fed PRO (replicates designated as PRO1M and PRO2M, respectively) and another two were fed SKE (replicates designated as SKE1M and SKE2M, respectively). The second collection was in July 2009 when four groups of 5 animals were fed PRO (replicates designated as PRO1L, PRO2L, PRO3L and PRO4L, respectively) and another four were fed SKE (replicates designated as SKE1L, SKE2L, SKE3L and SKE4L, respectively). The third sampling was in September when a third algae was introduced, RHO. Three groups of 40 specimens were fed RHO (replicates designated as RHO1S, RHO2S and RHO3S, respectively) and three were fed SKE (replicates designated as SKE1S, SKE2S and SKE3S, respectively).

During each sampling, animals were fed for 2 days *ad libitum* on either one of the three algal diets and were then transferred to filtered sea water (FSW) for 24 h to eliminate any algal residues in the gut. After this, each replicate was washed in 50 μl of FSW and carefully transferred to 500 μl Trizol Reagent (Invitrogen), frozen directly in liquid nitrogen and stored at −80 °C for a few weeks until RNA extraction. To study the extent to which the selected genes were differentially expressed in our experimental conditions, we extracted RNA and retro-transcribed it in complementary DNA (cDNA) (double-stranded DNA version of an mRNA molecule), which was used as the template for our molecular analyses.

2.2. RNA extraction and quantification

Total RNA was extracted using *Trizol* according to the manufacturer's protocol (Invitrogen). To remove hypothetically contaminating DNA, each sample was treated with DNaseI (Invitrogen) according to the instruction manual. RNA quantity was assured by *Nano-Drop* (ND-1000 UV–Vis spectrophotometer; NanoDrop Technologies) monitoring the absorbance at 260 nm; purity was determined by monitoring the 260/280 nm and 260/230 nm ratios using the same instrument. All samples were free from protein and organic solvents used during RNA extraction. RNA quality was also evaluated by gel electrophoresis showing minimal degradation of RNA, which was almost completely intact, with sharp 18S and 28S ribosomal bands.

Table 1
Copepod collections including information on sampling month, number of specimens fed and frozen for RNA extraction, algae used for feeding experiments and abbreviation of the treated groups.

Sampling time	Specimen number	Feeding	Abbreviation
May	20	PRO	PRO1M
	20	PRO	PRO2M
	20	SKE	SKE1M
	20	SKE	SKE2M
July	5	PRO	PRO1L
	5	PRO	PRO2L
	5	PRO	PRO3L
	5	PRO	PRO4L
	5	SKE	SKE1L
	5	SKE	SKE2L
	5	SKE	SKE3L
	5	SKE	SKE4L
September	40	RHO	RHO1S
	40	RHO	RHO2S
	40	RHO	RHO3S
	40	SKE	SKE1S
	40	SKE	SKE2S
	40	SKE	SKE3S

Author's personal copy

Table 2
PubMed accession numbers for candidate reference genes (RG) and genes of interest (GOI) for *Calanus helgolandicus* qPCR assays. Putative RGs were elongation factor 1α (EFA), adenosine 3-phosphate synthase (ATPs), histone 3 (HIST), glyceraldehyde-3-phosphate dehydrogenase (GAPDH), ribosomal units (18S, S7, and S20), ubiquitin (UBI), β-actin (ACT) and GOIs were α- and β-tubulins. Gene functions, primer sequences, amplicon sizes, oligo efficiencies (E^a) and correlation factors (R^2) are also given.

Gene name	Acc. no.	Function	Primer sequence 5'-3' (forward and reverse)	Amplicon size	E^a	R^2
Reference genes						
EFA	HQ270534	Translational elongation factor	GACAAGCCCCTCAGACTTCC GGAGAGACTCGTGGTGCATC	172	97%	0.9998
ATPs	HQ270507	Synthesis ATP	CTCCATCACTGACGGACAGATC TCAAGCTTCATGGAACCAGC	150	100%	0.9986
Hist3	HQ270530	Structure of chromatin	GAGGAGTGAAGAAGCCCCAC TGAAGTCCTGAGCAATCTCCC	137	100%	0.9969
18S	AY446908	Ribosomal protein	GAAACCAAAGCATTTGGGTTC GCTATCAATCTGTCAATCCTTCC	164	89%	0.9958
GAPDH	HQ270535	Oxidoreductase in glycolysis and gluconeogenesis	ATCTTTGATGCCAAGGCTGG GTCCTTGCCCTGCATGAAG	126	91%	0.9704
S20	HQ270531	Ribosomal protein	CGTAAGACTCCTTGTGGTGAGG GAAGTGATCTGCTTCACGATCTC	113	89%	0.9915
S7	HQ270532	Ribosomal protein	CGTGAGCTGGAAAAGAAGTTC CAGGATGGAGTTGTGGACAG	147	100%	0.9934
Ubi	HQ270536	Proteins degradation	GCAAGACCATCACCCTTGAG CAGCGAAAGATCAACCTCTG	113	100%	0.9984
Actin	HQ270533	Cytoskeleton structure	GGCACCACACTTTCTACAACG GTTGAAGGTCTCGAACATGATC	128	93%	0.9993
Genes of interest						
α tub	HQ270529	Microtubule subunit	ACAGCTTCTCCACCTTCTTCTC GTTGTTGGCGGCATCCTC	167	94%	0.9997
β tub	HQ270528	Microtubule subunit	GGATTTCAGCTGACCCACTC GTCTCATCAGTATTTTCCACCAG	206	97%	0.9862

[a] Oligo efficiency.

2.3. cDNA synthesis

The amount of RNA used for the reverse transcription steps was always 1 μg. This amount of RNA was converted into cDNA with the ProScript First Strand cDNA Synthesis Kit (New England Biolabs), following the manufacturer's instructions, and using the *GeneAmp PCR System 9700* (Perkin Elmer).The first reaction was carried out in 16 μl final volume with 1 μg of RNA, 50 μM of dt_{23} VN Primer, 15 μM of Random Primer 9, 2.5 μM of dNTP Mix and H_2O. The mix was first denatured by heating at 70 °C for 5 min. A second mix with 1% RT buffer, 10 units/μl of RNase Inhibitor and 25 units/μl of M-MuLV was added to reach a final volume of 20 μl, and the total reaction mix was incubated at 42 °C for 90 min and at 95 °C for 5 min. RNase H (2 units/μl) was added to eliminate non-converted (or potential contaminant) RNA by incubating at 37 °C for 20 min, followed by 5 min at 95 °C to stop the reaction. To evaluate the efficiency of cDNA synthesis, a PCR was carried out with primers of a constitutive gene, S20. The reaction was carried out on the *GeneAmp PCR System 9700* (Perkin Elmer) in 20 μl final volume with 2 μl 10× PCR reaction buffer Roche, 2 μl 0.1% BSA, 2 μl 10× 2 mM dNTP, 0.8 μl 5 U/μl Taq Roche, 1 μl

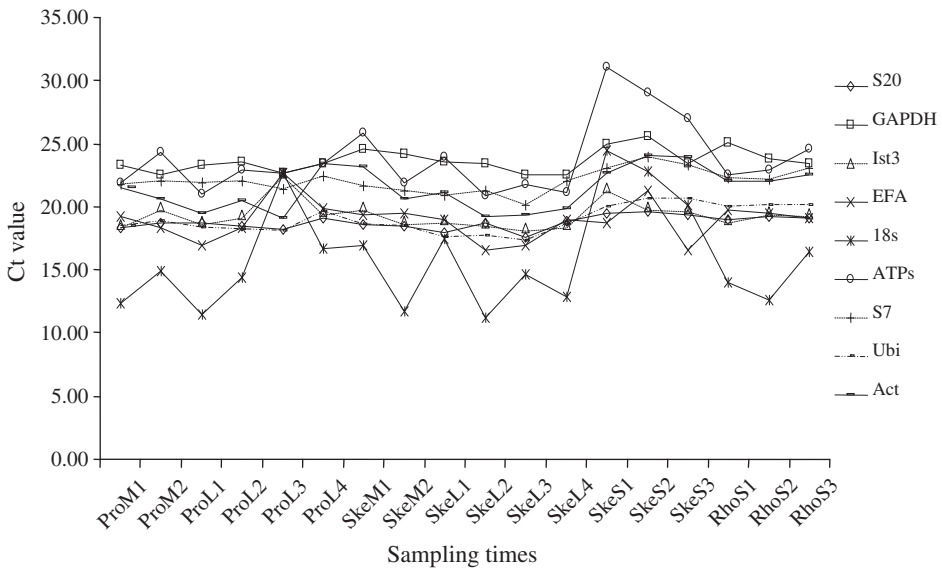

Fig. 1. Ct value profiles. The Ct values (ordinates) obtained for all candidate reference genes (RG) during all samplings (abscissa) for normalization in *C. helgolandicus* qPCR assays. Each curve represents the degree of stability of Ct values for each RG.

Author's personal copy

Table 3
BestKeeper results. Descriptive statistics of the derived crossing points for each putative RG, where n = number of samples; GM = geometric mean; AR = arithmetic mean; min and max = extreme values of the crossing points (CP); SD = standard deviation of CP; CV = coefficient of variance.

	S20	GAPDH	HIST3	EFA	18S	ATPS	S7	UBI	ACT
n	18	18	18	18	18	18	18	18	18
GM	18.73	23.62	19.52	18.86	15.52	23.66	22	18.91	21.35
AR	18.74	23.64	19.55	18.92	15.98	23.81	22.02	18.94	21.41
min	17.5	22.47	18.29	16.49	11.26	20.83	20.09	17.31	19.15
max	19.65	25.55	22.67	22.67	24.38	31.06	23.9	20.67	24.01
SD	0.42	0.68	0.76	1.11	3.29	2.1	0.67	0.94	1.41
CV	2.22	2.89	3.87	5.85	20.59	8.82	3.05	4.96	6.57

20 pmol/μl of each oligo, template cDNA and nuclease-free water to 20 μl. The PCR program consisted of a denaturation step at 95 °C for 3 min, 40 cycles at 95 °C for 30 s, 60 °C for 1 min and 72 °C for 30 s, and a final extension step at 72 °C for 7 min.

2.4. Primer design

To perform RT-qPCR in this copepod species we designed specific primers to isolate and amplify selected genes. Primers for hypothetical Reference Genes (RGs) and Genes of Interest (GOI) were designed considering the alignment of conserved domains in different arthropod species such as *Calanus finmarchicus*, *Calanus californicus*, *Tigriopus japonicus*, *Homarus americanus, Drosophila melanogaster* and *Anopheles gambiae*. Alignments were performed with Clustal W (Clustal) and BioEdit (BioEdit). Gene Runner, V3.05 (Hasting Software) was used to predict primer melting temperature (T_m) and check if primers formed dimers, hairpin, bulge and internal loops. The primers for 18S were designed from the known sequence (Accession number: AY446908) using Primer3 software, v. 0.4.0. RGs belonging to different functional classes were selected in order to reduce the possibility that they might be co-regulated (e.g. S20 and S7). The selected RGs were: β-actin (ACT), elongation factor 1α (EFA), glyceraldehyde-3-phosphate dehydrogenase (GAPDH), ribosomal components (18S, S7, and S20), adenosine-3-phosphate synthase (ATPs), and histone 3 (HIST). The GOI were the two microtubule subunits: α-tubulin (α tub) and β-tubulin (β tub). Table 2 lists gene functions, primers' sequences, amplicon size, correlation coefficient (R^2) and efficiency (E^a). Primers were synthesized commercially by Primm Labs. Primers were designed to amplify cDNA regions ranging from 100 to 200 bp in size, in order to facilitate cross-comparison of assays and assure equal PCR efficiencies. PCR conditions were optimized on a GeneAmp PCR System 9700 (Perkin Elmer). Reactions were carried out in 20 μl volume with 2 μl of 10× PCR reaction buffer Roche, 2 μl of 0.1% BSA, 2 μl of 10×2 mM dNTP, 0.8 μl of 5 U/μl Taq Roche, 1 μl of 20 pmol/μl for each oligo, template cDNA and nuclease-free water to 20 μl. The PCR program consisted of a denaturation step at 95 °C for 3 min, 40 cycles at 95 °C for 30 s, 60 °C for 1 min and 72 °C for 30 s, and a final extension step at 72 °C for 7 min. Amplified PCR products were analyzed by 1.5% agarose gel electrophoresis in TBE buffer. In order to verify the correct assignment of amplicons to target genes, the resulting bands were excised from the gel and extracted according to the *QIAquick Gel Extraction Kit* protocol (QIAGEN) and sequence analyzed. Sequence reactions were obtained by *BigDye Terminator Cycle Sequencing Technology* (Applied Biosystems) and purified using the *Agencourt CleanSEQ Dye terminator removal Kit* (Agencourt Bioscience Corporation) in automation by the robotic station *Biomek FX* (Beckman Coulter). Products were analyzed on the Automated Capillary Electrophoresis Sequencer *3730 DNA Analyzer* (Applied Biosystems). The identity of each sequence was confirmed using the bioinformatics tool BLAST (Basic local alignment search tool) (BLAST). The sequences are deposited in GenBank under the Accession numbers shown in Table 2.

2.5. Reverse transcription-quantitative real time polymerase chain reaction (RT-qPCR)

The fluorescent dye SYBR GREEN was used to evaluate expression levels of the selected genes by RT-qPCR. This dye shows maximal fluorescence only with double-strand DNA and was used to detect our amplicons. Fluorescence was monitored once per cycle after product extension and increased above background fluorescence at a cycle number that depended on the initial template concentration. RT-qPCR was performed in Bio-Rad 96-well reaction full skirted white plates with Microseal 'B' Adhesive Seals (BioRad) in a *Chromo4 TM Real-time Detector* (Biorad) thermal cycler, whereas fluorescence was measured using Opticon Monitor 3.1 (Biorad). The PCR volume for each sample was 25 μl, with 1× of *Fast Start SYBR Green Master Mix* (Roche), 2 μl of cDNA template and 0.7 pmol/μl for each oligo. The RT-qPCR thermal profile was obtained using the following procedure: 95 °C for 10 min, 40 times 95 °C for 15 s and 60 °C for 1 min, 72 °C for 5 min. The program was set to reveal the melting curve of each amplicon from 60 °C to 95 °C, and read every 0.5 °C. In RT-qPCR assays, the optimal quantity of template of 1:100 was assessed using serial dilutions, ranging from 1:1 to 1:10,000.

All RT-qPCR reactions were carried out in triplicate to capture intra-assay variability. Each assay included three no-template negative controls (NTC) for each primer pair. Five serial dilutions of cDNA were used to determine reaction efficiencies (E) for all primer pairs. These efficiencies (Table 2) were calculated generating for each oligonucleotide pair standard curves with at least five dilution points by using the

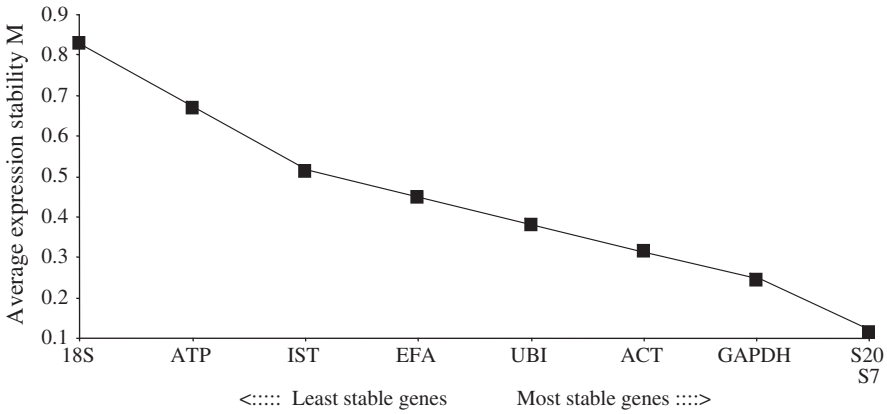

Fig. 2. Gene expression stability M of candidate RGs calculated by geNorm. The stepwise exclusion of genes that are more variable among samples using the geNorm program. Data points represent the average expression stability values of remaining RGs.

Author's personal copy

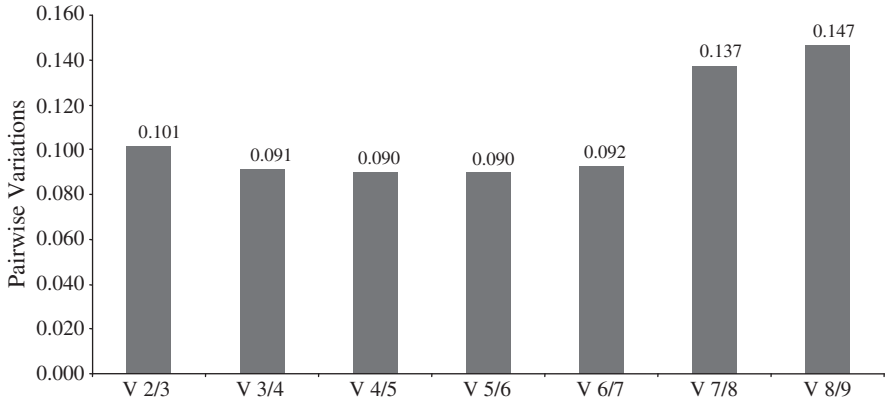

Fig. 3. Determination of the optimal number of control genes for normalization. Pair-wise variation to evaluate the effect of adding another RG to those already analyzed. The inclusion of additional RGs was not required below the cut-off value of 0.15. The two best RGs, S20 and S7, were sufficient for this analysis, but the third best RG, GAPDH, was also used because the two ribosomal proteins S20 and S7, belonging to the same functional class, might be co-regulated.

Cycle Threshold (Ct) value versus the logarithm of each dilution factor and using the equation $E = 10^{-1/slope}$. Primer efficiencies ranged from 89% to 100% while the linear correlation coefficient (R^2) ranged from 0.9704 to 0.9998 (Table 2). Each primer pair generated different and individual fluorescence patterns in the qPCR kinetics (Melting Curve). A 1:100 template dilution (4 ± 2 ng) was used which allowed almost all gene amplifications to fit in the optimal read window (from 15 to 25 cycles). Only a single peak in the melting-curve analyses of all genes was identified, confirming a gene-specific amplification and the absence of primer–dimers. No-template controls (NTC) were included in all RT-qPCR runs for each gene.

Three different algorithms were utilized to identify the best reference genes in our experimental design: BestKeeper (Pfaffl et al., 2004), geNorm (Vandesompele et al., 2002) and NormFinder (Andersen et al., 2004).

To study the expression of each target gene relative to the most stable RGs, we used REST tool (Relative expression software tool) (Pfaffl et al., 2002). This tool used a mathematical model based on the PCR efficiencies and the mean crossing point deviation between the sample and the control group. The advantage of REST is that this software tool tests the group differences for significance with the Pair-Wise Fixed Reallocation Randomization Test (Pfaffl et al., 2002).

Statistical analysis was performed using GraphPad Prim statistic software, V4.00 (GraphPad Software).

3. Results

3.1. Validation of best reference genes (RGs) for RT-qPCR

Raw Ct data of potential RGs are reported in Fig. 1. According to the mathematical approach of BestKeeper, RG expression stability considers the standard deviation of the Ct values (Table 3). Hence the most stable RGs have a standard deviation (SD) lower than 1 and these were S20, S7, GAPDH, HIST and UBI. BestKeeper analysis (Pfaffl et al., 2004) indicated S20 as the most stable gene, followed by S7 and GAPDH.

GeNorm analysis (Vandesompele et al., 2002) confirmed the results of BestKeeper, showing that the two most stable genes, with the lowest expression stability (M), were S20 and S7 (Fig. 2). Pair-wise variation was subsequently calculated to evaluate the effect of adding another RG to those already analyzed. Below the cut-off value of 0.15 the inclusion of additional RGs was not required. According to our results (Fig. 3), the two best RGs, S20 and S7, were sufficient for the analysis.

According to the statistical approach of NormFinder, our best candidate reference genes, with the lowest stability values, were S20, S7 and GAPDH, as reported in Fig. 4. The rank pattern was the same as for Bestkeeper and geNorm analyses as summarized in Table 4.

Although the three approaches agreed that the best RGs were S20 and S7 , we decided to also use the third best RG, GAPDH, because the

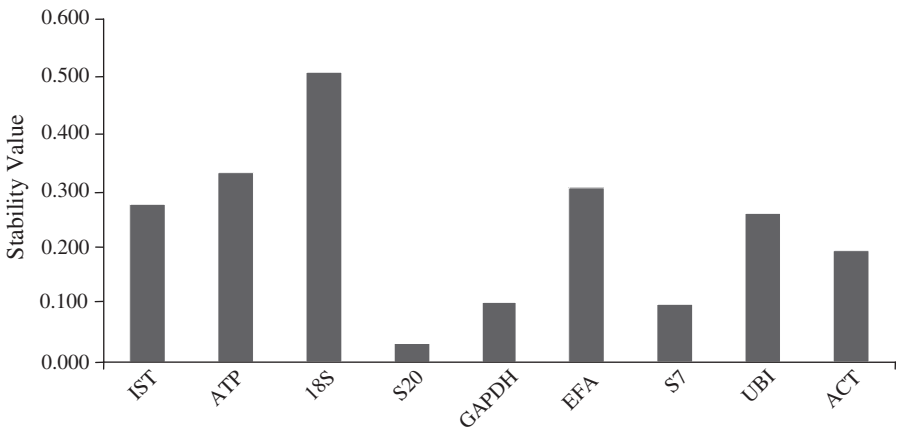

Fig. 4. Determination of the most stable RG using NormFinder. The NormFinder algorithm ranks the data set of candidate normalization genes according to their expression stability in a given experimental design. Blue bars represent the stability values of our candidate genes.

Author's personal copy

Table 4
Stability of putative RGs in *Calanus helgolandicus*. Candidate RGs are ranked from most to least stable using the three different softwares described in the text. Three best RGs used for the analysis were S20, S7 and GAPDH.

Rank	BestKeeper	GeNorm	NormFinder
1	S20	S20	S20
2	S7	S7	S7
3	GAPDH	GAPDH	GAPDH
4	HIST	ACT	ACT
5	UBI	UBI	UBI
6	EFA	EFA	EFA
7	ACT	HIST	EFA
8	ATPs	ATPs	ATPs
9	18S	18S	18S

two ribosomal proteins S20 and S7, belonging to the same functional class, might be co-regulated.

3.2. Expression level of genes of interest (GOI)

To investigate if microtubules in *C. helgolandicus* were affected by diets of SKE and RHO, we analyzed the relative expression levels of the two MT subunits: α- and β-tubulin (Fig. 5). The analyses were carried out on all samples using the three best RGs (S20, S7 and GAPDH) to normalize our data and considering copepods fed PRO as the control group using the Relative expression software tool (REST tool) (Pfaffl et al., 2002).

Fig. 5 shows that the expression levels of our GOI in copepods fed on the oxylipin-producing diatom SKE were significantly lower than on the flagellate RHO (Student's t-test, $p<0.0001$, for both genes). According to REST analysis, α-tubulin was about 2-fold down-regulated while β-tubulin was about 3-fold down-regulated in SKE treated samples. As expected, α- and β-tubulin gene expression in copepods fed RHO compared to copepods fed the control diet PRO did not show significantly different expression levels.

The behavior of GOI was confirmed by the replicates of the experiments (listed in table1) with a standard deviation (SD) of 0.194 and 0.052 for α-tubulin in SKE and RHO conditions, respectively, and 0.080 and 0.018 for β-tubulin for SKE and RHO, respectively (Fig. 5).

4. Discussion

Previous studies have shown that when *C. helgolandicus* is fed on *S. marinoi*, egg hatching success is impaired after 3 days of maternal feeding, with the production of apoptotic teratogenic nauplii that do not develop to adulthood (Ianora et al., 2004). Our results indicate that a diet of *S. marinoi* affects α- and β-tubulin gene expression levels in adult females after only 2 days of feeding by possibly reducing MT subunits and microtubule filament formation, with the cascading effect of altering pronuclear migration, DNA replication and mitotic events. Alternatively, PUAs and other oxylipins may affect protein and organelle transport along microtubules, impairing cellular homeostasis. Ingestion of *S. marinoi* induced a pronounced down regulation of tubulin genes, with about a 3-fold down-regulation of β-tubulin and 2-fold down-regulation of α-tubulin. By contrast, diets of the dinoflagellate *P. minimum* and the flagellate *R. baltica* induced no significant up- or down-regulation of these genes.

The best RGs for *C. helgolandicus* fed on the diatom *S. marinoi*, the dinoflagellate *P. minimum* and the flagellate *R. baltica* were S20, S7 and GAPDH. These results confirm the stability of the ribosomal protein S20 as reported for the salmon louse *L. salmonis* (Frost and Nilsen, 2003) even if this species belongs to a different copepod order. Glyceraldehyde-3-Phosphate Dehydrogenase (GAPDH) which is widely used in gene expression studies (Hansen et al., 2008a; Spinsanti et al., 2006; Toegel et al., 2007) has been shown to be up- or down-regulated in various conditions (Bustin, 2000). In our analysis GAPDH scored third. Gene expression profiles of Elongation factor (EFA), selected as RG in *C. finmarchicus* (Hansen et al., 2008a; Hansen et al., 2008b; Hansen et al., 2009; Hansen et al., 2010) and *L. salmonis* (Kvamme et al., 2004; Skern-Mauritzen et al., 2009), and of β-actin (ACT), used as RG in *Tigriopus japonicus* (Lee et al., 2007; Lee et al., 2008; Seo et al., 2006), were less stable in our test conditions and were therefore considered invalid for this analysis. Histone 3 (IST), Ubiquitin (UBI), ATP synthase (ATPs) and ribosomal protein 18S gene expression levels were less stable as well. In general, our results confirm that RGs are not universal but may change depending on the species and experimental conditions.

Interestingly, α- and β-tubulin subunits have also often been selected as putative RGs to normalize qPCR data (Andersen et al., 2004; Carvalho et al., 2010; Heckmann et al., 2006; Ransbotyn and

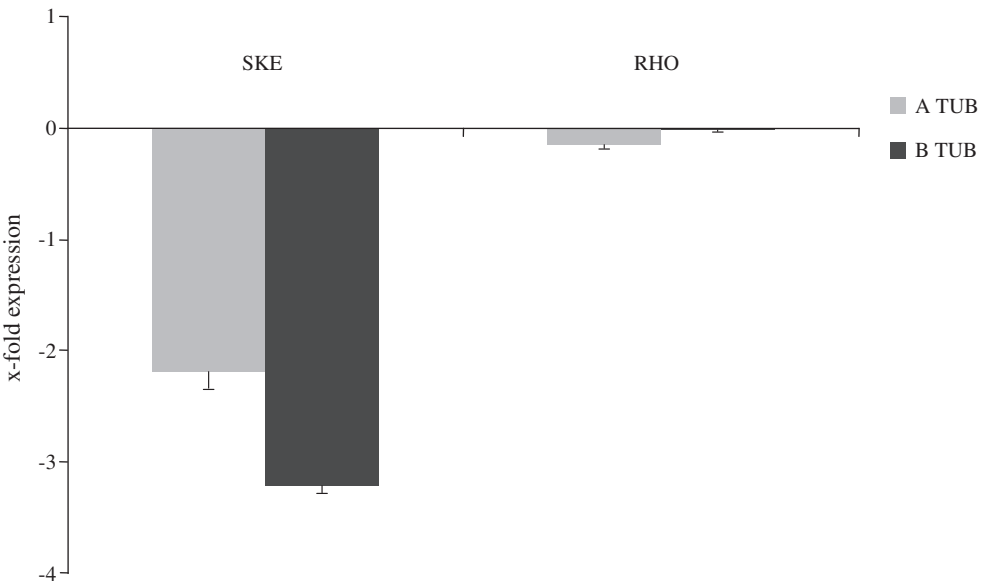

Fig. 5. Relative target gene expression in copepods fed on *Skeletonema marinoi* and *Rhodomonas baltica*. The figure shows α- and β-tubulin gene expression levels (y-axis, Mean ± SD) in copepods fed on the test diatom *Skeletonema marinoi* (SKE) and the flagellate *Rhodomonas baltica* (RHO), respectively. The data are normalized with our three best RGs, S20, S7 and GAPDH, using the dinoflagellate *Prorocentrum minimum* as a control alga.

Author's personal copy

Reusch, 2006; Sirakov et al., 2009), but in our experiments their expression levels were evidently affected by the oxylipin-producing diatom SKE.

Several studies have shown that the functioning of tubulin is affected by exposure to toxic compounds (Chavez et al., 2010; Lee et al., 2009), but these results have usually been obtained in humans. For example, exogenous exposure to another aldehyde, 4-hydroxy-2(E)-nonenal (HNE), in human monocytic THP-1 cells induced HNE-tubulin alpha-1B chain adducts leading to inhibition of tubulin polymerization (Chavez et al., 2010). Prenatal exposure to cocaine causes cyto-architectural alterations in the developing neocortex inducing impairments in fetal brain development and the down-regulation of cytoskeleton-related genes such as alpha 3d tubulin and alpha 8 tubulin in neural and/or A2B5+ progenitor cells (Lee et al., 2009).

Our results support, for the first time at the molecular level, previous findings by Buttino et al.(1999) and Hansen et al.(2004), that PUAs inhibit tubulin-polymerization affecting proper spindle formation and cell division. Future studies on the biological effects of these molecules should address whether the functioning of other important proteins are altered as well. Our results may help explain why recruitment processes in copepods during diatom blooms may be compromised with possible effects on cohort size of the next generation.

Acknowledgements

The authors thank Francesco Esposito for the preparation of algal cultures and assistance with the re-circulating copepod breeding system. We also thank Massimo Perna and Flora Palumbo of the FEEL Laboratory and the staff of the Molecular Biology Service of the SZN for their technical support. **[SS]**

References

Andersen, C.L., Jensen, J.L., Orntoft, T.F., 2004. Normalization of real-time quantitative reverse transcription-PCR data: a model-based variance estimation approach to identify genes suited for normalization, applied to bladder and colon cancer data sets. Cancer Research 64 (15), 5245–5250.

BioEdit, V 7.0.5.3 Biological Sequence Alignment Editor for Windows 95/98/NT/XP. [http://www.mbio.ncsu.edu/BioEdit/bioedit.html].

BLAST, Basic Local Alignment Search Tool. [http://www.ncbi.nlm.nih.gov/BLAST/].

Bustin, S.A., 2000. Absolute quantification of mRNA using real-time reverse transcription polymerase chain reaction assays. Journal of Molecular Endocrinology 25 (2), 169–193.

Bustin, S.A., Benes, V., Garson, J.A., Hellemans, J., Huggett, J., Kubista, M., Mueller, R., Nolan, T., Pfaffl, M.W., Shipley, G.L., Vandesompele, J., Wittwer, C.T., 2009. The MIQE guidelines: minimum information for publication of quantitative real-time PCR experiments. Clinical Chemistry 55 (4), 611–622.

Bustin, S.A., Beaulieu, J.F., Huggett, J., Jaggi, R., Kibenge, F.S.B., Olsvik, P.A., Penning, L.C., Toegel, S., 2010. MIQE precis: practical implementation of minimum standard guidelines for fluorescence-based quantitative real-time PCR experiments. BMC Molecular Biology 11.

Buttino, I., Miralto, A., Ianora, A., Romano, G., Poulet, S.A., 1999. Water-soluble extracts of the diatom *Thalassiosira rotula* induce aberrations in embryonic tubulin organisation of the sea urchin *Paracentrotus lividus*. Marine Biology 134 (1), 147–154.

Buttino, I., De Rosa, G., Carotenuto, Y., Mazzella, M., Ianora, A., Esposito, F., Vitiello, V., Quaglia, F., La Rotonda, M.I., Miralto, A., 2008. Aldehyde-encapsulating liposomes impair marine grazer survivorship. Journal of Experimental Biology 211 (9), 1426–1433.

Buttino, I., Ianora, A., Buono, S., Vitiello, V., Malzone, M.G., Rico, C., Langellotti, A.L., Sansone, G., Gennari, L., Miralto, A., in press. Experimental cultivation of the Mediterranean calanoid copepods *Temora stylifera* and *Centropages typicus* in a pilot re-circulating system. Aquaculture research.

Caldwell, G.S., 2009. The influence of bioactive oxylipins from marine diatoms on invertebrate reproduction and development. Marine Drugs 7 (3), 367–400.

Calligaris, D., Verdier-Pinard, P., Devred, F., Villard, C., Braguer, D., Lafitte, D., 2010. Microtubule targeting agents: from biophysics to proteomics. Cellular and Molecular Life Sciences 67 (7), 1089–1104.

Carvalho, K., de Campos, M.K.F., Pereira, L.F.P., Vieira, L.G.E., 2010. Reference gene selection for real-time quantitative polymerase chain reaction normalization in "Swingle" citrumelo under drought stress. Analytical Biochemistry 402 (2), 197–199.

Chavez, J., Chung, W.G., Miranda, C.L., Singhal, M., Stevens, J.F., Maier, C.S., 2010. Site-specific protein adducts of 4-hydroxy-2(E)-nonenal in human THP-1 monocytic cells: protein carbonylation is diminished by ascorbic acid. Chemical Research in Toxicology 23 (1), 37–47.

Clustal, W., [http://www.ebi.ac.uk/clustalw/].

Falkowski, P., 1994. The role of phytoplankton photosynthesis in global biogeochemical cycles. Photosynthesis Research 39 (3), 235–258.

Fontana, A., d'Ippolito, G., Cutignano, A., Romano, G., Lamari, N., Gallucci, A.M., Cimino, G., Miralto, A., Ianora, A., 2007. LOX-induced lipid peroxidation mechanism responsible for the detrimental effect of marine diatoms on zooplankton grazers. Chembiochem 8, 1810–1818.

Frost, P., Nilsen, F., 2003. Validation of reference genes for transcription profiling in the salmon louse, *Lepeophtheirus salmonis*, by quantitative real-time PCR. Veterinary Parasitology 118 (1–2), 169–174.

Hansen, E., Even, Y., Geneviere, A.M., 2004. The alpha, beta, gamma, delta-unsaturated aldehyde 2-trans-4-trans-decadienal disturbs DNA replication and mitotic events in early sea urchin embryos. Toxicological Sciences 81 (1), 190–197.

Hansen, B.H., Altin, D., Hessen, K.M., Dahl, U., Breitholtz, M., Nordtug, T., Olsen, A.J., 2008a. Expression of ecdysteroids and cytochrome P450 enzymes during lipid turnover and reproduction in *Calanus finmarchicus* (Crustacea: Copepoda). General and Comparative Endocrinology 158 (1), 115–121.

Hansen, B.H., Altin, D., Vang, S.H., Nordtug, T., Olsen, A.J., 2008b. Effects of naphthalene on gene transcription in *Calanus finmarchicus* (Crustacea: Copepoda). Aquatic Toxicology 86 (2), 157–165.

Hansen, B.H., Nordtug, T., Altin, D., Booth, A., Hessen, K.M., Olsen, A.J., 2009. Gene expression of GST and CYP330A1 in lipid-rich and lipid-poor female *Calanus finmarchicus* (Copepoda: Crustacea) exposed to dispersed oil. Journal of Toxicology and Environmental Health-Part a-Current Issues 72 (3–4), 131–139.

Hansen, B.H., Altin, D., Rørvik, S.F., Øverjordet, I.B., Olsen, A.J., Nordtug, T., 2010. Comparative study on acute effects of water accommodated fractions of an artificially weathered crude oil on *Calanus finmarchicus* and *Calanus glacialis* (Crustacea: Copepoda). Science of the Total Environment 409 (4), 704–709.

Harrison, M.R., Holen, K.D., Liu, G., 2009. Beyond taxanes: a review of novel agents that target mitotic tubulin and microtubules, kinases, and kinesins. Clinical Advances in Hematology and Oncology 7 (1), 54–64.

Heckmann, L.H., Connon, R., Hutchinson, T.H., Maund, S.J., Sibly, R.M., Callaghan, A., 2006. Expression of target and reference genes in *Daphnia magna* exposed to ibuprofen. BMC Genomics 7.

Ianora, A., Miralto, A., 2010. Toxigenic effects of diatoms on grazers, phytoplankton and other microbes: a review. Ecotoxicology 19 (3), 493–511.

Ianora, A., Miralto, A., Poulet, S.A., Carotenuto, Y., Buttino, I., Romano, G., Casotti, R., Pohnert, G., Wichard, T., Colucci-D'Amato, L., Terrazzano, G., Smetacek, V., 2004. Aldehyde suppression of copepod recruitment in blooms of a ubiquitous planktonic diatom. Nature 429 (6990), 403–407.

Jordan, M.A., Wilson, L., 2004. Microtubules as a target for anticancer drugs. Nature Reviews Cancer 4, 253–265.

Kvamme, B.O., Skern, R., Frost, P., Nilsen, F., 2004. Molecular characterisation of five trypsin-like peptidase transcripts from the salmon louse (*Lepeophtheirus salmonis*) intestine. International Journal for Parasitology 34 (7), 823–832.

Lee, Y.-M., Lee, K.-W., Park, H., Park, H.G., Raisuddin, S., Ahn, I.-Y., Lee, J.-S., 2007. Sequence, biochemical characteristics and expression of a novel Sigma-class of glutathione S-transferase from the intertidal copepod, *Tigriopus japonicus* with a possible role in antioxidant defense. Chemosphere 69 (6), 893–902.

Lee, K.-W., Raisuddin, S., Rhee, J.-S., Hwang, D.-S., Yu, I.T., Lee, Y.-M., Park, H.G., Lee, J.-S., 2008. Expression of glutathione S-transferase (GST) genes in the marine copepod *Tigriopus japonicus* exposed to trace metals. Aquatic Toxicology 89 (3), 158–166.

Lee, C.T., Lehrmann, E., Hayashi, T., Amable, R., Tsai, S.Y., Chen, J., Sanchez, J.F., Shen, J., Becker, K.G., Freed, W.J., 2009. Gene expression profiling reveals distinct cocaine-responsive genes in human fetal CNS cell types. Journal of Addiction Medicine 3 (4), 218–226.

Mauchline, J., 1998. The biology of calanoid copepods. Advances in Marine Biology 33, 1–710.

Miralto, A., Barone, G., Romano, G., Poulet, S.A., Ianora, A., Russo, G.L., Buttino, I., Mazzarella, G., Laabir, M., Cabrini, M., Giacobbe, M.G., 1999. The insidious effect of diatoms on copepod reproduction. Nature 402 (6758), 173–176.

Nelson, D.M., Tréguer, P., Brzezinski, M.A., Leynaert, A., Quéguiner, B., 1995. Production and dissolution of biogenic silica in the ocean: revised global estimates, comparison with regional data and relationship to biogenic sedimentation. Global Biogeochemical Cycles 9 (3), 359–372.

Nogales, E., Wolf, S.G., Downing, K.H., 1998. Structure of the alpha beta tubulin dimer by electron crystallography. Nature 391, 199–203.

Pfaffl, M.W., Horgan, G.W., Dempfle, L., 2002. Relative expression software tool (REST (c)) for group-wise comparison and statistical analysis of relative expression results in real-time PCR. Nucleic Acids Research 30 (9).

Pfaffl, M.W., Tichopad, A., Prgomet, C., Neuvians, T.P., 2004. Determination of stable housekeeping genes, differentially regulated target genes and sample integrity: BestKeeper–Excel-based tool using pair-wise correlations. Biotechnology Letters 26 (6), 509–515.

Ransbotyn, V., Reusch, T.B.H., 2006. Housekeeping gene selection for quantitative real-time PCR assays in the seagrass *Zostera marina* subjected to heat stress. Limnology and Oceanography-Methods 4, 367–373.

Romano, G., Miralto, A., Ianora, A., 2010. Teratogenic effects of diatom metabolites on sea urchin *Paracentrotus lividus* embryos. Marine Drugs 8 (4), 950–967.

Sashidhara, K.V., White, K.N., Crews, P., 2009. A selective account of effective paradigms and significant outcomes in the discovery of inspirational marine natural products. Journal of Natural Products 72 (3), 588–603.

Seo, J.S., Lee, K.-W., Rhee, J.-S., Hwang, D.-S., Lee, Y.-M., Park, H.G., Ahn, I.-Y., Lee, J.-S., 2006. Environmental stressors (salinity, heavy metals, H_2O_2) modulate expression

Author's personal copy

of glutathione reductase (GR) gene from the intertidal copepod *Tigriopus japonicus*. Aquatic Toxicology 80 (3), 281–289.

Sirakov, M., Zarrella, I., Borra, M., Rizzo, F., Biffali, E., Arnone, M.I., Fiorito, G., 2009. Selection and validation of a set of reliable reference genes for quantitative RT-PCR studies in the brain of the Cephalopod Mollusc *Octopus vulgaris*. BMC Molecular Biology 10.

Skern-Mauritzen, R., Frost, P., Dalvin, S., Kvamme, B.O., Sommerset, I., Nilsen, F., 2009. A trypsin-like protease with apparent dual function in early *Lepeophtheirus salmonis* (Kroyer) development. BMC Molecular Biology 10.

Spinsanti, G., Panti, C., Lazzeri, E., Marsili, L., Casini, S., Frati, F., Fossi, C.M., 2006. Selection of reference genes for quantitative RT-PCR studies in striped dolphin (*Stenella coeruleoalba*) skin biopsies. BMC Molecular Biology 7.

Tarrant, A.M., Baumgartner, M.F., Verslycke, T., Johnson, C.L., 2008. Differential gene expression in diapausing and active *Calanus finmarchicus* (Copepoda). Marine Ecology-Progress Series 355, 193–207.

Toegel, S., Huang, W.W., Piana, C., Unger, F.M., Wirth, M., Goldring, M.B., Gabor, F., Viernstein, H., 2007. Selection of reliable reference genes for qPCR studies on chondroprotective action. BMC Molecular Biology 8.

Vandesompele, J., De Preter, K., Pattyn, F., Poppe, B., Van Roy, N., De Paepe, A., Speleman, F., 2002. Accurate normalization of real-time quantitative RT-PCR data by geometric averaging of multiple internal control genes. Genome Biology 3 (7).

Molecular Evidence of the Toxic Effects of Diatom Diets on Gene Expression Patterns in Copepods

Chiara Lauritano*, Marco Borra, Ylenia Carotenuto, Elio Biffali, Antonio Miralto, Gabriele Procaccini, Adrianna Ianora

Stazione Zoologica Anton Dohrn, Napoli, Italy

Abstract

Background: Diatoms are dominant photosynthetic organisms in the world's oceans and are considered essential in the transfer of energy through marine food chains. However, these unicellular plants at times produce secondary metabolites such as polyunsaturated aldehydes and other products deriving from the oxidation of fatty acids that are collectively termed oxylipins. These cytotoxic compounds are responsible for growth inhibition and teratogenic activity, potentially sabotaging future generations of grazers by inducing poor recruitment in marine organisms such as crustacean copepods.

Principal Findings: Here we show that two days of feeding on a strong oxylipin-producing diatom (*Skeletonema marinoi*) is sufficient to inhibit a series of genes involved in aldehyde detoxification, apoptosis, cytoskeleton structure and stress response in the copepod *Calanus helgolandicus*. Of the 18 transcripts analyzed by RT-qPCR at least 50% were strongly down-regulated (aldehyde dehydrogenase 9, 8 and 6, cellular apoptosis susceptibility and inhibitor of apoptosis IAP proteins, heat shock protein 40, alpha- and beta-tubulins) compared to animals fed on a weak oxylipin-producing diet (*Chaetoceros socialis*) which showed no changes in gene expression profiles.

Conclusions: Our results provide molecular evidence of the toxic effects of strong oxylipin-producing diatoms on grazers, showing that primary defense systems that should be activated to protect copepods against toxic algae can be inhibited. On the other hand other classical detoxification genes (glutathione S-transferase, superoxide dismutase, catalase, cytochrome P450) were not affected possibly due to short exposure times. Given the importance of diatom blooms in nutrient-rich aquatic environments these results offer a plausible explanation for the inefficient use of a potentially valuable food resource, the spring diatom bloom, by some copepod species.

Citation: Lauritano C, Borra M, Carotenuto Y, Biffali E, Miralto A, et al. (2011) Molecular Evidence of the Toxic Effects of Diatom Diets on Gene Expression Patterns in Copepods. PLoS ONE 6(10): e26850. doi:10.1371/journal.pone.0026850

Editor: Howard Browman, Institute of Marine Research, Norway

Received July 13, 2011; **Accepted** October 5, 2011; **Published** October 28, 2011

Copyright: © 2011 Lauritano et al. This is an open-access article distributed under the terms of the Creative Commons Attribution License, which permits unrestricted use, distribution, and reproduction in any medium, provided the original author and source are credited.

Funding: The work was financed by Stazione Zoologica Anton Dohrn. The funders had no role in study design, data collection and analysis, decision to publish, or preparation of the manuscript.

Competing Interests: The authors have declared that no competing interests exist.

* E-mail: chiara.lauritano@szn.it

Introduction

Diatoms are dominant photosynthetic organisms in the world's oceans and are considered essential in the transfer of energy through marine food chains including important fisheries. However, numerous studies have shown that these unicellular plants at times produce secondary metabolites with toxic effects on reproductive processes in crustacean copepods [1,2,3] and cladocerans [4], echinoderm sea urchins [5] and sea stars [6,7], polychaete worms [8,9], and ascidians [10]. Diatom metabolites are the end-products of a lipoxygenase/hydroperoxide lyase metabolic pathway [11,12,13,14,15] initiated by damage to algal cells, as occurs through grazing by predators. Cell damage activates lipase enzymes, which liberate polyunsaturated fatty acids (PUFAs) from cell membranes that are immediately oxidized and cleaved within seconds to form polyunsaturated aldehydes (PUAs) and a plethora of other metabolites collectively termed oxylipins.

Oxylipins, and PUAs in particular, have important biological and biochemical properties including the disruption of gametogenesis, gamete functionality, fertilization, embryonic mitosis, and larval fitness and competence [7]. Although the effects of such toxins are less catastrophic than those inducing poisoning and death of predators, they are none-the-less insidious inducing abortions, birth defects and reduced larval survivorship [1,16]. Such antiproliferative compounds may discourage herbivory by sabotaging future generations of grazers, thereby allowing diatom blooms to persist when grazing pressure would otherwise have caused them to crash. Similar wound-activated compounds are also found in terrestrial plants where they play a pivotal role in defense because of their antibacterial, wound healing and antiproliferative activity [17].

In a recent study [18] the authors showed that alpha and beta tubulin gene expression levels were significantly reduced when females of the copepod *Calanus helgolandicus* were fed on the ubiquitous diatom-blooming species *Skeletonema marinoi* (*S. marinoi*) which is known to produce high quantities of PUAs and several other oxylipins including fatty acid hydroperoxides, hydroxyl- and keto-fatty acids, and epoxyalcohols [3]. The aim of the present study was to further explore the toxic effects of diatoms on copepod females at the gene level under two different experimen-

tal conditions: when females were fed for 2 days (2d) on *S. marinoi* compared to when they received a diet of another diatom *Chaetoceros socialis* (*C. socialis*) that does not produce PUAs and synthesizes only low levels of other oxylipins [3], and was thus, in theory, "less toxic" for copepods.

In addition to the previously investigated alpha and beta tubulins, here we analyzed the effects of these two diatom diets on the expression levels of genes which are known to have a primary role in generic stress responses, defense systems (e.g. aldehyde, free fatty acid and free radical detoxification) or apoptosis regulation in other organisms, from humans to marine organisms [19,20,21,22,23,24,25,26,27] (Figure 1). We expected an activation of enzymes and proteins involved in stress responses (e.g heat shock proteins, phase I and phase II enzymes), but, in particular, we hypothesized expression level increases of enzymes that could detoxify and/or metabolize toxic diatom PUAs.

To study the generic stress response of *C. helgolandicus* to diatom toxicity, we analyzed the heat shock protein families 40 and 70 (HSP40 and HSP70, respectively). HSPs are highly conserved proteins that are activated in response to various environmental stress factors [28,29]. HSP70 can be involved in the tolerance of hyperthermia, ischemia/hypoxia, resistance to hydrogen peroxide, escape from drug-induced cell cycle arrest, tolerance to ultraviolet radiation and apoptosis [28] whereas HSP40 is often co-localized with HSP70 and plays a role in regulating the ATPase activity of HSP70 [30].

Since oxylipins induce LPO and an increase in free fatty acids [31], we also analyzed the microsomal cytochrome P450 family 4 monooxygenases (CYP4) that generally catalyze the ω-hydroxylation of fatty acids, arachidonic acid and derivatives such as leukotrines and prostanoids [32]. Cytochrome P450 (CYP) enzymes, especially members of the CYP1, CYP2, CYP3, and CYP4 families are generally involved in oxidative modification (known as Phase I reaction) of chemicals into more hydrophilic metabolites to enhance their elimination or inactivation [33].

Diatom oxylipins are also known to induce an increase in free radicals, such as reactive oxygen species (ROS) [3] which induce oxidative stress and damage to DNA, RNA, proteins, lipids and carbohydrates. We therefore analyzed enzymes involved in ROS detoxification, such as catalase (CAT) and superoxide dismutase (SOD) [34] and antioxidant activity, such as glutathione synthase (GSH-S) and glutathione S-transferase (GST). Glutathione is an important cell scavenger molecule which facilitates dis-activation of radical compounds. GST is involved in phase II detoxification reactions, catalyzing the nucleophilic attack of glutathione on electrophilic substrates, decreasing their reactivity with cellular macromolecules, facilitating dissolution of the complex glutathione-substrate in the aqueous cellular and extracellular media and, consequently, its elimination from the body [35].

We also analyzed aldehyde dehydrogenases (ALDHs) which constitute a superfamily of enzymes that catalyze the oxidation of endogenous and exogenous aldehydes into their corresponding carboxylic acids. These enzymes are generally involved in many processes including amino acid catabolism, neurotransmitter metabolism, xenobiotic and drug biotransformation, protection from osmotic stress and detoxification reactions [26,36]. We selected several aldehyde dehydrogenase isoforms (ALDH2, ALDH3, ALDH6, ALDH7, ALDH8 and ALDH9) that are mainly involved in aldehyde detoxification due to lipid peroxidation (LPO) [26,37,38].

Previous studies have shown that PUAs and oxylipins also induce apoptosis and teratogenesis in the offspring of female copepods that have fed on diatoms for ≥5 d [16]. We therefore determined the transcription level of a protein belonging to the Inhibitor of apoptosis family (IAP), the cell cycle and apoptosis regulatory 1 protein (CARP) and the cellular apoptosis susceptibility protein (CAS). IAP levels increase in certain tumors probably contributing to resistance to apoptosis [39], CAS and CARP are also both involved in apoptosis [22,40,41]: CARP is a novel cell growth regulator [42] and CAS is necessary in the mitotic spindle checkpoint that ensures genomic stability during cell division [41]. In addition, we also analyzed microtubule subunits (alpha and beta tubulins), necessary for mitotic spindle formation. Microtubules (MTs) have many other cellular functions including development

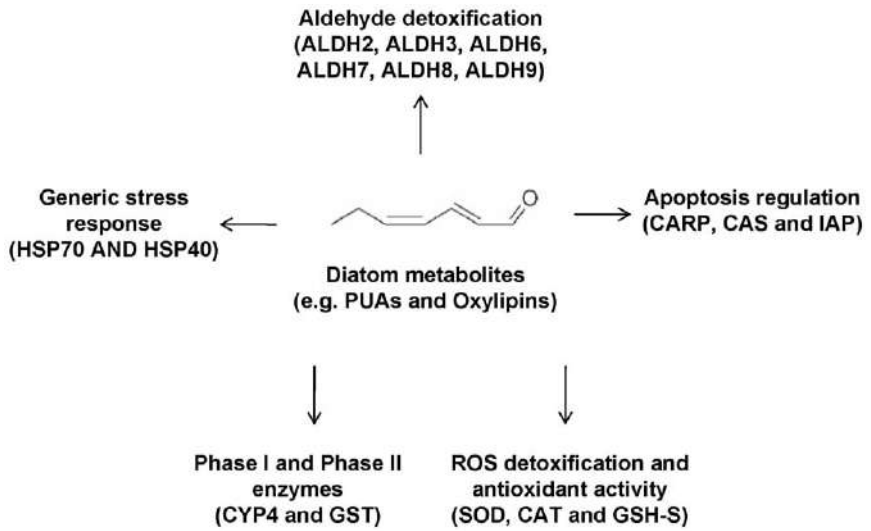

Figure 1. Putative systems affected by diatom metabolites in the copepod *Calanus helgolandicus*. A synopsis of the defense and detoxification systems and generic stress response (with selected genes in parenthesis) studied in *C. helgolandicus* females exposed to different diatom diets (*Skeletonema marinoi* and *Chaetoceros socialis*). Selected genes were six Aldehyde dehydrogenases (ALDH2, ALDH3, ALDH6, ALDH7, ALDH8, ALDH9), Cytochrome P450-4 (CYP4), Catalase (CAT), Superoxide Dismutase (SOD), Glutathione S-Transferase (GST), Glutathione Synthase (GSH-S), Inhibitor of Apoptosis Protein (IAP), Cell Cycle and Apoptosis Regulatory 1 Protein (CARP), Cellular Apoptosis Susceptibility Protein (CAS) and Alpha and Beta tubulins (ATUB and BTUB).
doi:10.1371/journal.pone.0026850.g001

and maintenance of cell shape, growth, signaling, protein movement, intracellular vesicle transport and organization and positioning of membranous organelles [43,44,45,46].

Materials and Methods

Microalgae culture

The planktonic diatoms *Skeletonema marinoi* (SMFE6; Adriatic Sea isolate FE6) and *Chaetoceros socialis* (CSFE17) were cultured as described in [47] and harvested during the stationary growth phase. Both species are part of the culture collection at the SZN. SMFE6 produces the PUAs 2-trans-4-cis-hepta-2,4-dienal as the dominant compound with smaller quantities of 2-trans-4-cis-octa-2,4-dienal and 2-trans-4-cis-octa- 2,4,7-trienal as well as a number of other products deriving from the oxidation of fatty acids including 9S-hydroxy-hexadecatrienoic acid, 11,9-hydroxy-epoxy-hexadienoic acid, 9S-hydroxy-hexatetraenoic acid, 5R- and 15S-hydroxy-eicosapentaenoic acids and 13,14S-hydroxy-epoxy-eicosatetraenoic acid, as described in [3,47]. CSFE17 produces 9S-hydroxy-eicosapentaenoic acid, 9S-hydroperoxy-eicosapentaenoic acid and 7,8-hydroxy-epoxy-eicosatetraenoic acid but not PUAs [3].

Copepod Feeding Experiments

Calanus helgolandicus specimens were collected in the North Adriatic Sea and transported to Naples where they were placed in a 500 L re-circulating copepod breeding system [48]. *C. helgolandicus* adult females were isolated under a Leica stereomicroscope, transferred to 1000 ml bottles (about 15–20 copepods/bottle) filled with 0.22 µm filtered sea water (FSW) at 20°C and fed either unialgal diets of the control flagellate *Rhodomonas baltica* (7500–8000 cells/ml) (which does not produce any oxylipins) or the test diatoms *S. marinoi* (45.000–60.000 cells/ml) and *C. socialis* (48.000–55.000 cells/ml) for two days (2 d). After 2 d, copepods were transferred to clean bottles with FSW for 24 h to eliminate any algal residues in the gut. For each diet, triplicate samples of 5 animals each were carefully transferred to 500 µl Trizol Reagent (Invitrogen), frozen directly in liquid nitrogen and stored at −80°C until RNA extraction.

RNA extraction and cDNA synthesis

Total RNA was extracted from each copepod replicate according to Trizol manufacturer's protocol (Invitrogen). Each sample was treated with DNaseI (Invitrogen) according to the instruction manual to remove hypothetically contaminating DNA. RNA quantity and purity was assured by Nano-Drop (ND-1000 UV-Vis spectrophotometer; NanoDrop Technologies), RNA quality by gel electrophoresis. 1 µg of each RNA sample was retro-transcribed in complementary DNA (cDNA) (doublestrand DNA version of an mRNA molecule) with the iScriptTM cDNA Synthesis Kit (BIORAD) following the manufacturer's instructions, using the GeneAmp PCR System 9700 (Perkin Elmer). The reaction was carried out in 20 µl final volume with 4 µl 5× iScript reaction mix, 1 µl iScript reverse transcriptase and H_2O. The mix was first incubated 5 min at 25°C, followed by 30 min at 42°C and finally heated at 85°C for 5 min.

Primer design

Primers were designed considering the alignment of conserved domains in other species. Table 1 lists primers' sequences, amplicon size, correlation coefficient (R^2) and efficiency (E). PCR conditions were optimized on a GeneAmp PCR System

Table 1. Reference Gene and Genes of Interest in the copepod *Calanus helgolandicus* RT-qPCR assays.

Acronym	Gene name	Acc. no.	Primer Forward (5′-3′)	Primer Reverse (5′-3′)	Amplicon size	E	R^2
S20	Ribosomal protein S20	HQ270531	CGTAAGACTCCTTGTGGTGAGG	GAAGTGATCTGCTTCACGATCTC	113	89%	0.9915
ATUB	Alpha tubulin	HQ270529	ACAGCTTCTCCACCTTCTTCTC	GTTGTTGGCGGCATCCTC	167	94%	0.9997
BTUB	Beta tubulin	HQ270528	GGATTTCAGCTGACCCACTC	GTCTCATCAGTATTTTCCACCAG	205	97%	0.9862
CYP4	Cytochrome P450-4	JF825512	CTGATCACTCCAACTTTTCACTTC	CCATTGCAGTCTCACAGATTATG	169	100%	0.959
ALDH2	Aldehyde Dehydrogenase 2	JF825506	GGACAAGGCAGATGTCAACAA	ATAGGGTTTGCCATTGTCAAG	181	100%	0.998
ALDH3	Aldehyde Dehydrogenase 3	JF825507	CCTCTTGGTGTTGTCCTGATC	CCAACTCTGATGGCTTGATG	117	95%	0.997
ALDH6	Aldehyde Dehydrogenase 6	JF825508	GAGCAGTGCTGCAGCAACAC	GGAACATCCAGAGGGGGATC	164	100%	0.989
ALDH7	Aldehyde Dehydrogenase 7	JF825509	CAGGAGTATGTTGACATCTGTGAC	GAAGTTGAAGGCGGTGATG	154	100%	0.988
ALDH8	Aldehyde Dehydrogenase 8	JF825510	CTGGAGGAGTTTGCAGTGG	GCCAGCCACACCAATAGG	198	100%	0.997
ALDH9	Aldehyde Dehydrogenase 9	JF825511	GGAAAACCAATCTGGGAAGC	CAAAGGGTAGTTCCAGGCTC	183	100%	0.988
GST	Glutathione S-Transferase	JF825513	CAACCCCCAGCACACTGTG	GGATAGACACAATCACCCATCC	210	83%	0.992
GSH-S	Glutathione Synthase	JF825516	GAGAAGGCAAAGGACTATGCTC	GGCAACCTTGTGCATCAAC	180	97%	0.998
CAT	Catalase	JF825517	TGTACATGCAAAGGGAGCTG	GGTGTCTGTTTGCCCACTTT	104	100%	0.998
SOD	Superoxide Dismutase	JF825518	GGAGATCTTGGCAATGTTCAG	CAGTAGCCTTGCTCAGTTCATG	166	97%	0.991
CAS	Cellular Apoptosis Susceptibility Protein	JF825520	CTACAACCACTACCTGTTCGAGT	CAGGGACATGATCTGGAACAC	169	100%	0.995
CARP	Cell Cycle and Apoptosis Regulatory 1 Protein	JF825519	GCCAAGAGTGGGAAGTTTGAC	GAACATTTCATTGAACAATTCTGC	126	98%	0.997
IAP	Inibitor of Apoptosis Protein	JF825521	CAGGATTCTTCTACACAGGCAG	CCATTTCTTGTGTTCTCCCC	108	100%	0.988
HSP70	Heat Shock Protein 70	JF825515	CTTCGTTTGGTATCCATGTTGGTA	CTCTGTGTCCTGGTAGGCGAC	130	100%	0.997
HSP40	Heat Shock Protein 40	JF825514	GGATTATTATAAAGTGCTGGGG	GTCACTAAGTACATCATAGGCCTC	163	100%	0.996

Table 1 shows Pubmed accession numbers, primer sequences, amplicon sizes (base pair), oligo efficiencies (E) and correlation factors (R^2) of the reference gene and genes of interest.

doi:10.1371/journal.pone.0026850.t001

9700 (Perkin Elmer). For a detailed description see [18]. Amplified PCR product sequences are deposited in GenBank under the Accession Numbers shown in Table 1.

Reverse Transcription-Quantitative Real Time Polymerase Chain Reaction (RT-qPCR)

RT-qPCR experiments were performed in a Chromo4 TM Real-time Detector (Biorad) thermal cycler, whereas fluorescence was measured using the Opticon Monitor 3.1 (Biorad). PCR volume for each sample was 25 µl, with 1× of Fast Start SYBR Green Master Mix (Roche), 2 µl of cDNA template and 0.7 pmol/µl for each oligo. The RT-qPCR thermal profile was obtained using the following procedure: 95°C for 10 min, 40 times 95°C for 15 sec and 60°C for 1 min, 72°C for 5 min. The program was set to reveal the melting curve of each amplicon from 60°C to 95°C, and read every 0.5°C. All RT-qPCR reactions were carried out in triplicate to capture intra-assay variability. Each assay included three no-template controls (NTC) for each primer pair. Five serial dilutions of cDNA were used to determine reaction efficiencies for all primer pairs. These efficiencies (Table 1) were calculated generating for each oligonucleotide pair standard curves with at least five dilution points by using the Cycle Threshold (Ct) value versus the logarithm of each dilution factor and using the equation $E = 10^{-1/slope}$. As for previous studies [18], a 1:100 template dilution (4±2 ng) was used for RT-qPCR experiments, in order to allow almost all gene amplifications to fit in the optimal detection window (from 15 to 25 cycles). All analyzed data were covered by the window defined by the standard curve generated for the calculation of the efficiency for each oligo pair.

Expression levels of each target gene in the tested experimental conditions (animals fed on *S. marinoi* and *C. socialis*) were compared to the control condition (animals fed on *R. baltica*) using the REST tool (Relative expression software tool) [49]. Data were normalized using the ribosomal protein S20, which had previously been identified as the best reference gene under different experimental conditions [18]. In the present analysis, the ribosomal protein S20 was confirmed to be stable, showing a variability always lower than ±1 cycle. The 1 x-fold expression level was therefore chosen as the threshold for significance of target genes. However, to validate our results, a statistical analysis was also performed using GraphPad Prism version 4.00 for Windows (GraphPad Software, San Diego California USA).

Results

The effects of diatom diets on *C. helgolandicus* females were evaluated by analyzing expression levels of genes involved in generic stress responses, defense systems, aldehyde detoxification or apoptosis regulation in other organisms (Figure 1). *C. helgolandicus* females fed the strong oxylipin and PUAs-producing diatom *S. marinoi* showed a general pattern of reduction in the expression levels of almost all the selected genes compared to females fed the control flagellate *R. baltica* (Figure 2, 3, 4). Both HSP40 and HSP70 transcript levels were reduced even if the change was only significant for HSP40 (p value<0.01, students't-test, GraphPad Software) (Figure 2). Expression levels of these genes in animals fed *C. socialis* did not change significantly. Enzymes involved in phase I and phase II reactions and anti-oxidant activity (CYP4, GST, GSH-S, CAT and SOD) did not show any significant changes in their expression levels in animals fed both diatom diets.

On the contrary, all six ALDH isoforms (ALDH2, ALDH3B1, ALDH6, ALDH7, ALDH8, and ALDH9) had lower expression levels in *C. helgolandicus* fed *S. marinoi* than those fed the control diet (Figure 3). However, only ALDH6, ALDH8 and ALDH9 were significantly affected, showing a 2–3 fold reduction in their expression levels (p value<0.001, students't-test, GraphPad Software). On the contrary, the expression levels for the same genes in copepods fed *C. socialis* did not show significant changes, indicating that these genes were not affected by this diatom diet.

Of the three proteins involved in apoptosis regulation (CARP, CAS and IAP) CAS and IAP expression levels were strongly

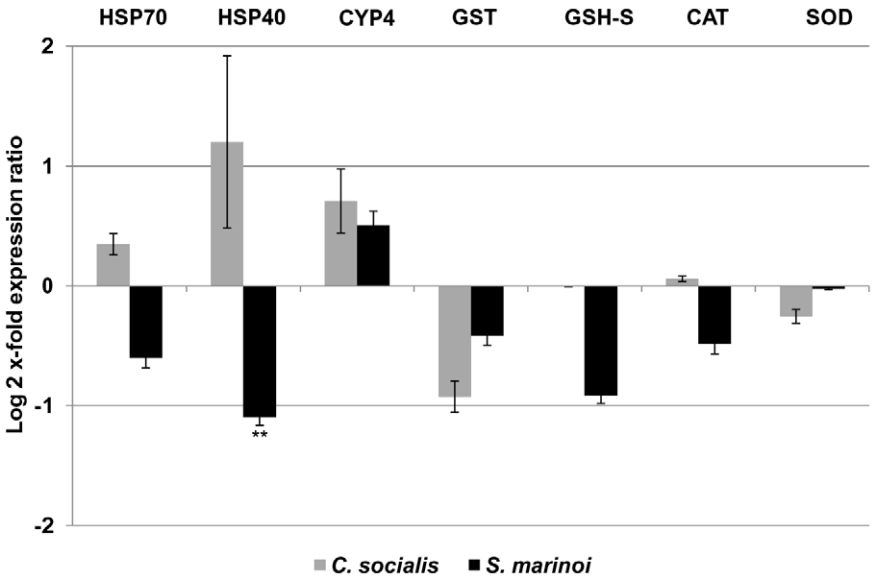

Figure 2. Expression levels of genes involved in stress and defense systems in the copepod *Calanus helgolandicus*. Changes in expression levels of Heat shock protein 70 (HSP70) and 40 (HSP40), Cytochrome P450-4 (CYP4), Glutathione S-Transferase (GST), Glutathione Synthase (GSH-S), Catalase (CAT) and Superoxide Dismutase (SOD) genes in *C. helgolandicus* fed either unialgal diets of *Skeletonema marinoi* (*S. marinoi*) or *Chaetoceros socialis* (*C. socialis*) compared to expression levels in females fed on the control *Rhodomonas baltica* (represented in the figure by x-axis) (** with p value<0.01, students't-test, GraphPad Software). The ribosomal protein S20 was used as reference gene to normalize the data.
doi:10.1371/journal.pone.0026850.g002

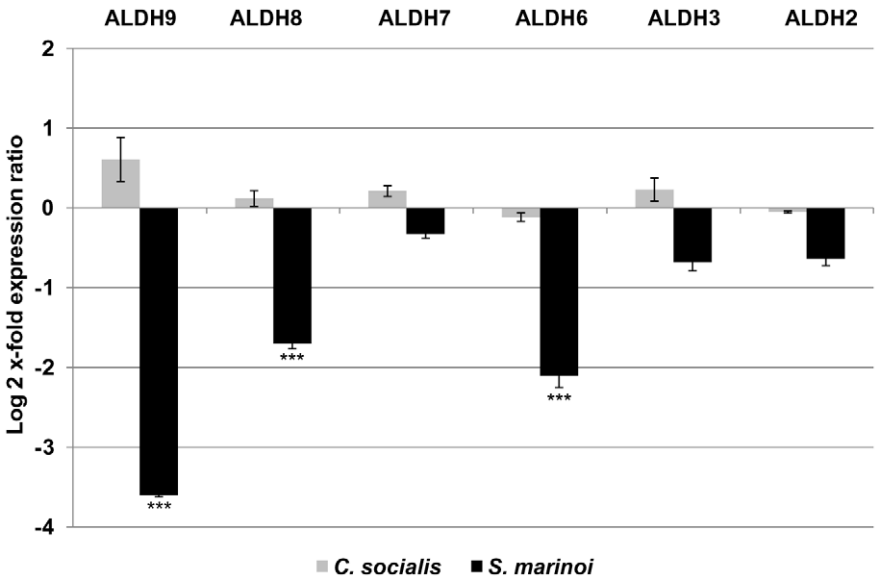

Figure 3. Relative gene expression levels of aldehyde dehydrogenases (ALDH) in the copepod *Calanus helgolandicus*. Changes in ALDH2, ALDH3, ALDH6, ALDH7, ALDH8 and ALDH9 gene expression levels in *C. helgolandicus* females fed either unialgal diets of *Skeletonema marinoi* (*S. marinoi*) or *Chaetoceros socialis* (*C. socialis*) compared to expression levels in females fed on the control *Rhodomonas baltica* (represented in the figure by x-axis) (*** with p value<0.001, students't-test, GraphPad Software). The ribosomal protein S20 was used as reference gene to normalize the data.
doi:10.1371/journal.pone.0026850.g003

reduced by *S. marinoi* compared to the control *R. baltica* and to *C. socialis*. In particular, CAS and IAP showed a significant 2-fold reduction (p value<0.001, students't-test, GraphPad Software) (Figure 4), while changes in CARP expression levels were close to zero. Gene expression profiles of alpha and beta tubulins, essential proteins for mitotic spindle formation, did not vary significantly in copepods fed on *C. socialis* compared to the control *R. baltica*. In contrast, *C. helgolandicus* fed *S. marinoi* showed a significant reduction of about 2-fold for alpha tubulin and 3-fold for beta tubulin (p value<0.001, students't-test, GraphPad Software) (Figure 4).

Discussion

Our results show that two days (2 d) of feeding of *C. helgolandicus* on *S. marinoi* is sufficient to inhibit a series of genes involved in

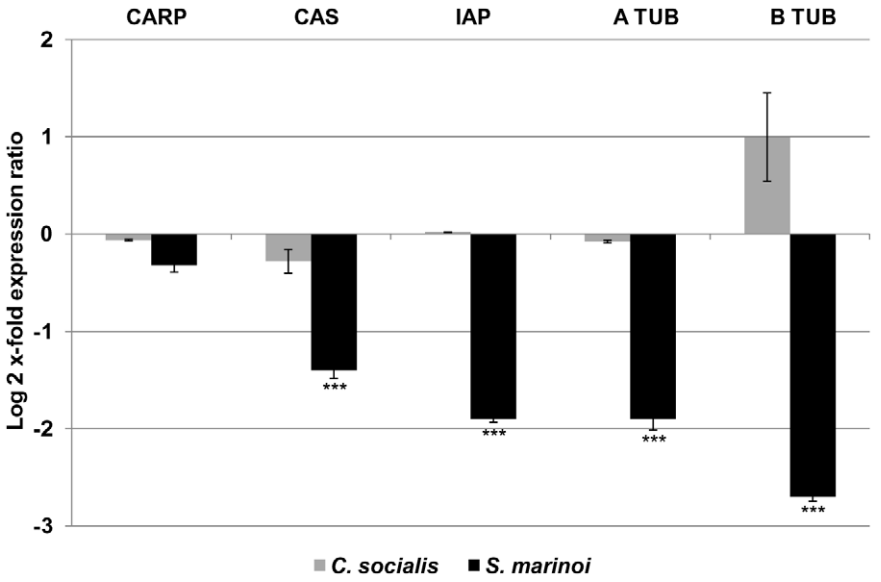

Figure 4. Expression analysis of genes involved in apoptosis and mitotic spindle formation in *C. helgolandicus*. Changes in expression levels of Cell Cycle and Apoptosis Regulatory 1 Protein (CARP), Cellular Apoptosis Susceptibility Protein (CAS), Inhibitor of Apoptosis Protein (IAP), and Alpha and Beta tubulins (ATUB and BTUB) genes in *C. helgolandicus* fed either unialgal diets of *Skeletonema marinoi* (*S. marinoi*) or *Chaetoceros socialis* (*C. socialis*) compared to expression levels in females fed on the control *Rhodomonas baltica* (represented in the figure by x-axis) (*** with p value<0.001, students't-test, GraphPad Software). The ribosomal protein S20 was used as reference gene to normalize the data.
doi:10.1371/journal.pone.0026850.g004

generic stress response, aldehyde detoxification and apoptosis regulation. Of the analyzed transcripts at least 50% were strongly reduced (ALDH9, ALDH8 and ALDH6, CAS, IAP, HSP40, alpha- and beta-tubulin) with a *S. marinoi* diet, while no significant gene expression changes were observed in animals fed on the other diatom *C. socialis*. Previous studies have shown that after 2 d of feeding on *S. marinoi* egg viability in *C. helgolandicus* is still high (>90%) and decreases to about 50% after 3 d [3]. On the contrary, with a *C. socialis* diet, egg viability is high (90%) even after 3 d [3] indicating that this diatom is less toxic for copepod reproduction. Fontana and co-workers [3] concluded that the lower toxicity of *C. socialis* was due to the fact that this diatom does not produce PUAs but only low quantities of hydroxyl-acids and epoxy-alcohols compared to *S. marinoi*. Our results indicate that there is a significantly different response in gene expression patterns in *C. helgolandicus* fed on these two diets thereby offering a possible explanation as to why in nature certain diatom blooms may be more toxic for copepods [1,16] compared to others [50,51].

Until now, gene expression studies in copepods have been performed after exposure to various toxicants such as naphtalene [52], diethanolamine [53] and mono ethanol amine (MEA), water-soluble fractions of oil (WSFs), trace metals [54] and endocrine-disrupting chemicals [55] (as reviewed by [56]). In most of these studies [52,53,57,58], detoxification gene expression levels increased when copepods were challenged with toxicants, but in our case there was a general pattern of decrease and both general stress systems and specific responses seemed to be inhibited.

Both HSP70 and HSP40 expression levels decreased in females fed on *S. marinoi* suggesting a reduction in chaperone activity in the folding of new proteins, repairing of unfolded and damaged proteins, and inhibition of protein aggregations, thereby leading to an increase in cellular damage. Romano et al. [59] have recently shown that sea urchins activate HSP70 when challenged with low concentrations (0.25 µg/ml) of the PUA decadienal thereby protecting embryos against the toxic effects of this aldehyde. This up-regulation was only found at 9 h post fertilization (hpf), while at 5, 24 and 48 hpf, expression levels were comparable to the control. Small changes in HSP70 mRNA levels were found in *C. finmarchicus* after naphtalene exposure [52], while Rhee and co-workers [60] showed a concentration-dependent increase in the expression of HSP70 transcripts after exposure to trace metals (i.e. copper, silver, and zinc), with an increase caused by bisphenol A (BPA) and a decrease by 4-nonylphenol (NP) and 4-t-octylpheno (OP).

Enzymes involved in antioxidant cell activity (GST and GSH-S) and in free radical detoxification (CAT and SOD) did not show significant expression level changes in *C. helgolandicus* fed either of the two diatom diets indicating that they were not involved in the defense response of this copepod species, at least after two days of exposure. Kozlowsky-Suzuki and co-workers (2008) also suggested that GST enzymatic activity did not seem to play a role in detoxification of copepods exposed to toxic dinoflagellate algae: *Alexandrium minutum* and *Alexandrium tamarense*, which contained Paralytic Shellfish Poisoning (PSP) toxins, and the dinoflagellate *Prorocentrum lima* with Diarrhetic Shellfish Poisoning (DSP) toxins. On the contrary, GST expression levels were affected in the copepod *Calanus finmarchicus* after exposure to naphthalene [52] and diethanolamine (DEA) [53] and in the copepod *Tigriopus japonicus* exposed to trace metals and hydrogen peroxide (H_2O_2) [58]. The responses were mainly concentration- and time-dependent and varied with the tested stressors. Hansen and co-workers [52] showed that only the lowest naphthalene concentration in *C. finmarchicus* led to increased mRNA levels of the ROS detoxification enzymes SOD and CAT, but no effects were found at medium and high concentrations, indicating no clear evidence for general cellular oxidative stress following naphthalene exposure. On the other hand, the transcription levels of the antioxidant glutathione synthase (GSH-S) and Cu/Zn-superoxide dismutase (SOD) changed with a concentration-dependent pattern following exposure to DEA in the same copepod species [53]. SODs expression levels in the harpacticoid copepod *Tigriopus japonicus* increased only at the highest heavy metal concentrations tested and showed different responses to endocrine disruptor chemicals (EDCs) depending on the specific stressor and its concentration [61].

The aldehyde dehydrogenase family, which should detoxify and inactivate aldehydes, was almost switched off in animals fed on the *S. marinoi* diet. Gene expression levels were significant reduced by about 4-fold for ALDH9 and 2-fold for ALDH8 and ALDH6. Until now, ALDH gene expression levels have been mostly analyzed in humans and this is the first time that they have been analyzed in a copepod species. It is widely known that ALDH are involved in protecting cells from the deleterious effects of xenobiotics and endogenous aldehydes such as those derived from lipid peroxidation [62]. Our results suggest that this enzyme family in copepods fed on the diatom *S. marinoi* is probably not able to detoxify high levels of toxic diatom aldehydes, and that therefore there is accumulation of these compounds in body tissues or formation of adducts.

Selected apoptosis regulatory proteins were also affected by the *S. marinoi* diet. The two proteins whose function in humans is to inhibit apoptosis, CAS and IAP, were significantly down-regulated by about 2-fold, yet apoptotic processes were not inhibited, at least after 2 d of feeding. The fact that CARP, a protein generally associated with an increase in apoptosis [63], did not respond to the diet suggests that there was no clear apoptosis induction in adult females in our experimental conditions. Buttino *et al.* [64] using aldehyde-encapsulating liposomes observed apoptotic regions in copepod female gonads only after 9 d of feeding. We therefore assume that induction of pro-apoptotic proteins may only occur after longer exposure to the toxic diet.

Alpha and beta tubulins, structural subunits of MTs and the targets of many natural toxins, were previously reported to be 2-fold and 3-fold down-regulated, respectively, with a *S. marinoi* diet [18]. Here we confirm our previous findings and also show that *C. socialis* does not induce the same pronounced reduction in the expression levels of these two genes. Future studies on PUAs-tubulin interactions may clarify if alpha and beta tubulins are the targets of toxic *S. marinoi* metabolites or if their gene expression reduction is a secondary effect of PUAs toxicity.

Our results provide molecular evidence for the toxic effects of certain diatom diets on grazers, showing that primary defense systems that should be activated to protect copepods against dangerous algae are inhibited. This exploratory study is currently being extended with the creation of a suppression subtractive hybridization library for *Calanus helgolandicus* which may further help to clarify which genes are differentially expressed in response to the ingestion of some diatom species. Given the importance of diatom blooms in nutrient-rich aquatic environments these preliminary results offer a plausible explanation for the inefficient use of a potentially valuable food resource—the spring diatom bloom—by some zooplankton [1,16]. Also terrestrial plants produce toxins which cause abortions, reproductive dysfunction and occasional birth defects when ingested by certain grazers [65] suggesting that interactions among organisms are regulated by similar mechanisms in terrestrial and marine ecosystems.

Acknowledgments

The authors thank Francesco Esposito for the preparation of algal cultures and assistance with the re-circulating copepod breeding system. We also thank Flora Palumbo and Massimo Perna of the FEEL laboratory and the staff of the Molecular Biology Service of Stazione Zoologica Anton Dohrn for their technical support.

Author Contributions

Conceived and designed the experiments: AI GP CL. Performed the experiments: CL YC. Analyzed the data: CL. Contributed reagents/materials/analysis tools: AM MB EB. Wrote the paper: CL AI GP YC MB.

References

1. Miralto A, Barone G, Romano G, Poulet SA, Ianora A, et al. (1999) The insidious effect of diatoms on copepod reproduction. Nature 402: 173–176.
2. Ianora A, Turner JT, Esposito F, Carotenuto Y, d'Ippolito G, et al. (2004) Copepod egg production and hatching success is reduced by maternal diets of a non-neurotoxic strain of the dinoflagellate *Alexandrium tamarense*. Marine Ecology-Progress Series 280: 199–210.
3. Fontana A, d'Ippolito G, Cutignano A, Romano G, Lamari N, et al. (2007) LOX-induced lipid peroxidation mechanism responsible for the detrimental effect of marine diatoms on Zooplankton grazers. Chembiochem 8: 1810–1818.
4. Carotenuto Y, Wichard T, Pohnert G, Lampert W (2005) Life-history responses of *Daphnia pulicaria* to diets containing freshwater diatoms: Effects of nutritional quality versus polyunsaturated aldehydes. Limnology and Oceanography 50: 449–454.
5. Romano G, Miralto A, Ianora A (2010) Teratogenic Effects of Diatom Toxins on Sea Urchin *Paracentrotus Lividus* Embryos. Marine Drugs 8: 950–967.
6. Guenther J, Wright AD, Burns K, de Nys R (2009) Chemical antifouling defences of sea stars: effects of the natural products hexadecanoic acid, cholesterol, lathosterol and sitosterol. Marine Ecology-Progress Series 385: 137–149.
7. Caldwell GS (2009) The influence of bioactive oxylipins from marine diatoms on invertebrate reproduction and development. Marine Drugs 7: 367–400.
8. Caldwell GS, Olive PJW, Bentley MG (2002) Inhibition of embryonic development and fertilization in broadcast spawning marine invertebrates by water soluble diatom extracts and the diatom toxin 2-trans,4-trans decadienal. Aquatic Toxicology 60: 123–137.
9. Simon CA, Bentley MG, Caldwell GS (2010) 2,4-Decadienal: Exploring a novel approach for the control of polychaete pests on cultured abalone. Aquaculture 310: 52–60.
10. Tosti E, Romano G, Buttino I, Cuomo A, Ianora A, et al. (2003) Bioactive aldehydes from diatoms block the fertilization current in ascidian oocytes. Molecular Reproduction and Development 66: 72–80.
11. Pohnert G (2000) Wound-activated chemical defense in unicellular planktonic algae. Angewandte Chemie-International Edition 39: 4352–4354.
12. d'Ippolito G, Tucci S, Cutignano A, Romano G, Cimino G, et al. (2004) The role of complex lipids in the synthesis of bioactive aldehydes of the marine diatom *Skeletonema costatum*. Biochimica Et Biophysica Acta-Molecular and Cell Biology of Lipids 1686: 100–107.
13. Cutignano A, d'Ippolito G, Romano G, Lamari N, Cimino G, et al. (2006) Chloroplastic glycolipids fuel aldehyde biosynthesis in the marine diatom *Thalassiosira rotula*. Chembiochem 7: 450–456.
14. Fontana A, d'Ippolito G, Cutignano A, Miralto A, Ianora A, et al. (2007) Chemistry of oxylipin pathways in marine diatoms. Pure and Applied Chemistry 79: 481–490.
15. d'Ippolito G, Lamari N, Montresor M, Romano G, Cutignano A, et al. (2009) 15S-Lipoxygenase metabolism in the marine diatom *Pseudo-nitzschia delicatissima*. New Phytologist 183: 1064–1071.
16. Ianora A, Miralto A, Poulet SA, Carotenuto Y, Buttino I, et al. (2004) Aldehyde suppression of copepod recruitment in blooms of a ubiquitous planktonic diatom. Nature 429: 403–407.
17. Andreou A, Brodhun F, Feussner I (2009) Biosynthesis of oxylipins in non-mammals. Progress in Lipid Research 48: 148–170.
18. Lauritano C, Borra M, Carotenuto Y, Biffali E, Miralto A, et al. (2011) First molecular evidence of diatom effects in the copepod *Calanus helgolandicus*. Journal of Experimental Marine Biology and Ecology 404: 79–86.
19. Bouraoui Z, Banni M, Ghedira J, Clerandeau C, Narbonne JF, et al. (2009) Evaluation of enzymatic biomarkers and lipoperoxidation level in *Hediste diversicolor* exposed to copper and benzo[a]pyrene. Ecotoxicology and Environmental Safety 72: 1893–1898.
20. Einsporn S, Bressling J, Koehler A (2009) Cellular localization of lead using an antobody-based detection system and enzyme activity chenges in the gills and digestive gland of the blue mussel *Mytilus edulis*. Environmental Toxicology and Chemistry 28: 402–408.
21. Hasselberg L, Meier S, Svardal A, Hegelund T, Celander MC (2004) Effects of alkylphenols on CYP1A and CYP3A expression in first spawning Atlantic cod (*Gadus morhua*). Aquatic Toxicology 67: 303–313.
22. Kim HE, Jiang XJ, Du FH, Wang XD (2008) PHAPI, CAS, and Hsp70 promote apoptosome formation by preventing Apaf-1 aggregation and enhancing nucleotide exchange on Apaf-1. Molecular Cell 30: 239–247.
23. Olsvik PA, Lie KK, Sturve J, Hasselberg L, Andersen OK (2009) Transcriptional effects of nonylphenol, bisphenol A and PBDE-47 in liver of juvenile Atlantic cod (*Gadus morhua*). Chemosphere 75: 360–367.
24. Salazar-Medina AJ, Garcia-Rico L, Garcia-Orozco KD, Valenzuela-Soto E, Contreras-Vergara CA, et al. (2010) Inhibition by Cu(2+) and Cd(2+) of a Mu-Class Glutathione S-Transferase from Shrimp *Litopenaeus vannamei*. Journal of Biochemical and Molecular Toxicology 24: 218–222.
25. Snyder MJ (2000) Cytochrome P450 enzymes in aquatic invertebrates: recent advances and future directions. Aquatic Toxicology 48: 529–547.
26. Vasiliou V, Pappa A, Estey T (2004) Role of human aldehyde dehydrogenases in endobiotic and xenobiotic metabolism. Drug Metabolism Reviews 36: 279–299.
27. Wan Q, Whang I, Choi CY, Lee JS, Lee J (2011) Validation of housekeeping genes as internal controls for studying biomarkers of endocrine-disrupting chemicals in disk abalone by real-time PCR. Comparative Biochemistry and Physiology C-Toxicology & Pharmacology 153: 259–268.
28. Feder ME, Hofmann GE (1999) Heat-shock proteins, molecular chaperones, and the stress response: Evolutionary and ecological physiology. Annual Review of Physiology 61: 243–282.
29. Bierkens JGEA (2000) Applications and pitfalls of stress-proteins in biomonitoring. Toxicology 153: 61–72.
30. Fan C-Y, Lee S, Cyr DM (2003) Mechanisms for regulation of Hsp70 function by Hsp40. Cell Stress & Chaperones 8: 309–316.
31. Fink P, Von Elert E, Juttner F (2006) Oxylipins from freshwater diatoms act as attractants for a benthic herbivore. Archiv Fur Hydrobiologie 167: 561–574.
32. Hsu MH, Savas U, Griffin KJ, Johnson EF (2007) Human cytochrome P450 family 4 enzymes: Function, genetic variation and regulation. Drug Metabolism Reviews 39: 515–538.
33. Goldstone JV, Hamdoun A, Cole BJ, Howard-Ashby M, Nebert DW, et al. (2006) The chemical defensome: Environmental sensing and response genes in the *Strongylocentrotus purpuratus* genome. Developmental Biology 300: 366–384.
34. Bigot A, Vasseur P, Rodius F (2010) SOD and CAT cDNA cloning, and expression pattern of detoxification genes in the freshwater bivalve *Unio tumidus* transplanted into the Moselle river. Ecotoxicology 19: 369–376.
35. Sheehan D, Meade G, Foley VM, Dowd CA (2001) Structure, function and evolution of glutathione transferases: implications for classification of non-mammalian members of an ancient enzyme superfamily. Biochemical Journal 360: 1–16.
36. Yoshida A, Rzhetsky A, Hsu LC, Chang C (1998) Human aldehyde dehydrogenase gene family. European Journal of Biochemistry 251: 549–557.
37. Marchitti SA, Brocker C, Stagos D, Vasiliou V (2008) Non-P450 aldehyde oxidizing enzymes: the aldehyde dehydrogenase superfamily. Expert Opinion on Drug Metabolism & Toxicology 4: 697–720.
38. Brocker C, Lassen N, Estey T, Pappa A, Cantore M, et al. (2010) Aldehyde dehydrogenase 7A1 (ALDH7A1) is a novel enzyme involved in cellular defense against hyperosmotic stress. Journal of Biological Chemistry 285: 18452–18463.
39. Lederman M, Meir T, Zeschnigk M, Pe'er J, Chowers I (2008) Inhibitor of apoptosis proteins gene expression and its correlation with prognostic factors in primary and metastatic uveal melanoma. Current Eye Research 33: 876–884.
40. Brinkmann U (1998) CAS, the human homologue of the yeast chromosome-segregation gene CSE1, in proliferation, apoptosis, and cancer. American Journal of Human Genetics 62: 509–513.
41. Tai CJ, Shen SC, Lee WR, Liao CF, Deng WP, et al. (2010) Increased cellular apoptosis susceptibility (CSE1L/CAS) protein expression promotes protrusion extension and enhances migration of MCF-7 breast cancer cells. Experimental Cell Research 316: 2969–2981.
42. Rishi AK, Zhang L, Yu Y, Jiang Y, Nautiyal J, et al. (2006) Cell cycle- and apoptosis-regulatory protein-1 is involved in apoptosis signaling by epidermal growth factor receptor. The Journal of Biological Chemistry 281: 13188–13198.
43. Jordan Mary Ann lW (2004) Microtubules as a target for anticancer drugs. Nature reviews.
44. Harrison MR, Holen KD, Liu G (2009) Beyond taxanes: a review of novel agents that target mitotic tubulin and microtubules, kinases, and kinesins. Clin Adv Hematol Oncol 7: 54–64.
45. Calligaris D, Verdier-Pinard P, Devred F, Villard C, Braguer D, et al. (2010) Microtubule targeting agents: from biophysics to proteomics. Cell Mol Life Sci 67: 1089–1104.
46. Nogales E, Wolf SG, Downing KH (1998) Structure of the alpha beta tubulin dimer by electron crystallography (vol 391, pg 199, 1998). Nature 393: 191–191.
47. Gerecht A, Romano G, Ianora A, d'Ippolito G, Cutignano A, et al. (2011) Plasticity of oxylipin metabolism among clones of the marine diatom *Skeletonema marinoi* (Bacillariophyceae). Journal of Phycology, In press.
48. Buttino I, Ianora A, Buono S, Vitiello V, Malzone MG, et al. (2011) Experimental cultivation of the Mediterranean calanoid copepods *Temora stylifera* and *Centropages typicus* in a pilot re-circulating system. Aquaculture research in press.
49. Pfaffl MW, Horgan GW, Dempfle L (2002) Relative expression software tool (REST (c)) for group-wise comparison and statistical analysis of relative expression results in real-time PCR. Nucleic Acids Research 30.

50. Koski M (2007) High reproduction of *Calanus finmarchicus* during a diatom-dominated spring bloom. Marine Biology 151: 1785–1798.
51. Irigoien X, Harris RP, Verheye HM, Joly P, Runge J, et al. (2002) Copepod hatching success in marine ecosystems with high diatom concentrations. Nature 419: 387–389.
52. Hansen BH, Altin D, Vang SH, Nordtug T, Olsen AJ (2008) Effects of naphthalene on gene transcription in *Calanus finmarchicus* (Crustacea: Copepoda). Aquatic Toxicology 86: 157–165.
53. Hansen BH, Altin D, Booth A, Vang SH, Frenzel M, et al. (2010) Molecular effects of diethanolamine exposure on *Calanus finmarchicus* (Crustacea: Copepoda). Aquatic Toxicology 99: 212–222.
54. Hansen BH, Altin D, Nordtug T, Olsen AJ (2007) Suppression subtractive hybridization library prepared from the copepod *Calanus finmarchicus* exposed to a sublethal mixture of environmental stressors. Comparative Biochemistry and Physiology D-Genomics & Proteomics 2: 250–256.
55. Lee YM, Park TJ, Jung SO, Seo JS, Park HG, et al. (2006) Cloning and characterization of glutathione S-transferase gene in the intertidal copepod *Tigriopus japonicus* and its expression after exposure to endocrine-disrupting chemicals. Marine Environmental Research 62: S219–S223.
56. Lauritano C, Procaccini G, Ianora A (2011) Gene expression patterns and stress response in marine copepods. Marine Environmental Research, In press.
57. Hansen BH, Altin D, Hessen KM, Dahl U, Breitholtz M, et al. (2008) Expression of ecdysteroids and cytochrome P450 enzymes during lipid turnover and reproduction in *Calanus finmarchicus* (Crustacea: Copepoda). General and Comparative Endocrinology 158: 115–121.
58. Lee K-W, Raisuddin S, Rhee J-S, Hwang D-S, Yu IT, et al. (2008) Expression of glutathione S-transferase (GST) genes in the marine copepod *Tigriopus japonicus* exposed to trace metals. Aquatic Toxicology 89: 158–166.
59. Romano G, Costantini M, Buttino I, Ianora A, Palumbo A (2011) Nitric oxide mediates the stress response induced by diatom adehydes in the sea urchin *Paracentrotus lividus*. PLoS One, In press.
60. Rhee JS, Raisuddin S, Lee KW, Seo JS, Ki JS, et al. (2009) Heat shock protein (Hsp) gene responses of the intertidal copepod *Tigriopus japonicus* to environmental toxicants. Comparative Biochemistry and Physiology C-Toxicology & Pharmacology 149: 104–112.
61. Kim B-M, Rhee J-S, Park GS, Lee J, Lee Y-M, et al. (2011) Cu/Zn- and Mn-superoxide dismutase (SOD) from the copepod *Tigriopus japonicus*: Molecular cloning and expression in response to environmental pollutants. Chemosphere 84: 1467–1475.
62. Canuto RA, Ferro M, Muzio G, Bassi AM, Leonarduzzi G, et al. (1994) Role of aldehyde metabolizing enzymes in mediating effects of aldehyde products of lipid-peroxidation in liver-cells. Carcinogenesis 15: 1359–1364.
63. Majumdar APN, Du JH, Yu YJ, Xu H, Levi E, et al. (2007) Cell cycle and apoptosis regulatory protein-1: a novel regulator of apoptosis in the colonic mucosa during aging. American Journal of Physiology-Gastrointestinal and Liver Physiology 293: G1215–G1222.
64. Buttino I, De Rosa G, Carotenuto Y, Mazzella M, Ianora A, et al. (2008) Aldehyde-encapsulating liposomes impair marine grazer survivorship. Journal of Experimental Biology 211: 1426–1433.
65. Green BT, Lee ST, Panter KE, Welch KD, Cook D, et al. (2010) Actions of piperidine alkaloid teratogens at fetal nicotinic acetylcholine receptors. Neurotoxicology and Teratology 32: 383–390.

OPEN ACCESS Freely available online

PLOS | ONE

Copepod Population-Specific Response to a Toxic Diatom Diet

Chiara Lauritano*, Ylenia Carotenuto, Antonio Miralto, Gabriele Procaccini, Adrianna Ianora

Stazione Zoologica Anton Dohrn, Villa Comunale, Napoli, Italy

Abstract

Diatoms are key phytoplankton organisms and one of the main primary producers in aquatic ecosystems. However, many diatom species produce a series of secondary metabolites, collectively termed oxylipins, that disrupt development in the offspring of grazers, such as copepods, that feed on these unicellular algae. We hypothesized that different populations of copepods may deal differently with the same oxylipin-producing diatom diet. Here we provide comparative studies of expression level analyses of selected genes of interest for three *Calanus helgolandicus* populations (North Sea, Atlantic Ocean and Mediterranean Sea) exposed to the same strain of the oxylipin-producing diatom *Skeletonema marinoi* using as control algae the flagellate *Rhodomonas baltica*. Expression levels of detoxification enzymes and stress proteins (e.g. glutathione S-transferase, glutathione synthase, superoxide dismutase, catalase, aldehyde dehydrogenases and heat shock proteins) and proteins involved in apoptosis regulation and cell cycle progression were analyzed in copepods after both 24 and 48 hours of feeding on the diatom or on a control diet. Strong differences occurred among copepod populations, with the Mediterranean population of *C. helgolandicus* being more susceptible to the toxic diet compared to the others. This study opens new perspectives for understanding copepod population-specific responses to diatom toxins and may help in underpinning the cellular mechanisms underlying copepod toxicity during diatom blooms.

Citation: Lauritano C, Carotenuto Y, Miralto A, Procaccini G, Ianora A (2012) Copepod Population-Specific Response to a Toxic Diatom Diet. PLoS ONE 7(10): e47262. doi:10.1371/journal.pone.0047262

Editor: Myron Peck, University of Hamburg, Germany

Received July 11, 2012; **Accepted** September 11, 2012; **Published** October 8, 2012

Copyright: © 2012 Lauritano et al. This is an open-access article distributed under the terms of the Creative Commons Attribution License, which permits unrestricted use, distribution, and reproduction in any medium, provided the original author and source are credited.

Funding: EU FP7 ASSEMBLE (grant agreement no. 227799) for financial support for copepod sampling in the Atlantic Ocean and North Sea. The funders had no role in study design, data collection and analysis, decision to publish, or preparation of the manuscript.

Competing Interests: The authors have declared that no competing interests exist.

* E-mail: chiara.lauritano@szn.it

Introduction

Diatoms are key phytoplankton organisms in the world's oceans and are considered essential in the transfer of energy through marine food chains. However, in the last 20 years, numerous studies have shown that these unicellular plants at times produce secondary metabolites with toxic effects on reproduction and development of marine organisms such as crustacean copepods [1,2,3] and cladocerans [4], echinoderm sea urchins [5] and sea stars [6,7], polychaete worms [8,9], and ascidians [10]. Diatom metabolites are the end-products of a lipoxygenase/hydroperoxide lyase metabolic pathway [11,12,13,14,15] initiated by damage to algal cells, as occurs through grazing by predators. Cell damage activates lipase enzymes, which liberate polyunsaturated fatty acids (PUFAs) from cell membranes that are immediately oxidized and cleaved within seconds to form polyunsaturated aldehydes (PUAs) and a plethora of other metabolites collectively termed oxylipins.

Oxylipins, and PUAs in particular, can compromise embryonic and larval development in marine organisms by inhibiting fertilization processes, reducing larval fitness and inducing malformations in the offspring of grazers that feed on these unicellular algae (as reviewed by [16]). Teratogenesis and reduction in egg production and hatching success have been observed also for wild copepods feeding on the natural winter/spring diatom-dominated bloom in the Mediterranean Sea (i.e. Adriatic Sea [1,2]), in North and South Pacific (i.e. Dabob Bay, Washington, USA [17] and the coastal zone off Dichato, Chile [18]) and in the Baltic Sea [19]. Such antiproliferative compounds may impact on herbivory by sabotaging future generations of grazers, thereby allowing diatom blooms to persist when grazing pressure would otherwise have caused them to crash.

In recent studies [20,21], we showed that expression levels of selected genes of interest (GOI) were significantly reduced when females of the copepod *Calanus helgolandicus* (*C. helgolandicus*) were fed for two days (d) on the diatom *Skeletonema marinoi* (*S. marinoi*) which is known to produce high quantities of PUAs and several other oxylipins including fatty acid hydroperoxides, hydroxyl- and keto-fatty acids, and epoxyalcohols [3]. On the contrary, a diet of *Chaetoceros socialis*, which does not produce any aldehydes, but only low levels of other oxylipins, did not induce significant expression levels changes [21]. Interestingly, after 2 d of feeding on *S. marinoi* egg viability in *C. helgolandicus* was still high (90%), and decreased rapidly to 10% after 5 d ([3], supporting material), indicating that changes in gene expression levels after 2 d could act as an early warning signal to denote a deterioration in copepod fitness.

The aim of the present study was to further explore the toxic effects of ingestion of *S. marinoi* on gene expression levels in three different *C. helgolandicus* populations: Swedish western coast (Gullmar Fjord, North Sea), English Channel (NE Atlantic Ocean) and North Adriatic Sea (Mediterranean Sea) populations. The three populations are exposed to different diatom blooms in terms of species composition [2,22,23,24]. All three *Calanus* populations co-exist with *S. marinoi*; in the Swedish west coast *S. marinoi* is differentiated in local populations and represents the most abundant diatom species reaching peak abundances almost twice

a year [24]; in the NE Atlantic this diatom occurs commonly, but it is never the most abundant diatom species, and is replaced by other oxylipin-producing diatoms (*Rhizosolenia delicatula*, *Thalassiosira rotula*, *Chaetoceros sp*., etc.; [25]); in the North Adriatic Sea *S. marinoi* is the most abundant species during the winter-spring phytoplankton bloom [2]. PUAs have been detected in all three sampling sites [25,26,27].

We analyzed expression levels of selected GOI in the three *Calanus* populations after 24 and 48 h of feeding on the stationary phase of growth of the same toxic *S. marinoi* clone used by Gerecht et al. [28]. The clone was isolated from the diatom bloom in the North Adriatic Sea in 1997 and was shown to produce 2.1 [SD 1.1] fmol PUAs cell^{-1} and 1.1 [SD 0.8] fmol cell^{-1} of nonvolatile oxylipins, such as hydroxy acids and epoxy alcohols, in the stationary phase of growth, more than 10 years after it was first isolated. PUA production measurements in other cultivated *S. marinoi* strains indicated PUA concentration between 0.1 and 25 fmol cell^{-1}, depending on the nutrient status of the diatom cells, while higher concentrations have been found at sea (up to 47.7 fmol cell^{-1}), probably due to optimum growth conditions of the field algal population [27,29,30]. Considering ingestion rates of about 1,000 diatom cells per hour [1], in our experiments *C. helgolandicus* had ingested 76.8 and 153.6 pmol of oxylipins after 24 h and 48 h, respectively.

The selected genes were utilized in previous studies on *C. helgolandicus* response to toxic diatom diets [21] and are known to have a primary role in generic stress responses, defense systems (e.g. aldehyde, free fatty acid and free radical detoxification) or apoptosis regulation in other organisms, from humans to marine organisms [31,32,33,34,35]. In particular, we analyzed the heat shock protein families 40 and 70 (HSP40 and HSP70, respectively) activated in response to various environmental stress factors [36], the microsomal cytochrome P450 family 4 monooxygenases (CYP4) involved in oxidative modification (known as Phase I reaction) of chemicals into more hydrophilic metabolites to enhance their elimination or inactivation [37], catalase (CAT) and superoxide dismutase (SOD) [38] responsible for detoxification of reactive oxygen species (ROS) [3], and the antioxidant activity of glutathione synthase (GSH-S) and glutathione S-transferase (GST). Six aldehyde dehydrogenase (ALDH) isoforms (ALDH2, ALDH3, ALDH6, ALDH7, ALDH8 and ALDH9) involved in aldehyde detoxification due to lipid peroxidation (LPO) [35,39] were examined because of their possible role in PUA detoxification. Finally, we analyzed 3 apoptosis-regulating genes, an inhibitor of the apoptosis protein (IAP), the cell cycle and apoptosis regulatory 1 protein (CARP), the cellular apoptosis susceptibility protein (CAS), and the microtubule subunits (alpha and beta tubulins) for their involvement in apoptosis regulation and cell-cycle progression [40,41,42].

Results

Population Identification

A 518 bp fragment of the mitochondrial Cytochrome Oxidase subunit I region (COI) was amplified for each *C. helgolandicus* population. COI sequence in animals collected from the Atlantic Ocean corresponded to the haplotype H1 typical of individuals of the NE Atlantic (GenBank accession number AY942600) as published by Papadopoulos and co-workers [43]. COI sequence in animals collected from the Adriatic Sea corresponded to the haplotype H8 (GenBank accession number AY942593) associated with specimens living in the NE Atlantic and/or Adriatic Sea. COI sequence in animals collected from the Swedish western coast corresponded to H1, H17 (GenBank accession number AY942591), H18 (GenBank accession number AY942595), HQ150067 or new haplotypes (GenBank accession number JX070087 and JX070088). COI sequences differed only for a maximum of 3 out of 518 nucleotides between the three populations. These nucleotide substitutions did not induce amino-acid changes.

Expression Level of Genes of Interest (GOI)

Swedish calanus helgolandicus population. After 24 h of feeding on *S. marinoi*, both primary defense and aldehyde detoxification genes increased. GST, SOD, ALDH2, ALDH7, ALDH9 and CAS expression levels were significantly up-regulated (p value$<$0.05 for all the genes; Figures 1a, 2a and 3a). After 48 h, there was a stronger response and many GOI were up-regulated (HSP70, HSP40, CYP, CAT, ALDH3, ALDH8, ALDH9, IAP and ATUB; p value$<$0.05 for all the genes) (Figures 1a, 2a and 3a).

English channel calanus helgolandicus population. After 24 h, CAT was up-regulated (p value$<$0.001) (Figure 1b) and there was also the activation of three out of six genes involved in the aldehyde detoxification complex: ALDH6, ALDH7 and ALDH8 were up-regulated (p value$<$0.001 for all the genes) (Figure 2b). BTUB expression levels significantly increased after 24 h of ingestion of *S. marinoi* (p value$<$0.001) (Figure 3b). After 48 h, no significant changes were observed, except for a significant reduction of CYP expression levels (p value$<$0.001) (Figure 1b).

Adriatic sea calanus helgolandicus population. Expression levels of genes belonging to primary defense system, or aldehyde detoxification and apoptosis regulation did not show significant changes in *C. helgolandicus* specimens fed *S. marinoi* for 24 h. After 48 h, many GOI showed a pattern of down-regulation: CYP, ALDH3, ALDH6, ALDH8, CAS, BTUB (p value$<$ 0.001 for all the genes) (Figures 1c, 2c and 3c).

Discussion

Our results provide new insight on the often debated toxic/non-toxic effects of diatoms on copepod reproduction and development in laboratory and field studies [1,2,44,45]. Of the three *Calanus helgolandicus* populations tested, the Swedish population seems to be better capable of coping with the toxic *S. marinoi* diet by activating almost all stress/detoxification proteins after 24 and 48 h. The Atlantic population only activated the free radical detoxification enzyme CAT and some aldehyde dehydrogenases soon after stress exposure (24 h), but not after prolonged exposure. On the contrary, the Adriatic population was unable to activate defense enzymes after both 24 and 48 h and showed a general pattern of down-regulation after 48 h of diatom exposure, as shown in previous experiments [21]. Thus it appeared to be the most sensitive population to the toxic diet. Accordingly, strong reduction in egg production and hatching success have been found for Adriatic *C. helgolandicus* fed on *S. marinoi* in laboratory experiments or during natural diatom blooms in the North Adriatic Sea [1,2], but these effects were not observed for Atlantic copepods [25,44]. Hence, gene expression patterns observed in this study may correlate with copepod physiological responses.

Analyses of population genetic diversity of Mediterranean and Atlantic *C. helgolandicus* populations suggest Pleistocene divergence between the two basins and species vicariance [43]. Our data concord with previous findings of low distinction between *C. helgolandicus* mtDNA haplotypes (genetic divergences between 0.22% and 0.57%, [43]), which is lower than interspecific

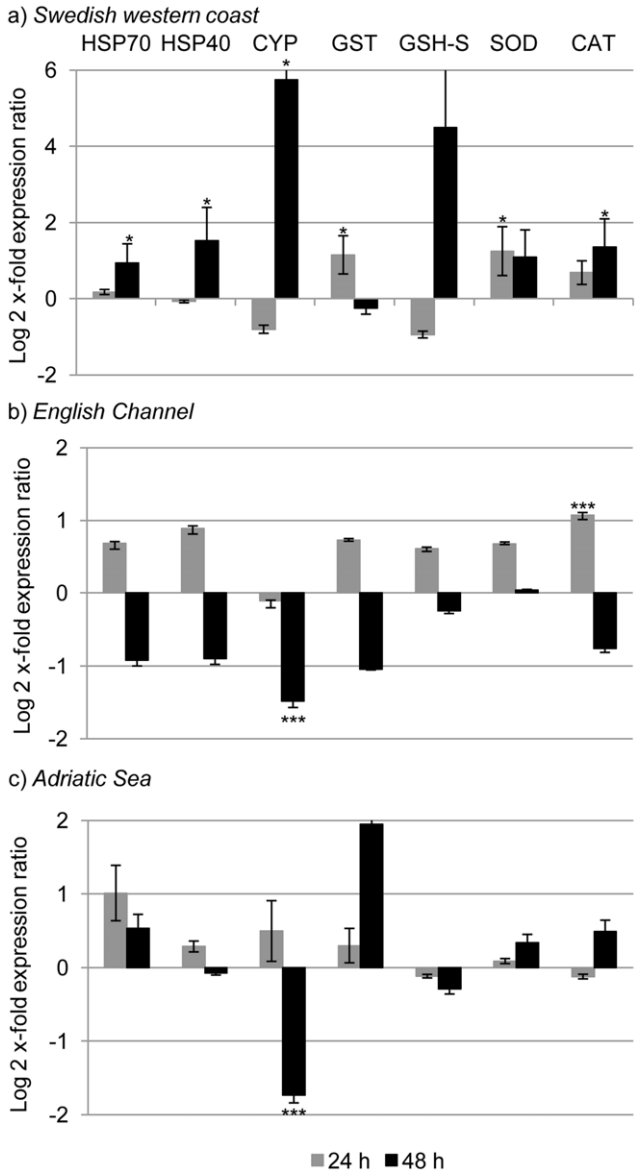

Figure 1. Expression levels of genes involved in stress and defense systems in the copepod *Calanus helgolandicus*. Changes in expression levels of Heat shock protein 70 (HSP70) and 40 (HSP40), Cytochrome P450-4 (CYP4), Glutathione S-Transferase (GST), Glutathione Synthase (GSH-S), Catalase (CAT) and Superoxide Dismutase (SOD) genes in Swedish (a), English Channel (b) and Adriatic (c) *C. helgolandicus* specimens fed *Skeletonema marinoi* (*S. marinoi*) for 24 or 48 h compared to expression levels in females fed on the control *Rhodomonas baltica* (represented in the figure by x-axis). The ribosomal protein S20 was used as reference gene to normalize the data.
doi:10.1371/journal.pone.0047262.g001

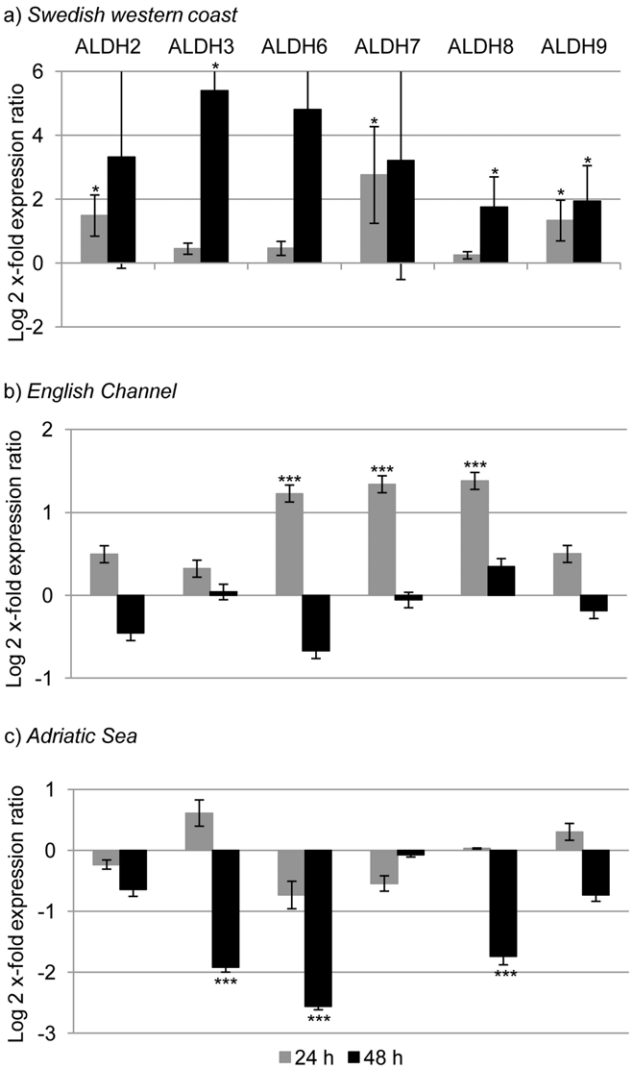

Figure 2. Relative gene expression levels of aldehyde dehydrogenases (ALDH) in the copepod *Calanus helgolandicus*. Changes in ALDH2, ALDH3, ALDH6, ALDH7, ALDH8 and ALDH9 gene expression levels in Swedish (a), English Channel (b) and Adriatic (c) *C. helgolandicus* females fed *Skeletonema marinoi* (*S. marinoi*) for 24 or 48 h compared to expression levels in females fed on the control *Rhodomonas baltica* (represented in the figure by x-axis). The ribosomal protein S20 was used as reference gene to normalize the data.
doi:10.1371/journal.pone.0047262.g002

divergence (17% to 22% between *Calanus finmarchicus*, *C. helgolandicus* and *Calanus glacialis*, [46]; 7–25% between ten *Calanus* species [47]). The Adriatic population does not seem to be connected by gene flow with the other two populations, since there is no common haplotype in the Mediterranean and extra-Mediterranean samples. The Atlantic and the North Sea populations, instead, share a single haplotype. Interestingly, despite the minor genetic differences among populations of *C. helgolandicus*, large physiological differences in tolerance to toxic oxylipins were present.

In recent years, numerous studies have focused on the effects of stressors on aquatic organisms, showing that responses to toxicants tend to be species-specific and may also be due to pre-adaptation to a given xenobiotic [48,49,50,51]. For example, pre-exposure of the aquatic oligochaete *Sparganophilus pearsei* to mercury in their native sediments influenced the resistance levels recorded during laboratory mercury exposure [51]. Colin and Dam [48] showed that when two geographically distant populations of the copepod *Acartia hudsonica* were reared on the toxic dinoflagellate *Alexandrium fundyense*, the one that had not experienced recurrent blooms of the toxic algae had lower somatic growth, size at maturity, egg production, and survival, compared to the other population that showed no effects on these life-history parameters. Our results confirmed these studies supporting and implementing them, for the first time, by gene expression studies.

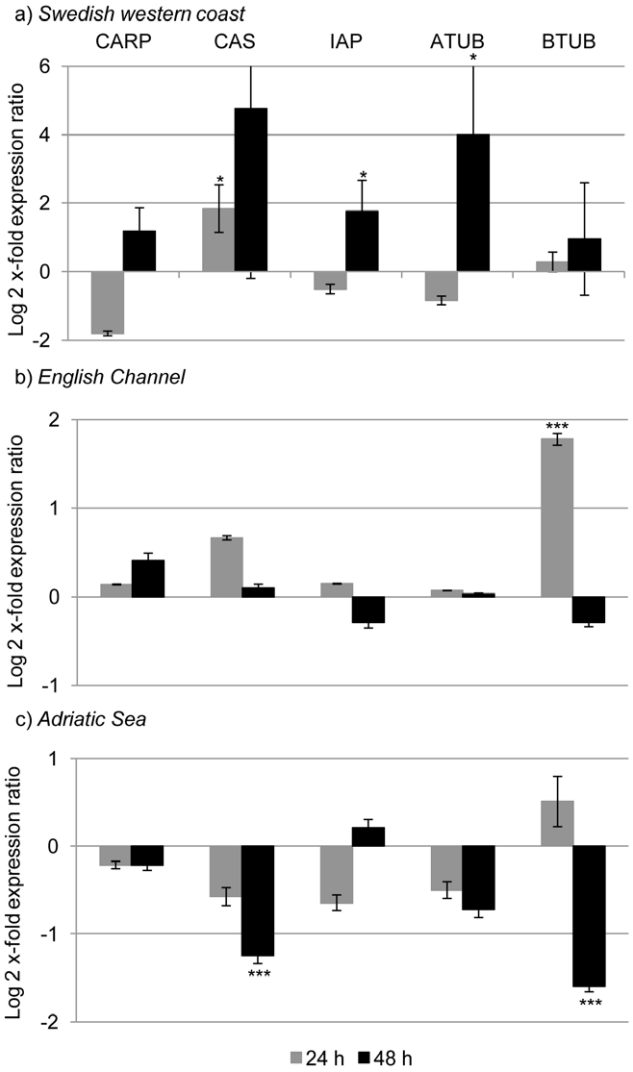

Figure 3. Expression analysis of genes involved in apoptosis and mitotic spindle formation in *Calanus helgolandicus*. Changes in expression levels of Cell Cycle and Apoptosis Regulatory 1 Protein (CARP), Cellular Apoptosis Susceptibility Protein (CAS), Inhibitor of Apoptosis Protein (IAP), and Alpha and Beta tubulins (ATUB and BTUB) genes in Swedish (a), English Channel (b) and Adriatic (c) *C. helgolandicus* fed *Skeletonema marinoi* (*S. marinoi*) for 24 or 48 h compared to expression levels in females fed on the control *Rhodomonas baltica* (represented in the figure by x-axis). The ribosomal protein S20 was used as reference gene to normalize the data.
doi:10.1371/journal.pone.0047262.g003

Defense and detoxification proteins, such as heat shock proteins, antioxidant and ROS detoxification enzymes, have been analyzed in copepods exposed to various environmental contaminants, such as heavy metals, endocrine disruptor chemicals and hydrocarbons. The data indicate high inter- and intra-species variability in copepod responses, depending on the type of stressor tested, the concentration and exposure time, and the enzyme isoform studied [50].

In this study, enzymes involved in free radical detoxification were up-regulated after both 24 and 48 h of exposure to a diatom diet in the Swedish population, after 24 h in the Atlantic population, but not in the Mediterranean population of *C. helgolandicus*. These data suggest an immediate specific capability of the Swedish and Atlantic populations to protect themselves against radical toxicants. A simultaneous increase in both SOD and CAT has also been observed in *C. finmarchicus* after 12 h of exposure to low naphthalene concentrations [52]. Thereafter levels for both antioxidants returned to basal levels, except after 48 h, when CAT levels were still elevated in copepods exposed to intermediate naphthalene concentrations. Whereas Hansen and co-workers [52] concluded that there was no clear relationship between antioxidant mRNA levels and exposure time/concentration, our data suggest that antioxidant defense genes (e.g. GST, SOD and CAT) and also a more specific detoxification system (ALDHs) could be activated in the Atlantic and Swedish populations soon after stress exposure (24 h).

In fact, ALDH2, ALDH7 and ALDH9 increased after 24 h of *S. marinoi* exposure, and all the six analyzed ALDHs increased after 48 h in the Swedish population (even if with high variability between replicates for some genes); ALDH6, ALDH7 and ALDH8 increased after 24 h in the Atlantic population; no ALDHs were up-regulated in the Mediterranean population. Since Atlantic and Swedish copepods are more frequently exposed to diatoms [23,24,25] they may have evolved mechanisms to better cope with deleterious diatom oxylipins.

After 48 h of *S. marinoi* exposure, HSP40 and HSP70 increased in the Swedish population suggesting a protective chaperoning activity. Romano et al. [53] have also recently shown that sea urchins activate HSP70 when challenged with low concentrations (0.25 mg/ml) of the PUA decadienal thereby protecting embryos against the toxic effects of this aldehyde. This up-regulation was only found at 9 h post fertilization (hpf), whereas at 5, 24 and 48 hpf, expression levels were comparable to the control.

A protective role is also suggested by the activation of the cellular apoptosis susceptibility protein (CAS) and the inhibitor of the apoptosis protein (IAP). IAP proteins are generally known for the control of cell death and the inhibition of apoptosis, however new emerging functions have been attributed to this protein family, such as cytoprotective and cellular stress response functions [54]. In this experiment, IAP expression levels significantly increased in the Swedish population after 48 h of exposure to the toxic diatom, while it showed no significant results for the other populations. CAS is essential for cell survival, can associate with microtubules and mitotic spindles, and is necessary for the mitotic checkpoint that assures the accurate segregation of chromosomes to daughter cells [40,55]. Supporting the hypothesis of a Swedish population more resistant to diatom toxins compared to the others is the fact that CAS expression levels increased in the Swedish population, and decreased in the Adriatic one (similar to our previous findings [21]). IAP was down-regulated in our previous experiments in Adriatic *C. helgolandicus* specimens fed on *S. marinoi* in the same experimental conditions, but, in the present study, values were comparable to the control, probably due to inter-individual variability.

Our results indicate strong population-level variations in copepod detoxification mechanisms to toxic diatoms and may explain why diatoms at times did not reduce hatching success in previous studies [44,45]. Such population-specific differences in tolerance to toxic metabolites suggest that co-evolution between diatoms and copepods is also based on a chemical arms race between plant defenses and animal offenses and the evolution of phenotypic traits among populations of a single herbivore species. These results are consistent with the hypothesis of evolved grazer resistance to toxins in copepod populations that have a longer history of exposure to pronounced and long-lasting spring phytoplankton blooms mainly dominated by diatoms such as those that occur in the North Atlantic Ocean [56].

Materials and Methods

Copepod Sampling and Feeding Experiments

No specific permits were required for the described field studies, the locations were not privately-owned or protected in any way and the field studies did not involve endangered or protected species.

Calanus helgolandicus specimens were collected in three different geographical locations: North Adriatic Sea (Mediterranean Sea), Swedish west coast (Gullmar Fjord) and North Atlantic Ocean. *C. helgolandicus* were collected in the North Adriatic Sea in April 2011, transported to Stazione Zoologica Anton Dohrn (SZN) in Naples and transferred to 10 L tanks. Specimens collected in the North Atlantic Ocean (May 2010) were transported to the CNRS of Roscoff (France) and transferred to 10 L tanks. Specimens collected in the Swedish west coast (May 2011) were transported to the Sven Lovén Centre for Marine Sciences, University of Gothenburg (Kristineberg) and transferred to 10 L tanks. In all the three cases, 120 adult female *C. helgolandicus* were sampled from the tanks under a Leica stereomicroscope and transferred to triplicate 1 L bottles (20 animals/bottle) filled with 0.22 µm filtered sea water (FSW) enriched with either unialgal diets of the control non-oxylipin producing flagellate *Rhodomonas baltica* (*R. baltica*) (7500–8000 cells/ml), that does not impair copepod egg production and hatching success [57], or the toxic oxylipin-producing diatom *Skeletonema marinoi* (*S. marinoi*) (45.000–60.000 cells/ml) provided ad libitum in the stationary phase of growth. Bottles containing copepods were maintained in temperature controlled rooms at 8–18°C (without altering the natural sea water temperature). To avoid settlement of diatom cells to container bottoms, bottles were gently rotated every 4 h. This was not necessary with bottles containing free-swimming flagellate cells.

Both algal strains belong to the SZN culture collection. *R. baltica* (Strain SZN FE202) was cultured in glass jars with 0.22 µm-FSW enriched with k medium at 20°C and on a 12:12 h dark:light cycle. The diatom *S. marinoi* (Strain SZN FE6) was cultured under the same experimental conditions but with F2 medium. Every day FSW and new food was added to each bottle at the same concentration as the day before. After 24 h and 48 h, triplicate sub-samples of 5 animals for each diet were collected and transferred to FSW for 24 h to eliminate any algal residues in the gut. After this, each replicate was carefully transferred to 500 µl Trizol Reagent (Invitrogen), frozen directly in liquid nitrogen and stored at −80°C until DNA or RNA extraction.

DNA Extraction and Population Identification

Total DNA was extracted from a pool of 5 animals from the Atlantic Ocean and Adriatic Sea copepod populations and from 22 single animals (22 replicates) from the Swedish population, according to Trizol manufacturer's protocol (Invitrogen). DNA quantity was assured by Nano-Drop (ND-1000 UV-Vis spectrophotometer; NanoDrop Technologies). In all the three cases, the following primers were used to amplify a 518 bp fragment of the mitochondrial Cytochrome Oxidase subunit I region (COI): ChelgCOI-F (5′-GGCCAAAACAGGGAGAGATA-3′) and ChelgCOI-R (5′-CGGGACTCAGTATAATTATTCGTCTA-3′) [43]. Reactions were carried out in 20 µl volume with 2 µl of 10× PCR reaction buffer Roche, 2 µl of 0.1% BSA, 2 µl of 10× 2 mM dNTP, 0.8 µl of 5 U/µl Taq Roche, 1 µl of 20 pmol/µl for each oligo, 1,5 µl template DNA and nuclease-free water to 20 µl. The PCR program consisted of a denaturation step at 94°C for 3 min, 35 cycles at 94°C for 1 min, 50°C for 45 sec and 72°C for 1 min, and a final extension step at 72°C for 7 min. Amplified PCR products were analyzed by 1.5% agarose gel electrophoresis in TBE buffer. In order to verify the correct assignment of amplicons to COI region, the resulting bands were excised from the gel and extracted according to the QIAquick Gel Extraction Kit protocol (QIAGEN) and sequences analyzed. The identity of each sequence was confirmed using the bioinformatics tool BLAST (Basic local alignment search tool).

RNA Extraction and cDNA Synthesis

Total RNA was extracted using Trizol manufacturer's protocol (Invitrogen). RNA quantity and purity was assured by Nano-Drop (ND-1000 UV-Vis spectrophotometer; NanoDrop Technologies), RNA quality by gel electrophoresis. 1 µg of each RNA was retrotranscribed into cDNA with the iScriptTM cDNA Synthesis Kit (BIORAD) following the manufacturer's instructions, using the GeneAmp PCR System 9700 (Perkin Elmer). The reaction was carried out in 20 µl final volume with 4 µl 5× iScript reaction mix, 1 µl iScript reverse transcriptase and H_2O. The mix was first incubated 5 min at 25°C, followed by 30 min at 42°C and finally heated at 85°C for 5 min.

Reverse Transcription-Quantitative Real Time Polymerase Chain Reaction (RT-qPCR)

The fluorescent dye SYBR GREEN was used to evaluate expression levels of the selected genes by RT-qPCR. Fluorescence was monitored once per cycle after product extension and increased above background fluorescence at a cycle number that depended on the initial template concentration. RT-qPCR was performed in MicroAmp Optical 384-Well reaction plate (Applied Biosystem) with Optical Adhesive Covers (Applied Biosystem) in a Viia7 Real Time PCR System (Applied Biosystem). The PCR volume for each sample was 10 µl, with 5 µl of Fast Start SYBR Green Master Mix (Roche), 1 µl of cDNA template and 0.7 pmol/µl for each oligo. The RT-qPCR thermal profile was obtained using the following procedure: 95°C for 10 min, 40 times 95°C for 15 sec and 60°C for 1 min, 72°C for 5 min. The programme was set to reveal the melting curve of each amplicon from 60°C to 95°C, and read every 0.5°C.

All RT-qPCR reactions were carried out in triplicate to capture intra-assay variability. Each assay included three no-template negative controls (NTC) for each primer pair. Reaction efficiencies for all primer pairs have been previously calculated using the equation $E = 10^{-1/slope}$ [21]. Primer's sequences, efficiencies and correlation coefficients, and gene accession numbers were previously published [21]. A 1:100 template dilution (4 ± 2 ng) was used which allowed almost all gene amplifications to fit in the optimal read window (from 15 to 25 cycles). Only a single peak in the melting-curve analyses of all genes was identified, confirming a gene-specific amplification and the absence of primer-dimers.

To study expression levels for each target gene relative to the most stable RG, S20 [20], we used the REST tool (Relative expression software tool) [58]. Copepods fed on the dinoflagellate *Rhodomonas baltica*, which does not produce any PUAs and oxylipins, were used as control condition. Statistical analysis was performed using GraphPad Prism version 4.00 for Windows (GraphPad Software, San Diego, California, USA).

Acknowledgments

The authors thank the Göteborg University, Sven Lovén Centre for Marine Sciences (Kristineberg) and the Station Biologique de Roscoff. We also thank Flora Palumbo, Francesco Esposito, Massimo Perna and the staff of the Molecular Biology Service of the Stazione Zoologica Anton Dohrn for their technical support.

Author Contributions

Conceived and designed the experiments: CL GP AI. Performed the experiments: CL YC. Analyzed the data: CL. Contributed reagents/materials/analysis tools: AM. Wrote the paper: CL GP AI.

References

1. Ianora A, Miralto A, Poulet SA, Carotenuto Y, Buttino I, et al. (2004) Aldehyde suppression of copepod recruitment in blooms of a ubiquitous planktonic diatom. Nature 429: 403–407.
2. Miralto A, Barone G, Romano G, Poulet SA, Ianora A, et al. (1999) The insidious effect of diatoms on copepod reproduction. Nature 402: 173–176.
3. Fontana A, d'Ippolito G, Cutignano A, Romano G, Lamari N, et al. (2007) LOX-induced lipid peroxidation mechanism responsible for the detrimental effect of marine diatoms on Zooplankton grazers. Chembiochem 8: 1810–1818.
4. Carotenuto Y, Wichard T, Pohnert G, Lampert W (2005) Life-history responses of *Daphnia pulicaria* to diets containing freshwater diatoms: Effects of nutritional quality versus polyunsaturated aldehydes. Limnology and Oceanography 50: 449–454.
5. Romano G, Miralto A, Ianora A (2010) Teratogenic Effects of Diatom Toxins on Sea Urchin *Paracentrotus lividus* Embryos. Marine Drugs 8: 950–967.
6. Guenther J, Wright AD, Burns K, de Nys R (2009) Chemical antifouling defences of sea stars: effects of the natural products hexadecanoic acid, cholesterol, lathosterol and sitosterol. Marine Ecology-Progress Series 385: 137–149.
7. Caldwell GS (2009) The influence of bioactive oxylipins from marine diatoms on invertebrate reproduction and development. Marine Drugs 7: 367–400.
8. Caldwell GS, Olive PJW, Bentley MG (2002) Inhibition of embryonic development and fertilization in broadcast spawning marine invertebrates by water soluble diatom extracts and the diatom toxin 2-trans,4-trans decadienal. Aquatic Toxicology 60: 123–137.
9. Simon CA, Bentley MG, Caldwell GS (2010) 2,4-Decadienal: Exploring a novel approach for the control of polychaete pests on cultured abalone. Aquaculture 310: 52–60.
10. Tosti E, Romano G, Buttino I, Cuomo A, Ianora A, et al. (2003) Bioactive aldehydes from diatoms block the fertilization current in ascidian oocytes. Molecular Reproduction and Development 66: 72–80.
11. Pohnert G (2000) Wound-activated chemical defense in unicellular planktonic algae. Angewandte Chemie-International Edition 39: 4352–4354.
12. d'Ippolito G, Tucci S, Cutignano A, Romano G, Cimino G, et al. (2004) The role of complex lipids in the synthesis of bioactive aldehydes of the marine diatom *Skeletonema costatum*. Biochimica Et Biophysica Acta-Molecular and Cell Biology of Lipids 1686: 100–107.
13. Cutignano A, d'Ippolito G, Romano G, Lamari N, Cimino G, et al. (2006) Chloroplastic glycolipids fuel aldehyde biosynthesis in the marine diatom *Thalassiosira rotula*. Chembiochem 7: 450–456.
14. Fontana A, d'Ippolito G, Cutignano A, Miralto A, Ianora A, et al. (2007) Chemistry of oxylipin pathways in marine diatoms. Pure and Applied Chemistry 79: 481–490.
15. d'Ippolito G, Lamari N, Montresor M, Romano G, Cutignano A, et al. (2009) 15S-Lipoxygenase metabolism in the marine diatom *Pseudo-nitzschia delicatissima*. New Phytologist 183: 1064–1071.
16. Ianora A, Miralto A (2010) Toxigenic effects of diatoms on grazers, phytoplankton and other microbes: a review. Ecotoxicology 19: 493–511.
17. Halsband-Lenk C, Pierson JJ, Leising AW (2005) Reproduction of *Pseudocalanus newmani* (Copepoda : Calanoida) is deleteriously affected by diatom blooms - A field study. Progress in Oceanography 67: 332–348.
18. Poulet SA, Escribano R, Hidalgo P, Cueff A, Wichard T, et al. (2007) Collapse of *Calanus chilensis* reproduction in a marine environment with high diatom concentration. Journal of Experimental Marine Biology and Ecology 352: 187–199.
19. Ask J, Reinikainen M, Bamstedt U (2006) Variation in hatching success and egg production of *Eurytemora affinis* (Calanoida, Copepoda) from the Gulf of Bothnia, Baltic Sea, in relation to abundance and clonal differences of diatoms. Journal of Plankton Research 28: 683–694.
20. Lauritano C, Borra M, Carotenuto Y, Biffali E, Miralto A, et al. (2011) First molecular evidence of diatom effects in the copepod *Calanus helgolandicus*. Journal of Experimental Marine Biology and Ecology 404: 79–86.
21. Lauritano C, Borra M, Carotenuto Y, Biffali E, Miralto A, et al. (2011) Molecolar evidence of the toxic effects of diatom diets on gene expression patterns in copepods. PLoS One 6: e26850.
22. Bonnet D, Richardson A, Harris R, Hirst A, Beaugrand G, et al. (2005) An overview of *Calanus helgolandicus* ecology in European waters. Progress in Oceanography 65: 1–53.
23. Poulet SA, Wichard T, Ledoux JB, Lebreton B, Marchetti J, et al. (2006) Influence of diatoms on copepod reproduction. I. Field and laboratory observations related to *Calanus helgolandicus* egg production. Marine Ecology-Progress Series 308: 129–142.
24. Godhe A, Harnstrom K (2010) Linking the planktonic and benthic habitat: genetic structure of the marine diatom *Skeletonema marinoi*. Molecular Ecology 19: 4478–4490.
25. Wichard T, Poulet SA, Boulesteix AL, Ledoux JB, Lebreton B, et al. (2008) Influence of diatoms on copepod reproduction. II. Uncorrelated effects of diatom-derived alpha,beta,gamma,delta-unsaturated aldehydes and polyunsaturated fatty acids on *Calanus helgolandicus* in the field. Progress in Oceanography 77: 30–44.
26. Taylor RL, Abrahamsson K, Godhe A, Wangberg S-A (2009) Seasonal variability in polyunsaturated aldehyde production potential among strains of *Skeletonema marinoi* (Bacillariophyceae). Journal of Phycology 45: 46–53.
27. Vidoudez C, Casotti R, Bastianini M, Pohnert G (2011) Quantification of dissolved and particulate polyunsaturated aldehydes in the Adriatic Sea. Marine Drugs 9: 500–513.
28. Gerecht A, Romano G, Ianora A, d'Ippolito G, Cutignano A, et al. (2011) Plasticity of oxylipin metabolism among clones of the marine diatom *Skeletonema marinoi* (Bacillaiophyceae). Journal of Phycology 47: 1050–1056.
29. Ribalet F, Vidoudez C, Cassin D, Pohnert G, Ianora A, et al. (2009) High plasticity in the production of diatom-derived polyunsaturated aldehydes under nutrient limitation: physiological and ecological implications. Protist 160: 444–451.
30. Wichard T, Poulet SA, Pohnert G (2005) Determination and quantification of alpha,beta,gamma,delta-unsaturated aldehydes as pentafluorobenzyl-oxime derivates in diatom cultures and natural phytoplankton populations: application in marine field studies. Journal of Chromatography B-Analytical Technologies in the Biomedical and Life Sciences 814: 155–161.
31. Bouraoui Z, Banni M, Ghedira J, Clerandeau C, Narbonne JF, et al. (2009) Evaluation of enzymatic biomarkers and lipoperoxidation level in *Hediste diversicolor* exposed to copper and benzo[a]pyrene. Ecotoxicology and Environmental Safety 72: 1893–1898.
32. Olsvik PA, Lie KK, Sturve J, Hasselberg L, Andersen OK (2009) Transcriptional effects of nonylphenol, bisphenol A and PBDE-47 in liver of juvenile Atlantic cod (*Gadus morhua*). Chemosphere 75: 360–367.
33. Salazar-Medina AJ, Garcia-Rico L, Garcia-Orozco KD, Valenzuela-Soto E, Contreras-Vergara CA, et al. (2010) Inhibition by Cu(2+) and Cd(2+) of a Mu-Class Glutathione S-Transferase from Shrimp *Litopenaeus vannamei*. Journal of Biochemical and Molecular Toxicology 24: 218–222.
34. Snyder MJ (2000) Cytochrome P450 enzymes in aquatic invertebrates: recent advances and future directions. Aquatic Toxicology 48: 529–547.
35. Vasiliou V, Pappa A, Estey T (2004) Role of human aldehyde dehydrogenases in endobiotic and xenobiotic metabolism. Drug Metabolism Reviews 36: 279–299.
36. Feder ME, Hofmann GE (1999) Heat-shock proteins, molecular chaperones, and the stress response: Evolutionary and ecological physiology. Annual Review of Physiology 61: 243–282.
37. Goldstone JV, Hamdoun A, Cole BJ, Howard-Ashby M, Nebert DW, et al. (2006) The chemical defensome: Environmental sensing and response genes in the *Strongylocentrotus purpuratus* genome. Developmental Biology 300: 366–384.
38. Bigot A, Vasseur P, Rodius F (2010) SOD and CAT cDNA cloning, and expression pattern of detoxification genes in the freshwater bivalve *Unio tumidus* transplanted into the Moselle river. Ecotoxicology 19: 369–376.
39. Marchitti SA, Brocker C, Stagos D, Vasiliou V (2008) Non-P450 aldehyde oxidizing enzymes: the aldehyde dehydrogenase superfamily. Expert Opinion on Drug Metabolism & Toxicology 4: 697–720.
40. Brinkmann U (1998) CAS, the human homologue of the yeast chromosome-segregation gene CSE1, in proliferation, apoptosis, and cancer. American Journal of Human Genetics 62: 509–513.
41. Rishi AK, Zhang L, Yu Y, Jiang Y, Nautiyal J, et al. (2006) Cell cycle- and apoptosis-regulatory protein-1 is involved in apoptosis signaling by epidermal growth factor receptor. The Journal of Biological Chemistry 281: 13188–13198.
42. Jordan Mary Ann lW (2004) Microtubules as a target for anticancer drugs. Nature reviews.
43. Papadopoulos LN, Peijnenburg K, Luttikhuizen PC (2005) Phylogeography of the calanoid copepods *Calanus helgolandicus* and *C. euxinus* suggests Pleistocene divergences between Atlantic, Mediterranean, and Black Sea populations. Marine Biology 147: 1353–1365.
44. Irigoien X, Harris RP, Verheye HM, Joly P, Runge J, et al. (2002) Copepod hatching success in marine ecosystems with high diatom concentrations. Nature 419: 387–389.
45. Koski M (2007) High reproduction of *Calanus finmarchicus* during a diatom-dominated spring bloom. Marine Biology 151: 1785–1798.
46. Bucklin A, Guarnieri M, Hill RS, Bentley AM, Kaartvedt S (1999) Taxonomic and systematic assessment of planktonic copepods using mitochondrial COI sequence variation and competitive, species-specific PCR. Hydrobiologia 401: 239–254.
47. Hill RS, Allen LD, Bucklin A (2001) Multiplexed species-specific PCR protocol to discriminate four N. Atlantic *Calanus* species, with an mtCOI gene tree for ten *Calanus* species. Marine Biology 139: 279–287.

48. Colin SP, Dam HG (2007) Comparison of the functional and numerical responses of resistant versus non-resistant populations of the copepod *Acartia hudsonica* fed the toxic dinoflagellate *Alexandrium tamarense*. Harmful Algae 6: 875–882.
49. Sotka EE, Whalen KE (2008) Herbivore Offense in the Sea: The Detoxification and Transport of Secondary Metabolites. In: Amsler CD, editor. Algal Chemical Ecology. Berlin, Germany: Springer-Verlag. 203–228.
50. Lauritano C, Procaccini G, Ianora A (2012) Gene expression patterns and stress response in marine copepods. Marine Environmental Research 76: 22–31.
51. Vidal DE, Horne AJ (2003) Mercury toxicity in the aquatic oligochaete *Sparganophilus pearsei*: I. Variation in resistance among populations. Archives of Environmental Contamination and Toxicology 45: 184–189.
52. Hansen BH, Altin D, Vang SH, Nordtug T, Olsen AJ (2008) Effects of naphthalene on gene transcription in *Calanus finmarchicus* (Crustacea : Copepoda). Aquatic Toxicology 86: 157–165.
53. Romano G, Costantini M, Buttino I, Ianora A, Palumbo A (2011) Nitric oxide mediates the stress response induced by diatom adehydes in the sea urchin *Paracentrotus lividus* PLoS One 6: e25980.
54. Altieri DC (2010) Survivin and IAP proteins in cell-death mechanisms. Biochemical Journal 430: 199–205.
55. Tai CJ, Hsu CH, Shen SC, Lee WR, Jiang MC (2010) Cellular apoptosis susceptibility (CSE1L/CAS) protein in cancer metastasis and chemotherapeutic drug-induced apoptosis. Journal of Experimental & Clinical Cancer Research 29.
56. Martin P, Lampitt RS, Perry MJ, Sanders R, Lee C, et al. (2011) Export and mesopelagic particle flux during a North Atlantic spring diatom bloom. Deep-Sea Research Part I-Oceanographic Research Papers 58: 338–349.
57. Carotenuto Y, Esposito F, Pisano F, Lauritano C, Perna M, et al. (2012) Multi-generation cultivation of the copepod *Calanus helgolandicus* in a re-circulating system. Journal of Experimental Marine Biology and Ecology 418: 46–58.
58. Pfaffl MW, Horgan GW, Dempfle L (2002) Relative expression software tool (REST (c)) for group-wise comparison and statistical analysis of relative expression results in real-time PCR. Nucleic Acids Research 30.

Harmful Algae 28 (2013) 23–30

Contents lists available at SciVerse ScienceDirect

Harmful Algae

journal homepage: www.elsevier.com/locate/hal

Changes in expression of stress genes in copepods feeding upon a non-brevetoxin-producing strain of the dinoflagellate *Karenia brevis*

Chiara Lauritano [a,*], Ylenia Carotenuto [a], Gabriele Procaccini [a], Jefferson T. Turner [b], Adrianna Ianora [a]

[a] Stazione Zoologica Anton Dohrn, Villa Comunale, 80121 Napoli, Italy
[b] Biology Department and School for Marine Science and Technology, University of Massachusetts Dartmouth, 285 Old Westport Road, North Dartmouth, MA 02747-2300, USA

ARTICLE INFO

Article history:
Received 6 March 2013
Received in revised form 14 May 2013
Accepted 14 May 2013

Keywords:
Copepods
Dinoflagellates
Egg morphology
Gene expression
Karenia brevis
RT-qPCR
Stress response

ABSTRACT

Effects of the toxic Gulf of Mexico dinoflagellate *Karenia brevis* on its copepod grazers are equivocal, in that this dinoflagellate is ingested by various copepods, but may be toxic to, and/or nutritionally inadequate for grazers. Recent studies have shown that when the Mediterranean copepod *Calanus helgolandicus* fed on *K. brevis*, egg production rates and egg viability declined steadily over time, reaching almost zero levels after 5 days of feeding (Turner et al., 2012). The *K. brevis* strain used in that study was chemically analyzed and shown not to contain any brevetoxins, but may have contained other harmful metabolites. Here we present gene expression analyses by reverse transcription-quantitative PCR (RT-qPCR) in *C. helgolandicus* after different exposure times (3, 5 and 8 days) to the same non-brevetoxin-containing *K. brevis* strain examined previously. The analyzed genes have a primary role in generic stress responses, defense systems (e.g. aldehyde, free fatty acid and free radical detoxification) and apoptosis regulation in other organisms. After 3 days of feeding on *K. brevis*, gene expression levels in copepods did not show significant changes. However, after 5 days of exposure, expression of stress-response genes was significantly reduced. After prolonged exposure for 8 days, expression of genes for 5 of 6 aldehyde dehydrogenases was strongly reduced, but expression of other genes was not coherently reduced, or increased. Microscopic observations revealed that after only a single day of feeding on *K. brevis*, freshly-spawned eggs were morphologically similar to those produced by copepods feeding on control diets, but after 3 days of feeding on *K. brevis*, eggs exhibited altered membrane cell morphology and apoptotic features such as granulation and degeneration of the cytoplasm matrix, compared to the unaltered eggs produced by copepods feeding on control diets. The changes in gene expression levels in copepods feeding on *K. brevis* were similar to those noted previously for copepods feeding upon diatoms that contained oxylipins, which interfered with copepod reproductive success. Changes in gene expression in copepods feeding upon toxic algal diets may offer important early warning signals of copepod stress responses to these diets.

© 2013 Elsevier B.V. All rights reserved.

1. Introduction

The toxic dinoflagellate *Karenia brevis* (formerly known as *Gymnodinium brevis*, *Gymnodinium breve*, and *Ptychodiscus brevis*) blooms annually in the Gulf of Mexico and occasionally in the Atlantic off the southeastern United States (Steidinger, 2009; Brand et al., 2012). *K. brevis* can naturally produce potent neurotoxins (Naar et al., 2007), termed brevetoxins (PbTx – named during the period when this dinoflagellate was known as *P. brevis*). PbTx-1, -2, and -3 are the dominant brevetoxins measured during *K. brevis* blooms, but brevetoxins are not the only bioactive compounds produced by this dinoflagellate (Waggett et al., 2012). *K. brevis* also produces multiple brevetoxin antagonists collectively known as brevenals (Baden et al., 2005; Bourdelais et al., 2004, 2005) that counteract the effects of brevetoxins (Baden et al., 2005; Bourdelais et al., 2004). A second potential brevetoxin antagonist, brevesin, has recently been characterized as an inhibitor of PbTx-3 (Satake et al., 2009). In addition, recent evidence suggests that *K. brevis* produces hemolytic toxins, which are compounds that lyse red blood cells, which may contribute to the overall toxicity of bloom events (Neely and Campbell, 2006).

Toxic harmful algal blooms (HABs) of *Karenia brevis* can cause various adverse effects. Massive fish kills can occur, as well as

* Corresponding author.
E-mail addresses: chiara.lauritano@szn.it (C. Lauritano), jturner@umassd.edu (J.T. Turner).

1568-9883/$ – see front matter © 2013 Elsevier B.V. All rights reserved.
http://dx.doi.org/10.1016/j.hal.2013.05.004

mortality of marine mammals, sea turtles, sea birds and benthic communities (Landsberg, 2002; Walsh et al., 2010; Brand et al., 2012). Human public health effects include shellfish contamination or inhalation of air-borne toxins (Pierce and Henry, 2008; Watkins et al., 2008). Indirect impacts include oxygen depletion due to decomposing phytoplankton and animal biomass, affecting benthic organisms, such as seagrasses and patch reef communities, which may require years for recovery (Pierce and Henry, 2008). HABs can have serious economic consequences for important fisheries, aquaculture and beach tourism. At the cellular level, *K. brevis* metabolites and/or neurotoxins are known to activate stress and detoxification responses, and induce DNA damage and cell death (apoptosis) in the oyster *Crassostrea gigas* and in cancer cells (Mello et al., 2012; Murrell and Gibson, 2009; Walsh et al., 2008).

It is often assumed that toxicity evolved in HAB phytoplankton to repel their zooplankton grazers (discussed by Turner et al., 1998; Turner, 2006). However, evidence for grazer deterrence due to such toxins is equivocal and/or contradictory. Some zooplankton grazers consume toxic HAB algae with no apparent adverse effects (Turner and Tester, 1989, 1997; and references therein), whereas in other cases, HAB toxins appear to repel some zooplankton grazers (Turner, 2006; Kubanek et al., 2007; and references therein). Additionally, some marine phytoplankton species contain chemical compounds that do not prevent copepod grazers from ingesting the algae, but cause subsequent adverse effects on copepod reproduction after ingestion of the algae by female copepods (reviewed by Ianora et al., 2003; Ianora and Miralto, 2010). Included are aldehydes and other chemical compounds found in certain diatoms or dinoflagellates, which reduce copepod egg production, egg hatching success, and/or survival of copepod nauplii (Ianora et al., 2003, 2004; Turner et al., 2001, 2012; and references therein).

Toxins in *Karenia brevis* may adversely affect their copepod grazers in various ways. Lower ingestion rates have been found for copepods fed diets dominated by *K. brevis* (Breier and Buskey, 2007; Speekmann et al., 2006). Egg production rates and egg viability for the copepod *Calanus helgolandicus* fed on *K. brevis* declined steadily over time, reaching almost zero levels after 5 days of feeding (Turner et al., 2012). The *K. brevis* strain used in the Turner et al. (2012) study was chemically analyzed and shown not to contain any brevetoxins, but other potentially-toxic metabolites (brevenal, brevesin and litic compounds) could not be quantified due to inability to obtain standards for these toxic compounds.

Aquatic organisms are constantly exposed to both physical (e.g. temperature and salinity) and chemical (e.g. endocrine disruptor chemicals, heavy metals, hydrocarbons and algal toxins) variations and stressors. Organisms react to stressors by activating a series of defense/detoxification genes. Studies on copepod responses to various stressors indicate high inter- and intra-species variability at the molecular level, depending on the type of stressor tested, the concentration and exposure time, and the enzyme isoform studied (reviewed by Lauritano et al., 2012a).

The aim of the present study was to use a molecular approach to investigate defense systems, stress responses and apoptosis regulation in the copepod *Calanus helgolandicus* fed on the same non-brevetoxin-containing strain of *Karenia brevis* that was used in the Turner et al. (2012) study. Expression level patterns of selected genes of interest (GOI) were analyzed in copepods after different periods of *K. brevis* ingestion (3, 5 and 8 days) by Reverse Transcription-Quantitative Polymerase Chain Reaction (RT-qPCR).

Changes in gene expression were quantified in terms of whether genes were up-regulated or down-regulated. Up-regulation is a process that occurs within a cell triggered by a signal (such as copepods feeding on *Karenia brevis*), which results in increased expression of one or more genes which may result in an increase in the protein(s) encoded by those genes. Hence, if there is an increase in a detoxification gene resulting in higher protein/enzyme levels, the copepod has a greater possibility of detoxifying the stressor. Conversely, down-regulation is a process resulting in decreased gene expression, which may correspond to a decrease in protein expression. If this leads to lower protein/enzyme levels copepods have a lower probability of detoxifying the stressor.

Changes in gene expression levels in copepods may offer important early-warning signals of copepod stress responses. Considering recent evidence that copepod stress response may depend on the different populations and haplotypes studied (Lauritano et al., 2012b), here we first analyzed the haplotype composition of the copepod sample in order to assess the haplotype-specific gene expression response. The analyzed genes were the heat-shock proteins 40 and 70 (HSP40 and HSP70, respectively), which have roles in response to various environmental stress factors (Feder and Hofmann, 1999), cytochrome P450 4 monooxygenase (CYP4) for its involvement in oxidative modifications (known as the Phase I reaction) of chemicals into more hydrophilic metabolites to enhance their elimination or inactivation (Snyder, 2000), catalase (CAT) and superoxide dismutase (SOD) (Bigot et al., 2010) responsible for detoxification of reactive oxygen species (ROS), the antioxidant enzymes glutathione synthase (GSH-S) and glutathione *S*-transferase (GST) (Eaton and Bammler, 1999; Martin and Teismann, 2009) and six aldehyde dehydrogenase (ALDH) isoforms (ALDH2, ALDH3, ALDH6, ALDH7, ALDH8 and ALDH9) for their aldehyde detoxification activity (Marchitti et al., 2008; Vasiliou et al., 2004). Finally, apoptosis-regulating genes were also selected: an inhibitor of the apoptosis protein (IAP), the cell cycle and apoptosis regulatory 1 protein (CARP), and the cellular apoptosis susceptibility protein (CAS) (Altieri, 2010; Brinkmann, 1998; Rishi et al., 2006).

The analyzed genes were previously investigated in *Calanus helgolandicus* after the ingestion of the oxylipin-producing diatom *Skeletonema marinoi* (Lauritano et al., 2011a, 2011b, 2012b). In addition, expression levels of a cysteine-aspartic acid protease (Caspase 3), with a central role in the execution-phase of cell apoptosis (Fehrenbacher et al., 2004), was also analyzed. Since there have been few studies on gene expression analysis via quantitative PCR (RT-qPCR) in the copepod *C. helgolandicus* (Lauritano et al., 2011a, 2011b, 2012b), and none of these studies have focused on exposure to *Karenia brevis*, here we also describe the evaluation of reference genes (RGs) as internal controls for RT-qPCR analyses in this new experimental condition. In fact, RGs are not universal but may change depending on the species and experimental conditions tested (Andersen et al., 2004; Bustin et al., 2010). Finally, considering the reduction in egg production and hatching success reported in *C. helgolandicus* after ingestion of *K. brevis* (Turner et al., 2012), images of eggs spawned by females fed on *K. brevis* or the control dinoflagellate *Prorocentrum minimum* for one or three days were also taken to investigate anomalies in egg morphology.

2. Materials and methods

2.1. Copepod sampling and feeding experiments

Adult female *Calanus helgolandicus* specimens were sampled in the Gulf of Naples (Mediterranean Sea) with a 200 μm-mesh plankton net, isolated under a Leica stereomicroscope and transferred to 1 L bottles (20 adult females per bottle) filled with 0.22 μm-filtered sea water (FSW) at about 20 °C. Copepods in each bottle were fed ad libitum unialgal diets of either the control non-oxylipin-producing dinoflagellate *Prorocentrum minimum* (5×10^3 cells ml^{-1}) (Fontana et al., 2007) or the non-neurotoxic dinoflagellate *Karenia brevis* (1×10^3 cells ml^{-1}). The *K. brevis* clone (Wilson clone) was isolated in 1953 (Lekan and Tomas, 2010), and obtained in 2008 from Patricia Tester, National Ocean

Service, NOAA, Beaufort, NC, USA. The *P. minimum* strain belongs to the Stazione Zoologica Anton Dohrn culture collection. *P. minimum* and *K. brevis* were cultured in glass jars with 0.22 μm-filtered FSW enriched with k-medium at 20 °C and on a 12:12 h dark:light cycle. Every day FSW was replaced in each bottle and new food was added at the same concentration as the previous day. After 3, 5 and 8 days of feeding, subsamples of 1 or 2 animals from each diet regime were collected and transferred to FSW for 24 h to eliminate any algal residues in the gut. Starvation was necessary to ensure RNA extraction only from copepods and not from algae. The control group was subjected to the same starvation treatment. After this, each replicate was carefully transferred to 0.500 ml Trizol Reagent (Invitrogen, San Diego, CA, USA), frozen directly in liquid nitrogen and stored at −80 °C until RNA extraction.

2.2. RNA extraction and cDNA synthesis

Animals were homogenized in 0.500 ml of TRIZOL® Reagent (Invitrogen) using the Tissuelyser (MM300, Retsch, Conquer Scientific, San Diego, CA) and Tungsten Carbide Beads (3 mm) (Qiagen, Valencia, CA) for 5 min (2 min followed by 3 min, without removing the samples from the instrument) at 20.1 Hz until all copepod individuals in the samples were completely homogenized. Samples were then centrifuged at 12,000 × *g* for 10 min at 4 °C and total RNA was extracted using Trizol manufacturer's protocol (Invitrogen). RNA quantity and purity was tested by Nano-Drop (ND-1000 UV–vis spectrophotometer; NanoDrop Technologies Inc., Wilmington, DE, USA), to ensure that 260/280 absorbance ratio was between 1.8 and 2.0, and 260/230 ratio was 2.0. RNA quality was monitored by gel electrophoresis. To remove hypothetically contaminating DNA, each sample was treated with DNaseI (Invitrogen), as in Lauritano et al. (2011a). Samples of 500 ng of each type of RNA were reverse-transcribed into cDNA with the iScriptTM cDNA Synthesis Kit (BIORAD, Hercules, CA) following the manufacturer's instructions, using the GeneAmp PCR System 9700 (Perkin Elmer, Applied Biosystems, Foster City, CA).

2.3. Population identification

The following primers were used to amplify a 518 bp fragment of the mitochondrial cytochrome oxidase subunit I region (COI): ChelgCOI-F (5′-GGCCAAAACAGGGAGAGATA-3′) and ChelgCOI-R (5′-CGGGACTCAGTATAATTATTCGTCTA-3′) (Papadopoulos et al., 2005). Reactions were carried out as in Lauritano et al. (2012b). Amplified PCR products were analyzed by 1.5% agarose gel electrophoresis in TBE buffer. In order to verify the correct assignment of amplicons to the COI region, the resulting bands were excised from the gel and extracted according to the QIAquick Gel Extraction Kit protocol (Qiagen) and sequences analyzed. The identity of each sequence was confirmed using the bioinformatics tool BLAST (Basic Local Alignment Search Tool).

2.4. Reverse Transcription-Quantitative Polymerase Chain Reaction (RT-qPCR)

In order to analyze expression levels of specific genes of interest (GOI), a panel of putative reference genes (RGs) was first screened to find the most stable genes in the new experimental conditions: elongation factor 1α (EFA), adenosine 3-phosphate synthase (ATPs), histone 3 (HIST), glyceraldehyde-3-phosphate dehydrogenase (GAPDH), ribosomal units (18S, S7, S20), ubiquitin (UBI), β-actin (ACT), and alpha- and beta-tubulins (TUBA and TUBB, respectively). Three different algorithms were utilized to identify the best RGs in our experimental design: BestKeeper (Pfaffl et al., 2004), geNorm (Vandesompele et al., 2002) and NormFinder (Andersen et al., 2004). Expression level analyses were then performed for specific GOIs: heat-shock proteins 40 and 70 (HSP40, HSP70), cytochrome P450-4 (CYP4), catalase (CAT), superoxide dismutase (SOD), glutathione *S*-transferase (GST), glutathione synthase (GSH-S), six aldehyde dehydrogenases (ALDH2, ALDH3, ALDH6, ALDH7, ALDH8, ALDH9), inhibitor of apoptosis protein (IAP), cell cycle and apoptosis regulatory 1 protein (CARP), cellular apoptosis susceptibility protein (CAS), caspase 3 (CASP3) and alpha and beta tubulins. Primers for RGs and GOI are already published in Lauritano et al. (2011a, 2011b), except for CASP3. For this gene, new primers (CASP3-F 5′-GGTCACTGAAGTGTGTGATGTGC-3′ and CASP3-R 5′-GGAGATCCCTTTATATTGTGAAAG-3′) were designed, considering the alignment of conserved domains in the caspase 3 sequences in the copepod *Calanus finmarchicus* and the mosquito *Anopheles gambiae*. Alignments were performed with Clustal W (Clustal) and BioEdit (BioEdit). Gene Runner, V3.05 (Hasting Software) was used to predict primer melting temperature (T_m) and to check if primers formed dimers, hairpin, bulge and internal loops. Serial dilutions of cDNA were used to determine CASP 3 primer reaction efficiency (100%), generating standard curves with five dilution points by using the cycle threshold (C_t) value versus the logarithm of each dilution factor and using the equation $E = 10^{-1/\text{slope}}$.

The fluorescent dye SYBR GREEN (Roche, Indianapolis, IN) was used to evaluate expression levels of the selected genes. RT-qPCR was performed in MicroAmp Optical 384-Well reaction plate (Applied Biosystem, Foster City, CA) with optical adhesive covers (Applied Biosystem) in a Viia7 real-time PCR system (Applied Biosystem). The PCR volume for each sample was 10 μl, with 5 μl of Fast Start SYBR Green Master Mix (Roche), 1 μl of cDNA template (1:50 template dilution) and 0.7 pmol μl^{-1} for each oligo. The RT-qPCR thermal profile was obtained using the following procedure: 95 °C for 10 min, 40 times 95 °C for 15 s, and 60 °C for 1 min, followed by one final step of 72 °C for 5 min. The program was set to reveal the melting curve of each amplicon from 60 to 95 °C, and read every 0.5 °C. Only a single peak was identified in the melting-curve analyses of all genes, confirming a gene-specific amplification and the absence of primer-dimers. All RT-qPCR reactions were carried out in triplicate to capture intra-assay variability. Each assay included three no-template negative controls (NTC) for each primer pair. To study expression levels for each target gene relative to the most stable RGs (EF1A, UBI and TUBA), we used the REST tool (Relative Expression Software Tool) (Pfaffl et al., 2002). Female copepods that were fed upon the dinoflagellate *Prorocentrum minimum*, which does not produce any known toxic compounds, were used as controls. Statistical analysis was performed using GraphPad Prim statistic software, V4.00 (GraphPad Software).

2.5. Microscopy

Images of newly spawned eggs were acquired for image analysis for females fed on the control (*Prorocentrum minimum*) or the tested diet (*Karenia brevis*); acquisition of images was performed until eggs hatched using a Zeiss-LSM 510 META confocal microscope (Laser 488, emission filter: BP 500–550).

3. Results

3.1. Population identification

A 518 bp fragment of the mitochondrial cytochrome oxidase subunit I region (COI) was amplified for 11 individuals. COI sequences confirmed the species identity of *Calanus helgolandicus*; the amplicons corresponded to the haplotype H1 (5 out of 11 sequences) typical of individuals of the NE Atlantic (GenBank accession number AY942600) (Papadopoulos et al., 2005) or to new

haplotypes (one out of 11 sequences, for GenBank accession numbers JX070089, JX070090, and JX070092, while three out of 11 for JX070091). The data confirmed the possible presence of multiple haplotypes in a single copepod population, as previously described by Papadopoulos et al. (2005). However, COI sequences differed for a maximum of 5 out of 518 nucleotides between the analyzed individuals. These nucleotide substitutions did not induce amino-acid substitutions.

3.2. Validation of best reference genes (RGs) for RT-qPCR

Results from the screening of putative RGs are reported in Table 1 and Fig. 1, and a synopsis of the results is summarized in Table 2. According to the mathematical approach of BestKeeper, EFA, which has the lowest standard deviation (SD), was the most-stable gene, followed by TUBA and GAPDH (Table 1). The geNorm analysis confirmed the results for BestKeeper, detecting as the two most-stable genes (i.e., with the lowest expression stability value, M) EFA and TUBA (Fig. 1A). GAPDH scored third. The chart indicates the average expression stability value of remaining reference genes at each step during a stepwise exclusion of the least stable reference gene. Starting from the least stable gene at the left, the genes are ranked according to increasing expression stability, ending with the two most-stable genes at the right (Vandesompele et al., 2002). Pair-wise variation was subsequently calculated to evaluate the effect of adding another RG to those already analyzed. The addition of other RGs is considered as unnecessary when the value is below the cutoff of 0.15. Accordingly, the three best RGs were sufficient for the normalization of GOI expression levels (Fig. 1B). According to the third statistical approach utilized, NormFinder, the best candidate reference gene was EFA, which showed the lowest stability value (Fig. 1C).

EFA was the most-stable RG using the three types of software while the stability rank of the other analyzed genes showed small differences depending on the software. Although the three approaches agreed that EFA was the best RG, we decided to use also the second- and third-best RGs, TUBA and GAPDH, according to GeNorm results and pair-wise variation analysis (Fig. 1C).

3.3. Expression level of genes of interest (GOI)

After 3 days of feeding on *Karenia brevis*, gene expression levels in copepods did not show significant changes due to high standard deviation. This result may suggest that, even if there could be gene expression up- or down-regulation between the treatments, it might have been masked by the high inter-replicate variability. After 5 days, some of the genes involved in generic stress responses, aldehyde detoxification and mitotic spindle formation

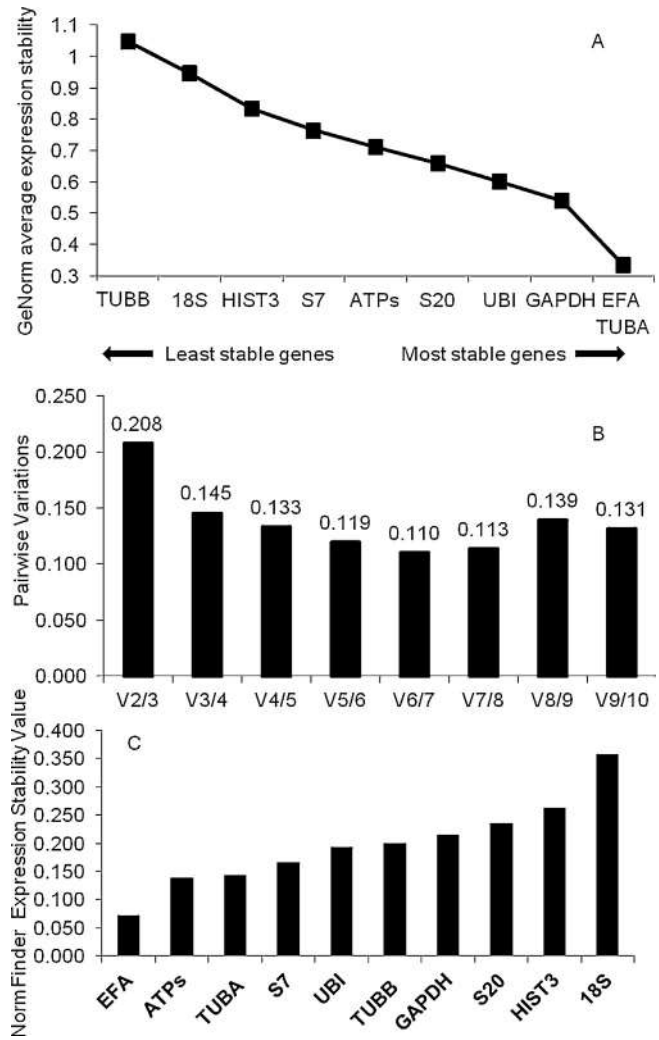

Fig. 1. Reference gene assessment. Ranking of the best reference genes (RGs) obtained with geNorm and NormFinder. (A) The stepwise exclusion of genes that are more variable among samples using the geNorm program. More stable genes with the lowest average expression stability value are indicated by the arrow (Vandesompele et al., 2002). (B) Pairwise variation (V) to evaluate the effect of adding another RG to the best couple already analyzed using geNorm (e.g. adding a third gene V2/3, a fourth V3/4, etc.). The inclusion of additional RGs was not required below the cutoff value of 0.15. (C) The NormFinder algorithm ranks the candidate RGs according to their expression stability. Lower stability values indicate more stable genes. Putative RGs were elongation factor 1α (EFA), adenosine 3-phosphate synthase (ATPs), histone 3 (HIST), glyceraldehyde-3-phosphate dehydrogenase (GAPDH), ribosomal proteins (S7, and S20), ubiquitin (UBI), β-actin (ACT), alpha and beta tubulins (TUBA and TUBB).

Table 1
Results of the BestKeeper analysis on the ten putative reference genes tested.

	S20	GAPDH	S7	UBI	TUBA	TUBB	ATPs	IST3	EFA	18S
n	13	13	13	13	13	13	13	13	13	13
GM	21.81	27.70	25.74	21.66	21.31	31.04	24.36	22.29	19.68	14.88
AM	21.83	27.71	25.76	21.67	21.32	31.06	24.38	22.32	19.69	14.91
min	20.09	26.41	23.14	20.40	20.55	28.01	22.67	21.06	19.01	13.72
max	24.26	29.78	27.12	22.71	23.03	33.53	25.57	25.24	20.87	16.76
SD	0.73	*0.50*	0.77	0.64	*0.46*	0.95	0.53	0.92	*0.33*	0.79
CV	3.33	1.81	2.99	2.97	2.17	3.05	2.17	4.12	1.70	5.29
min [*x*-fold]	−2.98	−2.31	−6.06	−2.39	−1.66	−7.77	−3.24	−2.34	−1.58	−2.08
max [*x*-fold]	4.78	3.83	2.60	2.07	3.12	5.44	2.31	7.74	2.24	3.33
SD [±*x*-fold]	1.59	1.38	1.63	1.51	1.34	1.83	1.40	1.80	1.24	1.65

Lowest standard deviation (SD) values are italicized.
n, number of samples; GM, geometric mean of C_t; AM, arithmetic mean of C_t; Min and Max, extreme values of C_t; SD, standard deviation of the C_t; CV, coefficient of variance, expressed as a percentage on the C_t level, extreme values of expression levels, expressed as an absolute *x*-fold over or under-regulation coefficient (Min [*x*-fold] and Max [*x*-fold]), and standard deviation of the absolute regulation coefficients (SD [±*x*-fold]) are given. According to BestKeeper, the most stable RG was EFA, which had the lowest standard deviation (SD), followed by TUBA and GAPDH.

Table 2
Best reference genes as given by BestKeeper, NormFinder and Genorm analyses. Putative RGs were elongation factor 1α (EFA), adenosine 3-phosphate synthase (ATPs), histone 3 (HIST), glyceraldehyde-3-phosphate dehydrogenase (GAPDH), ribosomal proteins (S7, and S20), ubiquitin (UBI), β-actin (ACT), alpha and beta tubulins (TUBA and TUBB).

GeNorm	BestKeeper	NormFinder
EFA	EFA	EFA
TUBA	TUBA	ATPs
GAPDH	GAPDH	TUBA
UBI	ATPs	S7
S20	UBI	UBI
ATPs	S20	TUBB
S7	S7	GAPDH
HIST	18S	S20
18S	HIST	HIST
TUBB	TUBB	18S

were significantly down-regulated: HSP40, GST, ALDH3 and TUBB (p value < 0.001 for all the genes) (Fig. 2A–C, respectively). After prolonged exposure (8 days), five out of six aldehyde dehydrogenases were strongly and significantly down-regulated: ALDH2, ALDH3, ALDH6, ALDH7, ALDH9 (p value < 0.001 for all the genes) (Fig. 2B); CYP4 and CAS were also significantly down-regulated, while HSP70 and CASP 3 were significantly up-regulated (p value < 0.001 for all the genes) (Fig. 2A and C). Time-dependent decreases were observed for SOD, ALDH2, ALDH3, ALDH6 and ALDH9 expression patterns (Fig. 2B), while CASP 3 expression levels increased with time reaching a 3-fold up-regulation after 8 d (Fig. 2C).

3.4. Microscopy

After one day of feeding on *Karenia brevis*, eggs collected soon after spawning were morphologically similar to the control (Fig. 3A), even if the cytoplasm and nuclei were not clearly defined (Fig. 3B). Conversely, after 3 days of feeding, eggs exhibited altered membrane cell morphology and apoptotic features such as granulation and degeneration of the cytoplasm matrix (Fig. 3C), whereas control eggs were identical to the first day (images not shown).

4. Discussion

Ingestion of *Karenia brevis* causes adverse effects on copepods. Included are alterations in copepod swimming and photobehavior, reduction in egg production and egg viability and, in some cases, reduced survival (Cohen et al., 2007; Prince et al., 2006; Turner

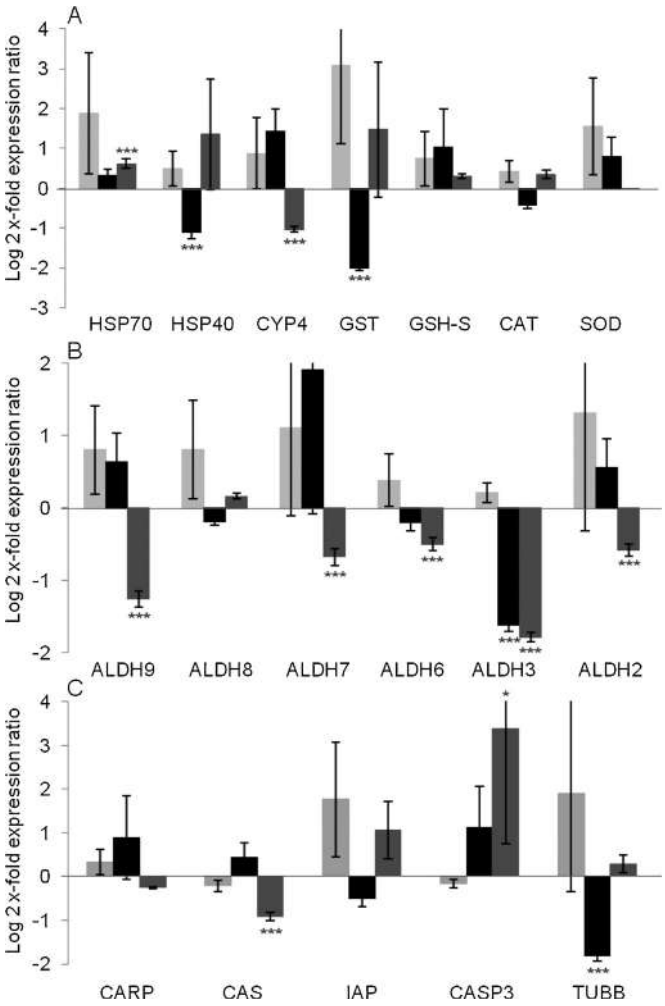

Fig. 2. Genes of interest expression levels. Relative gene expression levels of genes involved in (A) generic stress responses, (B) aldehyde dehydrogenases (ALDH) and (C) apoptosis regulation in the copepod *C. helgolandicus* feeding on *Karenia brevis*. Changes in expression levels of heat shock protein 70 (HSP70) and 40 (HSP40), cytochrome P450-4 (CYP4), glutathione *S*-transferase (GST), glutathione synthase (GSH-S), Catalase (CAT) and superoxide dismutase (SOD), aldehyde dehydrogenases (ALDH2, ALDH3, ALDH6, ALDH7, ALDH8, ALDH9), cell cycle and apoptosis regulatory 1 protein (CARP), cellular apoptosis susceptibility protein (CAS), inhibitor of apoptosis protein (IAP), caspase 3 (CASP 3) and beta tubulin (TUBB) genes in the copepod *C. helgolandicus* fed K. *brevis* for 3, 5 and 8 days compared to expression levels in females fed on the control algae *Prorocentrum minimum* (represented in the figure by *x*-axis). Three days of feeding are represented in the figure by histograms in gray, 5 days in black and 8 days in dark gray. The data are normalized with our three best RGs, EFA, TUBA and GAPDH.

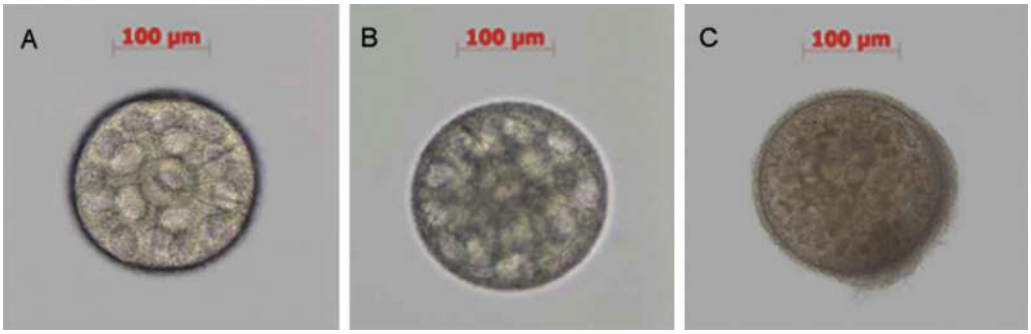

Fig. 3. Egg images. Confocal microscope images of eggs spawned by females fed on the dinoflagellate *Prorocentrum minimum* (A) for one day or *Karenia brevis* for one (B) or three days (C).

Table 3
Comparison between gene expression patterns in *C. helgolandicus* fed on *Skeletonema marinoi* or *Karenia brevis*. Timing in the gene regulation copepod response is different between the two algal species tested. However, genes showing pattern similarities are indicated with a double asterisk. Genes of interest (GOI) were heat shock protein 70 (HSP70) and 40 (HSP40), cytochrome P450-4 (CYP4), glutathione *S*-transferase (GST), glutathione synthase (GSH-S), catalase (CAT) and superoxide dismutase (SOD), aldehyde dehydrogenases (ALDH2, ALDH3, ALDH6, ALDH7, ALDH8, ALDH9), cell cycle and apoptosis regulatory 1 protein (CARP), cellular apoptosis susceptibility protein (CAS), inhibitor of apoptosis protein (IAP), caspase 3 (CASP 3), alpha and beta tubulins (TUBA and TUBB).

GOI	*S. marinoi*	*K. brevis*		
	2 days[a]	3 days	5 days	8 days
HSP70	ns	ns	ns	Up
HSP40[b]	Down	ns	Down	ns
CYP 4	ns	ns	ns	Down
GST	ns	ns	Down	ns
GSH-S	ns	ns	ns	ns
CAT	ns	ns	ns	ns
SOD	ns	ns	ns	ns
ALDH9[b]	Down	ns	ns	Down
ALDH8	Down	ns	ns	ns
ALDH7	ns	ns	ns	Down
ALDH6[b]	Down	ns	ns	Down
ALDH3[b]	ns	ns	Down	Down
ALDH2	ns	ns	ns	Down
CARP	ns	ns	ns	ns
CAS[b]	Down	ns	ns	Down
IAP	Down	ns	ns	ns
CASP 3[b]	Up	ns	ns	Up
TUBA	Down	ns	ns	ns
TUBB[b]	Down	ns	Down	ns

ns, not statistically significant gene expression changes.
[a] Data published in Lauritano et al. (2011b), except for CASP 3 results.
[b] Genes showing pattern similarities.

et al., 2012; Waggett et al., 2012). In our study, although none of the females died, expression patterns of selected genes involved in stress responses, detoxification mechanisms and apoptosis regulation were significantly affected.

The molecular responses in copepods that fed upon *Karenia brevis* were similar to those noted previously for copepods feeding on toxic diatoms (Lauritano et al., 2011a, 2011b, 2012a, 2012b), even if with different timing of response (summarized in Table 3). Previous studies on *Calanus helgolandicus* exposed to the oxylipin-producing diatom *Skeletonema marinoi* have shown that 2 d of feeding were sufficient to induce a strong down-regulation of a series of genes involved in aldehyde detoxification, apoptosis regulation and stress responses. However, other studies in copepods have also shown the down-regulation of antioxidant, metabolic or stress genes after exposure to chemicals or salinity/temperature variations. Hansen and co-workers showed the down-regulation of CYP330A1 and CYP1A2 at high naphthalene concentrations (Hansen et al., 2008) in the calanoid copepod *C. finmarchicus*. A reduction in the expression levels of the antioxidant enzyme glutathione reductase due to salinity variations (Seo et al., 2006a) and of the heat shock protein HSP20 after exposure to low temperature (Seo et al., 2006b) have also been reported in the harpacticoid copepod *Tigriopus japonicus*. Conversely, studies on *C. finmarchicus* and *T. japonicus* have shown that antioxidant and stress genes may be activated (up-regulated) soon after exposure to stressors, such as heavy metals (Lee et al., 2007, 2008), endocrine disruptor chemicals (Rhee et al., 2009) or hydrocarbons (Hansen et al., 2008, 2010). Down-regulation of a gene may occur, for example, when cell metabolism is focused on other metabolic pathways, at least after the tested exposure times, or when a cell is overstimulated by a stressor for a prolonged period of time and therefore the protein translated by that gene is no longer capable of protecting the cell (Morel and Barouki, 1998; Weber et al., 2006). On the other hand, gene up-regulation occurs, for example, when a cell needs more protection from a stress such as a toxin or drug, and therefore there is an increased production of the necessary protein (Hansen et al., 2008).

Recent studies of *Calanus helgolandicus* feeding on *Karenia brevis* (Wilson clone), showed that *K. brevis* ingestion reduced egg production to 25% and egg viability to 0% after 5 d of feeding, even if the algal strain tested did not produce any brevetoxins (Turner et al., 2012). The fifth day of *K. brevis* ingestion seems to be the time point with the strongest toxicity effects. In the present study, gene expression levels were investigated in adult females before, during and after this time point (3, 5 and 8 d). After 3 d of *K. brevis* ingestion, there were no significant changes in copepod gene expression, compared to the control. However, although not statistically significant, higher expression levels of many genes (HSP70, HSP40, CYP4, GST, GSH-S, SOD and ALDHs) involved in stress responses and detoxification mechanisms were observed after 3 d of *K. brevis* ingestion, due to high variability between replicates. Considering that our mtDNA haplotype analysis identified new haplotypes, besides the common H1 Atlantic haplotype, variability can be due to haplotype-specific response. This has been shown to occur in the *C. helgolandicus* response to *Skeletonema marinoi* exposure, in three different copepod populations, harboring diverse haplotypes (Lauritano et al., 2012b). After 8 d, only HSP70 was significantly up-regulated in the present study. SOD, CAT, GSH-S, ALDH8, CARP and IAP expression levels were comparable to the control during the whole experiment, while HSP40, CYP4 and the other ALDHs were significantly down-regulated after 5 and/or 8 d of *K. brevis* exposure.

Alpha-tubulin was very stable in animals fed on *Karenia brevis*, and the software used for the reference gene assessment (BestKeeper, NormFinder and GeNorm) scored it as one of the three most-stable genes within a panel of 10 putative reference genes (Table 2). Conversely, TUBA was significantly affected in our previous study (Lauritano et al., 2011a) where copepods were fed on *Skeletonema marinoi*, a diatom that produces secondary metabolites that alter tubulins and microtubule polymerization and their functions. In that case, the ribosomal protein S20 was the most-stable RG. Hence, our experiments suggest that the best RGs to use for RT-qPCR normalization are EFA, TUBA and GAPDH for *Calanus helgolandicus* fed on *K. brevis* and S20, S7 and GAPDH in *C. helgolandicus* fed on *S. marinoi* (Lauritano et al., 2011a). These results confirm that RGs are not universal but may change depending on the species and experimental conditions tested.

In this study, CASP 3, the major executioner protease in classic apoptosis, showed a time-dependent up-regulation, indicating increased apoptosis induction with time. CASP 3 expression levels also increased in *Calanus helgolandicus* fed for 48 h on *Skeletonema marinoi* (unpublished data), indicating apoptosis activation. However, the other apoptotic genes did not show a clear pattern. Image acquisition of eggs collected soon after spawning by females fed upon *Karenia brevis* for 3 days also showed that cell divisions were arrested, with abnormal egg morphology, granulation and degeneration of the cytoplasm, but in the absence of brevetoxins.

Hatching success decreased to 20% in *Calanus helgolandicus* after 6 days of ingestion of the diatom *Skeletonema marinoi* (Ianora et al., 2004), while it decreased to almost 0% in the same copepod species after 5 days of ingestion of *Karenia brevis* (Turner et al., 2012). This indicates a comparable or even stronger toxic effect with *K. brevis* than with *S. marinoi*. Even though different times of exposure were examined, there were many similarities between gene expression patterns in *C. helgolandicus* fed on *K. brevis* or *S. marinoi* (summarized in Table 3). These included the down-regulation of HSP40, ALDH6, ALDH9, CAS and beta-tubulin, and the up-regulation of CASP 3. These results suggest the impairment of the aldehyde detoxification machinery and an increase in cell

death via apoptosis in both cases. Even though the Wilson clone that we used did not produce brevetoxins, it exerted toxic effects similar to *S. marinoi*, suggesting that other metabolites may be responsible for these responses at the molecular level. Chemical analyses are in progress for the Wilson clone used in our work to identify what compound(s) may be responsible for the observed toxic effects on egg production and viability (Turner et al., 2012), and egg morphologies and/or gene expression patterns (present study). Although the chemical nature of these molecules remains unknown, our results provide evidence of the complexity of plant–animal chemical interactions in the plankton.

Acknowledgments

The authors thank Flora Palumbo, Francesco Esposito, Massimo Perna and the staff of the Molecular Biology Service of Stazione Zoologica Anton Dohrn for their technical support, and Cynthia Ladino of the University of Massachusetts Dartmouth for critical reading of an earlier version of the manuscript.[SS]

References

Altieri, D.C., 2010. Survivin and IAP proteins in cell-death mechanisms. Biochemical Journal 430, 199–205.

Andersen, C.L., Jensen, J.L., Orntoft, T.F., 2004. Normalization of real-time quantitative reverse transcription-PCR data: a model-based variance estimation approach to identify genes suited for normalization, applied to bladder and colon cancer data sets. Cancer Research 64, 5245–5250.

Baden, D.G., Bourdelais, A.J., Jacocks, H., Michelliza, S., Naar, J., 2005. Natural and derivative brevetoxins: historical background, multiplicity, and effects. Environmental Health Perspectives 113, 621–625.

Bigot, A., Vasseur, P., Rodius, F., 2010. SOD and CAT cDNA cloning, and expression pattern of detoxification genes in the freshwater bivalve *Unio tumidus* transplanted into the Moselle river. Ecotoxicology 19, 369–376.

BioEdit, Biological sequence alignment editor for Windows 95/98/NT/XP. <http://www.mbio.ncsu.edu/BioEdit/bioedit.html>.

Bourdelais, A.J., Campbell, S., Jacocks, H., Naar, J., Wright, J.L.C., Carsi, J., Baden, D.G., 2004. Brevenal is a natural inhibitor of brevetoxin action in sodium channel receptor binding assays. Cellular and Molecular Neurobiology 24, 553–563.

Bourdelais, A.J., Jacocks, H.M., Wright, J.L.C., Bigwarfe, P.M., Baden, D.G., 2005. A new polyether ladder compound produced by the dinoflagellate *Karenia brevis*. Journal of Natural Products 68, 2–6.

Brand, L.E., Campbell, L., Bresnan, E., 2012. *Karenia*: the biology and ecology of a toxic genus. Harmful Algae 14, 156–178.

Breier, C.F., Buskey, E.J., 2007. Effects of the red tide dinoflagellate *Karenia brevis*, on grazing and fecundity in the copepod *Acartia tonsa*. Journal of Plankton Research 29, 115–126.

Brinkmann, U., 1998. CAS, the human homologue of the yeast chromosome-segregation gene CSE1, in proliferation, apoptosis, and cancer. American Journal of Human Genetics 62, 509–513.

Bustin, S.A., Beaulieu, J.F., Huggett, J., Jaggi, R., Kibenge, F.S.B., Olsvik, P.A., Penning, L.C., Toegel, S., 2010. MIQE precis: practical implementation of minimum standard guidelines for fluorescence-based quantitative real-time PCR experiments. BMC Molecular Biology 11, 74.

Clustal, W. <http://www.ebi.ac.uk/clustalw/>.

Cohen, J.H., Tester, P.A., Forward Jr., R.B., 2007. Sublethal effects of the toxic dinoflagellate *Karenia brevis* on marine copepod behavior. Journal of Plankton Research 29, 301–315.

Eaton, D.L., Bammler, T.K., 1999. Concise review of the glutathione *S*-transferases and their significance to toxicology. Toxicological Sciences 49, 156–164.

Feder, M.E., Hofmann, G.E., 1999. Heat-shock proteins, molecular chaperones, and the stress response: evolutionary and ecological physiology. Annual Review of Physiology 61, 243–282.

Fehrenbacher, N., Gyrd-Hansen, M., Poulsen, B., Felbor, U., Kallunki, T., Boes, M., Weber, E., Leist, M., Jaattela, M., 2004. Sensitization to the lysosomal cell death pathway upon immortalization and transformation. Cancer Research 64, 5301–5310.

Fontana, A., d'Ippolito, G., Cutignano, A., Romano, G., Lamari, N., Gallucci, A.M., Cimino, G., Miralto, A., Ianora, A., 2007. LOX-induced lipid peroxidation mechanism responsible for the detrimental effect of marine diatoms on zooplankton grazers. ChemBiochem 8, 1810–1818.

Hansen, B.H., Altin, D., Vang, S.H., Nordtug, T., Olsen, A.J., 2008. Effects of naphthalene on gene transcription in *Calanus finmarchicus* (Crustacea Copepoda). Aquatic Toxicology 86, 157–165.

Hansen, B.H., Altin, D., Booth, A., Vang, S.H., Frenzel, M., Sorheim, K.R., Brakstad, O.G., Storseth, T.R., 2010. Molecular effects of diethanolamine exposure on *Calanus finmarchicus* (Crustacea: Copepoda). Aquatic Toxicology 99, 212–222.

Ianora, A., Miralto, A., 2010. Toxigenic effects of diatoms on grazers, phytoplankton and other microbes: a review. Ecotoxicology 19, 493–511.

Ianora, A., Poulet, S.A., Miralto, A., 2003. The effects of diatoms on copepod reproduction: a review. Phycologia 42, 351–363.

Ianora, A., Miralto, A., Poulet, S.A., Carotenuto, Y., Buttino, I., Romano, G., Casotti, R., Pohnert, G., Wichard, T., Colucci-D'Amato, L., Terrazzano, G., Smetacek, V., 2004. Aldehyde suppression of copepod recruitment in blooms of a ubiquitous planktonic diatom. Nature 429, 403–407.

Kubanek, J., Snell, T.W., Pirkle, C., 2007. Chemical defense of the red tide dinoflagellate *Karenia brevis* against rotifer grazing. Limnology and Oceanography 52, 1026–1035.

Landsberg, J.H., 2002. The effects of harmful algal blooms on aquatic organisms. Reviews in Fisheries Science 10, 113–390.

Lauritano, C., Borra, M., Carotenuto, Y., Biffali, E., Miralto, A., Procaccini, G., Ianora, A., 2011a. First molecular evidence of diatom effects in the copepod *Calanus helgolandicus*. Journal of Experimental Marine Biology and Ecology 404, 79–86.

Lauritano, C., Borra, M., Carotenuto, Y., Biffali, E., Miralto, A., Procaccini, G., Ianora, A., 2011b. Molecular evidence of the toxic effects of diatom diets on gene expression patterns in copepods. PLoS ONE 6 (10) e26850.

Lauritano, C., Procaccini, G., Ianora, A., 2012a. Gene expression patterns and stress response in marine copepods. Marine Environmental Research 76, 22–31.

Lauritano, C., Carotenuto, Y., Miralto, A., Procaccini, G., Ianora, A., 2012b. Copepod population-specific response to a toxic diatom diet. PLoS ONE 7 (10) e47262.

Lee, K.-W., Raisuddin, S., Rhee, J.-S., Hwang, D.-S., Yu, I.T., Lee, Y.-M., Park, H.G., Lee, J.-S., 2008. Expression of glutathione *S*-transferase (GST) genes in the marine copepod *Tigriopus japonicus* exposed to trace metals. Aquatic Toxicology 89, 158–166.

Lee, Y.-M., Lee, K.-W., Park, H., Park, H.G., Raisuddin, S., Ahn, I.-Y., Lee, J.-S., 2007. Sequence, biochemical characteristics and expression of a novel Sigma-class of glutathione *S*-transferase from the intertidal copepod, *Tigriopus japonicus* with a possible role in antioxidant defense. Chemosphere 69, 893–902.

Lekan, D.K., Tomas, C.R., 2010. The brevetoxin and brevenal composition of three *Karenia brevis* clones at different salinities and nutrient conditions. Harmful Algae 9, 39–47.

Marchitti, S.A., Brocker, C., Stagos, D., Vasiliou, V., 2008. Non-P450 aldehyde oxidizing enzymes: the aldehyde dehydrogenase superfamily. Expert Opinion on Drug Metabolism and Toxicology 4, 697–720.

Martin, H.L., Teismann, P., 2009. Glutathione—a review on its role and significance in Parkinson's disease. FASEB Journal 23, 3263–3272.

Mello, D.F., de Oliveira, E.S., Vieira, R.C., Simoes, E., Trevisan, R., Dafre, A.L., Barracco, M.A., 2012. Cellular and transcriptional responses of *Crassostrea gigas* hemocytes exposed *in vitro* to brevetoxin (PbTx-2). Marine Drugs 10, 583–597.

Morel, Y., Barouki, R., 1998. Down-regulation of cytochrome P450 1A1 gene promoter by oxidative stress. Journal of Biological Chemistry 273 (41) 26969–26976.

Murrell, R.N., Gibson, J.E., 2009. Brevetoxins 2, 3, 6, and 9 show variability in potency and cause significant induction of DNA damage and apoptosis in Jurkat E6-1 cells. Archives of Toxicology 83, 1009–1019.

Naar, J.P., Flewelling, L.J., Lenzi, A., Abbott, J.P., Granholm, A., Jacocks, H.M., Gannon, D., Henry, M., Pierce, R., Baden, D.G., Wolny, J., Landsberg, J.H., 2007. Brevetoxins, like ciguatoxins, are potent ichthyotoxic neurotoxins that accumulate in fish. Toxicon 50, 707–723.

Neely, T., Campbell, L., 2006. A modified assay to determine hemolytic toxin variability among *Karenia* clones isolated from the Gulf of Mexico. Harmful Algae 5, 592–598.

Papadopoulos, L.N., Peijnenburg, K., Luttikhuizen, P.C., 2005. Phylogeography of the calanoid copepods *Calanus helgolandicus* and *C. euxinus* suggests Pleistocene divergences between Atlantic, Mediterranean, and Black Sea populations. Marine Biology 147, 1353–1365.

Pfaffl, M.W., Horgan, G.W., Dempfle, L., 2002. Relative expression software tool (REST (c)) for group-wise comparison and statistical analysis of relative expression results in real-time PCR. Nucleic Acids Research 30, e36.

Pfaffl, M.W., Tichopad, A., Prgomet, C., Neuvians, T.P., 2004. Determination of stable housekeeping genes, differentially regulated target genes and sample integrity. BestKeeper—Excel-based tool using pair-wise correlations. Biotechnology Letters 26, 509–515.

Pierce, R.H., Henry, M.S., 2008. Harmful algal toxins of the Florida red tide (*Karenia brevis*): natural chemical stressors in South Florida coastal ecosystems. Ecotoxicology 17, 623–631.

Prince, E.K., Lettieri, L., McCurdy, K.J., Kubanek, J., 2006. Fitness consequences for copepods feeding on a red tide dinoflagellate: deciphering the effects of nutritional value, toxicity, and feeding behavior. Oecologia 147, 479–488.

Rhee, J.S., Raisuddin, S., Lee, K.W., Seo, J.S., Ki, J.S., Kim, C., Park, H.G., Lee, J.S., 2009. Heat shock protein (Hsp) gene responses of the intertidal copepod *Tigriopus japonicus* to environmental toxicants. Comparative Biochemistry and Physiology Part C: Toxicology and Pharmacology 149, 104–112.

Rishi, A.K., Zhang, L., Yu, Y., Jiang, Y., Nautiyal, J., Wali, A., Fontana, J.A., Levi, E., Majumdar, A.P.N., 2006. Cell cycle- and apoptosis-regulatory protein-1 is involved in apoptosis signaling by epidermal growth factor receptor. Journal of Biological Chemistry 281, 13188–13198.

Satake, M., Campbell, A., Van Wagoner, R.M., Bourdelais, A.J., Jacocks, H., Baden, D.G., Wright, J.L.C., 2009. Brevisin: an aberrant polycyclic ether structure from the dinoflagellate *Karenia brevis* and its implications for polyether assembly. Journal of Organic Chemistry 74, 989–994.

Seo, J.S., Lee, K.W., Rhee, J.S., Hwang, D.S., Lee, Y.M., Park, H.G., Ahn, I.Y., Lee, J.S., 2006a. Environmental stressors (salinity, heavy metals, H_2O_2) modulate expression of glutathione reductase (GR) gene from the intertidal copepod *Tigriopus japonicus*. Aquatic Toxicology 80, 281e289.

Seo, J.S., Lee, Y.M., Park, H.G., Lee, J.S., 2006b. The intertidal copepod *Tigriopus japonicus* small heat shock protein 20 gene (Hsp20) enhances thermotolerance of transformed *Escherichia coli*. Biochemical and Biophysical Research Communications 340, 901e908.

Snyder, M.J., 2000. Cytochrome P450 enzymes in aquatic invertebrates: recent advances and future directions. Aquatic Toxicology 48, 529–547.

Speekmann, C.L., Hyatt, C.J., Buskey, E.J., 2006. Effects of *Karenia brevis* diet on RNA: DNA ratios and egg production of *Acartia tonsa*. Harmful Algae 5, 693–704.

Steidinger, K.A., 2009. Historical perspective on *Karenia brevis* red tide research in the Gulf of Mexico. Harmful Algae 8, 549–561.

Turner, J.T., 2006. Harmful algae interactions with marine planktonic grazers. In: Granéli, E., Turner, J.T. (Eds.), Ecology of Harmful Algae. Springer-Verlag, Berlin, Heidelberg, pp. 259–270.

Turner, J.T., Tester, P.A., 1989. Zooplankton feeding ecology: copepod grazing during an expatriate red tide. In: Cosper, E.M., Bricelj, V.M., Carpenter, E.J. (Eds.), Novel Phytoplankton Blooms: Causes and Impacts of Recurrent Brown Tides and Other Unusual Blooms. Springer-Verlag, Berlin, Heidelberg, pp. 359–374.

Turner, J.T., Tester, P.A., 1997. Toxic marine phytoplankton, zooplankton grazers, and pelagic food webs. Limnology and Oceanography 42 (5 (Pt 2)) 1203–1214.

Turner, J.T., Hansen, P.J., Tester, P.A., 1998. Interactions between toxic marine phytoplankton and metazoan and protistan grazers. In: Anderson, D.M., Cembella, A., Hallegraeff, G. (Eds.), The Physiological Ecology of Harmful Algal Blooms. Springer-Verlag, Berlin, Heidelberg, pp. 453–474.

Turner, J.T., Ianora, A., Miralto, A., Laabir, M., Esposito, F., 2001. Decoupling of copepod grazing rates, fecundity and egg hatching success on mixed and alternating diatom and dinoflagellate diets. Marine Ecology Progress Series 220, 187–199.

Turner, J.T., Roncalli, V., Camarillo, P., Dell'Aversano, C., Fattorusso, E., Tartaglione, L., Carotenuto, Y., Romano, G., Esposito, F., Miralto, A., Ianora, A., 2012. Biogeographic effects of the Gulf of Mexico red tide dinoflagellate *Karenia brevis* on Mediterranean copepods. Harmful Algae 16, 63–73.

Vandesompele, J., De Preter, K., Pattyn, F., Poppe, B., Van Roy, N., De Paepe, A., Speleman, F., 2002. Accurate normalization of real-time quantitative RT-PCR data by geometric averaging of multiple internal control genes. Genome Biology 3 (7) , research0034.1-0034.11.

Vasiliou, V., Pappa, A., Estey, T., 2004. Role of human aldehyde dehydrogenases in endobiotic and xenobiotic metabolism. Drug Metabolism Reviews 36, 279–299.

Waggett, R.J., Hardison, D.R., Tester, P.A., 2012. Toxicity and nutritional inadequacy of *Karenia brevis*: synergistic mechanisms disrupt top-down grazer control. Marine Ecology Progress Series 444, 15–30.

Walsh, C.J., Leggett, S.R., Strohbehn, K., Pierce, R.H., Sleasman, J.W., 2008. Effects of in vitro brevetoxin exposure on apoptosis and cellular metabolism in a leukemic T cell line (Jurkat). Marine Drugs 6, 291–307.

Walsh, C.J., Leggett, S.R., Carter, B.J., Colle, C., 2010. Effects of brevetoxin exposure on the immune system of loggerhead sea turtles. Aquatic Toxicology 97, 293–303.

Watkins, S.M., Reich, A., Fleming, L.E., Hammond, R., 2008. Neurotoxic shellfish poisoning. Marine Drugs 6, 431–455.

Weber, C., Guigon, G., Bouchier, C., et al., 2006. Stress by heat shock induces massive down regulation of genes and allows differential allelic expression of the Gal/GalNAc lectin in *Entamoeba histolytica*. Eukaryotic Cell 5 (5) 871–875.

Aquatic Toxicology 156 (2014) 125–134

Contents lists available at ScienceDirect

Aquatic Toxicology

journal homepage: www.elsevier.com/locate/aquatox

Stress response to cadmium and manganese in *Paracentrotus lividus* developing embryos is mediated by nitric oxide

Oriana Migliaccio[a], Immacolata Castellano[a], Giovanna Romano[b], Anna Palumbo[a,*]

[a] Laboratory of Cellular and Developmental Biology, Stazione Zoologica Anton Dohrn, Villa Comunale, 80121 Naples, Italy
[b] Laboratory of Functional and Evolutionary Ecology, Stazione Zoologica Anton Dohrn, Villa Comunale, 80121 Naples, Italy

ARTICLE INFO

Article history:
Received 14 July 2014
Received in revised form 8 August 2014
Accepted 12 August 2014
Available online 20 August 2014

Keywords:
Cadmium
Development
Manganese
Nitric oxide
Paracentrotus lividus
Stress

ABSTRACT

Increasing concentrations of contaminants, often resulting from anthropogenic activities, have been reported to occur in the marine environment and affect marine organisms. Among these, the metal ions cadmium and manganese have been shown to induce developmental delay and abnormalities, mainly reflecting skeleton elongation perturbation, in the sea urchin *Paracentrotus lividus*, an established model for toxicological studies. Here, we provide evidence that the physiological messenger nitric oxide (NO), formed by L-arginine oxidation by NO synthase (NOS), mediates the stress response induced by cadmium and manganese in sea urchins. When NO levels were lowered by inhibiting NOS, the proportion of abnormal plutei increased. Quantitative expression of a panel of 19 genes involved in stress response, skeletogenesis, detoxification and multidrug efflux processes was followed at different developmental stages and under different conditions: metals alone, metals in the presence of NOS inhibitor, NO donor and NOS inhibitor alone. These data allowed the identification of different classes of genes whose metal-induced transcriptional expression was directly or indirectly mediated by NO. These results open new perspectives on the role of NO as a sensor of different stress agents in sea urchin developing embryos.
© 2014 Elsevier B.V. All rights reserved.

1. Introduction

Sea urchins are key species in structuring marine ecosystems through their grazing activity. Among them, *Paracentrotus lividus*, the dominant sea urchin in the Mediterranean Sea, locally controlling the dynamics of seaweed and seagrasses (Boudouresque and Verlaque, 2013), was considered a good model system to study the response of marine organisms to environmental stress. Indeed, the transparency of embryos/larvae, as well as their sensitivity to pollutants, made this organism particularly suitable for embryotoxicity tests and for monitoring or risk assessment programs (Beiras et al., 2003). *P. lividus* activates different protection strategies against a variety of stress-inducing agents, such as heat shock (Giudice et al., 1999), metals (Roccheri and Matranga, 2009; Pinsino et al., 2010), UVB radiation (Bonaventura et al., 2006), X-rays (Matranga et al., 2010; Bonaventura et al., 2011), natural toxins (Romano et al., 2010; Varrella et al., 2014) and endocrine disrupter compounds (Sugni et al., 2010). These strategies include activation of MAP kinases (Bonaventura et al., 2005), induction of metallothioneins (Ragusa et al., 2013), caspase 3 (Agnello et al., 2007) and different heat shock proteins (hsps) (Roccheri et al., 2004; Romano et al., 2011; Marrone et al., 2012).

Continuous exposure of *P. lividus* embryos to subacute/sublethal cadmium concentrations causes abnormal development with defects in skeleton elongation and patterning (Russo et al., 2003), coupled with a general reduction of protein synthesis, increased levels of specific hsps (Roccheri et al., 2004) and differential metallothionein expression (Ragusa et al., 2013). Parallel experiments have revealed that the amount of incorporated cadmium in sea urchin embryos highly increased with time (Agnello et al., 2007). Reduction and lack of arms and skeleton elongation were also observed in chronic long-term exposures at lower cadmium concentrations, mimicking moderately and highly polluted seawaters (Filosto et al., 2008). Cadmium treatment also induced apoptosis (Agnello et al., 2007; Filosto et al., 2008) and authophagy (Chiarelli et al., 2011). A functional relationship between the two processes has recently also been suggested (Chiarelli et al., 2014).

Manganese treatment resulted in developmental abnormalities, especially at the skeleton level, directly correlated to manganese accumulation in developing embryos. An increase of specific hsps without induction of apoptosis was reported (Pinsino et al., 2010). Manganese overload caused interference with calcium and perturbation of phosphorylation of the MAP kinases ERK and P38,

* Corresponding author. Tel.: +39 081 5833 293; fax: +39 081 7641355.
E-mail address: anna.palumbo@szn.it (A. Palumbo).

http://dx.doi.org/10.1016/j.aquatox.2014.08.007
0166-445X/© 2014 Elsevier B.V. All rights reserved.

resulting in the formation of embryos without skeletons (Pinsino et al., 2011, 2013).

Recently, it has been shown that in sea urchin embryos the physiological messenger nitric oxide (NO), produced by L-arginine oxidation by NO synthase (NOS), is involved in the stress response induced by the diatom aldehyde decadienal (Romano et al., 2011). At low decadienal concentrations, NO protected embryos from the toxic effect of the aldehyde, contributing to the activation of *hsp70* gene expression, whereas at high concentrations NO mediated initial apoptotic events through the generation of peroxynitrite. The involvement of NO in the stress response has also been reported in other organisms. Heat stress activated NO production in sponges (Giovine et al., 2001), and salinity and light stress gave rise to NO bursts in culture media of marine microalgae (Zhang et al., 2006). NO was also a central player in the surveillance system in a marine diatom in response to decadienal treatment (Vardi et al., 2006) and in coral bleaching (Bouchard and Yamasaki, 2008).

Our continuing interest in the biological functions of NO in marine invertebrates (Mattiello et al., 2010, 2012; Ercolesi et al., 2012; Castellano et al., 2014; Migliaccio et al., 2014) has prompted us to investigate if NO also mediates the response of *P. lividus* embryos to other stress agents, such as metal ions. We chose cadmium and manganese, two metals with different properties and known to affect sea urchin development (Russo et al., 2003; Filosto et al., 2008; Pinsino et al., 2010). Cadmium is a non-essential metal, without any biological role and it is a potent pollutant, whereas manganese is an essential element, naturally occurring metal which becomes toxic at high concentrations (Flick et al., 1971; CICAD, 2004).

Here, we show that NO is produced in sea urchin embryos in response to cadmium and manganese and its levels regulate directly or indirectly the transcriptional expression of some metal-induced genes involved in stress response, skeletogenesis, as well as in detoxification and multi drug efflux processes.

2. Materials and methods

2.1. Ethics statement

P. lividus (Lamarck) sea urchins were collected from a location that is not privately-owned nor protected in any way, according to the authorization of Marina Mercantile (DPR 1639/68, 09/19/1980 confirmed on 01/10/2000). The field studies did not involve endangered or protected species. All animal procedures were in compliance with the guidelines of the European Union (directive 609/86).

2.2. Gamete collection

Sea urchins were collected during the breeding season by SCUBA divers in the Gulf of Naples, transported in an insulated box to the laboratory within 1 h after collection and maintained in tanks with circulating sea water. The animals were acclimated for a minimum of 10 days until use and kept at 18 ± 2 °C in a controlled temperature chamber at a 12:12 light:dark cycle. The density of the individuals in the tanks was maximally 1 animal/5 L. Every 3 days animals were fed using fresh macroalgae (*Ulva* sp.). Feeding was interrupted for 2·days before experimental sampling. Very rare spontaneous spawning or mortalities were observed during the acclimation period. To induce gamete ejection, sea urchins were injected with 0.5 M KCl solution through the peribuccal membrane. Eggs from individual females were washed three times with 0.22 μm filtered sea water. Concentrated sperm was collected dry, mixing samples from at least three different males and kept undiluted at +4 °C. Ten μL of sperm mix was diluted in 10 mL SW just before fertilization and an aliquot (100 μL) of this solution was added to 100 mL of egg suspension. Sperm to egg ratio was 100:1 for both controls and treated embryos. The fertilization success was approximately 90%.

2.3. Embryo culture, treatments and morphological analysis

Eggs (150 eggs/mL) were fertilized as described above and allowed to develop at 18 ± 2 °C in a controlled temperature chamber at a 12:12 light:dark cycle. After 5 min from fertilization, the metals at different concentration were added under careful agitation. Nominal metal concentrations were 5×10^{-7} M (0.09 mg/L), 10^{-6} M (0.18 mg/L), 5.2×10^{-6} M (0.96 mg/L), 10^{-5} M (1.83 mg/L), 2×10^{-5} M (3.66 mg/L), 3×10^{-5} M (5.49 mg/L) for cadmium (cadmium chloride, Sigma–Aldrich, Milan, Italy) and 1.8×10^{-5} M (3.6 mg/L), 3.6×10^{-5} M (7.2 mg/L), 7.8×10^{-5} M (15.4 mg/L), 15.5×10^{-5} M (30.8 mg/L), 31.2×10^{-5} M (61.6 mg/L), 62.4×10^{-5} M (123.2 mg/L) for manganese (manganese chloride tetrahydrate, Sigma–Aldrich, Milan, Italy). Stock solutions of 10^{-4} M cadmium and 31.2×10^{-4} M manganese in sea water were prepared and diluted to the final experimental concentration. The same protocol was followed for treatments with the slow releasing NO donor (Z)-1-{N-(3-Aminopropyl)-N-(4-(3-aminopropylammonio)butyl)-amino}-diazen-1-ium-1,2-diolate) (spermine NONOate, sperNO) (Alexis, San Diego, California) and spermine (Sigma–Aldrich, Milan, Italy). Incubations with 1-(2-trifluoromethylphenyl)imidazole (TRIM) (Alexis, San Diego, California) were performed 20 min before fertilization. Stock solutions of 2×10^{-4} M TRIM (in 10^{-6} M DMSO), 4×10^{-4} M sperNO (in 10^{-2} M NaOH), 4×10^{-4} M spermine (in sea water) were prepared and diluted to the final experimental concentrations of 2×10^{-5} M, 5×10^{-5} M and 10^{-4} M TRIM, 4×10^{-5} M sperNO and 4×10^{-5} M spermine. Experiments were performed in triplicate using the eggs collected from three different females. The development was followed using an inverted microscope (Zeiss Axiovert 135 TV) and pictures were taken using a Zeiss Axiocam connected directly to the microscope. Morphological observations were performed approximately 48 h post fertilization (hpf) on plutei collected and fixed in 4% formalin. The percentage of normal and abnormal plutei was determined by counting at least 300 embryos from each well. Abnormalities were recorded following the criteria reported in Pagano et al. (1986). Embryos were considered normal if they satisfied all the morphological criteria defined elsewhere (Radenac et al., 2001; Kobayashi and Okamura, 2005), namely: (1) reached the pluteus stage of development, (2) exhibited a good body symmetry, (3) showed fully developed skeletal rods and (4) displayed a well differentiated gut. All the morphologies that did not satisfy the above-mentioned criteria were grouped and referred to as abnormal. In particular, the abnormalities were classified in two different levels according to the severity of the alterations, taking into account the classification reported in Carballeira et al. (2012) with some modifications. The level A was represented by plutei characterized by incorrect arrangement of skeletal rods, such as larvae with crossed tip, separated tip and fused arms. The level B was represented by larvae showing incomplete or absent skeletal rods and development blocked, such as plutei with folded tip, fractured ectoderm, fertilized eggs and blastula, gastrula, exogastrula, prisma and pre-pluteus stages.

2.4. Nitric oxide (NO) determination

The endogenous NO levels were measured by monitoring nitrite formation by the Griess reaction (Green et al., 1982). Fertilized eggs were treated as described above. Samples (about 15,000 embryos/larvae) were collected at 2-cell stage, 8-cell stage, early blastula, swimming blastula, prisma and pluteus by

centrifugation at 1800 rcf for 10 min in a swing out rotor at 4 °C. The pellet was washed with phosphate buffered saline and then frozen in liquid nitrogen and kept at −80 °C. Samples were homogenized in phosphate buffer (1:2, w/v) and centrifuged (12,000 rcf for 30 min at 4 °C), and the supernatants were analyzed for nitrite content. Aliquots (300 μL) were incubated for 2 h, at room temperature (25 °C) with nitrate reductase (1 U/mL) and enzyme co-factors FAD (100 μM) and NADPH (0.6 mM). Samples were incubated for 10 min in the dark with 300 μL of 1% (w/v) sulphanilamide in 5% H_3PO_4 and then for 10 min with 300 μL of 0.1% (w/v) N-(1-naphthy)-ethylenediaminedihydrochloride. The absorbance at 540 nm was determined and the molar concentration of nitrite in the sample was calculated from a standard curve generated using known concentrations of sodium nitrite (0–100 μM). NO in each sample was determined in triplicate. The efficacy of nitrate reduction by nitrate reductase was determined on known concentrations of nitrate and nitrite recovery was 90–100% over the entire range of sodium nitrite. The coefficient of variation between the different experiments was less than 5%.

2.5. RNA extraction and cDNA synthesis

About 1500 fertilized eggs were treated as described above and collected by centrifugation as reported in the above paragraph. Total RNA was extracted from each developmental stage using RNAqueous-Microkit (Ambion) according to the manufacturer's instructions. The amount of total RNA extracted was estimated by the absorbance at 260 nm and the purity by 260/280 and 260/230 nm ratios by Nanodrop (ND-1000 UV–Vis Spectrophotometer; NanoDrop Technologies). The integrity of RNA was evaluated by agarose gel electrophoresis. Intact rRNA subunits (28S and 18S) were observed on the gel indicating minimal degradation of the RNA. For each sample, 600 ng of total RNA extracted was retrotranscribed with iScript™ cDNA Synthesis kit (Biorad), following the manufacturer's instructions. cDNA was diluted 1:5 with H_2O prior to use in Real Time qPCR experiments.

2.6. Gene expression by real time qPCR

In this article the term gene expression refers to transcriptional expression, although it is acknowledged that gene expression can also be regulated, e.g., at translation or mRNA/protein stability level. For real time qPCR experiments the data from each cDNA sample were normalized using *Pl-Z12-1* as endogenous control. Its level remained constant during development (Costa et al., 2012; Ragusa et al., 2013). The programs geNorm VBA applet for Microsoft Excel and NormFinder version 19 (2009) were used to confirm *Pl-Z12-1* as the reference gene. The analyzed genes and the specific primers, used for amplification, are reported in supplementary Table 1. For *Pl-Z12-1*, *hsp70*, *hsp60*, *hsp56*, *sm30*, *sm50*, *p16*, *p19*, *msp130*, *bmp5-7*, *fg9/16/20*, *mt4*, *mt5*, *mt6*, *mt7* and *mt8* we used primers reported in the literature. In the case of *NOS*, *abc1a*, *abc4a*, *abc1b*, *abc8b*, specific primers were designed on the basis of nucleotide sequence with the help of Primer 3. The amplified fragments using Taq High Fidelity PCR System (Roche) were purified from agarose gel using QIAquick Gel extraction kit (Qiagen) and specificity of PCR products was checked by DNA sequencing. Specificity of amplification reactions was verified by melting curve analysis. The efficiency of each primer pair was calculated according to standard methods curves using the equation $E = 10^{-1/\text{slope}}$. Five serial dilutions were set up to determine Ct values and reaction efficiencies for all primer pairs. Standard curves were generated for each oligonucleotide pair using the Ct values versus the logarithm of each dilution factor. PCR efficiencies were calculated for control and target genes and were found to be about 2. Diluted cDNA was used as a template in a reaction containing a final concentration of 0.3 μM for each primer and 1× FastStart SYBR Green master mix (total volume of 10 μL). PCR amplifications were performed in a ViiA™ 7 Real Time PCR System (Applied Biosystems) thermal cycler using the following thermal profile: 95 °C for 10 min, one cycle for cDNA denaturation; 95 °C for 15 s and 60 °C for 1 min, 40 cycles for amplification; 72 °C for 5 min, one cycle for final elongation; one cycle for melting curve analysis (from 60 °C to 95 °C) to verify the presence of a single product. Each assay included a no-template control for each primer pair. To capture intra-assay variability all Real Time qPCR reactions were carried out in triplicate. Fluorescence was measured using ViiA™ 7 Software (Applied Biosystems). The expression of each gene was analyzed and internally normalized against *Pl-Z12-1* using Relative Expression Software Tool software (REST) based on the method by Pfaffl et al. (2002). Relative expression ratios above two cycles were considered significant.

2.7. Statistical analysis

Data are presented as means ± SD and analyzed by One-way ANOVA ($P < 0.05$) with Tukey's Multiple Comparison Test and Two-way ANOVA ($P < 0.05$), with Bonferroni post hoc test as reported in figure legends. Statistics was performed with GraphPad Prism 4.0 for Windows (Graphpad Software, San Diego, CA, USA).

3. Results

3.1. Involvement of NO in the abnormal development induced by cadmium and manganese

Previous studies have reported that treatment of *P. lividus* fertilized eggs with cadmium and manganese resulted in abnormal development. An increase in the number of plutei with abnormal skeletal patterning and developmental delay was dependent on metal concentration (Russo et al., 2003; Filosto et al., 2008; Pinsino et al., 2010). We treated fertilized eggs of sea urchin with cadmium and manganese at the concentrations reported in Section 2. After 48 h, morphological observations were performed in order to assess the proportion of normal and abnormal plutei. In detail, cone-shaped larvae with four fully developed arms and complete skeletal rods were considered normal, whereas larvae with defects in arm and skeleton elongation, larvae with a reduction of rudiment growth and developmentally delayed larvae were considered abnormal, following the criteria reported in Section 2. The exposure to increasing concentrations of cadmium resulted in an increase of percentage of abnormal plutei (Fig. 1) which reached values of 20 ± 1.87%, 28 ± 0.86% and 38 ± 2.98% at 5×10^{-7} M, 10^{-6} M and 5.2×10^{-6} M cadmium, respectively, compared to control (8 ± 1.33%) in the absence of cadmium. At the highest cadmium concentrations of 10^{-5} M, 2×10^{-5} M and 3×10^{-5} M the percentage of abnormal larvae was 62 ± 4.27%, 78 ± 3.12% and 100 ± 1.15%, respectively (data not shown). Defects were found mainly in the arms, which appeared malformed or absent. Often larvae showed some arms shorter than the others or in many cases the post-oral arms were absent. Moreover, a delay in development compared to control plutei was observed: treated larvae were much smaller in size and were often at gastrula or prisma stage.

As that with cadmium, manganese treatment resulted in a significant increase in the percentage of abnormal plutei with increasing manganese concentration (Fig. 1). In particular, the effect was significant starting from 1.8×10^{-5} M at which 17 ± 1.29% of the larvae appeared abnormal. At this concentration, defects mainly concerned the size of the larvae and the arm elongation and no lethal effects were observed, as shown by the normal swimming behavior of the larvae. At higher manganese concentrations of 3.6×10^{-5} M and 7.8×10^{-5} M, the percentage of abnormal

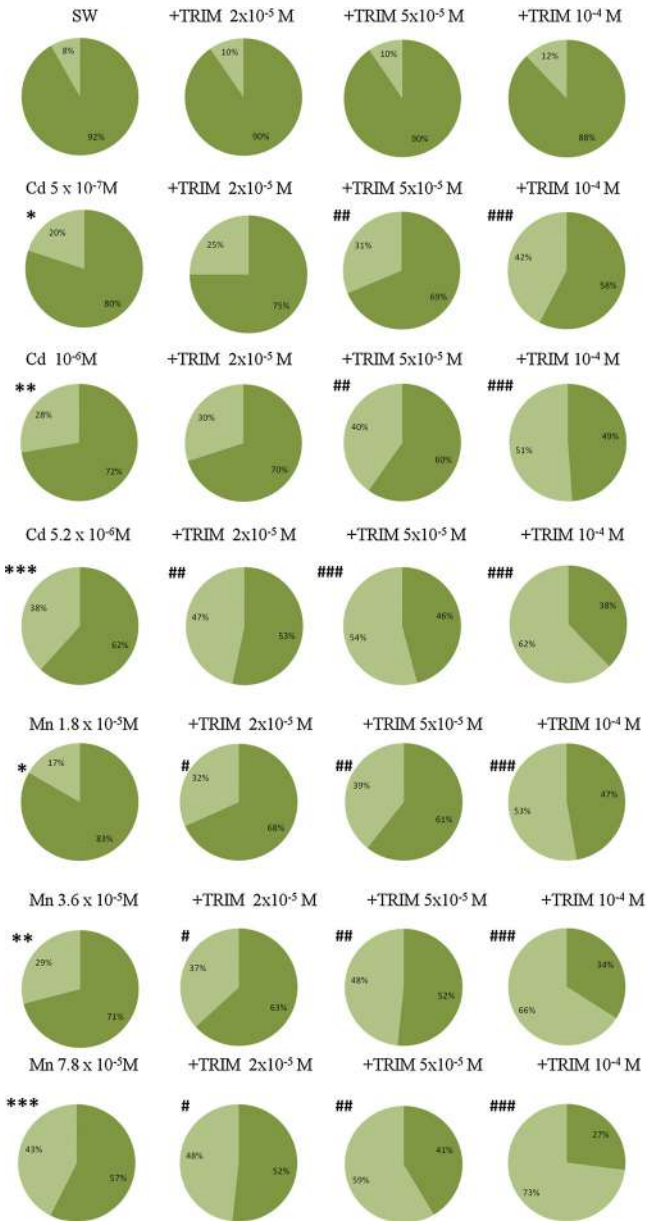

Fig. 1. Effects of cadmium and manganese on sea urchin development. Fertilized eggs were treated with the indicated cadmium and manganese concentrations in the absence and presence of TRIM, as described in Section 2. Development was monitored after 48 hpf. Significant differences compared to the control: $^{*}P<0.05$, $^{**}P<0.01$, $^{***}P<0.001$. Significant differences compared to the corresponding cadmium and manganese concentrations: $\#P<0.05$, $\#\#P<0.01$, $\#\#\#P<0.001$. One-way ANOVA ($P<0.05$), with Tukey's Multiple Comparison Test. Dark green: normal plutei. Light green: abnormal plutei. $N=3$.

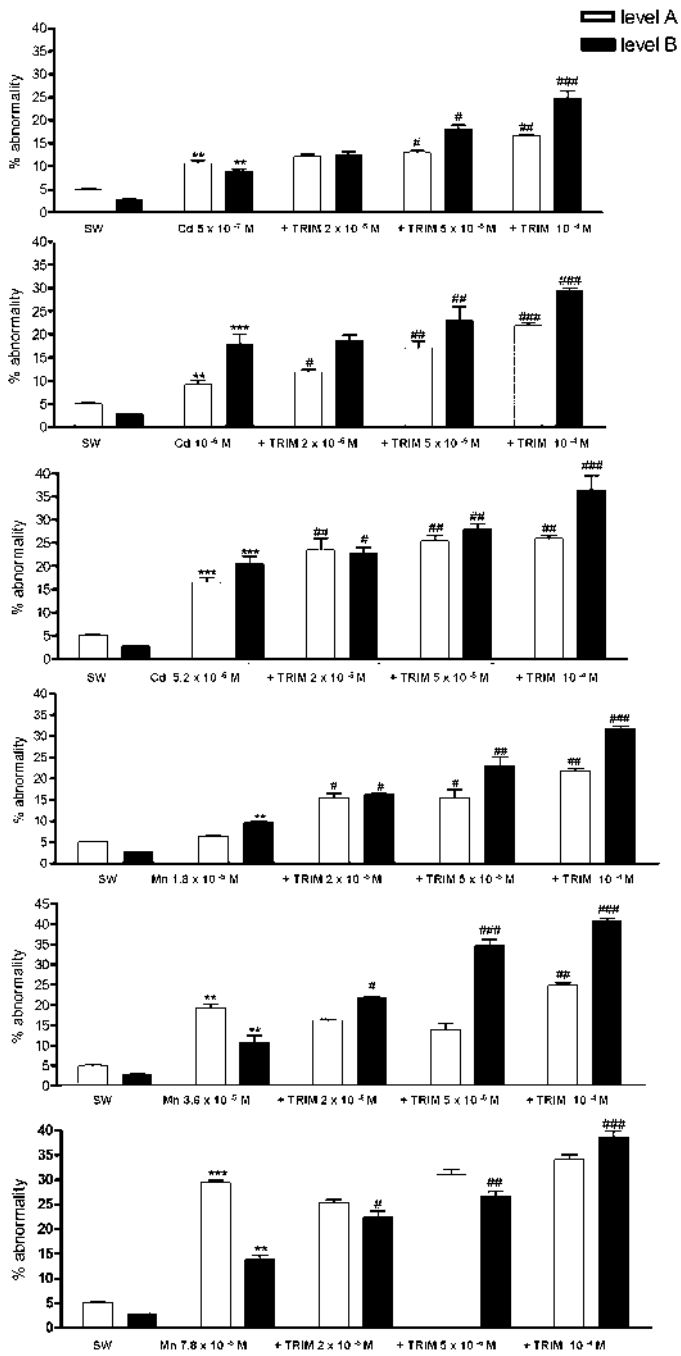

Fig. 2. Morphological analysis of the abnormal plutei following different treatments. Abnormal plutei obtained from cadmium or manganese exposure in the absence and presence of TRIM, were examined at the morphological level. The severity of the malformations were indicated as A and B, according to the criteria reported in Section 2. Significant differences compared to the control: $^{**}P<0.01$, $^{***}P<0.001$. Significant differences compared to the corresponding cadmium and manganese concentration: $\#P<0.05$, $\#\#P<0.01$, $\#\#\#P<0.001$. Two-way ANOVA, Bonferroni's post test ($P<0.05$). White: level A. Black: level B. $N=3$.

larvae was 29 ± 3.36 and $43\pm2.64\%$, respectively. At concentration values of 15.5×10^{-5} M, 31.2×10^{-5} M and 62.4×10^{-5} M, an increase in the malformations regarding arm elongation, skeletal abnormalities, developmental delay and mortality was observed and the percentage of abnormal larvae was $58\pm3.17\%$, $69\pm4.22\%$ and $98\pm5.11\%$, respectively (data not shown).

Based on these results, further experiments were performed to investigate the possible involvement of NO in the response of developing sea urchin embryos to cadmium and manganese. To this aim, metal treatments were performed in the presence of the NOS inhibitor, 1-(2-trifluoromethylphenyl)imidazole (TRIM), which interferes with the binding of both L-arginine and the cofactor BH_4 to the enzyme. To detect any morphological variation due to a reduction in the endogenous NO levels, we chose the metal concentrations which caused the formation of less than 50% of abnormal larvae. These were 5×10^{-7} M, 10^{-6} M, 5.2×10^{-6} M cadmium and 1.8×10^{-5} M, 3.6×10^{-5} M, 7.8×10^{-5} M manganese. The combined treatments of TRIM with cadmium or manganese (Fig. 1) resulted in an increase in the percentage of abnormal larvae compared to the treatment with metal alone, at all concentrations tested. TRIM alone at 2×10^{-5} M, 5×10^{-5} M and 10^{-4} M did not affect plutei morphology. This suggested the involvement of NO in the stress response induced by these metals.

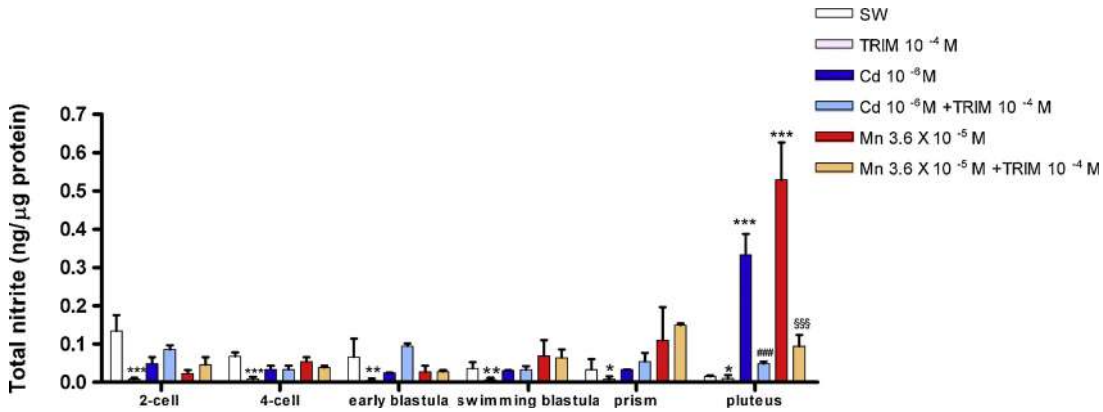

Fig. 3. Total NO concentration in sea urchin developing embryos. Embryos treated with cadmium 10^{-6} M and manganese 3.6×10^{-5} M in the absence and presence of TRIM, were examined at different developmental stages for nitrite content, as reported in Section 2. Significant difference compared to the control: *$P < 0.05$, **$P < 0.01$, ***$P < 0.001$. Significant difference compared to the cadmium treatment: ###$P < 0.001$. Significant difference compared to the manganese treatment: §§§$P < 0.001$. Two-way ANOVA, Bonferroni's post test ($P < 0.05$). $N = 3$.

A further morphological analysis of the abnormal plutei, obtained under these experimental conditions, was performed (Fig. 2). The abnormalities were classified in two different levels, A and B, as described in Section 2. They differed on the basis of the severity of the alterations. A and B were abnormal plutei with mild and severe malformations, respectively. The exposure to increasing cadmium and manganese concentrations led to an increase of both levels of malformations, although with different ratios between the two levels (Fig. 2). The combined treatments of metals with TRIM resulted in a significant increase of abnormalities at both levels at lower metal concentration and at the level B at higher metal concentrations. No significant differences between the two levels were found in larvae treated with TRIM alone (data not shown).

To further investigate the role of NO in the response to cadmium and manganese, the NO content of treated *P. lividus* embryos was examined at different developmental stages. In detail, fertilized eggs were incubated with metal concentrations resulting in a percentage of abnormal larvae of about 30%, i.e. 10^{-6} M cadmium and 3.6×10^{-5} M manganese in the absence and presence of TRIM. Then, the embryos at the following stages were collected: 2 cell, 4 cell, early blastula, swimming blastula, prisma and pluteus. NO levels were measured as total nitrite using the Griess assay. A significant increase in nitrite was observed after 48 h treatment of embryos with cadmium or manganese (Fig. 3). As expected, NO levels were reduced in the presence of TRIM. The NOS inhibitor also decreased NO levels of control samples at all developmental stages.

3.2. NO-mediated abnormal development: Gene expression

The quantitative expression levels of a series of genes implicated in different functional responses in sea urchins, including stress, skeletogenesis, detoxification and multidrug efflux, was followed. The genes encoding heat shock proteins *hsp70*, *hsp60* and *hsp56* were examined as stress genes. The genes involved in skeletogenesis included genes encoding the spicule matrix proteins *sm30*, *sm50*, *msp130*, the two proteins involved in skeleton formation *p16*, *p19*, the fibroblast growth factor *fg9/16/20*, coding for a protein involved in primary mesenchyme cell migration and skeletal morphology and the growth factor *bmp5–7*. The genes encoding metallothioneins *mt4*, *mt5*, *mt6*, *mt7* and *mt8* were investigated as genes involved in metal detoxification, whereas the genes encoding abc transporters *abc1a*, *abc1b*, *abc4a* and *abc8b* were examined for multidrug efflux in the protection system. Moreover, the expression of *NOS* was followed in relation to NO production. *Pl-Z12-1*was used as a control gene for Real Time qPCR experiments because its expression remained approximately constant in all developmental stages of sea urchin (Ragusa et al., 2013) and in different metal exposures (data not shown). Fig. 4 showed the relative expression ratios of the genes involved in the stress response (a), skeletogenesis (b), detoxification (c) and multidrug efflux (d) after cadmium (A) and manganese (B) treatment with respect to control embryos which developed in sea water without metals.

Among stress genes, *hsp70* and *hsp60* were up-regulated at the pluteus stage of 2.5- and 2.4-fold, respectively, by cadmium and manganese treatments (Fig. 4Aa, Ba). The expression of the skeletogenic genes *sm30*, *p16* and *msp130* increased at the early blastula stage 2.8-, 2.2- and 3.8-fold, respectively, after cadmium treatment (Fig. 4Ab). In contrast, the expression levels of the genes involved in skeletogenesis were not affected at this stage by manganese exposure (Fig. 4Bb). At the swimming blastula stage, in the presence of cadmium, the expression of *sm30* was down-regulated (2.4 fold), whereas *msp130* and *fg9/16/20* expression was up-regulated, showing a 6-fold increase for both genes (Fig. 4Ab). At the same stage, manganese treatment induced the expression of *p16*, *msp130* and *fg9/16/20* of 2.2-, 5.8- and 5.7-fold, respectively (Fig. 4Bb). At the prisma stage, no variation in the expression of skeletogenic genes was observed with either cadmium or manganese. At the pluteus stage, following cadmium treatment, we found a 3.2- and 3.9-fold up-regulation of *sm30* and *p19*, respectively, and a down-regulation of *msp130* of 3.9-fold (Fig. 4Ab). In the presence of manganese, the expression of *sm30* and *p19* was up-regulated by 3.8- and 3.9-fold, respectively (Fig. 4Bb). The expression of the detoxifying genes started to change at the prisma stage after metal treatment. During cadmium exposure, the expression of *mt4*, *mt5*, *mt6* and *mt8* was up-regulated by 2.9-, 4.3-, 4.1-, 2.3-fold, respectively (Fig. 4Ac). Manganese exposure caused a 2.8- and 2.7-fold up-regulation of *mt5* and *mt8*, respectively (Fig. 4Bc). At the pluteus stage, cadmium treatment induced an up-regulation of *mt4*, *mt5* and *mt8* by 2.3-, 4.9- and 2.4-fold, respectively, whereas manganese caused a 2.6-fold down-regulation of *mt6* expression (Fig. 4Ac, Bc). Regarding genes encoding abc transporters involved in multidrug efflux, the expression of *abc4a* was up-regulated (2.6-fold) by cadmium at the swimming blastula stage (Fig. 4Ad). Cadmium also caused down-regulation of *abc8b* (2.9 fold) and *abc1a* (3.3-fold) at the prisma and pluteus stages, respectively (Fig. 4Ad). In contrast, manganese treatment resulted only in the down-regulation (3.3-fold) of *abc1a* at the pluteus stage (Fig. 4Bd). No significant variations were found for the expression of *NOS*, at any developmental stage or after cadmium and manganese treatments (data not shown).

To investigate the involvement of NO in the transcription of the genes affected by cadmium or manganese treatment, their

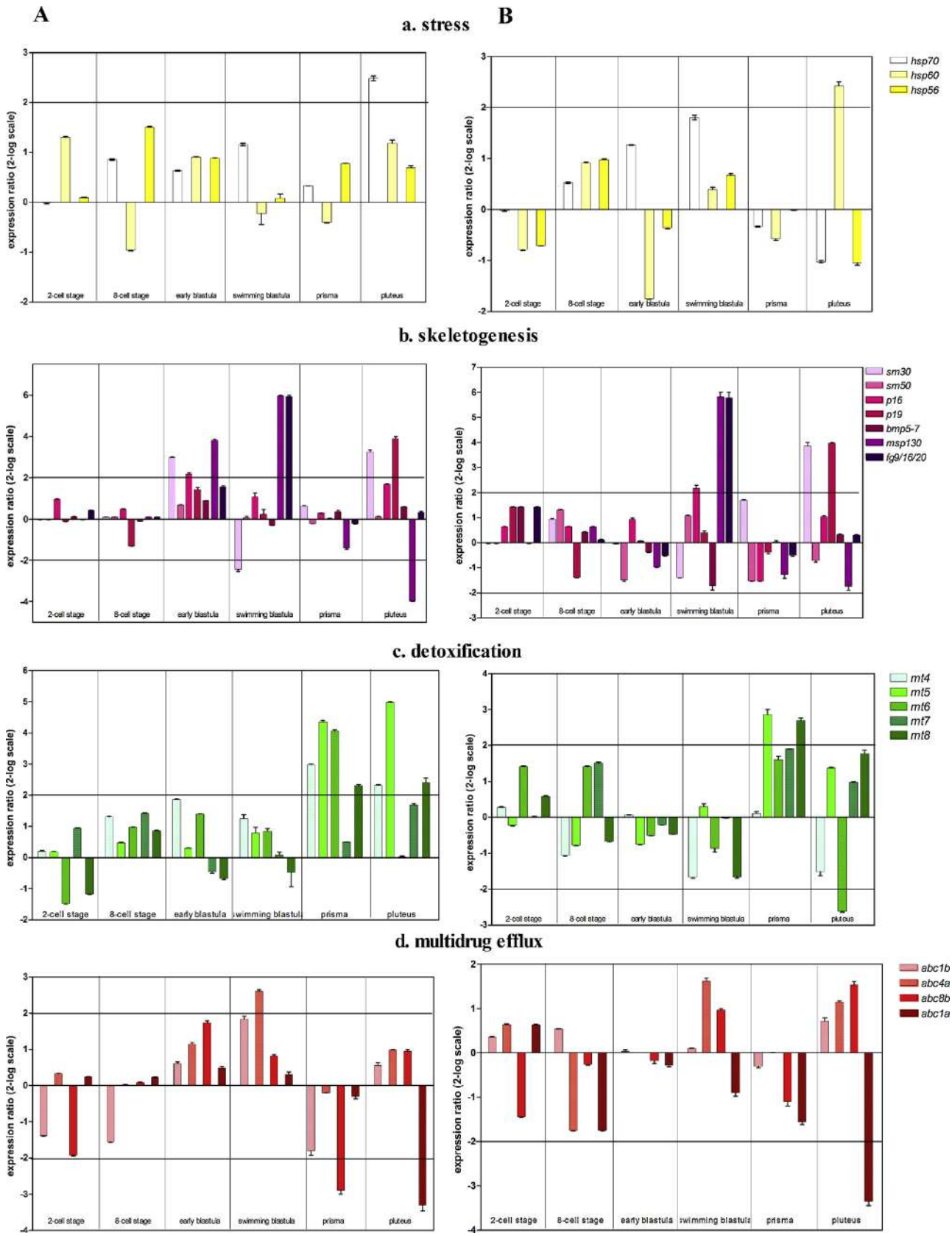

Fig. 4. Gene expression analysis in developing embryos after metal treatment. Fertilized eggs were treated with cadmium 10^{-6} M (A) and manganese 3.6×10^{-5} M (B) and different developmental stages (2-cell, 8-cell, early blastula, swimming blastula, prisma and pluteus) were examined for the transcriptional expression of genes involved in stress (a), skeletogenesis (b), detoxification (c) and multidrug efflux (d) by Real Time qPCR. Data are reported as a fold difference in the expression levels of the analyzed genes, compared to control (mean ± SD), embryos developed in sea water without metals. Fold differences greater than ±2 (see dotted horizontal guidelines at values of 2 and −2) were considered significant.

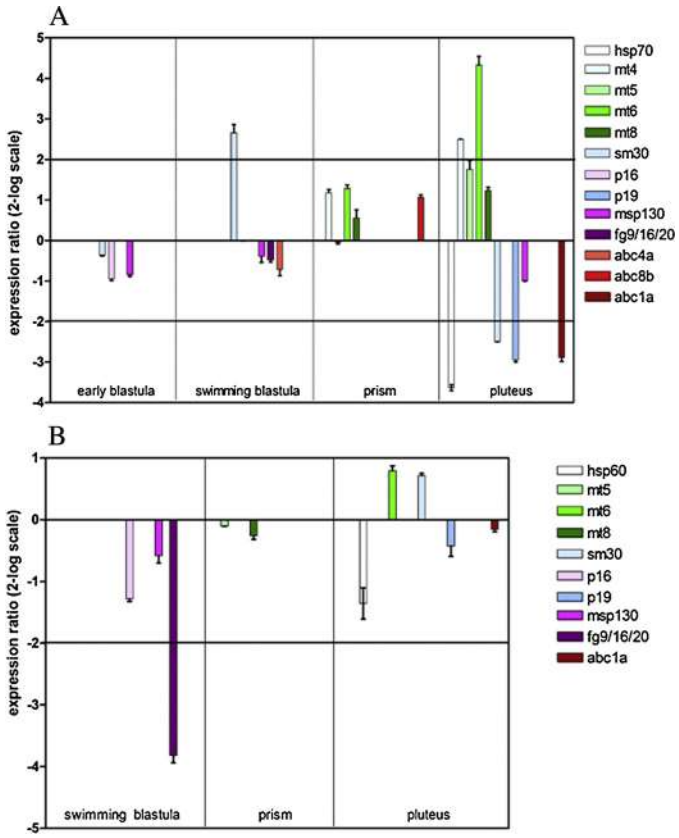

Fig. 5. Gene expression analysis in developing embryos treated with metals under low levels of NO. Fertilized eggs were treated with 10^{-6} M cadmium + TRIM 10^{-4} M (A) and 3.6×10^{-5} M manganese + TRIM 10^{-4} M (B). Samples collected at early blastula, swimming blastula, prism and pluteus stage were examined for gene expression by Real Time qPCR. Data are reported as a fold difference in the expression levels of the analyzed genes, compared to control (mean ± SD), embryos in sea water without metals. Fold differences greater than ±2 (see horizontal guidelines at values of 2 and −2) were considered significant.

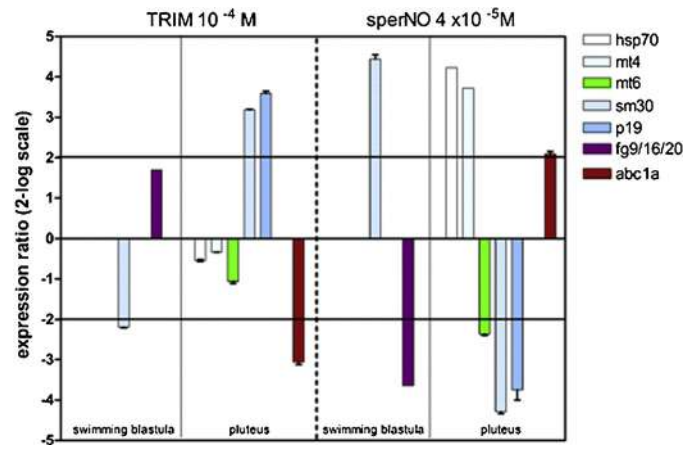

Fig. 6. Gene expression analysis in developing embryos under different NO levels. Fertilized eggs were treated with 10^{-4} M TRIM or 4×10^{-5} M sperNO. Samples, collected at swimming blastula and pluteus stage, were examined for gene expression by Real Time qPCR. Data are reported as a fold difference in the expression levels of the analyzed genes, compared to control (mean + SD), embryos in sea water or in the presence of spermine in the case of sperNO. Fold differences greater than ±2 (see horizontal guidelines at values of 2 and −2) were considered significant.

expression was analyzed under reduced levels of NO, i.e. in the presence of the NOS inhibitor TRIM. The expression of these genes was reported with respect to that of the metal alone (Fig. 5). During cadmium + TRIM exposure, *sm30* was up-regulated (2.6-fold) at the swimming blastula stage. At the pluteus stage, *mt4* (2.5-fold) and *mt6* (4.3-fold) were up-regulated, whereas *hsp70* (3.6-fold), *sm30* (2.5-fold), *p19* (2.9-fold) and *abc1a* (2.9-fold) were down-regulated (Fig. 5A). In the case of manganese, addition of TRIM caused down-regulation (3.8-fold) of *fg9/16/20* at the swimming blastula stage (Fig. 5B).

To further demonstrate that NO affected *hsp70*, *mt4*, *mt6*, *sm30*, *p19*, *fg9/16/20* and *abc1a* expression, their mRNA levels were measured after modifying endogenous NO levels with the NOS inhibitor TRIM and the NO donor sperNO (Fig. 6). As control for sperNO treatment, we used spermine, the product derived from sperNO after NO release. Under low levels of NO with TRIM, we found a down-regulation of *sm30* (2.2-fold) at the swimming blastula stage and an up-regulation of *sm30* (3.2-fold) and *p19* (3.6-fold) and down-regulation of *abc1a* (3.1-fold) at the pluteus stage. In the presence of sperNO, at the swimming blastula stage, *sm30* was up-regulated (4.4-fold) and *fg9/16/20* was down-regulated (3.6-fold). At the pluteus stage, *hsp70*, *mt4* and *abc1a* were up-regulated 4.2-, 3.7-, 2-fold, respectively, whereas *mt6*, *sm30* and *p19* were down-regulated 2.3-, 4.3- and 3.6-fold respectively.

Additional experiments were performed to detect if the expression of some genes was affected only by the combined treatment of metal + TRIM and not by metal or TRIM alone. During cadmium + TRIM exposure, *hsp60* and *fg9/16/20* were down-regulated (2.6- and 2.3-fold) at the swimming blastula and pluteus stage, respectively. In the case of manganese, the expression of *hsp60* (3.8-fold), *sm30* (5.7-fold), *sm50* (3.5-fold) and *p16* (2.49-fold) increased as a response to the metal + TRIM exposure at the early blastula stage, whereas *mt8* (2.48-fold) and *abc1b* (3.7-fold) were down-regulated. At the prisma stage, an up-regulation of *fg9/16/20* (2.5-fold) was observed.

4. Discussion

The results of this study expanded previous investigations on the effects of cadmium and manganese on sea urchin development (Filosto et al., 2008; Pinsino et al., 2010), providing new insights at phenotypic and gene levels and highlighting the involvement of NO in the stress response caused by these metals.

In this paper, a *vis-a-vis* comparison of the effects of cadmium and manganese on the developing embryos of *P. lividus* was performed for the first time, thus allowing us to identify analogies and differences between the two metals. In both cases, the percentage of abnormal plutei increased with increasing metal concentrations. However, some differences were evident. Cadmium exposure led to important skeletal malformations with high levels of larvae with delayed development, whereas manganese treatment caused more specific types of malformations, particularly in the arms, with a lower percentage of larvae with general delay in development, thus revealing a lower toxicity compared to cadmium, in agreement with previous experiments in *Arbacia crassispina* (Kobayashi and Okamura, 2005). Moreover, a series of genes encoding proteins involved in the stress response, skeletogenesis, detoxification and multidrug efflux were differentially modulated by these metals at environmentally relevant concentrations. In detail, the concentration of cadmium (10^{-6} M) used in this study corresponds to highly polluted sea water and that of manganese (3.6×10^{-5} M = 7124 $\mu g\,L^{-1}$) is close to the maximum value (10,000 $\mu g\,L^{-1}$) reported in natural water for this metal (CICAD, 2004). The different response of sea urchin embryos to cadmium and manganese is probably correlated to the different role of these metals. Cadmium is a potent pollutant (Flick et al., 1971), toxic even at very low concentrations (Foulkes, 2000); it does not have any biological role and its presence in the environment has grown

in the last years because of its large use in some industrial and agricultural activities (Rule et al., 2006). Manganese, on the other hand, is a naturally occurring metal required in trace amounts by the organisms where it plays a number of essential roles in many metabolic functions, in cellular protection, replication mechanisms and in bone mineralization processes (ATSDR, 2008; Daly, 2009; Santamaria, 2008). However, the exposure to high manganese levels can cause toxicity (CICAD, 2004; Gerber et al., 2002; Lima et al., 2008) and, due to the massive production of manganese-containing compounds, this metal is being considered as an emergent pollutant, especially in the aquatic environment (Satyanarayana and Saraf, 2007).

An important outcome of this study is the demonstration that NO was produced in response to cadmium and manganese treatments. Moreover, the examination of gene expression after metal treatments, as well as under different NO levels, has allowed us to get an insight into the involvement of NO in mediating the effects of cadmium and manganese on transcriptional gene expression. An overall picture of our results is schematically summarized in supplementary Table 2. Our finding that the expression of the genes *sm30*, *hsp70* and *p19* following cadmium treatment and *fg9/16/20* after manganese incubation was reversed by NOS inhibition with TRIM at some developmental stages, revealed that NO mediated the effect of the metals on the expression of these genes. The opposite effect of sperNO and TRIM on the expression of these genes indicates that NO levels could play a role in their regulation. A further insight was provided by the comparison of the effects of sperNO and metal alone. In particular, cadmium treatment for 48 h induced the expression of *hsp70*, similar to that observed with the NO donor sperNO. This result, together with data on NO determination, suggests that NO formed after cadmium treatment can directly up-regulate *hsp70* expression (Fig. 7A). The involvement of NO in inducing the expression of *hsp70* has been previously reported in sea urchin embryos in the case of another stress agent, the diatom toxin decadienal (Romano et al., 2011). Contrary to *hsp70*, the expression of *sm30* and *p19* regulated by cadmium, as well as *fg9/16/10* by manganese, showed an opposite trend compared to sperNO treatment alone. This finding suggests that the metals affect the expression of these genes not directly but through a *x*-factor, which is regulated by changes in NO levels after metal treatment (Fig. 7B). The lack of effect of TRIM on the expression of *mt4* and *abc1a* after cadmium treatment for 48 h suggested that NO is not involved in the regulation of these genes by cadmium (supplementary Table 2). The picture emerging from this study was further complicated considering that the expression of some genes (*hsp60*, *mt8*, *sm30*, *sm50*, *p16*, *abc1b* and *fg9/16/20*) at certain developmental stages was affected only by the combined treatment of the metals with TRIM and not by sperNO or TRIM alone (Fig. 7C). This result suggests that during metal treatment an already unknown *x*-factor was expressed, which, in response to changes in NO levels, regulated the expression of the studied genes. The lack of effect of sperNO or TRIM indicated that this factor is present only when sea urchin embryos are exposed to metals. Overall these findings demonstrate that NO differentially regulates gene expression in response to cadmium and manganese treatments. In conclusion, with cadmium, NO directly activated *hsp70* and indirectly regulated some stress (*hsp60*) and skeletogenic (*sm30*, *p19*, *fg9/16/20*) genes. On the other hand, with manganese, NO indirectly affected the expression of stress (*hsp60*), skeletogenic (*sm30*, *sm50*, *p16*, *fg9/16/20*) as well as multidrug efflux genes (*abc1b*) and detoxification genes (*mt8*).

The ability of NO to regulate gene expression has also been demonstrated in different cells and organisms (Heemskerk et al., 2007; Nakaya et al., 2000; Rossig et al., 2000). The kinetics of gene activation by NO was investigated in cultured fibroblasts exposed to NO donor and three distinct waves of gene activity were identified (Hemish et al., 2003). The first one was generated within 30 min of treatment and represented the primary gene targets, whereas the subsequent waves were due to further cascades of NO-induced gene expression. Specific signaling pathways used by NO to activate gene expression have been identified, including PI 3-kinase, PKC, NF-kappa B and p53. It has been reported that NO affected gene expression directly influencing the activity of transcription factors or modulating upstream signaling cascades, or mRNA stability and translation or the processing of the primary gene products (Bogdan et al., 2001).

In conclusion, our finding that NO mediated the stress response induced by different stress agents, such as cadmium and manganese (this work) and decadienal (Romano et al., 2011), pointed to NO as a mediator of different environmental stress agents in sea urchins.

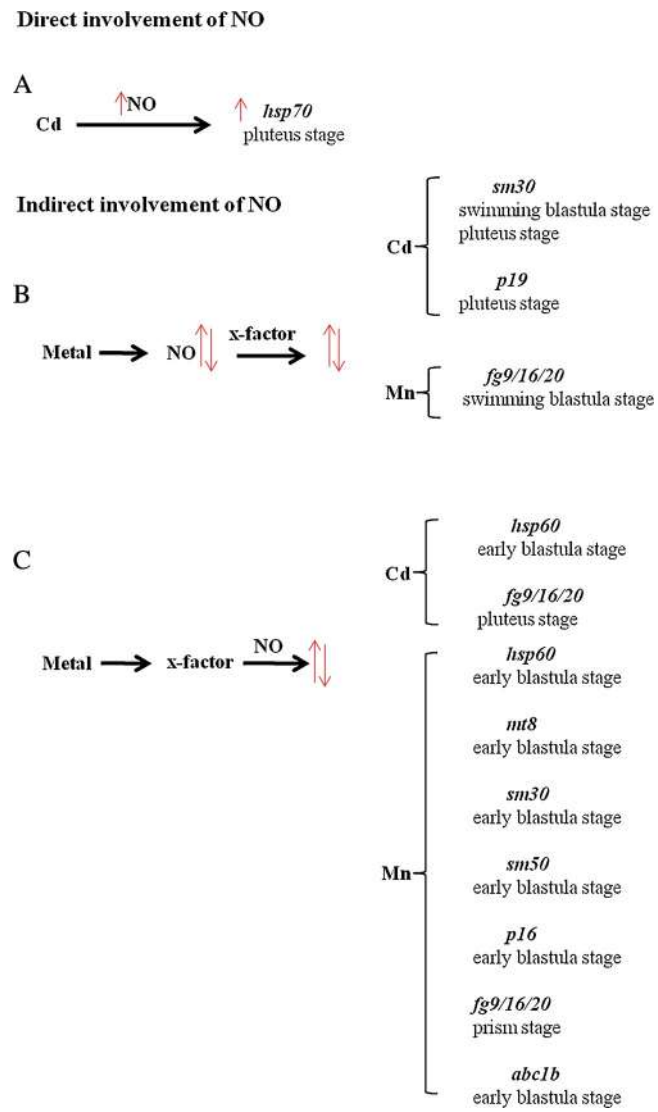

Fig. 7. Schematic representation of the NO involvement in the modulation of gene expression in developing embryos of sea urchin exposed to cadmium and manganese. (A) Direct involvement of NO: metal induces an increase of NO levels which up-regulates *hsp70* expression. (B) Indirect involvement of NO: metal treatment causes a variation in NO levels which affects an unknown factor, regulating gene expression. (C) Indirect involvement of NO: metal treatment affects an unknown factor which regulates gene expression through NO.

Acknowledgements

This work has been partially funded by the Flagship RITMARE – The Italian Research for the Sea – coordinated by the Italian National Research Council and funded by the Italian Ministry of Education, University and Research within the National Research Program 2011–2013. Oriana Migliaccio has been supported by a SZN PhD fellowship. Immacolata Castellano has been supported by a SZN post doc fellowship.

We thank the Molecular Biology Service for gene sequencing and Davide Caramiello and the service Marine Resources for Research for assistance with living organisms. We acknowledge Valeria Matranga for her helpful advice and discussion as external supervisor of Oriana Migliaccio PhD program. We acknowledge Thierry La Page for the use of the web site http://octopus.obs-vlfr.fr/blast/blast_oursin.html.

Appendix A. Supplementary data

Supplementary data associated with this article can be found, in the online version, at http://dx.doi.org/10.1016/j.aquatox.2014.08.007.

References

Agnello, M., Filosto, S., Scudiero, R., Rinaldi, A.M., Roccheri, M.C., 2007. Cadmium induces an apoptotic response in sea urchin embryos. Cell Stress Chaperones 12, 44e50.

ATSDR, 2008. Draft Toxicological Profile for Manganese. Agency for Toxic Substances and Disease Registry. Division of Toxicology and Environmental Medicine/Applied Toxicology Branch, Atlanta, Georgia.

Beiras, R., Fernandez, N., Bellas, J., Besada, V., Gonzalez-Quijano, A., Nunes, T., 2003. Integrative assessment of marine pollution in Galician estuaries using sediment chemistry, mussel bioaccumulation, and embryo-larval toxicity bioassays. Chemosphere 52, 1209–1224.

Bogdan, S., Senkel, S., Esser, F., Ryffel, G.U., Pogge, V., Strandmann, E., 2001. Misexpression of Xsiah-2 induces a small eye phenotype in Xenopus. Mech. Dev. 103, 61–69.

Bonaventura, R., Poma, V., Costa, C., Matranga, V., 2005. UVB radiation prevents skeleton growth and stimulates the expression of stress markers in sea urchin embryos. Biochem. Biophys. Res. Commun. 328, 150–157.

Bonaventura, R., Poma, V., Russo, R., Zito, F., Matranga, V., 2006. Effects of UV-B radiation on development and hsp70 expression in sea urchin cleavage embryos. Mar. Biol. 149, 79–86.

Bonaventura, R., Zito, F., Costa, C., Giarrusso, S., Celi, F., Matranga, V., 2011. Stress response gene activation protects sea urchin embryos exposed to X-rays. Cell Stress Chaperones 16, 681–687.

Bouchard, J.N., Yamasaki, H., 2008. Heat stress stimulates nitric oxide production in *Symbiodinium microadriaticum*: a possible linkage between nitric oxide and the coral bleaching phenomenon. Plant Cell Physiol. 49, 641–652.

Boudouresque, C.F., Verlaque, M., 2013. *Paracentrotus lividus*. In: Lawrence, J.M. (Ed.), Edible Sea Urchins: Biology and Ecology. Elsevier, Amsterdam, pp. 297–328.

Carballeira, C., Ramos-Gómez, J., Martín-Díaz, L., DelValls, T.A., 2012. Identification of specific malformations of sea urchin larvae for toxicity assessment: application to marine pisciculture effluents. Mar. Environ. Res. 77, 12–22.

Castellano, I., Ercolesi, E., Palumbo, A., 2014. Nitric oxide affects ERK signaling through down-regulation of MAP kinase phosphatase levels during larval development of the ascidian *Ciona intestinalis*. PLoS One 9 (7), e102907.

Chiarelli, R., Agnello, M., Roccheri, M.C., 2011. Sea urchin embryos as a model system for studying autophagy induced by cadmium stress. Autophagy 7, 1028–1034.

Chiarelli, R., Agnello, M., Bosco, L., Roccheri, M.C., 2014. Sea urchin embryos exposed to cadmium as an experimental model for studying the relationship between autophagy and apoptosis. Mar. Environ. Res. 93, 47–55.

CICAD, 2004. Manganese and its compounds: environmental aspects. Concise International Chemical Assessment Document, vol. 63. WHO, Geneva, Switzerland.

Costa, C., Karakostis, K., Zito, F., Matranga, V., 2012. Phylogenetic analysis and expression patterns of p16 and p19 in *Paracentrotus lividus* embryos. Dev. Genes Evol. 222, 245–251.

Daly, M.J., 2009. A new perspective on radiation resistance based on *Deinococcus radiodurans*. Nat. Rev. Microbiol. 7, 237–244.

Ercolesi, E., Tedeschi, G., Fiore, G., Negri, A., Maffioli, E., d'Ischia, M., Palumbo, A., 2012. Protein nitration as footprint of oxidative stress-related nitric oxide signaling pathways in developing *Ciona intestinalis*. Nitric Oxide. 27, 18–24.

Filosto, S., Roccheri, M.C., Bonaventura, R., Matranga, V., 2008. Environmentally relevant cadmium concentrations affect development and induce apoptosis of *Paracentrotus lividus* larvae cultured in vitro. Cell Biol. Toxicol. 24, 603–610.

Flick, D.F., Krayhill, H.F., Dimitroff, J.M., 1971. Toxic effects of cadmium. A review. Environ. Res. 4, 71–85.

Foulkes, E.C., 2000. Transport of toxic metal across cell membranes. Proc. Soc. Exp. Biol. Med. 223, 234–240.

Gerber, G.B., Leonard, A., Hantson, P., 2002. Carcinogenicity, mutagenicity and teratogenicity of manganese compounds. Crit. Rev. Oncol. Hematol. 42, 25–34.

Giovine, M., Pozzolino, M., Favre, A., Bavestrello, G., Cerrano, C., Ottaviani, F., Chiarantini, L., Cerasi, A., Cangiotti, M., Zocchi, E., Scarfì, S., Sarà, M., Benatti, U., 2001. Heat stress-activated, calcium-dependent nitric oxide synthase in sponges. Nitric Oxide 5, 427–431.

Giudice, G., Sconzo, G., Roccheri, M.C., 1999. Studies on heat shock protein in sea urchin development. Dev. Growth Differ. 41, 375–380.

Green, L.C., Wagner, D.A., Glogowski, J., 1982. Analysis of nitrate, nitrite and nitrate in biological fluids. Anal. Biochem. 126, 131–138.

Heemskerk, S., van Koppen, A., van den Broek, L., Poelen, G.J., Wouterse, A.C., Dijkman, H.B., Russel, F.G., Masereeuw, R., 2007. Nitric oxide differentially regulates renal ATP-binding cassette transporters during endotoxemia. Pflugers Arch. 454, 321–334.

Hemish, J., Nakaya, N., Mittal, V., Enikolopov, G., 2003. Nitric oxide activates diverse signaling pathways to regulate gene expression. J. Biol. Chem. 278, 42321–42329.

Kobayashi, N., Okamura, H., 2005. Effects of heavy metals on sea urchin embryo development. Part 2. Interactive toxic effects of heavy metals in synthetic mine effluents. Chemosphere 61, 1198–1203.

Lima, P.D.L., Vasconcellos, M.C., Bahia, M.O., Montenegro, R.C., Pessoa, C.O., Costa-Lotufo, L.V., Moraes, M.O., Burbano, R.R., 2008. Genotoxic and cytotoxic effects of manganese chloride in cultured human lymphocytes treated in different phases of cell cycle. Toxicol. In Vitro 22, 1032–1037.

Marrone, V., Piscopo, M., Romano, G., Ianora, A., Palumbo, A., Costantini, M., 2012. Defensome against toxic diatom aldehydes in the sea urchin *Paracentrotus lividus*. PLoS One 7, e31750.

Matranga, V., Zito, F., Costa, C., Bonaventura, R., Giarrusso, S., Celi, F., 2010. Embryonic development and skeletogenic gene expression affected by X-rays in the Mediterranean sea urchin *Paracentrotus lividus*. Ecotoxicology 19, 530–537.

Mattiello, T., Fiore, G., Brown, E.R., d'Ischia, M., Palumbo, A., 2010. Nitric oxide mediates the glutamate-dependent pathway for neurotransmission in *Sepia officinalis* chromatophore organs. J. Biol. Chem. 285, 24154–24163.

Mattiello, T., Costantini, M., Di Matteo, B., Livigni, S., Andouche, A., Bonnaud, L., Palumbo, A., 2012. The dynamic nitric oxide pattern in developing cuttlefish *Sepia officinalis*. Dev. Dyn. 241, 390–402.

Migliaccio, O., Castellano, I., Romano, G., Palumbo, A., 2014. Response of sea urchin to environmental stress. In: Edgar Raymond Banks (Ed.), Sea Urchins: Habitat, Embryonic Development and Importance in the Environment. Nova Science Publishers, Inc., New York, pp. 29–51.

Nakaya, N., Lowe, S.W., Taya, Y., Chenchik, A., Enikolopov, G., 2000. Specific pattern of p53 phosphorylation during nitric oxide-induced cell cycle arrest. Oncogene 19, 6369–6375.

Pagano, G., Cipollaro, M., Corsale, G., Esposito, A., Ragucci, E., 1986. The Sea Urchin: Bioassay for the Assessment of Damage from Environmental Contaminants. American Society for Testing and Materials, Philadelphia, pp. 67–92.

Pfaffl, M.W., Horgan, G.W., Dempfle, L., 2002. Relative expression software tool (REST) for group-wise comparison and statistical analysis of relative expression results in real-time PCR. Nucleic Acids Res. 30, e36.

Pinsino, A., Matranga, V., Trinchella, F., Roccheri, M.C., 2010. Sea urchin embryos as an in vivo model for the assessment of manganese toxicity: developmental and stress response effects. Ecotoxicology 19, 555–562.

Pinsino, A., Roccheri, M.C., Costa, C., Matranga, V., 2011. Manganese interferes with calcium, perturbs ERK signaling and produces embryos with no skeleton. Toxicol. Sci. 23, 217–230.

Pinsino, A., Roccheri, M.C., Matranga, V., 2013. Manganese overload affects p38 MAPK phosphorylation and metalloproteinase activity during sea urchin embryonic development. Mar. Environ. Res. 93, 64–69.

Radenac, G., Fichet, D., Miramand, P., 2001. Bioaccumulation and toxicity of four dissolved metals in *Paracentrotus lividus* sea-urchin embryo. Mar. Environ. Res. 51, 151–166.

Ragusa, M.A., Costa, S., Gianguzza, M., Roccheri, M.C., Gianguzza, F., 2013. Effect of cadmium exposure on sea urchin development assessed by SSH and RT-qPCR: metallothionein genes in marine invertebrates: focus on *Paracentrotus lividus* sea urchin development. Mol. Biol. Rep. 40, 2157–2167.

Roccheri, M.C., Agnello, M., Bonaventura, R., Matranga, V., 2004. Cadmium induces the expression of specific stress proteins in sea urchin embryos. Biochem. Biophys. Res. Commun. 321, 80–87.

Roccheri, M.C., Matranga, V., 2009. Cellular, biochemical and molecular effects of cadmium on *Paracentrotus lividus* sea urchin development. In: Parvau, R.G. (Ed.), Cadmium in the Environment. Nova Science Publishers, Inc., New York, pp. 1–30.

Romano, G., Miralto, A., Ianora, A., 2010. Teratogenic effects of diatom metabolites on sea urchin *Paracentrotus lividus* embryos. Mar. Drugs 8, 950–967.

Romano, G., Costantini, M., Buttino, I., Ianora, A., Palumbo, A., 2011. Nitric oxide mediates the stress response induced by diatom aldehydes in the sea urchin *Paracentrotus lividus*. PLoS One 6, e25980.

Rossig, L., Haendeler, J., Hermann, C., Malchow, P., Urbich, C., Zeiher, A.M., Dimmeler, S., 2000. Nitric oxide down-regulates MKP-3 mRNA levels: involvement in endothelial cell protection from apoptosis. J. Biol. Chem. 275, 25502–25507.

Rule, K.L., Comber, S.D., Ross, D., Thornton, A., Makropoulos, C.K., Rautiu, R., 2006. Diffuse sources of heavy metals entering an urban wastewater catchment. Chemosphere 63, 64–72.

Russo, R., Bonaventura, R., Zito, F., Schroeder, H.C., Müller, I., Müller, W.E.G., Matranga, V., 2003. Stress to cadmium monitored by metallothionein gene induction in *Paracentrotus lividus* embryos. Cell Stress Chaperones 8, 232–241.

Santamaria, A.B., 2008. Manganese exposure, essentiality and toxicity. Indian J. Med. Res. 128, 484–500.

Satyanarayana, Y.V., Saraf, R., 2007. Iron and manganese contamination: sources, adverse effects and control methods. J. Environ. Sci. Eng. 49, 333–336.

Sugni, M., Tremolada, P., Porte, C., Barbaglio, A., Bonasoro, F., Carnevali, M.D.C., 2010. Chemical fate and biological effects of several endocrine disrupters compounds in two echinoderm species. Ecotoxicology 19, 538–554.

Vardi, A., Formiggini, F., Casotti, R., De Martino, A., Ribalet, F., Miralto, A., Bowler, C., 2006. A stress surveillance system based on calcium and nitric oxide in marine diatoms. PLoS Biol. 4, e60.

Varrella, S., Romano, G., Ianora, A., Bentley, M.G., Ruocco, N., Costantini, M., 2014. Molecular response to toxic diatom-derived aldehydes in the sea urchin *Paracentrotus lividus*. Mar. Drugs 12, 2089–2113.

Zhang, Z.B., Liu, C.Y., Wu, Z.Z., Xing, L., Li, P.F., 2006. Detection of nitric oxide in culture media and studies on nitric oxide formation by marine microalgae. Med. Sci. Monit. 12, 75–85.

PLOS | ONE

RESEARCH ARTICLE

Maternal Exposure to Cadmium and Manganese Impairs Reproduction and Progeny Fitness in the Sea Urchin *Paracentrotus lividus*

Oriana Migliaccio[1], Immacolata Castellano[1], Paola Cirino[2], Giovanna Romano[3], Anna Palumbo[1]*

1 Department of Biology and Evolution of Marine Organisms, Stazione Zoologica Anton Dohrn, Villa Comunale, Naples, Italy, **2** Marine Resources for Research Service, Stazione Zoologica Anton Dohrn, Villa Comunale, Naples, Italy, **3** Department of Integrative Marine Ecology, Stazione Zoologica Anton Dohrn, Villa Comunale, Naples, Italy

* anna.palumbo@szn.it

CrossMark
click for updates

OPEN ACCESS

Citation: Migliaccio O, Castellano I, Cirino P, Romano G, Palumbo A (2015) Maternal Exposure to Cadmium and Manganese Impairs Reproduction and Progeny Fitness in the Sea Urchin *Paracentrotus lividus*. PLoS ONE 10(6): e0131815. doi:10.1371/journal.pone.0131815

Editor: Hector Escriva, Laboratoire Arago, FRANCE

Received: April 8, 2015

Accepted: June 7, 2015

Published: June 30, 2015

Copyright: © 2015 Migliaccio et al. This is an open access article distributed under the terms of the Creative Commons Attribution License, which permits unrestricted use, distribution, and reproduction in any medium, provided the original author and source are credited.

Data Availability Statement: All relevant data are within the paper and its Supporting Information files.

Funding: This work has been partially funded by the Flagship RITMARE—The Italian Research for the Sea—coordinated by the Italian National Research Council and funded by the Italian Ministry of Education, University and Research within the National Research Program 2011–2013. Oriana Migliaccio has been supported by a SZN PhD fellowship. Immacolata Castellano has been supported by a SZN post doc fellowship. The funders had no role in study design, data collection and

Abstract

Metal contamination represents one of the major sources of pollution in marine environments. In this study we investigated the short-term effects of ecologically relevant cadmium and manganese concentrations (10^{-6} and 3.6×10^{-5} M, respectively) on females of the sea urchin *Paracentrotus lividus* and their progeny, reared in the absence or presence of the metal. Cadmium is a well-known heavy metal, whereas manganese represents a potential emerging contaminant, resulting from an increased production of manganese-containing compounds. The effects of these agents were examined on both *P*. *lividus* adults and their offspring following reproductive state, morphology of embryos, nitric oxide (NO) production and differential gene expression. Here, we demonstrated that both metals differentially impaired the fertilization processes of the treated female sea urchins, causing modifications in the reproductive state and also affecting NO production in the ovaries. A detailed analysis of the progeny showed a high percentage of abnormal embryos, associated to an increase in the endogenous NO levels and variations in the transcriptional expression of several genes involved in stress response, skeletogenesis, detoxification, multi drug efflux processes and NO production. Moreover, we found significant differences in the progeny from females exposed to metals and reared in metal-containing sea water compared to embryos reared in non-contaminated sea water. Overall, these results greatly expanded previous studies on the toxic effects of metals on *P*. *lividus* and provided new insights into the molecular events induced in the progeny of sea urchins exposed to metals.

analysis, decision to publish, or preparation of the manuscript.

Competing Interests: The authors have declared that no competing interests exist.

Introduction

Metals have been considered highly toxic pollutants and their presence in the environment has been increased in the last decades due to anthropogenic activities [1]. Aquatic ecosystems can be exposed to a great variety of metals whose chemical forms and concentrations are determined by different processes [2]. They can be distinguished in essential metals, which are required to support biological activities, and non-essential metals with unknown biological functions [3]. Some metals, including cadmium, have been extensively studied for many years [4] and many features have been identified such as the environmental persistence, the capacity of long-range transport, the bio-magnification along the food chain and bio-accumulation in animal tissues and the potential impact on humans and environmental health [5]. Other metals, such as manganese, essential in low amount in the organisms but toxic at high concentrations [6, 7], have only recently begun to be explored as emergent factors in the environmental contamination for the increasing production of metal-containing compounds. Both metals also differ in many aspects. Cadmium is one of the most widely distributed and dangerous pollutants for marine organisms [8–10]. Its concentration in the sea ranges from 10^{-3} to 2 μg/L depending on different factors, such as seawater latitudes [11, 12], depth [13] and pollution of different sites [14–16]. In some particular cases due to urbanization and industrialization, higher levels (0.2–72 mg/L) have been reported [9, 17]. Manganese, on the other hand, is a naturally occurring metal, toxic only at high levels [18–20]. Manganese concentration in marine environments is governed by pH, oxygen concentration and redox conditions. In natural sea water it ranges from 10 to 10,000 μg/L [21] but during hypoxia can reach values up to 22 mg/L [22, 23]. Toxic effects of metals have been investigated using different marine model systems and performing various biological assays/tests. The sea urchin *Paracentrotus lividus*, a key species in the Mediterranean sea, provides a unique and suitable tool for the evaluation of metal toxicity. The easy gamete preparation, the embryo transparency useful to detect several kinds of malformations, the relative synchrony and rapidity of development and the embryos/larvae sensitivity make the planktonic life stages suitable for embryo-toxicity tests [24, 25] and monitoring or risk assessment programs [15]. Moreover, *P. lividus* life is influenced by human activities, especially in the coastal zones [26]. These characteristics, together with its world-wide distribution, abundance and sedentary habits, prompted also the use of adult sea urchins as biological–biochemical indicators of local pollution [25, 27, 28].

The toxic effects of cadmium and manganese on sea urchin developing embryos have been extensively investigated [6, 7, 9, 29–33]. Recently, we have demonstrated that the physiological messenger nitric oxide (NO), produced by NO synthase (NOS) trough oxidation of L-arginine, mediates the stress response induced by environmentally relevant concentrations of cadmium and manganese in *P. lividus* developing embryos. Moreover, by using pharmacological and molecular approaches we found that the transcriptional expression of some metal-induced genes involved in stress response, skeletogenesis, detoxification and multi-drug efflux was directly or indirectly regulated by NO [10]. Interestingly, NO is also involved in the response of *P. lividus* embryos to the toxic diatom-derived aldehyde decadienal [34]. On the contrary, only few studies have been performed to understand the effects of metals on adult sea urchins and their offspring. The progeny of *Strongylocentrotus intermedius* sea urchin, collected in the coastal zone of Amur Bay, characterized by an extensive pollution, showed a delayed development together with a large number of anomalies [8, 35, 36]. Similar results were also obtained in other studies on sea urchins collected from other polluted habitats (e.g. Naidenko) [37]. In *Sphaerechinus granularis* from the Bay of Brest, a large number of blocked and delayed embryos were observed, due to the presence of high levels of heavy metals in sea urchin gonads [38].

In this study we investigated the effects of cadmium and manganese, at concentrations mimicking polluted sea water, on female sea urchins *P. lividus* exposed for 2 and 9 days and on their offspring. Here, we show that both metals differentially impaired the fertilization process causing modifications in the reproductive state. Moreover, we found an abnormal development of the offspring of exposed females associated to a rise in NO levels in gonads and changes in the transcription of several genes involved in stress response, skeletogenesis, detoxification, multi drug efflux processes and NO production.

Materials and Methods

Ethics statement

Paracentrotus lividus (Lamarck) sea urchins were collected in the Gulf of Naples, near Castel dell'Ovo (40° 49' 41" latitude, 14° 14' 48" longitude), from a location that is not privately-owned nor protected in any way, according to the authorization of Marina Mercantile (DPR 1639/68, 09/19/1980, confirmed by D. Lgs. 9/01/2012 n.4). The field studies did not involve endangered or protected species. All animal procedures were in compliance with the guidelines of the European Union (directive 2010/63 and following D. Lgs. 4/03/2014 n.26).

Adult acclimation, treatments and gonads collection

Sea urchins were collected during the breeding season by SCUBA divers from the Gulf of Naples, transported in an insulated box to the laboratory within 1 h after collection and maintained in tanks with circulating sea water (1 animal/5 L). The animals were acclimated for a minimum of 10 days and kept in a controlled temperature chamber at 18±2°C with 12:12 light: dark cycle. Every 3 days animals were fed *ad libitum* by using fresh macroalgae (*Ulva* sp). Feeding was interrupted 2 days before experimental sampling. Rare spontaneous spawning and mortalities were observed during the acclimation period. Females (4.1 ± 0.98 cm), identified by Dr. Davide Caramiello from the service Marine Resources for Research of the Stazione Zoologica through observation at the stereomicroscope, were selected, weighed and transferred in experimental tanks. Each tank contained a group of 6 to 8 animals, as reported in figure legends, and 5 L of sea water per animal. Females were exposed to sea water containing cadmium 10^{-6} M (0.183 mg/L) or manganese $3.6x10^{-5}$ M (5.83 mg/L), prepared by stock solutions of 10^{-4} M cadmium (cadmium chloride, Sigma-Aldrich, Milan, Italy) and $31.2x10^{-4}$ M manganese (manganese chloride tetrahydrate, Sigma-Aldrich, Milan, Italy). Metal treatments were performed for 2 and 9 days. Control experiments were carried out by keeping the animals in sea water, in the tanks, as reported above, without addition of metals. The experimental tanks were artificially aerated and kept at 18±2°C with 12:12 light:dark cycle. Twice a week animals were fed with rations meal of *Ulva* sp. and 30% of the water was removed and replaced with new sea water containing the metal at the experimental concentration. All experiments were performed at least in triplicate. After 2 and 9 days, females were collected and weighed. Ovaries were removed, weighed, washed with PBS, frozen in liquid nitrogen and kept at -80°C until analysis. Moreover, eggs from single animals were collected and fertilized as described below.

Determination of gonadosomatic index, spawning and fertilization success

The gonadosomatic index (GSI) of the females was calculated as the ratio of the gonad mass to the whole-body wet mass (%). To induce gamete ejection, sea urchins were injected with 0.5 M KCl through the peribuccal membrane. Eggs from individual females were washed three times with 0.22 μm filtered sea water. Concentrated sperm was collected dry, mixing samples from at

least three different males and keeping undiluted at + 4°C. 10 μL of sperm mix was diluted in 10 mL sea water just before fertilization and an aliquot (100 μL) of this solution was added to 100 mL of egg suspension. Sperm to egg ratio was 100:1 for both controls and treated embryos. The fertilization success was approximately 90%. The spawning was determined as the ratio between the number of spawning females and the total number of females (%). The fertilization success was calculated as the ratio of the fertilized eggs observed at the first division (1h) respect to the number of total eggs (%).

Gamete collection, embryo culture, treatments and morphological analysis

Animals were sacrified and gonads were gently washed to allow egg release. The fertilization procedure was as described by Migliaccio et al. [10] with slight modifications. Briefly, eggs were collected from treated and control females and kept in sea water. The sperm from 3 control males was pooled and maintained dried in an eppendorf in cold conditions (+ 4°C) until fertilization. Diluted sperm (1:1000) was added to 100 mL of egg suspension (15000 eggs). Sperm to egg ratio were 100:1 for both controls and treated embryos. The mixture was carefully stirred to allow fertilization to take place. Five min after fertilization, eggs from treated animals were divided in two different groups. The eggs from the first group were reared in normal sea water whereas the eggs of the second group were reared in metal-containing sea water (cadmium 10^{-6} M or manganese 3.6 x 10^{-5} M). As control, eggs from females, maintained in tanks without metals for 2 and 9 days, were fertilized in sea water with a fertilization success approximately of 90%. Fertilized eggs were allowed to develop in a controlled temperature chamber at 18±2°C and 12:12 light:dark cycle. The development was followed by inverted microscope (Zeiss Axiovert 135 TV) until the pluteus stage, approximately 48 hours post fertilization (hpf). Morphological observations were performed on plutei fixed in 4% formalin. Embryos were considered normal if they reached the pluteus stage of development, exhibited good body symmetry, showed fully developed skeletal rods and displayed a well differentiated gut. All the morphologies that did not satisfy the above-mentioned criteria were grouped and referred to as abnormal [16, 39, 40].

NO determination

The endogenous NO levels were measured by monitoring nitrite formation by Griess reaction [10, 41]. Collected ovaries, washed in PBS and frozen in liquid nitrogen, were homogenized in 20 volumes of PBS and centrifuged at 25,000 x g for 20 min at + 4°C. The supernatants were analyzed for nitrite content. Sea urchin developing embryos were collected at different developmental stages (early blastula, swimming blastula, prism and pluteus stages) by centrifugation at 1800 g for 10 min in a swing out rotor at + 4°C. The pellet was washed with PBS, frozen in liquid nitrogen and kept at -80°C until use. Samples were homogenized in PBS (1:2 w/v) and centrifuged (12,000 g for 30 min at 4°C) and the supernatants were analyzed for nitrite content.

RNA extraction and cDNA synthesis

Embryos at different stages of development (about 1500) were collected by centrifugation as described above. Total RNA was extracted from each developmental stage, namely: early blastula, swimming blastula, prism and pluteus, using RNAqueous-Microkit (Ambion) according to the manufacturer's instructions. The amount of total RNA extracted was estimated by the absorbance at 260 nm and the purity by 260/280 and 260/230 nm ratios by Nanodrop (ND-1000 UV–Vis Spectrophotometer; NanoDrop Technologies). The integrity of RNA was also evaluated by agarose gel electrophoresis. Intact rRNA subunits (28S and 18S) were observed on

the gel indicating minimal degradation of the RNA. For each sample, 600 ng of total RNA extracted was retrotranscribed with iScript cDNA Synthesis kit (Biorad), following the manufacturer's instructions. cDNA was diluted 1:5 with H_2O prior to use in Real Time qPCR experiments.

Gene expression by real time qPCR

Real time qPCR experiments were performed on the offspring of sea urchin females exposed to cadmium and manganese for 2 and 9 days, with respect to the offspring of females reared in sea water in the absence of metals. The data from each cDNA sample were normalized using *Pl-Z12-1* as reference gene, because its level remained constant during development [10, 42]. The following genes were analyzed: *hsp70*, *hsp60*, *hsp56*, *sm30*, *sm50*, *p16*, *p19*, *msp130*, *bmp5-7*, *fg9/16/20*, *mt4*, *mt5*, *mt6*, *mt7*, *mt8*, *abc1a*, *abc4a*, *abc1b*, *abc8b* and *nos*. For all genes we used primers reported in Migliaccio et al. [10]. Diluted cDNA was used as a template in a reaction containing a final concentration of 0.3 μM for each primer and 1× FastStart SYBR Green master mix in a total volume of 10μL. PCR amplifications were performed in a ViiA7 Real Time PCR System (Applied Biosystems) thermal cycler using the following thermal profile: 95°C for 10 min, one cycle for cDNA denaturation; 95°C for 15 s and 60°C for 1 min, 40 cycles for amplification; 72°C for 5 min, one cycle for final elongation; one cycle for melting curve analysis (from 60°C to 95°C) to verify the presence of a single product. Each assay included a no-template control for each primer pair. To reduce intra-assay variability all Real Time qPCR reactions were carried out in triplicate. Moreover, at least 3 biological replicates were performed. Fluorescence was measured using ViiA7 Software (Applied Biosystems). The expression of each gene was analyzed and internally normalized against *Pl-Z12-1* using Relative Expression Software Tool software (REST) based on the method by Pfaffl et al. [43]. Relative expression ratios equal or greater than two fold were considered significant.

Statistical analysis

Data are presented as means ± SD. Two-way ANOVA ($P < 0.05$) with Bonferroni post hoc test was used to analyze data. Statistics was performed with GraphPad Prism 4.0 for Windows (GraphPad Software, San Diego, CA, USA). For Real Time qPCR analysis, significance was tested using the "Pair Wise Fixed Reallocation Randomisation Test", developed by REST software [43]. The number of experiments is reported in figure legends.

Results

Effects of cadmium and manganese on reproductive state and nitric oxide (NO) production in *P. lividus* females

Selected females were exposed for 2 and 9 days to cadmium 10^{-6} M and manganese 3.6 x 10^{-5} M. These metal concentrations were shown to be sublethal for developing *P. lividus* embryos, inducing a small percentage of abnormal plutei (28–29%) after treatment of fertilized eggs [10]. Then, the reproductive state was assessed by determination of gonadosomatic index (GSI), spawning and fertilization success. Moreover, NO content was measured in the ovaries as total nitrite by Griess assay. The exposure of sea urchin females to cadmium for 2 days caused a significant reduction in spawning (Fig 1C), fertilization success (Fig 1D) and NO production (Fig 1B), compared to the respective controls, females reared in sea water without metals. No effect was observed on GSI (Fig 1A). After 9 days, all parameters were affected by metal treatment. In particular, a significant reduction in GSI (Fig 1A), NO production (Fig 1B), spawning (Fig 1C) and fertilization success (Fig 1D) was recorded in cadmium-exposed sea urchins compared to

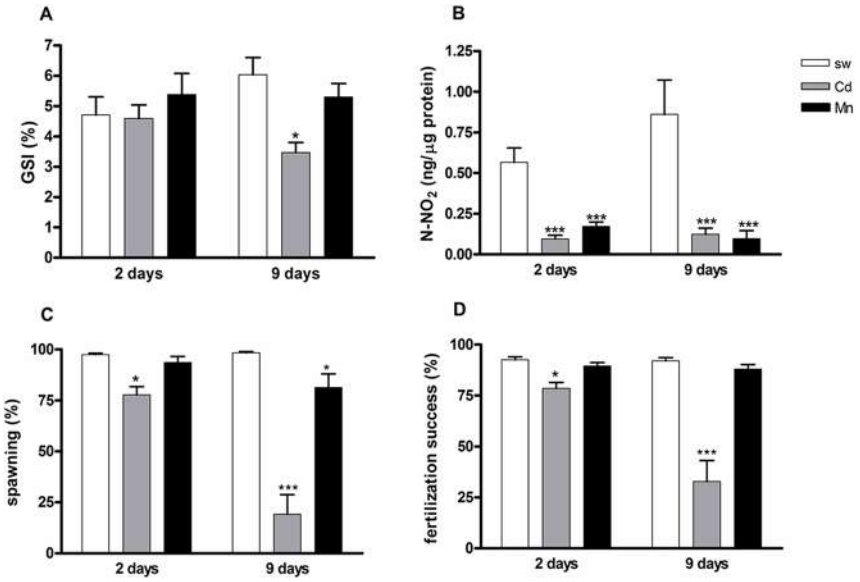

Fig 1. Reproductive state and nitric oxide (NO) production in *P. lividus* females exposed to cadmium and manganese. GSI (A), total NO concentration (B), spawning (C) and fertilization success (D) in females exposed to cadmium (Cd) 10^{-6} M and manganese (Mn) 3.6 x 10^{-5} M for 2 and 9 days. Significant differences compared to the controls (sw 2 and 9 days): *P<0.05, ***P<0.001. Two-way ANOVA, Bonferroni's post test (P<0.05). N = 8.

doi:10.1371/journal.pone.0131815.g001

the respective controls. Manganese exposure caused a decrease in NO levels at both experimental times (Fig 1B) and only a reduction in spawning after 9 days of treatment (Fig 1C).

Effects of cadmium and manganese on offspring of exposed *P. lividus* females

To investigate the effects of cadmium and manganese on the progeny of exposed sea urchins, the development of the offspring from females exposed to cadmium 10^{-6} M or manganese 3.6 x 10^{-5} M for 2 and 9 days and reared in the absence or in the presence of the metal was followed by morphological analysis, NO production and gene expression. We considered as control the offspring of females kept during the whole experimental period in sea water without addition of metals. Morphological analysis was performed at the pluteus stage, whereas NO production and gene expression were examined at different developmental stages: early blastula, swimming blastula, prism and pluteus.

Morphological analysis. For morphological analysis, we considered as normal plutei cone-shaped larvae with four fully developed arms and complete skeletal rods, whereas larvae with defects in arm and skeleton elongation and developmentally delayed were named abnormal, as previously described [10]. The exposure of females to both cadmium and manganese resulted in an increase in the percentage of abnormal plutei in the progeny (Fig 2A). In particular, the offspring of females exposed to cadmium 10^{-6} M reared in sea water showed 78±4.2% and 92±3.7% of abnormal plutei after 2 and 9 days respectively (Fig 2A), compared to the respective controls (7±1.2 and 9±0.73%). Defects were found in both arms and apex. The arms appeared often malformed or absent, whereas skeletal rods of the apex were folded, crossed or separated (Fig 2B). An increase in the number and type of abnormalities was found in the offspring of exposed females reared in the presence of cadmium with a percentage of abnormal plutei of 93±7.23 and 99±0.54% after 2 and 9 days, respectively, compared to controls in the

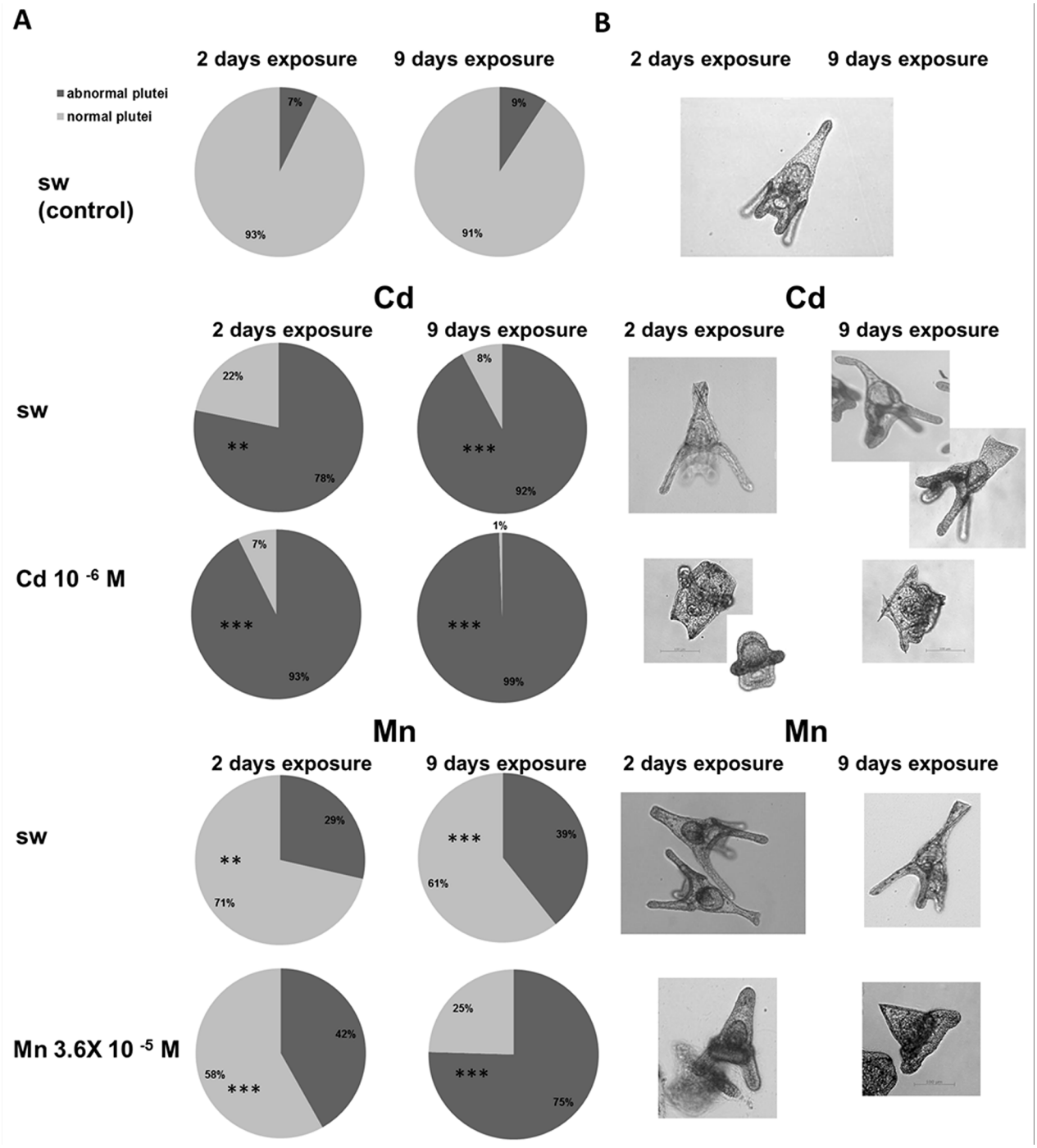

Fig 2. Morphological analysis of the progeny of *P. lividus* females exposed to cadmium and manganese. Females were treated for 2 and 9 days with cadmium (Cd) 10^{-6} M and manganese (Mn) 3.6 x 10^{-5} M, as described in Materials and Methods. Offspring was reared in sea water (sw) or in the presence of the metal. The development was monitored after 48 hpf. A. Percentage of normal and abnormal plutei; B. Representative pictures of the main abnormalities (bar = 100 μm). Significant differences compared to the control **P<0.01, ***P<0.001; Two-way ANOVA (P<0.05), with Bonferroni's Post Test. Light grey: normal plutei; dark grey: abnormal plutei. N = 8.

doi:10.1371/journal.pone.0131815.g002

absence of cadmium (Fig 2A). Larvae appeared severely affected by metal treatment with high percentage of gastrula and prism-like stages and arrested embryos (Fig 2B). The exposure of

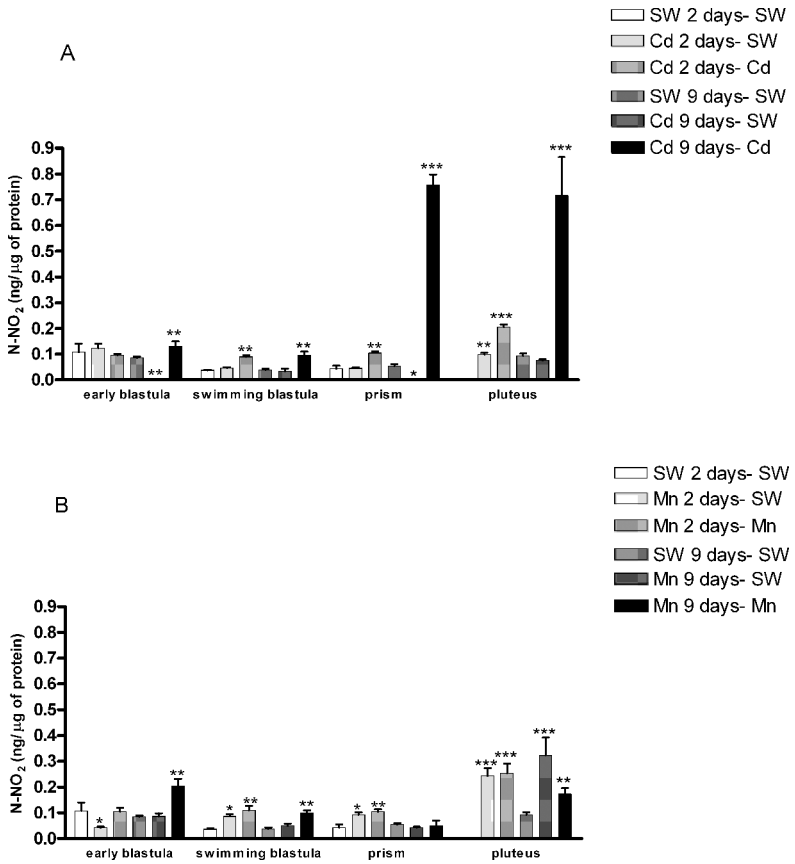

Fig 3. Total NO concentration in the progeny of *P. lividus* females exposed to cadmium and manganese. Different developmental stages of the offspring of females treated with cadmium (Cd) 10^{-6} M (A) or manganese (Mn) 3.6 x 10^{-5} M (B) for 2 and 9 days and reared in sea water (SW) or in SW containing metals were examined for nitrite content, as reported in Material and Methods. Significant differences compared to the respective control (SW 2 and 9 days) **P*<0.5, ***P*<0.01, ****P*<0.001. Two-way ANOVA, Bonferroni's post test (*P*<0.05). N = 6.

doi:10.1371/journal.pone.0131815.g003

females to manganese 3.6 x 10^{-5} M also caused abnormality in the offspring. In details, the embryos generated from those females and reared in sea water reached values of abnormalities of 29±3.23 and 39±4.65 after 2 and 9 days, respectively (Fig 2A), compared to the respective controls, offspring of females kept during the whole experimental period in sea water without metal. The abnormalities regarded especially the arms which appeared shorter than normal or malformed and the skeletal rods of the apex which were crossed or separated (Fig 2B). As in the case of cadmium treatment, an increase in the percentage and type of abnormalities was found in embryos reared in the presence of manganese which reached the values of 42±2.12 and 75±1.9% after 2 and 9 days, respectively, compared to controls. Larvae appeared much smaller in size and defects were found in both arms and apex (Fig 2B).

NO production. We examined the different developmental stages of the offspring of females exposed to cadmium and manganese for NO content, measured as total nitrite. As shown in Fig 3, the offspring of females treated for 2 days with cadmium 10^{-6} M and reared in normal sea water showed a significant increase in total nitrite with respect to the control, only at the pluteus stage, whereas embryos reared in the presence of cadmium showed increased NO production at the swimming blastula, prism and pluteus stages, compared to the respective controls. After 9 days of cadmium exposure, offspring reared in sea water without metal,

showed a decreased NO production at the early blastula and prism stages, compared to the respective controls, whereas embryos reared in the presence of cadmium exhibited an increased NO production at all developmental stages (Fig 3A), compared to the controls. Also manganese affected the production of NO. In fact, the offspring of females exposed for 2 days to manganese, reared in sea water, showed a reduction in total nitrite at the early blastula stage, whereas at all other developmental stages a significant increase was revealed compared to the controls. Also offspring reared in manganese-containing sea water showed an increased NO production at the swimming blastula, prism and pluteus stages, with respect to the controls (Fig 3B). The offspring reared for 9 days in normal sea water showed a significant increase in NO production at the pluteus stage. On the contrary, embryos reared in sea water containing manganese increased total nitrite at almost all developmental stages, except at the prism stage, compared to the respective controls.

Gene expression. Further experiments were performed to evaluate possible variation in the expression of genes involved in several processes, such as stress response (heat shock proteins *hsp70*, *hsp60* and *hsp56*), skeletogenesis (spicule matrix proteins *sm30*, *sm50* and *msp130*, the growth factor *bmp5-7*, the proteins involved in skeleton formation *p16* and *p19*, the fibroblast growth factor *fg9/16/20*), detoxification (metallothioneins *mt4*, *mt5*, *mt6*, *mt7* and *mt8*), multidrug efflux (abc transporter *abc1b*, *abc4a*, *abc8b*, *abc1a*) and NO production (*nos*). Their expression was followed at the different developmental stages in the offspring of females exposed to cadmium (Fig 4, S1 Table) and manganese (Fig 5, S1 Table) for 2 (A,B) and 9 days (C,D) and reared in sea water without metal (A,C) and in sea water containing metal (B,D). The data, obtained by Real Time qPCR, were normalized using as reference gene *Pl-Z12-1* and expressed with respect to the control values, offspring of females kept during the whole experimental period in sea water without addition of metals.

The offspring of females exposed to cadmium for both 2 and 9 days showed a great variation in gene expression when embryos were reared in sea water (Fig 4A and 4C, S1 Table) or in cadmium-containing sea water (Fig 4B and 4D, S1 Table), with respect to controls. In details, among the stress genes, *hsp70* was up-regulated in almost all developmental stages in the offspring of females exposed to cadmium for 2 or 9 days and reared both in sea water and in cadmium-containing sea water. The expression of *hsp60* and *hsp56* was up-regulated only at some developmental stages: *hsp60* at the early and swimming blastula (offspring of females exposed to cadmium for 2 days and reared in sea water and in cadmium-containing sea water, respectively) and *hsp56* at the swimming blastula and prism (offspring of females exposed to cadmium for 2 or 9 days and reared in metal-containing sea water, respectively). Among the skeletogenic genes, the spicule matrix protein 30, *sm30*, was up-regulated only at the early blastula and swimming blastula stages both in the offspring of females exposed for 2 days and reared in sea water and in cadmium-containing sea water. On the contrary, in the offspring of females exposed to cadmium for 9 days, this gene was down-regulated at all developmental stages when embryos were reared in cadmium-containing sea water and only at the prism and pluteus stages when development was performed in the absence of metal. Up-regulation of *sm50* was found only at the early blastula and swimming blastula stages in the offspring of females exposed to cadmium for 2 days and reared in sea water. A variation in the expression of *msp130* was mainly found in the offspring of females treated with cadmium for 2 or 9 days and reared in metal-containing water. The expression of *p16* and *p19* was also affected by the treatments. In the offspring of females exposed to cadmium for 2 days both genes were up-regulated at the initial stages (early and swimming blastula) and down-regulated at the prism and pluteus stages. The same trend (up-regulation at the initial stages and down-regulation at later stages) was observed for *p16* in the offspring of females exposed to cadmium for 9 days and reared in the presence of metal, whereas the expression of *p19* under these conditions increased

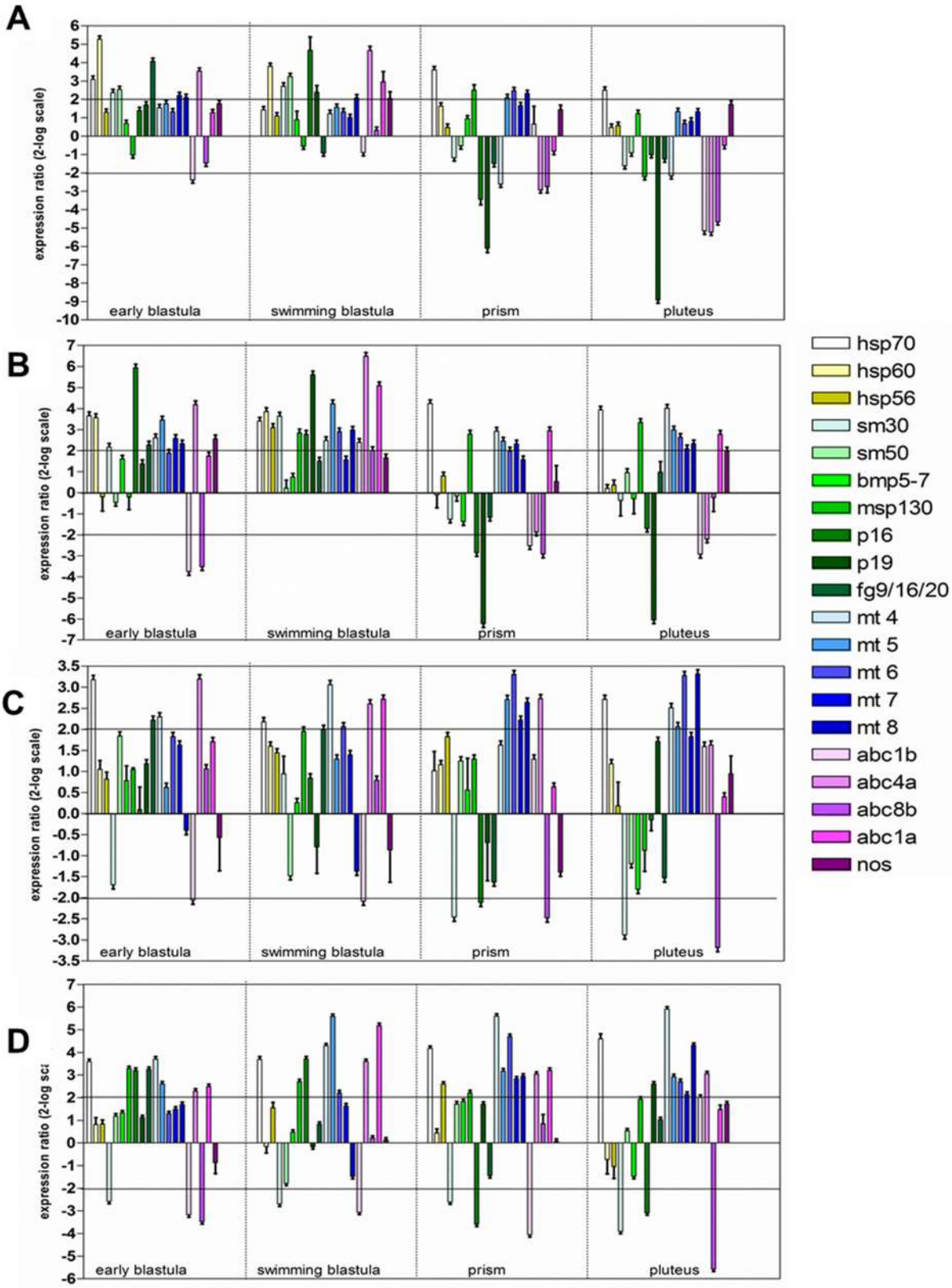

Fig 4. Gene expression analysis in the progeny of *P. lividus* females exposed to cadmium 10^{-6} M for 2 days (A,B) and 9 days (C,D). The embryos were reared in sea water (A,C) and in cadmium-containing sea water (B,D). Data are reported as a fold difference in the expression levels of the analyzed

genes, compared to controls (mean ± SD), offspring of females kept during the whole experimental period in sea water without addition of metal. Fold differences equal or greater than ± 2 (see horizontal guidelines at values of 2 and—2) were considered significant. Experiments were repeated at least on 3 biological replicates.

doi:10.1371/journal.pone.0131815.g004

only at the pluteus stage. The expression of *fg9/16/20* increased at early developmental stages in all experimental conditions. Among detoxification genes, the expression of metallothioneins increased to a different extent at almost all developmental stages in the offspring of females exposed to cadmium for 2 or 9 days and reared in metal-containing sea water. However, their expression was also up-regulated at some stages when development was performed in sea water without metal, except *mt4* which is down-regulated at the prism stage in the offspring of females exposed to cadmium for 2 days. Also the multidrug efflux genes showed variations in their expression following the different treatments. The transporters *abc1b* and *abc8b* were mostly down-regulated at different developmental stages and experimental conditions, except in some few conditions when they are up-regulated. The gene *abc1a* was always up-regulated at some developmental stages, whereas the expression of *abc4a* changed according to the time of adult exposure and developmental conditions. In the offspring of females exposed to cadmium for 2 days and reared in sea water or in metal-containing sea water the gene *abc4a* was up-regulated at the early and swimming blastula stages and down-regulated at late developmental stages. When females were exposed for 9 days, the offspring showed an up-regulation of this gene at all stages and conditions. The expression of *nos* was slightly affected only in the offspring of females exposed to cadmium for 2 days and reared in sea water and in cadmium-containing sea water.

In the presence of manganese, the greater effect on gene expression was found in the offspring after treatment with the metal for prolonged time (Fig 5, S1 Table). In detail, the expression of only *p19* was slightly affected in the offspring of females exposed for 2 days and reared in sea water (Fig 5A). When embryos were allowed to develop in manganese-containing seawater the expression of many genes was modified (Fig 5B). Among stress genes, *hsp70* was up-regulated at the swimming blastula, prism and pluteus stages, whereas *hsp60* only at the swimming blastula and prism stages. The expression of *sm30* decreased at the early and swimming blastula stages, while *sm50* was down-regulated only at the early blastula stage. Moreover, *mt7* and *mt8* were slightly up-regulated at the swimming blastula stage. Among the *abc* transporter, *abc4a* was up-regulated at the early blastula and prism stages and *abc1a* at the early blastula and pluteus stages. The offspring of females exposed for 9 days and reared in sea water showed an up regulation of some genes mostly at the early and swimming blastula stages. At the early blastula stage, *hsp60*, *sm50*, *msp130*, *p16*, *p19*, *fg9/16/20*, *abc4a* and *abc1a* were up-regulated. At the swimming blastula stage, *hsp70*, *hsp60*, *msp130*, *p16*, *p19* and *abc4a* increased their expression (Fig 5C). When embryos were reared in sea water containing manganese, the expression of these genes also changed (Fig 5D). However, under these conditions, *sm50* was down-regulated at the early blastula stage and up-regulated at the swimming blastula and prism stages. Moreover, *sm30* was down-regulated at all developmental stages and *mt8* and *abc1b* are slightly up-regulated at the pluteus and early blastula stages, respectively. The expression of *nos* was not modified by manganese treatment at all developmental stages analyzed.

Discussion

The results of this study on the effects of cadmium and manganese exposure for 2 and 9 days on *P. lividus* females and their offspring greatly expanded previous investigations on the impact of toxic metals on adult sea urchins [36, 44–46], providing also information on the transmission of the "maternal" stress to the progeny at morphological, biochemical and molecular level.

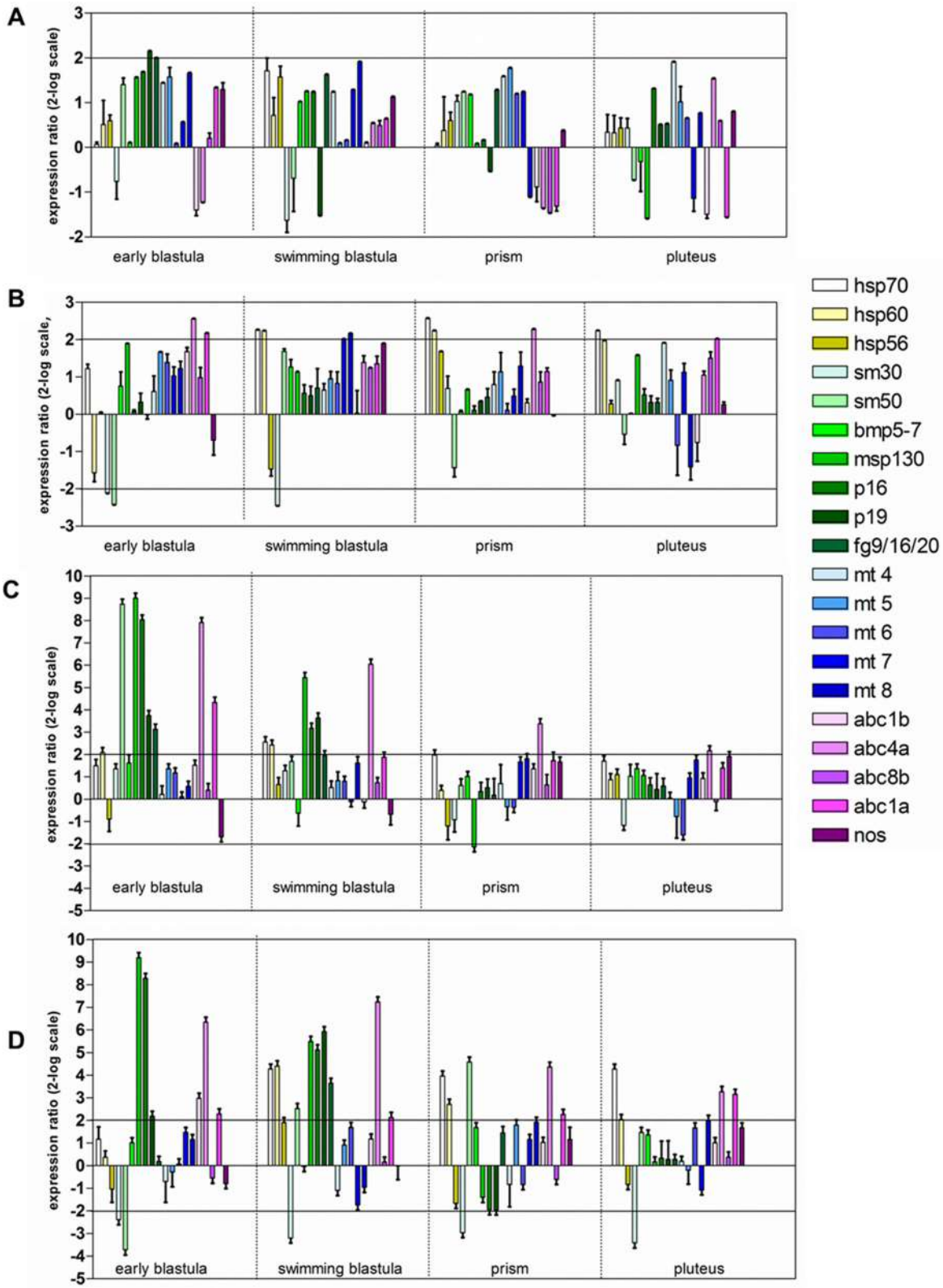

Fig 5. Gene expression analysis in the progeny of *P. lividus* females exposed to manganese 3.6 x 10^{-5} M for 2 days (A,B) and 9 days (C,D). The embryos were reared in sea water (A,C) and in manganese-containing sea water (B,D). Data are reported as a fold difference in the expression levels of the analyzed genes, compared to controls (mean ± SD), offspring of females kept during the whole experimental period in sea water without addition of metal.

Fold differences equal or greater than ± 2 (see horizontal guidelines at values of 2 and—2) were considered significant. Experiments were repeated at least on 3 biological replicates.

doi:10.1371/journal.pone.0131815.g005

Our findings that cadmium treatment impaired the ability of sea urchins to reproduce whereas manganese slightly affected the reproductive state indicated that the latter has "apparently" no toxic effects on adult sea urchins fertility. However, the exposure to both cadmium and manganese dramatically reduced the levels of NO in the ovaries. This signaling molecule has already been shown to mediate the response of sea urchin developing embryos to different stress agents [10, 34]. Therefore, it is likely that also manganese can affect female sea urchins defenses, although to a lesser extent than cadmium. These findings suggest that the measurements of the reproductive parameters, GSI, spawning and fertilization success, are not sufficient to assess the health of sea urchins, as also pointed out by Au et al. [45], whereas the determination of NO levels may represent an additional biomarker to monitor the wellness of the animals.

An important outcome of this study was provided by the analysis of the progeny of *P. lividus* females exposed to the metals and reared in sea water in the presence or in the absence of metals. Our findings clearly indicated that females exposed to cadmium and manganese produced an offspring with an high proportion of abnormal larvae also when the development was performed in normal sea water. As expected, the abnormalities increased with the time of female exposure and in the presence of the metal during embryo development. Phenotypic analysis of the progeny of females treated with environmentally relevant concentrations of cadmium and manganese confirmed previous results of a lower toxicity of manganese compared to cadmium [10,16]. Moreover, a general increase in NO levels especially at later developmental stages was found, similarly to the increase obtained by exposing directly developing embryos to the metals after fertilization [10]. However, an important result of this study was that with both cadmium and manganese, metal toxicity was exacerbated by maternal treatment. In fact, the percentage of abnormal plutei from treated females was much higher than those obtained when only embryos were exposed to metals [10]. This result suggested that maternal toxicity was transmitted to the progeny.

The present study provided first insights into the molecular mechanisms that mediate the toxic effects of cadmium and manganese on the progeny of exposed sea urchins. After maternal cadmium exposure for 2 days, significant changes in gene expression were found in developing embryos reared both in sea water with or without cadmium, whereas, after maternal manganese exposure for the same time, a significant modification in the expression of the selected genes was found only in developing embryos reared in sea water containing manganese. Our data, showing an up-regulation of the *hsps* in the offspring of females treated with cadmium and manganese, extend previous studies reporting the increase in hsps protein levels in larvae and adult cells or tissues of *P. lividus* after heat shock, X-ray, UVB, cadmium and manganese exposure [30, 47–51]. During the induction of heat shock proteins, cells are refractory to the toxicity of various agents and their protection is partially due to the inhibition of apoptosis [52]. The accumulation of damaged proteins acts as a signal for the induction of stress response and/or activation of the apoptotic program [53]. However, if the concentration of heat shock proteins is not enough to block the toxic effect of the metal, cells undergo to apoptosis [54]. Therefore, the up-regulation of *hsps* transcriptional levels confirms the activation of a defence mechanism to protect developing embryos against metals. Also the expression levels of some skeletogenic genes were modified by metal treatments. Sea urchin larvae have a simple skeleton consisting of a small number of spicules [55]. The skeleton is composed of magnesia calcite and spicule matrix proteins [56]. The cells responsible for the skeleton formation are the

primary mesenchyme cells (PMCs), which synthesize specific marker proteins, including msp 130, a cell surface glycoprotein likely involved in calcium transport [57], sm30 encoding an acidic glycoprotein of the spicule matrix [58], sm50 encoding a basic non glycosylated protein [59], found in Golgi and small vesicles, p16 and p19, small proteins involved in the formation of the biomineralized skeleton in embryos and adults [60]. The observed variations in the expression of these genes may be due to the need to carry on the development under stressful conditions. In fact, the expression of the skeletogenic genes has been reported to be affected by other stressors, such as X-rays [50], high CO_2 [61], heat shock [62], decadienal [34, 63], UVB exposure [49]. The finding that the expression level of the growth factor *bmp5-7* was not affected by cadmium or manganese treatment is in line with previous data showing that this gene is not involved during skeletogenesis [10,64]. Metals exposure also caused variations in the expression rate of the fibroblast growth factor *fg9/16/20*, coding for a protein involved in PMC migration and skeletal morphology, prefiguring the branching pattern of the skeleton. The inhibition of the production of these transcripts has a dramatic effect on sea urchin biomineralization because it leads to the absence of skeleton [65]. The observed up-regulation of this gene following cadmium and manganese treatment could prevent the inhibition of calcification in the PMCs, as also reported during CO_2 exposure [66]. Metals are also responsible for the variation in the expression of genes which may be involved in detoxification processes such as metallothioneins and abc transporters. Our finding that the expression of *mts* increased in the offspring of females exposed to cadmium and manganese and reared in metal-containing sea water confirmed that elevated expression of these proteins was a hallmark of metal exposure [67]. The abc-transporters are a conserved family of membrane proteins that use ATP to move compounds across membranes in both adult and embryo. They can transport peptides, metals, xenobiotics and ions necessary for homeostasis, protection, and signalling [68]. Sea urchin embryos use different abc-transporters during the early developmental stages. The importance of the abc-transporters in the response to environmental stress was demonstrated by Kurelec [69]. In particular, the authors showed that abc-transporters can protect organisms from several pollutants. Several studies demonstrated the modulation of *abc* genes and transport activities. In piscine cell line, for example, after 24h of exposure to four different metals ($CdCl_2$, $HgCl_2$, As_2O_3 or $K_2Cr_2O_7$) the *abcc2–4* genes were dose-dependently up-regulated by all metals, while *abcb1* and *abcc1* were less affected [70].

Analysis of the different classes of genes revealed little variations in the number and type of genes affected in embryos reared in cadmium-containing sea water, compared to embryos reared in sea water without metal, at both times of exposure (Fig 6). The situation was different in the offspring of females treated with manganese. When females were exposed for short periods (2 days) almost all classes of genes were affected only when offspring was reared in sea water containing manganese. At longer time of treatments (9 days) also in the offspring reared in sea water without metals the majority of classes of genes was regulated. The different response at gene level of sea urchin developing embryos from females exposed to cadmium and manganese is correlated to the different nature of these metals. Indeed, cadmium is a known heavy metal, toxic even at very low concentrations [71] and without any biological role, whereas manganese is a naturally occurring metal required in trace amounts by the organisms, toxic only at high levels. These results again confirmed the higher toxicity of cadmium compared to manganese. On the other hand, after maternal treatments for longer periods (9 days), the offspring of females exposed to both cadmium and manganese showed a great variation in the expression of the majority of the selected genes, indicating that the time of maternal exposure affects the molecular response of the offspring. However, considering that gene expression is only a part of the cascade processes leading to the elevated expression of a protein, future

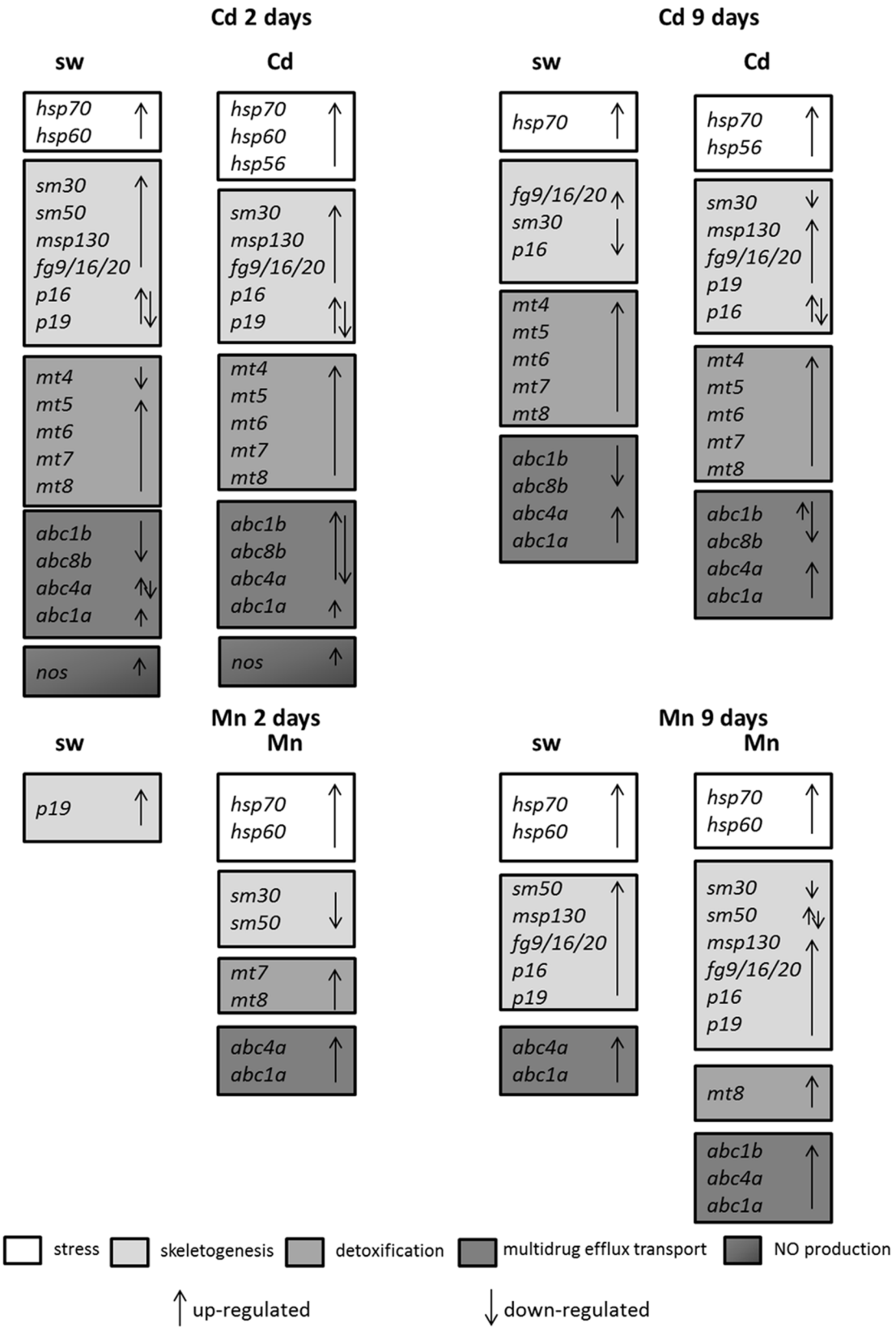

Fig 6. Synopsis of the patterns of up- and down-regulation of different classes of genes in the offspring of *P. lividus* females exposed to cadmium (Cd) or manganese (Mn) for 2 and 9 days. The two arrows indicate the up- or down-regulation of genes in different developmental stages.

doi:10.1371/journal.pone.0131815.g006

studies should be directed to obtain a clear picture of the dynamics of the defensome systems in *P*. *lividus* by investigating the protein expression patterns.

The variations in gene expression in the offspring of treated females could be correlated to changes in the endogenous levels of NO that, as we have previously shown [10], are able to affect gene expression in sea urchin developing embryos treated with cadmium and manganese after fertilization. In fact, a significant increase in NO production was found in the different developmental stages of the offspring derived from exposed females. The increase of NO could derive both by stimulation of nos activity e.g. by intracellular calcium concentration [72] or by regulation at the transcriptional level. Indeed, the slight up-regulation of *nos* at early developmental stages in the progeny of females exposed to cadmium for 2 days and the increase of NO levels at late stages may be explained with an early transcriptional regulation of *nos* gene, responsible for the later NO production. However, further investigation should be performed, by using NOS inhibitors and NO donors, to evaluate the differences found in embryos treated after fertilization [10] and the offspring of treated females (this work). Interestingly, *nos* was up-regulated in the offspring only when the metal treatment was performed on the females and not when fertilized eggs were treated with metals [10]. One speculation could be related to the presence of a sensitization mechanism in the offspring of treated females, in which *nos* is fast up-regulated in response to the metal.

In conclusion, our finding that cadmium and manganese, at environmentally relevant concentrations (10^{-6} M and 3.6 x 10^{-5} M, respectively) negatively affected both *P*. *lividus* females reproductivity and development of their progeny is of considerable ecological relevance, considering that maternal exposure to contaminants can impair reproduction and on a large-scale and long-term can affect recruitment of sea urchin populations habiting areas potentially exposed to contaminants (e.g. coastal or industrial zone).

Supporting Information

S1 Table. Variation in gene expression in the offspring of females exposed to cadmium and manganese. Different developmental stages of the offspring of females exposed to cadmium (Cd) and manganese (Mn) for 2 and 9 days and reared in sea water (SW) and in metal-containing SW were examined for gene expression. Values (mean ± SD) equal or greater than ± 2 are reported as a fold difference in the expression levels of the analyzed genes, compared to controls, offspring of females kept during the whole experimental period in sea water without addition of metal. Experiments were repeated at least on 3 biological replicates.
(DOC)

Acknowledgments

We thank the Molecular Biology Service for gene sequencing, Davide Caramiello and Alberto Macina and the service Marine Resources for Research for assistance with living organisms. We acknowledge Valeria Matranga for her helpful advice and discussion as external supervisor of Oriana Migliaccio PhD program. We acknowledge Thierry Lepage for the use of the web site http://octopus.obs-vlfr.fr/blast/blast_oursin.html.

Author Contributions

Conceived and designed the experiments: OM AP. Performed the experiments: OM. Analyzed the data: OM. Contributed reagents/materials/analysis tools: PC AP. Wrote the paper: OM IC GR AP.

References

1. Fan AM. An introduction to monitoring and environmental and human risk assessment of metal. In: Magos L, Suzuki T, editors. Toxicology of Metals. CRC Lewis Publishers: Boca Raton; 1996. pp. 5–9.
2. Perez-Lopez M, Alonso J, Novoa-Valinas MC, Melgar MJ. Assessment of heavy metal contamination of seawater and marine limpet, *Patella vulgata* L., from Northwest Spain. J Environ Sci Health A Tox Hazard Subst Environ Eng. 2003; 38: 2845–2856. PMID: 14672319
3. Roesijadi G, Robinson WE. Metal regulation in aquatic animals: mechanisms of uptake, accumulation, and release. In: Malins DC, Ostrander GK, editors. Aquatic Toxicology-Molecular, Biochemical, and Cellular Perspectives. Lewis Publishers: Boca Raton; 1994. pp. 387–420.
4. Migliaccio O, Castellano I, Romano G, Palumbo A. Response of sea urchin to environmental stress. In: Banks ER, editor. Sea Urchins: Habitat, Embryonic development and importance in the environment. Nova Science Publishers, Inc; 2014a. pp. 1–23.
5. Roccheri MC, Matranga V. Cellular, biochemical and molecular effects of cadmium on *Paracentrotus lividus* sea urchin development. In: Parvau R G, editor. Cadmium in the environment. Nova Science Publishers, Inc; 2009. pp. 1–30.
6. Pinsino A, Matranga V, Trinchella F, Roccheri MC. Sea urchin embryos as an in vivo model for the assessment of manganese toxicity: developmental and stress response effects. Ecotoxicology. 2010; 19: 555–562. doi: 10.1007/s10646-009-0432-0 PMID: 19882348
7. Pinsino A, Roccheri MC, Costa C, Matranga V. Manganese interferes with calcium, perturbs ERK signaling and produces embryos with no skeleton. Toxicol Sci. 2011; 23: 217–230.
8. Vaschenko MA, Luchsheva LN, Zhadan PM, Belcheva NN, Syasina IG Silina AV. Assessment of the ecological situation in Alekseev Bight (Peter the Great Bay, Sea of Japan) by biological and biochemical parameters. Biol Morya. 1999; 25: 96–97.
9. Filosto S, Roccheri MC, Bonaventura R, Matranga V. Environmentally relevant cadmium concentrations affect development and induce apoptosis of *Paracentrotus lividus* larvae cultured in vitro. Cell Biol Toxicol. 2008; 24: 603–610. doi: 10.1007/s10565-008-9066-x PMID: 18322810
10. Migliaccio O, Castellano I, Romano G, Palumbo A. Stress response to cadmium and manganese in *Paracentrotus lividus* developing embryos is mediated by nitric oxide. Aquat Toxicol. 2014b; 156: 125–134.
11. Kremling K, Streu P. Behaviour of dissolved Cd, Co, Zn, and Pb in North Atlantic near-surface waters (30° N/60° W to 60° N/2° W). Deep Sea Res I. 2001; 12: 2541–2567.
12. Pohl C, Hennings U. The coupling of long-term trace metal trends to seasonal diffusive trace metal fluxes at the oxic–anoxic interface in the Gotland Basin (57°19.20′ N; 20° 03.00′ E) Baltic Sea. J Mar Sys. 2005; 56: 207–225.
13. Kobayashi N, Okamura H. Effects of heavy metals on sea urchin embryo development. 1. Tracing the cause by the effects. Chemosphere. 2004; 55: 1403–1412. PMID: 15081783
14. Tankere SPC, Statham PJ. Distribution of dissolved Cd, Cu, Ni and Zn in the Adriatic Sea. Mar Pollut Bull. 1996; 32: 623–630.
15. Beiras R, Fernandez N, Bellas J, Besada V, Gonzalez-Quijano A, Nunes T. Integrative assessment of marine pollution in Galician estuaries using sediment chemistry, mussel bioaccumulation, and embryo-larval toxicity bioassays. Chemosphere. 2003; 52: 1209–1224. PMID: 12821002
16. Kobayashi N, Okamura H. Effects of heavy metals on sea urchin embryo development. Part 2. Interactive toxic effects of heavy metals in synthetic mine effluents. Chemosphere. 2005; 61: 1198–1203. PMID: 16263390
17. Fatoki OS, Mathabatha S. An assessment of heavy metal pollution in the East London and Port Elizabeth harbours. Water SA. 2001; 27: 233–240.
18. ATSDR. Draft Toxicological Profile for Manganese. Agency for Toxic Substances and Disease Registry. Division of Toxicology and Environmental Medicine/ Applied Toxicology Branch, Atlanta, Georgia. 2008.
19. Santamaria AB. Manganese exposure, essentiality and toxicity. Indian J Med Res. 2008; 128: 484–500. PMID: 19106442
20. Daly MJ. A new perspective on radiation resistance based on *Deinococcus radiodurans*. Nat Rev Microbiol. 2009; 7: 237–244. doi: 10.1038/nrmicro2073 PMID: 19172147
21. CICAD. Manganese and its Compounds: Environmental Aspects. In: Concise International Chemical Assessment Document, vol. 63. WHO, Geneva, Switzerland; 2004.
22. Trefry JH, Presley BJ, Keeney-Kennicutt WL, Trocine RP. Distribution and chemistry of manganese, iron, and suspended particulates in orca basin. Geo-Mar Lett. 1984; 4: 125–130.

23. Aller RC. The sedimentary Mn cycle in long island sound: its role as intermediate oxidant and the influence of bioturbation, O_2, and C_{org} flux on diagenetic reaction balances. J Mar Res. 1994; 52: 259–295.

24. Pagano G, Cipollaro M, Corsale G, Esposito A, Ragucci E. The Sea Urchin: Bioassay for the Assessment of damage from environmental contaminants. In: Philadelphia American Society for testing and materials. 1986. pp. 67–92.

25. Warnau M, Biondo R, Temara A, Bouquegneau JM, Jangoux M, Dubois P. Distribution of heavy metal in the echinoid *Paracentrotus lividus* (Lmk) from the Mediterranean *Posidonia oceanica* ecosystem: seasonal and geographical variations. J Sea Res. 1998; 39: 267–280.

26. Harmelin JG, Bouchon C, Hong JS. Impact de la pollution sur la distribution des échinodermes des substrats durs en Provence (Méditerranée Nord-occidentale). Téthys. 1981; 10: 13–36.

27. Bayed A, Quiniou F, Benrha A, Guillou M. The *Paracentrotus lividus* populations from the northern Moroccan Atlantic coast: growth, reproduction and health condition. J Mar Biol Assoc U K. 2005; 85: 999–1007.

28. Soualili D, Dubois P, Gosselin P, Pernet P, Guillou M. Assessment of seawater pollution by heavy metals in the neighbourhood of Algiers: use of the sea urchin, *Paracentrotus lividus*, as a bioindicator. ICES J Mar Sci. 2008; 65: 132–139.

29. Russo R, Bonaventura R, Zito F, Schroeder HC, Müller I, Müller WEG, et al. Stress to cadmium monitored by metallothionein gene induction in *Paracentrotus lividus* embryos. Cell Stress Chaperones. 2003; 8: 232–241. PMID: 14984056

30. Roccheri MC, Agnello M, Bonaventura R, Matranga V. Cadmium induces the expression of specific stress proteins in sea urchin embryos. Biochem Biophys Res Commun. 2004; 321: 80–87. PMID: 15358218

31. Agnello M, Filosto S, Scudiero R, Rinaldi AM, Roccheri MC. Cadmium induces an apoptotic response in sea urchin embryos. Cell Stress Chaperones. 2007; 12: 44–50. PMID: 17441506

32. Pinsino A, Roccheri MC, Matranga V. Manganese overload affects p38 MAPK phosphorylation and metalloproteinase activity during sea urchin embryonic development. Mar Environ Res. 2013; 93: 64–69. doi: 10.1016/j.marenvres.2013.08.004 PMID: 23998794

33. Chiarelli R, Agnello M, Bosco L, Roccheri MC. Sea urchin embryos exposed to cadmium as an experimental model for studying the relationship between autophagy and apoptosis. Mar Environ Res. 2014; 93: 47–55. doi: 10.1016/j.marenvres.2013.06.001 PMID: 23838188

34. Romano G, Costantini M, Buttino I, Ianora A, Palumbo A. Nitric oxide mediates the stress response induced by diatom aldehydes in the sea urchin *Paracentrotus lividus*. PLoS One. 2011; 6: e25980. doi: 10.1371/journal.pone.0025980 PMID: 22022485

35. Vaschenko MA, Zhadan PM, Medvedeva LA. Developmental disturbances in sea urchin *Strongylocentrotus intermedius* larvae from polluted regions of Peter the Great Bay, Sea of Japan. Biol Morya. 1999; 20: 137–147.

36. Vaschenko MA, Zhadan PM. Developmental disturbances in the progeny of sea urchins as an index of environmental pollution. Russ J Ecol. 2003; 34: 418–424.

37. Naidenko T. Abnormality of development in *Strongylocentrotus intermedius* (A. Agassiz) larvae from polluted habitat in Amursky Bay, Peter the Great Bay. Pub Seto Mar Biol Lab. 1997; 38: 1–11.

38. Quiniou F, Guillou M, Judas A. Arrest and delay in embryonic development in sea urchin populations of the bay of Brest (Brittany, France): link with environmental factors. Mar Poll Bull. 1999; 38: 401–406.

39. Radenac G, Fichet D, Miramand P. Bioaccumulation and toxicity of four dissolved metals in *Paracentrotus lividus* sea-urchin embryo. Mar Environ Res. 2001; 51: 151–166. PMID: 11468814

40. Carballeira C, Ramos-Gómez J, Martín-Díaz L, DelValls TA. Identification of specific malformations of sea urchin larvae for toxicity assessment: Application to marine pisciculture effluents. Mar Environ Res. 2012; 77: 12–22. doi: 10.1016/j.marenvres.2012.01.001 PMID: 22341183

41. Green LC, Wagner DA, Glogowski J. Analysis of nitrate, nitrite and nitrate in biological fluids. Anal Biochem. 1982; 126: 131–138. PMID: 7181105

42. Ragusa MA, Costa S, Gianguzza M, Roccheri MC, Gianguzza F. Effect of cadmium exposure on sea urchin development assessed by SSH and RT-qPCR: metallothionein genes in marine invertebrates: focus on *Paracentrotus lividus* sea urchin development. Mol Biol Rep. 2013; 40: 2157–2167. doi: 10.1007/s11033-012-2275-7 PMID: 23212613

43. Pfaffl MW, Horgan GW, Dempfle L. Relative expression software tool (REST) for group-wise comparison and statistical analysis of relative expression results in real-time PCR. Nucleic Acids Res. 2002; 30: e36. PMID: 11972351

44. Au DW, Lee CY, Chan KL, Wu RS. Reproductive impairment of sea urchins upon chronic exposure to cadmium. Part I: Effects on gamete quality. Environ Pollut. 2001a; 111: 1–9.

45. Au DW, Lee CY, Chan KL, Wu RS. Reproductive impairment of sea urchins upon chronic exposure to cadmium. Part II: Effects on sperm development. Environ Pollut. 2001b; 111: 11–20.

46. Manzo S, Buono S, Cremisini C. Cadmium, lead and their mixtures with copper: *Paracentrotus lividus* embryotoxicity assessment, prediction, and offspring quality evaluation. Ecotoxicology. 2010; 19: 1209–1223. doi: 10.1007/s10646-010-0506-z PMID: 20552397

47. Giudice G, Sconzo G, Roccheri MC. Studies on heat shock protein in sea urchin development. Dev Growth Differ. 1999; 41: 375–380. PMID: 10466924

48. Roccheri MC, Patti M, Agnello M, Gianguzza F, Carra E, Rinaldi AM. Localization of Mitochondrial Hsp58 chaperonine during sea urchin development. Biochem Biophys Res Commun. 2001; 287: 1093–1098. PMID: 11587534

49. Bonaventura R, Poma V, Costa C, Matranga V. UVB radiation prevents skeleton growth and stimulates the expression of stress markers in sea urchin embryos. Biochem Biophys Res Commun. 2005; 328: 150–157. PMID: 15670763

50. Matranga V, Zito F, Costa C, Bonaventura R, Giarrusso S, Celi F. Embryonic development and skeletogenic gene expression affected by X-rays in the Mediterranean sea urchin *Paracentrotus lividus*. Ecotoxicology. 2010; 19: 530–537. doi: 10.1007/s10646-009-0444-9 PMID: 19943107

51. Bonaventura R, Zito F, Costa C, Giarrusso S, Celi F, Matranga V. Stress response gene activation protects sea urchin embryos exposed to X-rays. Cell Stress Chaperones. 2011; 16: 681–687. doi: 10.1007/s12192-011-0277-3 PMID: 21720812

52. Samali A, Cotter TG. Heat shock proteins increase resistance to apoptosis. Exp Cell Res. 1996; 223: 163–170. PMID: 8635489

53. Latchman DS. Stress proteins: An overview. Handb Exp Pharmacol. 1999; 136: 1–7.

54. Hamada T, Tanimoto A, Sasaguri Y. Apoptosis induced by cadmium. Apoptosis. 1997; 2: 359–367. PMID: 14646532

55. Ameye L, Hermann R, Killian C, Wilt F, Dubois P. Ultrastructural localization of proteins involved in sea urchin biomineralization. J Histochem Cytochem. 1999; 47: 1189–1200. PMID: 10449540

56. Wilt FH. Developmental biology meets materials science: morphogenesis of biomineralized structures. Dev Biol. 2005; 280: 15–25. PMID: 15766744

57. Anstrom JA, Chin JE, Leaf DS, Parks AL, Raff RA. Localization and expression of msp 130 a primary mesenchyme lineage specific cell surface protein of the sea urchin embryo. Development. 1987; 101: 255–265. PMID: 3128442

58. George C, Killian CE, Wilt FH. Characterization and expression of a gene encoding a 30.6 kDa *Strongylocentrotus purpuratus* spicule matrix protein. Dev Biol. 1991; 147: 334–342. PMID: 1717322

59. Killian CE, Wilt FH. Characterization of the proteins comprising the integral matrix of *Strongylocentrotus purpuratus* embryonic spicules. J Biol Chem. 1997; 271: 9150–9159.

60. Costa C, Karakostis K, Zito F, Matranga V. Phylogenetic analysis and expression patterns of p16 and p19 in *Paracentrotus lividus* embryos. Dev Genes Evol. 2012; 222: 245–251. doi: 10.1007/s00427-012-0405-9 PMID: 22565340

61. Todgham AE, Hofmann GE. Transcriptomic response of sea urchin larvae *Strongylocentrotus purpuratus* to CO_2-driven seawater acidification. J Exp Biol. 2009; 212: 2579–2594. doi: 10.1242/jeb.032540 PMID: 19648403

62. Runcie D, Garfield DA, Babbitt CC, Wygoda JA, Mukjerjee S, Wray GA. Genetics of gene expression responses to temperature stress in a sea urchin gene network. Mol Ecol. 2012; 21: 4547–4562. doi: 10.1111/j.1365-294X.2012.05717.x PMID: 22856327

63. Marrone V, Piscopo M, Romano G, Ianora A, Palumbo A, Costantini M. Defensome against toxic diatom aldehydes in the sea urchin *Paracentrotus lividus*. PLoS One. 2012; 7: e31750. doi: 10.1371/journal.pone.0031750 PMID: 22363721

64. Zito F, Costa C, Sciarrino S, Poma V, Russo R. Expression of univin, a TGF-b growth factor, requires ectoderm-ECM interaction and promotes skeletal growth in the sea urchin embryo. Dev Biol. 2003; 264: 217–227. PMID: 14623243

65. Röttinger E, Saudemont A, Duboc V, Besnardeau L, McClay D, Lepage T. FGF signals guide migration of mesenchymal cells, control skeletal morphogenesis and regulate gastrulation during sea urchin development. Development. 2008; 135: 353–365. PMID: 18077587

66. Martin S, Richier S, Pedrotti ML, Dupont S, Castejon C, Gerakis Y, et al. Early development and molecular plasticity in the Mediterranean sea urchin *Paracentrotus lividus* exposed to CO_2-driven acidification. J Exp Biol. 2011; 214: 1357–1368. doi: 10.1242/jeb.051169 PMID: 21430213

67. Amiard JC, Amiard-Triquet C, Barka S, Pellerin J, Rainbow PS. Metallothioneins in aquatic invertebrates: their role in metal detoxification and their use as biomarkers. Aquat Toxicol. 2006; 76: 160–202. PMID: 16289342

68. Leslie EM, Deeley RG, Cole SP. Toxicological relevance of the multidrug resistance protein 1, MRP1 (ABCC1) and related transporters. Toxicology. 2001; 167: 13–23.

69. Kurelec B. The Multixenobiotic Resistance Mechanism in Aquatic Organisms. Crit Rev Toxicol. 1992; 22: 23–43. PMID: 1352103

70. Della Torre C, Zaja R, Loncar J, Smital T, Focardi S, Corsi I. Interaction of ABC transport proteins with toxic metals at the level of gene and transport activity in the PLHC-1 fish cell line. Chem Biol Interact. 2012; 198: 1–17. doi: 10.1016/j.cbi.2012.04.008 PMID: 22580103

71. Foulkes EC. Transport of toxic metal across cell membranes. Proc Soc Exp Biol Med. 2000; 223: 234–240. PMID: 10719835

72. Griffith OW, Stuehr DJ. Nitric oxide synthases: properties and catalytic mechanism. Annu Rev Physiol. 1995; 57: 707–736. PMID: 7539994

Available online at www.sciencedirect.com
ScienceDirect
The International Journal of Biochemistry & Cell Biology 39 (2007) 1902–1914
IJBCB
www.elsevier.com/locate/biocel

Feijoa sellowiana derived natural Flavone exerts anti-cancer action displaying HDAC inhibitory activities

Paola Bontempo [a], Luigi Mita [a], Marco Miceli [a], Antonella Doto [a], Angela Nebbioso [a], Floriana De Bellis [a,d], Mariarosaria Conte [a], Annunziata Minichiello [a], Fabio Manzo [a,d], Vincenzo Carafa [a], Adriana Basile [f], Daniela Rigano [g], Sergio Sorbo [f], Rosa Castaldo Cobianchi [f], Ettore Mariano Schiavone [e], Felicetto Ferrara [e], Mariacarla De Simone [e], MariaTeresa Vietri [a], Michele Cioffi [a], Vincenzo Sica [a], Francesco Bresciani [a], Angel R. de Lera [c], Lucia Altucci [a,b,*], Anna Maria Molinari [a]

[a] *Dipartimento di Patologia Generale, Seconda Università degli Studi di Napoli, vico L. De Crecchio 7, 80138 Napoli, Italy*
[b] *Centro di Oncogenomica AIRC, CEINGE Biotecnologia avanzata, Napoli, Italy*
[c] *Departamento de Quimica Orgánica, Facultad de Química, 36310 Vigo, Spain*
[d] *Department of Cell Biology and Signal Transduction, IGBMC/INSERM/CNRS, 67404 Illkirch, Strasbourg, France*
[e] *Ematologia con trapianto di cellule staminali, Ospedale Cardarelli, via Cardarelli 9, 80131 Napoli, Italy*
[f] *Dipartimento di Scienze Biologiche, sezione Biologia vegetale, Università di Napoli Federico II, Napoli, Italy*
[g] *Dipartimento di Chimica dei Prodotti naturali, Università di Napoli "Federico II", Italy*

Received 12 February 2007; received in revised form 4 May 2007; accepted 15 May 2007
Available online 25 May 2007

Abstract

Curative properties of some medicinal plants such as the *Feijoa sellowiana* Bert. (Myrtaceae), have been often claimed, although the corresponding molecular mechanism(s) remain elusive. We report here that the *Feijoa* acetonic extract exerts anti-cancer activities on solid and hematological cancer cells. *Feijoa* extract did not show toxic effects on normal myeloid progenitors thus displaying a tumor-selective activity. In the *Feijoa* acetonic extract, fractionation and subsequent purification and analyses identified Flavone as the active component. Flavone induces apoptosis which is accompanied by caspase activation and p16, p21 and TRAIL over-expression in human myeloid leukemia cells. Use of *ex vivo* myeloid leukemia patients blasts confirms that both the full acetonic *Feijoa* extract and its derived Flavone are able to induce apoptosis. In both cell lines and myeloid leukemia patients blasts the apoptotic activity of *Feijoa* extract and Flavone is accompanied by increase of histone and non-histone acetylation levels and by HDAC inhibition. Our findings show for the first time that the *Feijoa* apoptotic active principle is the Flavone and that this activity correlates with the induction of HDAC inhibition, supporting the hypothesis of its epigenetic pro-apoptotic regulation in cancer systems.
© 2007 Elsevier Ltd. All rights reserved.

Keywords: Cancer; Epigenetic drugs; Leukemia; Apoptosis; Cell biology

* Corresponding author at: Dipartimento di Patologia Generale, Seconda Università degli Studi di Napoli, vico L. De Crecchio 7, 80138 Napoli, Italy. Tel.: +39 0815667569; fax: +39 0812144840.
E-mail address: lucia.altucci@unina2.it (L. Altucci).

1357-2725/$ – see front matter © 2007 Elsevier Ltd. All rights reserved.
doi:10.1016/j.biocel.2007.05.010

1. Introduction

In many developing countries about 80% of available drugs come from medicinal plants, while frequently in industrialised countries the raw materials to synthesize pure chemical derivatives have plants origin. *Feijoa sellowiana* Berg. (Myrtaceae) is an evergreen bushy shrub originally native to South America and well acclimatized to the Mediterranean. *Feijoa* grows throughout the Mediterranean and it is widely used for human food (Aliev, Orudzhev, Aliev, & AKh, 1964). The edible fruit ripens in autumn as a spherical berry, 5–8 cm long, 20–30 g heavy. The fruit contains large quantities of vitamin C (28 mg/100 g fresh weight), hydrocarbons and minerals and iodine (3 mg/100 g) (Romero Rodriguez, Vazquez Oderiz, Lopez Hernandez, & Simal Lozano, 1992). The fruit contains terpenes, tannins, quinones, steroidal saponins, methyl- and ethyl-benzoate, responsible of the typical strong taste "*Feijoa-like*" (Binder & Flath, 1989; Foo & Porter, 1981). *Feijoa* contains also high amounts of bioflavonoids or vitamin P, (P)-active polyphenols, such as catechin, leucoanthocyanins, flavonols, proanthocyanidins, and naphthoquinones (Ielpo et al., 2000). Although the chemical composition of *Feijoa* fruit has been clearly reported (Herrmann, 1981), pharmaceutical studies of its constituents have barely been carried out. *Feijoa* showed potent antimicrobial activity against Gram-positive and Gram-negative bacteria as well as fungi and a sensible activity against *Helicobacter pylori* (Basile et al., 1997; Motohashi et al., 2000; Vuotto et al., 2000). Moreover, antioxidant activities of an aqueous extract on oxidative burst of human whole blood phagocytes as well as on isolated polymorphonuclear leukocytes have been reported. In addition, *Feijoa* peel contains components exhibiting MDR-modulation (Motohashi et al., 2000). These biological activities are interesting as emerging drug resistance is present among bacteria, virus and tumor cells. Finally, the tropical and subtropical countries where *Feijoa* is daily consumed have lower cancer incidence. Some anti-cancer activities of the full *Feijoa* extract have been reported (Abe et al., 2000; Nakashima, 2001), but a complete characterization of its active principles is lacking.

Here, we show that in different cancer cellular models the full acetonic extract of the *Feijoa* fruit exerts anti-cancer activities with low toxicity on normal cells. Moreover, we demonstrate that the anti-cancer potential is pharmacologically due to the Flavone contained in the fruit, that displays inhibitory activities on deacetylase enzymes thus hyper-acetylating histones and non-histone targets in leukemia cell lines and patients blasts. Finally, we identify p16, p21 and TRAIL as some of the molecular effectors of the pro-apoptotic *Feijoa* activity.

2. Materials and methods

2.1. Plant material

Feijoa sellowiana Berg. (Myrtaceae) fruits were collected from the Botanical Gardens of Naples (Italy). The identification was done by Prof. Adriana Basile—Section of Plant Biology of the Department of Biological Sciences of University Federico II of Naples. A voucher specimen (NAP 96-125) is deposited at the Herbarium Neapolitanum (NAP), Section of Plant Biology of the Department of Biological Sciences of University Federico II of Naples.

2.2. Preparation of the acetonic extract

Feijoa fruits, fresh or after storage at −5 °C, were treated with Triton X-100 0.8% water solution to remove epiphytic hosts normally found on the surface. After extensive washings in tap and distilled water, the fruits were dried on filter paper and then extracted with acetone for 15 min in a liquefied blender until homogenized. The acetonic extract (Basile et al., 1997) has been chosen after the screening for antibacterial activity in aqueous, acetonic and chloroform extracts. The extract was then centrifuged at 2800 × *g* and the supernatant is oven-dried at 45 °C. The test samples were prepared according to the method employed by Ieven, Vanden Berghe, Mertens, Vlietinck, and Lammens (1979) where 100 mg of the dry residues are dissolved in 10 ml of sterile physiological TRIS buffer (pH 7.4).

2.3. Extraction and isolation of active compounds

Six hundred and ninety grams of whole feijoa fruits were blended, freeze-dried and then extracted for 3 days with acetone at room temperature (3 × 5 l). After filtration, the solvent was evaporated under reduced pressure and moderate temperature (35 °C) to give a gum (46.45 g). An amount of the extract (5.8 g) was dissolved in CH_3OH and then subjected to column chromatography on silica gel 60 Merck (4 cm × 100 cm, 300 g, 70–230 mesh). Elution with *n*-hexane/EtOAc (from 100:0 to 0:100 stepwise gradient) and successively methanol afforded 11 fractions (A–M) of 100 ml each, gathered according to TLC analysis (eluent system *n*-hexane/EtOAc (1:1, v/v), spray reagent $Ce(SO_4)_2$ in H_2SO_4), that were submitted for biological testing: fraction A (57 mg,

eluted with 80:20 *n*-hexane/EtOAc), B (35.6 mg, eluted with 60:40 *n*-hexane/EtOAc), C (30.1 mg, eluted with 50:50 *n*-hexane/EtOAc), D (28.4 mg, eluted with 40:60 *n*-hexane/EtOAc), E (18.2 mg, eluted with 30:70 *n*-hexane/EtOAc), F (22 mg, eluted with 100% EtOAc), G (31.4 mg, eluted with 90:10 EtOAc/MeOH), H (457 mg, eluted with 70:30 EtOAc/MeOH), I (1.4 g, eluted with 60:40 EtOAc/MeOH), L (410 mg, eluted with 10:90 EtOAc/MeOH) and M (58.2 mg, eluted with 100% MeOH). Fraction B, which showed to be the most active, consisted of pure flavone (see Fig. 3, 0.75% dry wt.). The structure was determined by comparison of its spectroscopic data (UV, NMR and MS) with literature values (Agrawal, 1989).

Other 17.4 g of acetonic extract of *Feijoa sellowiana* were subjected to chromatographic separation with the procedure described above to obtain 106.8 mg of Flavone for the biological testing.

2.4. General experimental procedures

UV spectrum was obtained on a Jasco 7800 UV–Vis spectrophotometer. ^{1}H and ^{13}C NMR spectra were recorded on a Varian Mercury 400 MHz NMR spectrometer (^{1}H at 400.4 MHz, ^{13}C at 100.7 MHz), δ (ppm), J in Hz, using the residual solvent signal (δ 7.27 in ^{1}H and δ 77.0) as reference. ESIMS was obtained on Applied Biosystem API-2000 mass spectrometer. Merck Silica gel (70–230 mesh) was used for column chromatography. Thin-layer chromatography (TLC) was performed on plates coated with silica gel 60 F_{254} Merck, 0.25 mm. All solvents (analytical and deuterated grade) were purchased from Carlo Erba Reagenti, Milan, Italy. Commercial flavone (FS) was purchased from Sigma–Aldrich (Milan, Italy).

2.5. Cell lines, primary cells and materials

All cell lines have been obtained from ATCC and routinely cultured.

MCF7 and HeLa cells were grown at 37 °C in air and 5% CO_2 in Dulbecco's Modified Eagle Medium (DMEM, GIBCO, Grand Island, NY, USA) supplemented with 5% fetal bovine serum (FBS, GIBCO), 1% L-glutamine, 1% ampicillin/streptomycin and 0, 1% gentamicin. SKBR3 cells were grown at 37 °C in air and 5% CO_2 in Dulbecco's Modified Eagle Medium (DMEM, GIBCO, Grand Island, NY, USA) supplemented with 10% fetal bovine serum (FBS, GIBCO), 1% L-glutamine, 1% ampicillin/streptomycin and 0, 1% gentamicin. U937, MDA-MB231, LnCap and NB4 cells, were grown at 37 °C in air and 5% CO_2 in RPMI 1640 medium (GIBCO), supplemented with 10% heat-inactivated foetal bovine serum (FBS), 1% L-glutamine, 1% ampicillin/streptomycin and 0, 1% gentamicin. For the AML samples and normal CD34+ progenitors purifications and cultures have been carried out as previously described (Nebbioso et al., 2005). This study was approved by the Ethycal Committee of the Second University of Naples. All *trans* retinoic acid (SIGMA) (ATRA) was used resuspended in ethanol and at the final concentration of 1 μM. SAHA (kind gift of Merck) was resuspended in DMSO and thereby used at the final concentration of 1 μM. ICI 182, 780 was resuspended in ethanol and used at the final concentration of 1 μM.

2.6. Cell-based human HDAC1 assay

U937 cells for the HDAC1 assay were lysed in IP buffer (Tris–HCl pH 7.0, 50 mM, NaCl, 180 mM, NP-40, 0.15%, glycerol, 10%, $MgCl_2$, 1.5 mM, $NaMO_4$ 1 mM, NaF 0.5 mM) with protease inhibitor cocktail (Sigma), DTT 1 mM and PMSF 0.2 mM for 10 min in ice and centrifugated at 13,000 rpm for 30 min. One thousand micrograms of extracts were diluted in IP buffer up to 1 ml and pre-cleared by incubating with 20 μl A/G plus Agarose (Santa Cruz) for 30 min to 1 h on a rocking table at 4 °C. Supernatants were transferred into a new tube and the antibodies (3 μg of HDAC1, Abcam) were added and IP was allowed to proceed overnight at 4 °C on a rocking table. As negative control the same amount of protein extracts were immunoprecipitated with the corresponding purified IgG (Santa Cruz). The following day 20 μl A/G plus Agarose (Santa Cruz) were added to each IP and incubation was continued for 2 h. The beads were recovered by brief centrifugation and washed with cold IP buffer several times. The samples were than washed twice in PBS and resuspended in 20 μl of sterile PBS. The HDAC assay was carried out according to supplier's instructions (Upstate). Briefly, samples immunoprecipitated with HDAC1 or with purified IgG were pooled, respectively to homogenize all samples. Ten microliters of the IP was incubated with a previously labeled ^{3}H-Histone H4 peptide linked with streptavidine agarose beads (Upstate). In details, 120000 CPM of the H4-^{3}H-acetyl-peptide was used for each tube and incubated in 1× HDAC buffer with 10 μl of the sample in presence or absence of HDAC inhibitors with a final volume of 200 μl. Those samples were incubated over night at 37 °C in slow rotation. The following day 50 μl of a quenching solution were added and 100 μl of the samples were counted in duplicate after a brief centrifugation in a scintillation counter. Experiments have been carried out in quadruplicate.

2.7. Crystal violet and Trypan blu assays

In a 96 multiwell plate (BD), about 1200 cells/well were resuspended in 200 μl of cell cultures medium. After treatment with *Feijoa* extract, cells were fixed in 25 μl of 11% gluteraldehyde in PBS (SIGMA) for 15 min, washed in deionised water and dried. Wells were incubated for 20 min in 100 μl of Crystal violet (CV; Sigma), 1 mg/ml in 20% methanol, and than washed again. Wells were incubated immediately for 20 min in 100 μl of acetic acid (10%). Colorimetric assay carried out in triplicate was quantified by measuring OD_{595}. As alternative viability assay, we have performed a dye exclusion stain, where cells with an intact membrane are able to exclude the dye while cells without an intact membrane take up the colouring agent. The dye used for exclusion stain is the Trypan blue (SIGMA). Briefly cells have been mixed 1:1 with a 0.4% Trypan blu solution and counted in triplicate.

2.8. Cell cycle analysis

2.5×10^5 cells were collected and resuspended in 500 μl of a hypotonic buffer (0.1% Triton X-100, 0.1% sodium citrate, 50 μg/ml propidium iodide (PI), RNAse A). Cells were incubated in the dark for 30 min. Samples were acquired on a FACS-Calibur flow cytometer using the Cell Quest software (Becton Dickinson) and analysed with standard procedures using the Cell Quest software (Becton Dickinson) and the ModFit LT version 3 Software (Verity) as previously reported (De Luca et al., 2003). All the experiments were performed in triplicate.

2.9. FACS analysis of apoptosis

Apoptosis was measured with Annexin V/PI double staining detection (Roche and Sigma–Aldrich, respectively) as recommended by the suppliers; samples were analysed by FACS with Cell Quest technology (Becton Dickinson) as previously reported (Altucci et al., 2001; Nebbioso et al., 2005). We measured as apoptotic fraction the Annexin V positive, PI negative cells. As second assays the caspase 8 and 7, 3 detection (B-Bridge) was performed as recommended by suppliers and quantified by FACS (Becton Dickinson). Apoptotic assays and cell cycle analyses have been carried out separately and drawn later on together in the same figures.

2.10. Granulocytic differentiation assay

Granulocytic differentiation was carried out as previously described (Altucci et al., 2001; Nebbioso et al., 2005). Briefly, NB4 cells were harvested and resuspended in 10 μl phycoerythrine-conjugated CD11c (CD11c-PE) or 10 μl FITC-conjugated CD14 (CD14-FITC) (Pharmingen). Control samples were incubated with 10 μl PE or FITC conjugated mouse IgG1, incubated for 30 min at 4 °C in the dark, washed in PBS and resuspended in 500 μl PBS containing PI (0.25 μg/ml). Samples were analysed by FACS with Cell Quest technology (Becton Dickinson). PI positive cells have been excluded from the analysis.

2.11. RT-PCR analyses

RT-PCR analyses have been carried out as previously shown (Altucci et al., 2001). Sequences of used primers are: TRAIL forward CAACTCCGTCAGCTCGTTAGAAAG; TRAIL reverse TTAGACCAACAACTATTTCTAGCACT; β-actin forward CATGTACGTTGCATCCAGGC; β-actin reverse CTCCTTAATGTCACGCACGAT.

2.12. Western blot analyses

Forty micrograms of total protein extracts were separated on a 15% polyacrylamide gel and blotted as previously described (Mai et al., 2006). Western blots were shown for p21 (Transduction Laboratories, dilution 1:500), and for p16 (Santa Cruz) and total ERKs (Santa Cruz) were used to normalise for equal loading. For determination of α-tubulin acetylation, 25 μg of total protein extracts were separated on a 10% polyacrylamide gel and blotted. Western blots were shown for acetylated α-tubulin (Sigma, dilution 1:500) and total ERKs (Santa Cruz, dilution 1:1000) were used to normalise for equal loading. For quantification of histone H3 acetylation, 40 μg of total protein extracts were separated on a 15% polyacrylamide gel and blotted. Western blots were shown for acetylated histone H3 (Upstate cat. 06-599) and total tubulin (Sigma) was used to normalise for equal loading. For quantification of TRAIL protein, 100 μg of total protein extracts were separated on a 10% polyacrylamide gel and blotted. Western blots were shown for TRAIL (Chemicon) and Actin (Abcam) was used to normalise for equal loading.

2.13. Morphology and immunocitochemistry

NB4 cells were spun onto glass slides with a citospin centrifuge. Cell morphology were analysed after May-Grünwald Giemsa stain (SIGMA). To detect acetylated histone H3 cells were fixed for 5 min in 95%

absolute ethanol −5% acetic acid, washed thrice in PBS and incubated for 1 h in 4%BSA–2%FCS serum. The slides were washed in PBS and incubated overnight in PBS–0.2%BSA containing rabbit anti-acetylated histone H3 (Upstate) antibodies diluted 1:200. After three washes in PBS, the slides were incubated for 1 h with secondary FITC-conjugated donkey anti-rabbit antibody (Jackson ImmunoResearch) diluted 1:200 in PBS–0.2%BSA. Following five washes with PBS, slides were mounted in fluorescent mounting medium (Dako-Cytomation) and analysed with a ZEISS Axioscop 2 fluorescence microscope. All images shown are representative of the 20× magnification.

3. Results

3.1. Identification and characterization of cancer cells responsiveness to Feijoa extracts

The efficacy of different doses of the *Feijoa* acetonic extract was assessed in solid and hematological cancer cell lines (Fig. 1). Tested in proliferation curve with a Crystal violet assay, the crude *Feijoa* extract displayed anti-proliferative activity in some solid cancer cell lines such as HeLa (cervical cancer), MCF-7, SKBR-3, MDA-MB231 (breast cancer) cells. Moreover, this anti-growth action, measured by Trypan blu viability

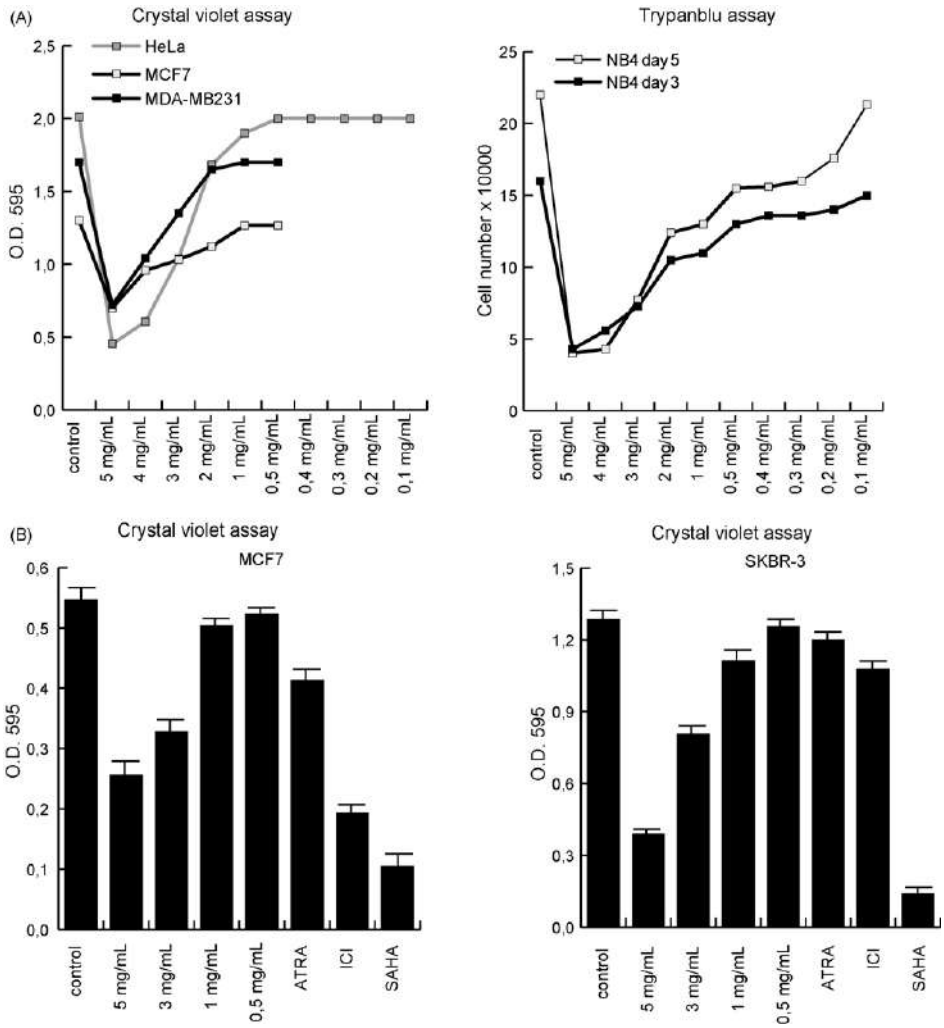

Fig. 1. Anti-proliferative potential of *Feijoa* acetonic extract. (A, left) Proliferation curves by Crystal violet assay in the indicated cell lines at day 5 of treatment. (A, right) Proliferation curve by Trypan blu assay in NB4 cells at day 3 and 5 after treatment with the indicated compounds. Results represent the media of triplicates. (B) Crystal violet assay carried out in MCF7 and SKBR-3 breast cancer cells after the treatment for 3 days with the indicated compounds. ATRA: all-*trans*-retinoic acid; ICI: ICI182780; SAHA: suberoylanilide hydroxamic acid.

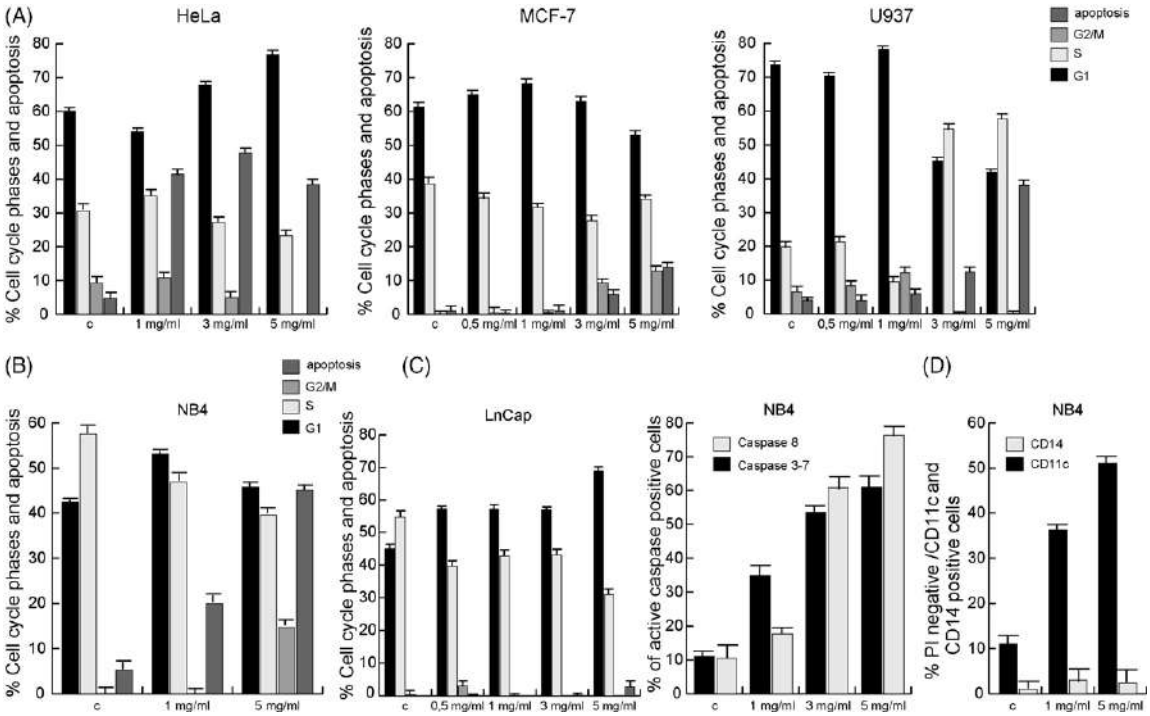

Fig. 2. *Feijoa* acetonic extract induce cell cycle block, differentiation and apoptosis in cancer cells. (A) Cell cycle and apoptosis in Hela, MCF7 and U937 cells after treatment with 1, 3 and 5 mg/ml (Hela cells) and 0.5, 1, 3 and 5 mg/ml (MCF7 and U937 cells) of Feijoa extracts for 3 days; B (left) Cell cycle analysis and apoptosis in NB4 cells after treatment with 1 and 5 mg of *Feijoa* extract for 3 days; B (right) Cell cycle analysis and apoptosis in LnCap cells after treatment with 0.5, 1, 3 and 5 mg/ml of *Feijoa* extract for 3 days; (C) Caspase 8 and 3, 7 assays carried out by FACS in NB4 cells after 2 days of incubation with the indicated amounts of *Feijoa* extract; (D) CD11c and CD14 expression levels measured by FACS after 48 h of treatment with the indicated amounts of *Feijoa* extract in NB4 cells. Note that PI positive cells have been excluded from the analysis.

assay, could also be shown in NB4 leukemia cells, the prototype of acute promyelocytic leukemia (APL), an acute myeloid leukemia (AML) classified as M3 according to the French-American-British (FAB) classification, which carries the chromosomal translocation *t*(15;17) leading to the expression of the fusion protein PML-RARα. Fig. 1A and B show that the anti-proliferative effect is dose dependent and not due to drug toxicity. Indeed prostate cancer cell lines, such as the LnCaP cancer cells, were weakly affected by the *Feijoa* treatment (Fig. 2C). In all the described cell lines, the major effect has been obtained using 5–3 mg/ml of the crude extract. The anti-proliferative effect has been compared to those of known anti-tumor growth agents such as retinoic acid (ATRA) (Altucci & Gronemeyer, 2001; Altucci et al., 2001; Altucci, Wilhelm, & Gronemeyer, 2004), the antiestrogen ICI182780 (Cicatiello et al., 2000) or the HDAC inhibitor SAHA (Altucci, Clarke, Nebbioso, Scognamiglio, & Gronemeyer, 2005; Insinga, Minucci, & Pelicci, 2005; Nebbioso et al., 2005) (Fig. 1A and B). Investigating for the anti-cancer potential of the full *Feijoa* acetonic extract, we tested its biological effects on cell cycle and apoptosis in solid cancer (HeLa, MCF7, LnCap cells) and in myeloid leukemia cell lines (U937, NB4). As shown in Fig. 2, four cell lines (HeLa, MCF7, U937, NB4) responded with apoptosis in a dose dependent manner, although displaying different sensitivities. Moreover, LnCap cells showed to be less sensitive (Fig. 2C) thus indicating a certain specificity for the *Feijoa* extract activity. In HeLa cells, increasing amounts of the *Feijoa* acetonic extract induced a G1 block of the cell cycle, whereas in MCF7, U937 and NB4 cells the block was in S or G2/M phases (Fig. 2A–D). These differences in the cell cycle block might be due to cellular context specific events. Finally, in the NB4 cellular system, we performed caspases 8 and 3, 7 assays, thus confirming the involvement of caspases in the induction of cell death by *Feijoa* extracts (Fig. 2D). Differentiation assays measured by CD11c and CD14 expression indicated that crude *Feijoa* extracts were able to induce granulocytic differentiation (Fig. 2D) in the NB4 cell line, suggesting that the cell cycle block induced

by the treatment was followed by differentiation and apoptosis.

3.2. *Feijoa chemical fractionation and analysis of the biological anti-cancer potential of the fractions*

Intrigued by the analyses of the biological action of the crude *Feijoa* extracts, we aimed to define which substance (or group of substances) are actively accounting for the anti-cancer action. For this purpose we have performed a fractionation procedure that yielded 11 fractions (A–M, see Section 2). For the biological testing, fraction A was not considered as it contained essentially ubiquitous constituents such as fatty acid derivatives, carotenoids and chlorophylls. The other fractions, i.e. B, C–E, F–H and I–M were tested for their potential to induce anti-cancer effects in comparison with the full *Feijoa* acetonic extract as shown in Fig. 3A and D. Clearly, only fraction B exerted anti-cancer potential being able to induce apoptosis in NB4 APL cells. Fraction B consisted of pure flavone (0.75% dry wt.). The structure was determined by comparison of its spectroscopic data (UV, NMR and MS) with literature values (Agrawal, 1989). As demonstrated by Fig. 3B, the purified Flavone (FP) was able to induce apoptosis in NB4 cells, identifying it as the chemical principle of the *Feijoa* anti-cancer action. Differently from the crude full extract, FP displayed a G1 cell cycle block indicating that different components in the full extract caused the *Feijoa* cell cycle activity. Finally, given that the Flavone is a commercially available compound (SIGMA) we compared the activity of different doses of FP to the

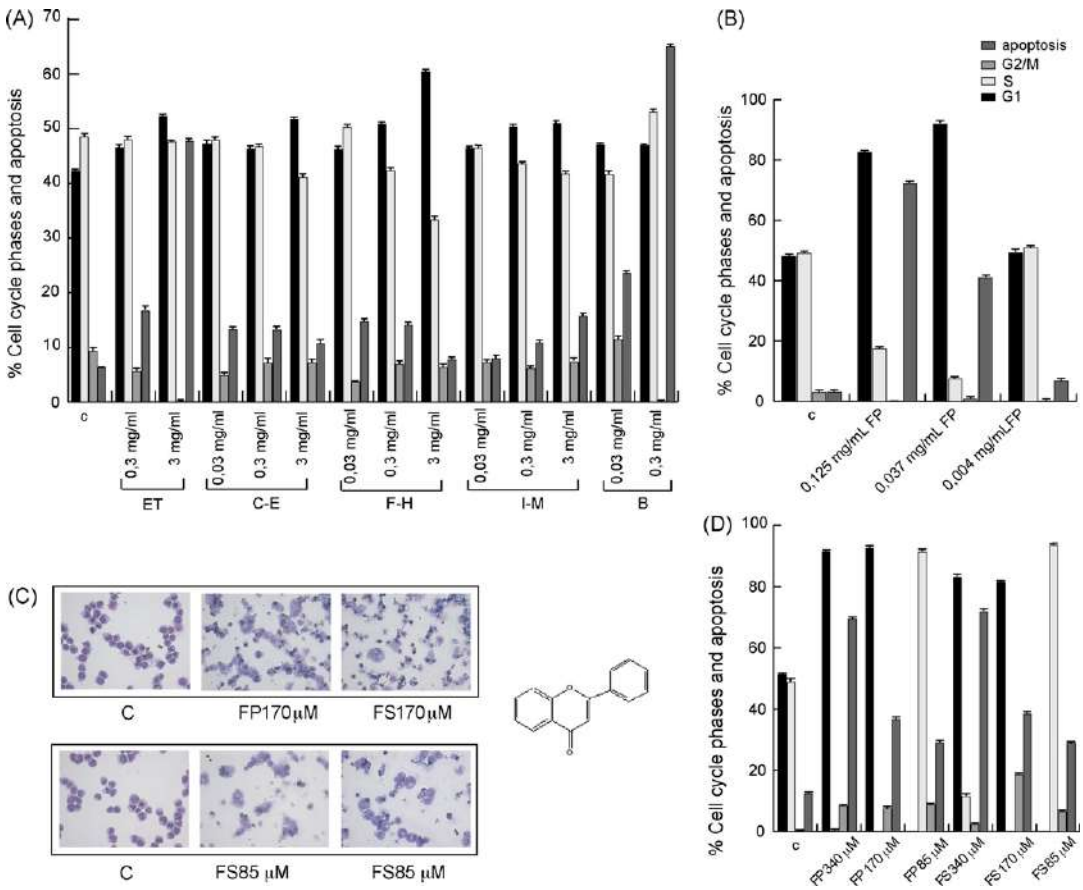

Fig. 3. Flavone is the *Feijoa* active principle that induces cancer cells apoptosis. (A) Cell cycle and apoptosis analyses carried out by FACS in NB4 cells treated for 3 days with the full extract (ET) or with the indicated fractions (see also Section 2) for 2 days. (B) Cell cycle analysis and apoptosis carried out by FACS in NB4 cells treated for 2 days with the flavone purified (FP) from the *Feijoa* extract. Note that 0.037 mg/ml of FP correspond to the 170 μM concentration; (C) Comparison of the effects on cell cycle and apoptosis carried out by FACS analysis of the FP and the commercial flavone (FS) in NB4 cells after 3 days of treatment. D (left): morphological analysis carried out in NB4 cells treated with the purified and commercial flavone (FP, FS) for 3 days with the indicated amounts of FP and FS; D (right): structure of the Flavone.

commercial compound (FS) (Fig. 3C and D). Note that our findings are in agreement with the current knowledge that flavones are able to induce block of proliferation and apoptosis in different cancer cellular systems (Chen, Shen, Chow, Ko, & Tseng, 2004; Daskiewicz et al., 2005; Erhart et al., 2005; Shen, Ko, Tseng, Tsai, & Chen, 2004) and that their activity is maximal at concentrations of 100–200 μM.

3.3. Molecular identification and characterization of the anti-cancer effect of Feijoa Flavones

To understand which molecular players could be involved in the *Feijoa* and Flavone anti-cancer action, we tested the expression levels of different known key factors in cell cycle and apoptosis (some of which have been previously reported (Chen et al., 2004)) in NB4

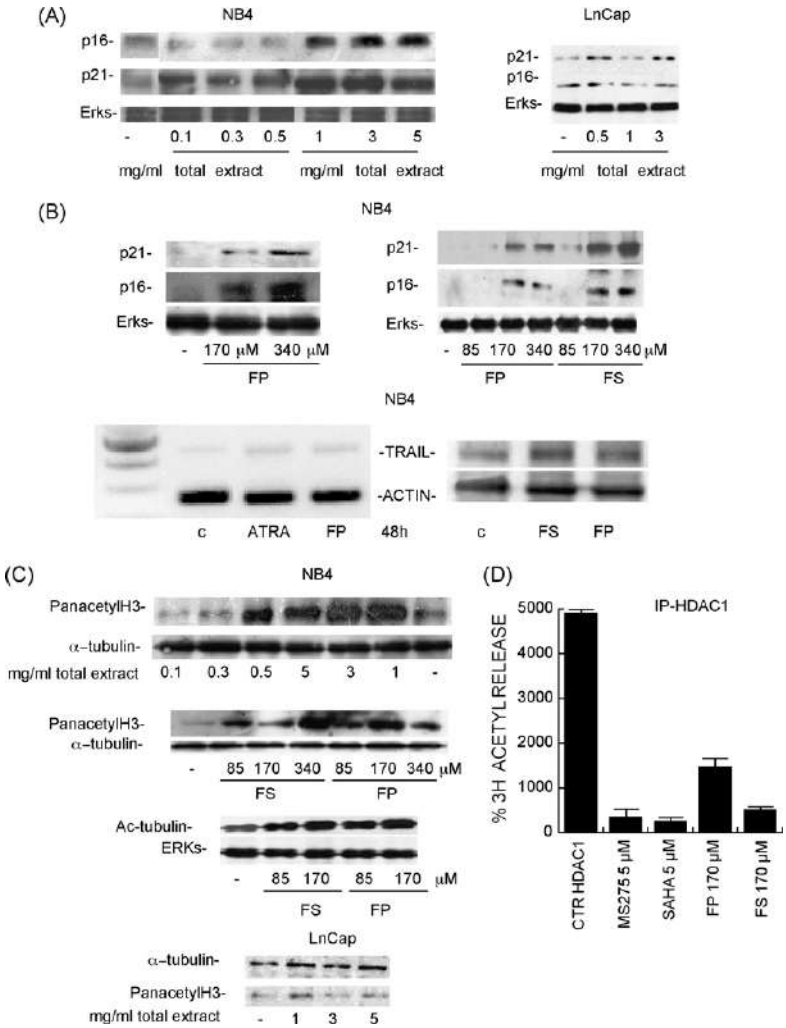

Fig. 4. Flavone induces p16, p21 and TRAIL up-regulation showing HDAC inhibitory action in NB4 cells. (A) Western blot analysis showing p21 and p16 expression levels in NB4 cells (left) and in LnCap cells (right) treated with the indicated doses of the *Feijoa* full extract for 3 days; total ERKs expression levels account for equal loading. B (upper part) Western blot analysis showing p21 and p16 expression levels in NB4 cells treated with the indicated doses of the purified flavone (FP) or with the commercial flavone (FS) for 3 days; total ERKs expression levels account for equal loading; B (lower part): left, TRAIL expression levels shown as RT-PCR after treatment of NB4 cells with the purified Flavone (FP); ATRA treatment has been used as positive control and actin signal stands for RT-PCR internal control; right, Western blot analysis of TRAIL expression levels after treatment with FP and FS at the indicated time and concentrations. Actin expression level account for equal loading. C (upper part) Analysis of the acetylation levels of Histone H3 and α-tubulin in NB4 cells treated for 3 days with *Feijoa* full extract or with Flavone (FP, FS); α-tubulin and ERKs expression levels account for equal loading; (lower part) Analysis of the acetylation levels of Histone H3 in LnCap cells treated for 3 days with *Feijoa* full extract; α-tubulin expression level account for equal loading; (D) HDAC1 inhibition due to FP and FS activity; SAHA and MS275 activities have been taken as positive controls.

cells upon treatments with *Feijoa* full extracts or with the FP and FS. As shown by Western blot analysis in Fig. 4A–C, both the *Feijoa* full extract and the FP were able to induce the cell cycle inhibitors p21 and p16 in NB4 cells. Fully in agreement with the weak sensitivity shown to *Feijoa* treatment, LnCap cells did not show p21 and p16 up-regulation upon treatment (Fig. 4A). Most interestingly the *Feijoa* derived purified Flavone and FS were also able to induce the TRAIL expression measured by semi-quantitative PCR and by Western blot analysis (Fig. 4B lower panel, RT-PCR at the left; Western blot at the right side). The extent of the TRAIL induction was comparable to that by ATRA, a known TRAIL regulator (Altucci et al., 2001).

Given that all the investigated molecular targets are also epigenetically inducible, we decided to establish whether the crude *Feijoa* extract as well as the FP and FS compounds affected histone and α-tubulin acetylation levels. As shown by Western blot in Fig. 4C, we found histone H3 and α-tubulin hyperacetylation induced by both *Feijoa* full extracts and FP–FS compounds (Fig. 4C). Note that α-tubulin was taken as example of non-histone target of acetylation. Finally, HDAC1 enzymatic assays showed that both FP and FS at the concentration of 170 μM were able to inhibit HDAC1 activity as known HDAC inhibitors, SAHA and MS275 (Mai et al., 2005). Thus the enzymatic inhibition might account for the anti-cancer potential of both *Feijoa* acetonic extract and of the Flavone purified from the extract.

3.4. *Feijoa and Flavone anti-cancer action on leukaemia primary blasts*

We aimed to verify whether our results could be corroborated and extended to other *ex vivo* models. We therefore tested the biological activities of *Feijoa* extract and of Flavone in AML blasts and in CD34+ normal progenitors. As shown in Fig. 5 and Table 1, all AML samples showed a clear induction of apoptosis upon addition of the compounds that correlated with increased histone hyperacetylation (see Fig. 5C). On the contrary, the biological effects induced by FS or FP on most CD34+ were minimal (see Table 1) suggesting no or very low toxicity of these compounds at the concentrations tested.

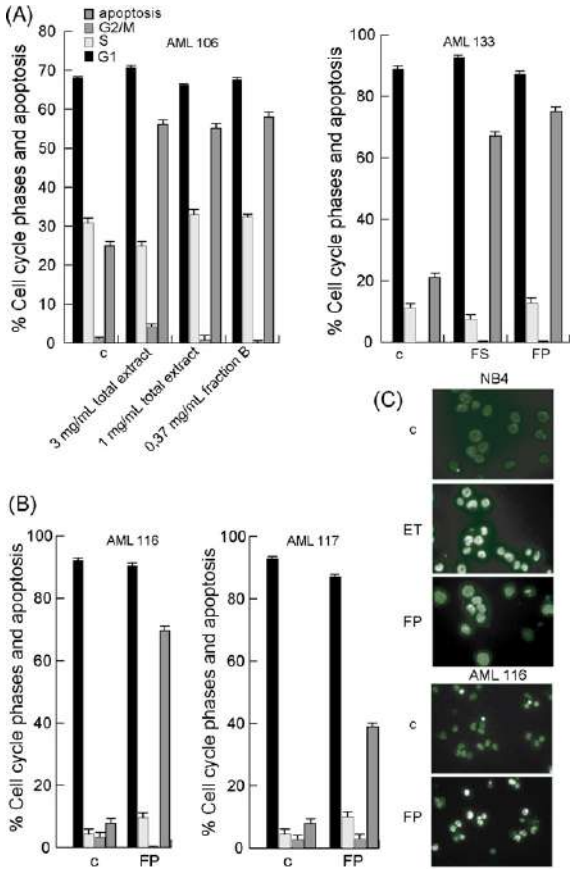

Fig. 5. Flavone induce apoptosis in myeloid leukaemia primary blasts increasing histone H3 acetylation levels. (A) Cell cycle and apoptosis analysis carried out by FACS in AML patient *ex vivo* blasts (#106, #133) after 24 h of treatment with the indicated doses of total *Feijoa* extract, fraction B or FP and FS, respectively. (B) Cell cycle and apoptosis analysis carried out by FACS in AML patient *ex vivo* blasts (#116, #117) after 20 h of treatment with the purified flavone FP. (C) Immunofluorescence analysis of Histone H3 acetylation levels induced after 20 h treatment with total *Feijoa* extract (ET) and with the purified flavone (FP) in NB4 cells (upper panels) and in *ex vivo* AML blasts #116 (lower panels).

4. Discussion

Already in the sixties it was postulated that the pharmacological properties of plants may be curative (Aliev et al., 1964; Alijew & Rachimowa, 1965). The application of natural products as drugs active in human pathologies is complicated because the molecular basis of such pharmacological activities and the identification and characterization of the chemical principles responsible of the biological effects is often missing. *F. sellowiana* has been reported to display an anti-bacterial, antioxidant and modulating activity in multi drug resistance (Basile et al., 1997; Motohashi et al., 2000; Vuotto et al., 2000). Anti-cancer activity of the full extract of the *Feijoa* fruit has been also reported (Abe et al., 2000; Nakashima, 2001), but a characterization of its active compound(s) has not been reported. Our results show that on a panel of different cancer cell lines, the total *Feijoa* acetonic extract exerted anti-proliferative effects accompanied by cell cycle and apoptosis modulation.

Table 1

No.	Apoptosis			FAB	Response to therapy	Karyotype	Immunophenotype
	FP	FS	Hours				
116	61		20	LAM-M1	Y	46, XX	DR+, CD13+, CD33+, CD117+, CD7+, CD44+, MPO-7+, CD19+−, CD34−
112	21	30	24	LAM-M4	N	Complex: 46XX, 1q+, del(9)(p13), del(11)(q21)	DR+, CD34−, CD13+, CD33+, CD117+/−, CD11c+, CD11b+, CD38+, CD56+, MPO-7+
106	33	30	60	LAM-M5a	Y	46, XY	CD34+, CD33+, CD117+
117	31	32	20	LAM-M1	N	46, XY	DR+, CD34+, CD13+, CD33−, CD44+, TdT+
123	2	3	50	AREB-T	Y	46, XY	CD34+, CD13+, CD33+, CD117+
119	1	4	40	LAL T-L2	Y	46, XY	CD7+, CD3−, CD5+, CD34+/−
125	16	18	40	LAM-M3	N	46, XX, *t*(15;17)	DR−, CD34−, CD13+, CD33+, CD117+, CD45RA+, CD45RO−, CD66b−, CD15−
120	24	28	48	LAM-M3 variant	Y	46, XX, neg for PML-RAR	Dr−, CD13+, CD33+, CD117+, CD11b+, CD11c+, CD34+/−
133	45	42	24	LAM-M4	N	N. E. (M)	DR+, CD34−, CD13+, CD33+, CD117+, CD36+, CD14+, CD11b+, CD11c+
134	3	2	24	LAM-M2	N	46, XY, *t*(8;21)	Dr+, CD34+, CD33+, CD19+
21	8	7	24	CD34+		46, XY	
20	10	2	20	CD34+		46, XX	
19	3	2	24	CD34+		46, XX	
18	0.3	0.1	24	CD34+		46, XY	
17	1	0.5	24	CD34+		46, XX	
16	0	0.1	24	CD34+		46, XY	
15	1	0.5	24	CD34+		46, XY	

In addition to FAB status, karyotype and immunophenotype, the response of 10 non-selected samples out of primary blasts, was characterized by FACS analysis to quantify apoptosis ("Apoptosis") relative to the corresponding vehicle treated control cultures (control cultures with levels higher than 25% were not used for the analysis. The apoptosis percentage of control cultures has been subtracted from the value of the treated culture). The patients' response to therapy is indicated, and details are available on request. Patients who showed response to appropriate chemotherapy programs and achieved a complete remission after the induction of the therapeutic phase are stated as Y, unresponsive patients are stated as N. Patients with a too early exitus are classified as not evaluable (NE). Note that AML No. 134 represents the culture of AML1-ETO expressing blasts at the third relapse of disease, post auto-transplantation. Samples 16, 17, 18, 19, 20, 21 represent primary cultures of normal myeloid CD34+ progenitors that have been cultured for the indicated time.

We could rule out that these effects were not due to toxicity because normal myeloid CD34+ progenitors in culture were not affected by the treatment, thus excluding adverse side effects. Note that LnCap prostate cancer cells were minimally sensitive to this treatment, reinforcing the notion that the *Feijoa* acetonic extract is not toxic and displays cancer-cell selectivity. In support of this we observed induction of caspase activity as a result of the treatment with *Feijoa* in NB4 APL cells. Intrigued by these data we set out to determine the biologically active fraction and identified Flavone as the compound responsible for the apoptotic action of the *Feijoa* extract in the cancer cells tested. Interestingly, although able to mimic *Feijoa* apoptotic action, the purified Flavone (FP) did not exert the same effects on cell cycle and differentiation as the crude acetonic extract, suggesting that other components present in this crude fraction might account for these activities. Evidence of the anti-proliferative and anti-cancer action of flavonoids is accumulating in the last decade. Although this large class of natural and synthetic compounds do represent an intriguing family of anti-cancer natural products, the underlying molecular mechanism(s) had not been clarified. Proteasome inhibition (Chen et al., 2005) as well as activation of the TRAIL pathway (Horinaka et al., 2005a, 2005b, 2006) have been correlated with the anti-cancer activities of some flavones. As a first step towards the characterization of the molecular basis for the apoptotic action of the purified Flavone (or the commercial one FS), we showed that they induce p21 and p16 in the responsive cells. The Flavone was also able to up-regulate TRAIL at both RNA and protein levels, thus confirming that this

pathway is involved in its apoptotic action. Intrigued by the observations that the apoptotic activities of flavones are correlated with the TRAIL pathway (Horinaka et al., 2005a, 2005b, 2006) and that TRAIL is a well known target of HDAC inhibitors (Insinga, Monestiroli, et al., 2005; Nebbioso et al., 2005), we assessed whether the *Feijoa* purified flavone was able to act as epigenetic modulator in cancer systems. Excitingly, Flavone induced histone H3 acetylation implying a role in epigenetic modulation in the NB4 APL cell line. Experiments with the *Feijoa* full acetonic extracts showed that this action is present in the total extract and correlates with the apoptotic activity of the full acetonic extract and its purified Flavone component.

Finally, enzymatic assays on HDAC1 activity showed that Flavone plays as a HDAC inhibitor, and this biological action may account for the observed induction of apoptosis and gene regulation. From a pharmacological perspective, the mechanism of HDAC inhibition by Flavone is most intriguing. It is commonly accepted that the enzyme deacetylates the ε-acetylamido lysine of histones and other targets following its occupancy of a narrow binding pocket of about 11 Å deep and subsequent hydrolysis (Biel, Wascholowski, & Giannis, 2005). Deep into the active site is a Zn^{2+} ion that activates bound water for nucleophilic addition. The tetrahedral zinc alkoxide intermediate is stabilized by enzyme residues and then releases the acetate and the lysine products. Crystal structures of the bacterial HDAC orthologue HDLP (Finnin et al., 1999) and of human HDAC8 (Somoza et al., 2004; Vannini et al., 2004) complexed with several natural and synthetic inhibitors support the mechanism of action of HDAC inhibitors through binding site occupancy of the channel and hydrolysis. In addition, a 14 Å long tube-like internal cavity below the active site has been documented (Wang, Wiest, Helquist, Lan-Hargest, & Wiech, 2004), and this has been suggested to be an exit channel for the acetate (Hildmann et al., 2006).

Consistent with the biochemical and structural insights gleaned from both the crystallographic and the Molecular Modeling studies, a prototypical HDAC inhibitor is structurally comprised of three regions: a Zn^{2+} ion chelating functional group (such as hydroxamic acid, thiol, mercaptoamide or trifluoromethylketon), a linker of variable length and nature, and a hydrophobic fragment for molecular recognition of the aminoacids of the binding pocket rim. This view of a canonical structure and mechanism of action for the HDAC inhibitors is however challenged by the characterization of a series of *bona fide* HDAC inhibitors, which are structurally unrelated amongst themselves to suggest a common and unique alternative mechanism of inhibition. In fact, their structure cannot be dissected into the traditional metal binding-linker-cap fragments of most HDACis and in most cases is dramatically different.

Indeed, the *o*-anilinobenzamide class represented by MS-275 has been suggested by Molecular Modeling to occupy the additional pocket (the exit channel) (Wang, Helquist, Wiech, & Wiest, 2005), and this might be shared by SB-429201 (Hu et al., 2003). The cyclic nature of the macrocyclic bis-pyridinium cyclostellettamine natural products (Oku et al., 2004) prevents the channel occupancy. Alternatively, these compounds might act by either blocking the entrance to the active site or inhibit the HDAC-chromatin recognition events given the presence of charged pyridinium ions. With regard to Flavone, one might suggest the occupation of the exit channel or additional more shallow binding sites in HDAC with possible allosteric modulatory effects (Bouchain & Delorme, 2003), as has been documented with certain kinase inhibitors.

Our new findings shed a novel light on the beneficial effects exerted by *F. sellowiana* extract, suggesting that the anti-cancer potential of this fruit might be due to its epigenetic modulation on responsive cells. We have dissected the therapeutic potential of the *Feijoa* extract into at least one of its molecular activities, i.e. to inhibit HDACs. It is likely that other biological activities contribute to the effect of the *Feijoa* extract on cell cycle and differentiation because the purified Flavone in contrast to the crude extract only minimally influenced differentiation indicating that other components of the *Feijoa* extract may be responsible for this activity and that differentiation and apoptotic pathways are separate events.

Taken together, our data provide a new perspective for the use of natural products in the treatment of human pathologies and indicate that plant components may exert anti-cancer activities via epigenetic modulation such as HDAC inhibition. Given the need of new 'smart' anti-cancer drugs, the development of products of natural origin with minimal side effects and with a well defined action on target cells may represent a new class of cancer selective death-inducers for the future.

Acknowledgements

We thank Prof. H.G. Stunnenberg for suggestions and for carefully reading the manuscript. *Grant Support*. European Union (EPITRON LSHC-CT2005-518417) to L.A. and A. de L.; the Ministero Italiano dell'Università e Ricerca PRIN 2006052835_003 to L.A. and the Ministerio de Educación y Ciencia (SAF04-07131/FEDER) to A.R. de L. Ricerca Finalizzata 2000-Ministero della

Sanità "Progetti speciali" Art 12 bis, comma 6 d. Igs 229/99. A.N., A.M. and M.M. have been financed within the LSHC-CT2005-518417 EU contract. F.M. is a PhD student supported by the Italian-French Association. F. De B. is a PhD student in co-tutele at the IGBMC.

References

Abe, I., Seki, T., Umehara, K., Miyase, T., Noguchi, H., Sakakibara, J., et al. (2000). Green tea polyphenols: Novel and potent inhibitors of squalene epoxidase. *Biochem. Biophys. Res. Commun.*, *268*, 767–771.

Agrawal, P. K. (1989). *NMR of flavonoids. Carbon-13*. London: Elsevier.

Aliev, R. K., Orudzhev, I. M., Aliev, T. A., & AKh, R. (1964). Juice from Feijoa Fruit. *Aptechn. Delo*, *13*, 24–26.

Alijew, R. K., & Rachimowa, A. C. (1965). Sucfejsel – the Juice of the Fruits of *Feijoa Sellowiana* Berg – in the Therapy of Thyrotoxicosis. *Pharm. Zentralhalle. Dtschl.*, *104*, 164–166.

Altucci, L., Clarke, N., Nebbioso, A., Scognamiglio, A., & Gronemeyer, H. (2005). Acute myeloid leukemia: Therapeutic impact of epigenetic drugs. *Int. J. Biochem. Cell Biol.*, *37*, 1752–1762.

Altucci, L., & Gronemeyer, H. (2001). The promise of retinoids to fight against cancer. *Nat. Rev. Cancer*, *1*, 181–193.

Altucci, L., Rossin, A., Raffelsberger, W., Reitmair, A., Chomienne, C., & Gronemeyer, H. (2001). Retinoic acid-induced apoptosis in leukemia cells is mediated by paracrine action of tumor-selective death ligand TRAIL. *Nat. Med.*, *7*, 680–686.

Altucci, L., Wilhelm, E., & Gronemeyer, H. (2004). Leukemia: Beneficial actions of retinoids and rexinoids. *Int. J. Biochem. Cell Biol.*, *36*, 178–182.

Basile, A., Vuotto, M. L., Violante, U., Sorbo, S., Martone, G., & Castaldo-Cobianchi, R. (1997). Antibacterial activity in *Actinidia chinensis*, *Feijoa sellowiana* and *Aberia caffra*. *Int. J. Antimicrobial. Agents*, *8*, 199–203.

Biel, M., Wascholowski, V., & Giannis, A. (2005). Epigenetics—an epicenter of gene regulation: Histones and histone-modifying enzymes. *Angew. Chem. Int. Ed. Engl.*, *44*, 3186–3216.

Binder, R. G., & Flath, R. A. (1989). Volatile components of pineapple guava. *J. Agric. Food Chem.*, *37*, 734–736.

Bouchain, G., & Delorme, D. (2003). Novel hydroxamate and anilide derivatives as potent histone deacetylase inhibitors: Synthesis and antiproliferative evaluation. *Curr. Med. Chem.*, *10*, 2359–2372.

Chen, D., Daniel, K. G., Chen, M. S., Kuhn, D. J., Landis-Piwowar, K. R., & Dou, Q. P. (2005). Dietary flavonoids as proteasome inhibitors and apoptosis inducers in human leukemia cells. *Biochem. Pharmacol.*, *69*, 1421–1432.

Chen, Y. C., Shen, S. C., Chow, J. M., Ko, C. H., & Tseng, S. W. (2004). Flavone inhibition of tumor growth via apoptosis in vitro and in vivo. *Int. J. Oncol.*, *25*, 661–670.

Cicatiello, L., Addeo, R., Altucci, L., Belsito Petrizzi, V., Boccia, V., Cancemi, M., et al. (2000). The antiestrogen ICI 182, 780 inhibits proliferation of human breast cancer cells by interfering with multiple, sequential estrogen-regulated processes required for cell cycle completion. *Mol. Cell. Endocrinol.*, *165*, 199–209.

Daskiewicz, J. B., Depeint, F., Viornery, L., Bayet, C., Comte-Sarrazin, G., Comte, G., et al. (2005). Effects of flavonoids on cell proliferation and caspase activation in a human colonic cell line HT29: An SAR study. *J. Med. Chem.*, *48*, 2790–2804.

De Luca, A., Baldi, A., Russo, P., Todisco, A., Altucci, L., Giardullo, N., et al. (2003). Coexpression of *Helicobacter pylori*'s proteins CagA and HspB induces cell proliferation in AGS gastric epithelial cells, independently from the bacterial infection. *Cancer Res.*, *63*, 6350–6356.

Erhart, L. M., Lankat-Buttgereit, B., Schmidt, H., Wenzel, U., Daniel, H., & Goke, R. (2005). Flavone initiates a hierarchical activation of the caspase-cascade in colon cancer cells. *Apoptosis*, *10*, 611–617.

Finnin, M. S., Donigian, J. R., Cohen, A., Richon, V. M., Rifkind, R. A., Marks, P. A., et al. (1999). Structures of a histone deacetylase homologue bound to the TSA and SAHA inhibitors. *Nature*, *401*, 188–193.

Foo, L. Y., & Porter, L. J. (1981). The structure of tannins of some edible fruits. *J. Sci. Food Agric.*, *32*, 711–716.

Herrmann, K. (1981). Review on chemical composition and constituents of some important exotic fruits (author's transl). *Z. Lebensm. Unters. Forsch.*, *173*, 47–60.

Hildmann, C., Wegener, D., Riester, D., Hempel, R., Schober, A., Merana, J., et al. (2006). Substrate and inhibitor specificity of class 1 and class 2 histone deacetylases. *J. Biotechnol.*, *124*, 258–270.

Horinaka, M., Yoshida, T., Shiraishi, T., Nakata, S., Wakada, M., Nakanishi, R., et al. (2005a). Luteolin induces apoptosis via death receptor 5 upregulation in human malignant tumor cells. *Oncogene*, *24*, 7180–7189.

Horinaka, M., Yoshida, T., Shiraishi, T., Nakata, S., Wakada, M., Nakanishi, R., et al. (2005b). The combination of TRAIL and luteolin enhances apoptosis in human cervical cancer HeLa cells. *Biochem. Biophys. Res. Commun.*, *333*, 833–838.

Horinaka, M., Yoshida, T., Shiraishi, T., Nakata, S., Wakada, M., & Sakai, T. (2006). The dietary flavonoid apigenin sensitizes malignant tumor cells to tumor necrosis factor-related apoptosis-inducing ligand. *Mol. Cancer Ther.*, *5*, 945–951.

Hu, E., Dul, E., Sung, C. M., Chen, Z., Kirkpatrick, R., Zhang, G. F., et al. (2003). Identification of novel isoform-selective inhibitors within class I histone deacetylases. *J. Pharmacol. Exp. Ther.*, *307*, 720–728.

Ielpo, M. T., Basile, A., Miranda, R., Moscatiello, V., Nappo, C., Sorbo, S., et al. (2000). Immunopharmacological properties of flavonoids. *Fitoterapia*, *71*(Suppl. 1), S101–S109.

Ieven, M., Vanden Berghe, D. A., Mertens, F., Vlietinck, A., & Lammens, E. (1979). Screening of higher plants for biological activities. I. Antimicrobial activity. *Planta Med.*, *36*, 311–321.

Insinga, A., Minucci, S., & Pelicci, P. G. (2005). Mechanisms of selective anticancer action of histone deacetylase inhibitors. *Cell Cycle*, *4*, 741–743.

Insinga, A., Monestiroli, S., Ronzoni, S., Gelmetti, V., Marchesi, F., Viale, A., et al. (2005). Inhibitors of histone deacetylases induce tumor-selective apoptosis through activation of the death receptor pathway. *Nat. Med.*, *11*, 71–76.

Mai, A., Massa, S., Pezzi, R., Simeoni, S., Rotili, D., Nebbioso, A., et al. (2005). Class II (IIa)-selective histone deacetylase inhibitors. 1. Synthesis and biological evaluation of novel (aryloxopropenyl)pyrrolyl hydroxyamides. *J. Med. Chem.*, *48*, 3344–3353.

Mai, A., Massa, S., Rotili, D., Simeoni, S., Ragno, R., Botta, G., et al. (2006). Synthesis and biological properties of novel, uracil-containing histone deacetylase inhibitors. *J. Med. Chem.*, *49*, 6046–6056.

Motohashi, N., Kawase, M., Shirataki, Y., Tani, S., Saito, S., Sakagami, H., et al. (2000). Biological activity of feijoa peel extracts. *Anticancer Res.*, *20*, 4323–4329.

Nakashima, H. (2001). Biological activity of Feijoa peel extracts. Kagoshima University Research Center for the Pacific Islands, Occasional Papers 34, pp. 169–175.

Nebbioso, A., Clarke, N., Voltz, E., Germain, E., Ambrosino, C., Bontempo, P., et al. (2005). Tumor-selective action of HDAC inhibitors involves TRAIL induction in acute myeloid leukemia cells. *Nat. Med.*, *11*, 77–84.

Oku, N., Nagai, K., Shindoh, N., Terada, Y., van Soest, R. W., Matsunaga, S., et al. (2004). Three new cyclostellettamines, which inhibit histone deacetylase, from a marine sponge of the genus Xestospongia. *Bioorg. Med. Chem. Lett.*, *14*, 2617–2620.

Romero Rodriguez, M. A., Vazquez Oderiz, M. L., Lopez Hernandez, J., & Simal Lozano, J. (1992). Determination of vitamin C and organic acids in various fruits by HPLC. *J. Chromatogr. Sci.*, *30*, 433–437.

Shen, S. C., Ko, C. H., Tseng, S. W., Tsai, S. H., & Chen, Y. C. (2004). Structurally related antitumor effects of flavanones in vitro and in vivo: Involvement of caspase 3 activation, p21 gene expression, and reactive oxygen species production. *Toxicol. Appl. Pharmacol.*, *197*, 84–95.

Somoza, J. R., Skene, R. J., Katz, B. A., Mol, C., Ho, J. D., Jennings, A. J., et al. (2004). Structural snapshots of human HDAC8 provide insights into the class I histone deacetylases. *Structure*, *12*, 1325–1334.

Vannini, A., Volpari, C., Filocamo, G., Casavola, E. C., Brunetti, M., Renzoni, D., et al. (2004). Crystal structure of a eukaryotic zinc-dependent histone deacetylase, human HDAC8, complexed with a hydroxamic acid inhibitor. *Proc. Natl. Acad. Sci. U.S.A.*, *101*, 15064–15069.

Vuotto, M. L., Basile, A., Moscatiello, V., De Sole, P., Castaldo-Cobianchi, R., Laghi, E., et al. (2000). Antimicrobial and antioxidant activities of *Feijoa sellowiana* fruit. *Int. J. Antimicrob. Agents*, *13*, 197–201.

Wang, D. F., Helquist, P., Wiech, N. L., & Wiest, O. (2005). Toward selective histone deacetylase inhibitor design: Homology modeling, docking studies, and molecular dynamics simulations of human class I histone deacetylases. *J. Med. Chem.*, *48*, 6936–6947.

Wang, D. F., Wiest, O., Helquist, P., Lan-Hargest, H. Y., & Wiech, N. L. (2004). On the function of the 14 A long internal cavity of histone deacetylase-like protein: Implications for the design of histone deacetylase inhibitors. *J. Med. Chem.*, *47*, 3409–3417.

Cell Proliferation

Cell Prolif., 2013, **46**, 183–192 doi: 10.1111/cpr.12022

Genista sessilifolia DC. extracts induce apoptosis across a range of cancer cell lines

P. Bontempo*, D. Rigano†, A. Doto†, C. Formisano†, M. Conte*, A. Nebbioso*, V. Carafa*, G. Caserta*, V. Sica*, A. M. Molinari* and L. Altucci*,‡

**Department of General Pathology, Seconda Università degli Studi di Napoli, Vico Luigi de Crecchio 7, Naples, 80138, Italy, †Department of Chemistry of Natural Compounds, University of Naples 'Federico II', Naples, I-80131, Italy and ‡CNR-IGB, Naples, 80100, Italy*

Received 17 September 2012; revision accepted 30 November 2012

Abstract

Objectives: Restorative properties of medicinal plants such as *Genista sessilifolia* DC. have often been suggested to occur, in epidemiological studies. However, full characterization of effective principles responsible for this action has never previously been performed. Here, we have characterized *G. sessilifolia*'s anti-cancer effects and identified the chemical components involved in this anti-tumour action.

Materials and methods: Cell cycle, apoptosis, necrosis, differentiation analyses, high-performance liquid chromatography, western blotting, RNA extraction, real-time PCR and primers have all been observed/used in the study.

Results: We report that *G. sessilifolia* methanol extract has anti-cancer activity on solid and haematological cancer cells. *G. sessilifolia* extract's anti-proliferative action is closely bound to induction of apoptosis, whereas differentiation is only weakly modulated. Analysis of *G. sessilifolia* extract, by high-performance liquid chromatography, identifies fraction 18–22 as the pertinent component for induction of apoptosis, whereas fractions 11–13 and 27–30 both seem to contribute to differentiation. *G. sessilifolia* extract induces apoptosis mediated by caspase activation and p21, Rb, p53, Bcl2-associated agonist of cell death (BAD), tumour necrosis factor receptor super-family, member 10 (TRAIL) overexpression and death receptor 5 (DR5). Accordingly, fraction 18–22 inducing apoptosis was able to induce TRAIL.

Conclusions: Our results indicate that *G. sessilifolia* extract and its fraction 18–22 containing genistin and isoprunetin, were able to induce anti-cancer effects supporting the hypothesis of a pro-apoptotic intrinsic content of this natural medicinal plant.

Correspondence: P. Bontempo and L. Altucci, Department of General Pathology, Seconda Università degli Studi di Napoli, vico Luigi de Crecchio 7, Naples 80138, Italy. Tel.: +39 0815 665 702; Fax: +39 0815 667 555; Tel.: +39 0815 667 569; Fax: +39 0812 144 840; E-mails: paola.bontempo@unina2.it and lucia.altucci@unina2.it

Introduction

The rational design of chemical compounds to target specific molecules often draws on components already existing in nature (1,2). Thus, improving and understanding biological effects of natural compounds represents a significant opportunity in biomedical sciences. As yet, emerging fields such as molecular biology and combinatorial chemistry have not appeared to be able to satisfy the requirements of the pharmaceutical industries. For example, by exploiting their natural properties, validation of natural target compounds might become useful for treatment of human diseases such as cancer (3–8).

In search of such beneficial compounds, a crucial prerequisite is their non-toxicity to normal cells, and as a consequence, there has been a focus on investigating components of traditional medicine for possible anti-cancer therapeutic use. Natural compounds, and particularly plant derivatives (9), are the subject of an increasing number of studies and growing interest is being directed to plants that are well known for general medicinal properties. Indeed, we (and others) have previously shown potential anti-cancer effects of components of *Psidium guajava* (10) and *Feijoa sellowiana* (11).

The genus *Genista* L. (Leguminosae, GL) consists of 87 species predominantly distributed in the Mediterranean area (12). Composition of GL plants is characterized by presence of flavones, quinolizidine alkaloids (13), glycoflavones, and above all, of isoflavones, particularly

© 2013 Blackwell Publishing Ltd

substituted-isoflavones such as 5-methylgenistein and O-glucosylated isoflavones (14). Daidzein, genistein and isoprunetin are the most representative compounds of the genus (15) and several *Genista* species have interesting biological properties, such as being hypoglycaemic, anti-inflammatory, anti-ulcer, spasmolytic, antioxidant, oestrogenic and cytotoxic in different human cancer cell lines (16–18). *Genista sessilifolia* DC. (syn. *Cytisus sessilifolius* L., GS) is a shrub with sessile or sub-sessile leaves and yellow flowers collected in racemes. GS occurs in two rather separate areas, one through Anatolia, and the other in south-eastern European countries such as Bulgaria, southern Romania, Macedonia, northern Greece (19, 20) and Italy, where it spreads though woods up to 800 m above sealevel (12). Previous reports indicate anabolic and anti-inflammatory properties of flavonoids extracted from the plant (21). Recently, we have studied effects of methanolic extracts from the aerial parts of *G. sessilifolia* DC. and *G. tinctoria* L., on pBR322 DNA cleavage induced by hydroxyl radicals (OH) generated from UV-photolysis of hydrogen peroxide (H_2O_2), and by nitric oxide (NO), and cell population growth inhibitory activity of these natural products, to human melanoma cell line (M14) (22). Previous results have shown that isoflavonoid components of extracts of *G. sessilifolia* and *G. tinctoria,* have prevented UV light and nitric oxide-mediated plasmid DNA damage and attenuated population growth of malignant melanoma cells, probably triggering apoptotic processes (22). Here, we report biological effects of *G. sessilifolia* DC. extracts, which include induction of cell cycle arrest and apoptosis. In fractionation experiments, we have been able to identify fraction 18–22 content of genistin and isoprunetin as active against malignant cells.

Materials and methods

Preparation of methanol extracts of G. sessilifolia

Aerial parts of *G. sessilifolia* were collected at full flowering stage in April 2005, from plants growing in the 'Parco Nazionale del Cilento' (Salerno, Italy). A voucher specimen (SN 033) was deposited at the Herbarium Neapolitanum (NAP), Faculty of Pharmacy, University of Naples 'Federico II'. For preparation of the extract, *G. sessilifolia* aerial parts (667 g) were air-dried, cut into small pieces, then sequentially extracted by cold maceration with petroleum ether (40–60 °C) (3 × 2.5 l), $CHCl_3$ (3 × 2.5 l) and CH_3OH (3 × 2.5 l). After filtration, the methanol solution was concentrated under reduced pressure to provide 72.8 g gum. Samples of extracts were used for biological assays.

High-performance liquid chromatography

Methanolic extract of *G. sessilifolia* was chromatographed in 2 g portions on a Sephadex LH-20 (Pharmacia, Uppsala, Sweden) column, eluting with CH_3OH to afford 35 fractions of 20 ml each. Fractions were analysed by TLC using *n*-BuOH/CH_3COOH/H_2O (60:15:25, v/v) as eluent and $Ce(SO_4)_2$ in H_2SO_4 as spray reagent, and gathered according TLC analysis. Fractions 18–19 (1.28 g), 20–22 (590 mg), 23–26 (369.3 mg) and 27–30 (72 mg), shown to be the most active in preliminary biological assays (data not shown), were further purified by HPLC on a C_{18} μ-Bondapak column, with the exception of fraction 23–26 that was constituted entirely of genistein (3) (15). Fraction 18–19 was eluted with CH_3OH/H_2O 50:50 to yield pure genistin (1; 33.1 mg; Rt = 7.5 min) (23). Fraction 20–22 was eluted with CH_3OH/H_2O 50:50 to yield pure isoprunetin (2; 3.4 mg; Rt = 15.5 min) (15). Fraction 27–30 was eluted with CH_3OH/H_2O 70:30 to yield pure orobol (4; 7.7 mg; Rt = 9.5 min) (15). Structures of these compounds were determined by comparison of their spectroscopic data (NMR and MS) with values found in the literature (15,23).

Cell lines and culture conditions

NB4 cells (human acute promyelocitic leukaemia) were obtained by DSMZ and were routinely cultured, while MCF-7, HeLa, MDA-MB231, LnCaP and U937 cell lines were obtained from ATCC and routinely cultured. MCF-7 and HeLa cells were grown at 37 °C in 5% CO_2 atmosphere in Dulbecco's modified Eagle's medium (DMEM; Gibco, Paisley, NY, USA), supplemented with 5% foetal bovine serum (FBS; Gibco), 1% l-glutamine, 1% ampicillin/streptomycin and 0.1% gentamicin. U937, MDA-MB231, LnCaP and NB4 cells were grown at 37 °C in 5% CO_2 atmosphere in RPMI-1640 medium (Gibco), supplemented with 10% heat-inactivated foetal bovine serum (FBS), 1% L-glutamine, 1% ampicillin/streptomycin and 0.1% gentamicin. SAHA (kindly provided by Merck) and MS275 (Alexis, Vinci-Biochem srl, Vinci, Italy) were resuspended in DMSO and used at final concentration of 5 μM. Cell morphological analysis (for all cell lines used) was performed using bright field light microscopy (20×).

Cell cycle analysis

Samples were applied to a FACS-Calibur flow cytometer and analysed following standard procedures using Cell Quest software (Becton Dickinson, Milan, Italy) and ModFit LT version 3 Software (Verity Software

© 2013 Blackwell Publishing Ltd

House, Topsham, ME, USA), as previously reported (24).

FACS analysis of apoptosis

Apoptotic levels were measured as pre-G1, analysed by FACS with Cell Quest software (Becton Dickinson), as previously reported (25,26). As second assays, caspases 8, 9 and 7–3 detection (B-Bridge) were performed as recommended by the suppliers and quantified using FACS (Becton Dickinson) analysis. Discrimination between necrosis and apoptosis was performed according to the manufacturer's instructions (ENZ-51002). Briefly, 2×10^5 cells were treated with the compound of interest for 24 h. Cells were washed in cold PBS and resuspended in dual detection reagent, provided with the kit. After 15 min incubation at RT, samples were analysed using flow cytometry.

Granulocyte differentiation assay

Granulocyte differentiation analysis was carried out as previously described (25,27). Briefly, NB4 cells were harvested and resuspended in 10 μl phycoerythrineconjugated CD11c (CD11c-PE) (Pharmingen, San Diego, California, US). Control samples were treated with 10 μl PE conjugated mouse IgG1, incubated for 30 min at 4 °C in the dark, washed in phosphate-buffered saline (PBS 1 × with 0.1% BSA) and resuspended in 500 μl PBS containing PI (0.25 μg/ml). Samples were analysed by FACS with Cell Quest software (Becton Dickinson). PI positive cells were excluded from the analysis.

Western blot analysis

Forty micrograms total protein extracts were separated on polyacrylamide gel and blotted as previously described (28). Western blots were performed for p21 (dilution 1:500; Transduction Laboratories, BD group), Rb and p53 (dilution 1:500; Santa Cruz, Santa Cruz, CA, USA). Total mitogen-activated protein kinases (ERKs) (dilution 1:1000; Santa Cruz) were used to normalize for equal loading. To quantify TRAIL, 40 μg total protein extract was separated on 12% polyacrylamide gel and blotted. Western blots were performed of TNF-related apoptosis inducing ligand (TRAIL) (dilution 1:200; Abcam, Cambridge, UK), ERKs (dilution 1:1000; Santa Cruz) being used for equal loading. For determination of BAD and Bcl2 expression levels, 40 μg total protein extracts were separated on 12% polyacrylamide gel and blotted. Antibodies used were: anti-BAD (dilution 1:500; Cell Signaling #9292, Danvers, MA, USA) and anti-Bcl2 (dilution 1:500, Bcl2 (Ab-1); Oncogene Science, Cambridge, MA, USA). Total ERKs were used to normalize for equal loading.

RNA extraction

Cells were collected by centrifugation and resuspended in 1 ml of TRIzol reagent (Invitrogen - Life Technologies, Monza, Italy), vigorously shaken, and stored at −20 °C overnight. The following day, samples were supplemented with 100 μl of 2-bromo-3-chloro propane (Sigma Aldrich, St Louse, MO, USA), shaken gently and incubated for 15 min at RT. After centrifugation for 15 min, 16000 g at 4 °C, supernatants were collected and dispensed into fresh tubes and supplemented with 500 μl cold isopropylicalcohol. RNA precipitation reaction was carried out for 1 h at −80 °C and followed by centrifugation for 15 min, 13 000 rpm at 4 °C. Pellets were then resuspended in 1 ml cold 75% ethanol and samples were centrifuged again for 10 min, 5300 g at 4 °C. Pellets were subsequently dried at 42 °C for several minutes and resuspended in DEPC-treated H_2O. RNA samples were quantified using a Nanodrop 1000 spectrophotometer.

Real-time PCR and primers

RNA samples were converted into c-DNA using VILO Invitrogen kit: 2 μg RNA was mixed with 1x VILO reaction mixture, 1x Super-Script Mix and DEPC-H_2O; samples were then incubated for 10 min at 25 °C, 60 min at 42 °C and 5 min at 85 °C. RT-PCR experiments for TRAIL, DR5, p21 and GAPDH were then performed. Thermal protocol was as follows: 95 °C for 5 min plus 35 cycles at 95 °C for 30 s, 60 °C for 30 s and 72 °C for 45 s, with final elongation of 10 min at 72 °C. For amplification, the following primers were used: TRAIL forward (5′-CAA CTC CGT CAG CTC GTT AGA-3′) and reverse (5′-TTA GAC CAA CAA CTA TTT CTA-3′); DR5 forward (5′-TGC AGC CGT AGT CTT GAT TG-3′) and reverse (5′-TCC TGG ACT TCC ATT TCC TG-3′); p21 forward (5′-GAC AAC CTCA CTC GTC AAA TC-3′) and reverse (5′-ACA GCA CTG TAA GAA TGA GC-3′); GAPDH forward (5′-GGA GTC AAC GGA TTT GGT-3′) and reverse (5′-CTT CCC GTT CTC AGC CTT-3′).

Results

Total GS extract induced anti-malignant effects in several cell models of cancer

Genista sessilifolia had anti-malignant cell activity and this property was initially confirmed by using total GS

© 2013 Blackwell Publishing Ltd

extract at different concentrations, for times of 24 and 48 h, on NB4 human acute promyelocitic leukaemia cells (APL) (Fig. 1a). Interestingly, effects of GS total extract were linear and dose-dependent (Fig. 1a). In agreement, morphological experiments clearly showed anti-proliferative effects on the NB4 cells after 24 h, suggesting that with GS incubation, they underwent proliferative arrest and apoptosis (Fig. 1b). When cell cycle effects were analysed, treatment with total GS extract (within ranges of biologically active doses) induced G1 cell cycle block (Fig. 1c) of around 70% at concentrations of 0.5/0.75/1.50 mg/ml. To establish whether GS extract was also able to induce differentiation, presence of CD11c, a specific marker for granulocytic differentiation, was evaluated on the NB4 cells after 48 h treatment. CD11c expression increased, even at concentration of 0.5 mg/ml, (Fig. 1d). Nevertheless, the differentiative effect was lower than that of MS (MS275, Entinostat), a well-known anti-tumour and pro-differentiative agent (25–27,29). To corroborate these data in different leukaemia models, we tested anti-cancer activity of GS on U937 cells after 48 h treatment. Both morphology and apoptosis evaluation indicate that action of GS was not restricted to NB4 cells, but was a more general anti-leukaemic cell property(Fig. 2a). To verify whether solid cancer model cell types would also respond to GS, with arrest of proliferation and apoptosis, we tested it on breast cancer (MCF7, MDA-MB231), cervical cancer (Hela) and prostate cancer (LNCaP) cell lines. As shown in Fig. 2b–e, all cancer cells displayed arrest of proliferation, and cell death, after 48 h GS incubation, despite some differences in sensitivity, MDA-MB231 and U937 cells being more sensitive than MCF7, Hela and LNCaP cells.

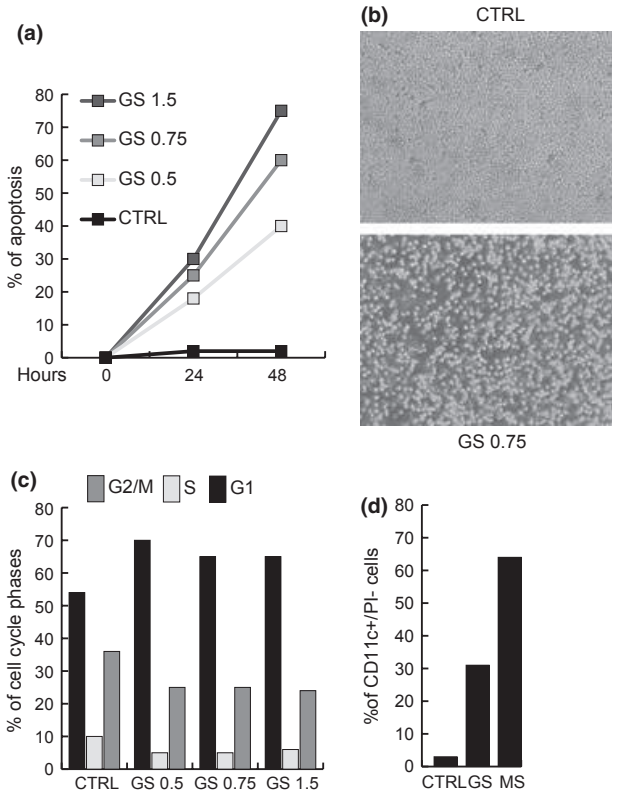

Figure 1. *Genista sessifolia* methanolic extract exerts anti-proliferative and differentiative action in leukaemia NB4 cells. (a) Apoptotic curve of NB4 cells at 24 and 48 h after treatment with *G. sessifolia* methanolic extract at reported concentrations. (b) Morphological analysis of NB4 cells after 24 h treatment with *G. sessifolia* methanolic extract at reported concentration. (c) Cell cycle analysis of NB4 cells at 24 h after treatment with *G. sessifolia* methanolic extract at reported concentrations. Results represent average of triplicates. (d) CD11c expression levels measured by FACS after 48 h treatment with indicated amounts of *G. sessifolia* methanolic extract, on NB4 cells. *Note*: PI positive cells were excluded from the analysis. MS (MS-275) used as positive pro-differentiative compound.

GS extract mediated caspase activation and apoptotic molecular events

To investigate molecular events underlying GS-induced cell death, caspase assays (caspase 8, 9 and caspase 3/7) were performed. As shown in Fig. 3a, caspases 8, 9 and 3/7 were mainly activated, suggesting that cell death was due to apoptosis of NB4 cells. To evaluate which molecular players might be involved in this anti-cancer action of GS total extract, expression levels of different known key factors in cell cycle progression and apoptosis were analysed by western blot analysis, in NB4 cells. As shown in Fig. 3b, after 48 h induction, total GS extract induced expression of p21, a known cell cycle inhibitor, and Rb, recognized to negatively regulate G1-S transition. Taken together, these data confirm the observation on cell cycle block (Figs 3b,1b). Under similar experimental conditions, expression levels of pro- and anti-apoptotic proteins were analysed. Interestingly, whereas Bcl2 remained unchanged, p53, TRAIL and BAD appeared to be induced after treatment with total GS extract (Fig. 3b), validating the pro-apoptotic action of the compound. In particular, that both mitochondrial (intrinsic) and death receptor (extrinsic) apoptotic pathways were activated strengthens the evidence suggested by caspase 8 and 9 activation (Fig. 2a).

Selective GS fractions induced anti-malignant effects on acute promyelocitic leukaemia NB4 cells

To investigate different components of the GS total extract involved in its anti-cancer effects, the extract was chromatographed to afford 35 fractions; these were then analysed for their action with respect to apoptosis,

© 2013 Blackwell Publishing Ltd

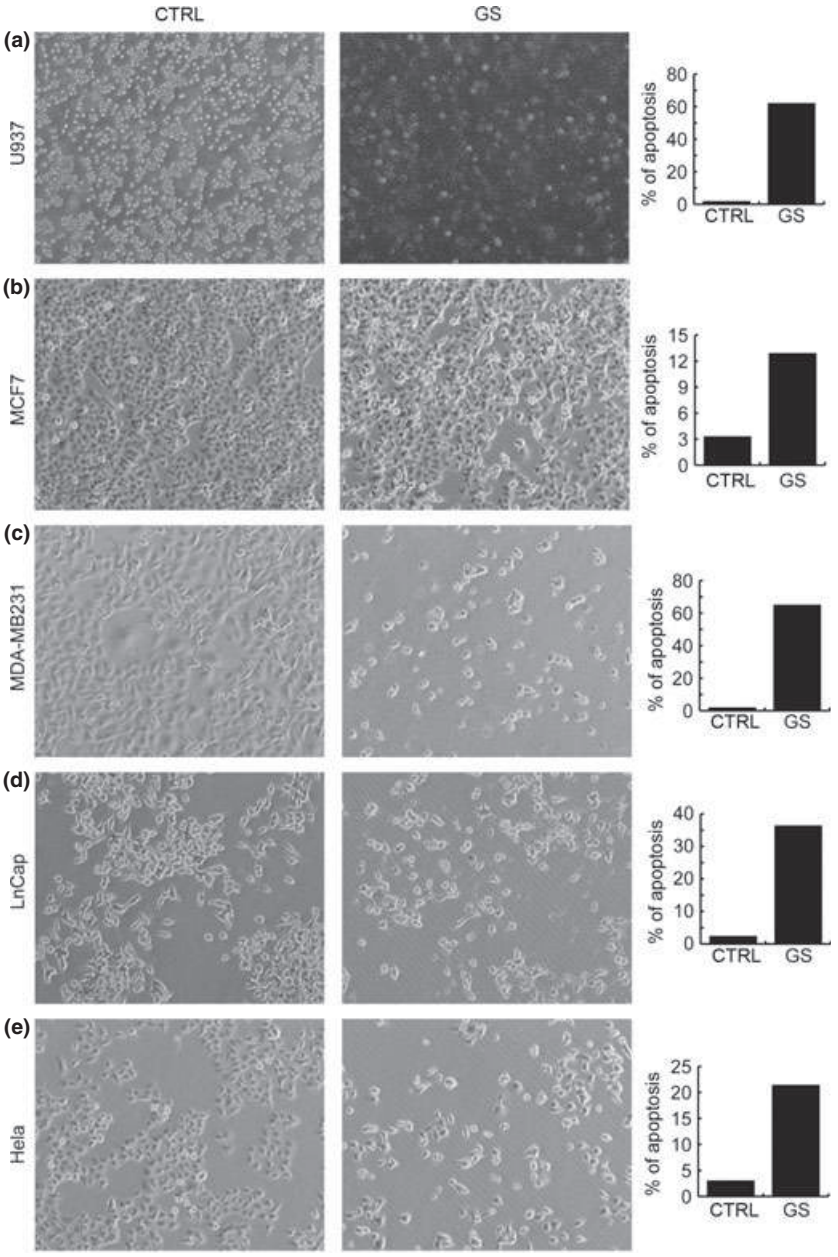

Figure 2. ***Genista sessifolia*** **methanolic extract exerts anti-cancer action in different cancer cell line models**. (a) Morphological analysis and percentage of apoptosis in U937 cells after 48 h treatment with *G. sessifolia* methanolic extract at indicated concentration. (b) Morphological analysis and percentage apoptosis, in MCF7 breast cancer cells after 48 h treatment with *G. sessifolia* methanolic extract at indicated concentration. (c) Morphological analysis and percentage of apoptosis of MDA-MB-231 breast cancer cells after 48 h treatment with *G. sessifolia* methanolic extract at indicated concentration. (d) Morphological analysis and percentage of apoptosis in LNCaP prostate cancer cells after 48 h treatment with *G. sessifolia* methanolic extract at indicated concentration (e) Morphological analysis and percentage of apoptosis in Hela cervical cancer cells after 48 h treatment with *G. sessifolia* methanolic extract at indicated concentration.

showing that fractions from 18 to 22 (18–22) gave rise to strong increase in pre-G1 phase (apoptotic fraction), whereas fractions 6–17 and 27–30 caused weaker increases in cell death (Fig. 4a). When CD11c was measured as a marker of differentiation, alone fractions 11–13 and 27–30 induced only a weak increase in CD11c expression at 48 h treatment (Fig. 4b). In comparison to total extract, effects of fractions 11–13 and 27–30 were much lower, suggesting that both fractions might contribute to the effect of GS total extract on induction of differentiation. Finally, in agreement with biological analyses shown in Fig. 4a, when fractions 18–22 had been tested by western blot analyses, stronger induction of effectors of apoptosis such as TRAIL and DR5 were detected at 0.2 mg/ml concentration at 48 h treatment (Fig. 4c), thus corroborating that components contained in these fractions accounted for cell death property of GS. Strongest apoptotic response triggered by fractions 18–19 and 20–22 were also confirmed by cytofluorimetric analysis using annexin V (Fig. 4d). Moreover, qPCR analyses of TRAIL, its death receptor DR5 and p21 indicate that there was modulation in fractions used (Fig. 4d). In particular, TRAIL was highly expressed in fraction 20–22 already at 0.2 mg/ml, while

© 2013 Blackwell Publishing Ltd

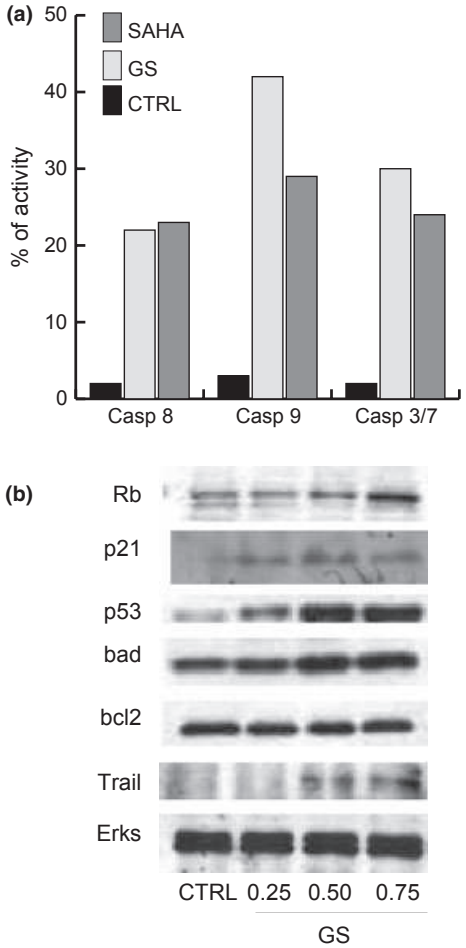

Figure 3. *Genista sessifolia* methanolic extract induced apoptosis by caspase activation in NB4 cells. (a) Apoptosis measured by caspase activation with FACS analysis in NB4 cells after 24 h induction with *G. sessifolia* methanolic extract. Data show average of triplicates. (b) Western blot evaluation of Rb, p21, p53, Bad, Bcl2 and TRAIL in NB4 cells after 24 h treatment with indicated concentrations of GS. Total Erks for equal loading.

DR5 and p21 induction were more detectable at higher concentrations.

Quantification of isoflavonoids

To determine major constituents, methanolic extract of *G. sessilifolia* was fractionated over Sephadex LH-20, yielding as the main constituents, genistin (1) (3,30–32), isoprunetin (2), genistein (3) and orobol (4) (22) (Fig. 5). These compounds were quantified using HPLC-PAD. Results of quantitative analyses of the isoflavones in methanolic extracts of *G. sessilifolia*, are shown in Table 1. Compounds were identified by comparison of their retention times (t_R), UV spectra and MS, with reference samples (Table 1); purity of peaks was checked by PAD (200–400 nm). UV spectra recorded at three different points per peak (up-slope, apex and down-slope) were compared with UV spectrum of the reference standard. Quantitative determination of genistin, isoprunetin, genistein and orobol was performed directly by HPLC-PAD using five-point regression curves in the range 1–25 μg/ml; all samples were injected three times at each level. Calibration curves for each compound, made by linear regression by graph, reporting area ratio of external standard against known concentration of external standard, were linear in the range 1–25 μg/ml for all isoflavones. Three aliquots of the methanol extract of *G. sessilifolia* were analysed to quantify genistin, isoprunetin, genistein and orobol. Results of quantitative analyses are shown in Table 1. Four isoflavones occurred as major constituents of *G. sessilifolia* (by methanolic extraction), in particular genistin and genistein were the most abundant compounds.

Discussion

Plants are an appreciated and natural font of therapeutic agents (33–36). At present, it is generally documented that intake of a number of native herbs and vegetables significantly contributes to improvement in human health, in terms of prevention and treatment of disease (37–42). In the region of 80% of existing drugs originate from medicinal plants, including several anti-tumoural agents as Paclitaxel (taxol) from *Taxus brevifolia* (43–46). Frequently in industrialized countries, raw ingredients used to synthesize pure chemicals originate from plants. The genus *Genista* L. (Leguminosae, GL), consisting of 87 species, is mostly found spread across the Mediterranean area (12). *Genista* L. is characterized by the presence of flavones, glycoflavones, and isoflavones, particularly substituted-isoflavones such as 5-methylgenistein and O-glucosylated isoflavones (14), whil daidzein, genistein and isoprunetin are the most represented of such compounds of the genus (15). Several *Genista* species have medical properties such as being hypoglycaemic, anti-inflammatory, anti-ulcer, spasmolytic, antioxidant, oestrogenic and as having cytotoxic activities against different human cancer cells (16,17). Recently, we have studied effects of extracts from aerial parts of *G. sessilifolia* DC. and *Genista tinctoria* L. on pBR322 DNA cleavage induced by hydroxyl radicals (OH) generated from UV-photolysis of hydrogen peroxide (H_2O_2) and by nitric oxide (NO) and cell population growth inhibitory activity of these natural products against human malignant melanoma cells (22).

Although a variety of components are present within them, the main one connected to anti-cancer action is genistin. Experimental indication that crude methanol

© 2013 Blackwell Publishing Ltd

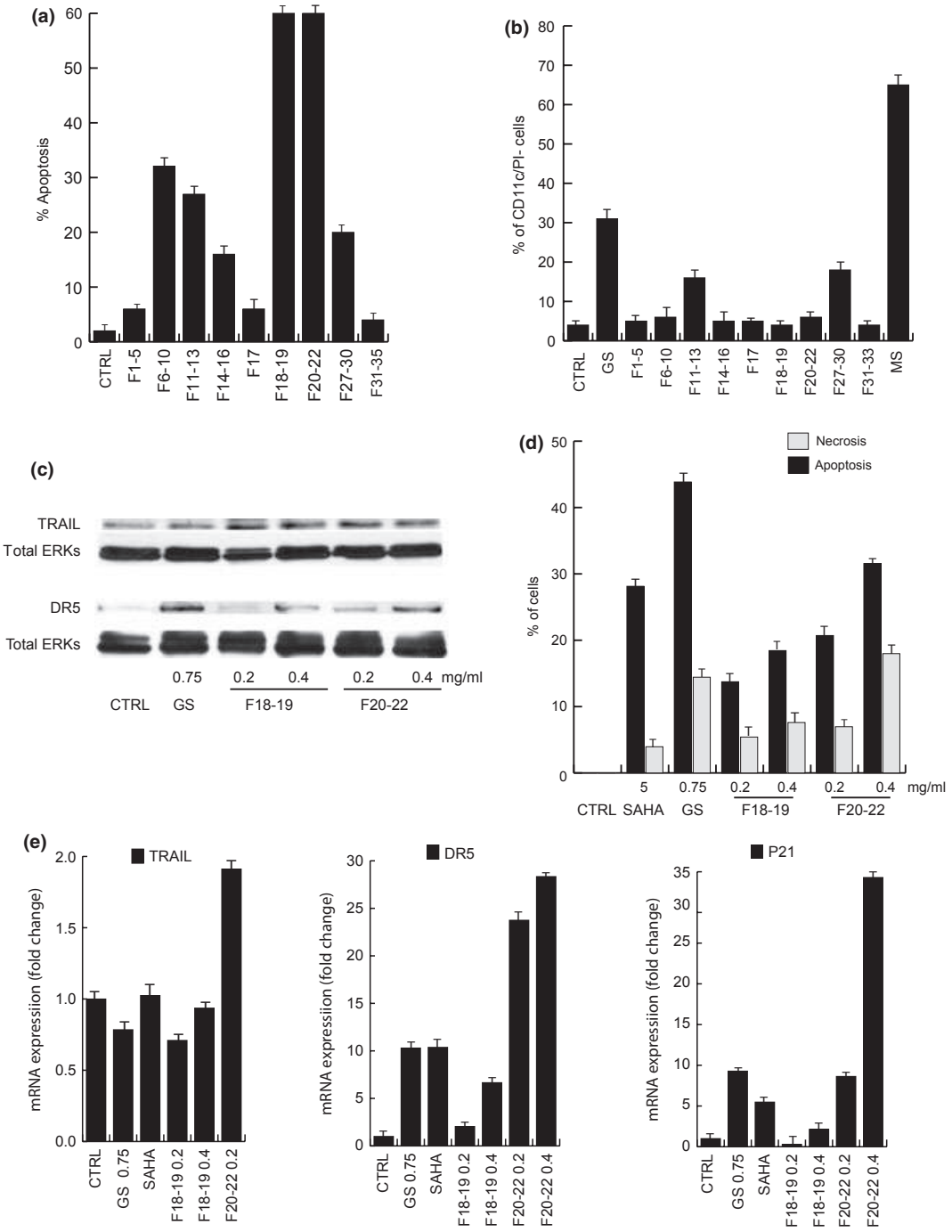

Figure 4. ***Genista sessifolia*** **fraction induced apoptosis in NB4 cells.** (a) Apoptotic curve of NB4 cells at 24 h after treatment with *G. sessifolia* fractions at concentration of 0.2 mg/ml. (b) CD11c expression levels on treatment with *G. sessifolia* fractions at concentration of 0.2 mg/ml for 48 h in NB4 cells. MS (MS-275) was used as positive pro-differentiative compound. (c) Western blot analysis of fraction 18–22 actions on TRAIL and DR5 induction at indicated concentrations, for 24 h. Total Erks account for equal loading. (d) Percentage of apoptotic and necrotic cells by GFP-certified apoptosis/necrosis detection kit using flow cytometry. SAHA was used as positive control for apoptotic induction. (e) Real-time PCR for TRAIL, DR5 and p21 for 18–19 and 20–22 fractions at the indicated concentrations.

extract was able to induce cell cycle arrest and cell death in NB4 cells confirmed our hypothesis that some components of the plant have anti-cancer activity. Methanol extract from *G. sessilifolia* was also capable of inducing CD11c expression (taken as ability to differentiate) in acute promyelocytic leukaemia (APL) cells,

© 2013 Blackwell Publishing Ltd

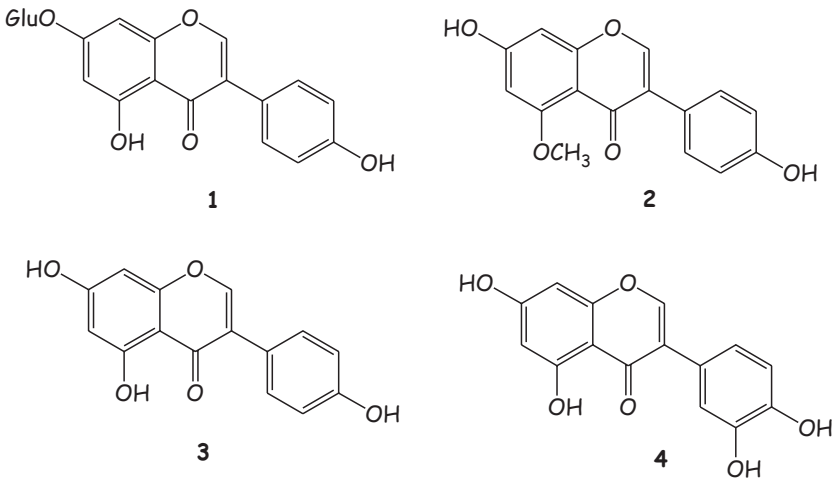

Figure 5. Active components of *Genista sessifolia* fractions: (1) Genistin; (2) Isoprunetin; (3) Genistein; (4) Orobol.

Table 1. Results of quantitative analysis

Compound	r^2	t_R (SD)	mg of compound/g of *Genista sessifolia* MeOH extract (SD)
Genistin (1)	0.9999	18.66 (0.08)	286.64 (3.41)
Isoprunetin (2)	0.9997	25.45 (0.13)	42.31 (0.13)
Genistein (3)	0.9993	35.98 (0.18)	123.54 (2.61)
Orobol (4)	0.9997	29.01 (0.16)	33.98 (2.41)

r = linear regression; SD = standard deviation.

despite lower levels than of known differentiating agents such as MS (MS-275, Entinostat). Apoptosis evaluation in different cancer cell line models indicated that anti-malignant action of GS is not restricted to NB4 cells, but is a general anti-cancer property, active in additional leukaemia models (U937) and against solid cancer cells (LnCaP, MDA-MB231, MCF7 and Hela). All cancer cell models tested here with GS methanol extract showed sensitivity (Fig. 2b–e); differential effects shown by different cancer cell lines. MDA-MB231 and U937 cells were more sensitive than MCF7, Hela and LNCaP cells, suggesting both some cell-selectivity and very low toxic effect of the extract.

Interestingly, we demonstrated that cell death, occurring on GS treatment, was caspase-mediated and able to activate both cell cycle and molecular death programmes (Fig. 3). Both initiator caspases (caspases 8 and 9) and effectors (caspases 3/7) were active after GS treatment, accompanied by induction of p21, Rb, p53, Bad and TRAIL (Fig. 3). These lines of evidence strongly suggest involvement of death receptors and mitochondrial-mediated death pathways in regulation of apoptosis induced by GS extract. Intrigued by these data, we set out to determine the most biologically active fraction and identified fractions 18–22 as responsible for apoptotic action of GS extracts in cancer cells tested. In agreement, fractions 18–22 were able to induce apoptosis as demonstrated by FACS analysis and by induction of TRAIL and DR5 (Fig. 4). In contrast, fractions 11–13 and 27–30 were the only ones able to slightly alter differentiation capability (as CD11c expression), indicating that multi-component action was needed to modulate CD11c expression levels in these settings. Interestingly, fractions 18–19 main component was genistin (Fig. 5) whose anti-cancer potential has already been recognized (31,47–49). Interestingly, fractions 20–22 main component was isoprunetin whose anti-cancer (50) and anti-oestrogenic (51) potentials have also been suggested.

Taken together, these data provide a new perspective for analysis and use of natural products in treatment of human pathologies, and indicate that plant components exert anti-cancer activities. Furthermore, identification of two components, genistin and isoprunetin, that account for the anti-cancer potential of GS, corroborates the knowledge of genistin action against cancer and strongly support further investigations of isoprunetin anti-cancer action. Given the need for new approaches into anti-cancer treatments, in-depth investigation of properties of natural products with minor side effects and targeted action represent a new approach for the future development of cancer-selective drugs and prevention strategies.

Acknowledgements

The authors thank Dr. Diego Di Novella for kindly providing the plant. Thanks are also to the C.S.I.A.S of University 'Federico II' of Naples for technical assistance. This study was supported by EU ('*Blueprint* contract no. 282510), by AIRC (Associazione Italiana per la

© 2013 Blackwell Publishing Ltd

Ricerca sul Cancro project no. 4625), by MIUR (PRIN_2009PX2T2E_004). We acknowledge Dr C. Fisher for kindly revising the manuscript. The authors declare that they have no conflict of interests.

References

1 Camp D, Davis RA, Campitelli M, Ebdon J, Quinn RJ (2012) Drug-like properties: guiding principles for the design of natural product libraries. *J. Nat. Prod.* **75**, 72–81.

2 Hann MM, Keserü GM (2012) Finding the sweet spot: the role of nature and nurture in medicinal chemistry. *Nat. Rev. Drug Discov.* **11**, 355–365.

3 Cragg GM, Newman DJ (2005) Plants as a source of anti-cancer agents. *J. Ethnopharmacol.* **1–2**, 72–79.

4 Ahmad A, Sakr WA, Rahman KM (2012) Novel targets for detection of cancer and their modulation by chemopreventive natural compounds. *Front. Biosci. (Elite Ed)* **4**, 410–425.

5 Mans DRA, da Rocha AB, Schwartsmann G (2000) Anti-cancer drug discovery and development in Brazil: targeted plant collection as a rational strategy to acquire candidate anti-cancer compounds. *Oncologist* **5**, 185–198.

6 Qurishi Y, Hamid A, Majeed R, Hussain A, Qazi AK, Ahmed M *et al.* (2011) Interaction of natural products with cell survival and signaling pathways in the biochemical elucidation of drug targets in cancer. *Future Oncol.* **7**, 1007–1021.

7 Russo P, Nastrucci C, Cesario A (2011) From the sea to anticancer therapy. *Curr. Med. Chem.* **18**, 3551–3562.

8 Shynu M, Gupta PK, Saini M (2011) Antineoplastic potential of medicinal plants. *Recent Pat. Biotechnol.* **5**, 85–94.

9 Verma PK, Bala M, Kumar N, Singh B (2012) Therapeutic potential of natural products from terrestrial plants as TNF-α antagonist. *Curr. Top. Med. Chem.* **12**, 1422–1435.

10 Bontempo P, Doto A, Miceli M, Mita L, Benedetti R, Nebbioso A *et al.* (2012) *Psidium guajava* L. anti-neoplastic effects: induction of apoptosis and cell differentiation. *Cell Prolif.* **1**, 22–31.

11 Bontempo P, Mita L, Miceli M, Doto A, Nebbioso A, De Bellis F *et al.* (2007) *Feijoa sellowiana* derived natural Flavone exerts anticancer action displaying HDAC inhibitory activities. *Int. J. Biochem. Cell Biol.* **10**, 1902–1914.

12 Pignatti S (1982) Edagricole (Ed.). *Flora d'Italia (Bologna)* **1**, 636.

13 Martins A, Wink M, Tei A, Brum-Bousquet M, Tillequin F, Rauter AP (2005) A phytochemical study of the quinolizidine alkaloids from Genista Tenera by gas chromatography-mass spectrometry. *Phytochem. Anal.* **16**, 264–266.

14 Harborne JB (1969) Chemosystematics of the Leguminosae. Flavonoid and isoflavonoid patterns in the tribe Genisteae. *Phytochemistry* **8**, 1449–1456.

15 Harborne JB, Turner BL (1984) Plant Chemosystematics. London, UK: Academy Press.

16 Ilarionov I, Rainova L, Nakov N (1979) Antinflammatory and antiulcer effect of some flavonoide isolated from the genus Genista. *Farmatsiya* **29**, 39–46.

17 Raja S, Ahamed HN, Kumar V, Mukerjee K, Bandyopadhyay A, Mukherjee PK (2007) Exploring the effect of Cytsius Scoparius on markers of oxidative stress in rats. *Iranian J. Pharmacol. Ther.* **6**, 15–21.

18 Rigano D, Russo A, Formisano C, Cardile V, Senatore F (2010) Antiproliferative and cytotoxic effects on malignant melanoma cells of essential oils from the aerial parts of *Genista sessilifolia* and *G. tinctoria*. *Nat. Prod. Commun.* **5**, 1127–1132.

19 Gibbs PE (1966) A revision of the genus *Genista* L. *Notes Royal Botanic Garden Edinburgh* **27**, 11–99.

20 Greuter W, Burdet HM, Long G (1989) Conservatoire et Jardin botaniques, Genève. *Med-Checklist* **4**, 91–105.

21 Ilarinov I (1988) Pharmacologic effects on the reproductive system and anti-inflammatory action of the total flavonoid mixtures contained in *Genista tintoria* and *Genista sessilifolia*. *Farmatsiya* **38**, 47–51.

22 Rigano D, Cardile V, Formisano C, Maldini MT, Piacente S, Bevilacqua J *et al.* (2009) *Genista sessilifolia* DC. and *Genista tinctoria* L. inhibit UV light and nitric oxide-induced DNA damage and melanoma cell growth. *Chem. Biol. Interact.* **180**, 211–219.

23 Rainova L, Nakov N, Bogdanova S, Minkov E, Staneva-Stoicheva D (1988) Ulceroprotective activity of the flavonoide of *Genista rumelica* Vel. *Phytother. Res.* **2**, 137–139.

24 De Luca A, Baldi A, Russo P, Todisco A, Altucci L, Giardullo N *et al.* (2003) Coexpression of *Helicobacter pylori*'s proteins CagA and HspB induces cell proliferation in AGS gastric epithelial cells, independently from the bacterial infection. *Cancer Res.* **63**, 6350–6356.

25 Nebbioso A, Clarke N, Voltz E, Germain E, Ambrosino C, Bontempo P *et al.* (2005) Tumor-selective action of HDAC inhibitors involves TRAIL induction in acute myeloid leukemia cells. *Nat. Med.* **11**, 77–84.

26 Altucci L, Rossin A, Raffelsberger W, Reitmair A, Chomienne C, Gronemeyer H (2001) Retinoic acid-induced apoptosis in leukemia cells is mediated by paracrine action of tumor-selective death ligand TRAIL. *Nat. Med.* **7**, 680–686.

27 Altucci L, Gronemeyer H (2001) The promise of retinoids to fight against cancer. *Nat. Rev. Cancer* **1**, 181–193.

28 Mai A, Massa S, Rotili D, Simeoni S, Ragno R, Botta G *et al.* (2006) Synthesis and biological properties of novel uracil-containing histone deacetylase inhibitors. *J. Med. Chem.* **49**, 6046–6056.

29 Altucci L, Wilhelm E, Gronemeyer H (2004) Leukemia: beneficial actions of retinoids and rexinoids. *Int. J. Biochem. Cell Biol.* **36**, 178–182.

30 Walter ED (1941) Genistin (an isoflavone glucoside) and its aglucone, genistein, from soybeans. *J. Am. Chem. Soc.* **62**, 3273–3276.

31 Coward L, Barnes NC, Setchell KDR, Barnes S (1993) Genistein, daidzein, and their β-glycoside conjugates: antitumor isoflavones in soybean foods from American and Asian diets. *J. Agric. Food Chem.* **41**, 1961–1967.

32 Du H, Huang Y, Tang Y (2010) Genetic and metabolic engineering of isoflavonoid biosynthesis. *Appl. Microbiol. Biotechnol.* **86**, 1293–1312.

33 Cragg GM, Newmann DJ, Snader KM (1997) Natural products in drug discovery and development. *Nat. Prod.* **60**, 52–60.

34 Harvey AL (1999) Medicines from nature: are natural products still relevant to drug discovery? *Trends Pharmacol. Sci.* **20**, 196–198.

35 Farnsworth NR (1984) The role of medicinal plants in drug development. In: Krogsgaard-Larsen P, Christensen SB, Kofod H, eds. Natural Products and Drug Development, pp. 8–98. London, UK: Ballière, Tindall, and Cox.

36 Cox PA (1994) The ethnobotanical approach to drug discovery: strengths and limitations. In: Chadwick DJ, Marsh J, eds. CIBA Foundation Symposium 185—Ethnobotany and the Search for New Drugs, pp. 25–47. Chichester, UK: John Wiley & Sons.

37 Kapiszewska M (2006) A vegetable to meat consumption ratio as a relevant factor determining cancer preventive diet. The Mediterranean versus other European countries. *Forum Nutr.* **59**, 130–153.

38 Shukla Y, George J (2011) Combinatorial strategies employing nutraceuticals for cancer development. *Ann. N. Y. Acad. Sci.* **1229**, 162–175.

© 2013 Blackwell Publishing Ltd

39 Amin AR, Kucuk O, Khuri FR, Shin DM (2009) Perspectives for cancer prevention with natural compounds. *J. Clin. Oncol.* **27**, 2712–2725.
40 Khan N, Afaq F, Mukhtar H (2008) Cancer chemoprevention through dietary antioxidants: progress and promise. *Antioxid. Redox Signal.* **10**, 475–510.
41 Kris-Etherton PM, Hecker KD, Bonanome A, Coval SM, Binkoski AE, Hilpert KF *et al.* (2002) Bioactive compounds in foods: their role in the prevention of cardiovascular disease and cancer. *Am. J. Med.* **113**, 71S–88S.
42 Trovato GM (2012) Behavior, nutrition and lifestyle in a comprehensive health and disease paradigm: skills and knowledge for a predictive, preventive and personalized medicine. *EPMA J.* **3**, 8.
43 Gotaskie GE, Andreassi BF (1994) Paclitaxel: a new antimitotic chemotherapeutic agent. *Cancer Pract.* **2**, 27–33.
44 Ferguson PJ, Phillips JR, Selner M, Cass CE (1984) Differential activity of vincristine and vinblastine against cultured cells. *Cancer Res.* **44**, 3307–3312.
45 Cormio G, Loizzi V, Gissi F, Camporeale A, De Mitri P, Leone L *et al.* (2011) Long-term topotecan therapy in recurrent or persistent ovarian cancer. *Eur. J. Gynaecol. Oncol.* **32**, 153–155.
46 Sinkule JA (1984) Etoposide: a semisynthetic epipodophyllotoxin. Chemistry, pharmacology, pharmacokinetics, adverse effects and use as an antineoplastic agent. *Pharmacotherapy* **4**, 61–73.
47 Hooshmand S, Khalil DA, Murillo G, Singletary K, Kamath SK, Arjmandi BH (2008) The combination of genistin and ipriflavone prevents mammary tumorigenesis and modulates lipid profile. *Clin. Nutr.* **27**, 643–648.
48 Choi EJ, Kim T, Lee M-S (2007) Pro-apoptotic effect and cytotoxicity of genistein and genistin in human ovarian cancer SK-OV-3 cells. *Life Sci.* **80**, 1403–1408.
49 Russo A, Cardile V, Lombardo L, Vanella L, Acquaviva R (2006) Genistin inhibits UV light-induced plasmid DNA damage and cell growth in human melanoma cells. *J. Nutr. Biochem.* **17**, 103–108.
50 Feng S, Hao J, Xu Z, Chen T, Qiu SX (2011) Polyprenylated isoflavanone and isoflavonoids from *Ormosia henryi* and their cytotoxicity and anti-oxidation activity. *Fitoterapia* **83**, 161–165.
51 Pinto B, Bertoli A, Noccioli C, Garritano S, Reali D, Pistelli L (2008) Estradiol-antagonistic activity of phenolic compounds from leguminous plants. *Phytother. Res.* **22**, 362–366.

© 2013 Blackwell Publishing Ltd

Bioorganic & Medicinal Chemistry 19 (2011) 3637–3649

Contents lists available at ScienceDirect

Bioorganic & Medicinal Chemistry

journal homepage: www.elsevier.com/locate/bmc

Epigenetic profiling of the antitumor natural product psammaplin A and its analogues

José García [a], Gianluigi Franci [b,f], Raquel Pereira [a], Rosaria Benedetti [b,c,e], Angela Nebbioso [b], Fátima Rodríguez-Barrios [a], Hinrich Gronemeyer [d], Lucia Altucci [b,f,*], Angel R. de Lera [a,*]

[a] Departamento de Química Orgánica, Universidade de Vigo, 36310 Vigo, Spain
[b] Dipartimento di Patologia generale, Seconda Università di Napoli, Vico L. De Crecchio 7, 80138 Napoli, Italy
[c] Università di Napoli Federico II, Dipartimento di Chimica Organica e Biochimica, Italy
[d] Department of Cancer Biology - Institut de Génétique et de Biologie Moléculaire et Cellulaire (IGBMC)/CNRS/INSERM/ULP, BP 163, 67404 Illkirch Cedex, C. U. de Strasbourg, France
[e] Università di Napoli Federico II, Dipartimento di Fisica, 6, CNR-IGB, Via P. Castellino, 80100, Napoli, , Italy
[f] CNR-IGB, Via Pietro Castellino 80100 Napoli, Italy

ARTICLE INFO

Article history:
Received 30 September 2010
Accepted 8 December 2010
Available online 15 December 2010

Keywords:
Psammaplin A
Epigenetics
HDAC
DNMT
Total synthesis
Natural products

ABSTRACT

A collection of analogues of the dimeric natural product psammaplin A that differ in the substitution on the (halo)tyrosine aryl ring, the oxime and the diamine connection has been synthesized. The effects on cell cycle, induction of differentiation and apoptosis of the natural-product inspired series were measured on the human leukaemia U937 cell line. Epigenetic profiling included induction of $p21^{WAF1}$, effects on global H3 histone and tubulin acetylation levels as well as in vitro enzymatic assays using HDAC1, DNMT1, DNMT3A, SIRT1 and a peptide domain with p300/CBP HAT activity. Whereas the derivatives of psammaplin A with modifications in the length of the connecting chain, the oxime bond and the disulfide unit showed lower potency, the analogues with changes on the bromotyrosine ring exhibited activities comparable to those of the parent compound in the inhibition of HDAC1 and in the induction of apoptosis. The lack of HDAC1 activity of analogues modified on the disulfide bond suggests that its cleavage must occur in cells to produce the monomeric Zn^{2+}-chelating thiol. This assumption is consistent with the molecular modelling of the complex of psammaplin A thiol with h-HDAC8. Only a weak inhibition of DNMT1, DNMT3A and residual activities with SIRT1 and a p300/CBP HAT peptide were measured for these compounds.

© 2010 Elsevier Ltd. All rights reserved.

1. Introduction

Psammaplin A (1, PsA, Scheme 1) is a symmetrical disulfide dimer derived from the condensation of modified tyrosine and cysteine units[1] (for a proposal of its biogenesis, see 2,3). Although it was first isolated in 1987 from an unidentified sponge[4] and from *Psammaplysilla* sp.,[5,6] PsA is found, together with biogenetically-related congeners, in several Verongidas[2,3,6–10] and in some associations of these species.[11,12]

Antibacterial and antitumor activities have been reported for PsA. The in vitro antibacterial activity of PsA against both *Staphylococcus aureus* (SA) and methicillin-resistant *Staphylococcus aureus* (MRSA) was considered the result of the inhibition of DNA gyrase[13] and induced arrest of bacterial DNA synthesis. PsA also inhibits topoisomerase II (topo II),[14] farnesyl protein transferase,[8] leucine aminopeptidase,[8] mycothiol-*S*-conjugate amidase,[15] chitinase,[10] Pol α-primase,[16] PPARγ[17–20] and mammalian aminopeptidase N (APN).[21] Targeting multiple proteins that impact on DNA topology, DNA replication, transcription, apoptosis, tumor invasion, and angiogenesis likely contributes to the significant cytotoxicity displayed by PsA in human lung (A549), ovarian (SKOV- 3), skin (SK-MEL-2), CNS (XF498), and colon (HCT15) cancer cell lines.[12]

PsA was also reported to inhibit in vitro the chromatin-modifying enzymes histone deacetylase (HDAC) and DNA methyl transferase (DNMT).[3] HDAC and DNMT are epigenetic enzymes that catalyze the covalent modifications of histone proteins and DNA in chromatin,[22] and therefore they are considered prime new targets[23] for the treatment and prevention of cancer[24–34] and other diseases.[35] The modification of chromatin is thus an addition to the list of potential mechanisms involved in the anticancer actions of the natural product PsA.

Histone acetylation is a dynamic process in which a cellular steady state is maintained by the opposing activities of histone acetyltransferases (HATs) and deacetylase enzymes (HDAC) acting at the ε-amino groups of evolutionally conserved lysine residues located at the histone N-termini. HATs transfer the acetyl moiety from acetyl CoA to the histone lysine residues whereas HDACs catalyze their removal. Individual HATs and HDACs display distinct

* Corresponding authors.
E-mail addresses: lucia.altucci@unina2.it (L. Altucci), qolera@uvigo.es (Angel R. de Lera).

0968-0896/$ - see front matter © 2010 Elsevier Ltd. All rights reserved.
doi:10.1016/j.bmc.2010.12.026

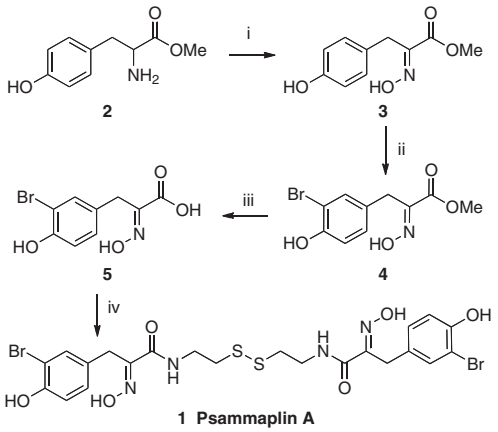

Scheme 1. Reagents and conditions: (i) Na_2WO_4, H_2O_2, 25 °C, 3 h (63%); (ii) NBS, CH_3CN, 25 °C, 2 h (82%); (iii) LiOH, THF–H_2O, 23 °C, 12 h (99%); (iv) DCC, *N*-hydroxyphthalimide, Et_3N, cystamine, 1,4-dioxane, MeOH, 25 °C, 12 h (60%).

specificities for certain individual lysine residues and particular histones. Although the factors responsible for the specificity are poorly understood they might reflect different biological functions of the various enzymes. Regardless of the details, it is widely accepted that histone acetylation is essential to establish a transcriptionally competent state of chromatin[22] and consequently contributes to the gene activation/gene repression transcriptional status of cells. Two histone deacetylase inhibitors (HDACis), suberoylanilide hydroxamic acid (SAHA, vorinostat, Zolinza®), and FK228 (romidepsin, Istodax®) are used as therapy for cutaneous T-cell lymphoma,[36] and several others are currently undergoing clinical trials as potential targeted cancer chemotherapeutic agents.[37–41]

In eukaryotes DNMTs catalyze the addition of methyl groups from *S*-adenosyl-L-methionine (SAM) to the C5 position of cytosine bases within the CpG-rich islands in DNA. Methylation of DNA is an epigenetic mark associated to a repressed chromatin state which inhibits gene transcription.[42,43] Several tumour supressor genes are hypermethylated in tumours, which suggest a link between aberrant DNA methylation and cancer.[44–47] DNA methyl transferase inhibitors (DNMTis)[48] structurally related to cytidine (5-azacytidine, Vidaza® and 5-aza-deoxycytidine, Dacogen®) are already in the clinic for the treatment of myelodysplastic syndrome.[49]

Since histone acetylation and DNA methylation play a key role in the pathophysiology of cells, dual inhibitors of HDAC or DNMT are therapeutically more appealing than combination of these drugs.[50,51] We thus became intrigued by the reports on the potent activity of psammaplin A (**1**) in the inhibition of these two epigenetic enzymes (HDAC: IC_{50} = 4.2 nM; DNMT: IC_{50} = 18.6 nM using in vitro cell-free enzyme assays)[3] as well as by the in vitro and in vivo inhibition of tumour growth induced by this natural product.[20] Despite the reports indicating some drawbacks for the development of **1** as a drug due to its poor physiological stability,[15,21,52] we undertook the synthesis of a family of analogues with the aim to discover more potent and selective derivatives of **1** as well as to shed light into the mechanism of epigenetic inhibition by **1**. Apart from the work of Nicolaou focused on antibacterial activities, no structure–activity relationship studies of the anticancer activities of PsA analogues have been reported, which are necessary for an eventual lead optimization project within this class of modified tetrapeptides.

2. Chemistry. Synthesis of psammaplin A and derivatives

All previous synthetic approaches to **1** have focused on the final construction of the dimeric disulfide structure by condensation of the corresponding carboxylic acid with the symmetrical diamine cystamine. Both Hoshino et al.[53] and Nicolaou et al.[54,55] installed the oxime function after the synthesis of the corresponding pyruvic acid derived from L-tyrosine, in a sequence that afforded **1** in moderate overall yields. Nicolaou then screened in antibacterial assays a 3828-membered library of heterodimeric psammaplin A analogues[15] obtained from symmetrical precursors by combinatorial scrambling via catalytically-induced disulfide exchange reactions. A recently described three-step (43% overall yield) synthesis of PsA **1** starts from the considerably more expensive and less versatile 4-hydroxyphenylpyruvic acid.[56]

We modified the above synthesis of **1** by performing the bromination of the phenol ring on the corresponding oxime **3** (Scheme 1).[57] As shown on Scheme 1, the amino group of L-tyrosine **2** was oxidized to the hydroxyimino ester **3** in 60% yield using Na_2WO_4 and H_2O_2 in ethanol.[58] A monobrominated product **4** was obtained by treatment of **3** with one equivalent of NBS in CH_3CN at 25 °C,[58,59] with no evidence of formation of the dibromo derivative or the dibrominated spirocyclic isoxazoline.[57] After saponification of **4** the carboxylic acid **5** was coupled with cystamine using Hoshino's conditions.[53] The overall yield for the synthetic sequence is 29%, with a slight improvement over the two routes previously described from L-tyrosine **2**. The synthetic scheme is advantageous for the preparation of diverse PsA analogues starting from commercial tyrosine derivatives.

Using the methodology depicted on Scheme 1, the synthesis of PsA homologues containing from three to six methylene units was completed, albeit in low yields (Scheme 2), using the non-commercial diamines **6a–d**, which were synthesized following a general methodology.[60]

Similarly, PsA analogues that preserve the native connecting cystamine unit but differ in the substituents at the aryl ring (Scheme 3) were synthesized using either commercially available tyrosine derivatives or the synthetic halogenated analogues (with bromine or iodine at C3) after oxidation of the amine to the oxime (Scheme 3). Some compounds of the series (**11a**, **11c**, **11d** and **11e**) have previously been described by Nicolaou on his search for new antibacterial agents.[55] Bromopsammaplin A **11f** is also a natural product isolated from an association of the sponges *Jaspis wondoensis* and *Poecillastra wondoensis*.[12]

Condensation of acid **5** with amines **12** and **14a–c** (Scheme 4) provided analogues **13** and **15a–c** which were designed to further our understanding of the mechanism underlying the biological activity of the parent PsA as HDAC inhibitor. The dimer **13** contains an ethylene group replacing the disulfide bond functionality. Products **15b**,**c** are monomers that have, respectively, methyl ether and methyl sulfide as end groups. The primary alcohol **16** was obtained by acidic (7:2:1 THF/HCO_2H/H_2O) deprotection of silyl ether **15a**.

The derivative lacking the oxime was also of interest to reveal whether this functional group is critical for the epigenetic activity of **1**. Compound **20** was prepared as described on Scheme 5. The bromination of methyl 3-(4-hydroxyphenyl)propanoate using the

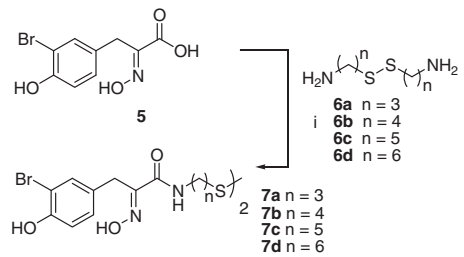

Scheme 2. Reagents and conditions: (i) DCC, *N*-hydroxyphthalimide, Et_3N, diamine **6**, 1,4-dioxane, MeOH, 25 °C, 12 h (**7a**, 16%; **7b**, 21%; **7c**, 34%; **7d**, 14%).

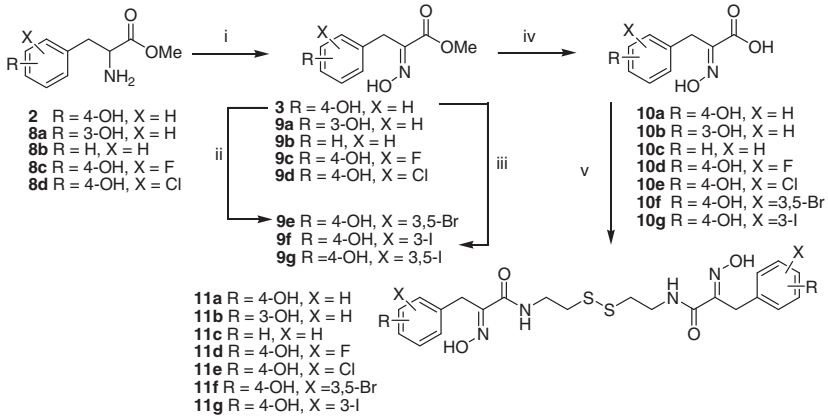

Scheme 3. Reagents and conditions: (i) Na_2WO_4, H_2O_2, 25 °C, 3 h (**9a**, 57%; **9b**, 50%; **9c**, 64%; **9d**, 80%); (ii) NBS, CH_3CN, 25 °C, 5 h (**9e**, 80%); (iii) I_2, Ag_2SO_4, MeOH, 25 °C, 15 min (**9f**, 51%; **9g**, 23%); (iv) LiOH, THF–H_2O, 23 °C, 12 h (**10a**, 99%; **10b**, 99%; **10c**, 99%; **10d**, 97%; **10e**, 98%; **10f**, 99%; **10g**, 99%); (v) DCC, *N*-hydroxyphthalimide, Et_3N, cystamine, 1,4-dioxane, MeOH, 25 °C, 12 h (**11a**, 46%; **11b**, 54%; **11c**, 15%; **11d**, 57%; **11e**, 57%; **11f**, 42%; **11g**, 52%).

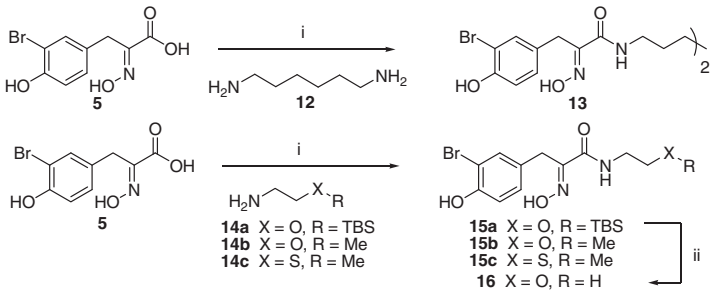

Scheme 4. Reagents and conditions: (i) DCC, *N*-hydroxyphthalimide, Et_3N, **12** or **14a–c**, 1,4-dioxane, MeOH, 25 °C, 14 h (**13**, 70%; **15a**, 83%; **15b**, 20%; **15c**, 18%); (ii) 7:2:1 THF/HCO_2H/H_2O, 25 °C, 14 h (76%).

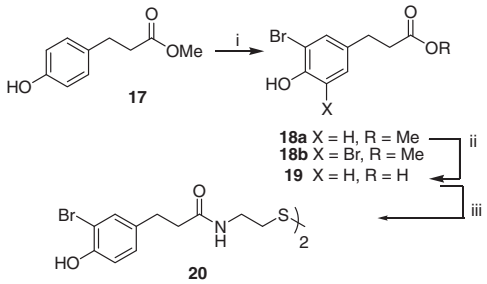

Scheme 5. Reagents and conditions: (i) NBS, DMF, 25 °C, 5 h (**18a**, 56%; **18b**, 17%); (ii) LiOH, THF–H_2O, 23 °C, 12 h (99%); (ii) DCC, *N*-hydroxyphthalimide, Et_3N, cystamine, 1,4-dioxane, MeOH, 25 °C, 14 h (40%).

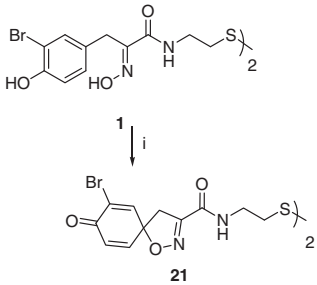

Scheme 6. Reagents and conditions: (i) MTA, CH_3CN, 25 °C, 15 h (5%).

conditions described for oxime **4** (NBS in CH_3CN) yielded a mixture of mono- and dibromo derivatives, **18a** and **18b**, respectively, in a 3:1 ratio. Hydrolysis of the former followed by the coupling of **19** with cystamine led to the desired disulfide **20** in moderate yield (Scheme 5).

Lastly the spirocyclic hexadienyl-isoxazoline **21**, a potential metabolite of PsA[1] could only be obtained, albeit in very low yield (5%), by the oxidative-induced cyclization[61] of PsA **1** with manganese(III) tris(acetylacetonate) (MTA)[62] (Scheme 6) after many other methods failed.

3. Biological characterization

Firstly, we focused on the reported inhibition of HDAC by PsA and the synthetic analogues, as well as on their effects on cell cycle, induction of differentiation and apoptosis on the U937 human acute myeloid leukemia cell line. In vitro tests of the compounds at 5 μM on human recombinant HDAC1, using SAHA as a positive control, confirmed the enzymatic inhibition of PsA **1** (Fig. 1A). In addition, some analogues (**11a–e**, **11g**) reduced the activity of HDAC1 more efficiently than **1**. The other compounds of the series (**7a–d**, **11f**, **13**, **15b–c**, **16**, **20** and **21**) did not noticeably affect HDAC1 activity. Compounds with longer chain connecting the disulfide to the hydroxyimino amide (**7a–d**) lack significant inhibitory activity. A similar result was observed for compounds having the disulfide replaced by methylene units (**13**) and for the monomers with either methyl ether –OMe, methyl thioether (–SMe) or alcohol (–OH) functionalities (**15b**, **15c** and **16**, respectively). In contrast, the inhibitory activity is maintained and even increased with compounds that preserve the general modified tetrapeptide scaffold of PsA regardless of the nature and pattern of the substituents at the aryl ring (**11a–f**). The more drastic change of the overall aryl ring structure imparted by the spirocycle together

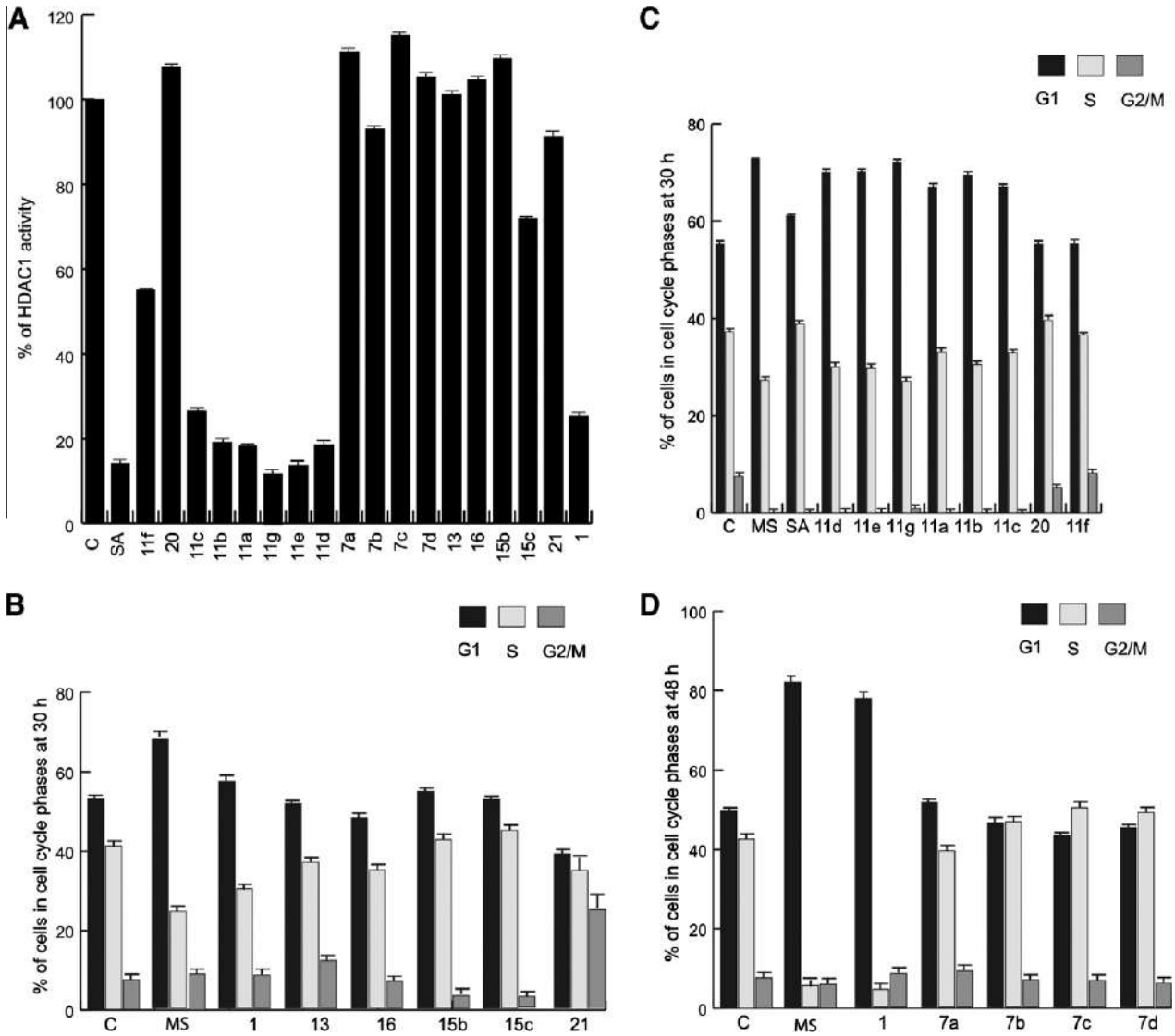

Figure 1. (A) HDAC1 fluorescent assay with the indicated compounds at 5 μM. The inhibition is reported as percentage of activity relative to the control (100%). (B–D) Cell cycle analysis and apoptosis in U937 cells treated with the indicated compounds at 5 μM for 30 h. The data represent the media of independent duplicates.

with the reduction of flexibility and the lack of free oxime in derivative **21** led to substantial loss of HDAC inhibitory activity.

Cell-based assays were performed on the U937 myeloid leukemia cells to determine the anti-proliferative potential and the ability of the compounds to revert myeloid tumor cells to differentiated granulocytes. Cell cycle progression, differentiation and amount of cells that undergo apoptosis following treatment with PsA **1** and analogues (5 μM) for 30, 40, and 48 h were determined (Figs. 1B and 2). Compared to the vehicle-treated cells and relative to the positive control represented by the known HDACis MS275 (HDAC1,2,3-selective) and SAHA (also HDAC6 inhibitor),[63,64] only PsA **1** and some analogues induced cell cycle arrest in G1 (Fig. 1, panels B–D). In particular after 30 h PsA induced a time-dependent accumulation of U937 cells in the G1 phase (60%), and analogues **11a–g** and **20** showed even greater arrest (80%), with values comparable to MS-275 (Fig. 1C). A clear correlation between the in vitro HDAC1 inhibition and the in vivo efficacy to induce cell cycle arrest was noticed for the most active compounds. Compound **21**, on the other hand, appears to block cell cycle at G2/M. The remaining analogues gave no detectable activities on cell cycle progression even after longer (48 h) treatment regimes (Fig. 1B and D).

The percentage of apoptotic cells (measured as caspase 3 activation by FACS analysis) increased when U937 cells were treated with **1** and series **11a–g** for 30 h (Fig. 2A). After 30 h induction with compounds **11a–e** and **11g** the percentage of apoptotic cells varied between 30% and 40%. Other compounds, including bromopsammaplin A (**11f**), and the derivative lacking the oxime function **20**, exhibited only minor effects even at longer incubation times (40 h). The results confirmed the in vitro findings since the most potent inducers of differentiation and apoptosis in U937 cells are the **11a–g** series of ring-modified PsA analogues (with the exception of bromopsammaplin A **11f**). Modifications in the chain length and the disulfide led to lower values of apoptosis, in agreement with the enzymatic assays. Interestingly, spiro derivative **21** showed comparable induction of apoptosis to parent **1**.

The differentiation of myeloid precursors to granulocytes was determined by measuring the presence on the cell membrane of the granulocytic differentiation marker CD11c antigen, which is highly expressed only on mature granulocytes, monocytes and certain lymphocytes, but not significantly on myeloid committed precursor cells. After treating the U937 cells with the PsA analogues at 5 μM for 30 and 40 h, low differentiation levels

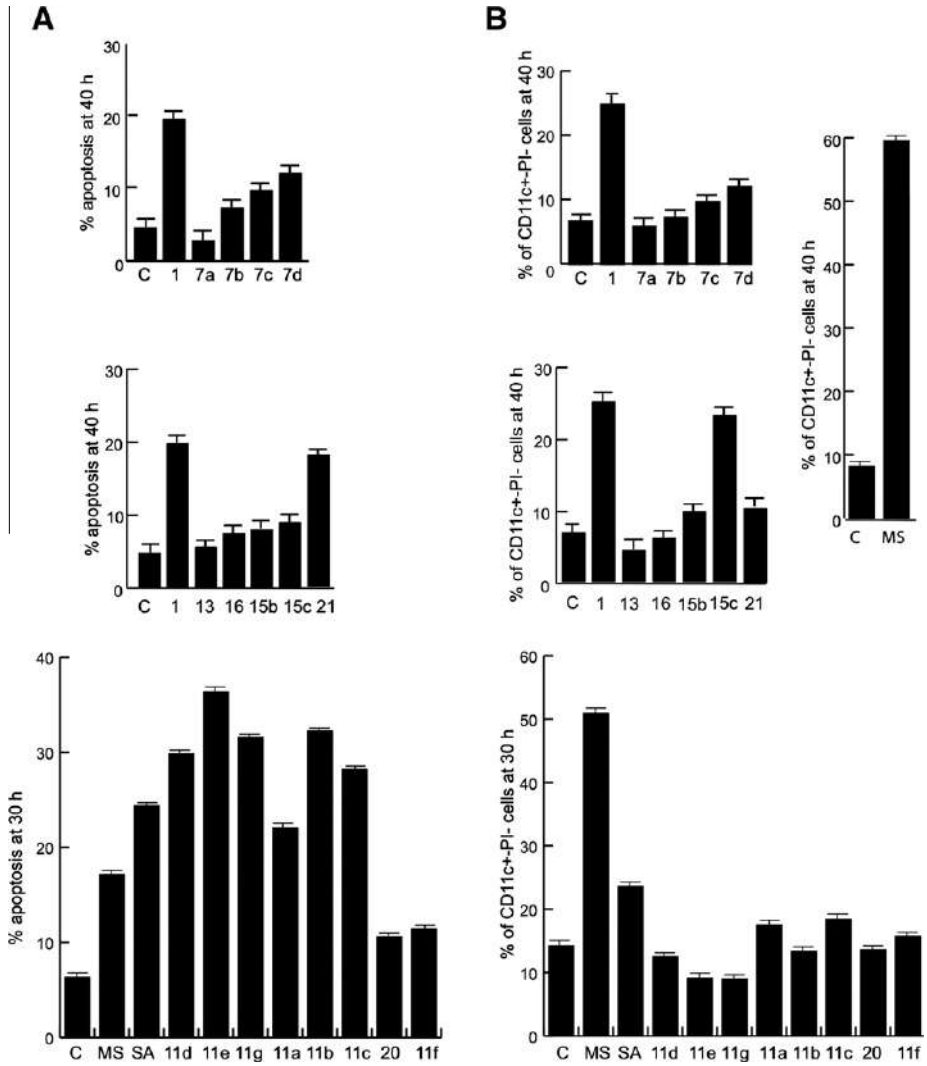

Figure 2. (A) Induction of apoptosis after treatment of U937 cells with the indicated compounds at 5 μM, for 30 h (for the series **11a**–**11g**) and 40 h. (B) Differentiation analysis in U937 cells after 30 h treatment with the indicated compounds at 5 μM. The percent value of CD11c positive/propidium iodide (PI) negative cells is represented. The data shown is the media of independent quadruplicates.

were measured (with the exception of parent **1** and methyl sulfide **15c**) relative to control (Fig. 2B) and to the class I-selective HDACi MS-275.

We next determined the expression levels of $p21^{WAF1}$, which is involved in the mechanism of tumor suppression, as well as the global acetylation status of histone (histone H3) and non-histone proteins (tubulin), that are substrates of HDACs family members. The up-regulation of $p21^{WAF1}$ and the increase of tubulin acetylation levels were evaluated by Western blot analyses on total extracts after treating the U937 cells for 24 h with the compounds at 5 μM (Fig. 3A–C). Compounds **7a–d**, **13**, **15b**, **16** and **21** failed to increase both $p21^{WAF1}$ and tubulin acetylation expression levels. Methyl sulfide **15c** increased weakly these levels in line with its noticeable effect on the induction of differentiation. While the **11a–g** series did not show a significant effect on tubulin acetylation, some members (**11b–e**) up-regulated $p21^{WAF1}$ to levels even higher than those of SAHA. The effect of the analogues on the level of histone acetylation was also analyzed by Western blot (Fig. 3D). After treating U937 cells for 24 h all compounds of the series **11a–g** displayed the ability to increase the level of acetylated histone H3, present in the histonic extract, as shown using the specific antibody.

In order to determine if the most potent analogues are endowed with additional epigenetic modulation activities, the series **11a–g** and **20** were also used in in vitro human SIRT1 fluorescent assay and in a radioactive assay on a peptide fragment having p300/CBP histone acetyl transferase (HAT) enzyme activity. As shown in Figure 4B, very weak SIRT1 inhibition was noted (ca. 30% relative to the control) for the majority of compounds at 50 μM, far lower than the activity of the SIRT1 inhibitor suramin at the same concentration. In addition, none of the analogues displayed modulation of a peptide fragment of CBP containing the enzymatically active HAT domain (Fig. 4A) relative to the control and to the effects of the known inhibitor anacardic acid (AA) at the same concentration,[65,66] thus confirming the specificity of the HDAC among other epigenetic inhibitory activities.

DNMT inhibition has also been reported for PsA.[3] To verify the effective physical interaction between PsA and its analogues and DNA methyl transferase enzymes, two in vitro radioactive assays were performed using DNMT1 and DNMT3A (Fig. 4C and D). DNMT1 was immunoprecipitated from K562 cells and used in radioactive assay that employs [^{3}H]-adenosyl-L-methionine as methyl donor and Poly dI-dC as methyl acceptor. The same conditions have been used for the DNMT3A radioactive assay, but the

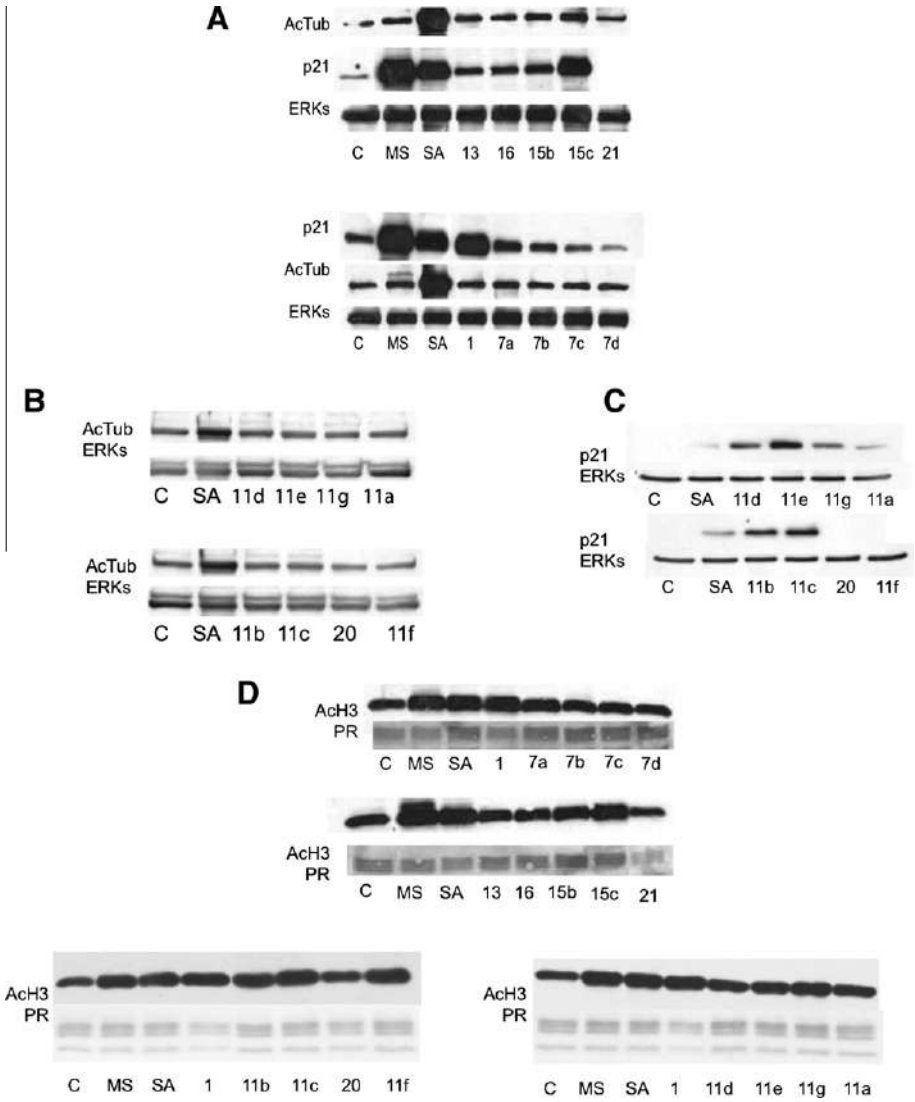

Figure 3. (A–C) Western blot analyses of $p21^{WAF1/CIP1}$ expression and α-tubulin acetylation in U937 cells after treatment with the indicated compounds at 5 μM for 24 h. ERK1 expression is shown as loading control. (D) Western blot analyses of histone H3 acetylation carried out in U937 cells, after 24 h induction with the compounds at 5 μM.

recombinant enzyme was produced in *Escherichia coli* BL21, as GST fused protein. In neither assay compounds **11a–g** and **20** showed significant inhibition at 50 μM (see Fig. 4C), in contrast to RG108[67] and SGI1027[68] at the same concentration for the DNMT1 assay.

Taken together, the enzymatic profiling suggests that the epigenetic activities of PsA are mainly restricted to the inhibition of the HDAC family in this context. Moreover, the HDAC activity of the series is likely linked to the formation of the monomeric thiol that originates from –S···S– bond cleavage (Scheme 7, vide infra), a known potent metal chelator. The Zn^{2+}-dependent histone deacetylase subfamily is composed of Class I HDACs (HDAC 1–3, 8 and 11) and Class II HDACs (HDAC 4–7, 9 and 10). In contrast, Class III (sirtuins), with seven members (SIRT1-7), require NAD^+ as a cofactor and release *O*-acetyl-ADP ribose and nicotinamide as a consequence of acetyl transfer from the acetylated lysine.[69]

Metalloproteinase-targeted HDAC inhibitors are typically substrate mimics of the linear acetyl-lysine side chain with a Zn^{2+}-chelating 'warhead' group that replaces the scissile acetamide, a connector chain and a 'cap' at the other end that extend beyond the enzyme substrate-binding channel. These features are exhibited by the thiol derived from PsA (Scheme 7), in which the active site binding/inactivating group is connected via a hydroxyimino amide linker to the HDAC recognition aryl group.

In order to address the nature of the interaction between the inhibitor and HDAC, the ab initio calculated structure of thiol **22** was docked into the active site of the human HDAC8-trichostatin A (TSA) crystal structure[70] after removal of the TSA ligand. The catalytic domain of about 390 amino acids responsible for the deacetylation is highly conserved among the metal-dependent HDACs, in particular the residues lining the ligand-binding pocket, but some differences can be exploited for the designed of selective Class I/Class II HDAC inhibitors.[71]

The highest scores using automated docking method for the interaction of the ligand with the Zn^{2+} ion in the active site, validated by the GRID maps, agree in having the thiol chelated to the metal, whereas the linker domain occupies the channel and the *o*-bromophenol is stabilized through interaction with Tyr100 and Phe152 at the rim of the active site entrance (Fig. 5 and Figs. S1–S3). This positioning facilitates the formation of a hydrogen bond between the oxime group and Asp101, which remains at a constant distance along the energy minimization and the simulation of the dynamic behaviour using unrestrained MD (Fig. S3). The Zn^{2+} ion is kept firmly coordinated to the four ligands (Asp178, Asp267, His180 and the thiol group of the inhibitor),

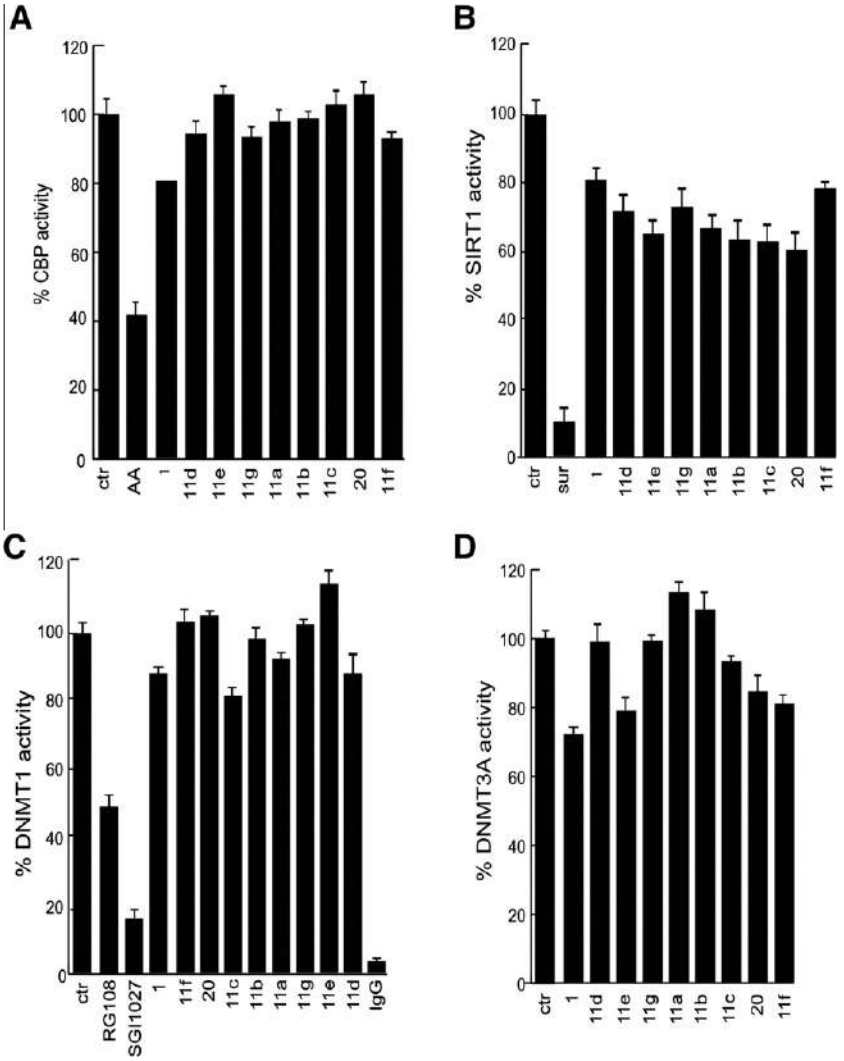

Figure 4. (A) CBP radioactive assay performed with 1 μg of recombinant CBP enzyme peptide fragment and the psammaplin A analogues at 50 μM. (B) SIRT1 fluorescence assay to measure the lysine deacetylase activity of the compounds at 50 μM on human recombinant SIRT1 enzyme (1 U). (C) DNMT1 radioactive assay with synthetic poly dI-dC as methyl acceptor (0.1 μg) and [^{3}H]-adenosyl-L-methionine (1 μCi) as methyl donor. DNMT1 was immunoprecipitated from K562 cells and the compounds **11a**–**g** were used at 50 μM. (D) DNMT1 radioactive assay to measure the inhibition of recombinant DNMT3a (1 μg, produced in *E. coli* BL21, as GST fused protein) by the compounds at 50 μM. In each panel the inhibition/activation of the enzyme is reported as percentage of activity relative to the control.

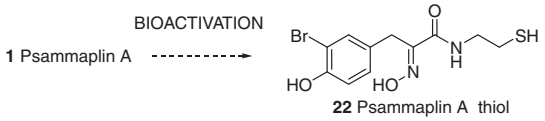

Scheme 7. Bioactivation of PsA **1** to thiol **22** by the reductive environment of the cells.

and the electrostatic term (−59.2191 ± 1.7841 kcal/mol) makes an important contribution to the overall energy. Favourable van der Waals interactions of the ligand with Phe152 and Phe208 residues also account for a fraction of the intermolecular energy component (Fig. S2).

4. Discussion

Psammaplin A **1** is the prototype of a collection of metabolites isolated from sponges[1] that are biosynthesized by linear connections of (bromo)tyrosines and modified cysteines.[12] Their biological activities, common to most of the bromotyrosine/cysteine constructs, range from antimicrobial[54] to anticancer.[1,6] The inhibition of several enzymes that impact different stages on the onset and progression of cancer such as topoisomerase II (growth),[14] the zinc-dependent metalloproteinase aminopeptidase N (APN, tumor cell invasion or angiogenesis),[21] HDAC and DNMT (chromatin remodeling),[3] among others, likely conspire to account for the reported anticancer activities of PsA in several cancer cell lines and in the A549 lung xenograft mouse model.[3,12] PsA was reported to activate Wnt signalling in a cell-based assay but the effect is likely due to HDAC inhibition rather than to an specific Wnt signalling pathway.[72]

More recent molecular and cellular studies[73] confirmed the potent inhibitory activity of PsA in enzymatic (HDAC inhibition) and in anti-proliferation assays, and also the selective induction of histone hyperacetylation. The anti-proliferative effects were linked to the overexpression of genes related to cell cycle arrest and apoptosis (p53-independent p21^{WAF1} expression).[74]

A series of PsA analogues modified at the aryl ring, with varying lengths of the amino thiol connecting unit, and some exchanges/deletions of functional groups have been prepared. These analogues have been characterized with regard to their enzymatic inhibitory potential and for their effects on cell cycle, differentia-

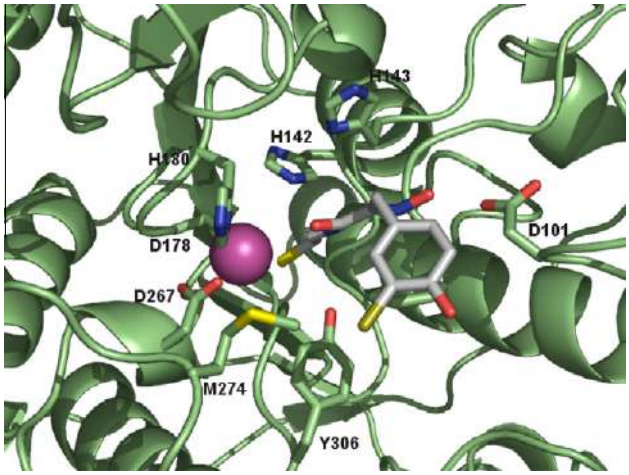

Figure 5. Proposed docking pose of biocleaved psammaplin A (thiol **22**) with HDAC8. The Cα trace of the enzyme is displayed as a ribbon, colored in green. The side chains of His142, His143, Asp178, Asp267, His180, Met274, Tyr306 are shown as sticks, with carbon atoms colored in green. The Zn^{2+} ion at the catalytic site is shown as a magenta sphere. The inhibitor is displayed also as sticks, but with carbon atoms colored in gray and the bromine atom colored in brown.

tion and apoptosis on the U937 acute myeloid leukemia cell line. For **1** and the most potent analogues, functional assays have also been carried out on the same cell line.

Enzymatic HDAC1 inhibition data for the series of analogues having chain lengths spanning from two to six methylene units (**7a–d**) established that the derivative of natural cystamine (the decarboxylated cysteine) present in psammaplin A was the most potent, and also that both the oxime and the disulfide functionalities were required for the HDAC inhibition activity, since analogues **13**, **15b–c**, **16** and **20** proved to be inactive (Fig. 1A). We then addressed the modifications of the aryl ring with analogues that preserve the same connecting diamine unit of the parent natural product. The substitution at the ring is well tolerated, and a general improvement in potency relative to PsA was noted when the ring was mono- (**11a**–**b**) or disubstituted (**11d**,**e**,**g**). The unsubstituted compound (the phenylalanine-derived **11c**) and the trisubstituted bromopsammaplin A **11f** were less active than **1**. Conversely the series of halogenated analogues **11d**,**e**,**g** exhibited greater potency than PsA and followed the order Br < F < Cl < I. The activities of the spiro derivative **21** are most intriguing, since it is the only compound showing a G2/M block (Fig. 1B) and strong induction of apoptosis (Fig. 2B), which appears not to be correlated with HDAC inhibition. A promising pro-differentiation profile is also noted for the methylsulfide **15c** (Fig. 2B), which merit further investigation.

It has previously been reported that human endometrial Ishikawa cancer cells treated with PsA showed accumulation of cells in the G1 phase and a significant decrease in the number of cells in the S phase,[74] a result in keeping with the effect of known HDAC inhibitors.[75] Our data confirm the time-dependent accumulation of cells in G1 upon treatment of human leukaemia U937 cells with PsA and analogues. Moreover, **1** and the **11a–g** series of related compounds induced apoptosis of U937 cells (Fig. 2B), an effect likely associated to their more selective inhibition of class I HDACs. The majority of these compounds (with the exception of **15c**) failed to induce tubulin acetylation (Fig. 3), which is a target of HDAC6 enzymes, and this finding is in agreement with previous reports for PsA in HeLa cells.[73] Although the result might suggest that psammaplin A show selectivity for histone proteins in preference to tubulin, it cannot be considered as a selective class I HDAC inhibitor, since it also inhibits HDAC4, a class II HDAC, in enzymatic assays (results not shown). Important differences between class I and class II metalo-HDACs are noticeable in their size (with class II being from two to three times larger), their cellular localization, the conservation of sequence motifs in the catalytic domains, the identity of the protein–protein interaction complexes and the tissue distribution.[76]

Western blot analysis of U937-treated cells confirmed the accumulation of acetylated histones using antibodies against acetylated H3 (Fig. 3D), in agreement with similar findings for PsA in endometrial cancer Ishikawa cells.[74] PsA and several analogues up-regulated cyclin-dependent kinase inhibitor $p21^{WAF1}$ (Fig. 3), which is one of the genes induced by HDAC inhibitors,[76] and this effect might be related to the suppression of cell proliferation and induction of apoptosis.

PsA and its 5-bromo derivative have been reported to inhibit the bacterial methyltransferase SssI. However, cultured HCT116 human colon carcinoma cells treated with 1 μM PsA did not reduce global genomic DNA methylation (the level of which was determined using a mass spectrometry assay) and failed to induce the hypomethylation or reactivation of cancer-testis antigen genes, known as methylation silenced genes.[56] Here, two different assays were performed on DNMT1 and DNMT3A (see Fig. 4C and D) to evaluate the inhibition of DNMT enzymes by PsA and derivatives (**11a–g**). Differently from expected, these compounds at 50 μM failed to inhibit DNMT1 and DNMT3a, thus indicating their inability to alter DNMT in vitro. Therefore, the action of these compounds on cell cycle progression and induction of apoptosis can be better correlated with the HDAC inhibitory activities. It is likely that the absence of hypomethylation is not due to the low affinity of PsA (and its analogues) for DNMT, but instead to the inefficient transport of these compounds through the nuclear membrane. Inefficient transportation of the compound into the nucleus or poor cell membrane penetration might also explain the much greater concentration of **1** (1800 times) required to obtain similar potencies in cell-based assays relative to the HDAC enzymatic inhibition assay.[52]

Lastly, no significant inhibition of SIRT1 and p300/CBP HAT enzymes was seen for the PsA-related series of analogues (Fig. 4A and B).

Other natural products of the depsipeptide class that act as inhibitors of HDAC also contain disulfide bonds, namely FK228 **23**, spiruchostatins **25** and FR901375 **26** (Fig. 6).[39,71] FK228 (romi-

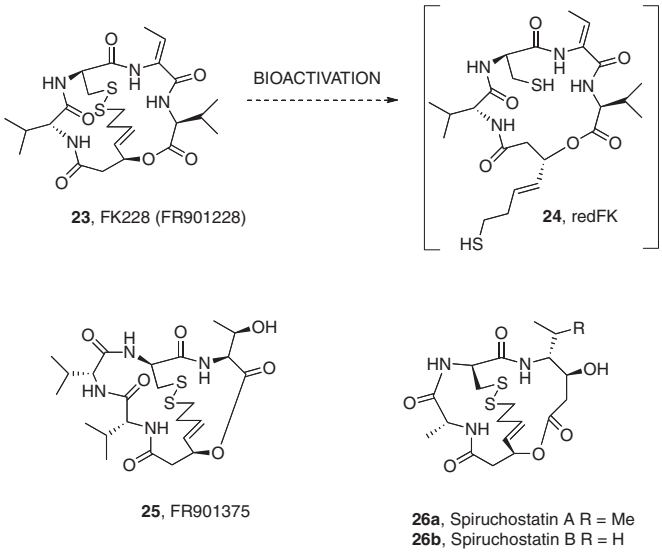

Figure 6. Natural depsipeptides **23**–**26** containing disulfide bonds are HDAC inhibitors. The structure of previously characterized active reduced form of FK228 (**24**, redFK) is shown by analogy with the reduced form of psammaplin A, **22**.

depsin, Istodax®) currently approved for T cell lymphoma is undergoing phase II clinical trials for the treatment of non-Hodgkin's lymphoma, acute myelogeneous leukemia, and pancreatic cancer (www.clinicaltrials.gov). It has been shown that the disulfide bond of FK228 becomes cleaved in the cells by the reducing activity of glutathione to afford redFK **24**, and the thiol then interacts with the Zn^{2+} ion in the active site of HDAC.[77] Moreover, mass spectrometry analysis of blood samples identified the thiol and glutathione conjugates of FK228.[78] Upon bio-reduction depsipeptides **25** and **26** must also release the Zn^{2+}-binding butenylthiol.[79] From an structural point of view both redFK **25** and PsA thiol **22** have Zn^{2+} ion connecting chains that are shorter than those of common hydroxamic acid-based inhibitors (TSA, SAHA...). Thiol chelating groups connected via a 5 atom saturated chain to cyclic tetrapeptides have also shown potent HDAC inhibitory activities.[80,81]

In agreement with these precedents, the dimer analogue lacking the disulfide bond (**13**) was inactive, which substantiates the proposal that PsA and analogues undergo thiolate exchange reaction with glutathione by –S···S– bond cleavage.[82] Interestingly, Wang et al. have shown that glutathione-depleted cells were not sensitive to PsA, implying that the reducing environment of the cells triggered the conversion of the disulfide of **1** to the corresponding thiol,[79] which would be the species responsible for the HDAC inhibitory activity of psammaplin A after uptake into the cells.

Based on the reported crystal structure, the HDAC8·Zn^{2+}·thiol **22** complex was constructed with the thiol group chelating the metal ion, and then refined using energy minimization. The dynamic behaviour of the complex using unrestrained molecular dynamics confirmed the feasibility of the proposed binding orientation and the mutual adaptation between HDAC8 and the ligand. The linker occupies the narrow channel whereas the bromophenol interacts with Tyr100 and Phe152 at the rim of the active site entrance, a pose that facilitates the formation of a robust hydrogen bond between the oxime group and Asp101 (Fig. 5).

Our results using alcohol **16**, ether **15b** and most importantly dimer **13** confirm the earlier findings with FK228[78] and suggest that psammaplin A **1** acts as a stable pro-drug[83] that is activated upon uptake by the reductive environment of the cells to afford thiol **22**, which then chelates the Zn^{2+} ion in the active site of the HDAC metalloenzymes.

5. Conclusion

PsA **1**, a natural product with a disulfide bond derived from the condensation of modified cystamine and tyrosine moieties, has been reported to display dual HDAC and DNMT epigenetic inhibitory activities. The intriguing ability to target simultaneously more than one member of the epigenetic machinery (epigenetic multiple ligands),[84] prompted us to synthesize a series of PsA analogues in an effort to determine the structural determinants for their epigenetic profile. We have analyzed the effects of the natural-product inspired collection on the human leukaemia U937 cell cycle, measuring induction of apoptosis and differentiation, induction of $p21^{WAF1}$ and tubulin acetylation levels and total histone H3, and also examined their HDAC1 enzyme-based inhibition profile. From the results it is concluded that Nature has optimized the design of the PsA scaffold to fulfil this epigenetic role, since only closely related synthetic derivatives (with modifications at the bromotyrosine ring) exhibited comparable or greater potency than the natural product. Modifications of the connecting chain, oxime bond and disulfide unit afforded either inactive or considerable less potent analogues. Exploring the possibility that PsA and derivatives might display additional epigenetic activities we have also tested them as inhibitors of DNMT1, DNMT3A, SIRT1 and a peptide containing the p300/CBP HAT domain, but the values measured were very low. Since epigenetic signalling by PsA appears to be restricted to inhibition of metalloproteinase HDACs, a model for the interaction of HDAC8 with the thiol derived from PsA **1** (by a presumed in vivo disulfide cleavage) was computed. The thiol binds the Zn^{2+} ion in the active site and the complex is additionally stabilized by a hydrogen bond interaction between the oxime group and the Asp101 residue located at the active site entrance. As with FK228, this bioactivation mechanism illustrates the ingenious solution adopted by Nature to protect the reactive zinc-binding thiol as a disulfide pro-drug with higher bioavailability. The increased levels of disulfide reductants (i.e., glutathione, thioredoxin and thioredoxin reductase) found in many cancer cells render such cells particularly susceptible to the action of PsA **1**.

Despite the failure to greatly improve the epigenetic inhibitory profile of PsA through the modifications reported, more significant skeletal alterations of the PsA structure might provide more potent derivatives, thus lending further support to the important role of natural products as inspiration[85] for the development of designed multiple ligands[50,51] as new anticancer drugs.[86,87]

6. Experimental section

6.1. General

Solvents were dried according to published methods and distilled before use. HPLC grade solvents were used for the HPLC purification. All other reagents were commercial compounds of the highest purity available. All reactions were carried out under argon atmosphere, and those not involving aqueous reagents were carried out in oven-dried glassware. Analytical thin layer chromatography (TLC) was performed on aluminium plates with Merck Kieselgel 60F254 and visualized by UV irradiation (254 nm) or by staining with a solution of phosphomolibdic acid. Flash column chromatography was carried out using Merck Kieselgel 60 (230–400 mesh) under pressure. Infrared spectra were obtained on JASCO FTIR 4200 spectrophotometer, from a thin film deposited onto a NaCl glass. ^{1}H NMR spectra were recorded in $CDCl_3$, CD_3OD, DMSO-d_6 and $(CD_3)_2CO$ at ambient temperature on a Bruker AMX-400 spectrometer at 400 MHz with residual protic solvent as the internal reference ($CDCl_3$, δ_H = 7.26 ppm; $(CD_3)_2CO$, δ_H = 2.05 ppm; CD_3OD, δ_H = 3.31 ppm; DMSO-d_6, δ_H = 2.50 ppm); chemical shifts (δ) are given in parts per million (ppm), and coupling constants (J) are given in Hertz (Hz). The proton spectra are reported as follows: δ (multiplicity, coupling constant J, number of protons, assignment). ^{13}C NMR spectra were recorded in $CDCl_3$ CD_3OD, DMSO-d_6 and $(CD_3)_2CO$ at ambient temperature on the same spectrometer at 100 MHz, with the central peak of $CDCl_3$ (δ_C = 77.0 ppm), CD_3OD (δ_C = 49.0 ppm), DMSO-d_6 (δ_C = 39.4 ppm) or $(CD_3)_2CO$ (δ_C = 30.8 ppm) as the internal reference. The DEPT135 sequence was used to aid in the assignment of signals on the ^{13}C NMR spectra. Melting points were determined on a Stuart SMP10 apparatus. Elemental analyses were determined on a Carlo Erba EA 1108 analyzer. MS experiments were performed on an APEX III FT-ICR MS (Bruker Daltonics, Billerica, MA), equipped with a 7T actively shielded magnet. Ions were generated using an Apollo API electrospray ionization (ESI) source (Bruker Daltonics, Billerica, MA), with a voltage between 1800 and 2200 V (to optimize ionisation efficiency) applied to the needle, and a counter voltage of 450 V applied to the capillary. Samples were prepared by adding a spray solution of 70:29.9:0.1 (v/v/v) methanol/water/formic acid to a solution of the sample at a v/v ratio of 1–5% to give the best signal-to-noise ratio. Data acquisition and data processing were performed using the XMASS software, version 6.1.2 (Bruker Daltonics). FAB experiments were performed on a VG AutoSpec instrument, using 3-nitrobenzylalcohol or glycerol as matrix.

6.2. General procedure for the oxidation of amines with Na_2WO_4

To a solution of amine (18.0 mmol) in EtOH (40 mL) at 0 °C were added $Na_2WO_4 \cdot 2H_2O$ (18 mmol), 30% H_2O_2 (16 mL) and H_2O (30 mL). The resulting mixture was stirred for 4 h at room temperature and the reaction was quenched with aqueous saturated NH_4Cl and extracted with EtOAc (3×). The combined organic extracts were washed with brine, dried over Na_2SO_4 and evaporated. The residue was purified by column chromatography on silica gel as indicated.

6.3. General procedure for the hydrolysis of esters

Lithium hydroxide (15 mmol) was added to a solution of ester (1 mmol) in a 1:1 THF/H_2O (16 mL) mixture. The solution was stirred at room temperature for 2 h, neutralized with 10% HCl and extracted with EtOAc (4×). The combined organic layers were washed with brine, dried over Na_2SO_4, filtered and the solvent was evaporated in vacuo. Crystallization of the residue provided the desired acid as indicated.

6.4. General procedure for the amidation of tyrosine acid derivatives with amines

N-Hydroxyphtalimide (1 mmol) and DCC (1 mmol) were added to a solution of the carboxylic acid (1 mmol) in dioxane (2.5 mL). After the mixture had been stirred for 2 h at room temperature, a solution of the amine (0.5 mmol), Et_3N (2 mmol) and MeOH (1 mL) was added. The resulting mixture was stirred for 12 h at room temperature and the reaction was quenched with H_2O and extracted with EtOAc (3×). The combined organic extracts were washed with brine, dried over Na_2SO_4 and evaporated. The residue was dissolved in THF, filtered off and the solvent was evaporated in vacuo. The resulting residue was then purified by column chromatography on silica gel as indicated.

6.4.1. (*E*)-Methyl 2-(hydroxyimino)-3-(4-hydroxyphenyl)propanoate (3)[88]

Following the general procedure for the oxidation of amines with $Na_2WO_4 \cdot 2H_2O$, L-tyrosine methyl ester **2** (3.45 g, 17.68 mmol) gave, after purification by column chromatography (SiO_2, 50:50 hexane/EtOAc), 2.24 g (60%) of oxime **3** as a white powder. ^{1}H NMR (CD_3COCD_3, 400.13 MHz): δ 11.35 (s, 1H, OH), 8.11 (s, 1H, OH), 7.11 (d, J = 8.5 Hz, 2H, ArH), 6.73 (d, J = 8.5 Hz, 2H, ArH), 3.84 (s, 2H, 2H3), 3.72 (s, 3H, CO_2CH_3) ppm.

6.4.2. (*E*)-Methyl 3-(3-bromo-4-hydroxyphenyl)-2-(hydroxyimino)propanoate (4)[61]

A solution of NBS (0.49 g, 2.75 mmol) in CH_3CN (6 mL) was added dropwise over 15 min to the solution of the oxime **3** (0.58 g, 2.75 mmol) in CH_3CN (6 mL). The reaction mixture was stirred at room temperature for 5 h, after which time the solvent was evaporated and the residue was treated with water and extracted with EtOAc (3×). The combined organic extracts were dried over Na_2SO_4, filtered, evaporated and the residue was purified by column chromatography (SiO_2, 50:50 hexane/EtOAc) to afford oxime **4** (0.65 g, 82%) as a yellow powder. ^{1}H NMR (CD_3COCD_3, 400.13 MHz): δ 11.49 (s, 1H, OH), 8.62 (s, 1H, OH), 7.44 (d, J = 1.6 Hz, 1H, H2′), 7.13 (dd, J = 8.3, 1.6 Hz, 1H, H6′), 6.90 (d, J = 8.3 Hz, 1H, H5′), 3.85 (s, 2H, 2H3), 3.74 (s, 3H, CO_2CH_3) ppm.

6.4.3. (*E*)-3-(3-Bromo-4-hydroxyphenyl)-2-(hydroxyimino)propanoic Acid (5)

In accordance with the general procedure for the hydrolysis of esters, ester **4** (0.61 g, 2.11 mmol) gave, after purification by column chromatography (SiO_2, 90:10 EtOAc/MeOH), 0.58 g (99%) of acid **5** as a white powder, mp: 147–148 °C (hexane/$CHCl_3$) (lit. 147–148 °C, dec.).[89] ^{1}H NMR (CD_3COCD_3, 400.13 MHz): δ 7.45 (s, 1H, H2′), 7.14 (d, J = 7.9 Hz, 1H, ArH), 6.90 (d, J = 7.9 Hz, 1H, ArH), 3.84 (s, 2H, 2H3) ppm.

6.4.4. (2*E*,2′*E*)-*N*,*N*′-[2,2′-Disulfanediylbis(ethane-2,1-diyl)]bis[3-(3-bromo-4-hydroxyphenyl)-2-(hydroxyimino)propanamide] (psammaplin A, 1)[56]

Following the general procedure for the amidation of tyrosine acid derivatives with amines, acid **5** (0.16 g, 0.59 mmol) afforded, after purification by column chromatography (SiO_2, gradient from 25:75 hexane/EtOAc to 95:5 CH_2Cl_2/MeOH), psammaplin A **1** (0.12 g, 60%) as a white foam. ^{1}H NMR (CD_3OD, 400.13 MHz) (data for monomer): δ 7.36 (s, 1H, H2′), 7.07 (d, J = 8.3 Hz, 1H, ArH), 6.76 (d, J = 8.3 Hz, 1H, ArH), 3.79 (s, 2H, 2H3), 3.52 (t, J = 6.7 Hz, 2H, 2H1″), 2.81 (t, J = 6.7 Hz, 2H, 2H2″), 2.15 (br, 2H, OH) ppm.

6.5. Molecular modeling of psammaplin A

6.5.1. Quantum mechanics calculations

The geometry of the thiol derived from psammaplin A was optimized using the ab initio quantum chemistry program Gaussian 03[90] and the HF/3-21G* basis set. A set of atom-centred RHF 6-31G*//3-21G* charges was then obtained by using the RESP methodology[91] as implemented in the AMBER suite of programs (http://amber.scripps.edu/). Covalent and nonbonded parameters for the inhibitor atoms were assigned, by analogy or through interpolation, from those already present in the AMBER force field[92] (parm99) or consistently derived, as explained in more detail elsewhere.[93]

6.5.2. Molecular docking

The genetic algorithm[94] implemented in AutoDock[95] and the h-HDAC8 (PDB code 1t64)[70] as the target protein upon removal of trichostatin A was used to generate different HDAC-Zn^{2+}-bound psammaplin A thiol conformers by randomly changing torsion angles and overall orientation of the molecule. A volume for exploration was defined in the shape of a three-dimensional cubic grid with a spacing of 0.3 Å that enclosed the residues that are known to make up the inhibitors binding pocket. At each grid point, the receptor's atomic affinity potentials for carbon, oxygen, nitrogen, sulfur, bromine and hydrogen atoms present in the ligand were precalculated for rapid intra- and intermolecular energy evaluation of the docking solution.

To obtain additional validation of the proposed binding mode for the ligands, the program GRID (http://www.moldiscovery.com/[96] was also used to search for sites on the enzyme that could be complementary to the functional groups present in this inhibitor. For the GRID calculations, a 18 × 21 × 21 Å lattice of points spaced at 0.5 Å was established at the binding site. The probes used were C1 = (aromatic carbon), N1 (neutral flat NH, eg amide), N:# (sp nitrogen with lone pair), O (sp2 carbonyl oxygen) and Br (bromine). The dielectric constants chosen were 4.0 for the macromolecule and 80.0 for the bulk water.

6.5.3. Molecular dynamics simulations

Ternary complexes (HDAC8-Zn^{2+}-psammaplin A thiol) representative of the most populated solutions were then refined using the second generation AMBER force field and 3000 steps of steepest descent energy minimization and 6000 steps of conjugate gradient of only the side chain of the protein and those atoms of the bound ligand. This procedure allowed readjustment of covalent bonds and van der Waals contacts without changing the overall conformation of the complex. The HDAC-psammaplin A thiol complex was then neutralized by addition of eight sodium ions[97] that were placed in electrostatically favored positions and immersed

in rectangular boxes each containing about 450 TIP3P water molecules[98] that extended 1 Å away from any solute atom. The cutoff distance for the non-bonded interactions was 9 Å, and periodic boundary conditions were applied. Electrostatic interactions were represented using the smooth particle mesh Ewald method with a grid spacing of ~1 Å. Unrestrained molecular dynamics (MD) simulations at 300 K and 1 atm were then run for 6 ns using the SANDER module in AMBER 8.[99] The coupling constants for the temperature and pressure baths were 1.0 and 0.2 ps, respectively. SHAKE[100] was applied to all bonds involving hydrogens, and an integration step of 2 fs was used throughout. The nonbonded pair list was updated every 10 steps. The simulation protocol involving a series of progressive energy minimizations followed by a 20 ps heating phase and a 70 ps equilibration period before data collection. System coordinates were saved every 2 ps for further analysis.

6.5.4. Analysis of the molecular dynamics trajectories

Three-dimensional structures and trajectories were visually inspected using the computer graphics program InsightII. The root-mean-square (rms) deviations from both the initial structures and the average structures, the inter-atomic distances, and the snapshot geometries were obtained using the PTRAJ module in AMBER. Intermolecular van der Waals energies for individual residues were calculated with the ANAL module, whereas the solvent-corrected residue-based electrostatic interaction energies were calculated with DelPhi, following the procedure described.[93]

All calculations were performed on the SGI R14000 Origin 3800 at CIEMAT (Madrid), on the SGI 1.5 GHz Itanium2 at CESGA (Santiago de Compostela) and locally on SGI R12000 Octane workstations.

6.6. Biological assays

6.6.1. Cell culture

Human leukaemia cell lines U937, K562 and HL60 were propagated in RPMI medium supplemented with 10% FBS (Foetal bovine serum; Hyclone) and antibiotics (100 U/mL penicillin, 100 μg/mL streptomycin and 250 ng/mL amphotericin-B). Cells were kept at the constant concentration of 200,000 cells per mL of culture medium.

6.6.2. Ligands and materials

SAHA (Merck) and MS-275 (a kind gift of Bayer-Schering AG) were dissolved in DMSO and used at 5×10^{-6} M. All other compounds described were dissolved in DMSO (Sigma-Aldrich) and used at 5 and 50 μM.

6.6.3. Cell cycle analysis

2.5×10^5 cells were collected and resuspended in 500 μL of hypotonic buffer (0.1% Triton X-100, 0.1% sodium citrate, 50 μg/mL propidium iodide, RNAse A). Cells were incubated in the dark for 30 min. Samples were acquired on a FACS-Calibur flow cytometer using the Cell Quest software (Becton Dickinson) and analysed with standard procedures using the Cell Quest software (Becton Dickinson) and the ModFit LT version 3 Software (Verity) as previously reported.[101,102] Apoptosis was revealed by monitoring nuclear fragmentation (the so-called 'sub-G1 DNA peak') by FACS and analysed by Cell Quest technology.

6.7. Caspase 3 activation assay

Caspase activity was detected in living U937 cells using the BIOMOL and B-BRIDGE Kits supplied with cell-permeable fluorescent substrates. The fluorescent substrate for caspase 3 was FAM-DEVD-FMK. ca. 1×10^6 cells were washed twice in cold PBS and incubated for 1 h in ice with the corresponding substrates as recommended by the suppliers. The cells were analysed after washing using the CellQuest software applied to a FACScalibur (BD). Experiments were performed in duplicate and values were expressed as mean ± SD.

6.7.1. Granulocyte differentiation

Granulocyte differentiation was carried out as previously described.[103] Briefly, U937 cells were harvested and resuspended in 10 μL phycoerythrin-conjugated CD11c (CD11c-PE). Control samples were incubated with 10 μL PE conjugated mouse IgG1 for 30 min at 4 °C in the dark, washed in PBS and resuspended in 500 μL PBS containing propidium iodide (0.25 μg/mL). Samples were analyzed by FACS with Cell Quest technology (Becton Dickinson). Propidium iodide (PI) positive cells have been excluded from the analysis.

6.7.2. Western blot analyses

Western blot analyses were performed according to standard procedures following suggestions of antibody suppliers. For the determination of $p21^{WAF1/CIP1}$ 50 μg of total protein extracts were separated on a 15% polyacrylamide gels and blotted. Western blots were shown for p21 (Transduction Laboratories, dilution 1:500) and total ERKs (Santa Cruz) were used to normalize for equal loading. For α-Tubulin acetylation 25 μg of total protein extracts were separated on a 10% polyacrylamide gels and blotted. Western blots where shown for acetylated α-tubulin (Sigma, dilution 1:500) and total ERKs (Santa Cruz) or total tubulin (Sigma) were used to normalise for equal loading.

6.8. Histone extraction protocol

Cells were harvested and washed twice with ice-cold PBS and lysed in Triton Extraction Buffer (TEB: PBS containing 0.5% Triton X 100 (v/v), 2 mM phenyl methyl sulfonyl fluoride (PMSF), 0.02% (w/v) NaN_3) at a cellular density of 10^7 cells per mL for 10 min on ice, with gentle stirring. After a brief centrifugation at 2000 rpm at 4 °C, the supernatant was removed and the pellet was washed in half the volume of TEB and centrifuged as before. The pellet was resuspended in 0.2 M HCl at a cell density of 4×10^7 cells per mL and acid extraction was left to proceed overnight at 4 °C on a rolling table. Next, the samples were centrifuged at 2000 rpm for 10 min at 4 °C, the supernatant was removed and protein content was determined using the Bradford assay.

6.9. Determination of histone H3 specific acetylations

For the histone H3 acetylation in U937 cells, 10 μg of histone extract was separated on 15% polyacrylamide gels and blotted. Western blots were shown for pan-acetylated histone H3 (Upstate).

6.10. Fluorimetric human recombinant HDAC1 assays

GST-HDAC1 has been cloned into the pAcG2T baculovirus transfer vector (BD) and purified by using glutathione beads. The BD BaculoGold transfection system (BD) has been used in Sf9 insect cells for expression following supplier's instructions. The HDAC assay has been carried out as follows: the HDAC Fluorescent Activity Assay is based on the Fluor de Lys Substrate and Developer combination (BioMol) and has been carried out according to supplier's instructions. Briefly, the Fluor de Lys Substrate, which comprises an acetylated lysine side chain, has been incubated with the purified recombinant HDAC enzymes in presence or absence of the inhibitors, for 0.5 h at 37 °C. When a different incubation time has been used, it is specified into the text. Deacetylation of the substrate sensitizes the substrate so that, in the second step, treatment

with the Developer for 30 min produces a fluorophore. The fluorophore is excited with a 360 nm light and the emitted light (460 nm) has been quantified with a TECAN Inphinite M200 station.

6.11. Human recombinant Sirt1 assay

Recombinant human Sirt1 was prepared in *E. coli* BL21 and purified by affinity chromatography. The enzymatic reaction consisted of 1 μg of Sirt1 incubated with the acetylated p53 peptide (AA 379–382), 1 mM dithiothreitol, and a range of inhibitor concentrations, as described. Reactions were carried out at 37 °C for 60 min. Assays were performed in the presence of 200 μM NAD^+ for each inhibitor. Fluorescence was measured with a fluorimetric reader (TECAN Inphinite M200 fluorescence plate reader) with excitation set at 360 nm and emission detection set at 450 nm. Results are expressed as the mean and standard deviation of four independent experiments as percentage of activity considering the untreated control as 100.

6.12. Human recombinant CBP assay

The recombinant CBP was prepared in *E. coli* BL21 and purified by affinity chromatography. Recombinant CBP fraction corresponded to amino acids 1098–1877. CBP was incubated in HAT buffer with 10 μg of histone H4 peptide (corresponding to amino acids 2–24) and 20 μM Acetyl CoA containing 0.5 μCi/mL [^{3}H]-Acetyl CoA in the presence of inhibitors. After 2 h a 37 °C, 5 μL of samples were spotted onto Whatman P81 paper (in triplicate). The paper squares were washed three times in 5% TCA and once in 100% acetone and then placed into scintillation vials containing scintillation fluid to allow the DPM reading. The DPM of enzyme samples was compared to DPM of negative control. Data have been expressed as percentage of activity considering the control without treatment as 100.

6.13. Human recombinant DNMT3A radioactive assay

DNMT3A was produced in *E. coli* BL21 according to standard procedures. The methyltransferase radioactive assay was performed in a volume of 25 μL/point, using [^{3}H]-adenosyl-L-methionine (1 μCi) as methyl donor and Poly dI-dC (0.1 γ) as methyl acceptor, while 30–50 ng of recombinant DNMT3A protein was used, depending on enzyme activity, stability and purity. The compounds were tested at 50 μM. After 2 h incubation at 37 °C, 5 μL of samples were spotted onto Whatman DE81 paper (in triplicate). The paper squares were washed three times in 5% Na_2HPO_4 and once in sterile water and then placed into scintillation vials containing 5 mL of scintillation fluid to allow the DPM reading. The DPM of enzyme samples was compared to the DPM of negative control. Data were expressed as a percentage of activity relative to control.

6.14. Immunoprecipitation of DNMT1 and radioactive assay

The K562 cells were cultured in the experimental conditions reported and lysed in TAP buffer pH 7–7.5 (50 mM Tris pH 7.0, 180 mM NaCl, 0.15% v/v NP40, 10% v/v glycerol, 1.5 mM $MgCl_2$, 1 mM Na_2MoO_4, 0.5 mM NaF, 1 mM DTT, 0.2 mM PMSF, 0.1 mM protease inhibitor cocktail) for 10 min in ice and centrifuged at 130,000 rpm for 30 min. 650 μg of extracts were diluted in TAP buffer up to 1 mL and pre-cleared by incubating with 20 μL A/G plus agarose (Santa Cruz) for 30 min to 1 h on a rocking table at 4 °C. Supernatant was transferred to a new tube and 3–5 μg of antibody against DNMT1 (Abcam) was added. IP was allowed to proceed overnight at 4 °C on a rocking table. As a negative control the same amount of protein extracts were immunoprecipitated with purified IgG rabbit (Santa Cruz). The following day, 50 μL A/G plus agarose were added and incubation was continued for 2 h. The beads were recovered by brief centrifugation and washed with cold TAP buffer several times. After the last washing 20 μL of 2X concentrated electrophoresis sample buffer (217 mM Tris–HCl pH 8.0, 5.3% SDS, 17.4% glycerol, 8.7% β-mercaptoethanol, 0.026% bromophenol blue) was added and the sample was boiled for 5 min. A fraction of supernatants was loaded onto an SDS–PAGE gel in order to check the immunoprecipitation product. 10 μL of resin binding DNMT1 were used in DNMT radioactive assay (see above) to test the inhibitory potency of the PsA derivatives.

Acknowledgments

This work was supported by the EU (Epitron LSHC-CT2005-518417; JG, RP, GLF and AN contracts; and ATLAS Contract 221952), the Spanish MICINN (SAF-07-63880-FEDER), Xunta de Galicia (INBIOMED), and the Italian Associazione Italiana per la ricerca contro il cancro.

Supplementary data

Supplementary data associated with this article can be found, in the online version, at doi:10.1016/j.bmc.2010.12.026.

References and notes

1. Peng, J.; Li, J.; Hamann, M. T. *Alkaloids: Chem. Biol.* **2005**, *61*, 59.
2. Jiménez, C.; Crews, P. *Tetrahedron* **1991**, *47*, 2097.
3. Piña, I. C.; Gautschi, J. T.; Wang, G. Y. S.; Sanders, M. L.; Schmitz, F. J.; France, D.; Cornell-Kennon, S.; Sambucetti, L. C.; Remiszewski, S. W.; Perez, L. B.; Bair, K. W.; Crews, P. *J. Org. Chem.* **2003**, *68*, 3866.
4. Arabshahi, L.; Schmitz, F. J. *J. Org. Chem.* **1987**, *52*, 3584.
5. Rodriguez, A. D.; Akee, R. K.; Scheuer, P. J. *Tetrahedron Lett.* **1987**, *28*, 4989.
6. Quiñoà, E.; Crews, P. *Tetrahedron Lett.* **1987**, *28*, 3229.
7. Suzuki, A.; Matsunaga, K.; Shin, H.; Tabudrav, J.; Shizuri, Y.; Ohizumi, Y. *J. Pharmacol. Exp. Ther.* **2000**, *292*, 725.
8. Shin, J.; Lee, H. S.; Seo, Y.; Rho, J. R.; Cho, K. W.; Paul, V. J. *Tetrahedron* **2000**, *56*, 9071.
9. Pham, N. B.; Butler, M. S.; Quinn, R. J. *J. Nat. Prod.* **2000**, *63*, 393.
10. Tabudravu, J. N.; Eijsink, V. G. H.; Gooday, G. W.; Jaspars, M.; Komander, D.; Legg, M.; Synstad, B.; Van Aalten, D. M. F. *Bioorg. Med. Chem.* **2002**, *10*, 1123.
11. Jung, J. H.; Sim, C. J.; Lee, C.-O. *J. Nat. Prod.* **1995**, *58*, 1722.
12. Park, Y.; Liu, Y.; Hong, J.; Lee, C. O.; Cho, H.; Kim, D. K.; Im, K. S.; Jung, J. H. *J. Nat. Prod.* **2003**, *66*, 1495.
13. Kim, D.; Lee, I. S.; Jung, J. H.; Yang, S. I. *Arch. Pharm. Res.* **1999**, *22*, 25.
14. Kim, D.; Lee, I. S.; Jung, J. H.; Lee, C. O.; Choi, S. U. *Anticancer Res.* **1999**, *19*, 4085.
15. Nicholas, G. M.; Eckman, L. L.; Ray, S.; Hughes, R. O.; Pfefferkorn, J. A.; Barluenga, S.; Nicolaou, K. C.; Bewley, C. A. *Bioorg. Med. Chem. Lett.* **2002**, *12*, 2487.
16. Jiang, Y.; Ahn, E. Y.; Ryu, S. H.; Kim, D. K.; Park, J. S.; Yoon, H. J.; You, S.; Lee, B. J.; Lee, D. S.; Jung, J. H. *BMC Cancer* **2004**, *4*, 70.
17. Fajas, L.; Egler, V.; Reiter, R.; Hansen, J.; Kristiansen, K.; Debril, M.-B.; Miard, S.; Auwerx, J. *Dev. Cell* **2002**, *3*, 903.
18. Fajas, L.; Egler, V.; Reiter, R.; Miard, S.; Lefebvre, A.-M.; Auwerx, J. *Oncogene* **2003**, *22*, 4186.
19. Fu, M.; Rao, M.; Bouras, T.; Wang, C.; Wu, K.; Zhang, X.; Li, Z.; Yao, T.-P.; Pestell, R. G. *J. Biol. Chem.* **2005**, *280*, 16934.
20. Mora, F. D.; Jones, D. K.; Desai, P. V.; Patny, A.; Avery, M. A.; Feller, D. R.; Smillie, T.; Zhou, Y. D.; Nagle, D. G. *J. Nat. Prod.* **2006**, *69*, 547.
21. Shim, J. S.; Lee, H.-S.; Shin, J.; Kwon, H. J. *Cancer Lett.* **2004**, *203*, 163.
22. Allis, C. D.; Jenuwein, T.; Reinberg, D.; Caparros, M.-L. *Epigenetics*; Cold Spring Harbor Laboratory Press: Cold Spring Harbor (NY), 2007.
23. Sippl, W.; Jung, M. In *Epigenetic Targets in Drug Discovery: Methods and Principles of Medicinal Chemistry*; Mannhold, R., Kubinyi, H., Folkers, G., Eds.; Wiley: Weinhem, 2009; Vol. 42.
24. Archer, S. Y.; Hodin, R. A. *Curr. Opin. Gene Dev.* **1999**, *9*, 171.
25. Marks, P. A.; Rifkind, R. A.; Richon, V. M.; Breslow, R.; Miller, T.; Kelly, W. K. *Nat. Rev. Cancer* **2001**, *1*, 194.
26. Rosato, R. R.; Grant, S. *Cancer Biol. Ther.* **2003**, *2*, 30.
27. Blanchard, F.; Chipoy, C. *Drug Discovery Today* **2005**, *10*, 197.
28. Bolden, J. E.; Peart, M. J.; Johnstone, R. W. *Nat. Rev. Drug Disc.* **2006**, *5*, 769.
29. Lin, H. Y.; Chen, C. S.; Lin, S. P.; Weng, J. R.; Chen, C. S. *Med. Res. Rev.* **2006**, *26*, 397.
30. Mei, S.; Ho, A. D.; Mahlknecht, U. *Int. J. Oncol.* **2004**, *25*, 1509.

31. Minucci, S.; Pelicci, P. G. *Nat. Rev. Cancer* **2006**, *6*, 38.
32. Fouladi, M. *Cancer Invest.* **2006**, *24*, 521.
33. Botrugno, O. A.; Santoro, F.; Minucci, S. *Cancer Lett.* **2009**, *280*, 134.
34. Mai, A.; Altucci, L. *Int. J. Biochem. Cell Biol.* **2009**, *41*, 199.
35. Kazantsev, A. G.; Thompson, L. M. *Nat. Rev. Drug Disc.* **2008**, *7*, 854.
36. Marks, P. A.; Dokmanovic, M. *Expert Opin. Invest. Drugs* **2005**, *14*, 1497.
37. Drummond, D. C.; Noble, C. O.; Kirpotin, D. B.; Guo, Z.; Scott, G. K.; Benz, C. C. *Ann. Rev. Pharmacol. Toxicol.* **2005**, *45*, 495.
38. Rodriquez, M.; Aquino, M.; Bruno, I.; De Martino, G.; Taddei, M.; Gomez-Paloma, L. *Curr. Med. Chem.* **2006**, *13*, 1119.
39. Paris, M.; Porcelloni, M.; Binaschi, M.; Fattori, D. *J. Med. Chem.* **2008**, *51*, 1505.
40. Smith, K. T.; Workman, J. L. *Int. J. Biochem. Cell Biol.* **2009**, *41*, 21.
41. Witt, O.; Lindemann, R. *Cancer Lett.* **2009**, *280*, 123.
42. Klose, R. J.; Bird, A. P. *Trends Biochem. Sci.* **2006**, *31*, 89.
43. Ooi, S. K. T.; Bestor, T. H. *Cell* **2008**, *133*, 1145.
44. Baylin, S.; Bestor, T. H. *Cancer Cell* **2002**, *1*, 299.
45. Esteller, M. *Oncogene* **2002**, *21*, 5427.
46. Das, P. M.; Singal, R. *J. Clin. Oncol.* **2004**, *22*, 4632.
47. Baylin, S. B. *Nat. Clin. Pract. Oncol.* **2005**, *2*, S4.
48. Brueckner, B.; Lyko, F. *Trends Pharm. Sci.* **2004**, *25*, 551.
49. Kaminskas, E.; Farrell, A.; Abraham, S.; Baird, A.; Hsieh, L.-S.; Lee, S.-L.; Leighton, J. K.; Patel, H.; Rahman, A.; Sridhara, R.; Wang, Y.-C.; Pazdur, R. *Clin. Cancer Res.* **2005**, *11*, 3604.
50. Morphy, R.; Kay, C.; Rankovic, Z. *Drug Discovery Today* **2004**, *9*, 641.
51. Morphy, R.; Rankovic, Z. *J. Med. Chem.* **2005**, *48*, 6523.
52. Remiszewski, S. W. *Curr. Med. Chem.* **2003**, *10*, 2393.
53. Hoshino, O.; Murakata, M.; Yamada, K. *Bioorg. Med. Chem. Lett.* **1992**, *2*, 1561.
54. Nicolaou, K. C.; Hughes, R.; Pfefferkorn, J. A.; Barluenga, S. *Chem. Eur. J.* **2001**, *7*, 4296.
55. Nicolaou, K. C.; Hughes, R.; Pfefferkorn, J. A.; Barluenga, S.; Roecker, A. J. *Chem. Eur. J.* **2001**, *7*, 4280.
56. Godert, A. M.; Angelino, N.; Woloszynska-Read, A.; Morey, S. R.; James, S. R.; Karpf, A. R.; Sufrin, J. R. *Bioorg. Med. Chem. Lett.* **2006**, *16*, 3330.
57. Boehlow, T. R.; Spilling, C. D. *Nat. Prod. Lett.* **1995**, *7*, 1.
58. Boehlow, T. R.; Harburn, J. J.; Spilling, C. D. *J. Org. Chem.* **2001**, *66*, 3111.
59. Carreño, M. C. R.; J.L.G.; Sanz, G.; Toledo, M. A.; Urbano, A. *Synlett* **1997**, 1241.
60. Pfammatter, M. J.; Siljegovic, V.; Darbre, T.; Keese, R. *Helv. Chim. Acta* **2001**, *84*, 678.
61. Nishiyama, S.; Yamamura, S. *Tetrahedron Lett.* **1982**, *23*, 1281.
62. Forrester, A. R. T.; R.H.; Woo, S. O. *J. Chem. Soc., Perkin Trans. 1* **1975**, 2340.
63. Khan, N.; Jeffers, M.; Kumar, S.; Hackett, C.; Boldog, F.; Khramtsov, N.; Qian, X.; Mills, E.; Berghs, S. C.; Carey, N.; Finn, P. W.; Collins, L. S.; Tumber, A.; Ritchie, J. W.; Jensen, P. B.; Lichenstein, H. S.; Sehested, M. *Biochem. J.* **2008**, *409*, 581.
64. Bradner, J. E.; Mak, R.; Tanguturi, S. K.; Mazitschek, R.; Haggarty, S. J.; Ross, K.; Chang, C. Y.; Bosco, J.; West, N.; Morse, E.; Lin, K.; Shen, J. P.; Kwiatkowski, N. P.; Gheldof, N.; Dekker, J.; DeAngelo, D. J.; Carr, S. A.; Schreiber, S. L.; Golub, T. R.; Ebert, B. L. *Proc. Natl. Acad. Sci. U.S.A.* **2010**, *107*, 12617.
65. Balasubramanyam, K.; Swaminathan, V.; Ranganathan, A.; Kundu, T. K. *J. Biol. Chem.* **2003**, *278*, 19134.
66. (a) Souto, J. A.; Conte, M.; Alvarez, R.; Nebbioso, A.; Carafa, V.; Altucci, L.; de Lera, A. R. *ChemMedChem* **2008**, *3*, 1435; (b) Souto, J. A.; Bebedetti, R.; Otto, K.; Miceli, M.; Alvarez, R.; Altucci, L.; de Lera, A. R. *ChemMedChem* **2010**, *5*, 1530; (c) Souto, J. A.; Vaz, E.; Lepore, I.; Pöppler, A.-C.; Franci, J. L.; Alvarez, R.; Altucci, L.; de Lera, A. R. *J. Med. Chem.* **2010**, *53*, 4654.
67. Siedlecki, P.; Boy, R. G.; Musch, T.; Brueckner, B.; Suhai, S.; Lyko, F.; Zielenkiewicz, P. *J. Med. Chem.* **2006**, *49*, 678.
68. Datta, J.; Ghoshal, K.; Denny, W. A.; Gamage, S. A.; Brooke, D. G.; Phiasivongsa, P.; Redkar, S.; Jacob, S. T. *Cancer Res.* **2009**, *69*, 4277.
69. Biel, M.; Wascholowski, V.; Giannis, A. *Angew. Chem., Int. Ed.* **2005**, *44*, 3186.
70. Somoza, J. R.; Skene, R. J.; Katz, B. A.; Mol, C.; Ho, J. D.; Jennings, A. J.; Luong, C.; Arvai, A.; Buggy, J. J.; Chi, E.; Tang, J.; Sang, B. C.; Verner, E.; Wynands, R.; Leahy, E. M.; Dougan, D. R.; Snell, G.; Navre, M.; Knuth, M. W.; Swanson, R. V.; McRee, D. E.; Tari, L. W. *Structure* **2004**, *12*, 1325.
71. Bieliauskas, A. V.; Pflum, M. K. H. *Chem. Soc. Rev.* **2008**, *37*, 1402.
72. McCulloch, M. W. B.; Coombs, G. S.; Banerjee, N.; Bugni, T. S.; Cannon, K. M.; Harper, M. K.; Veltri, C. A.; Virshup, D. M.; Ireland, C. M. *Bioorg. Med. Chem.* **2009**, *17*, 2189.
73. Kim, D. H. S. J.; Kwon, H. J. *Exp. Mol. Med.* **2007**, *39*, 47.
74. Ahn, M. Y.; Jung, J. H.; Na, Y. J.; Kim, H. S. *Ginecol. Oncol.* **2008**, *108*, 27.
75. Richon, V. M.; Sandhoff, T. W.; Rifkind, R. A.; Marks, P. A. *Proc. Natl. Acad. Sci. U.S.A.* **2000**, *97*, 10014.
76. Mai, A.; Massa, S.; Rotili, D.; Cerbara, I.; Valente, S.; Pezzi, R.; Simeoni, S.; Ragna, R. *Med. Res. Rev.* **2005**, *25*, 261.
77. Furumai, R.; Matsuyama, A.; Kobashi, N.; Lee, K. H.; Nishiyama, M.; Nakajima, H.; Tanaka, A.; Komatsu, Y.; Nishino, N.; Yoshida, M.; Horinouchi, S. *Cancer Res.* **2002**, *62*, 4916.
78. Xiao, J. J.; Byrd, J.; Marcucci, G.; Grever, M.; Can, K. K. *Rapid Commun. Mass Spectrom.* **2003**, *17*, 757.
79. Wang, D.; Helquist, P.; Wiest, O. *J. Org. Chem.* **2008**, *72*, 5446.
80. Nishino, N.; Jose, B.; Okamura, S.; Ebisusaki, S.; Kato, T.; Sumida, Y.; Yoshida, M. *Org. Lett.* **2003**, *5*, 5079.
81. Nishino, N.; Shivashimpi, G. M.; Soni, P. B.; Bhuiyan, M. P. I.; Kato, T.; Maeda, S.; Nishino, T. G.; Yoshida, M. *Bioorg. Med. Chem.* **2008**, *16*, 437.
82. Bach, R. D.; Dmitrenko, O.; Thorpe, C. *J. Org. Chem.* **2008**, *73*, 12.
83. Rautio, J.; Kumpulainen, H.; Heimbach, T.; Oliyai, R.; Oh, D.; Järvinen, T.; Savolainen, J. *Nat. Rev. Drug Disc.* **2008**, *7*, 255.
84. Mai, A.; Cheng, D.; Bedford, M. T.; Valente, S.; Nebbioso, A.; Perrone, A.; Brosch, G.; Sbardella, G.; De Bellis, F.; Miceli, M.; Altucci, L. *J. Med. Chem.* **2008**, *51*, 2279.
85. Li, J. W. H.; Vederas, J. C. *Science* **2009**, *325*, 161.
86. Newman, D. J. *J. Med. Chem.* **2008**, *51*, 2589.
87. Molinski, T. F.; Dalisay, D. S.; Lievens, S. L.; Saludes, J. P. *Nat. Rev. Drug Disc.* **2009**, *8*, 69.
88. Kotoku, N.; Tsujita, H.; Hiramatsu, A.; Mori, C.; Koizumi, N.; Kobayashi, M. *Tetrahedron* **2005**, *61*, 7211.
89. Knapp, S.; Amorelli, B.; Darout, E.; Ventocilla, C. C.; Goldman, L. M.; Huhn, R. A.; Minnihan, E. C. *J. Carbohydr. Chem.* **2005**, *24*, 103.
90. Frisch, M. J.; G. W. T., Schlegel, H. B.; Scuseria, G. E.; Robb, M. A.; Cheeseman, J. R.; Montgomery, Jr., J. A.; Vreven, T.; Kudin, K. N.; Burant, J. C.; Millam, J. M.; Iyengar, S. S.; Tomasi, J.; Barone, V.; Mennucci, B.; Cossi, M.; Scalmani, G.; Rega, N.; Petersson, G. A.; Nakatsuji, H.; Hada, M.; Ehara, M.; Toyota, K.; Fukuda, R.; Hasegawa, J.; Ishida, M.; Nakajima, T.; Honda, Y.; Kitao, O.; Nakai, H.; Klene, M.; Li, X.; Knox, J. E.; Hratchian, H. P.; Cross, J. B.; Bakken, V.; Adamo, C.; Jaramillo, J.; Gomperts, R.; Stratmann, R. E.; Yazyev, O.; Austin, A. J.; Cammi, R.; Pomelli, C.; Ochterski, J. W.; Ayala, P. Y.; Morokuma, K.; Voth, G. A.; Salvador, P.; Dannenberg, J. J.; Zakrzewski, V. G.; Dapprich, S.; Daniels, A. D.; Strain, M. C.; Farkas, Malick, O.; D. K.; Rabuck, A. D.; Raghavachari, K.; Foresman, J. B.; Ortiz, J. V.; Cui, Q.; Baboul, A. G.; Clifford, S.; Cioslowski, J.; Stefanov, B. B.; Liu, G.; Liashenko, A.; Piskorz, P.; Komaromi, I.; Martin, R. L.; Fox, D. J.; Keith, T.; Al-Laham, M. A.; Peng, C. Y.; Nanayakkara, A.; Challacombe, M.; Gill, P. M. W.; Johnson, B.; Chen, W.; Wong, M. W.; Gonzalez, C.; Pople, J. A. Gaussian, Pittsburg: 2004.
91. Bayly, C. I.; Cieplak, P.; Cornell, W. D.; Kollman, P. A. *J. Phys. Chem.* **1993**, *97*, 10269.
92. Cornell, W. D.; Cieplak, P.; Bayly, C. I.; Gould, I. R.; Merz, K. M.; Ferguson, D. M.; Spellmeyer, D. C.; Fox, T.; Caldwell, J. W.; Kollman, P. A. *J. Am. Chem. Soc.* **1995**, *117*, 5179.
93. Rodríguez-Barrios, F.; Pérez, C.; Lobatón, E.; Velázquez, S.; Chamorro, C.; San-Félix, A.; Pérez-Pérez, M. J.; Camarasa, M. J.; Pelemans, H.; Balzarini, J.; Gago, F. *J. Med. Chem.* **2001**, *44*, 1853.
94. Morris, G. M.; Goodsell, D. S.; Halliday, R. S.; Huey, R.; Hart, W. E.; Belew, R. K.; Olson, A. J. *J. Comput. Chem.* **1998**, *19*, 1639.
95. Morris, G. M.; Goodsell, D. S.; Huey, R.; Hart, W. E.; Halliday, S.; Belew, R.; Olson, A. J.; AutoDock, 3.0 ed. La Jolla, CA, 1999.
96. Goodford, P. J. *J. Med. Chem.* **1985**, *28*, 849.
97. Åqvist, J. *J. Phys. Chem.* **1990**, *94*, 8021.
98. Jorgensen, W. L.; Chandrasekhar, J.; Madura, J. D. *J. Chem. Phys.* **1983**, *79*, 926.
99. http://amber.scripps.edu/doc8.
100. Ryckaert, J. P.; Ciccoti, G.; Berendsen, H. J. C. *J. Comput. Phys.* **1977**, *23*, 327.
101. Nebbioso, A.; Clarke, N.; Voltz, E.; Germain, E.; Ambrosino, C.; Bontempo, P.; Alvarez, R.; Schiavone, E. M.; Ferrara, F.; Bresciani, F.; Weisz, A.; de Lera, A. R.; Gronemeyer, H.; Altucci, L. *Nat. Med.* **2005**, *11*, 77.
102. Scognamiglio, A.; Nebbioso, A.; Manzo, F.; Valente, S.; Mai, A.; Altucci, L. *Biochem. Biophys. Acta* **2008**, *1783*, 203.
103. Altucci, L.; Rossin, A.; Raffelsberger, W.; Reitmair, A.; Chomienne, C.; Gronemeyer, H. *Nat. Med.* **2001**, *7*, 680.

Journal of Medicinal Chemistry

Article

pubs.acs.org/jmc

Indole-Derived Psammaplin A Analogues as Epigenetic Modulators with Multiple Inhibitory Activities

Raquel Pereira,[†,#] Rosaria Benedetti,[‡,#] Santiago Pérez-Rodríguez,[†] Angela Nebbioso,[‡] José García-Rodríguez,[†] Vincenzo Carafa,[‡] Mayra Stuhldreier,[†] Mariarosaria Conte,[‡] Fátima Rodríguez-Barrios,[†] Hendrik G. Stunnenberg,[∥] Hinrich Gronemeyer,[⊥] Lucia Altucci,*[,‡,§] and Ángel R. de Lera*[,†]

[†]Departamento de Química Orgánica, Universidade de Vigo, 36310 Vigo, Spain

[‡]Dipartimento di Patologia Generale, Seconda Università degli Studi di Napoli, Vico L. de Crecchio 7, 80138 Napoli, Italy

[§]Institute of Genetics and Biophysics (IGB), CNR, Via P. Castellino 111, 80131 Napoli, Italy

[∥]NCMLS, Department of Molecular Biology, Radboud University, 6525 GA Nijmegen, The Netherlands

[⊥]Department of Cancer Biology, Institut de Génétique et de Biologie Moléculaire et Cellulaire (IGBMC), CNRS, INSERM, ULP, BP 163, 67404 Illkirch Cedex, C. U. de Strasbourg, France

Supporting Information

ABSTRACT: A SAR study has been carried out around a modified scaffold of the natural product psammaplin A obtained by replacing the *o*-bromophenol unit by an indole ring. A series of indole psammaplin A constructs were generated in a short synthetic sequence that starts with the functionalization of the C3 indole position with in situ generated nitrosoacrylate, and this is followed by protection of the β-indole-α-oximinoesters, saponification, condensation with symmetrical diamines, and deprotection. Biochemical and cellular characterization using U937 and MCF-7 cells confirmed that many of these analogues displayed more potent actitivies than the parent natural product. Moreover, in addition to the reported HDAC and DNMT dual epigenetic inhibitory profile of the parent compound, some analogues, notably **4a** (UVI5008), also inhibited the NAD^+-dependent SIRT deacetylase enzymes. The SAR study provides structural insights into the mechanism of action of these multiple epigenetic ligands and paves the way for additional structural exploration to optimize their pharmacological profiles. Because of their multi(epi)target features and their action in ex vivo samples, the indole-based psammaplin A derivatives are attractive molecules for the modulation of epigenetic disorders.

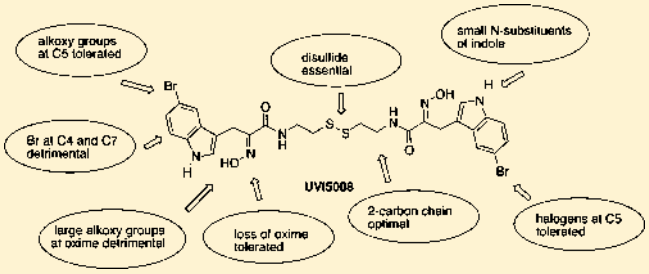

INTRODUCTION

In addition to its structural role in shaping the degree of DNA compaction, chromatin is considered the signal transduction interpreter that regulates all genome functions.[1] The basic unit of chromatin is the nucleosome, the 146 base-pair stretch of DNA wrapped 1.7 times around an octameric protein core containing two molecules each of histones H2A, H2B, H3, and H4. The flexible and highly conserved basic tail regions of the histones can be post-translationally modified primarily by acetylation, methylation, ADP-ribosylation, phosphorylation, sumoylation, and ubiquitylation.[2,3] The covalent modifications of DNA and histone proteins, most of which are reversible,[4,5] control the degree of compaction or relaxation of chromatin and act as recognition sites for regulatory factors/machineries. Ultimately, these events result in the regulation of fundamental cellular processes (such as replication, chromatin remodeling, repair, and transcription) through recognition, recruitment, and assembly of supramolecular structures (histone−histone and histone−DNA).[6] Because the alterations on gene expression are induced by mechanisms other than changes in DNA sequence, they are termed "epigenetic". The enzymes responsible for the most important covalent modifications of DNA and histones with small chemical marks are DNA methyltransferases (DNMTs), histone acetyltransferases (HATs), histone deacetylases (HDACs), histone methyltransferases (HMTs), and histone demethylases (HDMs).[7]

Emerging evidence suggests that the disruption of the balance of epigenetic networks and its interaction with the genome and the environment contribute to several major pathologies.[8−14] During onset and/or progression of disease, alterations of both the effectors of chromatin changes (e.g., histone and DNA modifiers)[15] and upstream signaling pathways[16−18] can occur.

DNA methylation at the cytosine C5 position within CpG dinucleotide-rich regions (CpG islands)[19] is promoted by the DNMT protein family,[20−22] which includes in mammals the

Received: May 3, 2012
Published: October 3, 2012

 © 2012 American Chemical Society

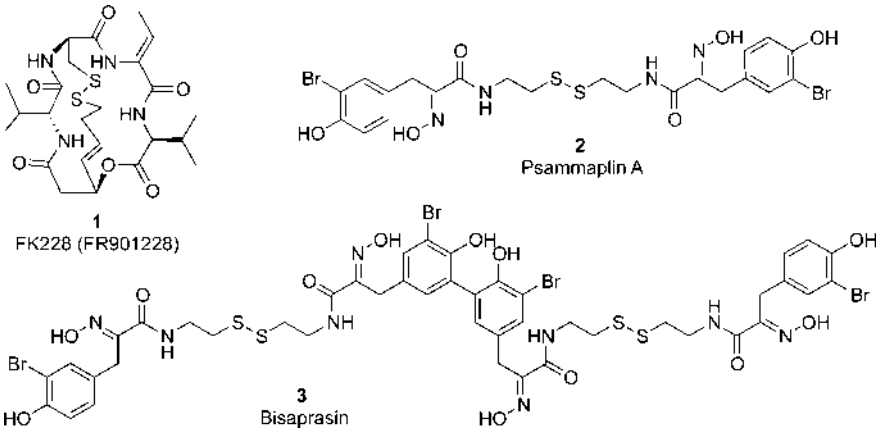

Figure 1. Disulfide-containing natural HDACis.

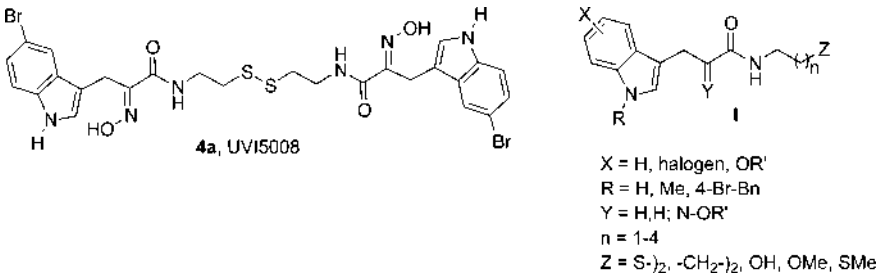

Figure 2. General structure of the indole derivatives prepared in the SAR study leading to the discovery of **4a**.

maintenance DNMT1 and the de novo methyltransferases DNMT2 and DNMT3 (a, b, and L).[23] The aberrant expression of DNMT1 induces site-specific hypermethylation and global hypomethylation of CpG islands, which are biological signatures of cancer.[9,24−29] Methylation of CpG islands in the promoter regions of tumor suppressor genes is associated with a silencing state.[30,31,28] Hypermethylation of DNA promoter and coding sequences is a major epigenetic mechanism that contributes to cancer progression by causing the inactivation of a number of tumor suppressor genes in a wide range of tumor types,[32] which is the most common molecular lesion of cancer cells.[12]

Post-translational reversible acetylation of histone lysine residues regulates gene expression and cell cycle progression. Many non-histone proteins also undergo acetylation,[33] and this modification alters, among other functions, DNA-binding activity, microtubule stabilization, protein−protein interactions, and small-molecule action. At the chromatin level, acetylation is controlled by the opposite activities of histone acetyltransferases (HATs) and histone deacetylases (HDACs).

Eighteen mammalian deacetylase enzymes comprise the superfamily of HDACs, which is conveniently divided into two families that differ in the overall mechanism of lysine deacetylation: the Zn^{2+}-dependent hydrolases (11 members consisting of class I with HDAC1, -2, -3, and -8; class IIa with HDAC4 and -10; class IIb with HDAC5, -6, -7, and -9; class IV with HDAC11) and the NAD^{+}-dependent deacetylases or sirtuins (7 members consisting of SIRT1−7).[34−36]

The Zn^{2+}-dependent HDAC hydrolases deacetylate the ε-acetylamidolysine by a nucleophilic attack of bound water to the Zn^{2+}-activated carbonyl group, creating a tetrahedral zinc alkoxide intermediate stabilized by enzyme residues which releases the acetyl group and the lysine product. Class I/II/IV HDAC inhibitors[37−39] contain three regions: a Zn^{2+}-chelating headgroup[40] (hydroxamates, benzamides, short-chain fatty acids, and thiolates, among others, are part of the metal-binding structure[38,39]), a linker/spacer that occupies the binding pocket of the native lysine, and a highly variable cap group that extends along the rim of the pocket. Sirtuins regulate a variety of cellular functions such as conservation of the genome, longevity, and metabolism of organisms ranging from bacteria to eukaryotes.[36,41−45] An increasing number of reports indicate the implication of multiple epigenetic enzymes in the onset or progression of cancer,[13] among them the sirtuins.[43]

The modulation of epigenetic enzymes by small molecules has been correlated with the induction of differentiation, cell cycle and growth arrest, and apoptosis in cancer cells.[46,47] Chromatin regulators ("epi drugs")[19,48,49] thus represent novel promising anticancer drugs.[8,13,50−52] Indeed, two DNMT inhibitors (DNMTis) (5-aza-cytidine, Vidaza; 5-aza-deoxycytidine, Dacogen)[21,53] have been approved for the treatment of myelodisplastic syndrome (MDS),[54] and two HDACis, namely, SAHA (suberoylanilide hydroxamic acid, vorinostat) and FK-228 **1** (depsipeptide), have also been marketed for the treatment of cutaneous T cell lymphoma (CTCL).

Depsipeptide **1** is a natural product isolated from *Chromobacterium violaceum* No. 968.[55] Its approval for therapy demonstrates that natural products continue to be a source of new medicines or the inspiration for the discovery of new drug leads.[56−60] It has been demonstrated that the disulfide bond of FK228 **1** (for other depsipeptides with disulfide bonds in bicyclic structures, such as the spiruchostatins and FR901375, see[58]) becomes reduced in cells by the activity of glutathione to afford a thiolate termed redFK, which then would interact with the Zn^{2+} ion in the active site of HDAC.[61]

A disulfide bond is also present in the dimeric natural product psammaplin A (**2**, Figure 1), a representative member of the symmetrical bromotyrosine−cysteine modified tetrapeptides. Isolated in 1987 from an unidentified sponge[62−64] and later,

Scheme 1[a]

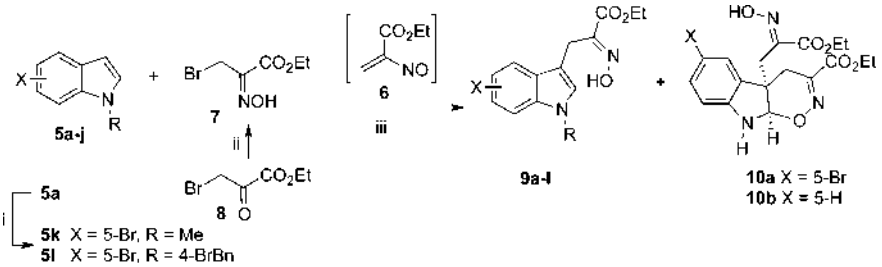

[a]Reagents and conditions: (i) MeI or 4-$BrC_6H_4CH_2Br$, KOH, DMF, 0 °C, 30 min (**5k**, 91%; **5l**, 53%); (ii) **8**, $CHCl_3$, $NH_2OH{\cdot}HCl$, MeOH/H_2O (1:1), 25 °C, 22 h (86%); (iii) K_2CO_3, CH_2Cl_2, 25 °C, 20 h (**9a–l**, Table 1).

Scheme 2[a]

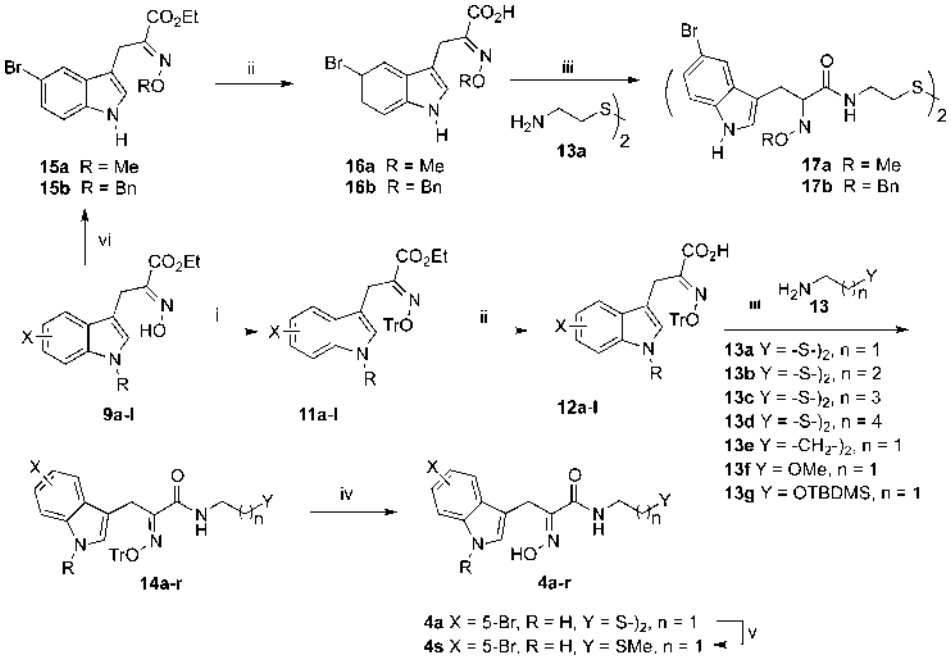

[a]Reagents and conditions: (i) K_2CO_3, CH_2Cl_2, TrCl, 25 °C, 20 h; (ii) LiOH·H_2O, THF/H_2O (1:1), 25 °C, 20 h (**12a–l**, Table 1, combined yield for the two steps); **16a**, 84%; **16b**, 99%; (iii) (i) EDC, NHS, dioxane, 25 °C, 2 h; (ii) cystamine **13a**, Et_3N, MeOH, dioxane, 25 °C, 15 h (**17a**, 80%; **17b**, 84%) or amines **13b–f**, Et_3N, MeOH, dioxane, 25 °C, 15 h; (iv) 1 M HCl in Et_2O, CH_2Cl_2, 25 °C, 2 h (**4a–r**, Table 1, combined yield for the two steps); (v) (i) $NaBH_4$, NaOH, EtOH, 25 °C, 0.5 h; (ii) MeI, 25 °C, 16 h (**4s**, 80%); (vi) MeI, Ag_2O, acetone, 25 °C, 14 h or BnBr, KO^{t}Bu, DME, 25 °C, 12 h (**15a**, 42%; **15b**, 72%).

together with **3**, from Verongid sponges (refs 65 and 66 and references cited therein), psammaplin A was shown to display antibacterial and antitumor activities.[67] In particular, **2** exhibited significant cytotoxicity against human lung (A549), ovarian (SKOV- 3), skin (SK-MEL-2), CNS (XF498), and colon (HCT15) cancer cell lines.[66] The dual inhibition of histone deacetylase (HDAC) and DNA methyltransferase (DNMT) enzymes reported for **2**[65] (note that DNMT inhibition by psammaplin A has been debated, being reported in refs 68–70 but not observed in a recent SAR study[71]) captured our interest,[72] given the promising results of ongoing clinical trials with combination therapies using HDACis and DNMTis.[20,73]

Inspired by the structure and likely mechanism of action of psammaplin A (**2**), we recently reported the synthesis and characterization of **4a** (Figure 2)[74] which, in addition to displaying a more potent inhibition of HDAC and DNMT than parent **1**, also targets at least one other family of epigenetic enzymes (SIRT). Here we report on the development of **4a** and SAR studies on this family of epigenetic modulators.

■ DESIGN AND SYNTHESIS

The structure of psammaplin A **2** contains a symmetrical tetrapeptide formed by condensation of two modified 2-bromotyrosine and cystamine units. It was considered that other amide moieties derived from heteroaryl-containing aminoacids incorporated into the scaffold could improve the reported HDAC and DNMT inhibitory profile of the parent compound. This assumption was supported by the discovery of highly potent HDACis with the indoleamide hydroxamic acid structure.[75,76]

Our purpose to undertake SAR studies called for a synthetic approach to these modified tetrapeptides that could yield analogues (general structure **I**, Figure 2) at the various positions by slight modifications of the sequence. Initial exploratory studies focused on the variations of the substituents at the indole ring including the group at N, the oxime functionality, and the size of the chain connecting the amide to the disulfide. Addressing some of these structural modifications, we expected

Table 1. Yields (%) for the Compounds of the Synthetic Sequence of Indole Psammaplins

9, 12	yield, 9	yield, 12	4	yield
a, X = 5-Br, R = H	60	73	**a**, X = 5-Br, R = H, Y = $(S\text{-})_2$, n = 1	70
b, X = H, R = H	67	87	**b**, X = H, R = H, Y = $(S\text{-})_2$, n = 1	50
c, X = 5-F, R = H	87	71	**c**, X = 5-F, R = H, Y = $(S\text{-})_2$, n = 1	38
d, X = 5-Cl, R = H	42	73	**d**, X = 5-Cl, R = H, Y = $(S\text{-})_2$, n = 1	30
e, X = 5-I, R = H	82	77	**e**, X = 5-I, R = H, Y = $(S\text{-})_2$, n = 1	13
f, X = 5-OMe, R = H	51	64	**f**, X = 5-OMe, R = H, Y = $(S\text{-})_2$, n = 1	4
g, X = 5-OBn, R = H	75	59	**g**, X = 5-OBn, R = H, Y = $(S\text{-})_2$, n = 1	20
h, X = 4-Br, R = H	65	61	**h**, X = 4-Br, R = H, Y = $(S\text{-})_2$, n = 1	54
i, X = 6-Br, R = H	43	49	**i**, X = 6-Br, R = H, Y = $(S\text{-})_2$, n = 1	41
j, X = 7-Br, R = H	43	37	**j**, X = 7-Br, R = H, Y = $(S\text{-})_2$, n = 1	30
k, X = 5-Br, R = Me	68	60	**k**, X = 5-Br, R = Me, Y = $(S\text{-})_2$, n = 1	71
l, X = 5-Br, R = 4-BrBn	68	45	**l**, X = 5-Br, R = 4-BrBn, Y = $(S\text{-})_2$, n = 1	32
			m, X = 5-Br, R = H, Y = $(S\text{-})_2$, n = 2	19
			n, X = 5-Br, R = H, Y = $(S\text{-})_2$, n = 3	42
			o, X = 5-Br, R = H, Y = $(S\text{-})_2$, n = 4	38
			p, X = 5-Br, R = H, Y = $(CH_2\text{-})_2$, n = 2	82
			q, X = 5-Br, R = H, Y = OMe, n = 1	37
			r, X = 5-Br, R = H, Y = OH, n = 1	37
			s, X = 5-Br, R = H, Y = SMe, n = 1	80

to additionally get further insights into the mechanism of action of **4a** in its epigenetic inhibitory activities, and for this purpose the terminal group was also chemically modified.

The synthesis of **4a** (Schemes 1 and 2) is representative of the preparation of the entire collection of indole psammaplins. It started with the attachment of the functionalized oxime ester side chain to indole derivative **5a** to provide **9a** using the method described by Gilchrist.[77] This entails reaction of **5a** with nitrosoacrylate **6**,[77] generated in situ from oxime **7**, itself prepared by the reaction of ethyl bromopyruvate **8** with hydroxylamine hydrochloride. Either an inverse electron-demand hetero-Diels–Alder cycloaddition or a Friedel–Crafts reaction followed by indole aromatization is fully compatible with the outcome of the condensation of **5a** and **6**. Other analogues **9b–e** were similarly obtained (Scheme 1, Table 1) starting from commercial and noncommercial bromoindoles. The latter compounds were synthesized by application of the Leimgruber–Batcho methodology[78] or by the Bartoli procedure.[79] N-Substituted indoles **5k** and **5l** were instead synthesized using the protocol described by Stadlwieser.[80]

Minor amounts of the cycloadducts **10** resulting from 2-fold condensation at the C3-position of indole and **7** were isolated and characterized in the case of X = 5-Br (**10a**, 4%) and X = H (**10b**, 7%). X-ray analysis of compounds **9b** and **10b** confirmed the *E* geometry of the oxime and for **10b** the *cis*-fusion of the indole and oxazine rings (Supporting Information). The amount of **10** could be minimized using an excess of indole derivative (2 equiv) and base (5.5 equiv) relative to oxime **7**.

Initial attempts to couple the oxime indole derivatives **9a** with amines using a variety of reaction conditions (DCC, HOBt,[81,82] PyBOP, $ClCO_2Et$[83]) were either unsuccessful or produced the product in low yields (<50% with DCC, *N*-hydroxyphthalimide).[84] Therefore, protection of the oxime of **9a** (Scheme 2, Table 1) as trityl derivative **11a** was required before saponification (to produce acid **12a**) and condensation with cystamine **13a** via activation as the *N*-succinimidyl ester, a sequence that produced disulfides **14**.[85] Cleavage of the trityl protecting group[85] afforded compound **4a** (Table 1).

Following identical sequence, indoles **9b–l** were transformed into disulfides **4b–l** using either cystamine **13a** or amines **13b–g** (Scheme 2, Table 1), some of which were synthesized using the general methodology described by Pfammatter.[86] Deprotection of the silyl ether of **14r** took place concomitantly with trityl deprotection. On the other hand, methyl sulfide **4s** was obtained by reduction of disulfide **4a** with $NaBH_4$ and methylation with MeI (Scheme 2).[87]

The same sequence provided the benzyl[88] and methyl[89] oximes (**15b** and **15a**, respectively, Scheme 2) following benzylation and methylation of **9a**, and along similar steps analogues **17a,b** were obtained from these intermediates.

Analogues **20a** and **20b**, which lack the oxime function, were synthesized by a similar sequence using a $ZrCl_4$-catalyzed[90] Friedel–Crafts type alkylation of 5-bromoindoles **5a** and **5k** with methyl acrylate followed by hydrolysis and condensation of acids **19a** and **19b** with cystamine **13a** via activation as the *N*-hydroxysuccinimidyl ester (Scheme 3).

Scheme 3[a]

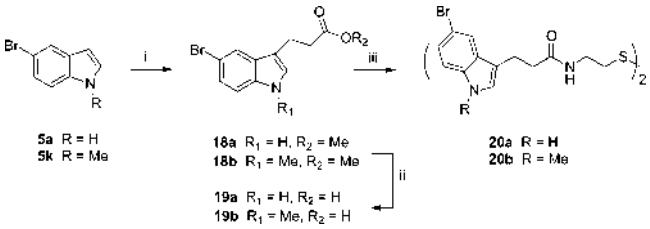

[a]Reagents and conditions: (i) methyl acrylate, $ZrCl_4$, CH_2Cl_2, 25 °C, 5 h; (ii) $LiOH{\cdot}H_2O$, THF/H_2O (1:1), 25 °C, 20 h (**19a**, 57%; **19b**, 75%; combined yield); (iii) (i) EDC, NHS, dioxane, 25 °C, 2 h; (ii) cystamine **13a**, Et_3N, MeOH, dioxane, 25 °C, 15 h (**20a**, 65%; **20b**, 42%).

■ BIOLOGICAL EFFECTS OF PSAMMAPLIN A DERIVATIVES IN CELLULAR CANCER MODELS

Following the confirmation of the epigenetic activities of psammaplin A **2** using in vitro assays on isolated enzymes and cellular experiments,[72] we undertook the search for more potent analogues, with a focus on the β-indole-α-oximinoamido scaffold. The series of indole derivatives synthesized (Schemes

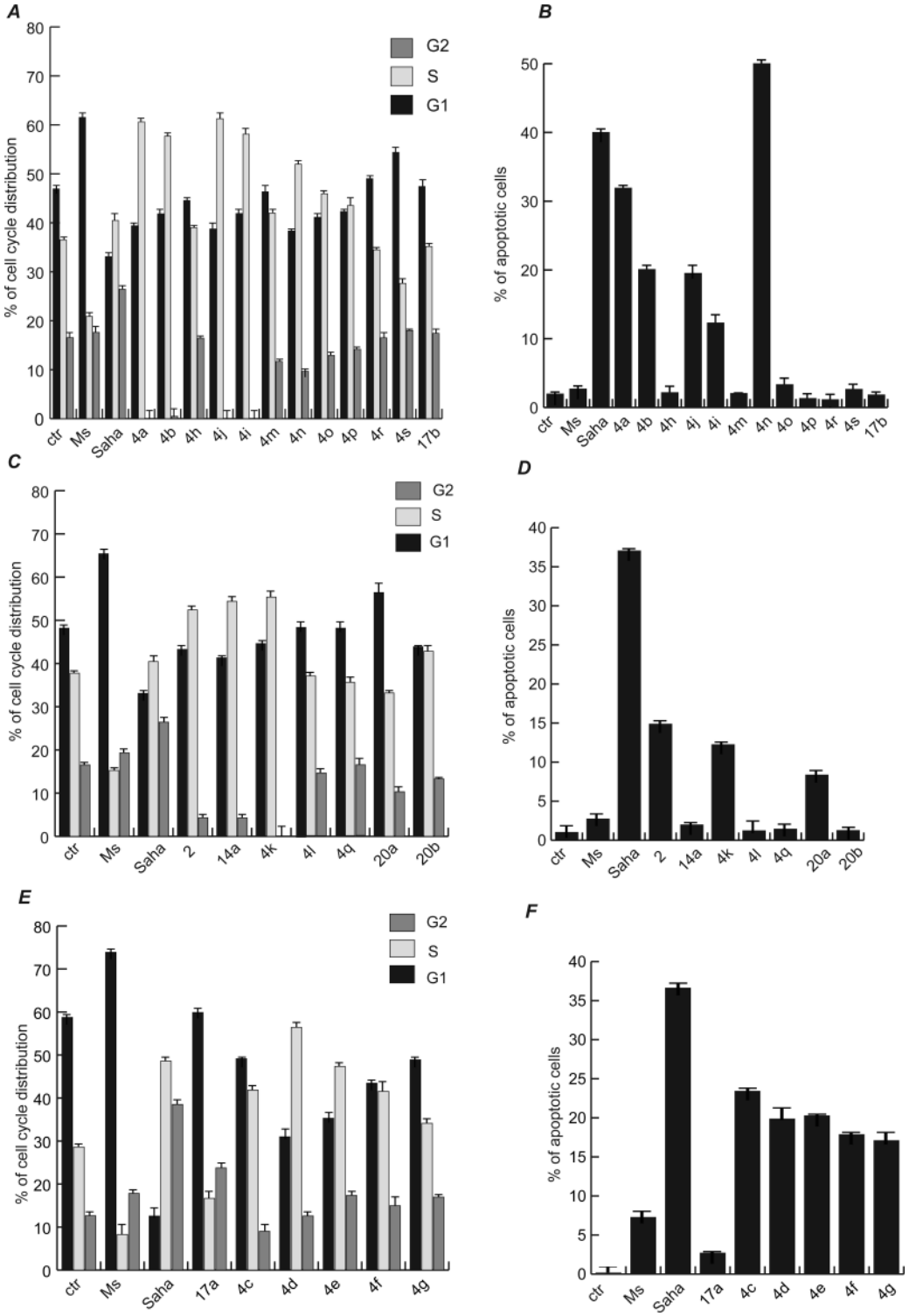

Figure 3. Analysis of the effects of cell cycle and apoptosis of U937 cells treated with indole-based psammaplin A analogues: (A, C, E) cytofluorimetric cell cycle analysis after treatment with the compounds at 5 μM for 24 h; (B, D, F) apoptosis analysis after treatment with the compounds at 5 μM for 30 h. MS-275 and SAHA (5 μM) were used as controls. Error bars represent standard deviation (SD) of biological triplicates.

2 and 3) were aimed at understanding the role of structural elements and functional groups in the modulation of different epigenetic enzymes and at the identification of the pharmacophore(s) of these inhibitors. We also addressed whether (i) the dimeric structure or just the monomer is necessary for their biological activity, (ii) if the disulfide bridge is dispensable, and (iii) if an uncleavable dimeric compound displays similar activities. By use of the U937 acute myeloid leukemia (AML) cell line, the activity readouts systematically investigated were cell cycle arrest and $p21^{WAF1/CIP1}$ induction, induction of differentiation, acetylation of histone H3, and for HDAC6 inhibition, the levels of α-tubulin acetylation.

As shown in Figure 3B, after 24 h of stimulation with the analogues at 5 μM, derivatives **4a** and **4n** showed a greater

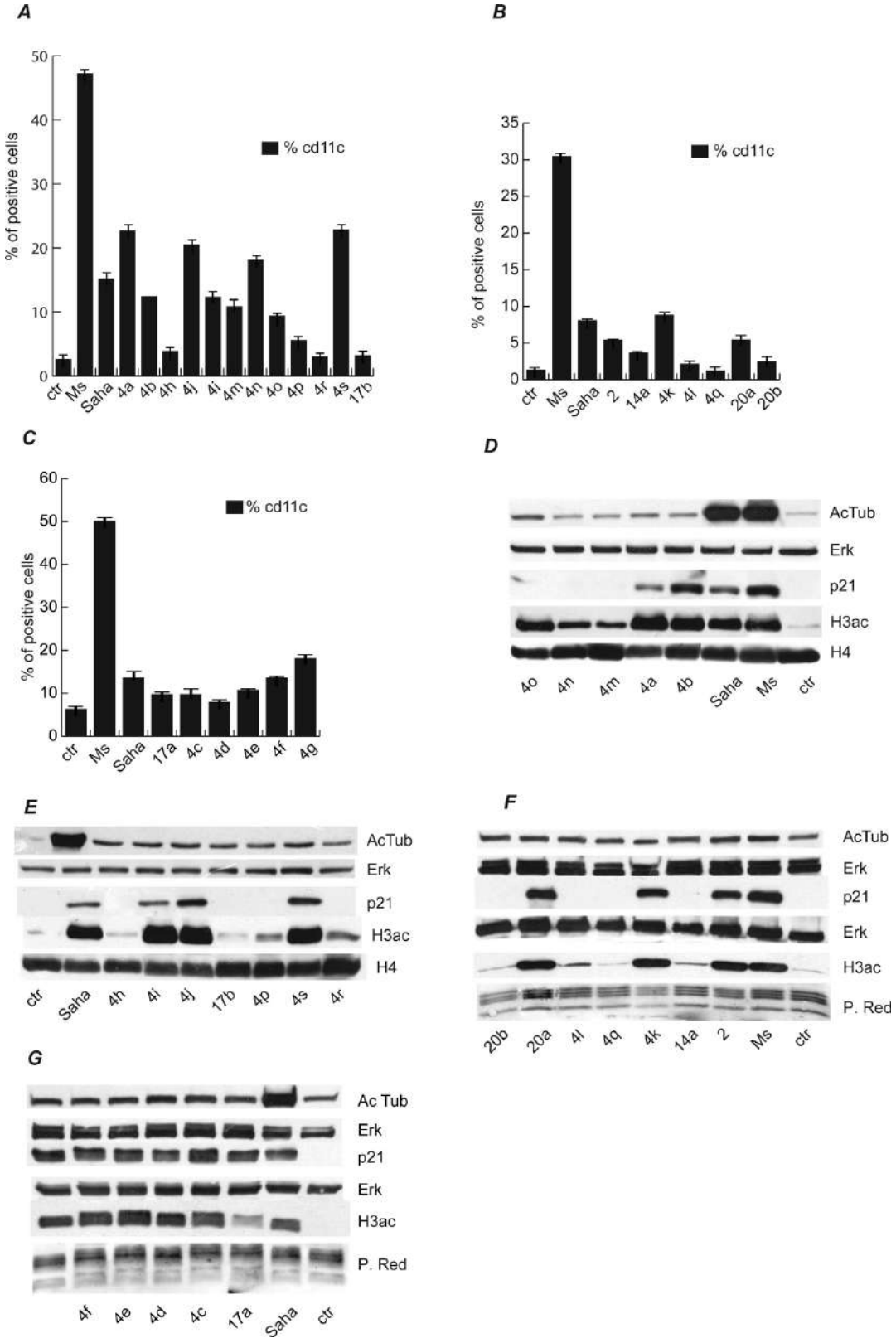

Figure 4. Analysis of cell differentiation (A−C) and Western blot analysis (D−G) of functional readouts of indole-based psammaplin A analogues. (A−C) Effects on granulocytic differentiation by cytofluorimetric analysis of CD11c expression after treatment of U937 acute myeloid leukemia cells with indole-based psammaplin A analogues at 5 μM for 30 h. SAHA and MS-275 (5 μM) were used as positive control. The data represent the average value of independent triplicates. Error bars represent standard deviation (SD) of biological triplicates. (D−G) Western blot analysis of p21, histone H3 acetylation, and α-tubulin acetylation in U937 cells after treatment with the indicated compounds at 5 μM for 24 h. Total ERKs were used to normalize for equal loading of total protein extraction. Total H4 or Ponceau red staining was used to normalize for equal loading of histone extracts. SAHA and MS-275 (5 μM) were used as controls.

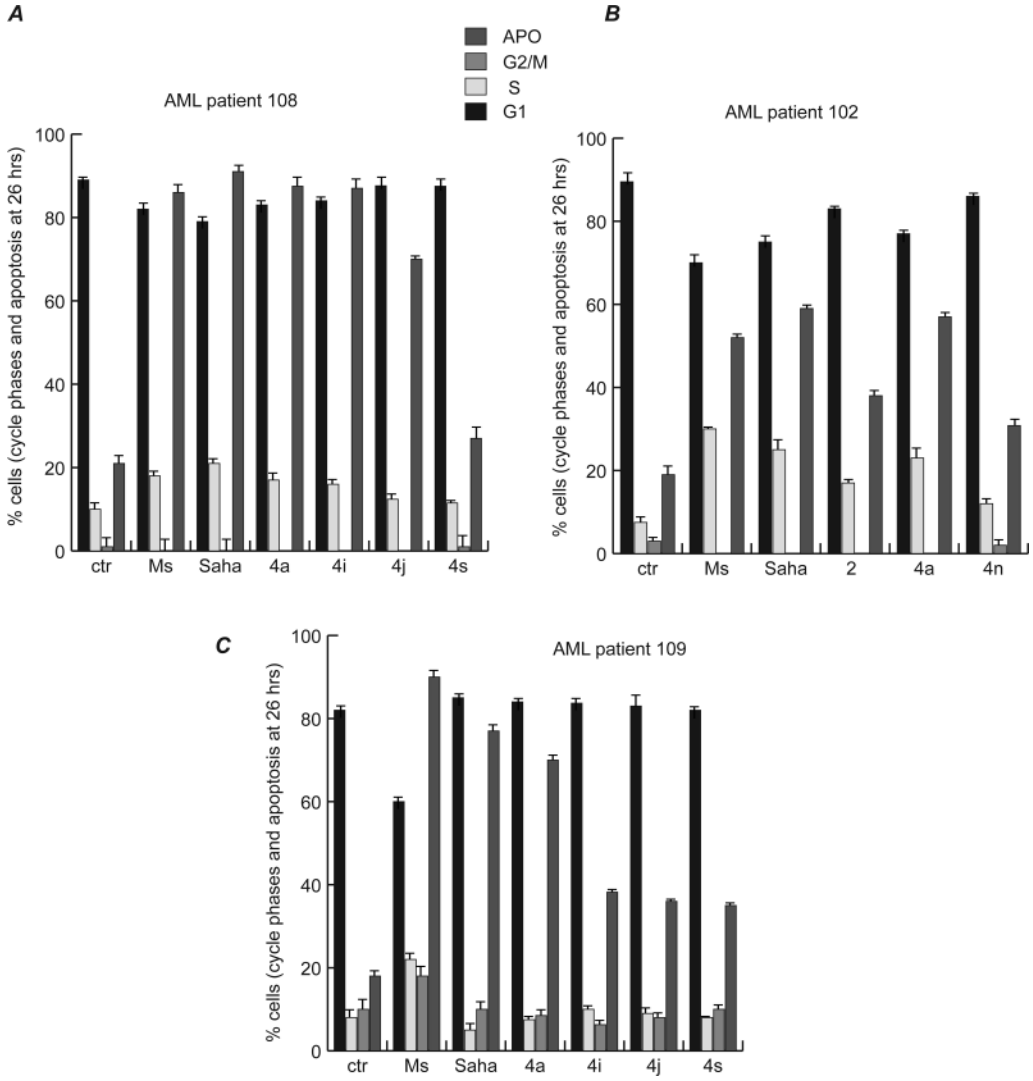

Figure 5. (A−C) Cell cycle analysis of ex vivo patient's blasts treated with selected indole-based psammaplin A analogues. Analysis of cell cycle and apoptosis was carried out with selected compounds at 5 μM in different AML patient blasts (indicated as numbers). SAHA and MS-275 (5 μM) were used as controls. Error bars represent standard deviation (SD) of biological triplicates.

induction of cell death than psammaplin A **2** (Figure 3D). To confirm these biological activities, cell cycle analyses were performed after 24 h of induction with psammaplin A **2** and its derivatives (Figure 3A,C). The proapoptotic activities of psammaplin A **2** and analogues **4a** and **4n** were also validated in the solid cancer cell lines derived from breast (ZR75.1, data not shown) and prostate (LnCap, data not shown) tumors. Cell death was observed for compounds **4i**, **4j**, **4k**, **20a**, **4c**−**g** (see Figure 3D and Figure 3F), but a lower number of cells underwent apoptosis compared to **4n**. Some compounds induced changes in the relative percentage of cells in the different phases of the cell cycle (Figure 3C and Figure 3E).

The parent compound formally derived from tryptophan (**4b**) displayed lower proapoptotic activity than the C5-bromoindole derivative (**4a**), but changing the substitution from C5 to C6 (**4i**) or C7 (**4j**) had only a minor effect on cell cycle arrest and apoptosis (Figure 3A and Figure 3B) and rather increased the induction of differentiation measured by expression of the CD11c marker (Figure 4A).

Figure 4A−C shows that most compounds (**4n**, **4i**, **4j**, **4s**, **4k**, **4f**, **4g**, and **4m**) derived from **4a** and **4b** induced the expression of CD11c (prodifferentiation surface marker), which is indicative of the differentiation of U937 cells to granulocytes.

Cell-based assays confirmed that the presence of one or two sulfur atoms and/or the disulfide bridge and/or the cell cleavage thiols derived from **2** and **4a** is required for cell cycle arrest, induction of apoptosis, and differentiation. Interestingly however, the methylthioether **4s** is inactive at inducing apoptosis (Figure 3B) and G2M phase accumulation but it induces cell arrest at G1 (Figure 3A) and the corresponding enhanced expression of $p21^{WAF1/CIP1}$, as shown in Figure 4A and Figure 4E. Further studies will be necessary to define the molecular pathways that are apparently differently affected by **4a** and **4s**.

Indole psammaplin A derivatives induced α-tubulin acetylation (a marker of HDAC6 inhibition), in some cases at levels similar to psammaplin A (**2**), as shown by Western blot analysis (Figure 4D−G). Moreover, most of the compounds increased histone H3 acetylation levels, with **4a** being clearly more efficient (Figure 4D). Note that despite its action on α-tubulin acetylation, **4n** did not show hyperacetylation of histone H3, suggesting a different mechanism of action.

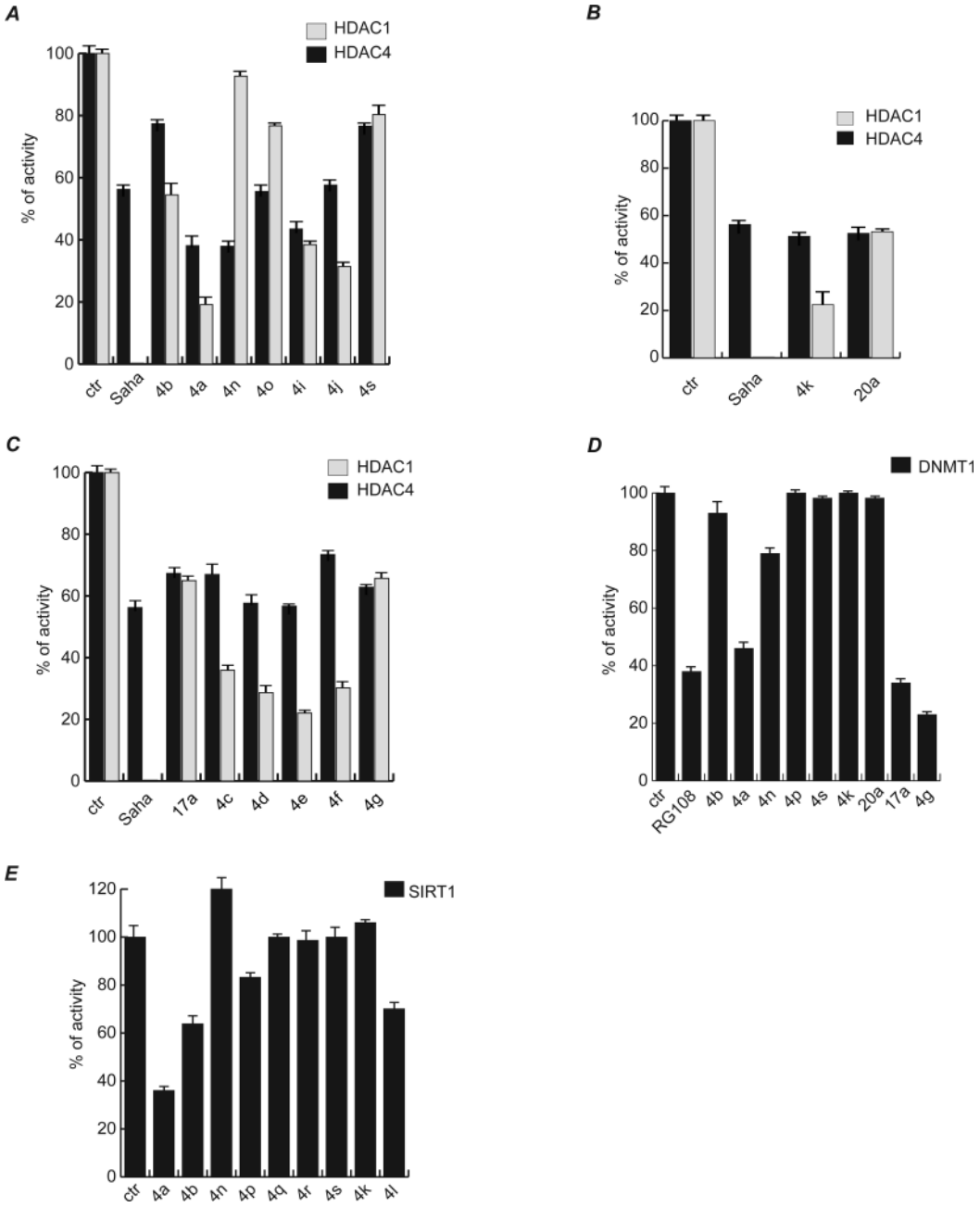

Figure 6. Modulation of epigenetic enzymes by indole-based psammaplin A analogues: (A−C) U937 cell-based HDAC1 and HDAC4 assay carried out with the indicated compounds at 5 μM; (D) in vitro DNMTs assay carried out in U937 extracts treated with the indicated compounds at 5 μM; (E) in vitro human recombinant SIRT1 assays with the indicated compounds at 5 μM. SAHA and RG-108 (5 μM) were used as controls. Error bars represent standard deviation (SD) of biological triplicates.

A correlation between hyperacetylation of histone H3 and expression of p21 protein exists. Indeed, as shown in Figure 4D−G, compounds for which the H3ac level is greater (**4b**, **4a**, **4i**, **4j**, **4s**, **4k**, **20a**, **4c−g**) also showed a stronger induction of p21 and the greatest percentage of cell death.

With regard to the effect of other substituents at the C5-indole ring position (OMe, **4f**; OBn, **4g**), including other halogens (F, **4c**; Cl, **4d**; I, **4e**), the biological evaluation indicates that the original scaffold is quite lenient at that position, since most of the C5-substituted indole derivatives showed the ability to induce p21, histone H3, and α-tubulin acetylation levels (Figure 4G) and, with the exception of **4c**, also p16 (see Figure 7).

Finally, the *N*-methyl derivative **4k** was found to induce apoptosis, change the cell cycle distribution, induce the acetylation of histone H3 and α-tubulin, and overexpress p21 (at levels comparable to **4a**), but the larger *N*-*p*-bromobenzyl analogue **4l** is quite inactive in these biological assays, showing a weak induction of p21 after 24 h of treatment of U937 cells (Figure 3C,D and Figure 4B,F).

■ INDOLE PSAMMAPLIN A DERIVATIVES INDUCE APOPTOSIS IN AML PATIENT'S BLASTS

The intriguing anticancer potential of these indole-based psammaplin A derivatives prompted us to test their activity in ex vivo AML patient blasts. As shown in Figure 5 B, **4a** induced

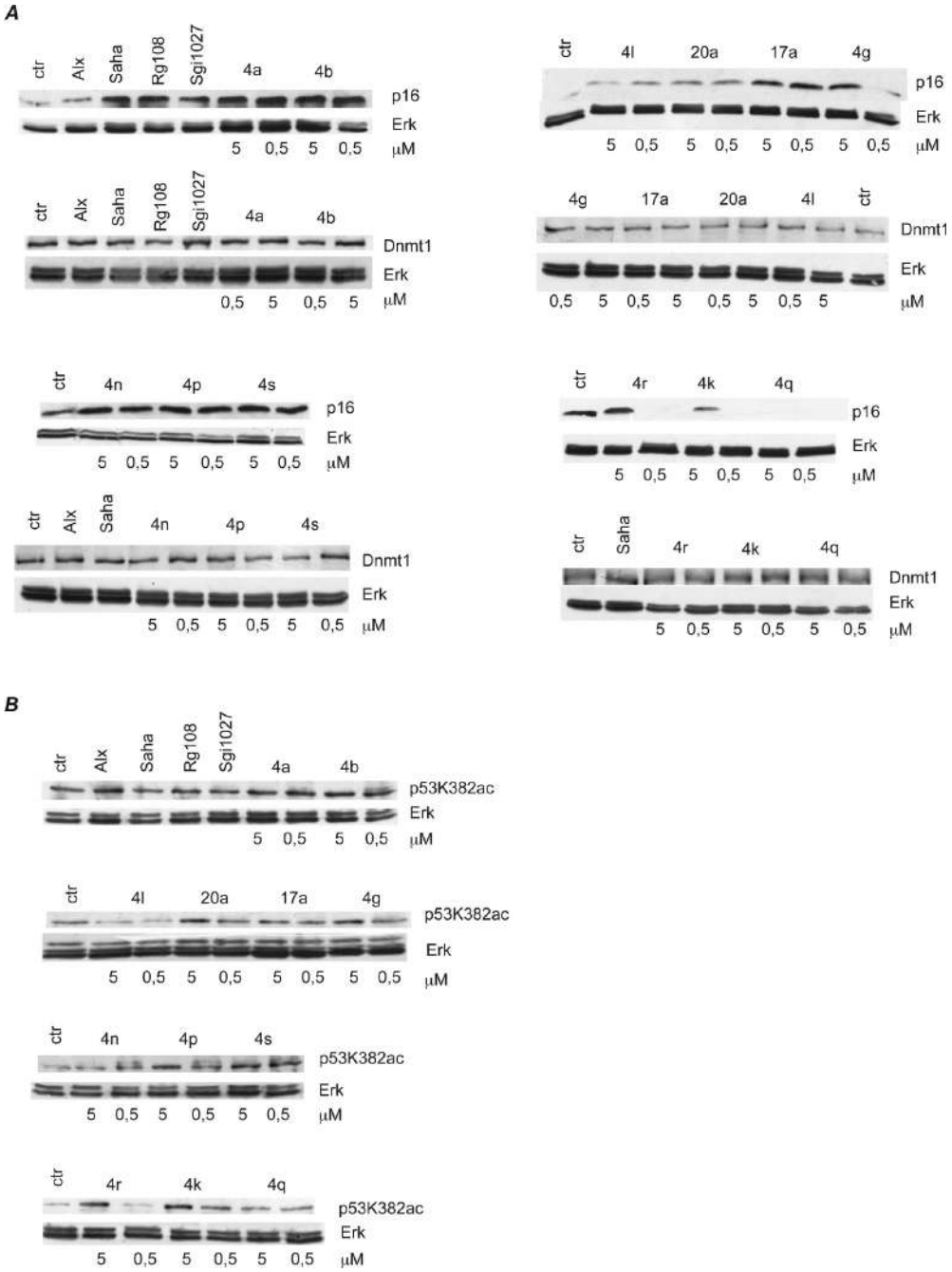

Figure 7. (A) Western blot analysis of p16 and DNMT1 levels after treatment of U937 cells with the indicated compounds at 5 and 0.5 μM for 24 h. Total ERKs were used to normalize for equal loading of total protein extraction. SAHA, RG108 (5 μM), SGI1027 (5 μM), and ALX (1 μM) were used as controls. (B) Western blot analysis of p53 acetylation on lysine 382 after treatment of MCF7 cells with the indicated compounds at 5 and 0.5 μM for 24 h. Total ERKs were used to normalize for equal loading of total protein extraction. SAHA, RG108 (5 μM), SGI1027 (5 μM), and ALX (1 μM) were used as controls.

cell cycle block and apoptosis as measured by FACS in AML no. 102 ex vivo blasts, similar to psammaplin A **2**. Known HDACis such as MS-275 (Entinostat) and SAHA (Vorinostat) displayed activities similar to that of **4a**. To verify the action of the selected derivatives on AML patient blasts, the activity of compounds **4a**, **4i**, **4j**, and **4s** was tested at 5 μM. As shown in Figure 5A,C, all these derivatives showed proapoptotic activity in two different samples of AML patient's blasts (no. 108 and no. 109). Methylthioether **4s** showed a weak induction of apoptosis, confirming data obtained with the U937 cell line.

INHIBITION OF EPIGENETIC ENZYMES BY INDOLE PSAMMAPLIN A DERIVATIVES

Having established the activity of the indole psammaplin A analogues in biological assays, the active compounds were also tested in vitro (on enzyme-based assays). Because acetylation levels of many targets were found to be modified after the treatment with selected compounds (see Figure 4D−G), those leading to the expression of p21, acetylation of histone H3, and acetylation of α-tubulin were tested (at 5 μM) as inhibitors of HDAC1 and HDAC4 enzymes.

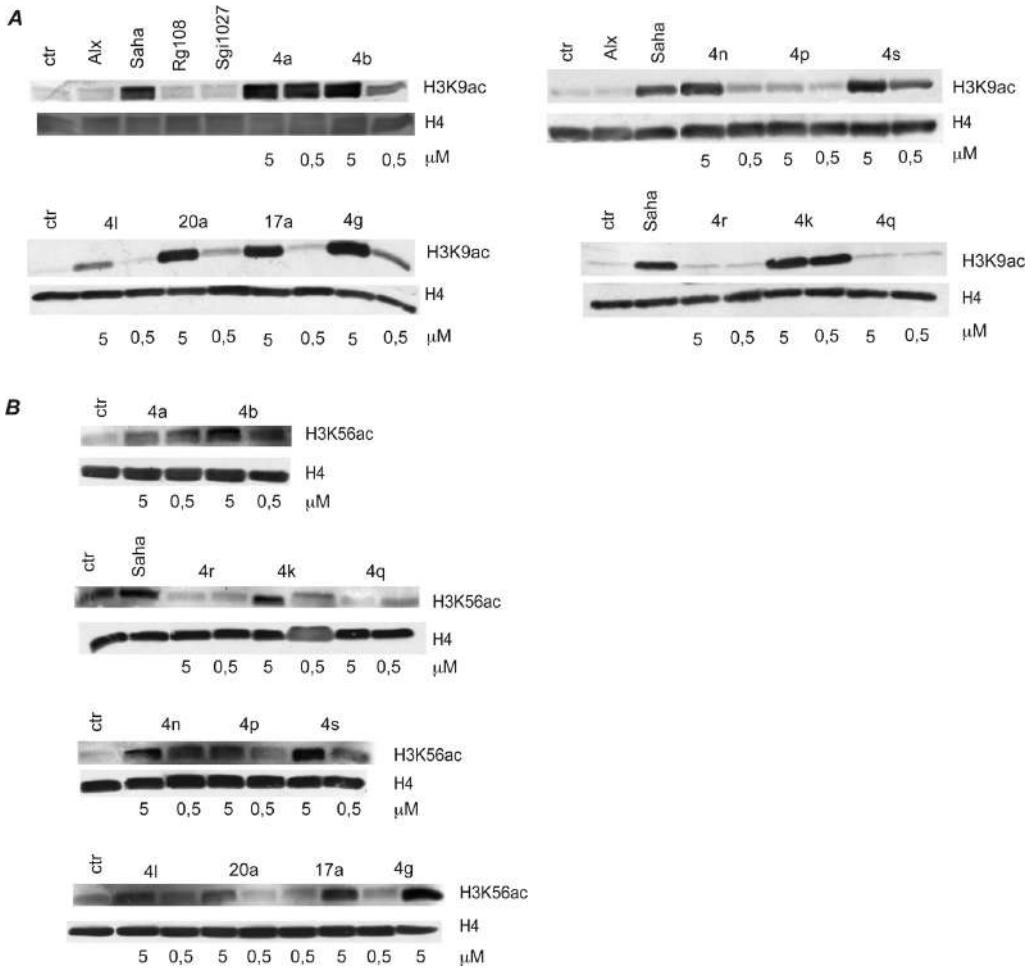

Figure 8. Western blot analysis of H3 acetylation on lysine K9 (A) and lysine K56 (B) after treatment of U937 cells with the indicated compounds at 5 and 0.5 μM for 24 h. Total H4 was used to normalize for equal loading of histone extracts. SAHA, RG108 (5 μM), SGI1027 (5 μM), and ALX (1 μM) were used as controls.

As shown in Figure 6A, compounds **4a**, **4i** and **4j** showed inhibitory activities (around 60−80%) against HDAC1. The same compounds were also active against HDAC4 (see black and gray bars in Figure 6A), although with lower potency (40−60% for compounds **4a** and **4j**). Other analogues followed the same trend (better inhibitors of HDAC1 than HDAC4) but were less effective inhibitors of both enzymes, with percentages of inhibition ranging from 20% (HDAC4) to 40% (HDAC1).

Compounds **4n** and **4o** were instead rather inactive against HDAC1 but acted as inhibitors of HDAC4 (in particular compound **4n**, for which the percentage of inhibition of HDAC4 is around 60%). Compounds **4k** and **20a** (see cell-based data in Figure 3C,D and Figure 4B,F) showed inhibition of HDAC4 (Figure 6B) and to a lesser extent of HDAC1 (**4k**).

The series of halogen and ether analogues at C5 (**4c−g**) reduced the activity of HDAC1 and HDAC4 in a variable way (different for each derivative) but in general showed a greater activity against HDAC1 than HDAC4 (Figure 6C). The inhibition induced by the methyloxime **17a** (Figure 6C) was similar to that of **4g**.

Likewise, the activity of mechanistically relevant analogues on other epigenetic enzymes was analyzed, in particular as inhibitors of DNMTs and SIRTs, in order to relate structure and activities. By use of recombinant DNMT1 enzyme and labeled *S*-adenosymethionine, the cofactor for methyl transfer (Figure 6D), it was shown that the desoximino compound (**20a**) was inactive but the methylated oxime (**17a**) was as active as **4a**, and the 5-OBn derivative (**4g**) exhibited even greater activity than **4a** and also than the known DNMT1 inhibitor RG-108.

As shown in Figure 6 E, **4a** displayed the greatest potency of the series on SIRT1 inhibition, with the presence of C5-Br being less important (**4b**) than other modifications. Whereas the *N*-Me-indole derivative **4k** proved to be inactive, the *N*-*p*-bromobenzyl derivative **4l** and the analogue with the all carbon connector between the amides (**4p**) showed weak activity. No SIRTi activity was noted for the corresponding monomers (**4s**, **4r**, **4q**).

■ INDOLE PSAMMAPLIN A ANALOGUES INDUCE CHANGES OF ACETYLATION AND EXPRESSION LEVELS OF EPIGENETIC TARGETS

Compounds that showed inhibitory activity on DNMT1 and SIRT1 enzymes were also tested in cell-based assays in order to confirm (by Western blot) if the in vitro activities correlated with changes of acetylation and expression states of selected epigenetic targets.

In Figure 7, the reactivation of p16 expression was evaluated after treatment of U937 cells for 24 h with selected compounds at two different concentrations (5 and 0.5 μM). Analogues **4a**,

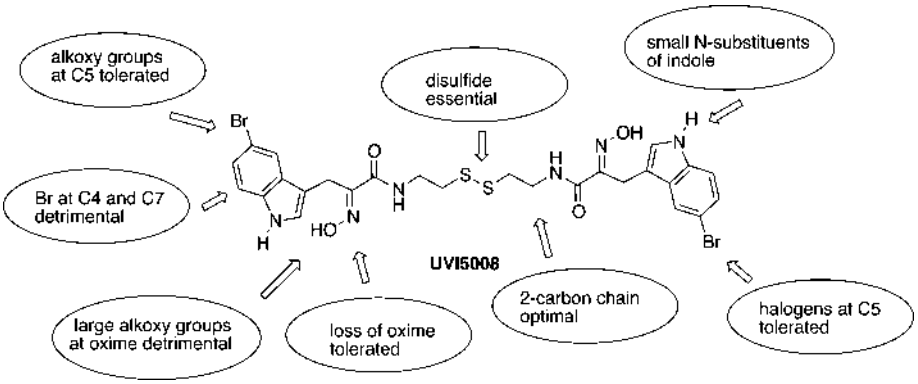

Figure 9. Summary of SAR studies on indole psammaplin A scaffold for HDAC inhibition.

17a, **4n**, **4p**, and **4s** proved to be the most active, since at 0.5 μM they induced the expression of p16 (which is causally linked to DNMT1 inhibition[74,91]). The level of DNMT1 protein remained roughly unchanged (Figure 7A). Compounds **4a**, **4g**, **4r**, and **4k** only induced p16 reactivation at 5 μM.

When compared to the data shown in Figure 6D, Figure 7 indicates a strong correlation between in vivo and cell-based assays for compounds **4a**, **4n**, **17a**, and **4g**. Surprisingly compounds **4p**, **4s**, and **4k** were inactive on in vitro DNMT1 assay (Figure 6D) but induced p16 reactivation (see Figure 7A).

The level of acetylation of SIRT1 epi-targets (as readout for SIRT inhibition) was also determined by treatment of U937 and MCF7 cells with indole psammaplin A derivatives at two concentrations. Figure 7B shows increased acetylation of p53 on residue K382 (a well-known SIRT1 target[92,93]) after treatment with selected compounds. Whereas some of those showed a dose-response trend (**4k**, **4r**, **4g**, and **20a**), others (**4s**, **4a**, and **4b**) were active only at the highest concentration (5 μM). Note that **4n** is the only compound of the series (Figure 6E) that neither increased p53K382ac levels nor inhibited SIRT in cell-based assays.

The reactivation of other reported SIRT1 targets (acetylation of H3K9[94,95] and H3K56[96]) was tested with the indole psammaplin A derivatives. Figure 8A,B shows that in general a correlation exists between concentration and level of acetylation of H3K9ac (Figure 8A) for the surveyed compounds. Compounds **4r** and **4q**, which lack the disulfide bond, did not show SIRT1 inhibition as demonstrated by their effects on H3K9 (Figure 8A) or H3K56 acetylation (Figure 8B), whereas the other analogues showed an effective proacetylation action, in particular **4k**, **4n**, **4p**, **4s**, **4l**.

■ SAR STUDIES ON INDOLE PSAMMAPLIN A DERIVATIVES

The biological results indicate that the indole derivatives of **2**[74] are more potent modulators of epigenetic enzymes than the natural product.[72] The 5-bromoindole analogue **4a** has been shown to highly efficiently induce cancer cell-selective death in a variety of models, and these activities were also demonstrated in several human tumor xenografts and genetic mouse models of human breast cancer in vivo.[74] Mechanistic studies proved that the anticancer activity of **4a** involves activation of death receptors and ROS production in a mutually independent manner. Importantly, cell death is efficiently induced in cells mutated or deficient for p53, Bcl-2 modifying factor, BMF, and/or TNF-related apoptosis inducing ligand, TRAIL.[74]

From the biochemical and cellular characterization of the analogues, it was concluded that positional isomers at the bromoindole ring such as **4i** and **4j** still showed cell cycle block, apoptosis induction (although to a lesser extent than **4a**), and CD11c differentiation of U937 cells (Figure 3A,B and Figure 4A,E). These derivatives increased α-tubulin acetylation and induced p21 expression similarly to **4a** and psammaplin A (**2**). On the contrary, protection of the oxime function as a trityl (**14a**) or benzyl derivative (**17b**) abolished activity (Figure 3A–D and Figure 4A,B,E,F). Furthermore **4p** (Figure 3A,B and Figure 4A,E) with a hydrocarbon linker was inactive, suggesting that the activity of these analogues must reside on the thiolate formed upon disulfide cleavage. Finally, incorporation of an alcohol functional group in place of the putative thiol as in **4r** (Figure 3A,B and Figure 4A,E) afforded a biologically inactive compound that kept a residual ability to induce α-tubulin acetylation. Altogether, the results confirm that the series of tetrapeptide disulfide dimers are prodrugs that get activated by reduction to afford the thiols, which are the functional group required for biological activity.

Capping the thiol as the methyl sulfide **4s** afforded a derivative with a distinct biological profile, since it blocked the cell cycle in G1 and induced p21 expression without increasing the differentiation of U937 cells. We note that its apoptogenic activity was only occurring in primary leukemic cells from AML patients but not in established U937 cells in culture. It will be interesting to study **4s** and other active compounds of this series in genetic mouse models for different types of (solid) human cancers, as reported for **4a**.[74]

HDAC1 and HDAC4 enzymatic inhibition studies revealed that the C5-Br could be replaced by other halogens (F, Cl, I) or oxygen substituents (OMe, OBn), since these analogues show roughly equal potency, but the absence of a substituent was detrimental. Positional isomers of the bromoindole (**4i–j**) showed reduced potency as HDAC inhibitors in enzymatic assays, as did the indole-*N*-methyl derivative (**4k**), in particular of HDAC4 (Figure 6A–C). Derivatization of the oxime as an alkyl derivative was tolerated for the small methyl group (**17a**) but not for the *O*-benzyl (**17b**) or *O*-trityl (**14a**) analogues (data not shown). The oxime group is dispensable (**20a**) if the indole N–H group is present, as the *N*-Me derivative (**20b**) lacks the activity (as confirmed by in vivo assays). Figure 9 summarizes the SAR study described in this work.

Regarding DNMT inhibition, Figure 6D shows the beneficial effect of the methylated oxime (**17a**) relative to **4a** and, more importantly, the presence of a *O*-Bn group in place of the bromine (**4g**). The data also conclude that the dimeric structure

Scheme 4[a]

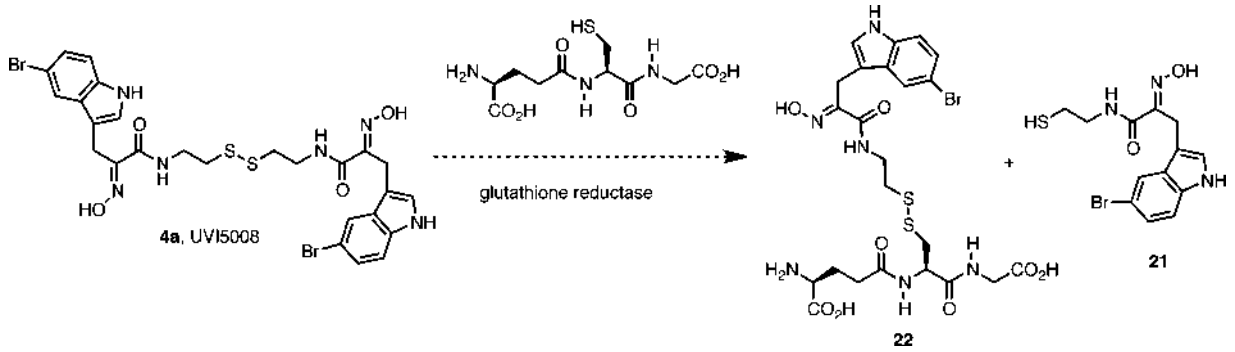

[a]In vivo conjugation of **4a** to glutathione.

is required for efficient inhibition, as monomeric analogues were inactive on DNMT1. We surmise that the disulfide could react with the enzyme after ocupation of the SAM binding pocket, perhaps undergoing capture by the invariant Cys81 active site residue[97] in a disulfide exchange reaction that might be reversible in vivo and therefore transient. Compounds that inhibited DNMT1 (**4a**, **4g**, **17a**) showed the ability to reactivate p16, an effect that was also shown by other analogues (**4n**, **4p**, **4s**; Figure 7A) but less efficiently (with the exception of **4b**).

We also studied the structural requirements for the inhibition of the SIRT NAD^+-dependent deacetylases by compound **4a**.[74] None of the analogues of **4a** assayed with SIRT1 showed equipotency to the parent compound (except **4b** and **4l**, Figure 6E), but the negative result also appears to suggest that the dimeric structure is required for the activity of **4a**, since the corresponding monomers (**4s**, **4r**, **4q**) proved to be inactive in our assay system, and both the *N*-*p*-bromobenzyl derivative **4l** and the analogue with the all carbon connector between the amides (**4p**) showed weak SIRT1 inhibitory activity. The modulation of SIRT1 targets (acetylation of p53 K382, H3K9, and H3K56, the last also linked to HDAC inhibition) was clearly consistent with the enzymatic assays for **4a**. The same correlation was noted for compounds **4p**, **4q**, and **4r**, for which the very weak inhibitory enzymatic activity (Figure 6E) is consistent with low levels of acetylation of H3K9 and H3K56 (Figure 8A). Complex readouts on the expression levels of the different SIRT1 targets hindered further SAR studies, although the disulfide bond also appears to be necessary for SIRT1 inhibition.

The entire data set suggests that the series of tetrapeptide disulfide dimers show greater activity in cell than in vitro assays (see Figure 6D and Figure 6C, cf. Figures 7 and 8), perhaps because of their prodrug nature. The inhibition of SIRT and DNMT enzymes is clearly indicated by the analysis of the levels of acetylation of sirtuin targets (p53 K382, H3K9, and H3K56) or by the reactivation of methylated genes (p16), respectively. The discrepancy between data from in vitro and cell-based assays could be understood and justified by the role of the disulfide group present in the molecular scaffold, which can be reduced (or undergo disulfide exchange, for example, with glutathione) upon cell uptake. This assumption is consistent with the weak activity displayed in both settings by alcohol **4r**. Other thiol-disguised prodrugs, such as the disulfide FK228 **1** and octanoyl derivative largazole, have also shown contrasting enzymatic potencies when compared to the corresponding reduced forms.[98,99]

Given their different enzymatic mechanism, sirtuins are not modulated by the inhibitors of classes I, II, and IV HDACs, such as suberoylanilide hydroxamic acid (SAHA) and trichostatin A (TSA), which have Zn^{2+} chelating groups. It is tempting to structurally relate the SIRT inhibition displayed by **4a** to the haloindole motif, which is found in related cyclic indole derivatives (EX243, GW5074, kenpaullones) that act as adenosine mimetics.[59]

■ MECHANISTIC INSIGHTS INTO THE MULTIPLE EPIGENETIC ACTIVITIES OF THE INDOLE-BASED PSAMMAPLIN A DERIVATIVES

With the data obtained thus far and the precedents on other sulfur containing inhibitors,[59] we surmise that the HDAC inhibition exhibited by these compounds is a consequence of disulfide reduction to the corresponding thiol-capped moiety, which likely binds the active site Zn^{2+}. Thiols such as **21** derived from the potent analogue **4a** (Scheme 4) feature the tripartite structure characteristic of most effective HDAC inhibitors, as it contains an HDAC rim-recognition element attached to an active site binding/inactivating group via a linker. The increased levels of native disulfide reductants (i.e., glutathione, thioredoxin, and thioredoxin reductase) found in many cancer cells likely render such cells particularly susceptible to the action of **4a** and analogues. Their cleavage would occur only following cellular entry after encountering a high glutathione concentration (typically 15 mM intracellular compared to 15 μM extracellular).[100]

Molecular modeling of **21** into the active site of HDAC8 shows the expected pose with the chelation of the thiol group to the Zn^{2+} ion and the additional stabilization by formation of a hydrogen bond between the indole N−H and Asp101. This model is also consistent with the inhibitory activities of the C5-indole analogue series and with the lack of activity of monomers lacking the thiol-chelating unit (Figure 10).

In support of the mechanism of action of these indole-based psammaplin A analogues, pharmacokinetic studies on lead compound **4a**[74] led to the detection by HPLC/MS of the mixed disulfide **22**, a glutathione adduct presumably formed by in-cell modification of the scissile disulfide bond as indicated in Scheme 4.

In addition to the disulfide present in other depsipeptides such as FK228 (**1**)[55] and in psammaplin A (**2**)[58] and to the octanoyl thiol ester of depsipeptide largazole,[102] the *S*-acetyl,[103] *S*-isobutyryl,[104] and *S*-2-methyl-3-phenylpropanoyl[105] thiol esters have also been developed as thiol surrogates in HDACis. Mixed disulfides have been used in lieu of the symmetrical

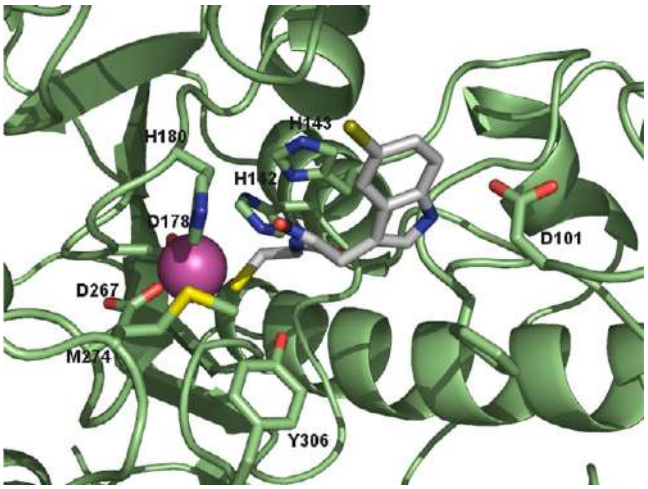

Figure 10. Proposed docking pose for **4a**-derived thiol **21** in HDAC8.[101] The Cα trace of the enzyme is displayed as a ribbon, colored in green. The side chains of His142, His143, Asp178, Asp267, His180, Met274, Tyr306 are shown as sticks, with carbon atoms colored in green. The Zn^{2+} at the catalytic site is shown as a magenta sphere. The inhibitor is displayed also as sticks but with carbon atoms colored in gray and the bromine atom colored in brown. The ab initio calculated structure of **4a**-derived thiol **21** was docked into the structure of human HDAC8[101] after removal of the trichostatin A (TSA) ligand. The highest scores using an automated docking method for the interaction with the Zn^{2+} ion in the active site was validated by the GRID maps. In these solutions, the thiolate group chelates the metal, the linker domain occupies the channel, and the bromoindole is stabilized through interaction with Tyr100 and Phe152 at the rim of the active site entrance. This positioning facilitates the formation of a hydrogen bond between the indole N−H and Asp101. The complex was refined using energy minimization, and its dynamic behavior was simulated using unrestrained MD (see Supporting Information).

dimeric structures.[106] All the above ligands are considered as prodrugs[107] that most likely release the thiolate group upon reaction with thioesterases or by thiol−disulfide exchange[108] induced by the addition of sulfhydryl groups of compounds present in the reductive environment of the cell such as glutathione. In addition, other sulfur-containing functional groups employed as headgroup of HDACis have been described, among them trithiocarbonates,[109] mercaptoacetamides,[110] mercaptoketones,[111] and methylsulfoxides.[112] The broad variety of functional groups further attests to the efficient and energetically favorable chelation of Zn^{2+} ion by sulfur-containing functional groups.[40]

■ CONCLUSION

To summarize, the scaffold of the psammaplin A natural product is amenable to synthetic reengineering without loss of epigenetic modulatory activity. In particular the *o*-bromophenol unit of psammaplin A **2** has been replaced by the more chemically robust and drug-friendly indole fragment. A series of indole psammaplin A constructs have been generated in a short synthetic sequence, and their biological evaluation has led to a better understanding of the structure−activity relationship of these epigenetic inhibitors (see Table 2 for a summary of enzymatic and cellular activities). Notably, the incorporation of the 5-bromoindole unit in **4a** replacing the *o*-bromophenol of **2** not only improved the potency of the parent compound with regard to the already reported HDAC and DNMT dual epigenetic inhibitory profile but interestingly added another activity, the inhibition of the NAD^+-dependent SIRT deacetylase enzymes.[74] In vivo pharmacokinetics revealed that this compound is a prodrug that gets rapidly transformed into the glutathione conjugate.[74] In keeping with the concept of targeting several pathways, it is encouraging that a large number of phase I/II clinical trials are currently exploring the combination of an HDAC together with the DNA methyltransferase inhibitor 5-aza-2′-deoxycytidine (decitabine) (http://clinicaltrials.gov). Indeed, the simultaneous block of at least three epigenetic targets offers a valid alternative to combination treatments as well as a unique strength to ensure delivery of an "all in one" drug to the cells.[59]

A major consequence of **4a**-mediated anticancer effects involves activation of different pathways of apoptosis in the cancer cells due to synergism between these inhibitory activities.[74] A balanced modulation of several epigenetic targets makes designed multiple ligands (DMLs)[113] a promising class of anticancer drugs with unanticipated therapeutic potential.[59] The fact that **4a** seems to be well tolerable in experimental mice models and that the maximal tolerable dose is higher than that of well-known HDAC inhibitors represents another important argument for its further development and use against cancer. The entire data set suggests that further investigation on the role of indole psammaplin A derivatives in controlling some biological processes, such as cellular death and regulation of epigenetic effectors/regulators, is warranted, particularly given their action on some hematological samples (Figure 5) in which, compared to other epi-drugs, selected compounds were able to efficiently induce cell death.

■ EXPERIMENTAL SECTION

General. Solvents were dried according to published methods and distilled before use. HPLC grade solvents were used for HPLC purification. All other reagents were commercial compounds of the highest purity available. All reactions were carried out under argon atmosphere, and those not involving aqueous reagents were carried out in oven-dried glassware. Analytical thin layer chromatography (TLC) was performed on aluminum plates with Merck Kieselgel 60F254 and visualized by UV irradiation (254 nm) or by staining with a solution of phosphomolybdic acid. Flash column chromatography was carried out using Merck Kieselgel 60 (230−400 mesh) under pressure. Infrared spectra were obtained on a JASCO FTIR 4200 spectrophotometer, from a thin film deposited onto a NaCl glass. ^{1}H NMR spectra were recorded in $CDCl_3$, CD_3OD, DMSO-d_6, and $(CD_3)_2CO$ at ambient temperature on a Bruker AMX-400 spectrometer at 400 MHz with residual protic solvent as the internal reference ($CDCl_3$, δ_H = 7.26 ppm; $(CD_3)_2CO$, δ_H = 2.05 ppm; CD_3OD, δ_H = 3.31; DMSO-d_6, δ_H = 2.50). Chemical shifts (δ) are given in parts per million (ppm), and coupling constants (J) are given in hertz (Hz). The proton spectra are reported as follows: δ (multiplicity, coupling constant J, number of protons, assignment). ^{13}C NMR spectra were recorded in $CDCl_3$, CD_3OD, DMSO-d_6, and $(CD_3)_2CO$ at ambient temperature on the same spectrometer at 100 MHz, with the central peak of $CDCl_3$ (δ_C = 77.0 ppm), CD_3OD (δ_C = 49.0 ppm), DMSO-d_6 (δ_C = 39.4 ppm), or $(CD_3)_2CO$ (δ_C = 30.8 ppm) as the internal reference. DEPT135 sequence was used to aid in the assignment of signals in the ^{13}C NMR spectra. Melting points were determined on a Stuart SMP10 apparatus. Elemental analyses were determined on a Carlo Erba EA 1108 analyzer. Crystallographic information was obtained from the corresponding single crystals analyzed by X-ray diffraction. Crystallographic data were collected on a single crystal Bruker SMART CCD6000 FR591 diffractometer equipped with a charge-coupled device (CCD) detector at 20 °C using graphite monochromated Mo Kα radiation (λ = 0.710 73 Å) and were corrected for Lorentz and polarization effects.

Mass Spectrometry. Experiments were performed on an APEX III FT-ICR MS instrument (Bruker Daltonics, Billerica, MA) equipped

Table 2. Summary of Compounds Activities[a]

	Cell cycle	Death	Cd11c	Acetylation	Expression	HDACs	SIRT1	DNMT1
2	■	■		■	■			
14a	■							
17a				■	■	■		■
17b								
20a			■	■	■	■		
20b								
4a	■	■	■	■	■	■	■	■
4b	■	■	■	■	■	■	■	
4c	■	■		■	■	■		
4d	■	■		■	■	■		
4e	■	■		■	■	■		
4f		■	■	■	■	■		
4g		■	■	■	■	■		■
4h								
4i	■	■	■	■	■	■		
4j	■	■	■	■	■	■		
4k	■	■	■	■	■	■		
4l							■	
4m			■	■				
4n	■	■	■	■		■		■
4o			■	■	■	■		
4p				■	■		■	
4q								
4r				■				
4s			■	■	■			

[a]Black boxes show, for each molecule, positive response to the tests. Column entries from left to right indicate the following: variations in cell cycle distribution (Cell cycle); induction of cell death (Death); induction of granulocytic differentiation (CD11c); variation of the acetylated state of proteins (Acetylation); expression of key and/or silenced proteins (Expression); in vitro activity against HDAC1/4 (HDACs); in vitro activity against SIRT1 (SIRT1); in vitro modulation of DNMT1 activity (DNMT1). The experimental details are reported in the Experimental Section and the numerical values in Figures 3−8.

with a 7 T actively shielded magnet. Ions were generated using an Apollo API electrospray ionization (ESI) source with a voltage between 1800 and 2200 V (to optimize ionization efficiency) applied to the needle and with a countervoltage of 450 V applied to the capillary. Samples were prepared by adding a spray solution of 70:29.9:0.1 (v/v/v) CH_3OH/water/formic acid to a solution of the sample at a v/v ratio of 1−5% to give the best signal-to-noise ratio.

Data acquisition and data processing were performed using the XMASS software, version 6.1.2 (Bruker Daltonics). FAB experiments were performed on a VG AutoSpec instrument, using 3-nitrobenzylalcohol or glycerol as matrices.

The purity of the compounds was established in most cases by elemental analysis and, for those that did not give suitable crystals, by HPLC and found to be greater than 95%.

General Procedure for the Reaction of Indoles with Ethylbromopyruvate-2-oxime. Oxime **7** (1.0 mmol) was dissolved in anhydrous dichloromethane (3 mL) with an excess of substrate (2.0 mmol). Anhydrous sodium carbonate (5.5 mmol) was then added, and the suspension was stirred for 24 h at room temperature. After filtration through silica gel, the solvent was removed and the residue was purified by column chromatography on silica gel as indicated.

General Procedure for the Protection of Oximes with TrCl. Trityl chloride (2.0 mmol) was added to a stirred suspension of the indole **9** (1.0 mmol) and Na_2CO_3 (2.0 mmol) in CH_2Cl_2 (10 mL) and THF (1.5 mL). The mixture was stirred at room temperature for 16 h, filtered through a pad of silica gel saturated with Et_3N, and the filtrate was concentrated. The residue was subjected to chromatography as indicated to afford **11**.

General Procedure for Hydrolysis of Esters. $LiOH{\cdot}H_2O$ (15 mmol) was added to a solution of the ester **11** (1.0 mmol) in a 1:1 THF/H_2O mixture (3.5 mL). After stirring for 16 h at room temperature, water was added and the solution was neutralized by addition of 10% HCl. Extraction with ethyl acetate and crystallization from hexane/$CHCl_3$ afforded the corresponding acid **12**.

General Procedure for the Coupling of Acids with Amines. To a solution of acid **12** (1.0 mmol) in dioxane (4 mL) was added EDC (1.9 mmol) and *N*-hydroxysuccinimide (1.7 mmol), and the resulting solution was stirred for 2 h at 25 °C. Then a solution of amine **13** (0.5 or 1.0 mmol) and Et_3N (5.5 mmol) in dioxane (4 mL) and MeOH (4 mL) was added. After the mixture had been stirred for 16 h at room temperature, water was added and the mixture extracted with ethyl acetate. The solvent was removed in vacuo, and the residue was subjected to column chromatography on silica gel as indicated. Some of those compounds **14** could not be fully characterized because of their instability upon attempted additional purification on silica gel.

General Procedure for the Cleavage of the Trityl Protecting Group. The corresponding indole (1.0 mmol) was dissolved in a 20:1 CH_2Cl_2/MeOH mixture (6 mL) and placed in a pressure flask, and anhydrous HCl (7.3 mmol of a 1.0 M solution in ether) was added. The solution was then stirred at 25 °C for 2h. The mixture was diluted with water and MeOH, washed with hexane, and the MeOH was evaporated in vacuo. EtOAc was then added, and the aqueous layer was extracted with EtOAc (3×). The combined organic extracts were dried over Na_2SO_4, filtered, and the solvent was evaporated in vacuo. The residue was subjected to column chromatography on silica gel (95:5 CH_2Cl_2/MeOH)..

(*E*)-Ethyl 3-(5-Bromo-1*H*-indol-3-yl)-2-(hydroxyimino)-propanoate (9a). Following the general procedure described for the reaction of indoles with ethyl bromopyruvate-2-oxime, indole **5a** (1.00 g, 5.10 mmol) gave, after purification by column chromatography (SiO_2, 35:65 EtOAc/hexane), oxime **9a** (0.50 g, 60%) as a white solid, mp 175−176 °C ($CHCl_3$/hexane), and oxazine **10a** (0.03 g, 4%) as a yellow solid,mp 161−162 °C ($CHCl_3$/hexane).

Data for (*E*)-Ethyl 3-(5-Bromo-1*H*-indol-3-yl)-2-(hydroxyimino)propanoate (9a). ^{1}H NMR (CD_3COCD_3, 400.13 MHz): δ 10.24 (br, 1H, NH), 7.92 (d, J = 1.7 Hz, 1H, H4′), 7.33 (d, J = 8.5 Hz, 1H, H7′), 7.27 (d, J = 2.3 Hz, 1H, H2′), 7.20 (dd, J = 8.5, 1.7 Hz, 1H, H6′), 4.19 (q, J = 7.1 Hz, 2H, $CO_2C\underline{H}_2CH_3$), 4.05 (s, 2H, 2H3), 1.22 (t, J = 7.1 Hz, 3H, $CO_2CH_2C\underline{H}_3$) ppm. ^{13}C NMR (CD_3COCD_3, 100.62 MHz): δ 165.6 (s), 152.9 (s), 136.9 (s), 131.1 (s), 127.4 (d), 125.7 (d), 123.3 (d), 114.9 (d), 113.5 (s), 111.0 (s), 62.6 (t), 21.6 (t), 15.3 (q) ppm. IR: ν 3500−3100 (br, N−H and O−H), 2983 (w, C−H), 1705 (s, C═O and C═N), 1426 (w), 1096 (w), 1014 (m), 864 (w) cm^{-1}. MS (FAB$^+$): m/z (%) 327 ([M + 1]$^+$ [^{81}Br], 61), 326 ([M]$^+$ [^{81}Br], 34), 325 ([M + 1]$^+$ [^{79}Br], 67), 324 ([M]$^+$ [^{79}Br], 26) 311 (62), 310 (35), 309 (84), 308 (25), 307 (26), 235 (22), 210 (99), 208 (100), 156 (24). HRMS (FAB$^+$) calcd for $C_{13}H_{13}{}^{81}BrN_2O_3$ and $C_{13}H_{13}{}^{79}BrN_2O_3$ ([M]$^+$), 326.0089 and 324.0110; found, 326.0100 and 324.0112. Anal. Calcd for $C_{13}H_{13}BrN_2O_3$: C, 48.02; H, 4.03; N, 8.62. Found: C, 48.02; H, 4.03; N, 8.65.

Data for (4a*R,9a*R**,*E*)-Ethyl 6-Bromo-4a-[3-ethoxy-2-(hydroxyimino)-3-oxopropyl]-4,4a,9,9a-tetrahydro[1,2]oxazino[6,5-*b*]-indole-3-carboxylate (10a).** ^{1}H NMR ($CDCl_3$, 400.13 MHz): δ 10.02 (br, 1H, NH), 7.10 (s, 2H, ArH), 6.42 (d, J = 8.5 Hz, 1H, ArH), 5.66 (s, 1H), 5.14 (s, 1H), 4.4−4.1 (m, 4H, 2 × $CO_2C\underline{H}_2CH_3$), 3.3−3.1 (m, 3H), 2.60 (d, J = 15.8 Hz, 1H, H4A), 1.3−1.2 (m, 6H, 2 × $CO_2CH_2C\underline{H}_3$) ppm. ^{13}C NMR ($CDCl_3$, 100.62 MHz): δ 163.6 (s), 162.0 (s), 159.3 (s), 148.9 (s), 147.3 (s), 131.7 (d), 131.3 (s), 126.5 (d), 110.9 (s), 110.4 (d), 94.8 (d), 62.4 (t), 62.3 (t), 50.6 (s), 32.9 (t), 27.8 (t), 13.9 (q, 2×) ppm. IR: ν 3500−3100 (br, N−H and O−H), 2986 (m, C−H), 1721 (s, C═O and C═N), 1606 (m), 1476 (m), 1435 (m), 1279 (s), 1167 (m), 1017 (m), 757 (s) cm^{-1}. HRMS (ESI$^+$) calcd for $C_{18}H_{20}{}^{81}BrN_3O_6Na$ and $C_{18}H_{20}{}^{79}BrN_3O_6Na$ ([M + Na]$^+$), 478.0407 and 476.0428; found, 478.0410 and 476.0428. Anal. Calcd for $C_{18}H_{20}BrN_3O_6$: C, 47.59; H, 4.44; N, 9.25. Found: C, 47.38; H, 4.44; N, 9.28.

(*E*)-Ethyl 3-(5-Bromo-1*H*-indol-3-yl)-2-(trityloxyimino)-propanoate (11a). In accordance with the general procedure described for the protection of oximes, indole **9a** (0.70 g, 2.10 mmol) afforded, after purification by column chromatography (SiO_2, 72:25:3 hexane/EtOAc/Et_3N), the protected oxime **11a** (0.90 g, 74%) as a white solid, mp 166−167 °C ($CHCl_3$/hexane). ^{1}H NMR (CD_3COCD_3, 400.13 MHz): δ 10.26 (br, 1H, NH), 7.90 (d, J = 1.4 Hz, 1H, H4′), 7.4−7.2 (m, 16H, ArH), 7.21 (dd, J = 8.6, 1.8 Hz, 1H, H6′), 7.18 (d, J = 2.0 Hz, 1H, H2′), 4.22 (s, 2H, 2H3), 4.11 (q, J = 7.1 Hz, 2H, $CO_2C\underline{H}_2CH_3$), 1.15 (t, J = 7.1 Hz, 3H, $CO_2CH_2C\underline{H}_3$) ppm. ^{13}C NMR (CD_3COCD_3, 100.62 MHz): δ 165.1 (s), 153.0 (s), 145.8 (s, 3×), 136.9 (s), 131.0 (d, 6×), 129.5 (d, 6×), 129.3 (d, 3×), 127.3 (d), 125.9 (d), 123.3 (d), 115.0 (d), 113.7 (s), 110.5 (s), 94.6 (s), 62.9 (t), 23.3 (t), 15.3 (q) ppm. IR: ν 3500−3300 (br, N−H), 3059 (w, C−H), 3028 (w, C−H), 2983 (w, C−H), 1716 (s, C═O and C═N), 1597 (w), 1450 (s), 1323 (m), 1195 (s), 754 (s) cm^{-1}. HRMS (ESI$^+$) calcd for $C_{32}H_{27}{}^{81}BrN_2O_3Na$ and $C_{32}H_{27}{}^{79}BrN_2O_3Na$ ([M + Na]$^+$), 591.1077 and 589.1097; found, 591.1063 and 589.1082. Anal. Calcd for $C_{32}H_{27}BrN_2O_3$: C, 67.73; H, 4.80; N, 4.94. Found: C, 67.82; H, 4.81; N, 4.98.

(*E*)-3-(5-Bromo-1*H*-indol-3-yl)-2-(trityloxyimino)propanoic Acid (12a). According to the general procedure described for the hydrolysis of esters, **11a** (0.70 g, 1.20 mmol) gave, after crystallization, acid **12a** (0.65 g, 99%) as a white solid, mp 171−172 °C (dec) (hexane/$CHCl_3$). ^{1}H NMR (CD_3COCD_3, 400.13 MHz): δ 10.23 (br, 1H, NH), 7.92 (d, J = 1.7 Hz, 1H, H4′), 7.4−7.2 (m, 16H, ArH), 7.19 (dd, J = 8.6, 1.7 Hz, 1H, H6′), 7.15 (s, 1H, H2′), 4.21 (s, 2H, 2H1) ppm. ^{13}C NMR (CD_3COCD_3, 100.62 MHz): δ 166.5 (s), 153.7 (s), 145.9 (s, 3×), 137.0 (s), 131.1 (s), 131.0 (d, 6×), 129.5 (d, 6×), 129.2 (d, 3×), 127.3 (d), 125.9 (d), 123.3 (d), 115.0 (d), 113.7 (s), 110.7 (s), 94.5 (s), 23.0 (t) ppm. IR: ν 3500−3200 (br, N−H and O−H), 3059 (w, C−H), 1756 (m, C═O), 1702 (m, C═N), 1597 (w), 1447 (s), 1216 (s), 972 (s), 757 (s), 700 (s) cm^{-1}. HRMS (ESI$^+$) calcd for $C_{30}H_{23}{}^{81}BrN_2O_3Na$ and $C_{30}H_{23}{}^{79}BrN_2O_3Na$ ([M + Na]$^+$), 563.0764 and 561.0784; found, 563.0755 and 561.0776. Anal. Calcd for $C_{30}H_{23}BrN_2O_3\cdot{}^1/_2H_2O$: C, 65.70; H, 4.41; N, 5.11. Found: C, 65.57; H, 4.50; N, 4.99.

(2*E*,2′*E*)-*N*,*N*′-[2,2′-Disulfanediylbis(ethane-2,1-diyl)]bis[3-(5-bromo-1*H*-indol-3-yl)-2-(trityloxyimino)propanamide] (14a). Following the general procedure described for the coupling of acids with amines, **12a** (0.60 g, 1.11 mmol) afforded, after purification by column chromatography (SiO_2, gradient from 47:50:3 hexane/EtOAc/Et_3N to 100% EtOAc), disulfide **14a** (0.56 g, 84%) as a white solid, mp 172−173 °C (hexane/$CHCl_3$). ^{1}H NMR (CD_3COCD_3, 400.13 MHz) (data for monomer): δ 10.24 (br, 1H, NH), 7.96 (s, 1H, ArH), 7.4−7.1 (m, 17H, ArH), 6.97 (s, 1H, ArH), 4.20 (s, 2H, 2H3), 3.4−3.2 (m, 2H, 2H1″), 2.87 (s, 1H, CONH), 2.60 (t, J = 6.3 Hz, 2H, 2H2″) ppm. ^{13}C NMR (CD_3COCD_3, 100.62 MHz) (data for monomer): δ 164.4 (s), 154.5 (s), 145.8 (s, 3×), 136.9 (s), 131.1 (s), 130.8 (d, 6×), 129.6 (d, 6×), 129.2 (d, 3×), 127.5 (d), 125.8 (d), 123.5 (d), 114.9 (d), 113.7 (s), 110.7 (s), 94.3 (s), 39.9 (t), 39.1 (t), 21.8 (t) ppm. IR: ν 3500−3200 (br, N−H), 3059 (w, C−H), 3022 (w, C−H), 1669 (s, C═O and C═N), 1520 (s), 1448 (s), 1217 (m), 971 (m), 755 (s), 701 (s) cm^{-1}. HRMS (ESI$^+$) calcd for $C_{64}H_{54}{}^{81}Br_2N_6O_4S_2Na$, $C_{64}H_{54}{}^{79}Br^{81}BrN_6O_4S_2Na$, and $C_{64}H_{54}{}^{79}Br_2N_6O_4S_2Na$ ([M + Na]$^+$), 1219.1866, 1217.1886, and 1215.1907; found, 1219.1852, 1217.1855, and 1215.1877. Anal. Calcd for $C_{64}H_{54}Br_2N_6O_4S_2\cdot 2H_2O$: C, 62.44; H, 4.75; N, 6.83; S, 5.21. Found: C, 62.50; H, 4.97; N, 6.32; S, 4.67.

(2*E*,2′*E*)-*N*,*N*′-[2,2′-Disulfanediylbis(ethane-2,1-diyl)bis(3-(5-bromo-1*H*-indol-3-yl)-2-(hydroxyimino)propanamide] (4a). In accordance with the general procedure described for the cleavage of the trityl group, **14a** (0.09 g, 0.08 mmol) gave, after purification by column chromatography (SiO_2, 95:5 CH_2Cl_2/MeOH), disulfide **4a** (0.04 g, 81%) as a yellowish solid, mp 179−180 °C (hexane/EtOAc). ^{1}H NMR (CD_3OD, 400.13 MHz) (data for monomer): δ 7.83 (d, J = 1.8 Hz, 1H, H4′), 7.15 (d, J = 8.5 Hz, 1H, H7′), 7.10 (dd, J = 8.5, 1.8 Hz, 1H, H6′), 7.09 (s, 1H, H1′), 3.97 (s, 2H, 2H3), 3.40 (t, J = 6.7 Hz, 2H, 2H1″), 2.65 (t, J = 6.7 Hz, 2H, 2H2″) ppm. ^{13}C NMR (CD_3OD, 100.62 MHz) (data for monomer): δ 166.2 (s), 153.6 (s), 136.3 (s), 130.4 (s), 126.5 (d), 124.9 (d), 122.6 (d), 113.7 (d), 112.9 (s), 110.2 (s), 39.6 (t), 38.4 (t), 19.7 (t) ppm. IR: ν 3500−3100 (br, N−H and OH), 3061 (w, C−H), 2925 (w, C−H), 1705 (m), 1662 (s, C═O and C═N), 1526 (s), 1448 (s), 1360 (m), 1226 (m), 793 (w) cm^{-1}. HRMS (ESI$^+$) calcd for $C_{26}H_{27}{}^{81}Br_2N_6O_4S_2$, $C_{26}H_{27}{}^{79}Br^{81}BrN_6O_4S_2$, and $C_{26}H_{27}{}^{79}Br_2N_6O_4S_2$ ([M + H]$^+$), 712.9855, 710.9876, and 708.9896; found, 712.9831, 710.9851, and 708.9879. Anal. Calcd for $C_{26}H_{26}Br_2N_6O_4S_2$: C, 43.95; H, 3.69; N, 11.83; S, 9.03. Found: C, 44.40; H, 3.94; N, 11.62; S, 9.21.

(2*E*,2′*E*)-*N*,*N*′-[2,2′-Disulfanediylbis(ethane-2,1-diyl)]bis[2-(hydroxyimino)-3-(1*H*-indol-3-yl)propanamide] (4b). In accordance with the general procedure for the cleavage of trityl groups, **14b** (0.08 g, 0.07 mmol) gave, after purification by column chromatography (SiO_2, 95:5 CH_2Cl_2/MeOH), disulfide **4b** (0.04 g, 78%) as a yellow oil. ^{1}H NMR (CD_3OD, 400.13 MHz) (data for monomer): δ 7.64 (d, J = 7.9 Hz, 1H, ArH), 7.21 (d, J = 8.1 Hz, 1H, ArH), 7.01 (s, 1H, H2′), 6.98 (t, J = 7.5 Hz, 1H, ArH), 6.91 (t, J = 7.4 Hz, 1H, ArH), 3.98 (s, 2H, 2H3), 3.36 (t, J = 6.7 Hz, 2H, 2H1″), 3.27 (br, 1H, CONH), 2.60 (t, J = 6.7 Hz, 2H, 2H2″) ppm. ^{13}C NMR (CD_3OD, 100.62 MHz) (data for monomer): δ 166.3 (s), 154.0 (s), 137.7 (s), 128.5 (s), 124.7 (d), 122.2 (d), 119.9 (d), 119.5 (d), 112.0 (d), 110.2 (s), 39.4 (t), 38.3 (t), 19.8 (t) ppm. IR: ν 3500−3000 (br, N−H and O−H), 3057 (w, C−H), 2925 (m, C−H), 2855 (w, C−H), 1702 (w, C═O), 1660 (s, C═N), 1527 (s), 1457 (s), 1423 (s), 1356 (m), 1227 (m), 1009 (m), 744 (s) cm^{-1}. HRMS (ESI$^+$) calcd for $C_{26}H_{28}N_6O_4S_2Na$ ([M + Na]$^+$), 575.1506; found, 575.1492.

(2*E*,2′*E*)-*N*,*N*′-[2,2′-Disulfanediylbis(ethane-2,1-diyl)]bis[3-(5-fluoro-1*H*-indol-3-yl)-2-(hydroxyimino)propanamide] (4c). In accordance with the general procedure for the cleavage of trityl groups, **14c** (0.30 g, 0.28 mmol) gave, after purification by column chromatography, disulfide **4c** (0.11 g, 38% in two steps) as a yellow oil. ^{1}H NMR (CD_3COCD_3, 400.13 MHz) (data for monomer): δ 10.13

(br, 1H, NH), 7.60 (t, J = 5.2 Hz, 1H, CONH), 7.50 (dd, $^3J_{H-F}$ = 10.2 Hz, J_{H-H} = 2.1 Hz, 1H, H4′), 7.32 (dd, J_{H-H} = 8.8 Hz, $^4J_{H-F}$ = 4.5 Hz, 1H, H7′), 7.27 (s, 1H, H2′), 6.85 (td, $^3J_{H-F}$ = J_{H-H} = 9.2 Hz, J_{H-H} = 2.3 Hz, 1H, H6′), 4.02 (s, 2H, 2H3), 3.53 (q, J = 6.5 Hz, 2H, NHC$\underline{H}_2$), 2.81 (t, J = 6.5 Hz, 2H, CH_2S) ppm. ^{13}C NMR (CD_3COCD_3, 100.62 MHz MHz) (data for monomer): δ 165.4 (s), 159.2 (s, J_{C-F} = 231.2 Hz), 154.7 (s), 134.8 (s), 129.7 (s, $^3J_{C-F}$ = 10.3 Hz), 128.1 (d), 113.8 (d, $^3J_{C-F}$ = 9.8 Hz), 111.6 (s, $^4J_{C-F}$ = 4.6 Hz), 111.0 (d, $^2J_{C-F}$ = 26.6 Hz), 105.6 (d, $^2J_{C-F}$ = 23.9 Hz), 40.1 (t), 39.3 (t), 20.5 (t) ppm. IR: ν 3500−3000 (br, N−H and O−H), 2925 (w, C−H), 1698 (m, C═O), 1658 (s, C═N), 1527 (s), 1482 (m), 1430 (s), 1356 (m), 1220 (s), 1011 (s), 854 (m), 791 (s), 713 (m) cm^{-1}. HRMS (ESI)$^+$ calcd for $C_{26}H_{27}F_2N_6O_4S_2$ ([M + H]$^+$), 589.1498, found 589.1470.

(2*E*,2′*E*)-*N*,*N*′-[2,2′-Disulfanediylbis(ethane-2,1-diyl)]bis[3-(5-chloro-1*H*-indol-3-yl)-2-(hydroxyimino)propanamide] (4d). In accordance with the general procedure for the cleavage of trityl groups, **14d** (0.13 g, 0.12 mmol) gave, after purification by column chromatography, disulfide **4d** (0.05 g, 30% in two steps) as a yellow oil. ^{1}H NMR (CD_3COCD_3, 400 MHz) (data for monomer): δ 11.06 (br, 1H, OH), 10.20 (br, 1H, NH), 7.81 (d, J = 1.8 Hz, 1H, H4′), 7.58 (t, J = 5.7 Hz, 1H, CONH), 7.34 (d, J = 8.6 Hz, 1H, H7′), 7.27 (s, 1H, H2′), 7.04 (dd, J = 8.6, 2.0 Hz, 1H, H6′), 4.03 (s, 2H, 2H3), 3.54 (q, J = 6.6 Hz, 2H, NHC$\underline{H}_2$), 2.83 (t, J = 6.6 Hz, 2H, CH_2S) ppm. ^{13}C NMR (CD_3COCD_3, 100.62 MHz) (data for monomer): δ 165.3 (s), 154.7 (s), 136.7 (s), 130.6 (s), 127.8 (d), 125.8 (s), 123.0 (d), 120.4 (d), 114.4 (d), 111.4 (s), 40.1 (t), 39.4 (t), 20.4 (t) ppm. IR: ν 3500−3000 (br, N−H and O−H), 3063 (w, C−H), 2920 (m, C−H), 1702 (s, C═O), 1658 (s, C═N), 1525 (s), 1461 (s), 1423 (s), 1359 (s), 1226 (s), 1011 (m), 980 (m), 900 (m), 794 (s) cm^{-1}. HRMS (ESI)$^+$ calcd for $C_{26}H_{27}{}^{37}Cl_2N_6O_4S_2$, $C_{26}H_{27}{}^{37}Cl^{35}ClN_6O_4S_2$, and $C_{26}H_{27}{}^{35}Cl_2N_6O_4S_2$ ([M + H]$^+$), 625.0808, 623.0845, and 621.0880; found, 625.0862, 623.0882, and 621.0907.

(2*E*,2′*E*)-*N*,*N*′-[2,2′-Disulfanediylbis(ethane-2,1-diyl)]bis[2-(hydroxyimino)-3-(5-iodo-1*H*-indol-3-yl)propanamide] (4e). In accordance with the general procedure for the cleavage of trityl groups, **14e** (0.15 g, 0.11 mmol) gave, after purification by column chromatography, disulfide **4e** (0.05 g, 13% in two steps) as a yellow oil. ^{1}H NMR (CD_3COCD_3, 400 MHz) (data for monomer): δ 10.23 (br, 1H, NH), 8.16 (br, 1H, H2′), 7.60 (t, J = 5.7 Hz, 1H, CONH), 7.33 (dd, J = 8.5, 1.5 Hz, 1H, H6′), 7.21 (d, J = 8.3 Hz, 1H, H7′), 7.20 (d, J = 1.2 Hz, 1H, H2′), 4.01 (s, 2H, 2H3), 3.53 (q, J = 6.6 Hz, 2H, NHC$\underline{H}_2$), 2.84 (t, J = 6.6 Hz, 2H, CH_2S) ppm. ^{13}C NMR (CD_3COCD_3, 100.62 MHz) (data for monomer): δ 165.3 (s), 154.7 (s), 137.3 (s), 132.1 (s), 131.1 (d), 130.0 (d), 127.2 (d), 115.4 (d), 111.0 (s), 83.6 (s), 40.2 (t), 39.4 (t), 20.4 (t) ppm. IR: ν 3500−3000 (br, N−H and O−H), 3064 (w, C−H), 2923 (w, C−H), 1690 (s, C═O), 1662 (s, C═N), 1529 (s), 1451 (s), 1253 (s), 1015 (m), 794 (m) cm^{-1}. HRMS (ESI)$^+$ calcd for $C_{26}H_{27}I_2N_6O_4S_2$ ([M + H]$^+$), 804.9619, found 804.9582.

(2*E*,2′*E*)-*N*,*N*′-[2,2′-Disulfanediylbis(ethane-2,1-diyl)]bis[2-(hydroxyimino)-3-(5-methoxy-1*H*-indol-3-yl)propanamide] (4f). In accordance with the general procedure for the cleavage of trityl groups, **14f** (0.04 g, 0.04 mmol) gave, after purification by column chromatography, disulfide **4f** (0.02 g, 4% in two steps) as a yellow oil. ^{1}H NMR (CD_3COCD_3, 400 MHz) (data for monomer): δ 9.86 (br, 1H, NH), 7.52 (t, J = 5.3 Hz, 1H, CONH), 7.32 (d, J = 2.1 Hz, 1H, H4′), 7.21 (d, J = 8.8 Hz, 1H, H7′), 7.13 (s, 1H, H2′), 6.71 (dd, J = 8.8, 2.3 Hz, 1H, H6′), 4.01 (s, 2H, 2H3), 3.78 (s, 3H, OCH_3), 3.52 (q, J = 6.5 Hz, 2H, NHC$\underline{H}_2$), 2.83 (t, J = 6.6 Hz, 2H, CH_2S) ppm. ^{13}C NMR (CD_3COCD_3, 100.62 MHz) (data for monomer): δ 165.4 (s), 155.6 (s), 155.1 (s), 133.4 (s), 129.9 (d), 126.5 (d), 113.5 (d), 113.2 (d), 111.1 (s), 102.8 (d), 56.7 (q), 40.1 (t), 39.4 (t), 20.5 (t) ppm. IR: ν 3500−3100 (br, N−H and O−H), 2429 (s, C−H), 2818 (w, C−H), 1658 (s, C═O and C═N), 1526 (s), 1484 (s), 1216 (s), 1051 (m), 739 (m) cm^{-1}. HRMS (ESI$^+$) calcd for $C_{28}H_{32}N_6NaO_6S_2$ ([M + H]$^+$), 635.1722, found 635.1717.

(2*E*,2′*E*)-*N*,*N*′-[2,2′-Disulfanediylbis(ethane-2,1-diyl)]bis[3-(5-(benzyloxy)-1*H*-indol-3-yl)-2-(hydroxyimino)propanamide] (4g). In accordance with the general procedure for the cleavage of trityl groups, **14g** (0.10 g, 0.08 mmol) gave, after purification by column chromatography, disulfide **4g** (0.02 g, 20% in two steps) as a yellow oil. ^{1}H NMR (CD_3COCD_3, 400.13 MHz) (data for monomer): δ 10.95 (s, 1H, OH), 9.83 (br, 1H, NH), 7.52 (d, J = 6.6 Hz, 1H), 7.51 (d, J = 7.4 Hz, 2H, ArH), 7.45 (d, J = 2.3 Hz, 1H, H4′), 7.38 (t, J = 7.4 Hz, 2H, ArH), 7.30 (t, J = 7.4 Hz, 1H, ArH), 7.22 (d, J = 8.7 Hz, 1H, H7′), 7.14 (d, J = 2.1 Hz, 1H, H2′), 6.80 (dd, J = 8.7, 2.4 Hz, 1H, H6′), 5.09 (s, 2H, CH_2Ph), 4.02 (s, 2H, 2H3), 3.52 (q, J = 6.6 Hz, 2H, NHC$\underline{H}_2$), 2.81 (t, J = 6.6 Hz, 2H, CH_2S) ppm. ^{13}C NMR (CD_3COCD_3, 100.62 MHz) (data of monomer): δ 165.4 (s), 155.1 (s), 154.7 (s), 140.2 (s), 133.7 (s), 130.2 (d, 2×), 129.9 (s), 129.5 (d, 2×), 129.4 (d), 126.7 (d), 113.8 (d), 113.6 (d), 111.2 (s), 104.5 (d), 72.1 (t), 40.1 (t), 39.4 (t), 20.6 (t) ppm. IR: ν 3500−3000 (br, N−H and O−H), 3058 (w, C−H), 2926 (s, C−H), 2864 (w, C−H), 1660 (s, C═O and C═N), 1527 (s), 1477 (s), 1456 (s), 1213 (s), 1016 (s), 796 (m), 753 (s), 703 (m) cm^{-1}. HRMS (ESI$^+$) calcd for $C_{40}H_{41}N_6O_6S_2$ ([M + H]$^+$), 765.2523, found 765.2498.

(2*E*,2′*E*)-*N*,*N*′-[2,2′-Disulfanediylbis(ethane-2,1-diyl)]bis[3-(4-bromo-1*H*-indol-3-yl)-2-(hydroxyimino)propanamide] (4h). In accordance with the general procedure for the cleavage of trityl groups, **14h** (0.09 g, 0.08 mmol) gave, after purification by column chromatography (SiO_2, 95:5 CH_2Cl_2/MeOH), disulfide **4h** (0.04 g, 81%) as a brown oil. ^{1}H NMR (CD_3COCD_3, 400.13 MHz) (data for monomer): δ 10.95 (br, 1H), 10.29 (br, 1H), 7.74 (s, 1H, ArH), 7.34 (dd, J = 7.9, 3.9 Hz, 1H, ArH), 7.19 (dd, J = 7.2, 3.9 Hz, 1H, ArH), 7.0−6.9 (m, 2H, ArH), 4.43 (s, 2H, 2H3), 3.7−3.5 (m, 2H, 2H1″), 3.0−2.8 (m, 2H, 2H2″) ppm. ^{13}C NMR (CD_3COCD_3, 100.62 MHz) (data for monomer): δ 165.5 (s), 155.1 (s), 140.0 (s), 127.1 (s), 125.7 (d), 124.9 (d), 124.1 (d), 115.4 (s), 112.9 (d), 112.1 (s), 40.2 (t), 39.6 (t), 22.9 (t) ppm. IR: ν 3500−3100 (br, N−H and O−H), 3020 (m, C−H), 2927 (w, C−H), 1709 (m, C═O), 1663 (s, C═N), 1528 (s), 1426 (s), 1361 (m), 1218 (s), 760 (s) cm^{-1}. HRMS (ESI$^+$) calcd for $C_{26}H_{27}{}^{81}Br_2N_6O_4S_2$, $C_{26}H_{27}{}^{79}Br^{81}BrN_6O_4S_2$, and $C_{26}H_{27}{}^{79}Br_2N_6O_4S_2$ ([M + H]$^+$), 712.9855, 710.9876, and 708.9896; found, 712.9845, 710.9864, and 708.9884.

(2*E*,2′*E*)-*N*,*N*′-[2,2′-Disulfanediylbis(ethane-2,1-diyl)]bis[3-(6-bromo-1*H*-indol-3-yl)-2-(hydroxyimino)propanamide] (4i). In accordance with the general procedure for the cleavage of trityl groups, **14i** (0.10 g, 0.08 mmol) gave, after purification by column chromatography (SiO_2, 95:5 CH_2Cl_2/MeOH), disulfide **4i** (0.03 g, 54%) as a brown oil. ^{1}H NMR (CD_3COCD_3, 400.13 MHz) (data for monomer): δ 11.02 (br s, 1H), 10.18 (br s, 1H), 7.73 (d, J = 8.5 Hz, 1H, H4′), 7.55 (d, J = 1.8 Hz, 1H, H7′), 7.23 (s, 1H, H2′), 7.14 (dd, J = 8.5, 1.8 Hz, 1H, H5′), 4.05 (s, 2H, 2H3), 3.55 (q, J = 6.5 Hz, 2H, 2H1″), 2.85 (t, J = 6.7 Hz, 2H, 2H2″) ppm. ^{13}C NMR (CD_3COCD_3, 100.62 MHz) (data for monomer): δ 165.3 (s), 154.7 (s), 139.1 (s), 128.5 (s), 127.0 (d), 123.4 (d), 122.6 (d), 116.2 (s), 115.8 (d), 111.8 (s), 40.1 (t), 39.4 (t), 20.3 (t) ppm. IR: ν 3500−3100 (br, N−H and OH), 3065 (w, C−H), 2925 (w, C−H), 1703 (s, C═O), 1661 (s, C═N), 1528 (s), 1454 (s), 1361 (m), 1226 (m), 1048 (m), 807 (m) cm^{-1}. HRMS (ESI$^+$) calcd for $C_{26}H_{27}{}^{81}Br_2N_6O_4S_2$, $C_{26}H_{27}{}^{79}Br^{81}BrN_6O_4S_2$, and $C_{26}H_{27}{}^{79}Br_2N_6O_4S_2$ ([M + H]$^+$), 712.9855, 710.9876, and 708.9896; found, 712.9852, 710.9870, and 708.9890.

(2*E*,2′*E*)-*N*,*N*′-[2,2′-Disulfanediylbis(ethane-2,1-diyl)]bis[3-(7-bromo-1*H*-indol-3-yl)-2-(hydroxyimino)propanamide] (4j). In accordance with the general procedure for the cleavage of trityl groups, **14j** (0.07 g, 0.06 mmol) gave, after purification by column chromatography (SiO_2, 95:5 CH_2Cl_2/MeOH), disulfide **4j** (0.02 g, 60%) as a brown oil. ^{1}H NMR (CD_3COCD_3, 400.13 MHz) (data for monomer): δ 10.92 (br, 1H), 10.08 (br, 1H), 7.70 (d, J = 7.8 Hz, 1H, ArH), 7.47 (t, J = 5.7 Hz, 1H, CONH), 7.19 (s, 1H, ArH), 7.18 (d, J = 7.8 Hz, 1H, ArH), 6.85 (t, J = 7.8 Hz, 1H, H5′), 3.96 (s, 2H, 2H3), 3.45 (q, J = 6.5 Hz, 2H, 2H1″), 2.74 (t, J = 6.8 Hz, 2H, 2H2″) ppm. ^{13}C NMR (CD_3COCD_3, 100.62 MHz) (data for monomer): δ 165.3 (s), 154.7 (s), 136.5 (s), 131.1 (s), 127.1 (d), 125.6 (d), 121.8 (d), 120.6 (d), 113.0 (s), 105.9 (s), 40.1 (t), 39.5 (t), 20.6 (t) ppm. IR: ν 3500−3100 (br, N−H and OH), 3063 (w, C−H), 2933 (m, C−H), 2860 (w, C−H), 1661 (s, C═O and C═N), 1528 (s), 1433 (s), 1340 (m), 1203 (m), 1015 (m), 837 (m), 787 (m) cm^{-1}. HRMS (ESI$^+$) calcd for $C_{26}H_{27}{}^{81}Br_2N_6O_4S_2$, $C_{26}H_{27}{}^{79}Br^{81}BrN_6O_4S_2$, and $C_{26}H_{27}{}^{79}Br_2N_6O_4S_2$ ([M + H]$^+$), 712.9855, 710.9876, and 708.9896; found, 712.9839, 710.9860, and 708.9882.

(2*E*,2′*E*)-*N*,*N*′-[2,2′-Disulfanediylbis(ethane-2,1-diyl)]bis[3-(5-bromo-1-methyl-1*H*-indol-3-yl)-2-(hydroxyimino)-propanamide] (4k). In accordance with the general procedure described for the cleavage of trityl groups, **14k** (0.12 g, 0.10 mmol) gave, after purification by column chromatography (SiO_2, 95:5 CH_2Cl_2/MeOH), disulfide **4k** (0.07 g, 91%) as a white solid. ^{1}H NMR (CD_3COCD_3, 400.13 MHz) (data for monomer): δ 11.04 (s, 1H, NOH), 7.94 (d, J = 1.7 Hz, 1H, H4′), 7.55 (t, J = 5.3 Hz, 1H, CONH), 7.26 (d, J = 8.7 Hz, 1H, H6′), 7.21 (dd, J = 8.7, 1.7 Hz, 1H, H7′), 7.12 (s, 1H, H2′), 3.98 (s, 2H, 2H3), 3.53 (q, J = 6.6 Hz, 2H, 2H1″), 2.84 (s, 3H, NCH_3), 2.84 (t, J = 6.6 Hz, 2H, 2H2″) ppm. ^{13}C NMR (CD_3COCD_3, 100.61 MHz) (data for monomer): δ 165.2 (s), 154.6 (s), 137.4 (s), 131.9 (d), 131.5 (s), 125.5 (d), 123.8 (d), 113.5 (s), 112.9 (d), 110.4 (s), 40.1 (t), 39.4 (t), 33.8 (q), 20.2 (t) ppm. IR: ν 3500−3100 (br, O−H), 2924 (w, C−H), 1658 (s, C═N and C═O), 1527 (s), 1475 (s), 1422 (m), 1218 (s), 772 (s) cm^{-1}. HRMS (ESI$^+$) calcd for $C_{28}H_{30}{}^{81}Br_2N_6O_4S_2Na$, $C_{28}H_{30}{}^{81}Br^{79}BrN_6O_4S_2Na$, and $C_{28}H_{30}{}^{79}Br_2N_6O_4S_2Na$ ([M + Na]$^+$) 762.9988, 761.0008, and 759.0029; found, 762.9994, 761.0016, and 759.0042.

(2*E*,2′*E*)-*N*,*N*′-[2,2′-Disulfanediylbis(ethane-2,1-diyl)]bis[3-(5-bromo-1-[4-bromobenzyl]-1*H*-indol-3-yl)-2-(hydroxyimino)-propanamide] (4l). In accordance with the general procedure described for the cleavage of trityl groups, **14l** (0.14 g, 0.10 mmol) gave, after purification by column chromatography (SiO_2, 95:5 CH_2Cl_2/MeOH), disulfide **4l** (0.06 g, 59%) as a white foam. ^{1}H NMR (CD_3COCD_3, 400.13 MHz) (data for monomer): δ 7.97 (d, J = 1.8 Hz, 1H, H4′), 7.59 (t, J = 5.9 Hz, 1H, CONH), 7.45 (d, J = 8.5 Hz, 2H, ArH), 7.30 (s, 1H, H2′), 7.26 (d, J = 8.7 Hz, 1H, H7′), 7.17 (dd, J = 8.7, 1.9 Hz, 1H, H6′), 7.08 (d, J = 8.5 Hz, 2H, ArH), 5.34 (s, 2H, NCH_2Ar), 4.01 (s, 2H, 2H3), 3.53 (q, J = 6.6 Hz, 2H, 2H1″), 2.87 (s, 1H, NOH), 2.82 (t, J = 6.6 Hz, 2H, 2H2″) ppm. ^{13}C NMR (CD_3COCD_3, 100.61 MHz) (data for monomer): δ 165.2 (s), 154.4 (s), 139.4 (s), 136.8 (s), 133.5 (d, 2×), 131.9 (s), 131.4 (d), 130.8 (d, 2×), 125.8 (d), 124.0 (d), 122.7 (s), 113.9 (s), 113.5 (d), 111.3 (s), 50.6 (t), 40.1 (t), 39.3 (t), 20.2 (t) ppm. IR: ν 3500−3100 (br, O−H), 2922 (w, C−H), 1656 (s, C═N and C═O), 1525 (s), 1463 (m), 1010 (s), 786 (s), 717 (s) cm^{-1}. HRMS (ESI$^+$) calcd for $C_{40}H_{36}{}^{81}Br_4N_6O_4S_2Na$, $C_{40}H_{36}{}^{81}Br_2{}^{79}Br_2N_6O_4S_2Na$, and $C_{40}H_{36}{}^{79}Br_4N_6O_4S_2Na$ ([M + Na]$^+$) 1072.8813, 1070.8829, and 1068.8849; found, 1072.8812, 1070.8828, and 1068.8846.

(2*E*,2′*E*)-*N*,*N*′-[3,3′-Disulfanediylbis(propane-3,1-diyl)]bis[3-(5-bromo-1*H*-indol-3-yl)-2-(hydroxyimino)propanamide] (4m). In accordance with the general procedure described for the cleavage of the trityl group, **14m** (0.07 g, 0.05 mmol) gave, after purification by column chromatography (SiO_2, 95:5 CH_2Cl_2/MeOH), disulfide **4m** (0.01 g, 19% two steps) as a yellow oil. ^{1}H NMR (CD_3COCD_3, 400.13 MHz) (data for monomer): δ 10.28 (br, 1H, OH), 7.96 (s, J = 1.8 Hz, 1H, H4′), 7.51 (t, J = 4.9 Hz, 1H, NH), 7.31 (d, J = 8.6 Hz, 1H, H7′), 7.25 (s, 1H, H2′), 7.16 (dd, J = 8.6, 1.8 Hz, 1H, H6′), 4.03 (s, 2H, 2H3), 3.34 (q, J = 7.0 Hz, 2H, 2H1″), 2.63 (t, J = 7.0 Hz, 2H, 2H3″), 1.85 (quint, J = 7.0 Hz, 2H, 2H2″) ppm. ^{13}C NMR (CD_3COCD_3, 100.62 MHz) (data for monomer): δ 165.4 (s), 155.0 (s), 137.0 (s), 131.3 (s), 127.6 (d), 125.6 (d), 123.6 (d), 114.9 (d), 113.5 (s), 111.4 (s), 39.6 (t), 37.5 (t), 31.1 (t), 20.4 (t) ppm. IR: ν 3500−3100 (br, N−H and O−H), 3060 (w, C−H), 2927 (w, C−H), 1701 (m, C═O), 1656 (s, C═N), 1626 (m, C═N), 1530 (s), 1446 (s), 1423 (s), 1363 (m), 1207 (m), 1094 (w), 1039 (w), 987 (m), 881 (s), 792 (s) cm^{-1}. HRMS (ESI$^+$) calcd for $C_{28}H_{30}{}^{81}Br_2N_6O_4S_2$, $C_{28}H_{30}{}^{81}Br^{79}BrN_6O_4S_2$, and $C_{28}H_{30}{}^{79}Br_2N_6O_4S_2$ ([M + Na]$^+$) 762.9992, 761.0010, 759.0029; found, 762.9985, 761.0031, and 759.0007.

(2*E*,2′*E*)-*N*,*N*′-[4,4′-Disulfanediylbis(butane-4,1-diyl)]bis[3-(5-bromo-1*H*-indol-3-yl)-2-(hydroxyimino)propanamide] (4n). In accordance with the general procedure described for cleavage of the trityl group, **14n** (0.09 g, 0.08 mmol) gave, after purification by column chromatography (SiO_2, 95:5 CH_2Cl_2/MeOH), disulfide **4n** (0.03 g, 42% two steps) as a yellow oil. ^{1}H NMR (CD_3COCD_3, 400.13 MHz) (data for monomer): δ 10.22 (br, 1H, OH), 7.93 (d, J = 1.8 Hz, 1H, H4′), 7.40 (br, 1H, NH), 7.27 (d, J = 8.6 Hz, 1H, H7′), 7.21 (d, J = 1.3 Hz, 1H, H2′), 7.11 (dd, J = 8.6, 1.8 Hz, 1H, H6′), 4.00 (s, 2H, 2H3), 3.23 (q, J = 6.4 Hz, 2H, 2H1″), 2.59 (t, J = 6.4 Hz, 2H, 2H4″), 1.6−1.5 (m, 4H, 2H2″ + 2H3″) ppm. ^{13}C NMR (CD_3COCD_3, 100.62 MHz) (data for monomer): δ 165.3 (s), 155.0 (s), 136.9 (s), 131.3 (s), 127.7 (d), 125.6 (d), 123.6 (d), 114.8 (d), 113.5 (s), 111.4 (s), 40.2 (t), 39.9 (t), 30.1 (t), 28.1 (t), 20.4 (t) ppm. IR: ν 3500−3100 (br, N−H and O−H), 3058 (w, C−H), 2930 (w, C−H), 1702 (m, C═O), 1656 (s, C═N), 1626 (m, C═N), 1530 (s), 1448 (s), 1423 (s), 1362 (m), 1226 (m), 1205 (m), 993 (s), 881 (s), 792 (s) cm^{-1}. HRMS (ESI$^+$) calcd for $C_{30}H_{34}{}^{81}Br_2N_6O_4S_2$, $C_{30}H_{34}{}^{81}Br^{79}BrN_6O_4S_2$, and $C_{30}H_{34}{}^{79}Br_2N_6O_4S_2$ ([M + H]$^+$) 791.0306, 789.0323, and 787.0342; found, 791.0255, 789.0318, and 787.0346.

(2*E*,2′*E*)-*N*,*N*′-[5,5′-Disulfanediylbis(pentane-5,1-diyl)]bis[3-(5-bromo-1*H*-indol-3-yl)-2-(hydroxyimino)propanamide] (4o). In accordance with the general procedure described for cleavage of the trityl group, **14o** (0.08 g, 0.07 mmol) gave, after purification by column chromatography (SiO_2, 95:5 CH_2Cl_2/MeOH), disulfide **4o** (0.03 g, 38% two steps) as a yellow oil. ^{1}H NMR (CD_3COCD_3, 400.13 MHz) (data for monomer): δ 10.27 (br, 1H, OH), 7.97 (s, 1H, H4′), 7.38 (t, J = 5.4 Hz, 1H, NH), 7.31 (d, J = 8.6 Hz, 1H, H7′), 7.25 (s, 1H, H2′), 7.17 (dd, J = 8.6, 1.6 Hz, 1H, H6′), 4.03 (s, 2H, 2H3), 3.24 (q, J = 6.6 Hz, 2H, 2H1″), 2.63 (t, J = 7.2 Hz, 2H, 2H5″), 1.63 (quint, J = 7.2 Hz, 2H, $-CH_2$), 1.50 (quint, J = 7.2 Hz, 2H, $-CH_2$), 1.34 (quint, J = 7.2 Hz, 2H, $-CH_2$) ppm. ^{13}C NMR (CD_3COCD_3, 100.62 MHz) (data for monomer): δ 165.2 (s), 155.0 (s), 136.9 (s), 131.3 (s), 127.7 (d), 125.6 (d), 123.6 (d), 114.8 (d), 113.5 (s), 111.4 (s), 40.6 (t), 40.1 (t), 30.9 (t), 30.4 (t), 27.3 (t), 20.4 (t) ppm. IR: ν 3500−3100 (br, N−H and O−H), 2929 (w, C−H), 2858 (w, C−H), 1703 (s, C═O), 1656 (s, C═N), 1627 (m, C═N), 1531 (s), 1456 (s), 1423 (s), 1362 (s), 1227 (s), 1092 (m), 1040 (m), 992 (s), 881 (s), 792 (s) cm^{-1}. HRMS (ESI$^+$) calcd for $C_{32}H_{39}{}^{81}Br_2N_6O_4S_2$, $C_{32}H_{39}{}^{81}Br^{79}BrN_6O_4S_2$, and $C_{32}H_{39}{}^{79}Br_2N_6O_4S_2$ ([M + H]$^+$) 797.0801, 795.0817, and 793.0835; found, 797.0746, 795.0812, and 793.0800.

(2*E*,2′*E*)-*N*,*N*′-(Hexane-1,6-diyl)bis[3-(5-bromo-1*H*-indol-3-yl)-2-(hydroxyimino)propanamide] (4p). In accordance with the general procedure described for the cleavage of trityl groups, **14p** (0.10 g, 0.09 mmol) gave, after purification by column chromatography (SiO_2, 97:3 CH_2Cl_2/MeOH), disulfide **4p** (0.06 g, 98%) as a yellow solid, mp 240−214 °C (dec) (MeOH/EtOAc). ^{1}H NMR (CD_3COCD_3, 400.13 MHz) (data for monomer): δ 10.96 (br s, 1H), 10.25 (br, 1H), 7.95 (br, 1H, ArH), 7.29 (dd, J = 8.6, 1.9 Hz, 1H, H6′), 7.24 (br, 1H, ArH), 7.16 (d, J = 8.6 Hz, 1H, H7′), 4.04 (s, 2H, 2H3), 3.3−3.2 (m, 2H, 2H1″), 1.3−1.2 (m, 2H), 1.2−1.1 (m, 2H) ppm. ^{13}C NMR (DMSO-d_6, 100.62 MHz): δ 163.3 (s), 152.5 (s), 134.5 (s), 128.8 (s), 125.5 (d), 123.2 (d), 121.0 (d), 113.2 (d), 110.9 (s), 108.7 (s), 38.5 (t), 28.9 (t), 25.9 (t), 18.8 (t) ppm. IR: ν 3500−3000 (br, N−H and O−H), 2930 (m, C−H), 2858 (w, C−H), 1668 (s, C═O and C═N), 1539 (m), 1456 (m), 1206 (s), 1143 (m), 799 (w) cm^{-1}. HRMS (ESI$^+$) calcd for $C_{28}H_{30}{}^{81}Br_2N_6O_4Na$, $C_{28}H_{30}{}^{79}Br^{81}BrN_6O_4Na$, and $C_{28}H_{30}{}^{79}Br_2N_6O_4Na$ ([M + Na]$^+$), 699.0552, 697.0573, and 695.0593; found, 699.0556, 697.0568, and 695.0584.

(*E*)-3-(5-Bromo-1*H*-indol-3-yl)-2-(hydroxyimino)-*N*-(2-methoxyethyl)propanamide (4q). In accordance with the general procedure described for the cleavage of trityl groups, **14q** (0.05 g, 0.09 mmol) gave, after purification by column chromatography (SiO_2, 97:3 CH_2Cl_2/MeOH), disulfide **4q** (0.02 g, 71%) as a colorless oil. ^{1}H NMR (CD_3OD, 400.13 MHz): δ 7.85 (d, J = 1.8 Hz, 1H, H4′), 7.20 (d, J = 8.6 Hz, 1H, H7′), 7.13 (dd, J = 8.6, 1.8 Hz, 1H, H6′), 7.11 (s, 1H, H2′), 3.98 (s, 2H, 2H3), 3.4−3.3 (m, 4H, 2H1″+ 2H2″), 3.27 (s, 3H, OCH_3) ppm. ^{13}C NMR (CD_3OD, 100.62 MHz): δ 166.2 (s), 153.6 (s), 136.4 (s), 130.4 (s), 126.5 (d), 124.9 (d), 122.7 (d), 113.7 (d), 112.9 (s), 110.3 (s), 71.9 (t), 58.9 (q), 40.0 (t), 19.7 (t) ppm. IR: ν 3500−3100 (br, N−H and O−H), 3057 (w, C−H), 2928 (w, C−H), 2877 (w, C−H), 1659 (s, C═O and C═N), 1533 (s), 1453 (m), 1200 (m), 1097 (m), 994 (m), 876 (m) cm^{-1}. MS (FAB$^+$): m/z (%) 357 ([M + 1]$^+$ [^{81}Br], 19), 356 ([M]$^+$ [^{81}Br], 90), 355 ([M + 1]$^+$ [^{79}Br], 33), 354 ([M]$^+$ [^{79}Br], 100), 338 (24), 233 (31), 210 (24), 208 (24). HRMS (FAB$^+$) calcd for $C_{14}H_{17}{}^{81}BrN_3O_3$ and $C_{14}H_{19}{}^{79}BrN_3O_3$ ([M + 1]$^+$), 356.0433 and 354.0453; found, 356.0442 and 354.0461.

(*E*)-3-(5-Bromo-1*H*-indol-3-yl)-*N*-(2-hydroxyethyl)-2-(hydroxyimino)propanamide (4r). A solution of **14r** (0.06 g, 0.09

mmol) in a 6:3:1 THF/HCO_2H/H_2O mixture was stirred for 19 h. Water was added, and the reaction mixture was extracted with EtOAc. The organic extracts were washed with brine and dried over Na_2SO_4. The solvent was removed in vacuo to yield a yellow oil. The residue was dissolved in a 20:1 CH_2Cl_2/MeOH mixture (0.6 mL), placed in a Schlenk flask, and anhydrous HCl (0.63 mmol of a 1.0 M ether solution) was added. The solution was then stirred at 25 °C for 1 h. The mixture was diluted with 1:1 MeOH/H_2O mixture and washed with hexane. The MeOH was removed in vacuo, and the aqueous layer was extracted with EtOAc. The combined organic extracts were dried over Na_2SO_4 and filtered, and the solvent was removed in vacuo. The residue was subjected to column chromatography (SiO_2, 95:5 CH_2Cl_2/MeOH) to afford amide **4r** (0.02 g, 59%) as a colorless oil. ^{1}H NMR (CD_3COCD_3, 400.13 MHz): δ 11.02 (s, 1H), 10.17 (br, 1H), 7.79 (d, J = 7.9 Hz, 1H, ArH), 7.57 (t, J = 5.3 Hz, 1H, CONH), 7.28 (s, 1H, ArH), 7.27 (d, J = 7.4 Hz, 1H, ArH), 6.95 (t, J = 7.8 Hz, 1H, ArH), 4.05 (s, 2H), 3.54 (q, J = 6.5 Hz, 2H, 2H2″), 2.84 (t, J = 6.7 Hz, 2H, 2H1″) ppm. ^{13}C NMR (CD_3COCD_3, 100.62 MHz): δ 165.3 (s), 154.7 (s), 136.9 (s), 131.3 (s), 127.7 (d), 125.6 (d), 123.6 (d), 114.8 (d), 113.4 (s), 111.4 (s), 62.6 (t), 43.6 (t), 20.2 (t) ppm. IR: ν 3500−3100 (br, N−H and O−H), 3069 (w, C−H), 2931 (w, C−H), 2884 (w, C−H), 1702 (m, C═O or C═N), 1657 (s, C═O or C═N), 1534 (s), 1459 (s), 1227 (m), 1064 (m), 1041 (m), 883 (w), 794 (m) cm^{-1}. MS (FAB$^+$): m/z (%) 342 ([M + 1]$^+$ [^{81}Br], 87), 341 ([M]$^+$ [^{81}Br], 55), 340 ([M + 1]$^+$ [^{79}Br], 100), 339 ([M]$^+$ [^{79}Br], 40), 257 (23), 255 (23), 237 (30), 236 (38), 235 (36), 234 (35), 210 (44), 208 (46), 173 (41), 159 (25), 157 (24), 156 (33), 155 (30), 154 (33). HRMS (FAB$^+$) calcd for $C_{13}H_{14}{}^{81}BrN_3O_3$ and $C_{13}H_{14}{}^{79}BrN_3O_3$ ([M]$^+$), 341.0198 and 339.0219; found, 341.0214 and 339.0218.

(*E*)-3-(5-Bromo-1*H*-indol-3-yl)-2-(hydroxyimino)-*N*-[2-(methylthio)ethyl]propanamide (4s). $NaBH_4$ (2 mg, 0.06 mmol) was added to a solution of **4a** (0.01 g, 0.01 mmol) and NaOH (2 mg, 0.05 mmol) in dry MeOH (0.1 mL) at room temperature. The reaction mixture was stirred for 0.5 h, and then MeI (0.01 mL, 0.11 mmol) was added. After 16 h, the methanol was evaporated and the residue dissolved in CH_2Cl_2, washed with water, and dried with Na_2SO_4. The solvent was removed in vacuo and the residue was purified by column chromatography (SiO_2, 97:3 CH_2Cl_2/MeOH) to afford 8 mg (80%) of **4s** as a yellow oil. ^{1}H NMR (CD_3COCD_3, 400.13 MHz): δ 11.00 (br, 1H), 10.22 (br, 1H), 7.97 (d, J = 1.8 Hz, 1H, H4′), 7.48 (br, 1H, CONH), 7.31 (d, J = 8.6 Hz, 1H, H7′), 7.25 (d, J = 2.2 Hz, 1H, H2′), 7.17 (dd, J = 8.6, 1.8 Hz, 1H, H6′), 4.02 (s, 2H, 2H3), 3.45 (q, J = 6.4 Hz, 2H, 2H1″), 2.61 (t, J = 7.0 Hz, 2H, 2H2″), 2.06 (s, 3H, SCH_3) ppm. ^{13}C NMR (CD_3COCD_3, 100.62 MHz): δ 165.0 (s), 154.7 (s), 136.9 (s), 131.3 (s), 127.7 (d), 125.5 (d), 123.6 (d), 114.8 (d), 113.4 (s), 111.4 (s), 39.9 (t), 34.9 (t), 20.3 (t), 15.9 (q) ppm. IR: ν 3500−3100 (br, N−H and O−H), 3064 (w, C−H), 2921 (m, C−H), 1661 (s, C═O and C═N), 1529 (s), 1453 (s), 1225 (m), 1036 (m), 998 (m), 793 (m) cm^{-1}. MS (FAB$^+$): m/z (%) 372 ([M + 1]$^+$ [^{81}Br], 92), 371 ([M]$^+$ [^{81}Br], 62), 370 ([M + 1]$^+$ [^{79}Br], 100), 369 ([M]$^+$ [^{79}Br], 43), 322 (39), 236 (31), 235 (23), 234 (30), 210 (33), 208 (34), 165 (29), 161 (30), 159 (32), 155 (45), 154 (79). HRMS (FAB$^+$) calcd for $C_{14}H_{16}{}^{81}BrN_3O_2S$ and $C_{14}H_{16}{}^{79}BrN_3O_2S$ ([M]$^+$), 371.0126 and 369.0147; found, 371.0125 and 369.0150.

(*E*)-Ethyl 3-(5-Bromo-1*H*-indol-3-yl)-2-(methoxyimino)-propanoate (15a). Silver(I) oxide (0.04 g, 0.17 mmol) and iodomethane (0.15 mL, 2.40 mmol) were added to a solution of ester **9a** (0.05 g, 0.15 mmol) in acetone (0.5 mL). After being stirred at room temperature for 14 h, the solution was filtered through a pad of Celite and the solvent was evaporated. The residue was purified by column chromatography (SiO_2, 75:25 hexane/EtOAc) to afford indole **15a** (0.02 g, 42%) as a colorless oil. ^{1}H NMR (CD_3COCD_3, 400.13 MHz): δ 10.28 (br, 1H, NH), 7.81 (d, J = 1.9 Hz, 1H, H4′), 7.34 (d, J = 8.6 Hz, 1H, H7′), 7.23 (d, J = 2.4 Hz, 1H, H2′), 7.20 (dd, J = 8.6, 1.9 Hz, 1H, H6′), 4.20 (q, J = 7.1 Hz, 2H, $CO_2C\underline{H}_2CH_3$), 4.08 (s, 3H, $NOCH_3$), 3.98 (s, 2H, 2H3), 1.24 (t, J = 7.1 Hz, 3H, $CO_2CH_2C\underline{H}_3$) ppm. ^{13}C NMR (CD_3COCD_3, 100.62 MHz): δ 165.1 (s), 152.7 (s), 137.0 (s), 131.0 (s), 127.5 (d), 125.8 (d), 123.2 (d), 115.0 (d), 113.6 (s), 110.6 (s), 64.3 (q), 63.0 (t), 22.4 (t), 15.4 (q) ppm. IR: ν 3500−3100 (br, NH), 2980 (w, C−H), 2938 (w, C−H), 1719 (s, C═O and C═N), 1458 (m), 1323 (m), 1205 (m), 1116 (m), 1046 (s), 793 (m) cm^{-1}. MS (FAB$^+$): m/z (%) 341 ([M + 1]$^+$ [^{81}Br], 92), 340 ([M]$^+$ [^{81}Br], 96), 339 ([M + 1]$^+$ [^{79}Br], 100), 338 ([M]$^+$ [^{79}Br], 84), 238 (17), 236 (28), 235 (29), 233 (26), 210 (82), 209 (16), 208 (81). HRMS (FAB$^+$) calcd for $C_{14}H_{15}{}^{81}BrN_2O_3$ and $C_{14}H_{15}{}^{79}BrN_2O_3$ ([M]$^+$), 340.0246 and 338.0266; found, 340.0277 and 338.0277.

(*E*)-Ethyl 2-(Benzyloxyimino)-3-(5-bromo-1*H*-indol-3-yl)-propanoate (15b). To a solution of oxime **9a** (0.10 g, 0.31 mmol) and potassium *tert*-butoxide (0.04 g, 0.38 mmol) in 1,2-dimethoxyethane (DME) (6 mL) was added a solution of benzyl bromide (0.05 mL, 0.43 mmol) in DME (2 mL). The mixture was stirred for 15 h at room temperature, and the solvent was removed under reduced pressure. A solution of the residue in CH_2Cl_2 was washed successively with 10% HCl and brine and subsequently dried over Na_2SO_4. The residue was subjected to column chromatography (SiO_2, 70:30 hexane/EtOAc) to give the *O*-benzyloxime **15b** (0.09 g, 72%) as a yellow oil. ^{1}H NMR ($CDCl_3$, 400.13 MHz): δ 8.07 (br, 1H, NH), 7.83 (s, 1H, ArH), 7.5−7.3 (m, 5H, ArH), 7.3−7.2 (m, 1H, ArH), 7.17 (d, J = 8.5 Hz, 1H, ArH), 7.02 (s, 1H, ArH), 5.36 (s, 2H, OCH_2Ph), 4.28 (q, J = 7.0 Hz, 2H, $CO_2C\underline{H}_2CH_3$), 4.01 (s, 2H, 2H3), 1.31 (t, J = 7.1 Hz, 3H, $CO_2CH_2C\underline{H}_3$) ppm. ^{13}C NMR ($CDCl_3$, 100.62 MHz): δ 163.4 (s), 151.0 (s), 136.2 (s), 134.4 (s), 128.9 (s), 128.7 (d, 2×), 128.6 (d, 2×), 128.3 (d), 124.8 (d), 124.6 (d), 121.9 (d), 112.8 (s), 112.4 (d), 109.5 (s), 77.9 (t), 61.9 (t), 21.1 (t), 14.1 (q) ppm. IR: ν 3500−3100 (br, N−H), 3031 (w, C−H), 2982 (w, C−H), 2935 (w, C−H), 1718 (s, C═O and C═N), 1454 (s), 1323 (m), 1199 (s), 1012 (s), 772 (s) cm^{-1}. MS (FAB$^+$): m/z (%) 417 ([M + 1]$^+$ [^{81}Br], 95), 416 ([M]$^+$ [^{81}Br], 90), 415 ([M + 1]$^+$ [^{79}Br], 100), 414 ([M]$^+$ [^{79}Br], 72), 325 (24), 323 (24), 309 (26), 307 (34), 210 (46), 208 (46), 155 (23), 154 (63). HRMS (FAB$^+$) calcd for $C_{20}H_{19}{}^{81}BrN_2O_3$ and $C_{20}H_{19}{}^{79}BrN_2O_3$ ([M]$^+$), 416.0559 and 414.0579; found, 416.0569 and 414.0575.

(*E*)-3-(5-Bromo-1*H*-indol-3-yl)-2-(methoxyimino)propanoic Acid (16a). According the general procedure described for the hydrolysis of esters, indole **15a** (0.15 g, 0.44 mmol) gave, after crystallization, acid **16a** (0.11 g, 84%) as a yellow solid, mp 154−155 °C (hexane/CH_2Cl_2/MeOH). ^{1}H NMR (CD_3COCD_3, 400.13 MHz): δ 10.28 (br, 1H, NH), 7.84 (d, J = 1.9 Hz, 1H, H4′), 7.34 (d, J = 8.6 Hz, 1H, H7′), 7.23 (d, J = 1.9 Hz, 1H, H2′), 7.20 (dd, J = 8.6, 1.9 Hz, 1H, H6′), 4.08 (s, 3H, $NOC\underline{H}_3$), 3.97 (s, 2H, 2H3) ppm. ^{13}C NMR (CD_3COCD_3, 100.62 MHz): δ 165.6 (s), 152.5 (s), 137.0 (s), 131.1 (s), 127.5 (d), 125.8 (d), 123.3 (d), 115.0 (d), 113.6 (s), 110.6 (s), 64.4 (q), 22.0 (t) ppm. IR: ν 3500−3100 (br, OH) 3410 (s, NH), 2985 (w, C−H), 2933 (w, C−H), 1711 (s, C═O and C═N), 1429 (m), 1211 (w), 1044 (s), 785 (m). MS (FAB$^+$): m/z (%) 313 ([M + 1]$^+$ [^{81}Br], 61), 312 ([M]$^+$ [^{81}Br], 59), 311 ([M + 1]$^+$ [^{79}Br], 62), 310 ([M]$^+$ [^{79}Br], 51), 281 (24), 210 (100), 208 (99), 185 (22), 156 (21). HRMS (FAB$^+$) calcd for $C_{12}H_{11}{}^{81}BrN_2O_3$ and $C_{12}H_{11}{}^{79}BrN_2O_3$ ([M]$^+$), 311.9933 and 309.9953; found, 311.9957 and 309.9966.

(*E*)-2-(Benzyloxyimino)-3-(5-bromo-1*H*-indol-3-yl)propanoic Acid (16b). According to the general procedure described for the hydrolysis of esters, indole **15b** (0.07 g, 0.17 mmol) gave, after crystallization, acid (0.65 g, 99%) as a white solid. ^{1}H NMR (CD_3COCD_3, 400.13 MHz): δ 10.26 (br, 1H), 7.90 (s, 1H), 7.45 (d, J = 7.0 Hz, 2H), 7.4−7.3 (m, 5H), 7.24 (s, 1H), 7.22 (d, J = 8.6 Hz, 1H), 5.35 (s, 2H, OCH_2Ph), 4.06 (s, 2H, 2H3) ppm. ^{13}C NMR (CD_3COCD_3, 100.62 MHz): δ 165.5 (s), 152.7 (s), 138.6 (s), 136.8 (s), 130.9 (s), 130.2 (d, 2×), 130.1 (d, 2×), 129.9 (d), 127.5 (d), 125.7 (d), 123.1 (d), 114.9 (d), 113.6 (s), 110.3 (s), 79.1 (t), 22.1 (t) ppm.

(2*E*,2′*E*)-*N*,*N*′-[2,2′-Disulfanediylbis(ethane-2,1-diyl)]bis[3-(5-bromo-1*H*-indol-3-yl)-2-(methoxyimino)propanamide] (17a). Following the general procedure described for the coupling of acids with amines, acid **16a** (0.11 g, 0.35 mmol) afforded, after purification by column chromatography (SiO_2, 95:5 CH_2Cl_2/MeOH), disulfide **17a** (0.10 g, 77%) as a colorless oil. ^{1}H NMR (CD_3COCD_3, 400.13 MHz) (data for monomer): δ 10.22 (br, 1H, NH), 7.87 (d, J = 1.8 Hz, 1H, H4″), 7.68 (t, J = 5.2 Hz, 1H, CONH), 7.31 (d, J = 8.6 Hz, 1H, H7″), 7.21 (d, J = 2.1 Hz, 1H, H2″), 7.17 (dd, J = 8.6, 1.8 Hz, 1H, H6″), 3.98 (s, 3H, $NOCH_3$), 3.97 (s, 2H, 2H3′), 3.55 (q, J = 6.8 Hz, 2H, 2H1), 2.85 (t, J = 6.8 Hz, 2H, 2H2) ppm. ^{13}C NMR (CD_3COCD_3, 100.62 MHz) (data for monomer): δ 164.6 (s), 154.4 (s), 137.0 (s), 131.2 (s),

127.6 (d), 125.7 (d), 123.5 (d), 114.9 (d), 113.5 (s), 110.9 (s), 64.0 (q), 40.4 (t), 39.3 (t), 21.1 (t) ppm. IR: ν 3500−3100 (br, NH), 3008 (w, C−H), 2976 (w, C−H), 2936 (w, C−H), 1664 (s, C═O and C═N), 1523 (s), 1458 (m), 1218 (m), 1047 (s), 760 (s) cm^{-1}. MS (FAB^+): m/z (%) 741 ($[M + 1]^+$ $[^{81}Br]$, 42), 740 ($[M]^+$ $[^{81}Br]$, 42), 739 ($[M + 1]^+$ $[^{81}Br]$ $[^{79}Br]$, 71), 738 ($[M + 2]^+$ $[^{79}Br]$, 40), 737 ($[M + 1]^+$ $[^{79}Br]$, 39), 708 (12), 707 (19), 664 (42), 663 (100), 662 (60), 648 (28), 647 (57). HRMS (FAB^+) calcd for $C_{28}H_{31}{}^{81}Br_2N_6O_4S_2$, $C_{28}H_{31}{}^{81}Br^{79}BrN_6O_4S_2$, and $C_{28}H_{31}{}^{79}Br_2N_6O_4S_2$ ($[M + 1]^+$), 741.0174, 739.0194, and 737.0215; found, 741.0184, 739.0203, and 737.0237.

(2*E*,2′*E*)-*N*,*N*′-[2,2′-Disulfanediylbis(ethane-2,1-diyl)]bis[2-(benzyloxyimino)-3-(5-bromo-1*H*-indol-3-yl)propanamide] (17b). Following the general procedure described for the coupling of acids with amines, indole **16b** (0.18 g, 0.46 mmol) gave, after purification by column chromatography (SiO_2, 50:50 hexane/EtOAc), disulfide **17b** (0.16 g, 80%) as a yellow oil. ^1H NMR (CD_3COCD_3, 400.13 MHz) (data for monomer): δ 10.23 (br, 1H, NH), 7.88 (d, J = 1.6 Hz, 1H, H4′), 7.71 (t, J = 5.4 Hz, 1H, CONH), 7.4−7.3 (m, 6H, ArH), 7.19 (d, J = 2.2 Hz, 1H, H2′), 7.17 (dd, J = 8.6, 1.9 Hz, 1H, H6′), 5.23 (s, 2H, OCH_2Ph), 4.01 (s, 2H, 2H3), 3.54 (t, J = 6.5 Hz, 2H, 2H1″), 2.9−2.8 (m, 2H, 2H2″) ppm. ^{13}C NMR (CD_3COCD_3, 100.62 MHz) (data for monomer): δ 164.6 (s), 154.8 (s), 139.0 (s), 136.9 (s), 131.2 (s), 130.3 (d, 2×), 130.2 (d, 2×), 129.9 (d), 127.7 (d), 125.7 (d), 123.5 (d), 114.9 (d), 113.6 (s), 110.7 (s), 78.8 (t), 40.4 (t), 39.3 (t), 21.3 (t) ppm. IR: ν 3500−3100 (br, N−H), 3032 (w, C−H), 2930 (w, C−H), 1666 (s, C═O and C═N), 1521 (s), 1455 (s), 1362 (m), 1226 (m), 1207 (m), 1013 (s), 793 (m) cm^{-1}. HRMS (ESI^+) calcd for $C_{40}H_{38}{}^{81}Br_2N_6O_4S_2$, $C_{40}H_{38}{}^{79}Br^{81}BrN_6O_4S_2$, and $C_{40}H_{38}{}^{79}Br_2N_6O_4S_2$ ($[M]^+$), 893.0794, 891.0815, and 889.0835; found, 893.0811, 891.0836, and 889.0841.

Methyl 3-(5-Bromo-1*H*-indol-3-yl)propanoate (18a). Methyl acrylate (0.88 g, 10.20 mmol) and $ZrCl_4$ (0.15 mL, 2.40 mmol) were added to a solution of 5-bromo-1*H*-indole **5a** (1.00 g, 5.10 mmol) in CH_2Cl_2 (0.5 mL). After the mixture was stirred at room temperature for 5 h, water was added and the solution was extracted with EtOAc (3×). The combined organic extracts were dried over Na_2SO_4, filtered, evaporated and the residue was purified by column chromatography (SiO_2, 70:30 hexane/EtOAc) to afford 0.83 g (58%) of ester **18a** as a white solid and 0.07 g (7%) of starting 5-bromo-1*H*-indole. ^1H NMR (CD_3COCD_3, 400.13 MHz): δ 10.18 (br, 1H, NH), 7.75 (d, J = 2.0 Hz, 1H, H4′), 7.35 (d, J = 8.4 Hz, 1H, H7′), 7.21 (s, 1H, H2′), 7.20 (dd, J = 8.4, 2.0 Hz, H6′), 3.61 (s, 3H, CO_2CH_3), 3.04 (t, J = 7.5 Hz, 2H), 2.69 (t, J = 7.5 Hz, 2H) ppm. ^{13}C NMR (CD_3COCD_3, 100.62 MHz): δ 174.8 (s), 137.3 (s), 131.1 (s), 125.7 (d), 125.6 (s), 122.7 (d), 115.8 (s), 115.0 (d), 113.4 (s), 52.6 (q), 39.3 (t), 22.0 (t) ppm. IR: ν 3335 (s, NH), 2950 (w, C−H), 2917 (w, C−H), 2855 (w, C−H) 1712 (s, C═O), 1438 (m), 1382 (m), 1302 (m), 1193 (s), 1170 (s), 981 (m), 882 (m), 791 (s) cm^{-1}. MS (FAB^+): m/z (%) 284 ($[M + 1]^+$ $[^{81}Br]$, 37), 283 ($[M]^+$ $[^{81}Br]$, 94), 282 ($[M + 1]^+$ $[^{79}Br]$, 52), 281 ($[M]^+$ $[^{79}Br]$, 100), 280 (14), 224 (13), 223 (12), 222 (12), 221 (12), 211 (11), 210 (82), 209 (13), 208 (86), 207 (12), 203 (13). HRMS (FAB^+) calcd for $C_{12}H_{12}{}^{81}BrNO_2$ and $C_{12}H_{12}{}^{79}BrNO_2$ ($[M]^+$), 283.0031 and 281.0051; found, 283.0024 and 281.0056.

Methyl 3-(5-Bromo-1-methyl-1*H*-indol-3-yl)propanoate (18b). Following the general procedure, indole **5k** (0.50 g, 2.39 mmol) afforded, after purification by column chromatography (SiO_2, 85:15 hexane/EtOAc), ester **18b** (0.56 g, 79%) as a colorless oil. ^1H NMR (CD_3COCD_3, 400.13 MHz): δ 7.74 (s, 1H, ArH), 7.26 (s, 2H, ArH), 7.06 (s, 1H, ArH), 3.73 (s, 3H, OCH_3), 3.61 (s, 3H, NCH_3), 3.01 (t, J = 7.5 Hz, 2H, CH_2), 2.66 (t, J = 7.5 Hz, 2H, CH_2) ppm. ^{13}C NMR (CD_3COCD_3, 100.61 MHz): δ 174.1 (s), 137.6 (s), 131.2 (s), 130.0 (d), 125.6 (d), 122.8 (d), 114.8 (s), 113.4 (s), 113.0 (d), 52.6 (q), 36.3 (t), 33.8 (q), 21.8 (t) ppm. IR: ν 2949 (w, C−H), 1732 (s, C═O), 1476 (s), 1425 (w), 1422 (w), 1245 (m), 1198 (m), 1155 (s), 1047 (w), 790 (s) cm^{-1}. MS (ESI^+): m/z (%) 298 ($[M + H]^+$ $[^{81}Br]$, 98), 297 ($[M]^+$ $[^{81}Br]$ $[^{79}Br]$, 25), 296 ($[M + H]^+$ $[^{79}Br]$, 100), 223 (31), 221 (30). HRMS (ESI^+) calcd for $C_{13}H_{15}{}^{81}BrNO_2$, $C_{13}H_{15}{}^{79}BrNO_2$ ($[M + H]^+$) 298.0261, 296.0281; found, 298.0254 and 296.0273.

3-(5-Bromo-1*H*-indol-3-yl)propanoic Acid (19a). According to the general procedure described for the hydrolysis of esters, **18a** (0.06 g, 0.20 mmol) gave, after crystallization, acid **19a** (0.05 g, 98%) as a white solid, mp 86−87 °C (hexane/CH_2Cl_2/MeOH). ^1H NMR (CD_3OD, 400.13 MHz): δ 7.66 (d, J = 1.7 Hz, 1H, H4′), 7.24 (d, J = 8.6 Hz, 1H, H7′), 7.16 (dd, J = 8.6, 1.7 Hz, 1H, H7′), 7.08 (s, 1H, H2′), 3.00 (t, J = 7.5 Hz, 2H, CH_2), 2.65 (t, J = 7.5 Hz, 2H, CH_2) ppm. ^{13}C NMR (CD_3OD, 100.62 MHz): δ 177.4 (s), 136.7 (s), 130.3 (s), 125.0 (d), 124.6 (d), 121.8 (d), 114.8 (s), 113.9 (d), 112.7 (s), 36.0 (t), 21.7 (t) ppm. IR: ν 3500−3100 (br, OH and NH), 2923 (w, C−H), 2851 (w, C−H), 1706 (s, C═O), 1623 (s), 1566 (m), 1541 (m), 1450 (s), 1212 (m), 822 (s), 801 (s), 785 (s), 680 (s) cm^{-1}. MS (FAB^+): m/z (%) 270 ($[M + 1]^+$ $[^{81}Br]$, 61), 269 ($[M]^+$ $[^{81}Br]$, 100), 268 ($[M + 1]^+$ $[^{79}Br]$, 70), 267 ($[M]^+$ $[^{79}Br]$, 92), 210 (34), 208 (34). HRMS (FAB^+) calcd for $C_{11}H_{11}{}^{81}BrNO_2$ and $C_{11}H_{11}{}^{79}BrNO_2$ ($[M + 1]^+$), 268.9874 and 266.9895; found, 268.9872 and 266.9886.

3-(5-Bromo-1-methyl-1*H*-indol-3-yl)propanoic Acid (19b). According to the general procedure described for the hydrolysis of esters, **18b** (0.20 g, 0.68 mmol) gave, after crystallization, **19b** (0.18 g, 95%) as a brown solid, mp 157−160 °C (hexane/$CHCl_3$). ^1H NMR (CD_3OD, 400.13 MHz): δ 7.65 (s, 1H, ArH), 7.20 (d, J = 8.6 Hz, 1H, ArH), 7.18 (d, J = 8.6 Hz, 1H, ArH), 6.97 (s, 1H, ArH), 3.69 (s, 3H, NCH_3), 2.98 (t, J = 7.4 Hz, 2H, CH_2), 2.62 (t, J = 7.4 Hz, 2H, CH_2) ppm. ^{13}C NMR (CD_3OD, 100.61 MHz): δ 177.0 (s), 137.3 (s), 130.8 (s), 129.1 (d), 125.2 (d), 122.1 (d), 114.5 (s), 113.0 (s), 111.9 (d), 36.0 (t), 32.8 (q), 21.4 (t) ppm. IR: ν 3500−2500 (br, O−H), 1700 (s, C═O), 1481 (m), 1433 (m), 1402 (m), 1368 (w), 1310 (s), 1201 (s), 907 (m), 788 (s) cm^{-1}. MS (EI^+): m/z (%) 284 ($[M + 1]^+$ $[^{81}Br]$, 3), 283 ($[M]^+$ $[^{81}Br]$, 24), 281 ($[M]^+$ $[^{79}Br]$, 20), 225 ($[M - CH_3 - CO_2 + 1]^+$ $[^{81}Br]^+$, 10), 224 ($[M - CH_3 - CO_2]^+$ $[^{81}Br]^+$,100), 223 ($[M - CH_3 - CO_2 + 1]^+$ $[^{79}Br]^+$, 12), 222 ($[M - CH_3 - CO_2]^+$ $[^{79}Br]^+$,99), 203 ($[M - Br + 1]^+$, 16), 157 (17), 144 (57), 143 (44), 142 (10). HRMS (EI^+) calcd for $C_{12}H_{12}{}^{81}BrNO_2$, $C_{12}H_{12}{}^{79}BrNO_2$ $[M]^+$, 283.0031 and 281.0051; found, 283.0028 and 281.0048. Anal. Calcd for $C_{12}H_{12}BrNO_2$: C, 51.09; H, 4.29; N, 4.96. Found: C, 50.92; H, 4.29; N, 4.96.

***N*,*N*′-[2,2′-Disulfanediylbis(ethane-2,1-diyl)]bis[3-(5-bromo-1*H*-indol-3-yl)propanamide] (20a).** Following the general procedure described for the coupling of acids with amines, **19a** (0.05 g, 0.20 mmol) afforded, after purification by column chromatography (SiO_2, 95:5 CH_2Cl_2/MeOH), disulfide **20a** (0.04 g, 65%) as a colorless oil. ^1H NMR (CD_3COCD_3, 400.13 MHz) (data for monomer): δ 10.19 (br, 1H, NH), 7.73 (s, 1H, H4″), 7.47 (br, 1H, CONH), 7.32 (d, J = 8.6 Hz, 1H, H7″), 7.18 (d, J = 2.1 Hz, 1H), 7.17 (d, J = 2.1 Hz, 1H), 3.43 (t, J = 6.6 Hz, 2H, CH_2), 3.04 (t, J = 7.4 Hz, 2H, CH_2), 2.73 (t, J = 6.6 Hz, 2H, CH_2), 2.56 (t, J = 7.4 Hz, 2H, CH_2) ppm. ^{13}C NMR (CD_3COCD_3, 100.62 MHz) (data for monomer): δ 174.1 (s), 137.2 (s), 131.2 (s), 125.7 (d), 125.5 (d), 122.8 (d), 116.2 (s), 114.8 (d), 113.2 (s), 40.1 (t), 39.5 (t), 38.5 (t), 22.7 (t) ppm. IR: ν 3500−3100 (br, NH), 2920 (m, C−H), 1623 (s, C═O), 1539 (s), 1453 (s), 1212 (m), 1098 (m), 881 (m), 794 (s), 753 (s) cm^{-1}. MS (FAB^+): m/z (%) 655 ($[M]^+$ $[^{81}Br]$, 59), 654 ($[M + 2]^+$ $[^{81}Br]$ $[^{79}Br]$, 40), 653 ($[M]^+$ $[^{81}Br]$ $[^{79}Br]$, 100), 652 ($[M + 2]^+$ $[^{79}Br]$, 31), 651 ($[M + 1]^+$ $[^{79}Br]$, 54), 327 (88), 325 (77). HRMS (FAB^+) calcd for $C_{26}H_{29}{}^{81}Br_2N_4O_2S_2$, $C_{26}H_{29}{}^{81}Br^{79}BrN_4O_2S_2$, and $C_{26}H_{29}{}^{79}Br_2N_4O_2S_2$ ($[M + 1]^+$), 655.0058, 653.0078, and 651.0099; found, 655.0072, 653.0081, and 651.0084.

***N*,*N*′-[2,2′-Disulfanediylbis(ethane-2,1-diyl)]bis[3-(5-bromo-1-methyl-1*H*-indol-3-yl)propanamide] (20b).** Following the general procedure described for the coupling of acids with amines, **19b** (0.06 g, 0.21 mmol) afforded, after purification by column chromatography (SiO_2, 95:5 CH_2Cl_2/MeOH), disulfide **20b** (0.05 g, 42%) as a white foam. ^1H NMR (CD_3COCD_3, 400.13 MHz) (data for monomer): δ 7.71 (d, J = 1.7 Hz, 1H, H4″), 7.48 (br, CONH), 7.28 (d, J = 8.6 Hz, 1H, H7″), 7.22 (dd, J = 8.6, 1.7 Hz, 1H, H6″), 7.04 (s, 1H, H2″), 3.73 (s, 3H, NCH_3), 3.42 (q, J = 6.6 Hz, 2H, CH_2), 3.00 (t, J = 7.4 Hz, 2H, CH_2), 2.73 (t, J = 6.6 Hz, 2H, CH_2), 2.54 (t, J = 7.4 Hz, 2H, CH_2) ppm. ^{13}C NMR (CD_3COCD_3, 100.62 MHz) (data for monomer): δ 174.1 (s), 137.8 (s), 131.5 (s), 130.2 (d), 125.5 (d), 123.1 (d), 115.5 (s), 113.3 (s), 113.0 (d), 40.1 (t), 39.6 (t), 38.7 (t),

33.8 (q), 22.7 (t) ppm. IR: ν 3300 (m, NH), 2918 (w, C−H), 1634 (s, C═O), 1549 (s), 1478 (m), 1266 (w), 810 (w) cm^{-1}. MS (FAB^+): m/z (%) 683 ($[M + 1]^+$ [^{81}Br], 38), 679 ($[M + 1]^+$ [^{79}Br], 38), 561 (15), 559 (15), 342 (18), 341 (22), 340 (21), 225 (14), 224 (97), 222 (100). HRMS (FAB^+) calcd for $C_{28}H_{33}{}^{81}Br_2N_4O_2S_2$ ($[M + 1]^+$), $C_{28}H_{33}{}^{79}Br_2N_4O_2S_2$ ($[M + 1]^+$), 683.0371 and 679.0412; found, 683.0400 and 679.0394.

Biology. Cell Culture. U937 (human leukemic monocyte lymphoma cell line, ATCC) were grown in RPMI 1640 medium (Euroclone) supplemented with 10% heat-inactivated FBS (Euroclone), 1% glutamin (Lonza), 1% penicillin/streptomycin (Euroclone), and 0.1% gentamycin (Lonza) at 37 °C in air and 5% CO_2. MCF7 (human breast cancer cell line, ATCC) were cultured in Dulbecco's modified Eagle's medium (DMEM, Euroclone) supplemented with 10% FCS (Sigma), 50 mg/mL penicillin−streptomycin (Gibco), and 2 mM glutamine (Gibco). Cell lines were maintained at 37 °C in a humidified atmosphere of 95% air, 5% CO_2 as previously reported.

Ligands and Materials. SAHA (Alexis), MS-275 (a kind gift of Schering AG), SGI1027, and indole-derived psammaplin A analogues were dissolved in DMSO (Sigma-Aldrich) and used at 5 or 0.5 μM. RG108 was dissolved in ethanol and used at 5 μM. ALX (Alexis) was dissolved in DMSO and used at a final concentration of 1 μM.

Cell Cycle Analysis. 2.5×10^5 U937 cells were collected by centrifugation after 24 h of stimulation with reference or testing compounds at 5 μM. The cells were resuspended in 500 μL of hypotonic buffer (0.1% NP-40, 0.1% sodium citrate, 50 μg/mL PI, RNase A) and incubated in the dark for 30 min. The analysis was performed by FACS-Calibur (Becton Dickinson) using the Cell Quest Pro software (Becton Dickinson) and ModFit LT, version 3, software (Verity). The experiment was performed in triplicate.

Granulocytic Differentiation Analysis. 2.5×10^5 U937 cells were collected by centrifugation after 30 h of stimulation with reference compound MS-275 at 5 μM or indole derivatives at 5 μM. The cells were washed with PBS and incubated in the dark at 4 °C for 30 min with 10 μL of PE-conjugated anti-CD11c surface antigen antibody or with 10 μL of PE-conjugated IgG in order to define the background signal. At the end of the incubation the samples were washed again and resuspended in 500 μL of PBS containing 0.25 μg/mL PI. The analysis was performed by FACS-Calibur (Becton Dickinson) using the Cell Quest Pro software (Becton Dickinson). The experiment was performed in triplicate, and PI positive cells were excluded from the analysis.

Histone Extraction. After stimulation with compounds, the cells were collected by centrifugation and washed two times with PBS. Then the samples were resuspended in Triton extraction buffer (PBS containing 0.5% Triton X-100 (v/v), 2 mM PMSF, 0.02% (w/v) NaN_3), and the lysis was performed for 10 min at 4 °C. Next, the samples were centrifuged at 2000 rpm for 10 min at 4 °C, and the pellets were washed in TEB (half the volume). After a new centrifugation under the same conditions, the samples were resuspended in 0.2 N HCl and the acid histone extraction was carried out overnight at 4 °C. The supernatant was recovered by centrifugation and the protein content was ensured by BCA protein assay (Pierce).

Total Protein Extraction. U937 cells were harvested and washed once with cold PBS and lysed in a lysis buffer containing 50 mM Tris-HCl, pH 7.4, 150 mM NaCl, 1% NP40, 10 mM NaF, 1 mM PMSF (phenylmethylsulfonyl fluoride) and protease inhibitor cocktail (Roche). The lysates were centrifuged at 14 000 rpm × 30 min at 4 °C. Protein concentrations were estimated by Bradford assay (Bio-Rad).

Western Blot Analyses. The 50 mg of total protein and 10 mg of histone extract were denaturated by boiling samples in buffer (0.25 M Tris-HCl, pH 6.8, 8% SDS, 40% glycerol, 5% 2-mercaptoethanol, 0.05% bromophenol blue) for 3 min before electrophoresis. Proteins were subjected to SDS−PAGE (8%−10%−15% polyacrylamide) in Tris−glycine−SDS (25 mM Tris, 192 mM glycine, 0.1% SDS). After electrophoresis, proteins were transferred to nitrocellulose membranes (Schleicher-Schuell, Germany) in a buffer containing Tris-glycine (25 mM Tris, 192 mM glycine) (Bio-Rad, Italy) and 20% MeOH. The complete transfer was assessed using Ponceau Red (Sigma Aldrich, U.S.) staining. After blocking with 5% nonfat dry milk in TBS 1×/Tween 0.1% (10 mM Tris-HCl, pH 8.0, 150 mM NaCl, 0.1% Tween-20), the membrane was incubated with the primary antibody overnight at 4 °C. After washing with TBS 1×/Tween 0.1%, membranes were incubated with the horseradish peroxidase conjugated secondary antibody (1:5000) for 60 min at room temperature, and the reaction was detected with a chemoluminescence detection system (Amersham Biosciences, U.K.). The antibodies used were p21 (BD), p16 (Santa Cruz), acetyltubulin (Sigma), H3ac (Diagenode), H3K9ac (Abcam), DNMT1 (Abcam), p53K382ac (Abcam), and H3K56ac. Total ERKs (Santa Cruz) were used to normalize for equal loading of total protein extraction. H4 (Cell Signalling) or Ponceau red staining was used to normalize for equal loading of histone extracts.

HDACs Fluorimetric Assay. HDACs assays were performed in the presence of 3 mM HDAC buffer (16.7 mM Tris-HCl, pH 8, 45.7 mM NaCl, 0.9 mM KCl, 0.3 mM $MgCl_2$) and 5 μg of BSA. For these experiments 0.25 μg of HDAC1 (BPS Bioscience) or 2.5 ng of HDAC4 (BPS Bioscience) was added to the reaction mix, and after a preincubation of 15 min at 37 °C was also added to the specific substrate at 5 μM. The reaction was carried out for 2 h at 37 °C in gentle shaking, and in the end fluorescence was quantified with a TECAN Infinite M200 station.

DNMT1 Assay. DNMT1 Immunoprecipitation. The U937 cells were lysed in TAP buffer, pH 7−7.5 (50 mM Tris, pH 7.0, 180 mM NaCl, 0.15% NP40 v/v, 10% glycerol v/v, 1.5 mM $MgCl_2$, 1 mM $NaMnO_4$, 0.5 mM NaF, 1 mM DTT, 0.2 mM PMSF, and protease inhibitor cocktail) for 10 min in ice and centrifuged at 13 000 rpm for 30 min. An amount of 650 μg of extracts was diluted in TAP buffer up to 1 mL and precleared by incubating with 20 μL of A/G plus agarose (Santa Cruz) for 1 h on a rocking table at 4 °C. The supernatant was transferred to a new tube. Then 3.25 μg of antibody against DNMT1 (Abcam) was added and IP was allowed to proceed overnight at 4 °C on a rocking table. As negative control, the same amount of protein extracts was immunoprecipitated with purified rabbit IgG (Santa Cruz). The following day 50 μL of A/G and agarose were added, and incubation was continued for 2 h. The beads were recovered by brief centrifugation and washed with cold TAP buffer several times. At this point the resin was resuspended in 10 μL of DNMT buffer (5 mM EDTA, 0.2 mM DTT, 26 mM NaCl, 20 mM Tris HCl, pH 7.4) in order to proceed with the radioactive assay.

DNMT1 Radioactive Assay. DNMT1 assays were performed in the presence of the analogues at 5 μM plus a reaction mixture composed of 10 μL of DNMT1-bound resin, 5 μCi *S*-adenosyl-L-[methyl-^{3}H]methionine (radioactive methyl donor, 12−18 Ci/mmol), 0.1 μg of poly dI-dC (methyl acceptor), and DNMT buffer. The reaction was carried out for 2 h at 37 °C with gentle stirring, and the experiment was performed in duplicate. Subsequently each sample was spread on Whatman DE-81 paper (in quadruplicate) and the papers were washed three times with 5% Na_2HPO_4 and once with distilled water. The papers were then transferred to the scintillation vials containing 5 mL of scintillation fluid (Perkin-Elmer) in order to read the DPM values.

SIRT Assay. Dilution of the enzyme (no. BML-SE239) from 5 to 0.2 U/μL in SIRT1 assay buffer (no. KI-286: 50 mM Tris-HCl, pH 8, 137 mM NaCl, 2.7 mM KCl, 1 mM $MgCl_2$, BSA 1 mg/mL) was followed by the preparation of a combined 2× solution by diluting the Fluor de Lys (substrate KI-177, 50 mM stock solution) and NAD^+ (no. KI-282, 10 mM stock solution) to 500 μM and 1 mM, respectively, in SIRT1 assay buffer. The plate was prepared as shown in Table 3.

The reaction was carried out for 1.5 h at 37 °C in gentle shaking table. Then 50 μL/well developer solution (39 μL of trypsin buffer

Table 3

well	assay buffer	SIRT1 (0.2 U/μL)	2× solution	compd
control	20 μL	5 μL	25 μL	
+ inhibitor	15 μL	5 μL	25 μL	5 μL
blank	25 μL	25 μL		

(Tris-HCl, pH 8, 50 mM, NaCl 100 mM), 3 μL of nicotinamide (diluted at 50 mM in assay buffer from a 120 mM stock solution in DMSO), and 8 μL of trypsin (6 mg/mL)) was added. After incubation for 30 min, the fluorescence was quantified with a TECAN Infinity 200 station at 360 nm excitation, 460 nm emission.

Molecular Modeling. (a) Quantum Mechanics Calculations. The geometry of **4a**-derived thiol **21** was optimized using the ab initio quantum chemistry program Gaussian 03[114] and the HF/3-21G* basis set. A set of atom-centered RHF 6-31G*//3-21G* charges was then obtained by using the RESP methodology[115] as implemented in the AMBER suite of programs. Covalent and nonbonded parameters for the inhibitor atoms were assigned, by analogy or through interpolation, from those already present in the AMBER force field[116] (parm99) or consistently derived, as explained in more detail elsewhere.[117]

(b) Molecular Docking. The genetic algorithm[118] implemented in AutoDock[119] and the HDAC8 (PDB code 1t64)[101] as the target protein upon removal of trichostatin A was used to generate different HDAC-Zn-bound **4a**-derived thiol **21** conformers by randomly changing torsion angles and overall orientation of the molecule. A volume for exploration was defined in the shape of a three-dimensional cubic grid with a spacing of 0.3 Å that enclosed the residues that are known to make up the inhibitor's binding pocket. At each grid point, the receptor's atomic affinity potentials for carbon, oxygen, nitrogen, sulfur, bromine, and hydrogen atoms present in the ligand were precalculated for rapid intra- and intermolecular energy evaluation of the docking solution.

To obtain additional validation of the proposed binding mode for the ligands, the program GRID (http://www.moldiscovery.com/)[120] was also used to search for sites on the enzyme that could be complementary to the functional groups present in this inhibitor. For the GRID calculations, a 18 Å × 21 Å × 21 Å lattice of points spaced at 0.5 Å was established at the binding site. The probes used were C1═ (aromatic carbon), N1 (neutral flat NH, eg amide), N:# (sp nitrogen with lone pair), O (sp^2 carbonyl oxygen), and Br (bromine). The dielectric constants chosen were 4.0 for the macromolecule and 80.0 for the bulk water.

(c) Molecular Dynamics Simulations. Ternary complexes (HDAC8−Zn^{2+}−thiol **21**) representative of the most populated solutions were then refined using the second generation AMBER force field and 3000 steps of steepest descent energy minimization and 6000 steps of conjugate gradient of only the side chain of the protein and those atoms belonging to the bound ligand. This procedure allowed readjustment of covalent bonds and van der Waals contacts without changing the overall conformation of the complex. The HDAC−**21** complex was then neutralized by addition of eight sodium ions[121] that were placed in electrostatically favored positions and immersed in rectangular boxes each containing about 450 TIP3P water molecules[122] that extended 8 Å away from any solute atom. The cutoff distance for the nonbonded interactions was 9 Å, and periodic boundary conditions were applied. Electrostatic interactions were represented using the smooth particle mesh Ewald method with a grid spacing of ∼1 Å. Unrestrained molecular dynamics (MD) simulations at 300 K and 1 atm were then run for 6 ns using the SANDER module in AMBER 8.[123] The coupling constants for the temperature and pressure baths were 1.0 and 0.2 ps, respectively. SHAKE[124] was applied to all bonds involving hydrogens, and an integration step of 2 fs was used throughout. The nonbonded pair list was updated every 10 steps. The simulation protocol involved a series of progressive energy minimizations followed by a 20 ps heating phase and a 70 ps equilibration period before data collection. System coordinates were saved every 2 ps for further analysis.

(d) Analysis of the Molecular Dynamics Trajectories. Three-dimensional structures and trajectories were visually inspected using the computer graphics program InsightII. Root-mean-square (rms) deviations from both the initial and the average structures, interatomic distances, and snapshot geometries were obtained using the PTRAJ module in AMBER. Intermolecular van der Waals energies for individual residues were calculated with the ANAL module, whereas the solvent-corrected residue-based electrostatic interaction energies were calculated with DelPhi, following the procedure described.[124]

All calculations were performed on the SGI R14000 Origin 3800 at CIEMAT (Madrid, Spain), on the SGI 1.5 GHz Itanium2 at CESGA (Santiago de Compostela, Spain), and locally on SGI R12000 Octane workstations.

■ ASSOCIATED CONTENT

Supporting Information

Experimental procedures, molecular modeling, crystalographic data for compounds **9b** and **10b**, and NMR spectra. This material is available free of charge via the Internet at http://pubs.acs.org.

■ AUTHOR INFORMATION

Corresponding Author

*For L.A.: phone, 39-081-5667569; e-mail, lucia.altucci@unina2.it. For Á.R.d.L.: phone, 34-986-812316; e-mail, qolera@uvigo.es.

Author Contributions

#These authors contributed equally to this work.

Notes

The authors declare the following competing financial interest(s): H. G. Stunnenberg, Á. R. de Lera, H. Gronemeyer, and L. Altucci are inventors for the patent WO2008/125988 entitled "Novel Derivatives of Psammaplin A, a Method for Their Synthesis and Their Use for the Prevention or Treatment of Cancer".

■ ACKNOWLEDGMENTS

This work was supported by the European Union Grant LSHC-CT-2005-518417 "Epitron"; the Italian IHEC (Flag Project EPIGEN); the Italian Association for Cancer Research (Contract No. 11812); the Italian Ministry of University and Research (Grants PRIN_2009PX2T2E_004, PON002782, PON0101227); La Ligue Contre le Cancer (HG, équipe labellisée); Association pour la Recherche sur le Cancer (ARC to H.G.); Grant ANR-07-EMPB-012-01 "EPI_DRUG"; MINECO (Grant SAF2010-17935 FEDER to Á.R.d.L.); and Xunta de Galicia (Consolidación, INBIOMED, to Á.R.d.L.). Mayra Stuhldreier was an Erasmus student from Georg-August Universität Göttingen, Germany.

■ DEDICATION

This paper is dedicated to the memory of Annamaria Scognamiglio.

■ ABBREVIATIONS USED

AML, acute myeloid leukemia; APL, acute promyelocytic leukemia; CTCL, cutaneous T cell lymphoma; DNMT, DNA methyltransferase; DNMTis, DNA methyltransferase inhibitors; HAT, histone acetyltransferase; HDAC, histone deacetylase; HDACis, histone deacetylase inhibitors; HDM, histone demethylase; HMT, histone methyltransferase; MDS, myelodysplastic syndrome; NAD, nicotine adenine dinucleotide; SAH, *S*-adenosyl homocysteine (AdoHcy); SAHA, suberoylanilide hydroxamic acid; SAM, *S*-adenosylmethionine (AdoMet); SAR, structure−activity relationship

■ REFERENCES

(1) Wolffe, A. P. *Chromatin: Structure and Function*; Academic Press: London, 1992.

(2) Kouzarides, T. Chromatin modifications and their function. *Cell* **2007**, *128*, 693−705.

(3) Bannister, A. J.; Kouzarides, T. Regulation of chromatin by histone modifications. *Cell Res.* **2011**, *21*, 381−395.
(4) Bhaumik, S. R.; Smith, E.; Shilatifard, A. Covalent modifications of histones during development and disease pathogenesis. *Nat. Struct. Mol. Biol.* **2007**, *14*, 1008−1016.
(5) Voigt, P.; Reinberg, D. Histone tails: ideal motifs for probing epigenetics through chemical biology approaches. *ChemBioChem* **2011**, *12*, 236−252.
(6) Taverna, S. D.; Li, H.; Ruthenburg, A. J.; Allis, C. D.; Patel, D. J. How chromatin-binding modules interpret histone modifications: lessons from professional pocket pickers. *Nat. Struct. Mol. Biol.* **2007**, *14*, 1025−1040.
(7) Allis, C. D.; Berger, S. L.; Cote, J.; Dent, S.; Jenuwein, T.; Kouzarides, T.; Pillus, L.; Reinberg, D.; Shi, Y.; Shiekhattar, R.; Shilatifard, A.; Workman, J. L.; Zhang, Y. New nomenclature for chromatin-modifying enzymes. *Cell* **2007**, *131*, 633−636.
(8) Egger, G.; Liang, G.; Jones, P. A. Epigenetics in human disease and prospects for epigenetic therapy. *Nature* **2004**, *429*, 457−463.
(9) Feinberg, A. P. Phenotypic plasticity and the epigenetics of human disease. *Nature* **2007**, *447*, 433−440.
(10) Portela, A.; Esteller, M. Epigenetic modifications and human disease. *Nat. Biotechnol.* **2010**, *28*, 1057−1068.
(11) Petronis, A. Epigenetics as a unifying principle in the aetiology of complex traits and diseases. *Nature* **2010**, *465*, 721−727.
(12) Rodriguez-Paredes, M.; Esteller, M. Cancer epigenetics reaches mainstream oncology. *Nat. Med.* **2011**, *17*, 330−339.
(13) Dawson, M. A.; Kouzarides, T. Cancer epigenetics: from mechanism to therapy. *Cell* **2012**, *150*, 12−27.
(14) You, J. S.; Jones, P. A. Cancer genetics and epigenetics: two sides of the same coin? *Cancer Cell* **2012**, *22*, 9−20.
(15) Varambally, S.; Dhanasekaran, S. M.; Zhou, M.; Barrettemgrt, T. R.; Kumar-Sinha, C.; Sanda, M. G.; Ghosh, D.; Pienta, K. J.; Sewalt, R. G. A. B.; Otte, A. P. The polycomb group protein EZH2 is involved in progression of prostate cancer. *Nature* **2002**, *419*, 624−629.
(16) Varier, R. A.; Timmers, H. T. M. Histone lysine methylation and demethylation pathways in cancer. *Biochim. Biophys. Acta, Rev. Cancer* **2011**, *1815*, 75−89.
(17) Lee, J.-S.; Smith, E.; Shilatifard, A. The language of histone crosstalk. *Cell* **2010**, *142*, 682−685.
(18) Chi, P.; Allis, C. D.; Wang, G. G. Covalent histone modifications: miswritten, misinterpreted and mis-erased in human cancers. *Nat. Rev. Cancer* **2010**, *10*, 457−469.
(19) Biel, M.; Wascholowski, V.; Giannis, A. Epigenetics—an epicenter of gene regulation: histones and histone-modifying enzymes. *Angew. Chem., Int. Ed.* **2005**, *44*, 3186−3216.
(20) Hellebrekers, D. M. E. I.; Griffioen, A. W.; van Engeland, M. Dual targeting of epigenetic therapy in cancer. *Biochim. Biophys. Acta, Rev. Cancer* **2007**, *1775*, 76−91.
(21) Cheng, X.; Blumenthal, R. M. Mammalian DNA methyltransferases: a structural perspective. *Structure* **2008**, *16*, 341−350.
(22) Chen, Z.-x.; Riggs, A. D. DNA methylation and demethylation in mammals. *J. Biol. Chem.* **2011**, *286*, 18347−18353.
(23) El-Osta, A. DNMT cooperativity: the developing links between methylation, chromatin structure and cancer. *BioEssays* **2003**, *25*, 1071−1084.
(24) Das, P. M.; Singal, R. DNA methylation and cancer. *J. Clin. Oncol.* **2004**, *22*, 4632−4642.
(25) Klose, R. J.; Bird, A. P. Genomic DNA methylation: the mark and its mediators. *Trends Biochem. Sci.* **2006**, *31*, 89−97.
(26) Jones, P. A.; Baylin, S. B. The epigenomics of cancer. *Cell* **2007**, *128*, 683−692.
(27) Feinberg, A. P. Epigenetics at the epicenter of modern medicine. *JAMA, J. Am. Med. Assoc.* **2008**, *299*, 1345−1350.
(28) Esteller, M. Epigenetics in Cancer. *N. Engl. J. Med.* **2008**, *358*, 1148−1159.
(29) Jurkowska, R. Z.; Jurkowski, T. P.; Jeltsch, A. Structure and function of mammalian DNA methyltransferases. *ChemBioChem* **2011**, *12*, 206−222.
(30) Altucci, L.; Leibowitz, M. D.; Ogilvie, K. M.; de Lera, A. R.; Gronemeyer, H. RAR and RXR modulation in cancer and metabolic disease. *Nat. Rev. Drug Discovery* **2007**, *6*, 793−810.
(31) Chen, J.; Odenike, O.; Rowley, J. D. Leukaemogenesis: more than mutant genes. *Nat. Rev. Cancer* **2010**, *10*, 23−36.
(32) Baylin, S. B. DNA methylation and gene silencing in cancer. *Nat. Clin. Pract. Oncol.* **2005**, *2*, S4−S11.
(33) Hodawadekar, S. C.; Marmorstein, R. Chemistry of acetyl transfer by histone modifying enzymes: structure, mechanism and implications for effector design. *Oncogene* **2007**, *26*, 5528−5540.
(34) De Ruijter, A. J. M.; Van Gennip, A. H.; Caron, H. N.; Kemp, S.; Van Kuilenburg, A. B. P. Histone deacetylases (HDACs): characterization of the classical HDAC family. *Biochem. J.* **2003**, *370*, 737−749.
(35) Ekwall, K. Genome-wide analysis of HDAC function. *Trends Genet.* **2005**, *21*, 608−615.
(36) Finkel, T.; Deng, C.-X.; Mostoslavsky, R. Recent progress in the biology and physiology of sirtuins. *Nature* **2009**, *460*, 587−591.
(37) Miller, T. A.; Witter, D. J.; Belvedere, S Histone deacetylase inhibitors. *J. Med. Chem.* **2003**, *46*, 5097−5114.
(38) Paris, M.; Porcelloni, M.; Binaschi, M.; Fattori, D. Histone deacetylase inhibitors: from bench to clinic. *J. Med. Chem.* **2008**, *51*, 1505−1529.
(39) Bieliauskas, A. V.; Pflum, M. K. H. Isoform-selective histone deacetylase inhibitors. *Chem. Soc. Rev.* **2008**, *37*, 1402−1413.
(40) Wang, D.; Helquist, P.; Wiest, O. Zinc binding in HDAC inhibitors: a DFT study. *J. Org. Chem.* **2008**, *72*, 5446−5449.
(41) Longo, V. D.; Kennedy, B. K. Sirtuins in aging and age-related disease. *Cell* **2006**, *126*, 257−268.
(42) Guarente, L. Sirtuins as potential targets for metabolic syndrome. *Nature* **2006**, *444*, 868−874.
(43) Liu, T.; Liu, P. Y.; Marshall, G. M. The critical role of the class III histone deacetylase SIRT1 in cancer. *Cancer Res.* **2009**, *69*, 1702−1705.
(44) Zhong, L.; D'Urso, A.; Toiber, D.; Sebastian, C.; Henry, R. E.; Vadysirisack, D. D.; Guimaraes, A.; Marinelli, B.; Wikstrom, J. D.; Nir, T.; Clish, C. B.; Vaitheesvaran, B.; Iliopoulos, O.; Kurland, I.; Dor, Y.; Weissleder, R.; Shirihai, O. S.; Ellisen, L. W.; Espinosa, J. M.; Mostoslavsky, R. The histone deacetylase SIRT6 regulates glucose homeostasis via Hif1α. *Cell* **2010**, *140*, 280−293.
(45) Lavu, S.; Boss, O.; Elliot, P. J.; Lambert, P. D. Sirtuins—novel therapeutic targets to treat age-associated disorders. *Nat. Rev. Drug Discovery* **2008**, *7*, 841−853.
(46) Kelly, T. K.; De Carvalho, D. D.; Jones, P. A. Epigenetic modifications as therapeutic targets. *Nat. Biotechnol.* **2010**, *28*, 1069−1078.
(47) Nebbioso, A.; Clarke, N.; Voltz, E.; Germain, E.; Ambrosino, C.; Bontempo, P.; Alvarez, R.; Schiavone, E. M.; Ferrara, F.; Bresciani, F.; Weisz, A.; de Lera, A. R.; Gronemeyer, H.; Altucci, L. Tumor-selective action of HDAC inhibitors involves TRAIL induction in acute myeloid leukemia cells. *Nat. Med.* **2005**, *11*, 77−84.
(48) Sippl, W.; Jung, M. *Epigenetic Targets in Drug Discovery*; Wiley-VCH: Weinheim, Germany, 2009; Vol. *42*.
(49) Szyf, M. Epigenetics, DNA methylation and chromatin modifying drugs. *Annu. Rev. Pharmacol. Toxicol.* **2009**, *49*, 243−263.
(50) Minucci, S.; Pelicci, P. G. Histone deacetylase inhibitors and the promise of epigenetic (and more) treatments for cancer. *Nat. Rev. Cancer* **2006**, *6*, 38−51.
(51) Minucci, S.; Pelicci, P. G. Histone deacetylase inhibitors and the promise of epigenetic (and more) treatments for cancer. *Nat. Rev. Cancer* **2006**, *6*, 38−51.
(52) Satterlee, J. S.; Schubeler, D.; Ng, H.-H. Tackling the epigenome: challenges and opportunities for collaboration. *Nat. Biotechnol.* **2010**, *28*, 1039−1044.
(53) Brueckner, B.; Lyko, F. DNA methyltransferase inhibitors: old and new drugs for an epigenetic cancer therapy. *Trends Pharmacol. Sci.* **2004**, *25*, 551−554.
(54) Kaminskas, E.; Farrell, A.; Abraham, S.; Baird, A.; Hsieh, L.-S.; Lee, S.-L.; Leighton, J. K.; Patel, H.; Rahman, A.; Sridhara, R.; Wang, Y.-C.; Pazdur, R. Approval summary: azacitidine for treatment of

myelodysplastic syndrome subtypes. *Clin. Cancer Res.* **2005**, *11*, 3604−3608.
(55) Shigematsu, N.; Ueda, H.; Takase, S.; Tanaka, H.; Yamamoto, K.; Tada, T. FR901228, a novel antitumor bicyclic depsipeptide produced by *Chromobacterium violaceum* No. 968. II. Structure determination. *J. Antibiot.* **1994**, *47*, 311−314.
(56) Newman, D. J. Natural products as leads to potential drugs: an old process or the new hope for drug discovery? *J. Med. Chem.* **2008**, *51*, 2589−2599.
(57) Koehn, F. E.; Carter, G. T. The evolving role of natural products in drug discovery. *Nat. Rev. Drug Discovery* **2005**, *4*, 206−220.
(58) Newkirk, T. L.; Bowers, A. A.; Williams, R. M. Discovery, biological activity, synthesis and potential therapeutic utility of naturally occurring histone deacetylase inhibitors. *Nat. Prod. Rep.* **2009**, *26*, 1293−1320.
(59) Álvarez, R.; Gronemeyer, H.; Altucci, L.; de Lera, A. R. Epigenetic multiple modulators. *Curr. Top. Med. Chem.* **2011**, *11*, 2749−2787.
(60) Gerwick, W. H.; Moore, B. S. Lessons from the past and charting the future of marine natural products drug discovery and chemical biology. *Chem. Biol.* **2012**, *19*, 85−98.
(61) Furumai, R.; Matsuyama, A.; Kobashi, N.; Lee, K. H.; Nishiyama, M.; Nakajima, H.; Tanaka, A.; Komatsu, Y.; Nishino, N.; Yoshida, M.; Horinouchi, S. FK228 (depsipeptide) as a natural prodrug that inhibits class I histone deacetylases. *Cancer Res.* **2002**, *62*, 4916−4921.
(62) Arabshahi, L.; Schmitz, F. J. Brominated tyrosine metabolites from an unidentified sponge. *J. Org. Chem.* **1987**, *52*, 3584−3586.
(63) Rodriguez, A. D.; Akee, R. K.; Scheuer, P. J. Two bromotyrosine-cysteine derived metabolites from a sponge. *Tetrahedron Lett.* **1987**, *28*, 4989−4992.
(64) Quiñoà, E.; Crews, P. Phenolic constituents of *Psammaplysilla*. *Tetrahedron Lett.* **1987**, *28*, 3229−3232.
(65) Piña, I. C.; Gautschi, J. T.; Wang, G. Y. S.; Sanders, M. L.; Schmitz, F. J.; France, D.; Cornell-Kennon, S.; Sambucetti, L. C.; Remiszewski, S. W.; Perez, L. B.; Bair, K. W.; Crews, P. Psammaplins from the sponge *Pseudoceratina purpurea*: inhibition of both histone deacetylase and DNA methyltransferase. *J. Org. Chem.* **2003**, *68*, 3866−3873.
(66) Park, Y.; Liu, Y.; Hong, J.; Lee, C. O.; Cho, H.; Kim, D. K.; Im, K. S.; Jung, J. H. New bromotyrosine derivatives from an association of two sponges, *Jaspis wondoensis* and *Poecillastra wondoensis*. *J. Nat. Prod.* **2003**, *66*, 1495−1498.
(67) Remiszewski, S. W. The discovery of NVP-LAQ824: from concept to clinic. *Curr. Med. Chem.* **2003**, *10*, 2393−2402.
(68) Amatori, S.; Bagaloni, I.; Donati, B.; Fanelli, M. DNA demethylating antineoplastic strategies. *Genes Cancer* **2010**, *1*, 197−209.
(69) Baud, M. G. J.; Leiser, T.; Meyer-Almes, F.-J.; Fuchter, M. J. New synthetic strategies towards psammaplin A, access to natural product analogues for biological evaluation. *Org. Biomol. Chem.* **2011**, *9*, 659−662.
(70) Kim, H. J.; Kim, J. H.; Chie, E. K.; Da Young, P.; Kim, I. A.; Kim, I. H. DNMT (DNA methyltransferase) inhibitors radiosensitize human cancer cells by suppressing DNA repair activity. *Radiat. Oncol.* **2012**, *7*, 39.
(71) Baud, M. G. J.; Leiser, T.; Haus, P.; Samlal, S.; Wong, A. C.; Wood, R. J.; Petrucci, V.; Gunaratnam, M.; Hughes, S. M.; Buluwela, L.; Turlais, F.; Neidle, S.; Meyer-Almes, F.-J.; White, A. J. P.; Fuchter, M. J. Defining the mechanism of action and enzymatic selectivity of psammaplin A against its epigenetic targets. *J. Med. Chem.* **2012**, *55*, 1731−1750.
(72) García, J.; Franci, G.; Pereira, R.; Benedetti, R.; Nebbioso, A.; Rodríguez-Barrios, F.; Gronemeyer, H.; Altucci, L.; de Lera, A. R. Epigenetic profiling of the antitumor natural product psammaplin A and its analogues. *Bioorg. Med. Chem.* **2011**, *19*, 3637−3649.
(73) Belinsky, S. A.; Grimes, M. J.; Picchi, M. A.; Mitchell, H. D.; Stidley, C. A.; Tesfaigzi, Y.; Channell, M. M.; Liu, Y.; Casero, R. A.; Baylin, S. B.; Reed, M. D.; Tellez, C. S.; March, T. H. Combination therapy with Vidaza and Entinostat suppresses tumor growth and reprograms the epigenome in an orthotopic lung cancer model. *Cancer Res.* **2011**, *71*, 454−462.
(74) Nebbioso, A.; Pereira, R.; Khanwalkar, H.; Matarese, F.; García-Rodríguez, J.; Miceli, M.; Logie, C.; Kedinger, V.; Ferrara, F.; Stunnenberg, H. G.; de Lera, A. R.; Gronemeyer, H.; Altucci, L. *Mol. Cancer Ther.* **2011**, *10*, 2394−2404.
(75) Dai, Y.; Guo, Y.; Guo, J.; Pease, L. J.; Li, J.; Marcotte, P. A.; Glaser, K. B.; Tapang, P.; Albert, D. H.; Richardson, P. L.; Davidsen, S. K.; Michaelides, M. R. Indole amide hydroxamic acids as potent inhibitors of histone deacetylases. *Bioorg. Med. Chem. Lett.* **2003**, *13*, 1897−190.
(76) Dai, Y.; Guo, Y.; Curtin, M. L.; Li, J.; Pease, L. J.; Guo, J.; Marcotte, P. A.; Glaser, K. B.; Davidsen, S. K.; Michaelides, M. R. A novel series of histone deacetylase inhibitors incorporating hetero aromatic ring systems as connection units. *Bioorg. Med. Chem. Lett.* **2003**, *13*, 3817−3820.
(77) Gilchrist, T. L.; Roberts, T. G. Addition and cycloaddition reactions of the electrophilic vinyl nitroso compounds 3-nitrosobut-3-en-2-one, 2-nitrosopropenal, and ethyl 2-nitrosopropenoate. *J. Chem. Soc., Perkin Trans. 1* **1983**, 1283−1292.
(78) Moyer, M. P.; Shiurba, J. F.; Rapoport, H. Metal−halogen exchange of bromoindoles. A route to substituted indoles. *J. Org. Chem.* **1986**, *51*, 5106−5110.
(79) Nicolaou, K. C.; Chen, D. Y. K.; Huang, X.; Ling, T.; Bella, M.; Snyder, S. A. Chemistry and biology of diazonamide A: first total synthesis and confirmation of the true structure. *J. Am. Chem. Soc.* **2004**, *126*, 12888−12896.
(80) Stadlwieser, J. F.; Dambaur, M. E. Convenient synthesis of 1*H*-indol-1-yl boronates via palladium(0)-catalyzed borylation of bromo-1*H*-indoles with pinacolborane. *Helv. Chim. Acta* **2006**, *89*, 936−946.
(81) Zhu, G.; Yang, F.; Balachandran, R.; Hook, P.; Vallee, R. B.; Curran, D. P.; Day, B. W. Synthesis and biological evaluation of purealin and analogues as cytoplasmic dynein heavy chain inhibitors. *J. Med. Chem.* **2006**, *49*, 2063−20766.
(82) Kotoku, N.; Tsujita, H.; Hiramatsu, A.; Mori, C.; Koizumi, N.; Kobayashi, M. Efficient total synthesis of bastadin 6, an anti-angiogenic brominated tyrosine-derived metabolite from marine sponge. *Tetrahedron* **2005**, *61*, 7211−7218.
(83) Reddy, A. S.; Kumar, M. S.; Reddy, G. R. A convenient method for the preparation of hydroxamic acids. *Tetrahedron Lett.* **2000**, *41*, 6285−6288.
(84) Hoshino, O.; Murakata, M.; Yamada, K. A convenient synthesis of a bromotyrosine derived metabolite, psammaplin A, from *Psammaplysilla* sp. *Bioorg. Med. Chem. Lett.* **1992**, *2*, 1561−1562.
(85) Nicolaou, K. C.; Hughes, R.; Pfefferkorn, J. A.; Barluenga, S.; Roecker, A. J. Combinatorial synthesis through bisulfide exchange: discovery of potent psammaplin A type antibacterial agents active against methicillin-resistant *Staphylococcus aureus* (MRSA). *Chem.—Eur. J.* **2001**, *7*, 4280−4295.
(86) Pfammatter, M. J.; Siljegovic, V.; Darbre, T.; Keese, R. Synthesis of ω-substituted alkanethiols and (bromomethyl)methylthiomalonates. *Helv. Chim. Acta* **2001**, *84*, 678−689.
(87) Schneider, P. H.; Schrekker, H. S.; Silveira, C. C.; Wessjohann, L. A.; Braga, A. L. First generation cysteine- and methionine-derived oxazolidine and thiazolidine ligands for palladium-catalyzed asymmetric allylations. *Eur. J. Org. Chem.* **2004**, 2715−2722.
(88) Plate, R.; Nivard, R. J. F.; Ottenheijm, H. C. J. Conversion of *N*-hydroxytryptophans into α,β-dehydrotryptophan. An approach to the neoechinulin series. *J. Chem. Soc., Perkin Trans. 1* **1987**, 2473−2480.
(89) Hermkens, P. H. H.; van Maarseveen, J. H.; Cobben, P. L. H. M.; Ottenheijm, H. C. J.; Kruse, C. G.; Scheerent, H. W. Syntheses of 1,3-disubstituted *N*-oxy-[beta]-carbolines by the Pictet−Spengler reactions of *N*-oxy-tryptophan and -tryptamine derivatives. *Tetrahedron* **1990**, *46*, 833−846.
(90) Kumar, V.; Kaur, S.; Kumar, S. $ZrCl_4$ catalyzed highly selective and efficient Michael addition of heterocyclic enamines with [alpha], [beta]-unsaturated olefins. *Tetrahedron Lett.* **2006**, *47*, 7001−7005.
(91) Datta, J.; Ghoshal, K.; Denny, W. A.; Gamage, S. A.; Brooke, D. G.; Phiasivongsa, P.; Redkar, S.; Jacob, S. T. A new class of quinoline-

based DNA hypomethylating agents reactivates tumor suppressor genes by blocking DNA methyltransferase 1 activity and inducing its degradation. *Cancer Res.* **2009**, *69*, 4277−4285.

(92) Solomon, J. M.; Pasupuleti, R.; Xu, L.; McDonagh, T.; Curtis, R.; DiStefano, P. S.; Huber, L. J. Inhibition of SIRT1 catalytic activity increases p53 acetylation but does not alter cell survival following DNA damage. *Mol. Cell. Biol.* **2006**, *26*, 28−38.

(93) Lara, E.; Mai, A.; Calvanese, V.; Altucci, L.; López-Nieva, P.; Martínez-Chantar, M. L.; Varela-Rey, M.; Rotili, D.; Nebbioso, A.; Ropero, S.; Montoya, G.; Oyarzabal, J.; Velasco, S.; Serrano, M.; Witt, M.; Villar-Garea, A.; Inhof, A.; Mato, J. M.; Esteller, M.; Fraga, M. F. Salermide, a sirtuin inhibitor with a strong cancer-specific proapoptotic effect. *Oncogene* **2009**, *28*, 781−791.

(94) Vaquero, A.; Scher, M. B.; Lee, D. H.; Sutton, A.; Cheng, H.-L.; Alt, F. W.; Serrano, L.; Sternglanz, R.; Reinberg, D. SIRT2 is a histone deacetylase with preference for histone H4 Lys 16 during mitosis. *Genes Dev.* **2006**, *20*, 1256−1261.

(95) Pruitt, K.; Zinn, R. L.; Ohm, J. E.; McGarvey, K. M.; Kang, S. H.; Watkins, D. N.; Herman, J. G.; Baylin, S. B. *PLoS Genet.* **2006**, *2*, e40.

(96) Yuan, J.; Pu, M.; Zhang, Z.; Lou, Z. Histone H3-K56 acetylation is important for genomic stability in mammals. *Cell Cycle* **2009**, *8*, 1747−1753.

(97) Verdine, G. L. The flip side of DNA methylation. *Cell* **1994**, *76*, 197.

(98) Bowers, A.; West, N.; Taunton, J.; Schreiber, S. L.; Bradner, J. E.; Williams, R. M. Total synthesis and biological mode of action of largazole: a potent class I histone deacetylase inhibitor. *J. Am. Chem. Soc.* **2008**, *130*, 11219−11222.

(99) Bowers, A. A.; Greshock, T. J.; West, N.; Estiu, G.; Schreiber, S. L.; Wiest, O.; Williams, R. M.; Bradner, J. E. Synthesis and conformation−activity relationships of the peptide isosteres of FK228 and largazole. *J. Am. Chem. Soc.* **2009**, *131*, 2900−2905.

(100) Saito, G.; Swanson, J. A.; Lee, K.-D. Drug delivery strategy utilizing conjugation via reversible disulfide linkages: role and site of cellular reducing activities. *Adv. Drug Delivery Rev.* **2003**, *55*, 199−215.

(101) Somoza, J. R.; Skene, R. J.; Katz, B. A.; Mol, C.; Ho, J. D.; Jennings, A. J.; Luong, C.; Arvai, A.; Buggy, J. J.; Chi, E.; Tang, J.; Sang, B. C.; Verner, E.; Wynands, R.; Leahy, E. M.; Dougan, D. R.; Snell, G.; Navre, M.; Knuth, M. W.; Swanson, R. V.; McRee, D. E.; Tari, L. W. Structural snapshots of human HDAC8 provide insights into the class I histone deacetylases. *Structure* **2004**, *12*, 1325−1334.

(102) Taori, K.; Paul, V. J.; Luesch, H. Structure and activity of largazole, a potent antiproliferative agent from the floridian marine cyanobacterium *Symploca* sp. *J. Am. Chem. Soc.* **2008**, *130*, 1806−1807.

(103) Suzuki, T.; Kouketsu, A.; Itoh, Y.; Hisakawa, S.; Maeda, S.; Yoshida, M.; Nakagawa, H.; Miyata, N. Highly potent and selective histone deacetylase 6 inhibitors designed based on a small-molecular substrate. *J. Med. Chem.* **2006**, *49*, 4809−4812.

(104) Itoh, Y.; Suzuki, T.; Kouketsu, A.; Suzuki, N.; Maeda, S.; Yoshida, M.; Nakagawa, H.; Miyata, N. Design, synthesis, structure−selectivity relationship, and effect on human cancer cells of a novel series of histone deacetylase 6-selective inhibitors. *J. Med. Chem.* **2007**, *50*, 5425−5438.

(105) Suzuki, T.; Hisakawa, S.; Itoh, Y.; Maruyama, S.; Kurotaki, M.; Nakagawa, H.; Miyata, N. Identification of a potent and stable antiproliferative agent by the prodrug formation of a thiolate histone deacetylase inhibitor. *Bioorg. Med. Chem. Lett.* **2007**, *17*, 1558−1561.

(106) Nishino, N.; Jose, B.; Okamura, S.; Ebisusaki, S.; Kato, T.; Sumida, Y.; Yoshida, M. Cyclic tetrapeptides bearing a sulfhydryl group potently inhibit histone deacetylases. *Org. Lett.* **2003**, *5*, 5079−5082.

(107) Rautio, J.; Kumpulainen, H.; Heimbach, T.; Oliyai, R.; Oh, D.; Järvinen, T.; Savolainen, J. Prodrugs: design and clinical applications. *Nat. Rev. Drug Discovery* **2008**, *7*, 255−270.

(108) Bach, R. D.; Dmitrenko, O.; Thorpe, C. Mechanism of thiolate−disulfide interchange reactions in biochemistry. *J. Org. Chem.* **2008**, *73*, 12−21.

(109) Dehmel, F.; Weinbrenner, S.; Julius, H.; Ciossek, T.; Maier, T.; Stengel, T.; Fettis, K.; Burkhardt, C.; Wieland, H.; Beckers, T. Trithiocarbonates as a novel class of HDAC inhibitors: SAR studies, isoenzyme selectivity, and pharmacological profiles. *J. Med. Chem.* **2008**, *51*, 3985−4001.

(110) Kozikowski, A. P.; Chen, Y.; Gaysin, A.; Chen, B.; D'Annibale, M. A.; Suto, C. M.; Langley, B. C. Functional differences in epigenetic modulators—superiority of mercaptoacetamide-based histone deacetylase inhibitors relative to hydroxamates in cortical neuron neuroprotection studies. *J. Med. Chem.* **2007**, *50*, 3054−3061.

(111) Hassig, C. A.; Symons, K. T.; Guo, X.; Nguyen, P.-M.; Annable, T.; Wash, P. L.; Payne, J. E.; Jenkins, D. A.; Bonnefous, C.; Trotter, C.; Wang, Y.; Anzola, J. V.; Milkova, E. L.; Hoffman, T. Z.; Dozier, S. J.; Wiley, B. M.; Saven, A.; Malecha, J. W.; Davis, R. L.; Muhammad, J.; Shiau, A. K.; Noble, S. A.; Rao, T. S.; Smith, N. D.; Hager, J. H. KD5170, a novel mercaptoketone-based histone deacetylase inhibitor that exhibits broad spectrum antitumor activity in vitro and in vivo. *Mol. Cancer Ther.* **2008**, *7*, 1054−1065.

(112) Suzuki, T.; Matsuura, A.; Kouketsu, A.; Hisakawa, S.; Nakagawa, H.; Miyata, N. Design and synthesis of non-hydroxamate histone deacetylase inhibitors: identification of a selective histone acetylating agent. *Bioorg. Med. Chem.* **2005**, *13*, 4332−4342.

(113) Morphy, R.; Rankovic, Z. Designed multiple ligands. An emerging drug discovery paradigm. *J. Med. Chem.* **2005**, *48*, 6523−6543.

(114) Frisch, M. J.; Trucks, G. W.; Schlegel, H. B.; Scuseria, G. E.; Robb, M. A.; Cheeseman, J. R.; Montgomery, J. A., Jr.; Vreven, T.; Kudin, K. N.; Burant, J. C.; Millam, J. M.; Iyengar, S. S.; Tomasi, J.; Barone, V.; Mennucci, B.; Cossi, M.; Scalmani, G.; Rega, N.; Petersson, G. A.; Nakatsuji, H.; Hada, M.; Ehara, M.; Toyota, K.; Fukuda, R.; Hasegawa, J.; Ishida, M.; Nakajima, T.; Honda, Y.; Kitao, O.; Nakai, H.; Klene, M.; Li, X.; Knox, J. E.; Hratchian, H. P.; Cross, J. B.; Bakken, V.; Adamo, C.; Jaramillo, J.; Gomperts, R.; Stratmann, R. E.; Yazyev, O.; Austin, A. J.; Cammi, R.; Pomelli, C.; Ochterski, J. W.; Ayala, P. Y.; Morokuma, K.; Voth, G. A.; Salvador, P.; Dannenberg, J. J.; Zakrzewski, V. G.; Dapprich, S.; Daniels, A. D.; Strain, M. C.; Farkas, O.; Malick, D. K.; Rabuck, A. D.; Raghavachari, K.; Foresman, J. B.; Ortiz, J. V.; Cui, Q.; Baboul, A. G.; Clifford, S.; Cioslowski, J.; Stefanov, B. B.; Liu, G.; Liashenko, A.; Piskorz, P.; Komaromi, I.; Martin, R.L.; Fox, D. J.; Keith, T.; Al-Laham, M. A.; Peng, C. Y.; Nanayakkara, A.; Challacombe, M.; Gill, P. M. W.; Johnson, B.; Chen, W.; Wong, M. W.; Gonzalez, C.; Pople, J.A. *Gaussian 03*, revision D.02; Gaussian, Inc.: Wallingford, CT, 2004.

(115) Bayly, C. I.; Cieplak, P.; Cornell, W. D.; Kollman, P. A. A well-behaved electrostatic potential based method using charge restraints for deriving atomic charges: the RESP model. *J. Phys. Chem.* **1993**, *97*, 10269−10280.

(116) Cornell, W. D.; Cieplak, P.; Bayly, C. I.; Gould, I. R.; Merz, K. M.; Ferguson, D. M.; Spellmeyer, D. C.; Fox, T.; Caldwell, J. W.; Kollman, P. A. A second generation force field for the simulation of proteins, nucleic acids, and organic molecules. *J. Am. Chem. Soc.* **1995**, *117*, 5179−5197.

(117) Rodríguez-Barrios, F.; Pérez, C.; Lobatón, E.; Velázquez, S.; Chamorro, C.; San-Félix, A.; Pérez-Pérez, M. J.; Camarasa, M. J.; Pelemans, H.; Balzarini, J.; Gago, F. Identification of a putative binding site for [2′,5′-bis-*O*-(*tert*-butyldimethylsilyl)-*β*-D-ribofuranosyl]-3′-spiro-5″-(4″-amino-1″,2″-oxathiole-2″,2″-dioxide)thymine (TSAO) Derivatives at the p51-p66 Interface of HIV-1 Reverse Transcriptase. *J. Med. Chem.* **2001**, *44*, 1853−1865.

(118) Morris, G. M.; Goodsell, D. S.; Halliday, R. S.; Huey, R.; Hart, W. E.; Belew, R. K.; Olson, A. J. Automated docking using Lamarckian genetic algorithm and an empirical binding free energy function. *J. Comput. Chem.* **1998**, *19*, 1639−1662.

(119) Morris, G. M.; Goodsell, D. S.; Huey, R.; Hart, W. E.; Halliday, S.; Belew, R.; Olson, A. J. *AutoDock, Automated Docking of Flexible Ligands to Receptors*, version 3.0; The Scripps Research Institute: La Jolla, CA, 1999.

(120) Goodford, P. J. A computational procedure for determining energetically favorable binding sites on biologically important macromolecules. *J. Med. Chem.* **1985**, *28*, 849−857.

(121) Åqvist, J. Ion−water interaction potentials derived from free energy perturbation simulations. *J. Phys. Chem.* **1990**, *94*, 8021−8024.

(122) Jorgensen, W. L.; Chandrasekhar, J.; Madura, J. D. Comparison of simple potential functions for simulating liquid water. *J. Chem. Phys.* **1983**, *79*, 926−935.
(123) Case, D. A.; Darden, T. A.; Cheatham, T. E., III; Simmerling, C. L.; Wang, J.; Duke, R. E.; Luo, R.; Merz, K. M.; Wang, B.; Pearlman, D. A.; Crowley, M.; Brozell, S.; Tsui, V.; Gohlke, H.; Mongan, J.; Hornak, V.; Cui, G.; Beroza, P.; Schafmeister, C.; Caldwell, J. W.; Ross, W. S.; Kollman, P. A. *AMBER 8*; University of California, San Francisco, 2004.
(124) Ryckaert, J. P.; Ciccoti, G.; Berendsen, H. J. C. Numerical integration of the Cartesian equations of motion of a system with constraints: molecular dynamics of *n*-alkanes. *J. Comput. Phys.* **1977**, *23*, 327−341.

Published OnlineFirst October 6, 2011; DOI: 10.1158/1535-7163.MCT-11-0525

Molecular Cancer Therapeutics

Preclinical Development

Death Receptor Pathway Activation and Increase of ROS Production by the Triple Epigenetic Inhibitor UVI5008

Angela Nebbioso[1], Raquel Pereira[4], Harshal Khanwalkar[5], Filomena Matarese[6], José García-Rodríguez[4], Marco Miceli[1], Colin Logie[6], Valerie Kedinger[5], Felicetto Ferrara[3], Hendrik G. Stunnenberg[6], Angel R. de Lera[4], Hinrich Gronemeyer[5], and Lucia Altucci[1,2]

Abstract

Deregulation of the epigenome is recognized as cause of cancer and epigenetic factors are receiving major attention as therapeutic targets; yet, the molecular mode of action of existing epi-drugs is largely elusive. Here, we report on the decryption of the mechanism of action of UVI5008, a novel epigenetic modifier, that inhibits histone deacetylases, sirtuins, and DNA methyltransferases. UVI5008 highly efficiently induces cancer cell–selective death in a variety of models and exerts its activities in several human tumor xenografts and genetic mouse models of human breast cancer *in vivo*. Its anticancer activity involves independent activation of death receptors and reactive oxygen species production. Importantly, UVI5008 action is not critically dependent on p53, Bcl-2 modifying factor, and/or TNF-related apoptosis-inducing ligand as cell death is efficiently induced in cells mutated or deficient for these factors limiting the risk of drug resistance development and maximizing its application spectrum. The simultaneous modulation of multiple (epigenetic) targets promises to open new avenues with unanticipated potential against cancer. *Mol Cancer Ther; 10(12); 2394–404. ©2011 AACR.*

Introduction

Cancer is a multistep process involving acquisition of unlimited replicative potential, self-sustained growth with loss of sensitivity toward apoptogenic and checkpoint controls (1). These aberrations are caused by a series of genetic events that involve proto-oncogene activation, tumor suppressor gene (TSG) inactivation, and senescence escape. Studies on leukemogenesis have revealed the intimate relationship between initial somatic mutations, often a chromosomal translocation, and epigenetic deregulation (2, 3). In the case of acute promyelocytic leukemia (APL), the formation of a PML–RARα oncofusion protein leads to multiple deregulations, which include histone deacetylase (HDAC) recruitment (4) to retinoic acid target genes, resulting in obstruction of differentiation programs (2, 5). While aberrant HDAC recruitment is a hallmark of APL, recent data suggest that HDAC mistargeting is necessary, but not sufficient for leukemogenesis (6), supporting the novel concept that multiple targeting by combination therapy may achieve maximal anticancer effects. This concept is also supported by the multiple genetic and epigenetic aberrations present in cancer that might need a multitarget therapy approach. It has become clear that cancer originates from and is supported by epigenetic deregulation (7–9). Deposition of epigenetic marks on chromatin is accomplished by enzymes residing in multisubunit complexes (10). The control of the enzymatic machinery including histone acetylation/deacetylation and methylation/demethylation (11) or DNA methylation (DNMT; ref. 12) is central to transcription regulation. Chromatin-modifying enzymes, in particular HDACs and DNMTs, have emerged as new anticancer targets. The fact that epigenetic modifications can be reversed makes epi-drugs promising for antitumor therapy (13). Proof-of-principle

Authors' Affiliations: [1]Dipartimento di Patologia generale, Seconda Università di Napoli, Vico L. de Crecchio 7; [2]CNR-IGB, Via P. Castellino; [3]Ospedale Cardarelli, Napoli, Italy; [4]Departamento de Química Orgánica, Facultade de Química, Universidade de Vigo, Vigo, Spain; [5]Department of Cancer Biology, Institut de Génétique et de Biologie Moléculaire et Cellulaire, Illkirch Cedex, Strasbourg, France; and [6]NCMLS, Department of Molecular Biology, Radboud University, GA Nijmegen, the Netherlands

Note: Supplementary data for this article are available at Molecular Cancer Therapeutics Online (http://mct.aacrjournals.org/).

A. Nebbioso, R. Pereira, and H. Khanwalkar are equal first authors.

H.G. Stunnenberg, A.R. de Lera, H. Gronemeyer, and L. Altucci are equal last authors and have contributed equally to this work.

Current address for H. Khanwalkar: Lupin Limited (Research Park), 46A/47A, Nande village, Pune 411 042, Maharashtra, India.

Current address for V. Kedinger: Polyplus-transfection, Bioparc, Blvd S. Brant, 67401 Illkirch, France.

Corresponding Author: Lucia Altucci, Dipartimento di Patologia generale, Seconda Università degli Studi di Napoli, Vico L. De Crecchio 7, 80138 Napoli, Italy. Phone: 39-081-5667569; Fax: 39-081-2144840; E-mail: lucia.altucci@unina2.it

doi: 10.1158/1535-7163.MCT-11-0525

©2011 American Association for Cancer Research.

Downloaded from mct.aacrjournals.org on March 6, 2016. © 2011 American Association for Cancer Research.

Published OnlineFirst October 6, 2011; DOI: 10.1158/1535-7163.MCT-11-0525

comes from studies with HDAC inhibitors (HDACi) that are in clinical practice (14).

HDACs are considered leading targets for therapy to reverse epi-aberrations (15). The 18 mammalian HDACs are divided in 2 families, the Zn^{+2}-dependent HDACs (Class I: HDAC1–3, 8; Class II: HDAC4–7, 9, 10; Class IV: HDAC11) and the NAD^{+}-dependent sirtuins (Class III: SIRTs1–7; ref. 16). SIRT1 has only recently been implicated in malignancies (17). DNMTs are responsible for CpG methylation within the genome. Three active enzymes have been identified in mammals: DNMT1 responsible for maintenance of preexisting methylation and DNMT3a/b for *de novo* methylation (18). Notwithstanding the clinical use of HDAC and other inhibitors, little is known about the molecular mode of action. We and others have shown that HDACis induce TRAIL-apoptosis (TNF-related apoptosis inducing ligand/TNSF10/Apo2L) in acute myeloid leukemia (AML) cells, *in vivo* AML models and *ex vivo* blasts (19, 20). Here we report on UVI5008 molecular characterization and anticancer activities. UVI5008 inhibits 3 epi-enzymes and independently affects the death receptor (DR) pathway and reactive oxygen species (ROS) production. UVI5008 targets p53, the Bcl-2 modifying factor (BMF), and/or TRAIL in cancer cells harboring the wild-type factors as well as tumors, which are deficient for one of them.

Materials and Methods

Cell lines

Cell lines and primary cell cultures are deeply described as Supplementary Methods. Briefly, U937, K562, K812-F, HL60 (leukemia), DU-145 (prostate), HCT116 (colon), MDA-MB231, and MCF7 (breast) cancer cells were obtained from American Type Culture Collection. HCT116 $p53^{-/-}$ and HCT116-DK0 colon cancer cells were a gift from B. Vogelstein, John Hopkins Kimmel Cancer Center, Baltimore, MD. BJ, normal foreskin fibroblast, and Ras transformed BJELR cells were a gift from W. C. Hahn (Dana-Farber Cancer Institute, Boston, MA). For AML primary samples, bone marrow containing 80% to 90% leukemic blasts was purified over Ficoll and processed as previously described (20). Primary $CD34^{+}$ normal progenitors (obtained from donors) have been cultured in *ex vivo* medium as recommended by the supplier. This study was approved by the Ethical Committee of the Second University of Naples. KD clones used in this study have been published previously (20), or have been created by standard procedures using the Mission technology (Sigma).

Inhibitors

Suberoylanilide hydroxamic acid (SAHA; Merck), AZA (Sigma), EX527 (Alexis), and MS-275 (Bayer Schering Pharma) were dissolved in dimethyl sulfoxide (DMSO) and used at 5×10^{-6} mol/L or as indicated. All other compounds described were dissolved in DMSO and used at 1 or 5 μmol/L. Cell-cycle, differentiation, and cell death assays are described as Supplementary Methods and carried out as in references (20, 21).

Western blot analyses

Western blot analyses were carried out following supplier's suggestions. For the determination of $p21^{WAF1/CIP1}$ and $p16^{INK4}$, 100 μg of extracts was separated on 15% polyacrylamide gels and blotted. Western blot analyses are shown for p21 (Transduction Laboratories), p16, and total ERKs (Santa Cruz). For α-tubulin acetylation, 25 μg of extracts were separated on 10% polyacrylamide gels and blotted. Western blot analyses are shown for acetylated α-tubulin, total tubulin (Sigma), and total ERKs (Santa Cruz). For the detection of histone H3 acetylation, we used Upstate antibodies, whereas for histone H3K9 trimethylation and H3K9, H3K14, and H3K18 acetylations we used Abcam antibodies.

Histone extraction protocol and MS analysis, P53K382 acetylation, p21 expression, and histone extraction in xenograft tumors, xenograft and MMTV-MYC mouse models, and isolation and digestion of genomic DNA are described as Supplementary Methods.

In vitro methylation of genomic DNA

Digested DNA was methylated with 8U of Sss1 methylase (New England Biolabs) in the presence of 3.2 mmol/L SAM for 2 hours at 37°C. After phenol–chloroform extraction, DNA was precipitated and resuspended with 20 μL water.

Bisulfite treatment and PCR for RARβ and p16 methylation

Bisulfite treatment and PCR for RARβ and p16 methylation are described in the Supplementary Methods.

Fluorimetric human cell–based HDAC1 and 4 assays and *in vitro* HDAC assays

HDAC assays were carried out as previously described (21, 22).

In vitro assays of Sirt1 and Sirt2, DNMTs assay, chromatin immunoprecipitation (ChIP) assay, and immunofluorescence assays are described in the Supplementary Methods. ChIP assays have been carried out as in reference (23).

RNA preparation for RNA-Seq, Illumina high-throughput sequencing, and MethylCap-seq are described in the Supplementary Methods and in references (2, 24, 25).

Results

UVI5008 efficiently induces apoptosis

We tested the activity of UVI5008 (Fig. 1A) activity on a series of cancer cells. UVI5008 induced cell death (Fig. 1B) and apoptosis by activation of both initiator, executor caspases (Fig. 1C), and loss of mitochondrial membrane potential in cancer cells derived from leukemias (U937, Ku-812F, and K562) or solid tumors, such as breast (MCF7), osteosarcoma (U2OS), prostate (DU145), colon

Downloaded from mct.aacrjournals.org on March 6, 2016. © 2011 American Association for Cancer Research.

Published OnlineFirst October 6, 2011; DOI: 10.1158/1535-7163.MCT-11-0525

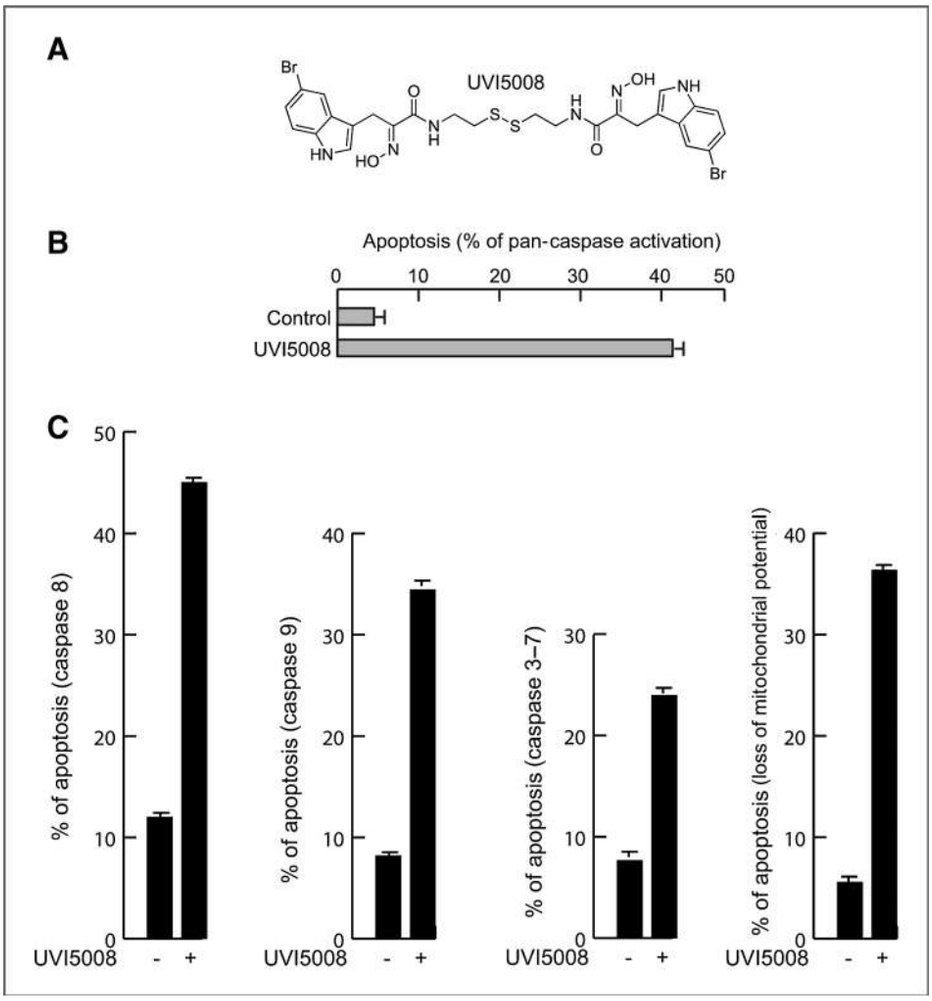

Figure 1. Structure and apoptogenic action of UVI5008 in U937 cells. A, structure of UVI5008. B, apoptosis of UVI5008 at 40 hours revealed by pan-caspase activation assays. C, selective assays for activation of caspases 8, 9, and 3–7. In B and C, UVI5008 was used at micromolar UVI5008. Evaluation of the loss of mitochondrial potential after UVI5008 treatment (5 μmol/L).

carcinoma (HCT116), and melanoma (A375; Supplementary Fig. S1A and data not shown). Several cell lines derived from colon, breast, and prostate carcinomas exhibited antiproliferative responses with IC_{50}s ranging from about 200 nmol/L to 3.1 μmol/L (Supplementary Methods and data not shown).

UVI5008 anticancer action *in vivo and ex vivo*

To test UVI5008 antitumor activity *in vivo*, xenograft assays were carried out with luciferase-expressing human cancer cells. At 40 mg/kg UVI5008 [molecular weight (MW) 710.46 g/mol] efficiently blocked HCT116 colon carcinoma growth as visualized by *in vivo* imaging (Fig. 2A) and quantified by direct photon counting (Fig. 2B). No adverse side effects were noticed, whereas the same dose of SAHA (Vorinostat; MW 264.33 g/mol) was lethal (data not shown). Similarly, UVI5008 strongly inhibited MCF7 breast cancer growth *in vivo* in the presence of estradiol; tamoxifen cotreatment attenuated the growth without affecting the median overall tumor size (Fig. 2C, left). Importantly, UVI5008 strongly reduced tumor growth in a genetic mouse model (MMTV-myc) of human breast cancer, when treatment was initiated as soon as the tumors became palpable (Fig. 2C, right). The weight profiles of the treated versus control groups supported the absence of toxicity. Similar tumor growth inhibition by 40 mg/kg UVI5008 was observed in the MMTV-cerbB2 breast cancer model (data not shown). Thus, UVI5008 displays a strong anticancer effect not only in xenografts, but also in 2 genetic mouse models that mimic human breast cancer. Pharmacokinetics analyses revealed half-lives of up to approximately 7 hours (oral application) for the *in vivo* formed glutathione conjugate of UVI5008 (see Supplementary Methods).

UVI5008 mediated tumor-selective apoptosis

To assess the cancer-selective potential of UVI5008, we first used the isogenic BJ stepwise cellular tumorigenesis model (26). While primary fibroblasts (BJ) were largely insensitive to UVI5008, 80% of the transformed BJELR cells were killed (Fig. 2D, left).

The efficient induction of tumor selective cell death by UVI5008 prompted us to test its efficacy in *ex vivo* assays in

Downloaded from mct.aacrjournals.org on March 6, 2016. © 2011 American Association for Cancer Research.

Published OnlineFirst October 6, 2011; DOI: 10.1158/1535-7163.MCT-11-0525

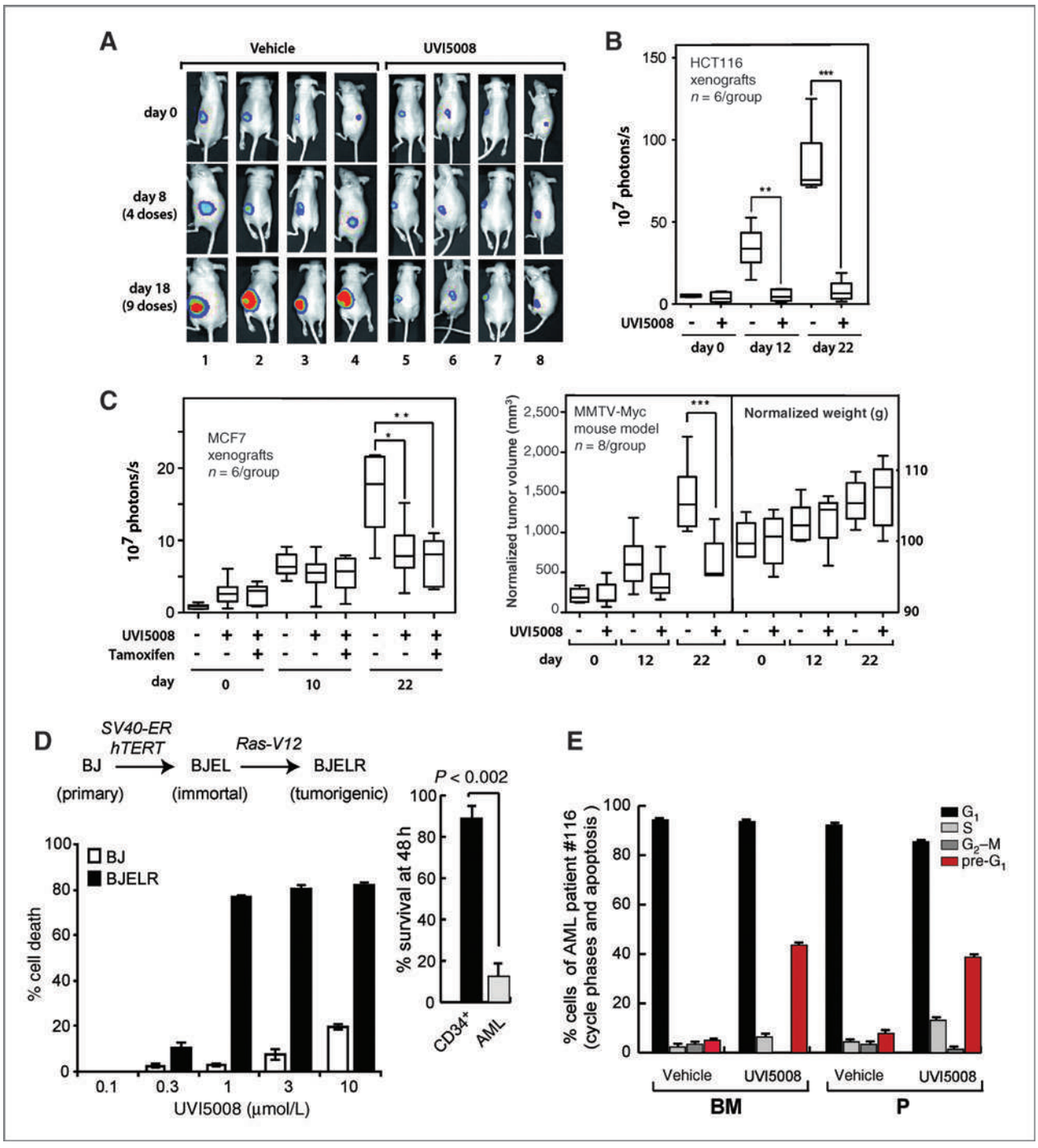

Figure 2. UVI5008 displays anticancer action *in vivo* and tumor-selective apoptosis. A, false-color images revealing tumor growth *in vivo* of luciferase-tagged HCT116 cells, xenografted into nude mice and treated with vehicle or 40 mg/kg of UVI5008; the increase of luminescence determined by direct photon counting reveals the growth-inhibitory effects. B, kinetics of tumor mass development (as in A). C, left, tumor mass development as in A of MCF7-xenografted mice treated with 40 mg/kg of UVI5008; right, tumor mass development in MMTV-Myc transgenic mice treated with 40 mg/kg of UVI5008; treatment was initiated when tumors became palpable; normalized mouse weights are shown on the right side. D, left, primary BJ fibroblasts and their tumorigenic derivatives were exposed to UVI5008 and survival was measured by MTT assays; right, survival rate of $CD34^+$ cells and AML blasts upon UVI5008 (5 μmol/L) treatment after 48 hours. E, example of the apoptotic UVI5008 action (20 hours, 5 μmol/L) in the AML blast #116, both in bone marrow (BM) and periphery (P).

primary AML blasts. Within 24 hours, UVI5008 induced caspase 3 activation and apoptosis in 14/14 independent *ex vivo* blasts (Fig. 2E and Supplementary Fig. S1B). No significant toxicity was seen in normal $CD34^+$ progenitors, whereas all AML blasts were sensitive (Fig. 2D, right).

Downloaded from mct.aacrjournals.org on March 6, 2016. © 2011 American Association for Cancer Research.

Published OnlineFirst October 6, 2011; DOI: 10.1158/1535-7163.MCT-11-0525

UVI5008 is a triple HDAC, DNMT, and SIRT inhibitor

To decipher the basis of UVI5008 anticancer activity, we assessed inhibition of DNMT. Using methylation-specific PCR, we corroborated that UVI5008, like its parental compound psammaplin A (27), induced significant demethylation of the *RAR*β and *p16*^{INK4a} promoters (Supplementary Fig. S2A). In keeping with the p16 promoter reactivation, UVI5008 induced an increase of p16 protein levels in U937 cells that was higher than the one seen upon combined treatment with 5-aza-cytidine (5-aza-C) and SAHA (Supplementary Fig. S2B, top). *In vitro* assays showed that UVI5008 acted as a direct inhibitor of DNMT3a (Supplementary Fig. S2B) and only marginally inhibited DNMT1 (Supplementary Fig. S2B, bottom), when compared with the DNMT1 inhibitors RG108 (28) or SGI-1027 (29). To the best of our knowledge, UVI5008 is the first DNMT3a-selective inhibitor.

Next, we assessed whether UVI5008, like psammaplin A (30, 31), acts as HDACi. UVI5008 blocked the activity of HDAC1–4 both *in vitro* and in cell-based assays (Fig. 3A and Supplementary Fig. S3). Moreover, UVI5008 treatment of U937 cells induced the well-known HDACi target p21, inhibited deacetylation of the HDAC6/SIRT2 substrate α-tubulin, and affected histone acetylation (H3K9, H3K14, and H3K18; Fig. 3B). UVI5008 also induced global histone H3 hyperacetylation in *ex vivo* blasts as exemplified for AML #116 (Fig. 3C and data not shown), thus acting both *in vitro* and *ex vivo*. Immunoblotting of tumors derived from both HCT116-xenografted mice and MMTV-myc model treated with UVI5008 revealed global (pan-H3) and specific (H3K9, H3K14) hyperacetylation, thereby confirming UVI5008 HDACi action in tumori. Immunohistochemical analysis showed a stronger induction of H3K9 acetylation in HCT116 xenografts of mice treated with UVI5008 than in animals treated with SAHA (Fig. 3D bottom).

To investigate whether UVI5008 induced other histone modifications, we defined the spectrum of modifications in bulk histones from U937 cells treated with UVI5008 (4 hours) using mass spectrometric analyses. In addition to the increase of histone H3 acetylation expected for an HDACi, we identified a histone H3–derived peptide that is acetylated at K56 (Supplementary Fig. S2C and Table S1). In yeast, deacetylation of H3K56ac is mediated by the SIRT homologues Hst3 and Hst4 (32), and in humans H3K56ac acts as Sirt1 substrate (33). Hence, we investigated whether UVI5008 possesses SIRT inhibitory (SIRTi) activity. *In vitro* assays with recombinant human SIRT1 and 2 revealed that UVI5008 is a powerful inhibitor of SIRT1 and SIRT2 (Fig. 4A). Analyses with anti-H3K56ac antibodies (34) revealed H3K56 acetylation in UVI5008-

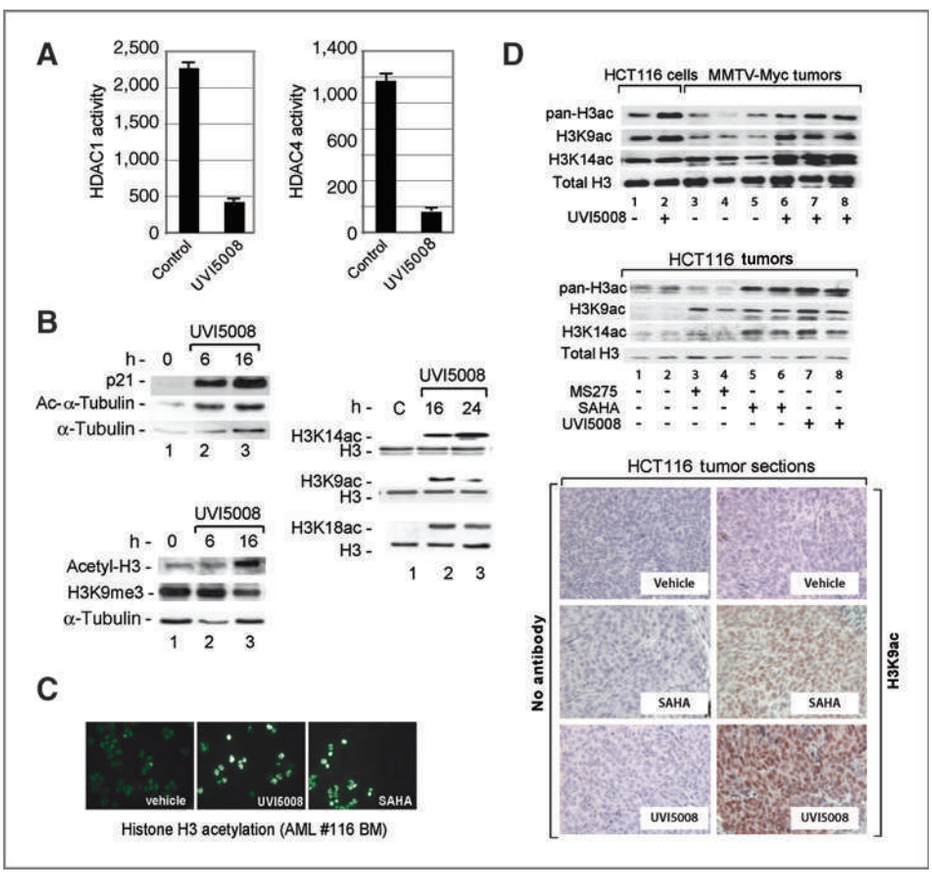

Figure 3. HDAC inhibitory activities of UVI5008 *in vitro*, *ex vivo*, and *in vivo*. A, cell-based HDAC1 and HDAC4 assay carried out in MCF7 cells with UVI5008 at 5 μmol/L. B, Western blot analyses of p21, α-tubulin, and histone H3 acetylation, H3K9me3 and H3K9, H3K14, H3K18 acetylations (ac) in U937 cells after 24 hours with UVI5008 at 5 μmol/L. C, immunofluorescence of histone H3 acetylation levels in *ex vivo* AML #116 blasts. D, stimulation of histone H3-specific acetylations both in the tumors of MMTV-Myc transgenic mice (data with HCT116 cells treated *in vitro* are shown for comparison) and in xenografted HCT116 p53$^{+/+}$ tumors treated with 40 mg/kg dose of UVI5008 and 20 mg/kg dose of SAHA analyzed at day 22. Immunohistochemical staining for H3K9 acetylation in tumor sections from UVI5008- or SAHA-treated HCT116-xenografted mice. BM, bone marrow.

Downloaded from mct.aacrjournals.org on March 6, 2016. © 2011 American Association for Cancer Research.

Published OnlineFirst October 6, 2011; DOI: 10.1158/1535-7163.MCT-11-0525

treated U937 cells, U2OS osteosarcoma cells (Fig. 4A and B), and other cell lines (Fig. 4B and data not shown). The observation that tumors from HCT116-xenografted mice and from the MMTV-myc breast cancer genetic mouse model revealed increased H3K56ac when treated with UVI5008 but not SAHA, established the *in vivo* SIRTi activity of UVI5008 (Fig. 4B and C).

Considering that acetylation activates p53 (35) and that SIRT1 deacetylates p53K382 (36), we hypothesized that UVI5008 may sustain p53 activity. Indeed, treatment of MCF7 and HCT116 cells with etoposide and UVI5008 increased p53K382 acetylation similar to the SIRT1i EX527 (37), thus extending our observations that UVI5008 inhibits SIRTs (Fig. 4C). Immunohistochemical analysis in tumors from HCT116-xenografted mice treated with UVI5008 confirmed efficient SIRTi *in vivo* (Fig. 4D; ref. 37). Our *in vivo* studies confirm that UVI5008, which displays a favorable pharmaokinetic (see Supplementary Methods for pharmacokinetic and pharmacodynamic study), reaches tumors *in vivo* to exert HDACi and SIRTi activity and to display anticancer action at doses that may be tolerable and efficacious in the context of a clinical trial. These results show that UVI5008 is a potent HDAC and SIRTi *in vitro* and *in vivo*.

UVI5008 reactivates TSG programs

A measure of importance for the activity of epigenetic inhibitors and their application as anticancer drugs is the ability to induce growth arrest by altering the expression of TSG such as the cyclin-dependent kinase inhibitor $p21^{Waf1/Cip1}$ CDKN1A (38). UVI5008 efficiently induced transcription of $p21^{Waf1/Cip1}$ in HCT116 cells and in the corresponding xenografts *in vivo* (Fig. 5A). UVI5008 also induced $p21^{Waf1/Cip1}$ expression in $p53^{-/-}$ HCT116 cells and xenografts, indicating that p21 targeting is p53 independent (Fig. 5A). Expression of secreted frizzled-related protein 1 and 2 (SFRP1, SFRP2) and MLH1 TSGs was strongly induced in UVI5008-treated HCT116 cells (Fig. 5A, right), HCT116-xenografts, MDA-MB231 and

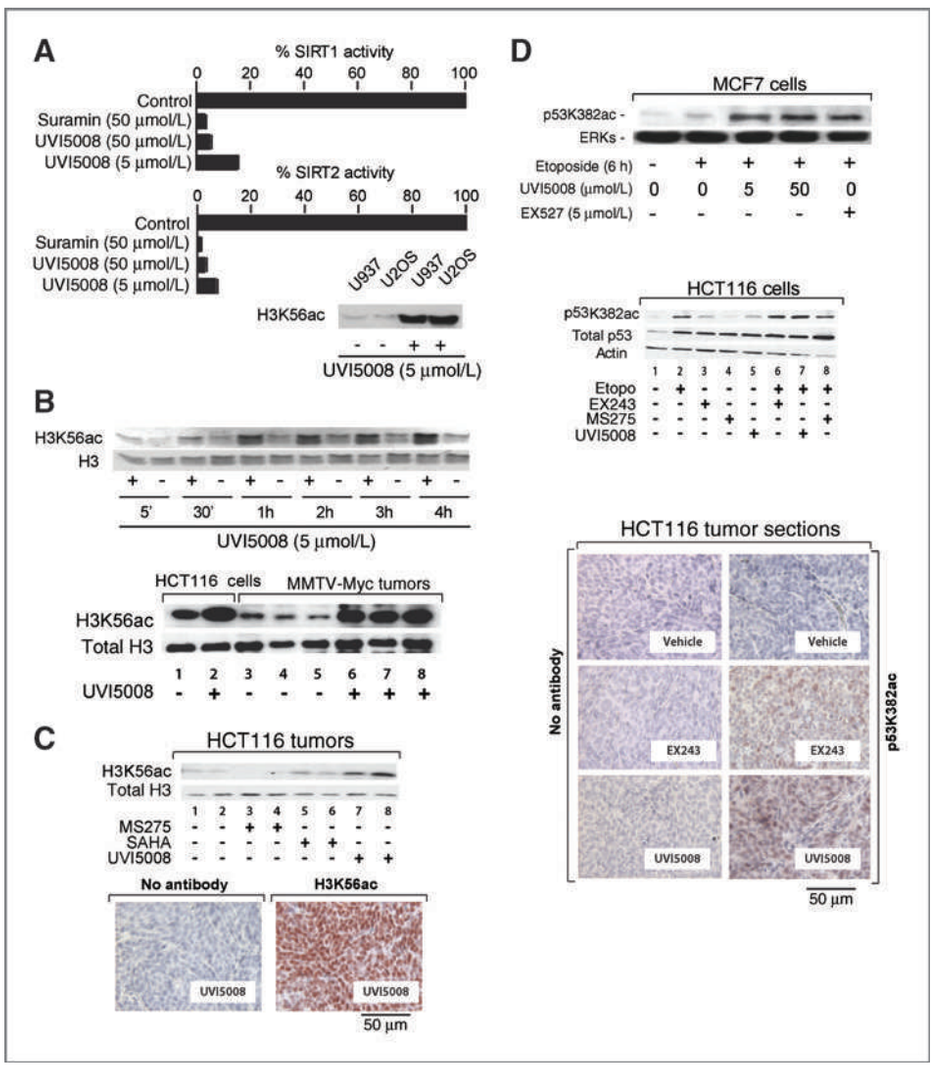

Figure 4. SIRTi activities of UVI5008 *in vitro*, *ex vivo*, and *in vivo*. A, human recombinant SIRT1 and 2 assays *in vitro* with the indicated compounds; histone H3K56 acetylation in U937 and U2OS cells treated for 24 hours with UVI5008 (5 μmol/L). B, Western blot analyses of H3K56 acetylation in histone extracts of U937 cells treated with UVI5008 (5 μmol/L). C, stimulation with UVI5008 (40 mg/kg dose) induced H3K56-specific acetylation in both tumors of MMTV-Myc transgenic mice (data with HCT116 cells treated *in vitro* are shown for comparison) and in xenografted HCT116 $p53^{+/+}$ tumors analyzed at day 22; H3K56ac immunohistochemical staining of tumor sections from UVI5008-treated HCT116-xenografted mice. D, top, analysis of p53K382 acetylation in MCF7 cells after 6-hour treatment with the indicated compounds; middle, p53K382 acetylation levels in HCT116 cells treated *in vitro*; bottom, p53K382 acetylation immunohistochemical staining of tumor sections from HCT116-xenografted mice treated with 40 mg/kg of UVI5008. Both UVI5008 and EX243, but not MS275, stimulate p53K382 acetylation in HCT116 cells *in vitro* (middle) and in tumors in treated xenografted mice (bottom). ERK, extracellular signal-regulated kinase.

Downloaded from mct.aacrjournals.org on March 6, 2016. © 2011 American Association for Cancer Research.

Published OnlineFirst October 6, 2011; DOI: 10.1158/1535-7163.MCT-11-0525

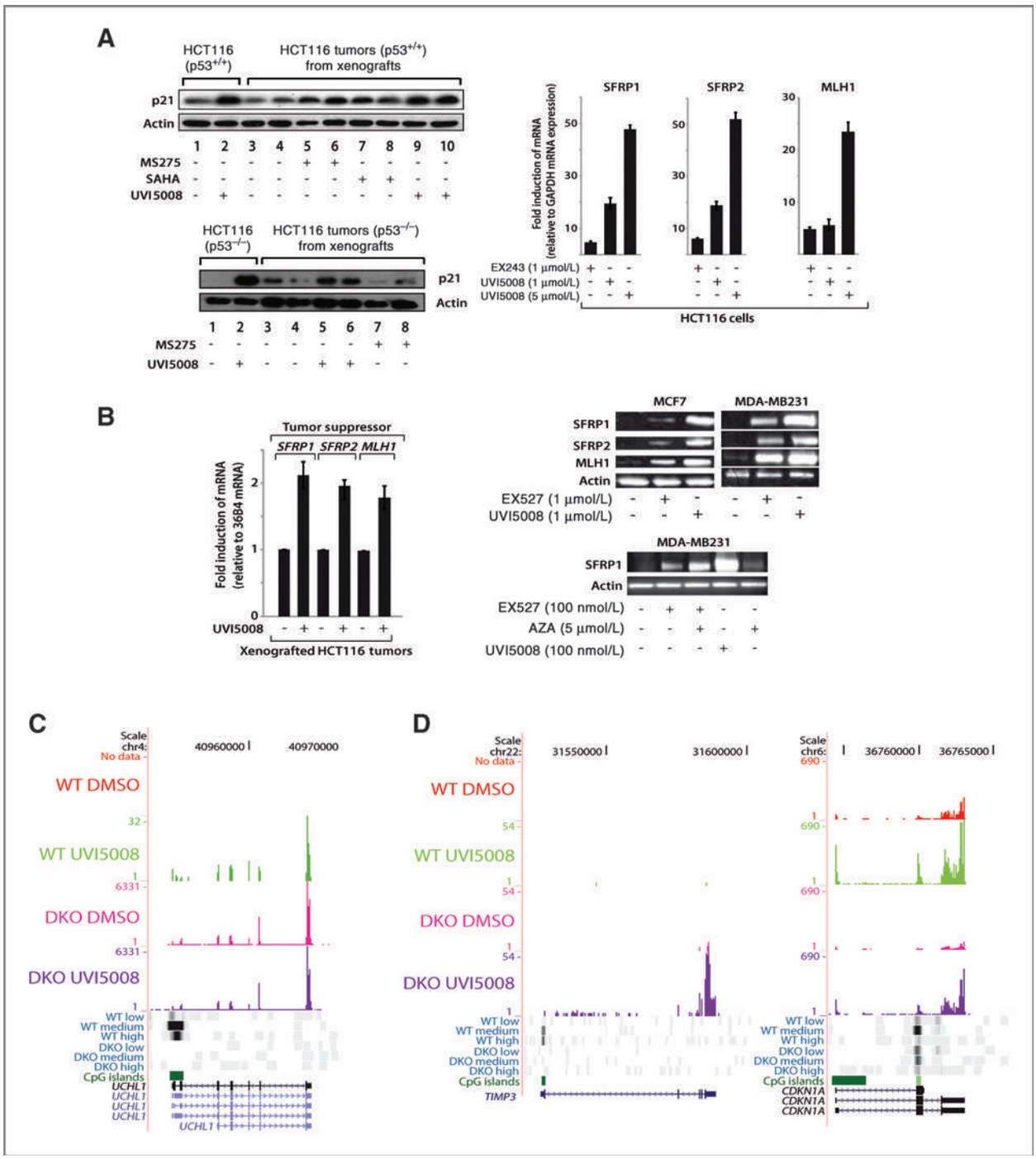

Figure 5. UVI5008 displays TSG reactivation *in vitro* and *in vivo*. A, left, Western blot analyses revealing p21 expression in HCT116 cells and in mice bearing HCT116 p53$^{+/+}$ and HCT116 p53$^{-/-}$ tumors; right, 48-hour treatment of UVI5008 reactivates TSGs in HCT116 cells. B, left panel, UVI5008 reactivates TSGs in HCT116-based xenografts; 36B4 is an inert internal control that RNA used for normalization; (right, top) UVI5008 reactivates TSG in breast cancer cells treated for 30 hours; (right, bottom) combined treatment with UVI5008 and AZA or EX527 and AZA (36 hours) synergizes in gene reexpression in MDA-MB231 cells. C, reactivation of *UCHL1* gene: browser screenshot of RNA-seq and DNMT (MethylCap-seq) profiling of HCT116 (wild-type; WT) and HCT116–DKO cells after treatment with UVI5008 at 5 μmol/L for 24 hours. RNA-seq was carried out using poly(A) + RNA. In MethylCap, fragmented genomic DNA (average 400–500 bp) is separated into 3 fractions (low, medium, and highly methylated DNA). The degree of methylation is graded from black (high) to white (unmethylation). Green boxes indicate CpG islands. The organization of the gene is schematically indicated. D, DNMT-dependent and -independent reactivation of *TIMP3* and *CDKNIA* (p21) genes. Browser screenshots (as in C). GAPDH, glyceraldehyde-3′phosphate dehydrogenase.

Downloaded from mct.aacrjournals.org on March 6, 2016. © 2011 American Association for Cancer Research.

Published OnlineFirst October 6, 2011; DOI: 10.1158/1535-7163.MCT-11-0525

MCF7 cells, supporting the SIRTi activity of UVI5008 (Fig. 5B). Note that UVI5008 mediated higher activation of SFRP1 expression when compared with exposure to SIRTi or DNMTi alone (Fig. 5B).

We also tested the ability of UVI5008 to activate transcription from genes with DNMT CpG-island in HCT116 cells and a double knockout of DNMT1 and DNMT3b [HCT116–double knockout (DKO) cells] by RNA-seq; in parallel, the DNMT status was determined by MethylCap (25). UVI5008 was able to partially reactivate loci such as UCHL1 gene whose CpG-island is methylated in line with its albeit weak DNMTi action (Fig. 5C). Upon complete loss of DNMT at this CpG-island as in HCT116–DKO, the gene is strongly reactivated. UVI5008 treatment of HCT116–DKO did not further enhance transcription as compared with the parental HCT116 suggesting that its DNMT but not HDAC and/or SIRTi caused the low but significant activation of the UCHL1 locus in wild-type cells. TIMP3, a TSG known both to be repressed by DNMT (39, 40) and to be SIRT1 target (41) was reactivated by UVI5008 only in HCT116–DKO cells and not in the untreated or wild-type cells (Fig. 5C). Possibly because of its low DNMT-inhibitory activity, UVI5008 could not overcome the repressive action of DNMT. Induction of $p21^{Waf1/Cip1}$ (CDKN1A) expression by UVI5008 in wild-type and DKO cells (Fig. 5D) is most likely because of the non-DNMTi activities of UVI5008, as the promoter–proximal CpG-island is not DNMT in wild-type or DKO HCT116 cells.

Mechanisms of pro-apoptotic UVI5008 action

The induction of apoptosis in cells, *ex vivo* and *in vivo* by UVI5008, and its bona fide tumor-specific action prompted us to decipher the underlying molecular pathway(s). Reverse transcriptase PCR and ELISA assays showed a strong increase of TNF superfamily 10 (TNFSF10) mRNA and protein levels upon UVI5008 exposure (Supplementary Fig. S4A) extending our previous findings that the TRAIL is a target of HDACi (19, 20). In line with the transcription activation of the TNFSF10 promoter by UVI5008, ChIP assays (23) revealed a rapid increase in histone H3 acetylation at the TNFSF10 promoter as exemplified by H3K9ac spreading to the TNFSF10 intron within 2 hours of treatment (Supplementary Fig. S4B). Similar activation was seen at the promoter of the DR-5 (DR5/TRAIL-R2; data not shown). These results show that UVI5008 activates the tumor-selective TRAIL pathway, which accounts for, or contributes to its tumor selectivity.

To assess the contribution of the TRAIL pathway to tumor-selective activity of UVI5008, we expressed a dominant-negative FADD (dnFADD) and the nonfunctional FADD mutant (dnFADDmut); the dnFADD reduced UVI5008-induced death only to approximately 50%, while completely blocking TNFSF10-induced apoptosis (Supplementary Fig. S4C). Similarly, only a moderate reduction of apoptosis was detectable in UVI5008-treated U937 cells expressing stably integrated shTNFSF10 (KD; ref. 20), whereas a complete reduction was obtained upon MS275, a bona fide pure HDACi (Supplementary Fig. S4C). Moreover, neither the simultaneous knockdown of TNFSF10 and p21 nor the blocking of DR-mediated death pathways by neutralizing antibodies affected UVI5008 death (Supplementary Fig. S5A and S5B). These observations strongly suggest that while TRAIL induction is a key factor in HDACi apoptosis, this is not the only mechanism by which UVI5008 induces apoptotic pathways distinct from or additional to TRAIL.

Concomitant death receptors and ROS activation cause UVI5008-mediated apoptosis

To gain further insight into the UVI5008 death activities, we assessed the implication of p53 and BMF. The *p53* gene is a SIRT target, whereas BMF silencing was reported to rescue cells from HDACi-induced apoptosis (42) in some cancers. Despite efficient knockdown of *BMF* and *p53*, no significant rescue from UVI5008-induced apoptosis was detected (Fig. 6A) suggesting that neither p53 nor BMF are singly essential. In agreement with these results, strong antitumor action of UVI5008 was observed in HCT116 $p53^{-/-}$ xenografts *in vivo* (Fig. 6A, right), reemphasizing its therapeutic potential for the therapy of p53 mutant or deficient cancers. On the other hand, caspases 8 and 9 inhibition, or caspase 8 silencing resulted in a major inhibition (Fig. 6B), implicating both the extrinsic and intrinsic pathways in UVI5008-induced death. Interestingly, while necroptosis inhibition by Nec-1 did not affect UVI5008-mediated death, *N*-acetyl-cysteine (NAC), a scavenger of ROS, significantly decreased it (Fig. 6C; compare lanes 3 and 7 with lanes 2 or 6). Most importantly, NAC fully blocked UVI5008-induced apoptosis in cells stably expressing shTNFSF10 (compare lanes 14 and 15). Strikingly, experiments carried out *ex vivo* in primary AML blasts, corroborated the dual involvement of the TRAIL-induced death signaling and ROS production as the main apoptotic mechanism of action of UVI5008 (Fig. 6D, lane 6). Thus, the anticancer activity of UVI5008 originates from the cumulative activation of multiple pathways due to the concomitant activation of death receptors and ROS production. More specifically, the triple action inhibitor UVI5008 displays (i) strong anticancer action *in vitro*, *ex vivo*, and *in vivo*, (ii) reactivation of TSGs *in vitro* and *in vivo*, and (iii) antitumor efficacy independent of p53 and BMF *in vitro* and *in vivo*.

Discussion

The fact that epigenetic modifications can be reversed by epi-drugs makes epi-compounds highly promising for antitumor therapy. However, the results have been lagging behind expectation. Investigation of the spectrum of epi-mutations in cancer has only recently started and Food and Drug Administration-approved epi-drugs are currently limited by a number of factors. Because of their moderate toxicities, HDACis and DNMTis entered therapy without a detailed molecular characterization. Beside this, no real markers for their apoptotic action or patient's response have been reported so far, thus currently

Downloaded from mct.aacrjournals.org on March 6, 2016. © 2011 American Association for Cancer Research.

Published OnlineFirst October 6, 2011; DOI: 10.1158/1535-7163.MCT-11-0525

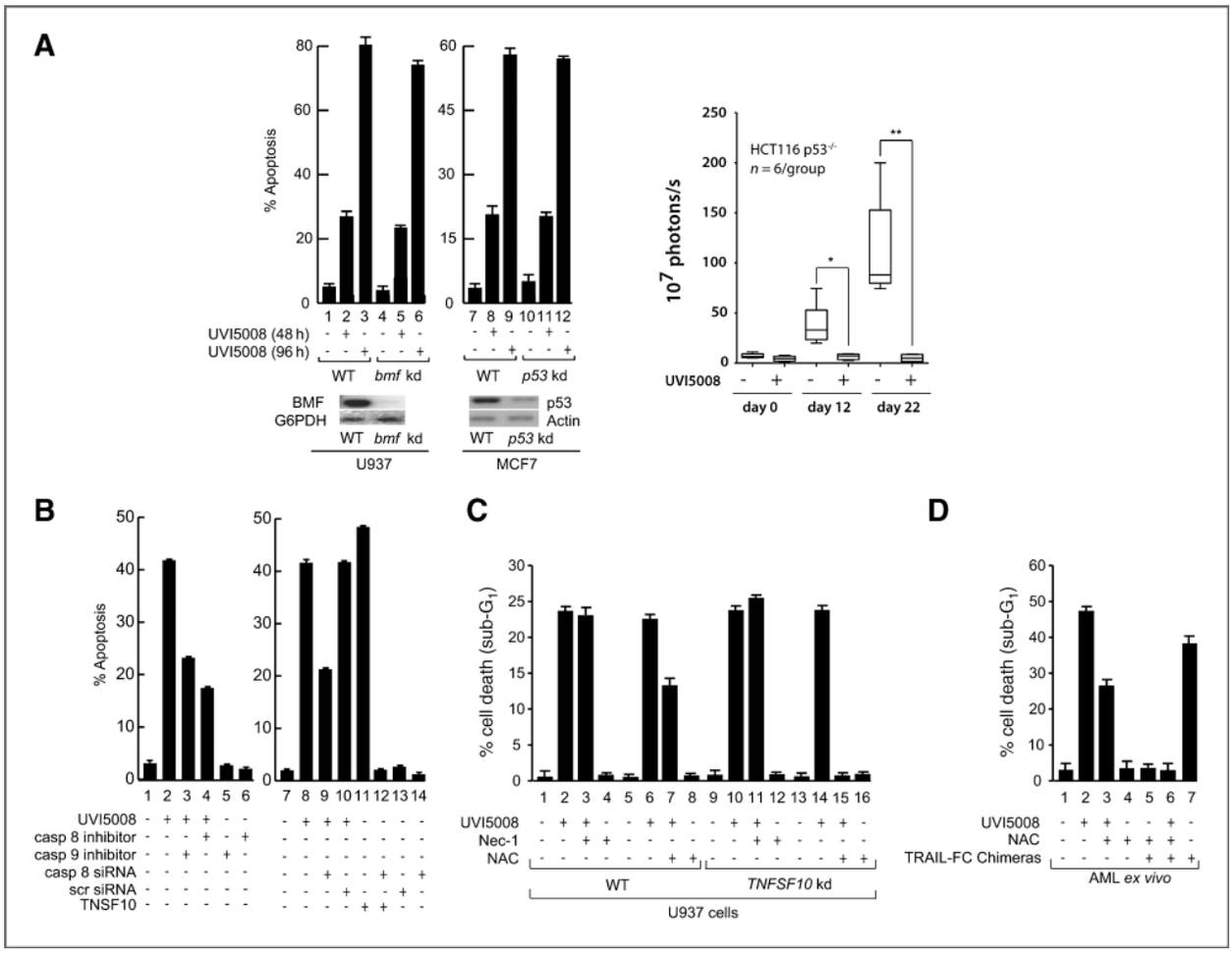

Figure 6. Only multiple pathway interventions can block UVI5008 action *in vitro* and *in vivo*. A, left, caspases 3–7 assay in wild-type (WT) and BMF KD U937 cells upon treatment with UVI5008 at 5 μmol/L; Annexin V assay carried out in MCF7 cells WT or p53 KD upon treatment with UVI5008 at 5 μmol/L; right, tumor growth kinetics of luciferase-tagged HCT116 p53$^{-/-}$ mouse xenografts exposed to vehicle or 40 mg/kg UVI5008. B, caspase (casp) 8 and 9 inhibitors (50 μmol/L) and short interfering RNA (siRNA) targeting Casp8 do not fully impair UVI5008 apoptosis in U937 cells. As control, TRAIL-mediated apoptosis was fully blocked by si-Casp8. C, NAC, but not NEC1, blocks apoptosis in TRAIL KD but not in WT U937 cells treated with UVI5008. D, only the combined action of NAC and TRAIL blockage impairs apoptosis in primary *ex vivo* AML blasts treated with UVI5008 (24 hours). Scr, scramble.

hampering clinical stratification. This lack of knowledge about pathways and targets might have led to unfocused therapeutic applications of epi-drugs.

We have identified and characterized the mechanism resulting in the apoptogenic action of UVI5008 in detail. We have previously reported that induction of TRAIL is part of the action spectrum of HDACis (19, 20). Hence, the contribution of TRAIL tumor-selective death by UVI5008 is likely to be linked to its HDACi action. Our observation that both TNFSF10-silenced and TNFSF10-deficient cells (cell lines and blasts) undergo apoptosis upon UVI5008 treatment strongly supports the contribution of SIRT and DNMT inhibition to UVI5008 anticancer action. Our data suggests that UVI5008 may be effective even in HDACi-resistant and hyper-mutated tumors. The same applies to tumors in which p53 is silenced or mutated (Figs. 5 and 6). Importantly, p53, BMF and TRAIL are often altered in cancers, thus suggesting the beneficial application of UVI5008 in multiple settings. Considering that SIRT1 mediates resistance to intrinsic apoptosis in cancer (43), SIRT1i may enforce the higher UVI5008 apoptotic activity possibly enhanced by its other inhibitory activities. We show that UVI5008 anticancer activity is causally linked to DR pathway activation and ROS production (Fig. 6). Although the involvement of oxidative stress in TRAIL-mediated apoptosis has been reported (44), our data shows that only the concomitant impairment of both pathways fully blocks UVI5008 action. Thus the targeting of these 2 molecular pathways in both *in vitro* and *ex vivo* settings by UVI5008 is independent (Fig. 6). Interestingly, SIRT1 inhibits apoptosis induced by oxidative stress. SIRT1 deacetylates and activates FOXO1 (45), FOXO3a (46), and FOXO4 (47), promoting expression of the DNA repair factor GADD45, and of the mitochondrial

Downloaded from mct.aacrjournals.org on March 6, 2016. © 2011 American Association for Cancer Research.

Published OnlineFirst October 6, 2011; DOI: 10.1158/1535-7163.MCT-11-0525

antioxidant enzyme manganese superoxide dismutase (MnSOD). These proteins may contribute to the induction of ROS tolerance by SIRT1 in tumors. Perturbation of the mechanisms that tightly couple ROS production, oxidative stress signaling, and FOXO activity to the subsequent cellular response is a pivotal step in cancer. Consequently, the ROS-FOXO pathway is a promising therapeutic target in cancer, not only as it mediates chemotherapy response, but also because it underpins drug resistance. As the intimate, reciprocal relation between FOXO and ROS is being unraveled (48), new applications arise to apply SIRTis to circumvent resistance to conventional drugs. The tight link between SIRTis and ROS production (48) may explain UVI5008 ROS-dependent action and its higher anticancer action when compared with single HDACi and SIRTi.

Analyzing DNMT3a inhibition, UVI5008 effect on DNMT on the p16 promoter is comparable to that of 5-azacytidine, whereas the induction of p16 protein expression by UVI5008 is higher (Supplementary Fig. S3), which likely results from the simultaneous inhibition of DNMT3a and SIRT1/2. Indeed, the indication that upon induction of DNA double-strand breaks, SIRT1 recruitment to the E-cadherin promoter is a prerequisite for DNMT3 recruitment and subsequent heritable CpG methylation at the promoter strongly favors the use of an anticancer drug that targets both SIRT and DNMT. The reported deregulation/overexpression of HDACs, DNMTs, and SIRTs in cancer (17, 33), also rationalizes UVI5008 use.

As suggested for HDACi and DNMTi combinations (49), also SIRT1i reactivates TSGs without altering DNA hypermethylation (8). The fact that TSGs, such as TIMP3 (Fig. 5), become reexpressed upon UVI5008 exposure is relevant. The mechanism of TIMP3 silencing in colon cancer and its role in tumorigenesis remain elusive. That DNA demethylation fails to reactivate the gene indicates that multiple activities potentiated by UVI5008 are needed for its reexpression. A further illustration that UVI5008 fulfills the criteria of a multiple targeting drug is the activation of SFRP1 (Fig. 5), which is far higher with UVI5008 than with canonical combo-treatments, supporting the winning strategy of applying a single drug exerting multiple-interventions against cancer.

The use of a single drug with multiple epi-activities, such as UVI5008, has great promise for therapy, as the synergies between its activities may reduce both the effective dose and development of resistance (50). The pharmaceutical development of a single compound is less complex than that of combinatorial therapies, complicated by divergent pharmacokinetic, pharmacodynamic, and complex ADMET profiles. UVI5008 belongs to this novel class of compounds, as it inhibits 3 distinct classes of epigenetic enzymes, namely DNMT3a, HDACs, and SIRTs. The rationale at the basis of targeting drugs could radically shift with the introduction of molecules interfering simultaneously with multiple targets as this might be more effective than single target agents thus representing a new generation of anticancer drugs. In this view, the inhibition of at least 3 epi-enzymes offers a promising alternative to combo-treatments of cancer using poly-pharmacology approaches. Given the ability of cancer to bypass signaling routes via complex networks, the simultaneous modulation of multiple epi-targets promises to open new avenues against cancer.

Disclosure of Potential Conflict of Interest

H.G. Stunnenberg, A.R. de Lera, H. Gronemeyer, and L. Altucci are inventors for the patent no. WO2008/125988 entitled: "Novel Derivatives of Psammaplin A, a method for their synthesis and their use for the prevention or treatment of cancer."

Acknowledgments

The authors thank W. Hahn and R. Weinberg for stepwise tumorigenesis model; P. Jansen, C. Erb, and G. Lemaire for technical help; E. Carrillo de Santa Pau and H. Marks for bioinformatics analysis; and V. Carafa and F. Rodríguez-Barrios for technical help and discussions.

Grant Support

The study was supported by Associazione Italiana ricerca contro il cancro (AIRC; L. Altucci), MIUR ('EpiGen' Italian IHEC Flag project) to L. Altucci, Association for International Cancer Research (AICR 00-108; H. Gronemeyer), Ligue National Contre le Cancer (H. Gronemeyer), ANR-07-EMPB-012-01 "*EPI_DRUG*", MEC (SAF2010-17935 FEDER; A.R. de Lera), Programmi di Ricerca Scientifica di Rilevante Interesse Nazionale (PRIN2009PX2T2E; L. Altucci), EU LSHC-CT-2005-518417 (EPITRON), HEALTH-F4-2007-200767 (APO-SYS), HEALTH-F2-2007-200620 (CANCERDIP), HEALTH-F4-2009-221952 (ATLAS).

The costs of publication of this article were defrayed in part by the payment of page charges. This article must therefore be hereby marked *advertisement* in accordance with 18 U.S.C. Section 1734 solely to indicate this fact.

Received July 17, 2011; revised September 9, 2011; accepted September 18, 2011; published OnlineFirst October 6, 2011.

References

1. Hanahan D, Weinberg RA. Hallmarks of cancer: the next generation. Cell 2011;144:646–74.
2. Martens JH, Brinkman AB, Simmer F, Francoijs KJ, Nebbioso A, Ferrara F, et al. PML-RARalpha/RXR alters the epigenetic landscape in acute promyelocytic leukemia. Cancer Cell 2010;17:173–85.
3. Martens JH, Stunnenberg HG. The molecular signature of oncofusion proteins in acute myeloid leukemia. FEBS Lett 2010;584:2662–9.
4. Grignani F, De Matteis S, Nervi C, Tomassoni L, Gelmetti V, Cioce M, et al. Fusion proteins of the retinoic acid receptor-alpha recruit histone deacetylase in promyelocytic leukaemia. Nature 1998;391:815–8.
5. Altucci L, Leibowitz MD, Ogilvie KM, de Lera AR, Gronemeyer H, RAR and RXR modulation in cancer and metabolic disease. Nat Rev Drug Discov 2007;6:793–810.
6. Matsushita H, Scaglioni PP, Bhaumik M, Rego EM, Cai LF, Majid SM, et al. *In vivo* analysis of the role of aberrant histone deacetylase recruitment and RAR alpha blockade in the pathogenesis of acute promyelocytic leukemia. J Exp Med 2006;203:821–8.
7. Baylin SB, Ohm JE. Epigenetic gene silencing in cancer—a mechanism for early oncogenic pathway addiction? Nat Rev Cancer 2006; 6:107–16.

Downloaded from mct.aacrjournals.org on March 6, 2016. © 2011 American Association for Cancer Research.

Published OnlineFirst October 6, 2011; DOI: 10.1158/1535-7163.MCT-11-0525

8. Pruitt K, Zinn RL, Ohm JE, McGarvey KM, Kang SH, Watkins DN, et al. Inhibition of SIRT1 reactivates silenced cancer genes without loss of promoter DNA hypermethylation. PLoS Genet 2006;2:e40.
9. Rodriguez-Paredes M, Esteller M. Cancer epigenetics reaches mainstream oncology. Nat Med 2011;17:330–9.
10. Bantscheff M, Hopf C, Savitski MM, Dittmann A, Grandi P, Michon AM, et al. Chemoproteomics profiling of HDAC inhibitors reveals selective targeting of HDAC complexes. Nat Biotechnol 2011;29:255–65.
11. Chi P, Allis CD, Wang GG. Covalent histone modifications–miswritten, misinterpreted and mis-erased in human cancers. Nat Rev Cancer 2010;10:457–69.
12. Szyf M. Epigenetics, DNA methylation and chromatin modifying drugs. Ann Rev Pharmacol Toxicol 2009;49:243–63.
13. Mai A, Altucci L. Epi-drugs to fight cancer: from chemistry to cancer treatment, the road ahead. Int J Biochem Cell Biol 2009;41:199–213.
14. Lane AA, Chabner BA. Histone deacetylase inhibitors in cancer therapy. J Clin Oncol 2009;27:5459–68.
15. Bolden JE, Peart MJ, Johnstone RW. Anticancer activities of histone deacetylase inhibitors. Nat Rev Drug Discov 2006;5:769–84.
16. Finkel T, Deng CX, Mostoslavsky R. Recent progress in the biology and physiology of sirtuins. Nature 2009;460:587–91.
17. Huffman DM, Grizzle WE, Bamman MM, Kim JS, Eltoum IA, Elgavish A, et al. SIRT1 is significantly elevated in mouse and human prostate cancer. Cancer Res 2007;67:6612–8.
18. Ooi SK, Bestor TH. The colorful history of active DNA demethylation. Cell 2008;133:1145–8.
19. Insinga A, Monestiroli S, Ronzoni S, Gelmetti V, Marchesi F, Viale A, et al. Inhibitors of histone deacetylases induce tumor-selective apoptosis through activation of the death receptor pathway. Nat Med 2005;11:71–6.
20. Nebbioso A, Clarke N, Voltz E, Germain E, Ambrosino C, Bontempo P, et al. Tumor-selective action of HDAC inhibitors involves TRAIL induction in acute myeloid leukemia cells. Nat Med 2005;11:77–84.
21. Nebbioso A, Manzo F, Miceli M, Conte M, Manente L, Baldi A, et al. Selective class II HDAC inhibitors impair myogenesis by modulating the stability and activity of HDAC-MEF2 complexes. EMBO Rep 2009;10:776–82.
22. Lahm A, Paolini C, Pallaoro M, Nardi MC, Jones P, Neddermann P, et al. Unraveling the hidden catalytic activity of vertebrate class IIa histone deacetylases. Proc Natl Acad Sci U S A 2007;104:17335–40.
23. Denissov S, van Driel M, Voit R, Hekkelman M, Hulsen T, Hernandez N, et al. Identification of novel functional TBP-binding sites and general factor repertoires. EMBO J 2007;26:944–54.
24. Akkers RC, van Heeringen SJ, Jacobi UG, Janssen-Megens EM, Francoijs KJ, Stunnenberg HG, et al. A hierarchy of H3K4me3 and H3K27me3 acquisition in spatial gene regulation in Xenopus embryos. Dev Cell 2009;17:425–34.
25. Brinkman AB, Simmer F, Ma K, Kaan A, Zhu J, Stunnenberg HG. Whole-genome DNA methylation profiling using MethylCap-seq. Methods 2010;52:232–6.
26. Hanahan D, Weinberg RA. The hallmarks of cancer. Cell 2000;100: 57–70.
27. Piña IC, Gautschi JT, Wang GYS, Sanders ML, Schmitz FJ, France D, et al. Psammaplins from the sponge *Pseudoceratina purpurea*: inhibition of both histone deacetylase and DNA methyltransferase. J Org Chem 2003;68:3866–73.
28. Brueckner B, Boy RG, Siedlecki P, Musch T, Kliem HC, Zielenkiewicz P, et al. Epigenetic reactivation of tumor suppressor genes by a novel small-molecule inhibitor of human DNA methyltransferases. Cancer Res 2005;65:6305–11.
29. Datta J, Ghoshal K, Denny WA, Gamage SA, Brooke DG, Phiasivongsa P, et al. A new class of quinoline-based DNA hypomethylating agents reactivates tumor suppressor genes by blocking DNA methyltransferase 1 activity and inducing its degradation. Cancer Res 2009;69:4277–85.
30. Ahn MY, Jung JH, Na YJ, Kim HS. A natural histone deacetylase inhibitor, Psammaplin A, induces cell cycle arrest and apoptosis in human endometrial cancer cells. Gynecol Oncol 2008;108:27–33.
31. Garcia J, Franci G, Pereira R, Benedetti R, Nebbioso A, Rodriguez-Barrios F, et al. Epigenetic profiling of the antitumor natural product psammaplin A and its analogues. Bioorg Med Chem 2011;19:3637–49.
32. Maas NL, Miller KM, DeFazio LG, Toczyski DP. Cell cycle and checkpoint regulation of histone H3 K56 acetylation by Hst3 and Hst4. Mol Cell 2006;23:109–19.
33. Das C, Lucia MS, Hansen KC, Tyler JK. CBP/p300-mediated acetylation of histone H3 on lysine 56. Nature 2009;459:113–7.
34. Ozdemir A, Spicuglia S, Lasonder E, Vermeulen M, Campsteijn C, Stunnenberg HG, et al. Characterization of lysine 56 of histone H3 as an acetylation site in *Saccharomyces cerevisiae*. J Biol Chem 2005; 280:25949–52.
35. Tang Y, Zhao W, Chen Y, Zhao Y, Gu W. Acetylation is indispensable for p53 activation. Cell 2008;133:612–26.
36. Avalos JL, Celic I, Muhammad S, Cosgrove MS, Boeke JD, Wolberger C. Structure of a Sir2 enzyme bound to an acetylated p53 peptide. Mol Cell 2002;10:523–35.
37. Solomon JM, Pasupuleti R, Xu L, McDonagh T, Curtis R, DiStefano PS, et al. Inhibition of SIRT1 catalytic activity increases p53 acetylation but does not alter cell survival following DNA damage. Mol Cell Biol 2006;26:28–38.
38. Gui CY, Ngo L, Xu WS, Richon VM, Marks PA. Histone deacetylase (HDAC) inhibitor activation of p21WAF1 involves changes in promoter-associated proteins, including HDAC1. Proc Natl Acad Sci U S A 2004;101:1241–6.
39. Bai YX, Yi JL, Li JF, Sui H. Clinicopathologic significance of BAG1 and TIMP3 expression in colon carcinoma. World J Gastroenterol 2007;13:3883–5.
40. Durr ML, Mydlarz WK, Shao C, Zahurak ML, Chuang AY, Hoque MO, et al. Quantitative methylation profiles for multiple tumor suppressor gene promoters in salivary gland tumors. PLoS One 2010;5:e10828.
41. Cardellini M, Menghini R, Martelli E, Casagrande V, Marino A, Rizza S, et al. TIMP3 is reduced in atherosclerotic plaques from subjects with type 2 diabetes and increased by SirT1. Diabetes 2009;58: 2396–401.
42. Zhang Y, Adachi M, Kawamura R, Imai K. BMF is a possible mediator in histone deacetylase inhibitors FK228 and CBHA-induced apoptosis. Cell Death Differ 2006;13:129–40.
43. Cohen HY, Lavu S, Bitterman KJ, Hekking B, Imahiyerobo TA, Miller C, et al. Acetylation of the C terminus of Ku70 by CBP and PCAF controls Bax-mediated apoptosis. Mol Cell 2004;13:627–38.
44. Lee MW, Park SC, Kim JH, Kim IK, Han KS, Kim KY, et al. The involvement of oxidative stress in tumor necrosis factor (TNF)-related apoptosis-inducing ligand (TRAIL)-induced apoptosis in HeLa cells. Cancer Lett 2002;182:75–82.
45. Motta MC, Divecha N, Lemieux M, Kamel C, Chen D, Gu W, et al. Mammalian SIRT1 represses forkhead transcription factors. Cell 2004;116:551–63.
46. Brunet A, Sweeney LB, Sturgill JF, Chua KF, Greer PL, Lin Y, et al. Stress-dependent regulation of FOXO transcription factors by the SIRT1 deacetylase. Science 2004;303:2011–5.
47. van der Horst A, Tertoolen LG, de Vries-Smits LM, Frye RA, Medema RH, Burgering BM. FOXO4 is acetylated upon peroxide stress and deacetylated by the longevity protein hSir2(SIRT1). J Biol Chem 2004; 279:28873–9.
48. Myatt SS, Brosens JJ, Lam EW. Sense and sensitivity: FOXO and ROS in cancer development and treatment. Antioxid Redox Signal 2011;14: 675–87.
49. Jones PA, Baylin SB. The fundamental role of epigenetic events in cancer. Nat Rev Genet 2002;3:415–28.
50. Overington JP, Al-Lazikani B, Hopkins AL. How many drug targets are there? Nat Rev Drug Discov 2006;5:993–6.

Downloaded from mct.aacrjournals.org on March 6, 2016. © 2011 American Association for Cancer Research.

Published OnlineFirst October 6, 2011; DOI: 10.1158/1535-7163.MCT-11-0525

American Association for Cancer Research

Molecular Cancer Therapeutics

Death Receptor Pathway Activation and Increase of ROS Production by the Triple Epigenetic Inhibitor UVI5008

Angela Nebbioso, Raquel Pereira, Harshal Khanwalkar, et al.

Mol Cancer Ther 2011;10:2394-2404. Published OnlineFirst October 6, 2011.

Updated version	Access the most recent version of this article at: doi:10.1158/1535-7163.MCT-11-0525
Supplementary Material	Access the most recent supplemental material at: http://mct.aacrjournals.org/content/suppl/2011/10/03/1535-7163.MCT-11-0525.DC1.html

Cited articles	This article cites 50 articles, 12 of which you can access for free at: http://mct.aacrjournals.org/content/10/12/2394.full.html#ref-list-1
Citing articles	This article has been cited by 4 HighWire-hosted articles. Access the articles at: http://mct.aacrjournals.org/content/10/12/2394.full.html#related-urls

E-mail alerts	Sign up to receive free email-alerts related to this article or journal.
Reprints and Subscriptions	To order reprints of this article or to subscribe to the journal, contact the AACR Publications Department at pubs@aacr.org.
Permissions	To request permission to re-use all or part of this article, contact the AACR Publications Department at permissions@aacr.org.

Downloaded from mct.aacrjournals.org on March 6, 2016. © 2011 American Association for Cancer Research.

Food and Chemical Toxicology 55 (2013) 304–312

Contents lists available at SciVerse ScienceDirect

Food and Chemical Toxicology

journal homepage: www.elsevier.com/locate/foodchemtox

Antioxidant, antimicrobial and anti-proliferative activities of *Solanum tuberosum* L. var. Vitelotte

Paola Bontempo [a,*], Vincenzo Carafa [a], Roberto Grassi [b], Adriana Basile [c], Gian Carlo Tenore [d], Carmen Formisano [e], Daniela Rigano [e,*], Lucia Altucci [a,f,*]

[a] Department of General Pathology, Second University of Naples, Vico L. de Crecchio 7, 80138 Napoli, Italy
[b] Medical-Surgical Department of Internal and Experimental Clinic 'Magrassi-Lanzara', Second University of Naples, Via Pansini 5, 80100 Naples, Italy
[c] Department of Plant Biology, University of Naples "Federico II", Via Foria 223, 80139 Naples, Italy
[d] Department of Pharmaceutical Chemistry, University of Naples "Federico II", Via D. Montesano, 49, 80131 Naples, Italy
[e] Department of Chemistry of Natural Compounds, University of Naples "Federico II", Via D. Montesano, 49, 80131 Naples, Italy
[f] Institute of Genetics and Biophysics 'Adriano Buzzati Traverso', IGB, Via P. Castellino 111, 80131 Naples, Italy

ARTICLE INFO

Article history:
Received 29 October 2012
Accepted 26 December 2012
Available online 11 January 2013

Keywords:
Solanum tuberosum L. var. Vitelotte
Anthocyanin
Antibacterial
Antifungal
Anticancer action

ABSTRACT

Solanum tuberosum L. var. Vitelotte is a potato variety widely used for human consumption. The pigments responsible for its attractive color belong to the class of anthocyanins. The objectives of this study were to characterize and measure the concentration of anthocyanins in pigmented potatoes and to evaluate their antioxidant and antimicrobial activities and their anti-proliferative effects in solid and hematological cancer cell lines. Anthocyanins exert anti-bacterial activity against different bacterial strains and a slight activity against three fungal strains. The Gram-positive bacterium *Staphylococcus aureus* and the fungus *Rhyzoctonia solani* were the most affected microorganisms. Antioxidant activities were evaluated by DPPH and FRAP methods; the extract showed a higher reducing capability than anti-radical activity. Moreover, we found that in different cancer cell models the anthocyanins cause inhibition of proliferation and apoptosis in a dose dependent manner. These biological activities are likely due to the high content of malvidin 3-O-*p*-coumaroyl-rutinoside-5-O-glucoside and petunidin 3-O-*p*-coumaroyl-rutinoside-5-O-glucoside.

© 2013 Elsevier Ltd. All rights reserved.

1. Introduction

Solanum tuberosum L. var. Vitelotte is a potato variety with deep blue skin and violet flesh widely used for human consumption and well appreciated for its good nutritional characteristics. In recent years there has been an increasing interest in red- and purple-fleshed potato varieties because of their color appeal, outstanding taste and "mashability". There has been consumer interest in potatoes with colored flesh for use in salads and novelty crisps, especially since color is retained after cooking or frying (Lewis et al., 1999). The pigments responsible for the attractive color of these potatoes varieties are anthocyanins, whose concentration vary in large ranges and correlates with the degree of pigmentation in potato flesh. The pigments in colored potatoes have been identified as the 5-glucoside-3-rhamnosylglucoside derivatives of all the common anthocyanidins, monoacylated with *p*-coumaric or ferulic acids (Andersen et al., 2002; Harborne, 1960; Lewis et al., 1999). A good correlation between the total anthocyanins and the biological activities of the tubers was found. It is known that these pigments are rapidly adsorbed at the stomach level (Passamonti et al., 2003). Recently, *in vivo* absorption of anthocyanins from an extract of *Ipomea batatas* L. was also demonstrated in rats and humans after their addition to the diet. Acylated anthocyanins, the main constituents of potato, were detected in plasma and urine after ingestion (Harada et al., 2004). Anthocyanins are known to possess different pharmacological properties and are used by humans for therapeutic purpose (Kong et al., 2003). More and more

Abbreviations: AML, Acute Myeloid Leukemia; APL, Acute Promyelocytic Leukemia; COX-2, cyclooxygenase-2; DPPH, Free Radical Scavenging Ability; FAB, French-American-British; FAS, TNF receptor superfamily, member 6; FASL, FAS ligand; FRAP, Ferric Reducing/Antioxidant Power; HPLC-DAD, high performance liquid chromatography-diode array detector; HPLC–ESI–MS, high performance liquid chromatography- electrospray ionization mass spectrometry; MBC, Minimum Bactericidal Concentration; MIC, Minimal inhibitory concentration; NF-κb, Nuclear Factor-kappa B; PML-RAR, Promyelocytic Leukemia-Retinoic Acid Receptor; ROS, Reactive Oxygen Species; TE, Trolox Equivalent; TNF-α, Tumor Necrosis Factor alpha; VEGF, Vascular Endothelial growth factor.

* Corresponding authors. Address: Department of general Pathology, Second University of Naples, Vico L. de Crecchio 7, 80138 Napoli, Italy. Tel.: +39 0815667569; fax: +39 081450169 (L. Altucci). Tel.: +39 0815665702; fax: +39 081450169 (P. Bontempo). Tel.: +39 081678546; fax: +39 081678552 (D. Rigano).

E-mail addresses: paola.bontempo@unina2.it (P. Bontempo), drigano@unina.it (D. Rigano), lucia.altucci@unina2.it (L. Altucci).

0278-6915/$ - see front matter © 2013 Elsevier Ltd. All rights reserved.
http://dx.doi.org/10.1016/j.fct.2012.12.048

studies show that anthocyanins have demonstrated ability to protect against a myriad of human diseases such as liver dysfunction, hypertension, vision disorders, microbial infections, and diarrhea (Rice-Evans and Packer, 1998; Smith et al., 2000; Wang et al., 2000). Due to this fact, a high intake of anthocyanin-rich food has been linked to health preventive effects and reduced risk of pathologies such as aged-related macular degeneration, cancer or cardiovascular disorders. Indeed, the consumption of anthocyanins lowers the risk of cardiovascular disease, diabetes, arthritis and cancer due, at least in part, to their anti-oxidant and anti-inflammatory activities (Afaq et al., 2005; Huang et al., 2002; Prior and Wu, 2006; Reddy et al., 2005; Rodrigo et al., 2006). The anticancer action of anthocyanins has also been reported. Pure anthocyanins and anthocyanin-rich extracts from fruits and vegetables have exhibited anti-proliferative activity towards multiple cancer cell types *in vitro* (Rodrigo et al., 2006; Zhang et al., 2005). Cell proliferation was inhibited by the ability of anthocyanins to block various stages of the cell cycle by acting on regulatory proteins (e.g., p53, p21, p27, cyclin D1, cyclin A, etc.). Interestingly, several investigations have compared the antiproliferative effects of anthocyanins on normal vs. cancer cells and found that they selectively inhibit the growth of cancer cells with relatively little or no effect on the growth of normal cells (Galvano et al., 2004; Hakimuddin et al., 2004). Furthermore, anthocyanin-rich extracts from berries and grapes, and several pure anthocyanins and anthocyanidins, have exhibited pro-apoptotic effects in multiple cell types *in vitro* (Afaq et al., 2007; Chen et al., 2005; Martin et al., 2003; Olsson et al., 2004; Reddivari et al., 2007; Seeram et al., 2006), acting via both the mitochondrial and the extrinsic death pathways (Chang et al., 2005; Reddivari et al., 2007). In the intrinsic pathway, anthocyanin treatment alters mitochondrial membrane potential, leading to cytochrome *c* release and modulation of caspase-dependent apoptosis. In the extrinsic pathway, anthocyanins modulate the expression of FAS and FASL (FAS ligand) in cancer cells. In addition, treatment of cancer cells, but not normal cells, with anthocyanins leads to an accumulation of ROS (reactive oxygen species) and subsequent apoptosis, suggesting that the ROS-mediated mitochondrial caspase-independent pathway is important for anthocyanin-induced apoptosis (Feng et al., 2007). Not surprisingly, anthocyanins also exhibit antioxidant and anti-inflammatory effects. Inflammation has been shown to play a role in the promotion of some types of cancer in animals, and probably in humans (Kwon et al., 2007). Abnormal up-regulation of two inflammatory proteins, nuclear factor-kappa B (NF-κB) and cyclooxygenase-2 (COX-2), is a common occurrence in many cancers, and inhibitors of these proteins usually exhibit significant chemo-preventive potential (Chang et al., 2005;Martin et al., 2003). Interestingly, through their ability to inhibit the mRNA and/or protein expression levels of COX-2, NF-κB and various interleukins, the anthocyanins have exhibited anti-inflammatory effects in multiple cell types *in vitro* (Afaq et al., 2005; Huang et al., 2002; Reddy et al., 2005;Rodrigo et al., 2006). In addition, the anticancer potential can also be correlated to the anthocyanins anti-angiogenic effects that have been investigated in endothelial (Bagchi et al., 2004), oral cancer (Rodrigo et al., 2006) and mouse epidermal JB6 cells (Huang et al., 2006). Anthocyanins have been shown to suppress angiogenesis through several mechanisms such as: inhibition of H_2O_2-and tumor necrosis factor alpha (TNF-α)-induced VEGF expression in epidermal keratinocytes (Bagchi et al., 2004), and by reducing VEGF and VEGF receptor expression in endothelial cells. Anthocyanin extracts (2.5–100 μM) from different berry types, black rice and eggplant have been evaluated for their ability to inhibit the invasion of multiple cancer cell types in Matrigel (Coates et al., 2007; Nagase et al., 1998). Prevention and treatment of cancer through the induction of cellular differentiation offers a cell-specific approach to cancer prevention and treatment that is likely to be less toxic than standard radio/chemotherapy (Fimognari et al., 2004).

The objectives of this study were to characterize and measure the concentration of anthocyanins in pigmented potatoes and to evaluate their antioxidant, antibacterial and antifungal activities and their anti-proliferative effects in solid and hematological cancer cell lines. Our results indicate the therapeutic value of *S. tuberosum* extracts and its contained anthocyanins as potential antimicrobial, antioxidant and anticancer agents.

2. Materials and methods

2.1. Chemicals

DPPH (1,1-diphenyl-2-picrilhydrazyl), 2,4,6-tris-2,4,6-tripiridyl-2-triazine (TPTZ), ferric chloride dry, 6-hydroxy-2,5,7,8-tetramethylchroman-2-carboxylic acid (Trolox), L-ascorbic acid, tert-butyl-4-hydroxy toluene (BHT), gallic acid, were purchased from Sigma Chemical Co. (St. Louis, MO). Methanol (RPE) was purchased from Carlo Erba (Milano, Italy).

2.2. Plant material

S. tuberosum L. var. Vitelotte (718 g) was collected at Nusco (Avellino) in Southern Italy, on June 2010. All the tubers had pigmented peel and pigmented flesh. They were washed in running tap water, cut into pieces of approximately 0.5 cm, dried in a heated air drier, and then pulverized by the disintegrator. After drying the weight of potatoes was 157 g. Samples were kept at 4 °C.

2.3. Preparation of anthocyanins extract

Several extraction methods have been proposed to obtain extracts rich in anthocyanin, usually based on solvents as methanol, ethanol, acetone, water or mixtures. The addition of a small amount of hydrochloric acid or formic acid is recommended to prevent the degradation of the non-acylated compounds (Kjell and Øyvind, 2005). The optimum condition for anthocyanin extraction of potatoes was determined according to a previous paper (Fan et al., 2008).

Pigmented potato powder was put into a 50 ml conical flask, then added in acid–ethanol (HCl, 1.5 mol/l) with a solid–liquid ratio 1:32 and put in thermostatic water bath at a selected temperature (80 °C) for 60 min, then, centrifuged at 4000 rpm for 15 min. The supernatant was collected and transferred into a 50 ml volumetric flask for the determination of anthocyanins yield. About 1 g of the samples was used for each treatment.

2.4. Antimicrobial activity assays Microorganisms

Nine bacterial strains from the American Type Culture Collection (ATCC; Rockville, MD, USA) were employed. They included Gram-positive (G+) bacteria: *Staphylococcus aureus* (ATCC 13709) and *Enterococcus faecalis* (ATCC 14428), and the following Gram-negative (G−) bacteria: *Proteus mirabilis* (ATCC 7002), *Proteus vulgaris* (ATCC 12454), *Pseudomonas aeruginosa* (ATCC 27853), *Salmonella typhi* (ATCC 19430), *Enterobacter aerogenes* (ATCC 13048), *Enterobacter cloacae* (ATCC 10699), and *Klebsiella pneumoniae* (ATCC 27736). The same bacterial strains, clinically isolated, were used to compare the sensitivity to the extract.

The extract was added with 5×10^{-2} M stock solution in DMSO, and diluted from 0.01 to 1000 μg/ml concentrations in sterile physiological Tris buffer (pH 7.4, 0.05 M) (Ieven et al., 1979) immediately before being used.

2.5. MIC and MBC determination

Bacterial strains were grown on MH agar plates (DIFCO, Detroit, MI) and suspended in MH (Mueller Hinton) broth (DIFCO). The MIC values against bacterial strains were performed using the Ericcson and Sherris (1971) broth-dilution method (MH broth). The inoculum suspensions were prepared from 6 h broth cultures and adjusted to obtain a 0.5 McFarland standard turbidity. The extract was sterilized by filtration through Millipore filters (0.45 μm) and added to MH broth medium. Serial 10-fold dilutions were made for a concentration range between 0.01 and 1000 μg/ml. In the range between the minimum active and the maximum inactive concentrations were tested 2-fold dilutions to obtain a more precise measure of the MIC. The bacterial suspensions were aerobically incubated for 24 h at 37 °C. The MIC was defined as the lowest concentration able to inhibit any visible bacterial growth. Cultures containing only sterile physiological TRIS buffer (pH 7.4, 0.05 M), which did not influence bacterial growth, were used as controls. The MIC values were also determined for tetracycline hydrochloride (Pharmacia, Milano), benzyl penicillin sodium (Cynamid, Catania) and cefotaxime sodium (Roussel Pharma, Milano) in MH broth using standard method.

The MBC determination was carried out transferring to the fresh MH broth aliquots of bacterial suspensions from the test tubes containing extract concentrations equal or higher (up to 1000 μg/ml) than the MIC. The extract was tested in triplicate; the experiment was performed four times.

2.6. Antifungal activity assays

Antifungal tests were done against three fungal strains: the clinically isolated (CI) yeast *Candida albicans*, potentially pathogenic for humans, and the two filamentous phytopathogenic fungi *Botrytis cinerea* and *Rhyzoctonia solani*, kindly provided by the Plant Pathology Department of the University Federico II of Naples (Italy).

The fungi were maintained on Sabouraud glucose agar (SGA) medium (Diagnostic Pasteur).

Two methods were used for the *in vitro* assays: (1) method of agar incorporation (dilution on a solid medium) and (2) the minimal inhibitory concentration (MIC) which inhibits the visible growth of fungi was determined by the standardized broth micro-dilution method. Both the methods are fully described in a previous paper (Basile et al., 2010). Positive control cultures were made culturing the fungi without and with ketoconazole (Sigma Aldrich, Milan).

2.7. Cell lines and materials

NB4 cells were provided by M. Lanotte (INSERM U-496, Centre G. Hayem Hospital Saint-Louis Paris, France). MCF-7, HeLa, MDA-MB231, LNCaP and U937 cell lines have been obtained from ATCC and routinely cultured. MCF-7 and HeLa cells were grown at 37 °C in 5% CO2 atmosphere in Dulbecco's Modified Eagle Medium (DMEM, Gibco, NY, USA), supplemented with 5% fetal bovine serum (FBS, Gibco), 1% L-glutamine, 1% ampicillin/streptomycin and 0.1% gentamicin. U937, MDA-MB231, LNCaP and NB4 cells, were grown at 37 °C in 5% CO2 atmosphere in RPMI-1640 medium (Gibco, NY, USA), supplemented with 10% heat-inactivated fetal bovine serum (FBS), 1% L-glutamine, 1% ampicillin/streptomycin and 0.1% gentamicin. 3T3L1 (ATCC) fibroblasts were grown – formulated Dulbecco's Modified Eagle Medium (DMEM, Gibco, NY, USA), completed with bovine calf serum to a final concentration of 10%.

2.8. Crystal violet and Trypan blu assays

In a 96 multiwell plate (BD), about 1200 cells/well were suspended in 200 μl of cell cultures medium. After treatment with extract, cells were fixed in 25 μl of 11% gluteraldehyde in PBS (SIGMA) for 15 min, washed in deionized water and dried. Wells were incubated for 20 min in 100 μl of Crystal violet (CV; Sigma), 1 mg/ml in 20% methanol, and then washed again. Wells were incubated immediately for 20 min in 100 l of acetic acid (10%). Colorimetric assay carried out in triplicate was quantified by measuring OD595. As alternative viability assay, we have performed a dye exclusion stain, where cells with an intact membrane are able to exclude the dye while cells without an intact membrane take up the coloring agent. The dye used for exclusion stain is the Trypan blue (SIGMA). Briefly cells have been mixed 1:1 with a 0.4% Trypan blu solution and counted in triplicate.

2.9. Cell cycle analysis

2.5×10^5 cells were collected and suspended in 500 μl of a hypotonic buffer (0.1% Triton X-100, 0.1% sodium citrate, 50 μg/ml propidium iodide (PI), RNAse A). Cells were incubated in the dark for 30 min. Samples were acquired on a FACS-Calibur flow cytometer using Cell Quest software (Becton Dickinson) and analyzed with standard procedures using Cell Quest software (Becton Dickinson) and the ModFit LT version 3 Software (Verity) as previously reported (Nebbioso et al. 2011). All the experiments were performed in triplicate.

2.10. Analysis of apoptosis

Apoptosis was measured as pre-G1 analyzed by FACS with Cell Quest software (Becton Dickinson) as previously reported (Altucci et al., 2001; Nebbioso et al., 2005). Moreover, analysis of apoptosis was measured as activation of caspases 8 and 3–7 (B-Bridge) or DAPI staining following the manufacturer's instructions.

2.11. Total monomeric anthocyanin content

The total monomeric anthocyanin content of the potatoes extract was evaluated by applying a pH-differential method. An aliquot of 1 ml of the sample was added to two vials containing 10 ml of acetate buffer (pH 3.6) and HCl 1 N, respectively. The difference between the absorbance read at 530 nm was calculated. Total anthocyanin content was expressed as mg malvin equivalents (ME)/100 ml of potato extract.

2.12. Determination of antioxidant capacity

Both sample and analytical standards were dissolved in methanol in order to obtain 1 mg/100 ml solutions, which was chosen as appropriate concentration for assessing antioxidant activity after preliminary studies of the different concentrations. For each antioxidant assay, a Trolox aliquot was used to develop a 0.5–10 mmol/l standard curve. All data were then expressed as Trolox Equivalents (mmol/l) and antioxidant activity referred to as Trolox Equivalents Antioxidant Capacity (TEAC).

2.12.1. Ferric reducing/antioxidant power (FRAP method)

The total antioxidant potential of the extract was determined by using the ferric reducing antioxidant power (FRAP) assay of Benzie and Strain (1996). A solution of 10 mmol/l TPTZ in 40 mmol/l HCl and 12 mmol/l ferric chloride was diluted in 300 mmol/l sodium acetate buffer (pH 3.6) at a ratio of 1:1:10. Aliquots (40 μl) of extract solutions were added to 3 ml of the FRAP solution, and allowed to react for 90 min. at 37 °C, before reading the absorbance at 593.

2.12.2. Free radical scavenging ability (DPPH method)

The ability of the extract to scavenge the DPPH radical was measured using the method of Brand-Williams et al. (1995). Aliquots (40 μl) of extract solutions were added to 3 ml of DPPH solution (6×10^{-5} mol/l) and the absorbance was determined at 515 nm after 90 min.

2.13. Anthocyanin separation, identification and quantification

HPLC separation of anthocyanin extract was performed according to earlier studies (Downey and Rochfort, 2008). Identification was possible by monitoring anthocyanins at 520 nm and by comparing their spectra and retention times with those of commercial standards and with those reported in previous works (Downey and Rochfort, 2008). The sample (20 μl) was directly injected after filtration through a 0.45 μm membrane filter. Elution conditions consisted of 10% formic acid in water (solvent A) and 10% formic acid in a methanol (solvent B) gradient at a flow rate of 1.0 ml/min. The column selected was a C-18 Zorbax (150 mm × 4.6 mm, 5 μm packing; Agilent, USA) protected by an Agilent C-18 guard column. Analyses were run on a Finnigan HPLC system (Thermo Electron Corporation, San Jose, CA) provided with photodiode array detector (DAD). The gradient conditions were: 0 min, 18% B; 14 min, 29% B; 16 min, 32% B; 18 min, 41% B; 18.1 min, 30% B; 29 min, 41% B; 32 min, 50% B; 34.5 min, 100% B; 35–38 min, 18% B. Calibration curves consisted in 0.001–1 mg/ml quercetin- 3-O-glucoside and 0.05–1 mg/ml malvidin-3-O-glucoside standard solutions. The identity of anthocyanins was confirmed with LC–ESI/MS/MS experiments and the data were compared with previous works (Downey and Rochfort, 2008). The same chromatographic conditions were applied to a HP1100 HPLC system (Agilent, USA) coupled to a PE-Sciex API-2000 triple-quadruple mass spectrometer (MS) (Warrington, Cheshire, UK) equipped with a turbo-spray (TSI) source. MS detection was carried out in positive ion mode at unit resolution using a mass range of 150–1500 m/z and a mass peak width of 0.7 ± 0.1. Selected ion monitoring (SIM) experiments were carried out using the following operational parameters: vaporizer, 350 °C; heated capillary, 150–200 °C; carrier gas, nitrogen, at a sheath pressure of 70 psi; auxiliary gas, nitrogen, to assist in nebulization, at a pressure of 30 psi; de-clustering potential, 44.0 eV; focusing potential, 340.0 eV; entrance potential, 10.0 eV; collision energy, 33.0 eV for ion decomposition in the collision cell at 0.8 mTorr. (Tenore et al., 2011).

2.14. Statistical analysis

Triplicate analyses for each measurement were conducted for each sample. Differences between the means were evaluated with ANOVA, using the Graf Pad Instat 3 (Microsoft Software) statistic program. The significance of the model was evaluated by ANOVA. The significance of the regression cients was evaluated by Student's *t* test. The significance level was fixed at 0.05 for all the statistical analysis. Correlation coefficients (*R*), to determine the relationship between antioxidant activity and phenol content, were calculated by using Microsoft Office Excel application.

3. Results

3.1. Antibacterial and antifungal effects of Anthocyanins extract from S. tuberosum

Anthocyanins showed a high antibacterial activity against all the nine standard bacterial strains tested. Both Gram-positive and Gram-negative bacteria were inhibited, but the Gram-positive bacteria were the most sensible to the action of the extract. Minimal inhibitory concentrations (MICs) were in the range of 16–250 μg/ml, and ATCC strains were generally more inhibited on respect to CI (Table 1). *Staphylococcus aureus* from both standard and clinical sources showed a very high sensitivity to the extract (MIC = 15.6 μg/mL for standard strains and 31.3 μg/mL for clinical isolates), displaying also good minimum bactericidal concentration (MBC) values.

Table 1
MIC and MBC values (μg/ml) of anthocyanins extract from *Solanum tuberosum* L. var Vitelotte and MICs of reference antibiotics.

	MIC(μg/mL)				MBC
	Anthocyanins	CTAX	PENG	TET	Anthocyanins
S. aureus ATCC 13709	15.6	2	0.03	2	62.5
S. aureus CI	31.3	*R*	*R*	*R*	125
E. faecalis ATCC 14428	15.6	*R*	8	2	*R*
E. faecalis CI	31.3	*R*	*R*	*R*	*R*
P. vulgaris ATCC 12454	31.3	2	4	*R*	*R*
P. vulgaris CI	62.5	32	*R*	*R*	*R*
P. mirabilis ATCC 7002	31.3	0.03	4	32	*R*
P. mirabilis CI	62.5	32	*R*	*R*	*R*
S. typhi ATCC 19430	31.3	0.5	4	1	*R*
S. typhi CI	62.5	1	2	1	*R*
E. cloacae ATCC 10699	31.3	*R*	4	*R*	*R*
E. cloacae CI	62.5	*R*	*R*	*R*	*R*
E. aerogenes ATCC 13048	31.3	*R*	4	*R*	*R*
E. aerogenes CI	62.5	*R*	*R*	*R*	*R*
P. aeruginosa ATCC 27853	62.5	16	*R*	32	*R*
P. aeruginosa CI	62.5	32	*R*	*R*	*R*
K. pneumoniae ATCC 27736	125	0.1	*R*	16	*R*
K. pneumoniae CI	250	32	*R*	*R*	*R*

CTAX = cefotaxime; PENG = Benzyl Penicillin Sodium; TET = Tetracycline; CI = Clinical Isolated.

The antifungal activity of the anthocyanins extract of *S. tuberosum* var. Vitelotte was studied against three strains of fungi, including one potentially pathogenic yeast (*C. albicans* CI) and two filamentous phyto-pathogenic fungi (*B. cinerea* and *R. solani*). Anthocyanins inhibited the three fungi: in particular, *R. solani* from 0% to 50% and *C. albicans* and *B. cinerea* from 0% and 25%. Because only the samples with a fungal growth inhibition superior or equal to 50% (high) were the object of MIC determination, anthocyanins were successively tested. Results indicate that the samples had a fungi-static effect on all the fungi tested, *R. solani* being the most sensitive strain (MIC = 250 μg/mL) (Table 2).

3.2. Anthocyanins extract from S. tuberosum exerts antioxidant action

Antioxidant activities were evaluated using 2,2-diphenyl-1-picrylhydrazyl (DPPH) radical scavenging potential and FRAP assays. DPPH and FRAP tests are expressed as trolox equivalents (TEs). In both assays the extract antioxidant activity was compared with that of three standard solutions: the extract showed a higher reducing capacity than anti-radical activity (1.42 ± 0.2 and 4.25 ± 0.4 mmol Trolox/L for DPPH and FRAP, respectively). The steady state was reached after 110 min in both assays and results are shown in Figs. 1 and 2.

3.3. Anthocyanins extract from S. tuberosum exerts anticancer action in solid and hematological cancer cell lines by inducing anti-proliferative and apoptotic effects

The efficacy of different doses of the anthocyanins extract was assessed in solid and hematological cancer cell lines (Fig. 3). Tested in proliferation curve with a Crystal violet assay, the crude anthocyanins extract displayed anti proliferative activity in some solid cancer cell lines such as HeLa (cervical cancer), MCF-7, MDA-MB231 (breast cancer) and LnCaP (prostate cancer) cells (Fig. 3A). Moreover, this anti-growth action, measured by Trypan blu viability assay, could also be shown in myeloid leukemia cells such as U937 and NB4 (the prototype of acute promyelocytic leukemia, APL) (Fig. 3B). As shown in Fig. 3A and B, the anti-proliferative effect is dose dependent. In all the described cell lines, the major effect has been obtained using 5 mg/ml of the crude extract. Investigating for the anti-cancer potential of the anthocyanins extract, we tested its biological effects on cell cycle in solid cancer (HeLa, MDA-MB231, MCF7, LnCap) and in myeloid leukemia cell

Table 2
Antifungal activity of anthocyanins from *S. tuberosum* L. var. Vitelotte.

	MIC (μg/mL)		MFC
	Anthocyanins	KCON	Anthocyanins
R. solani	250	0.2	–
B. cinerea	500	0.2	–
C. albicans CI	500	0.4	–

KCON, ketoconazole. A dash indicates not active.

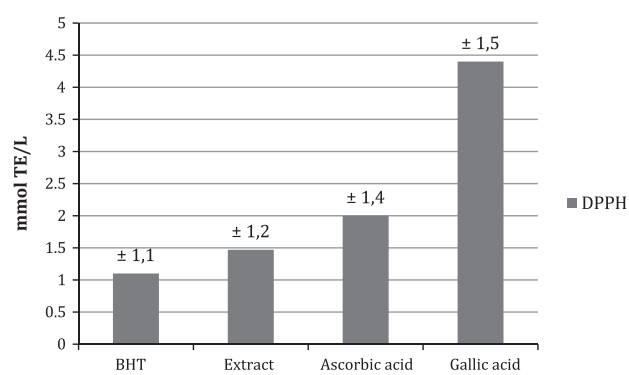

Fig. 1. Antioxidant capability of anthocyanins extract vs. three antioxidant standards measured by using the DPPH method.

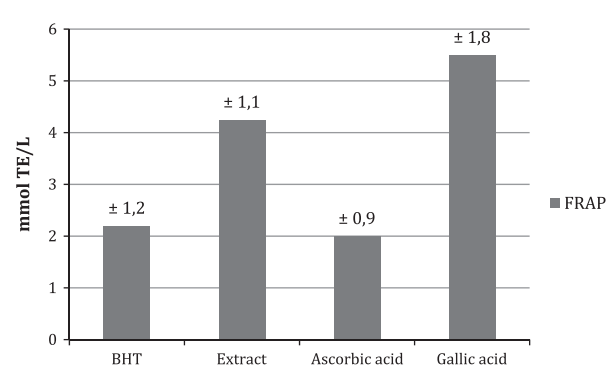

Fig. 2. Antioxidant capability of anthocyanins extract vs. three antioxidant standards measured by using the FRAP method.

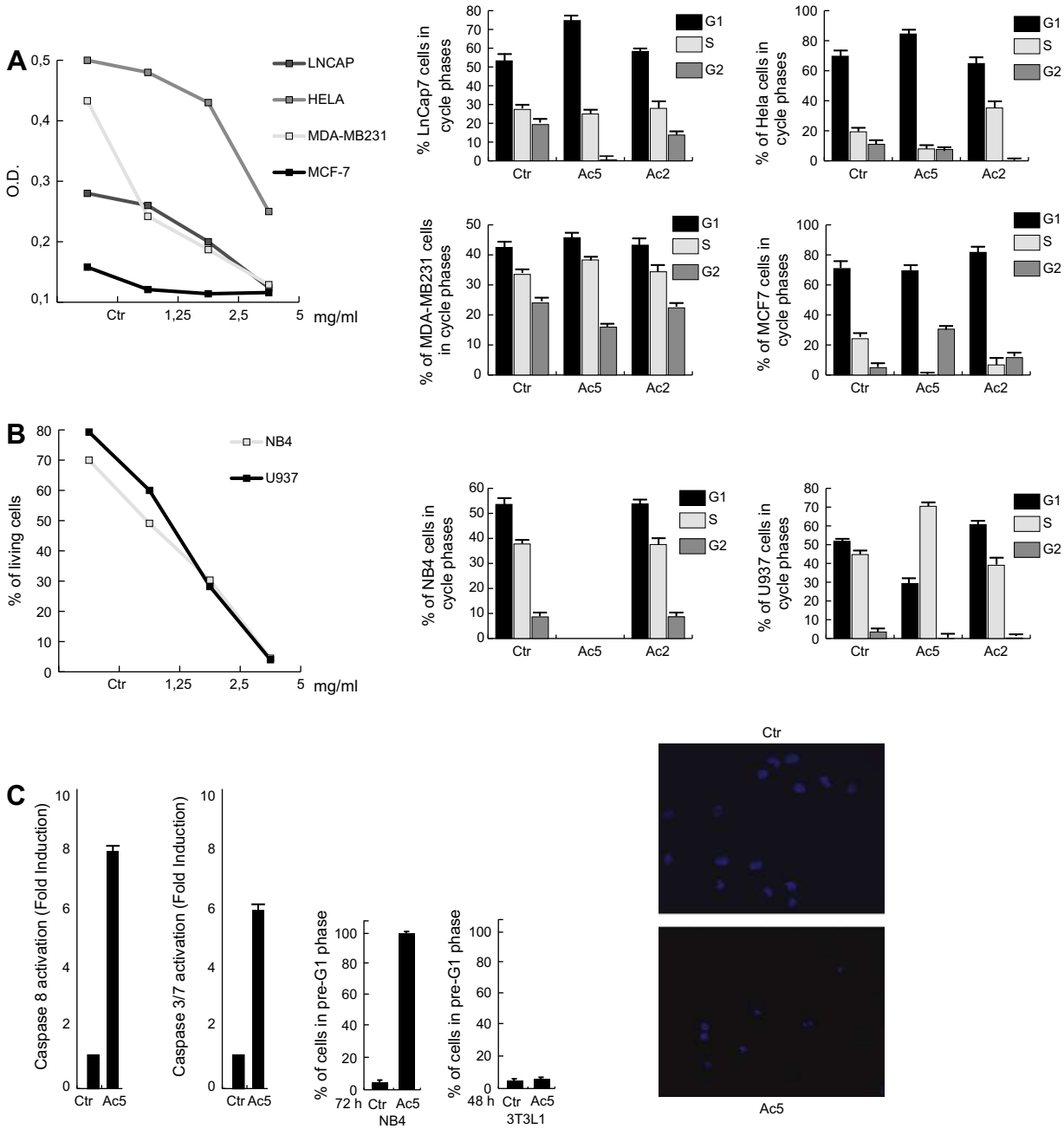

Fig. 3. Anti-proliferative potential of *Anthocyanins* extract. (A) Proliferation curves by Crystal violet assay and cell cycle analysis in the indicated cell lines at day 3 of treatment. (B) Proliferation curve by Trypan blu assay and cell cycle analysis in NB4 and U937 cells at day 3 after treatment with the indicated compound (Ac2 and Ac5 correspond to the 2 and 5 mg/mL concentrations). Results represent the media of triplicates. (C) Caspase 8 and 3–7 activation in NB4 cells upon 48 h treatment as indicated; apoptosis measured as pre-G1 pick in NB4 and 3T3L1 cells after 72 and 48 h of treatment respectively as indicated; nuclear morphology by DAPI staining after vehicle or 48 h treatment in NB4 cells as indicated.

lines (U937, NB4). As shown in Fig. 3A and B, the majority of the cell lines responded with a dose dependent block in G1 phase of cell cycle; only U937 cells showed a dual effect with a S phase block for the higher dose and a G1 block for the lower dose. In agreement, while normal 3T3L1 fibroblasts did not show induction of apoptosis (Fig. 3C), NB4 leukemia cells displayed nearly 100% of cells in pre-G1 pick at 72 h and a high induction of caspases 8 and 3–7 activation after 48 h of treatment (Fig. 3C). In these settings also nuclear morphology stained with DAPI showed a high rate of fragmentation, supporting the induction of a time dependent apoptosis (Fig. 3C). Indeed, all cancer cell lines (but not normal cells) responded with apoptosis to the treatment with anthocyanin extract (Fig. 4), although displaying different sensitivities that might be related to the intrinsic cell line context. These data were fully supported by the morphological analyses showing the anti-proliferative effect accompanying the apoptotic events.

3.4. Identification and quantification of the active Anthocyanins

Although more than six distinct chromatographic peaks were detected for the sample, some were present only in trace amounts, thus making their identification and quantification difficult. Their identification was based on MS experiments, UV–VIS absorption spectra, and chromatographic retention times, which were compared with both reference compounds and data from other studies (Downey and Rochfort, 2008). Single anthocyanin contents (Table 3)

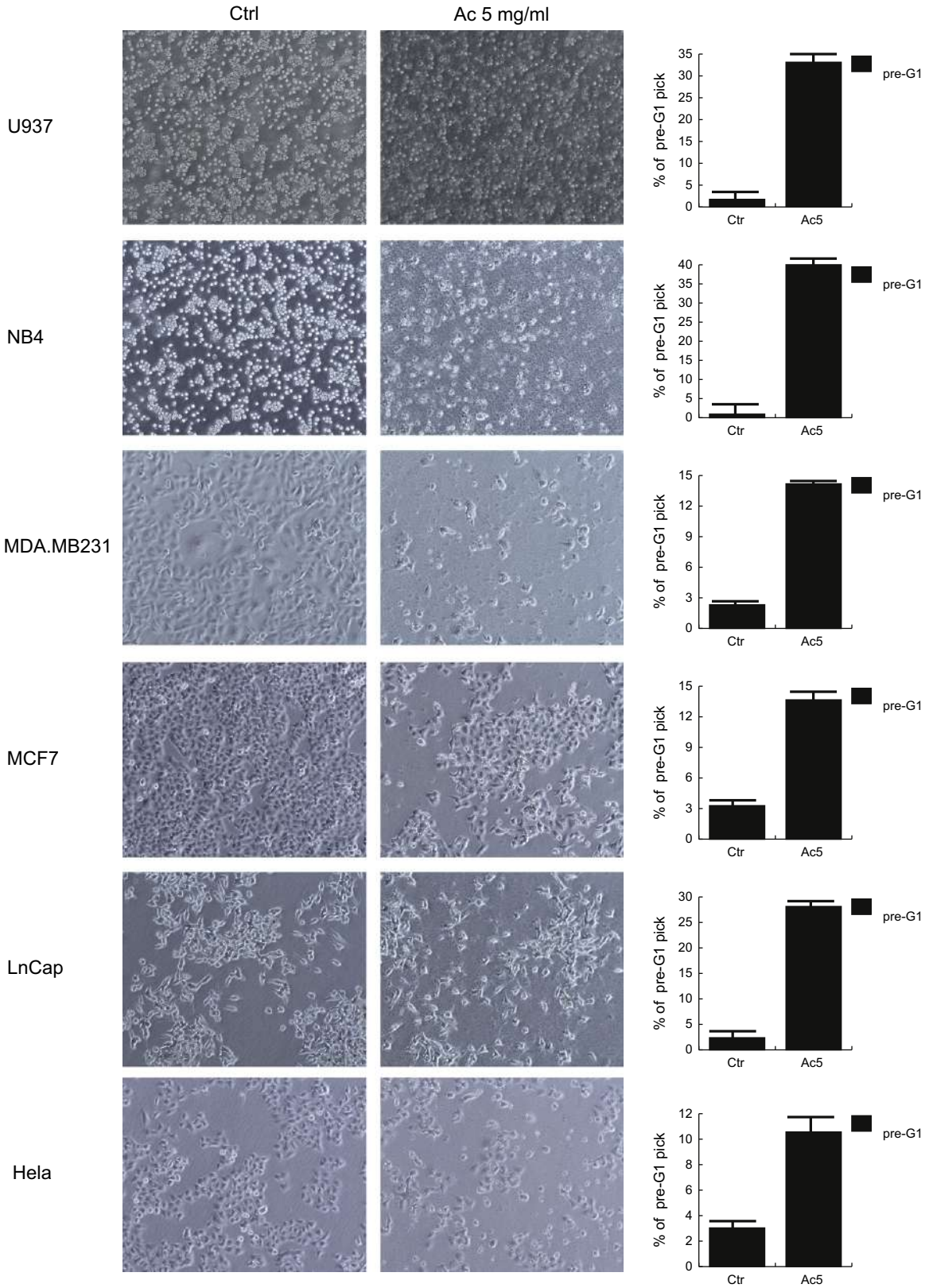

Fig. 4. *Anthocyanins* extract induce proliferative block and apoptosis in cancer cells. Apoptosis in the indicated cell lines at day 2 of treatment with 5 mg/ml together with the morphological analyses of the corresponding points.

results were generally higher than those reported previously (Ieri et al., 2011). As reported by Ieri et al. (2011), the compound malvidin 3-O-*p*-coumaroyl-rutinoside-5-O-glucoside was found as the main monomeric anthocyanin (Table 3). This anthocyanin was followed by petunidin 3-O-*p*-coumaroyl-rutinoside-5-O-glucoside, while the remaining ranged from 20.2 ± 1.2 to 27.2 ± 1.3 mg ME/L.

Table 3
LC/MS data of tentatively identified anthocyanins in pigmented potatoes extract and their quantitative analysis using DAD at 520 nm.

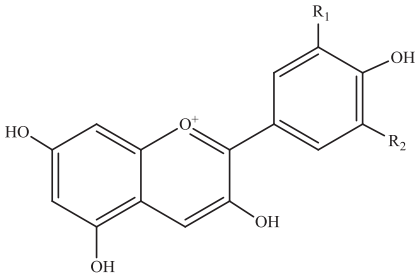

Name	R_1	R_2
Delphinidin	OH	OH
Petunidin	OCH_3	OH
Malvidin	OCH_3	OCH_3

Peak	Compound	mg ME/L[a]	Retention time[b] (min)	m/z $[M+H]^+$	Fragment ion (m/z)[c]
1	Mal-3-*O*-rut-5-*O*-glu	20.21 ± 1.1	5.14 ± 0.2	801	331, 493, 639
2	Delp-3-*O*-p-coum-rut-5-*O*-glu	23.75 ± 1.2	6.62 ± 0.3	919	303, 465, 757, 773
3	Mal-3-*O*-caf-rut-5-*O*-glu	27.22 ± 1.4	8.12 ± 0.4	963	331, 493, 801
4	Pet-3-*O*-p-coum-rut-5-*O*-glu	147.83 ± 1.0	10.07 ± 0.5	933	317, 479, 771, 787
5	Mal-3-*O*-p-coum-rut-5-*O*-glu	360.70 ± 1.9	11.50 ± 0.6	947	331, 493, 785, 801
6	Mal-3-*O*-ferul-rut-5-*O*-glu	23.22 ± 1.5	15.44 ± 0.7	977	331, 493, 801, 815

Abbreviations used: Pet, Petunidin; Mal, Malvidin; Delp, Delphinidin; Rut, Rutinoside; Glu, Glucoside; Ferul, Feruloyl; p-Coum, para-Coumaroyl; Caf, Caffeoyl.
Standards of cyanidin, delphinidin, malvidin, peonidin, pelargonidin and petunidin were purchased from Fluka (Buchs, Switzerland). Caffeic acid (⩾98% HPLC), ferulic acid (⩾99% HPLC), para-coumaric acid (⩾98% HPLC), chlorogenic acid (⩾99% HPLC) were obtained from Sigma–Aldrich Co. (St. Louis, USA).
[a] ME: Malvidin-3-*O*-glucoside Equivalents, expressed as value ± SD.
[b] Expressed as mean value ± SD.
[c] Base peak (100%) is underlined.

4. Discussion

Anthocyanins both in fruit and vegetables serve two functions – they improve the overall appearance, but also contribute to consumers' health and well-being. They are widely ingested by humans and their daily intake has been estimated at around 180 mg (Passamonti et al., 2003). An important attribute of these pigments is that they are potent antioxidants in the diet and are known to possess different pharmacological properties and are used by humans for therapeutic purpose (Rice-Evans and Packer, 1998; Smith et al., 2000; Wang et al., 2000). They are mainly contained in red and purple colored potato cultivars in the skins and flesh of tubers; previous reports on anthocyanins from various potatoes reveal a dominance of one or more of the *p*-coumaroyl-5-glucoside-3-rhamnoglucosides of pelargonidin, cyanidin, peonidin, delphinidin, petunidin and malvidin. So, colored potatoes may serve as a potential source for natural anthocyanin pigments, since they are a low cost crop.

Anthocyanin extract from *S. tuberosum* var. Vitelotte showed a high antibacterial activity against nine standard bacterial strains and the same bacterial strains clinically isolated. The Gram-positive bacteria were the most sensible to the action of the extract, and *Staphylococcus aureus* from both standard and clinical sources showed a very high sensitivity (MIC = 15.6 μg/mL for standard strains and 31.3 μg/mL for clinical isolates), showing also good Minimum bactericidal concentration (MBC) values. This is a significant datum considering that, so far, *Staphylococcus aureus* infections are particularly tricky given its intrinsic resistance to multiple classes of antibiotics and its ability to acquire adaptive resistance during a therapeutic course (Cowan, 1999). The anthocyanin extract of *S. tuberosum* var. Vitelotte had also a fungi-static effect against three strains of fungi, including one potentially pathogenic yeast (*C. albicans* CI) and two filamentous phytopathogenic fungi (*B. cinerea* and *R. solani*), and was particularly active against *R. solani* (MIC = 250 μg/mL). Moreover, antioxidant activities of anthocyanins were evaluated using two complementary assays methods, namely 2,2-diphenyl-1-picrylhydrazyl (DPPH) radical scavenging potential and FRAP assays. The reduction of DPPH absorption is indicative of the capacity of the extract to scavenge free radicals, independently of any enzymatic activity, while the FRAP method is used to determine the capacity of reductants in a sample. FRAP test showed a higher reducing activity of anthocyanin extract from *S. tuberosum* than antiradical activity evaluated by DPPH test. This result is of great interest since generally anthocyanins are well known for their hydrogen donating ability by which they are considered potent free radical scavengers. In both assays the extract antioxidant activity was compared with that of three standard solutions showing an appreciable activity, keeping into consideration that the comparison was made between an extract (a complex mixture of compounds characterized by very different levels of biological properties) and standard solutions composed by pure substances.

Also the anticancer activity of anthocyanin extract from *S. tuberosum* var. Vitelotte has been thoroughly investigated in our study. The efficacy of different doses of the anthocyanin extract was assessed in solid and hematological cancer cell lines (Fig. 3). The crude anthocyanin extract displayed anti proliferative activity in some solid cancer cell lines such as HeLa (cervical cancer), MCF-7, 3, MDA-MB231 (breast cancer) cells and LnCaP (prostate cancer). Moreover, this anti-growth action, could also be shown in myeloid leukemia cells such as U937 and NB4 the prototype of acute promyelocytic leukemia (APL), an acute myeloid leukemia (AML) classified as M3 according to the French-American-British (FAB) classification, which carries the chromosomal translocation *t*(15;17) leading to the expression of the fusion protein PML-RAR-alpha. As shown in Fig. 1a and b the anti-proliferative effect is dose dependent. In all the described cell lines, the major effect has been obtained using 5 mg/ml of the crude extract. Investigating for the anti-cancer potential of the anthocyanins extract, we tested its biological effects on cell cycle and apoptosis. As shown in Fig. 4, four cell lines (HeLa, MCF7, U937, NB4) responded with apoptosis in a dose dependent manner, although displaying different

sensitivities. These differences in the cell cycle block might be due to cellular context specific events. In all the described cell lines, the major effect has been obtained using 5 mg/ml of the crude extract.

Because biological activity of potato anthocyanins results from the synergistic effect of each anthocyanin pigment, it is important to assess the pigmented potato cultivar for individual anthocyanin content. For this reason, we have characterized and measured the concentration of anthocyanins in pigmented potatoes, with the results shown in Table 3. Our findings are consistent with results of Ieri et al. (2011) who by means of rapid HPLC/DAD/MS found for the Vitelotte Noire variety dominant malvidin and petunidin. In our research, the identity of the major pigments was confirmed by HPLC-DAD and HPLC–ESI–MS analyses as malvidin 3-O-*p*-coumaroyl-rutinoside-5-O-glucoside and petunidin 3-O-*p*-coumaroyl-rutinoside-5-O-glucoside (Table 3). Regarding the structure of these anthocyanidins, a high degree of hydroxylation and methoxylation of their aromatic rings suggests their higher contribution to antioxidant activity of this potato cultivar (Prior and Wu, 2006).

5. Conclusions

On the whole, our results show that anthocyanins extract of *S. tuberosa* Vitelotte is able to exert different biological activities. It is characterized by a worthy radical scavenging and reducing capacity and causes inhibition of proliferation and apoptosis in a dose dependent manner in different solid and hematological cancer cell lines. We have also demonstrated for the first time the efficacy of colored potatoes extract against a particularly resistant bacterium such as *Staphylococcus aureus* and its antifungal activity. The identification of components that account for the biological potential of pigmented potatoes corroborates the knowledge of anthocyanins action against cancer and as antimicrobial and antioxidant agents. The different biological properties of pigmented potatoes and the increased concern regarding their toxicological safety indicate that they have a potential use for the nutraceutical industry and might represent promising sources of natural colorants with added value for the food industry and human health.

Conflict of Interest

The authors declare that there are no conflicts of interest.

Acknowledgements

This study was supported by: EU ('Blueprint Contract No. 282510), AIRC (Associazione Italiana per la Ricerca sul Cancro, Project No. 4625), by MIUR (PRIN_2009PX2T2E_004; PRIN_2007RZWFBZ_004; PON002782; PON0101227). We acknowledge Dr. C. Fisher for kindly revising the manuscript.

References

Afaq, F., Malik, A., Syed, D., Maes, D., Matsui, M.S., Mukhtar, H., 2005. Pomegranate fruit extract modulates UVB-mediated phosphorylation of mitogen-activated protein kinases and activation of nuclear factor kappa B in normal human epidermal keratinocytes. Photochem. Photobiol. 81, 38–45.

Afaq, F., Syed, D.N., Malik, A., Hadi, N., Sarfaraz, S., Kweon, M.H., Khan, N., Zaid, M.A., Mukhtar, H., 2007. Delphinidin, an anthocyanidin in pigmented fruits and vegetables, protects human HaCaT keratinocytes and mouse skin against UVB-mediated oxidative stress and apoptosis. J. Invest. Dermatol. 127, 222–232.

Altucci, L., Rossin, A., Raffelsberger, W., Reitmair, A., Chomienne, C., Gronemeyer, H., 2001. Retinoic acid-induced apoptosis in leukemia cells is mediated by paracrine action of tumor-selective death ligand TRAIL. Nat. Med. 7, 680–686.

Andersen, A.W., Tong, C.B.S., Krueger, D.E., 2002. Comparison of periderm color and anthocyanins of four red potato cultivars. Am. J. Potato Res. 79, 249–253.

Bagchi, D., Sen, C.K., Bagchi, M., Atalay, M., 2004. Anti-angiogenic, antioxidant, and anti-carcinogenic properties of a novel anthocyanin-rich berry extract formula. Biochemistry (Mosc.) 69, 75–80.

Basile, A., Conte, B., Rigano, D., Senatore, F., Sorbo, S., 2010. Antibacterial and antifungal properties of acetonic extract of *Feijoa sellowiana* fruits and its effect on *Helicobacter pylori* growth. J. Med. Food 13, 189–195.

Benzie, I.F.F., Strain, J.J., 1996. The ferric reducing ability of plasma (FRAP) as a measure of "antioxidant power": The FRAP assay. Anal. Biochem. 239, 70–76.

Brand-Williams, W., Cuvelier, M.E., Berset, C., 1995. Use of free radical method to evaluate antioxidant activity. Lebenson. Wiss. Technol. 28, 25–30.

Chang, Y.C., Huang, H.P., Hsu, J.D., Yang, S.F., Wang, C.J., 2005. Hibiscus anthocyanins rich extract-induced apoptotic cell death in human promyelocytic leukemia cells. Toxicol. Appl. Pharmacol. 205, 201–212.

Chen, P.N., Chu, S.C., Chiou, H.L., Chiang, C.L., Yang, S.F., Hsieh, Y.S., 2005. Cyanidin 3-glucoside and peonidin 3-glucoside inhibit tumor cell growth and induce apoptosis *in vitro* and suppress tumor growth *in vivo*. Nutr. Cancer 53, 232–243.

Coates, E.M., Popa, G., Gill, C.I., McCann, M.J., McDougall, G.J., Stewart, D., Rowland, I.I., 2007. Colon-available raspberry polyphenols exhibit anti-cancer effects on *in vitro* models of colon cancer. J. Carcinog. 6, 4.

Cowan, M.M., 1999. Plant products as antimicrobial agents. Clin. Microbiol. Rev. 12, 564–582.

Downey, M.O., Rochfort, S., 2008. Simultaneous separation by reversed-phase high-performance liquid chromatography and mass spectral identification of anthocyanins and flavonols in Shiraz grape skin. J. Chromatogr. A 1201, 43–47.

Ericcson, H.M., Sherris, J.C., 1971. Antibiotic sensitivity testing: report of an international collaborative study. Acta Pathol. Microbiol. Scand. 217, 1–90.

Fan, G., Han, Y., Gu, Z., Chen, D., 2008. Optimizing conditions for anthocyanins extraction from purple sweet potato using response surface methodology (RSM). LWT-Food Sci. Technol. 41, 155–160.

Feng, R., Ni, H.M., Wang, S.Y., Tourkova, I.L., Shurin, M.R., Harada, H., Yin, X.M., 2007. Cyanidin-3-rutinoside, a natural polyphenol antioxidant, selectively kills leukemic cells by induction of oxidative stress. J. Biol. Chem. 282, 13468–13476.

Fimognari, C., Berti, F., Nüsse, M., Cantelli-Forti, G., Hrelia, P., 2004. Induction of apoptosis in two human leukemia cell lines as well as differentiation in human promyelocytic cells by cyanidin-3-O-betaglucopyranoside. Biochem. Pharmacol. 67, 2047–2056.

Galvano, F., La Fauci, L., Lazzarino, G., Fogliano, V., Ritieni, A., Ciappellano, S., Battistini, N.C., Tavazzi, B., Galvano, G., 2004. Cyanidins: metabolism and biological properties. J. Nutr. Biochem. 15, 2–11.

Hakimuddin, F., Paliyath, G., Meckling, K., 2004. Selective cytotoxicity of a red grape wine flavonoid fraction against MCF-7 cells. Breast Cancer Res. Treat. 85, 65–79.

Harada, K., Kano, M., Takayanagi, T., Yamacawa, O., Ishikawa, F., 2004. Absorption of acylated antocyanins in rats and humans after ingesting an extract of *Ipomoea batatas* purple sweet potato tuber. Biosci. Biotechnol. Biochem. 68, 1500–1507.

Harborne, J.B., 1960. Plant polyphenols 1. Anthocyanin production in the cultivated potato. Biochem. J. 74, 262–269.

Huang, C., Huang, Y., Li, J., Hu, W., Aziz, R., Tang, M.S., Sun, N., Cassady, J., Stoner, G.D., 2002. Inhibition of benzo (a)pyrene diol-epoxide-induced transactivation of activated protein 1 and nuclear factor kappaB by black raspberry extracts. Cancer Res. 62, 6857–6863.

Huang, C., Li, J., Song, L., Zhang, D., Tong, Q., Ding, M., Bowman, L., Aziz, R., Stoner, G.D., 2006. Black raspberry extracts inhibit benzo(a)pyrene diol-epoxide-induced activator protein 1 activation and VEGF transcription by targeting the phosphotidylinositol 3 kinase/Akt pathway. Cancer Res. 66, 581–587.

Ieri, F., Innocenti, M., Andrenelli, L., Vecchio, V., Mulinacci, N., 2011. Rapid HPLC/DAD/MS method to determine phenolic acids, glycoalkaloids and anthocyanins in pigmented potatoes (*Solanum tuberosum* L.) and correlations with variety and geographical origin. Food Chem. 125, 750–759.

Ieven, M., Vanden Berghe, D.A., Mertens, F., Vlietinck, A., Lammens, E., 1979. Screening of higher plants for biological activities. I. Antimicrobial activity. Planta Med. 36, 311–321.

Kjell, T., Øyvind, M.A., 2005. Color stability of anthocyanins in aqueous solutions at various pH values. Food Chem. 89, 427–440.

Kong, J.M., Chia, L.S., Goh, N.K., Chia, T.F., Brouillard, R., 2003. Analysis and biological activities of anthocyanins. Phytochemistry 64, 923–933.

Kwon, J.Y., Lee, K.W., Hur, H.J., Lee, H.J., 2007. Peonidin inhibits phorbol-ester-induced COX-2 expression and transformation in JB6 P+ cells by blocking phosphorylation of ERK-1 and -2. Ann. NY. Acad. Sci. 1095, 513–520.

Lewis, C.E., Walker, J.R.L., Lancaster, J.E., 1999. Changes in anthocyanin, flavonoid and phenolic acid concentrations during development and storage of coloured potato (*Solanum tuberosum* L.) tubers. J. Sci. Food Agric. 79, 311–316.

Martin, S., Giannone, G., Andriantsitohaina, R., Martinez, M.C., 2003. Delphinidin, an active compound of red wine, inhibits endothelial cell apoptosis via nitric oxide pathway and regulation of calcium homeostasis. Br. J. Pharmacol. 139, 1095–1102.

Nagase, H., Sasaki, K., Kito, H., Haga, A., Sato, T., 1998. Inhibitory effect of delphinidin from *Solanum melongena* on human fibrosarcoma HT-1080 invasiveness *in vitro*. Planta Med. 64, 216–219.

Nebbioso, A., Clarke, N., Voltz, E., Germain, E., Ambrosino, C., Bontempo, P., Alvarez, R., Schiavone, E.M., Ferrara, F., Bresciani, F., Weisz, A., de Lera, A.R., Gronemeyer, H., Altucci, L., 2005. Tumor-selective action of HDAC inhibitors involves TRAIL induction in acute myeloid leukemia cells. Nat. Med. 11, 77–84.

Nebbioso, A., Pereira, R., Khanwalkar, H., Matarese, F., García-Rodríguez, J., Miceli, M., Logie, C., Kedinger, V., Ferrara, F., Stunnenberg, H.G., de Lera, A.R., Gronemeyer, H., Altucci, L., 2011. Death receptor pathway activation and increase of ROS production by the triple epigenetic inhibitor UVI5008. Mol. Cancer Ther. 10, 2394–2404.

Olsson, M.E., Gustavsson, K.E., Andersson, S., Nilsson, A., Duan, R.D., 2004. Inhibition of cancer cell proliferation *in vitro* by fruit and berry extracts and correlations with antioxidant levels. J. Agric. Food Chem. 52, 7264–7271.

Passamonti, S., Vrhovsek, U., Vanzo, A., Mattivi, F., 2003. The stomach as a site for anthocyanins absorption from food. FEBS Lett. 544, 210–213.

Prior, R.L., Wu, X., 2006. Anthocyanins: structural characteristics that result in unique metabolic patterns and biological activities. Free Radic. Res. 40, 1014–1028.

Reddivari, L., Vanamala, J., Chintharlapalli, S., Safe, S.H., Miller Jr., J.C., 2007. Anthocyanin fraction from potato extracts is cytotoxic to prostate cancer cells through activation of caspase-dependent and caspaseindependent pathways. Carcinogenesis 28, 2227–2235.

Reddy, M.K., Alexander-Lindo, R.L., Nair, M.G., 2005. Relative inhibition of lipid peroxidation, cyclooxygenase enzymes, and human tumor cell proliferation by natural food colors. J. Agric. Food Chem. 53, 9268–9273.

Rice-Evans, C., Packer, L. (Eds.), 1998. Flavonoids in Health and Disease. Marcel Dekker Inc., New York.

Rodrigo, K.A., Rawal, Y., Renner, R.J., Schwartz, S.J., Tian, Q., Larsen, R.E., Mallery, S.R., 2006. Suppression of the tumorigenic phenotype in human oral squamous cell carcinoma cells by an ethanol extract derived from freeze-dried black raspberries. Nutr. Cancer 54, 58–68.

Seeram, N.P., Adams, L.S., Zhang, Y., Lee, R., Sand, D., Scheuller, H.S., Heber, D., 2006. Blackberry, black raspberry, blueberry, cranberry, red raspberry, and strawberry extracts inhibit growth and stimulate apoptosis of human cancer cells *in vitro*. J. Agric. Food Chem. 54, 9329–9339.

Smith, M., Marley, K., Seigler, D., Singletary, K., Meline, B., 2000. Bioactive properties of wild blueberry fruits. J. Food Sci. 65, 352–356.

Tenore, G.C., Troisi, J., Di Fiore, R., Manfra, M., Novellino, E., 2011. Nutraceutical value and toxicological profile of selected red wines from Morocco. Food Chem. 129, 792–798.

Wang, C., Wang, J., Lin, W., Chu, C., Chou, F., Tseng, T., 2000. Protective effect of *Hibiscus* anthocyanins against tert-butyl hydroperoxide-induced hepatic toxicity in rats. Food Chem. Toxicol. 38, 411–416.

Zhang, Y., Vareed, S.K., Nair, M.G., 2005. Human tumor cell growth inhibition by nontoxic anthocyanidins, the pigments in fruits and vegetables. Life Sci. 76, 1465–1472.